# Regime Shift Detection Techniques for Determining the Year of Positive 0°C Crossing in the Northern Hemisphere for Late-Winter and Spring

by

Shabnam Sorkhi

A thesis
presented to the University of Waterloo
in fulfillment of the
thesis requirement for the degree of
Master of Applied Science
in
Civil Engineering

Waterloo, Ontario, Canada, 2011

I hereby declare that I am the sole author of this thesis. This is a true copy of the thesis, including any required final revisions, as accepted by my examiners.

I understand that my thesis may be made electronically available to the public.

## Abstract

The temperature of 0°C, the phase change point of water-ice, is among the most influential factors on the hydrology of the temperate regions that experience winter. Many cryospheric processes, such as snow and ice melt, avalanches, freshwater ice breakup, and ice jam floods, are triggered by the arrival of the above-0°C air temperatures. Moreover, such 0°C based changes can have significant cascading impacts on other parts of the physical environment as well as related socio-economic activities. This research adopts an extensive analytical approach to examine the changes in the sign of mean JFM (January-February-March) and MAM (March-April-May) air temperatures, in the $0.5° \times 0.5°$ land grid cells of the Northern Hemisphere (20.25°N-89.75°N), during the period 1901-2009. The goal is to identify grid cells in which JFM or MAM temperatures used to be primarily below freezing, however, changed sign permanently some time during 1901-2009 due to an advancement in the arrival timing of the annual above-0°C temperature. Considering that air temperature fluctuates and can cross 0°C several times during the entire period of study, four different modelling techniques are employed to detect the shift points in the trend function as well as mean level of the time series and to determine the year when the model rises above 0°C ($y_0$) in a given location. Model-specific criteria are set to determine $y_0$ in cases of multiple positive 0°C crossings. The techniques applied include i) trend shift detection techniques: Model 2 and Model 3 (Perron and Yabu, 2009b; Kim and Perron, 2009), ii) Multivariate Adaptive Regression Splines (Friedman, 1991), and iii) the R method (Rodionov, 2004, 2006). This thesis provides a thorough discussion of these techniques and reviews their strengths and weaknesses relative to the research goals.

In addition to $y_0$, the time of the onset of warming that causes a time series to permanently rise above 0°C ($y_w$) is identified. The applied methods divide the entire domain of the time series into sub-regions in which the data are approximated by polynomials of degree zero or one. The segment which encompasses $y_0$ is termed the 'segment of interest' ($S_{interest}$). The combination of $S_{interest}$ and the segment(s) with positive slope that immediately follows $S_{interest}$ forms a section referred to as the 'section of total warming' ($S_{W_{total}}$). The non-parametric Mann-Kendall test, following the modified trend-free prewhitening approach (Burn et al., 2004), is conducted to examine if the warming during $S_{interest}$, which causes the temperature to turn positive, is significant. The same test is applied to $S_{W_{total}}$ to determine if the total warming subsequent to $y_w$ is significant. Only the locations with significant warming during $S_{interest}$ and $S_{W_{total}}$ are selected. A bootstrap

analysis (Cunderlik and Burn, 2002), conducted to determine the field significance of the results, indicates that local trends are also globally significant.

A thorough comparative evaluation of all the above-mentioned techniques determines that Model 2 is the technique that best meets the analysis goals. Analytical results indicate that during JFM, $y_0$ most commonly takes place in the following zones (referred to as '*transition area*'). It should be noted that only the grid cells with significant warming during $S_{interest}$ and $S_{W_{total}}$ are considered: i) North America, western U.S; ii) Europe, highest density in central Europe; iii) southwestern and central Asia, a small region consisting of some parts of Uzbekistan, Kazakhstan, and Iran; iv) central-eastern Asia, a small area in western China most of which lies in the Taklamakan Desert; v) easternmost Asia, some grid cells from east-central China, South Korea, and Japan. During MAM, over North America, the *transition area* of Model 2 is principally located in Canada and extends from northeastern British Columbia to the Atlantic regions. In Eurasia, northern Europe, European Russia, southern Russia, northern Mongolia, and northeastern China form the great portion of the *transition area*. It should be noted that except for a few high-elevation regions located in lower latitudes, the grid cells with $y_0$ taking place during MAM are located north of those with $y_0$ occurring during JFM.

Results also indicate that $y_0$ of the majority of locations occurs during the 1960-2008 interval. During MAM, the *transition area* of Model 2 in east-central Canada and Eurasia exhibits a clear pattern of increase in $y_0$ values with latitude. This characteristic is also observed in some regions during JFM. The $y_w$ values are most commonly distributed over the period 1901-1980 with a peak during 1960-1980. The rate of warming over $S_{interest}$ and $S_{W_{total}}$ generated by Model 2 is $\sim 0.01-0.1\,(^{\circ}\mathrm{C/year})$. The spatial and temporal variability in the results is believed to be related to variations in climate, elevation effects, and/or large-scale atmosphere and ocean circulations, all of which require further evaluation for proper attribution of effects.

**Acknowledgements**

I would like to sincerely thank my advisor, Prof. Donald H. Burn, for supporting me step by step in this research and also for being available whenever I needed feedback/help. Moreover, I have to thank Prof. Terry D. Prowse for being my co-supervisor during masters studies. Although he worked from far away, he guided me significantly in my research through long distance. Similarly, I would like to express my gratitude to Prof. Barrie R. Bonsal for helping us with organizing and processing the raw data used in this work.

I am also grateful to Nicholas J. Gralewicz, an alumni of the University of Victoria, for proposing the initial idea of MARS (explained in Chapters 2 and 3). We kept our contact through e-mail during the course of my research which helped me significantly in developing this thesis. I would like to express my appreciation to all of my colleagues at the University of Waterloo, especially Ms. Nicole O'Brien for her kind support and sharing her computer when I needed one.

Finally, I have to express my love and gratitude to my parents, Jafar and Mahin, for their continuous love and support. Without their selfless love, I could not succeed in the life. I am also thankful to my siblings, Roya and Mohammad; they supported me all my life as their younger sister. Last but not least, I should thank my husband, Shervan Fashandi, who unconditionally loved and kindly supported me during my graduate studies.

This research was supported by grants to my supervisors from Natural Sciences and Engineering Research Council (NSERC) and the Faculty of Engineering in the University of Waterloo.

# Table of Contents

# List of Tables

# List of Figures

# List of Abbreviations

| | |
|---|---|
| AIC | Akaike information criterion. |
| AO | Arctic Oscillation. |
| Aout | additive outlier. |
| AR(1) | first-order autoregressive model. |
| BF | basis function. |
| BIC | Bayesian information criterion. |
| CRU | Climate Research Unit. |
| ENSO | El Nino-Southern Oscillation. |
| EOF | empirical orthogonal function. |
| FGLS | feasible generalized least squares. |
| GCV | generalized cross-validation. |
| GHG | greenhouse gas. |
| GLS | generalized least squares. |
| i.i.d. | independent and identically distributed. |
| IO | innovational outlier. |
| IP4 method | bias correction technique (inverse proportionality with 4 corrections), described in Section 3.2.2. |

| | |
|---|---|
| JFM | January-February-March. |
| KPY method | trend shift detection technique (after Kim, Perron, and Yabu), described in Section 3.4. |
| MAM | March-April-May. |
| MARS | multivariate adaptive regression spline. |
| MK | Mann-Kendall. |
| MPK method | bias correction technique (after Marriott, Pope, and Kendall), described in Section 3.2.2. |
| NAO | North Atlantic Oscillation. |
| NP | North Pacific. |
| OLS | ordinary least square. |
| PCA | principal component analysis. |
| PDO | Pacific Decadal Oscillation. |
| PNA | Pacifice North American. |
| QA | quality assurance. |
| R method | climate regime shift detection technique (after Rodionov), described in Section 3.2. |
| RSI | regime shift index. |
| RSS | residual sum of squares. |
| SCA | snow-covered area. |
| SFE | winter-total snowfall water equivalent. |

| | |
|---|---|
| SO | Southern Oscillation. |
| SSE | sum of squared errors. |
| SST | sea surface temperature. |
| SWE | snow water equivalent. |
| TFPW | trend-free pre-whitening. |

# List of Frequently Used Symbols

| | |
|---|---|
| $I(0)$ | stationary process. |
| $I(1)$ | unit root process. |
| $l$ | cut-off length of the climate regimes. |
| $m$ | subsample size for the estimation of the lag-1 autoregressive coefficient. |
| $\mathrm{S}_{\mathrm{interest}}$ | segment of interest, described in Section 4.4. |
| $\mathrm{S}_{\mathrm{W}_{\mathrm{total}}}$ | section of total warming, described in Section 4.4. |
| $\mathrm{W}_{\mathrm{total}}$ | total warming, described in Section 4.4. |
| $\mathrm{y}_0$ | year of 0°C crossing, described in Section 4.4. |
| $\mathrm{y}_\mathrm{w}$ | start year of warming, described in Section 4.4. |

# Chapter 1

# Introduction

## 1.1 Motivation

The impact of human activities on the natural energy balance of the earth is increasingly receiving greater attention, with a major focus on the role of greenhouse gases (GHGs). The increased emissions of GHGs from anthropogenic activities, such as from burning fossil fuels, are believed to be the key factor that alters the composition of the atmosphere and radiation exchanges and ultimately, interferes with the energy balance of the earth. Given increasing growth in population, urbanization, and industrial expansion, the production of GHGs is likely to grow. This trend, combined with the long atmospheric lifetimes of emitted GHGs, indicate that greater future consequences can be expected beyond those already documented (Karl and Trenberth, 2003). Therefore, in addition to preventive actions that should be taken to mitigate or impede further changes, it is critical that environmental and socio-economic systems adapt to new conditions. Precise climate change adaptation plans necessitate the assessment of the past events as well as developing effective techniques to project future conditions.

Many analyses of climate-induced changes (temporal and spatial) still rely on relatively simple climate variables such as air temperature, rather than complex suites of meteorological variables (e.g., wind, pressure, humidity, short and long wave radiation) (e.g., Zhang et al., 2000; Bonsal and Prowse, 2003; Prowse et al., 2007; Ivanov and Evtimov, 2010; Prowse et al., 2010). Air temperature acts as an index for a complex set of heat fluxes

(i.e., sensible, latent, radiative) that determine surface energy budgets. Hence, many hydrological observations are highly correlated with air temperature. For example, within the environment of cold regions, a few days of mild above-freezing air temperature in winter can initiate rapid hydrologic responses, such as rapid snowmelt, premature river ice breakup, and ice jam floods (Beltaos, 2002; Prowse and Beltaos, 2002). Furthermore, as temperature cools after such events, refreezing can produce relatively impermeable ice layers that can have a variety of bio-physical effects. Using winter ecology as another example of temperature-related effects, such ice layers can make plants inaccessible to foraging animals and have been identified as one of the factors causing the population decline of some animal and plant species (Forchhammer and Boertmann, 1993; Putkonen and Roe, 2003). It is because of these types of examples that there is a strong interest in examining specific changes and critical shifts in air temperature, such as those related to 0°C conditions described next.

Although trends and variability in air temperature are well documented for the Northern Hemisphere, the critical phase change temperature of the cryosphere, 0°C, has only been the subject of a few studies (see Section 1.2). Air temperature changes around 0°C are most meaningful in the climate of cold regions, particularly, those characterized by seasonal snow and ice covers, where many hydrological and ecological processes as well as human social and economic activities are influenced by the change in the sign of temperature on the annual basis. The time of spring ice breakup, autumn freeze-up, and animal hibernation, type of precipitation (snowfall versus rainfall), road, rail, and marine transportation, hydroelectric power generation, etc. are examples of the processes affected by the arrival and retreat of sub-freezing temperatures (Bonsal and Prowse, 2003). Given that the timing of the first positive or negative air temperatures produces such a wide range of impacts, an assessment of how climate change has produced spatial and temporal changes in 0°C conditions is pre-requisite to evaluating the full scope of its historical and potential future effects.

## 1.2 Related Work

Bonsal and Prowse (2003) investigated the temporal and spatial patterns of spring and autumn 0°C isotherm dates in Canada to evaluate the impact of global warming on them. According to this study, the spring 0°C isotherm is defined as the date when the mean daily

temperature rises above 0°C in a given year. Based on this approach, Duguay et al. (2006) conducted a correlation study on the recent trends of lake ice freeze-up/breakup dates and spring and autumn 0°C isotherm dates in Canada. In most of the regions of the country, strong correlations are observed. Furthermore, the temporal and spatial characteristics of the two variables resemble each other. Since the most significant changes in temperature have occurred in high latitudes, and various models forecast higher future warming for these regions, Prowse et al. (2010) performed a similar 0°C-isotherm analysis on four of the largest Arctic flowing rivers. As they noted, the timing of ice breakup events and spring freshet in such rivers is highly influenced by ambient air temperature. The unequal heating along these rivers poses challenges to flood forecasting and creates risks to humans and aquatic life. This study points to the importance of understanding spring 0°C-isotherm conditions as indicators of spring melt conditions in the analysis of hydrological trends.

The study by Bonsal and Prowse (2003) is focused on spring and autumn 0°C isotherms during the $20^{\text{th}}$ century. The study area is fixed and limited to Canada, and the first negative and positive temperatures in autumn and spring are determined for each station by analysing the time series of mean daily temperature in a given year. The mean spring (autumn) 0°C isotherm date for a given station over the time period of study (e.g., the latter half of the $20^{\text{th}}$ century) is the average of all the spring (autumn) 0°C isotherm dates determined for the years encompassed in the entire period of study. By contrast, this thesis focuses on two fixed time periods: i) late winter and early spring; i.e., January-February-March (JFM), ii) spring; i.e., March-April-May (MAM). In many parts of the Northern Hemisphere, particularly along central latitudes, JFM or MAM is the time of the year when temperature sign changes are expected to occur and produce hydrological changes similar to those noted above. This thesis focuses on identifying land grid cells in the extra-tropical Northern Hemisphere (20.25°N-89.75°N) that have experienced permanent changes in the sign of temperature from below 0°C to above 0°C during JFM or MAM, in the period 1901-2009. The spatial resolution is 0.5° latitude-longitude, and the temporal resolution is 1 year. It means that the time series for each $0.5° \times 0.5°$ grid cell comprises 109 data points, and each data point is the mean temperature of JFM or MAM for the corresponding year. The time of permanent positive 0°C crossing for a specific grid cell (if it applies) is defined as the year when the primarily negative temperature turns positive. This thesis also attempts to determine the start year of warming that eventually leads to the temperature sign change.

Due to temperature fluctuations, the line of 0°C is crossed more than one time during

the entire period of study. Bonsal and Prowse (2003) used a 31-day moving average to smooth such variability. The spring (autumn) 0°C isotherm was then defined as the time when the moving average crosses 0°C in the positive (negative) direction. In this thesis, four techniques are applied to model the original temperature time series. The time of positive 0°C crossing ($y_0$) as well as the start year of warming ($y_w$) are then determined based on these models. The techniques are as follows:

- **Trend shift detection techniques**
  These techniques are applied to detect the breaks in the trend function of a time series. Based on the type of the shift they detect, these techniques are divided into three categories: i) Model 1, which detects the shift in the intercept of the trend function; ii) Model 2, which is used to test for the break in slope; iii) Model 3, which detects the simultaneous shift in intercept and slope. The two segments of the time series, preceding and following the break time, are modelled by ordinary least square (OLS) regression lines. These techniques were originally developed for the analysis of econometric time series (Perron and Yabu, 2009b; Kim and Perron, 2009). They have, however, also been applied in the analysis of air temperature time series in the Northern Hemisphere by Ivanov and Evtimov (2010).

  Specifically, Ivanov and Evtimov (2010) applied Model 3 to the time series of annual mean anomalies of the air temperature in the Northern Hemisphere. The study concludes that a break occurs in 1963, and a new regime starts in 1970, after the transitional period of 6 years. Following the approach of Ivanov and Evtimov (2010) and due to the unique characteristics of the trend shift detection techniques, this thesis selected Model 2 and Model 3 to analyse the temperature time series of the Northern Hemisphere.

- **Multivariate Adaptive Regression Splines (MARS)**
  This technique, developed by Friedman (1991), is the subset of the methods used in adaptive computations. MARS is a hybrid of the classical spline approach and a more modern way of partitioning data into sub-regions. Knots are predetermined in the classical spline approach. However, MARS identifies best knot placements automatically over the course of the process. It should be noted that only significant knots are detected by the algorithm; for example, if a single line is the best fit, no interior knot placement would occur. Nicholas J. Gralewicz (personal communication) conducted some preliminary analyses on climate time series using MARS. Based on

the outcomes of his assessment and inspired by the unique features of MARS, this technique is also employed in this thesis.

- **A sequential algorithm for climate regime shift detection (R method)** Developed by Rodionov (2004, 2006), this technique detects abrupt shifts in the mean level of a time series. More than one shift point may be found by this technique. The behaviour of most of the regime shift detection techniques deteriorates close to the ends of time series. However, the R method is able to discover the discontinuities that occur close to the ends of time series.

All the above-indicated techniques have some common characteristics which make them suitable to achieve the analysis goals of this thesis:

- The algorithm of these techniques could be automated to analyse the large data set of this research.
- The shift points are detected by the algorithms, and *a priori* knowledge of the time of shifts is not required.
- The original time series are analysed by the techniques. Since it is not required to convert the data to anomalies, the ambiguity regarding the definition of a base period is avoided.

When the length of a time series is relatively short (a hundred or so), it is difficult to attribute a specific function to it (Rodionov, 2006). This was the main reason that motivated the selection of a range of different methods in this thesis. This study provides an unprecedented discussion about the techniques mentioned above. The strengths and weaknesses of the methods are indicated in light of the research goals. The analysis of the time series is conducted by applying all of the techniques and presenting all of their results for comparison. Therefore, although this thesis eventually selects one technique as the method which best suits its goals, the comparisons and results provided could act as a helpful guide for additional research and other applications. Researchers may select one or more of these techniques that best meets their analytical objectives and particular data constraints of their projects.

## 1.3 Research Objectives

The specific objectives and key methodological approaches of this thesis are to:

1. identify locations in the Northern Hemisphere that have experienced positive 0°C crossings using the above-noted modelling techniques
2. determine $y_w$ and $y_0$ and develop criteria to identify such values in cases of multiple crossings of the 0°C threshold
3. determine the rate of the increase in temperature that begins at $y_w$ and leads to $y_0$
4. test the local and global significance of the warming that results in the JFM or MAM temperature rising above 0°C using the non-parametric Mann-Kendall test following a modified trend-free pre-whitening (TFPW) (Burn et al., 2004) approach and a bootstrap analysis (Cunderlik and Burn, 2002)
5. conduct non-parametric comparisons of the results of the various methods using two non-parametric techniques: Wilcoxon signed-rank test for paired observations and Wilcoxon rank-sum test (Miller, 1986; Glantz, 2002; Gibbons and Chakraborti, 2003; Montgomery and Runger, 2003)
6. examine the connection between the techniques in terms of their mathematical bases and select the best model based on the analysis results and with respect to the research goals
7. provide rationale for the observed trends by comparing them with those from studies of temporal and spatial trends in hydrologic and cryospheric processes strongly influenced by 0°C conditions

## 1.4 Organization of the Thesis

The remainder of the thesis is organized as follows. Chapter 2 first provides a brief summary of the studies focussed on the impact of climate change on the spatial and temporal characteristics of the hydrological processes in cold regions. Related changes in ecosystem

and human socio-economic activities are also discussed. The chapter then reviews the previous work with regard to non-parametric trend tests as well as the various regime shift detection techniques used in this thesis to model the time series. Chapter 3 describes the mathematical bases and the details of the algorithms of the techniques used in modelling, non-parametric comparison, non-parametric trend testing, as well as the bootstrapping technique applied in this research. Chapter 4 introduces the data used for the study. The chapter gives some information about the source of data and how the data were collected, homogenized, and adjusted to be the indicators of monthly climate variations. Furthermore, Chapter 4 gives an overview of the steps followed in the assessment of the final database to fulfil the research goals. Chapter 5 provides a description of all the variables which are examined including $y_w$ and $y_0$. Following a technique-specific discussion about the input arguments as well as the rules of $y_w$ and $y_0$ determination, the results of the corresponding method are presented in the form of descriptive tables, histograms, and maps. The final section of Chapter 5 discusses the results and includes the mathematical comparison of the techniques as well as description and comparison of the results depicted by histograms and maps. This discussion leads to the choice of the most suitable model. The section ends with providing some cryospheric evidence from the related work for the observed spatial and temporal patterns in this thesis. Finally, conclusions are provided in Chapter 6.

# Chapter 2

# Literature Review

## 2.1 Introduction

This chapter first focuses on climate change impacts on the hydrology of cold regions and presents a brief summary of the available literature. The climate change in cold regions has broad-scope effects observed in subsurface to atmospheric processes, vegetation and plants to human subsystems, and so on. This chapter only aims to describe those consequences caused by the phase change of water such as changes in the type of precipitation, floating ice, glaciers, and permafrost. The discussion then continues with reviewing the available literature on trend detection; the statistical tools suitable for the analysis of the behaviour of climate data are illustrated. Due to specific characteristics of environmental data, this section is mostly concentrated on non-parametric techniques. Following the topic of trend analysis, the rest of this chapter provides a thorough description of the techniques that could be applied in climate shift detection. The focus of this section is on the techniques which could be easily automated for the analysis of large data sets.

## 2.2 Climate Change

Our planet receives sun's radiation. The solar energy is partially reflected back to space by the earth surface, aerosols, clouds, and atmospheric gases. The rest of this energy, after undergoing several processes, eventually radiates back to space as infrared radiation at low

energy (longwave radiation). The processes which cause the absorbed energy to leave and balance the energy of the earth (+atmosphere) include i) thermals (e.g., warming of the air surrounding the earth surface with the absorbed energy by the surface), ii) evapotranspiration, iii) latent heat emitted by clouds (Kiehl and Trenberth, 1997). Greenhouse gases (GHGs) also play a key role in the energy balance of the earth. The primary GHGs are water vapor, Carbon Dioxide, Ozone, and trace gases such as Methane and Nitrous Oxide. The reason behind this terminology (greenhouse gases) is that these gases partially absorb and back-radiate the longwave energy leaving the earth which causes greanhouse effect. Our planet would be colder without the presence of these gases.

Humans alter the atmospheric composition and interfere with the natural energy balance of the earth. The most drastic anthropogenically induced changes are caused by GHG emissions resulted from various human activities. These activities include burning fossil fuels that increases the concentration of Carbon Dioxide in the atmosphere. Part of the human impact on the climate is through changes in land-use such as urbanization. Although changes in land-use are usually regional rather than global and restricted only to areas where people live, the effects are significant and detectable. Due to long atmospheric lifetimes of the emitted GHGs, developing urban areas, and advancements in technology, the recently started climate change is expected to last for a long time. Therefore, it is of paramount importance to plan to adapt to new and upcoming conditions besides efforts devoted to mitigating or preventing further changes. In order to make as precise plans as possible, more studies should be conducted on the quality and quantity of changes in the past as well as developing effective techniques to forecast future changes (Karl and Trenberth, 2003).

### 2.2.1 Impacts of Climate Change on Cold Regions Hydrology

Analysing the effect of climate change on the hydrological parameters is a practically important issue. Some of the most affected hydrological parameters in cold regions can be listed as extent of the land ice and permafrost, sea and lake levels, degree of soil moisture, as well as rate of ice melt, run-off, river discharge, and groundwater discharge. These hydrological parameters in turn play a critical role in the frequency of extreme events such as floods or drought periods and have pronounced impacts on biological and social systems.

The ‘science of climate change’ has been reviewed by a succession of assessment reports

produced by the Intergovernmental Panel On Climate Change (IPCC). The most recent assessment report is the 4$^{th}$ assessment report (2007). 'The Physical Science Basis' is the contribution of 'Working Group I' to the 4$^{th}$ assessment report of IPCC (IPCC, 2007). This comprehensive report includes information on changes in the temperature of land, air, and ocean. It provides a detailed description of the changes in glaciers, ice cover, frozen ground, etc. caused by changes in climate. As a post-product to the 4$^{th}$ assessment report (2007), IPCC produced a special report, IPCC (2008), which focuses only on the issue of water. The report includes the details of the relationship between climate change and water resources. It investigates the changes in climate pertinent to water such as changes in precipitation, snow and land ice, etc. This section is a brief synopsis of the major processes influenced by climate change in cold regions. Only the processes that concern the study area of this research are discussed.

#### 2.2.1.1 Precipitation

Any form of water falling from clouds is called precipitation. Studies indicate that over the 20$^{th}$ century, atmospheric water vapour has increased over oceans. This is an artifact of increases in sea surface temperatures. Therefore, the amount, frequency, intensity, and type of precipitation are influenced by the observed changes in water vapour pressure in the atmosphere (IPCC, 2007, 2008).

##### 2.2.1.1.1 Change in Precipitation Amount, Intensity, and Frequency

Madden and Williams (1978) examined the 64-year (1897-1960) precipitation and temperature time series of 98 stations in North America and Europe (72 and 26 stations in North America and Europe, respectively). They reported high correlations between seasonal mean temperature and amount of precipitation. The correlation observed in summer (June, July, and August) is negative, whereas both positive and negative correlations are observed equally in other seasons. Trenberth and Shea (2005) studied the relationship between monthly mean surface air temperature and precipitation data that span the period of 1979-2002 over the globe. According to this study, negative correlations appear on land. However, high latitudes during northern cold season months (January, February, March, April, and May) feature positive correlations. This phenomenon occurs because providing that sufficient surface moisture is available, an increase in temperature leads to

more evaporation. On the other hand, in extra-tropical high latitudes, there is a positive correlation between the water holding capacity of the atmosphere and temperature. This implies that under cold conditions, the water holding capacity of the atmosphere decreases, which limits precipitation. It should be noted that in these regions, general increases in precipitation are less apparent since warmer conditions lead to increased drying as well (IPCC, 2007).

As indicated, temperature increases lead to increases in water vapour content of the atmosphere. As one would expect, this may lead to heavy rain and snow events. Although positive trends of total annual rainfall have been observed in the middle to northern latitudes, in some regions like the Mediterranean region, studies show decreasing trends. Alpert et al. (2002) examined 265 stations in the Mediterranean region from 1951 to 1995. The obtained trends feature decreasing annual rainfall in spite of increasing intense daily rainfall. Since there has been an increase in the frequency and persistence of subtropical anticyclones, the observed changes in rainfall are associated with this phenomenon that in turn has been caused by GHG warming. Furthermore, aerosols, which have recently increased due to human activities, reflect part of sun's radiation. Therefore, it takes longer to increase the water vapour pressure of the atmosphere. This increases the potential for heavy precipitation. On the other hand, after precipitation, it takes longer to fill the water vapour supply of the atmosphere, which may lead to drought events (Allan and Soden, 2008). Min et al. (2011) also discussed human contributions to intensified precipitation. According to Min et al. (2011), in the latter half of the $20^{\text{th}}$ century, anthropogenically induced increases in GHGs are very influential in the intensity and frequency of extreme precipitation events over two-third of the grid cells in the Northern hemisphere. These grid cells are located below 60°N and over North America and Eurasia. Based on the comparison of observations to the simulation results of 22 coupled climate models, Min et al. (2010) concluded that the spatial and temporal patterns of changes in precipitation are influenced by anthropogenically induced increases in GHGs and sulfate aerosols. Their study area is confined to Arctic land areas located north of 55°N, and the data span the second half of the $20^{\text{th}}$ century.

#### 2.2.1.1.2 Change in Precipitation Form

The increase in temperature increases the probability of the change in the type of winter precipitation. This implies that more precipitation could fall as rain instead of snow. Some

of the most significant impacts of the change in precipitation form include: i) decrease in snowfall: Reductions in snowfall lead to reductions in snowpacks. Snowpacks are important water supplies in summertime, and observed droughts in some regions are the consequence of this phenomenon (Leung and Wigmosta, 1999); ii) winter floods: The likelihood of wintertime flooding would increase due to increased rainfall and snowmelt (caused by warming climate) (Leung and Wigmosta, 1999); iii) mid-winter breakup and ice jams: A few days of mild temperature in winter, particularly if it is accompanied by rainfall, can cause quick rises in river flow. This in turn leads to premature breakup of river ice, which has numerous socio-economic and ecological impacts such as flood events caused by ice jams (Beltaos, 2002; Prowse and Beltaos, 2002); iv) snow avalanche formation: Rain on snow events, which can happen as a consequence of above freezing temperatures in winter, change the properties of the surface layers. This causes the formation of wet slabs on snowpacks and increases the risk of snow avalanches (Schweizer et al., 2003).

Using a regional climate model, Leung and Wigmosta (1999) simulated the present-day surface climate as well as the climate conditions under the scenario of doubled $CO_2$ concentrations. The results indicate that under warmer conditions, more precipitation occurs in the form of rain rather than snow. This leads to 60% and 18% reductions in snowpacks of American River and Middle Fork Flathead River, respectively.

Zhang et al. (2000) investigated the trends of precipitation and temperature in Canada using temperature and total precipitation data as well as snowfall to total precipitation ratios. Results reveal increasing temperatures in southern and western Canada, whereas negative temperature trends are observed in the northeast over the period of 1950-1998. Total precipitation and the ratio of snowfall to total precipitation have increased over the entire country. However, significant negative trends are reported during spring in the south of Canada.

Arora and Boer (2001) studied the effects of global warming on the hydrology of 23 major rivers around the world. They simulated the run-off using Coupled General Circulation models of Canadian Centre for Climate Modelling and Analysis. It is reported that due to reductions in snowfall as well as early spring snowmelt, the hydrological cycles of the rivers of middle to high latitudes (e.g., Amur, Yenisey, Lena, Ob, Volga, and Yukon) have changed. It is also emphasized that the observed trends and changes in precipitation, evapotranspiration, and soil moisture are not uniform all around the globe. For example, the hydrological cycles of the low-latitude rivers (e.g., Yangtze and Ganges) are not as

much influenced by the warmer climate as the middle- to high-latitude rivers.

In their study of effects of temperature and precipitation variability on snowpacks, in the western United States, Hamlet et al. (2005) simulated the linear trends of April 1$^{st}$ Snow Water Equivalent (SWE) using the Variable Infiltration Capacity (VIC) hydrologic model. In order to determine the type of precipitation using the data generated by VIC model, the following rules are set: Temperature data above 0.5°C result in 100% rainfall and temperature data below -0.5°C result in 100% snowfall; a linear relation is established between these two values. This implies that in the regions with temperatures close to 0°C, the probability of getting more rain than snow is higher; only small increases in temperature could cause sign changes (from below 0°C to above 0°C). This in turn could lead to the change in the type of precipitation according to the above criteria. In agreement with these statements, IPCC (2007) reports changes in the type of precipitation observed in many places including middle to high latitudes of the Northern Hemisphere over land.

Studying streamflow data from 89 stations in the western United States for the time period of 1950-1999, Regonda and Rajagopalan (2005) reported that one of the factors influencing hydrological cycles is the general increase in winter precipitation most of which occurs in the form of rain. The observed changes are more significant in lower elevations and in the Northwest Pacific (at elevations between 1000 and 2000 m (Leung and Ghan, 1999)); winter temperatures are closer to 0°C in these regions, and small changes in climate have a significant effect on the hydrology of them. Barnett et al. (2008) also studied the hydrological changes in the time period of 1950-1999, in the western United States. It is reported that there has been a shift in the type of precipitation, and records show more winter precipitation in the form of rain instead of snow.

Knowles et al. (2006) studied the earlier run-off due to more precipitation falling as rain instead of snow, in the western United States, during the time period of 1949-2004. The study reveals a decreasing trend in the ratio of the 'winter-total snowfall water equivalent' (SFE) to 'winter-total precipitation'. Similar to the previous studies, this research indicates that these changes mostly happen in the regions with near freezing temperatures. The most significant decreases in SFE are observed in the areas where the average of winter wet-day minimum temperatures are above -5°C. In these areas, average warmings of 0°C to 3°C have led to significant reductions in SFE. If temperatures are low enough, increasing temperatures do not change the character of precipitation in the region.

#### 2.2.1.1.3 Snow Cover in the Northern Hemisphere

Section 2.2.1.1.2 briefly refers to the impact of global warming on the type of precipitation; that is, changes from primarily nival to primarily pluvial regimes have been observed which in turn lead to smaller snowpacks. In order to study the influence of changing climate on snow, the combined effects of precipitation and temperature should be considered. As indicated in Section 2.2.1.1.2, due to the decreased winter precipitation occurring in the form of snow, there is a reduction in the total winter snow accumulation. Furthermore, warmer climate has led to shorter winters and durations of snow season as well as earlier spring thaws (Burn, 1994, 2008). Stewart (2009) studied the impact of climate change on snowpack and snowmelt run-off in mountainous regions during the past several decades. The study indicates that in the global scale, mountain snowpack is influenced by both precipitation and temperature; however, the nature of this impact is complex since it varies based on factors such as elevation and latitude. Generally, in the middle elevations with increased precipitation, the effect of warmer climate dominates. Therefore, decreased snowpack and earlier snowmelt run-off are observed. On the other hand, in the high elevations with well below 0°C temperatures, an increase in precipitation increases snow accumulation. According to the map of changes in SWE, in western U.S., during the time period of 1949-2004, most of the stations exhibit significant decreasing trends in mountain snowpack except the stations that are located in cold and high-elevation areas or regions with an overall increase in precipitation that offsets the decrease in SWE. According to the map of spring pulse onset in Stewart (2009), most of the stations in western U.S. experience earlier spring pulse onset (approximately 15-20 days).

Temperature variations have a great impact on the extent of the snow-covered area (SCA) in the Northern Hemisphere. Snow has a very high albedo ($\sim 0.8 - 0.9$ for fresh snow). There are several factors affecting the albedo of snow such as depth of snow cover and age of snow cover. The high albedo of snow has a significant impact on reflecting the solar energy reaching the earth. Thus, it plays an important role in the energy balance of the earth. There exists a positive feedback process which is called 'snow albedo feedback'; that is, the decease in snow cover due to warming leads to decreasing snow albedo. Consequently, more solar energy is absorbed and temperatures increase even more (Groisman et al., 1994). Due to the snow-albedo feedback phenomenon, there is a strong correlation between the extent of SCA and temperature in the "*latitudinal band of greatest variability in SCA*" (IPCC, 2007).

As indicated, the duration and extent of snow cover have a significant impact on the radiative energy balance of the globe. Additionally, the annual cycle of snow cover disappearance and onset as well as the snow-free period affect soil water recharge and the active radiation received by soil for photosynthesis. This implies that snow cover has significant terrestrial effects which are not geographically limited to the region periodically covered by snow (Gerland et al., 2000). Hence, climate change may potentially lead to ecosystem change by spatially and temporally altering snow cover. Due to the consequences of observed changes in snow cover, this section is devoted to the observed patterns in snow cover.

Dye (2002) studied the annual cycle of snow cover in land areas located above 45°N in high altitudes of the **Northern Hemisphere**. The data span the time period of 1972-2000. The study reveals that i) '*the week of the last observed snow cover*' has been moved to earlier time by the rate of 3 to 5 days per decade, ii) the snow-free season has been increased by the rate of 5 to 6 days per decade, iii) looking at the big picture, i.e., the Northern Hemisphere as a whole, no significant shift in the beginning of snow season in autumn ('*the first-observed snow cover in autumn*') is detected. However, in the smaller scale, i.e., continental scale, earlier onset of snow season is observed in November in North America, whereas SCA has been decreased in western Eurasia in October (late onset of snow season). Brown and Mote (2009) investigated another aspect of the response of snow cover in the Northern Hemisphere to changing climate. According to the study, snow cover duration (SCD) is the most sensitive variable to climate change in the regions of the Northern Hemisphere that have seasonal snow cover. Climate regime and elevation are the two factors that influence this sensitivity. The greatest impact is observed in the snow cover of the coastal regions with extensive snowfall. The interior regions of the continents with relatively cold and dry winters show the least sensitivity. The study reveals that the most significant decreasing trends of SCD over the time period of 1966-2007 are observed in the regions with maritime climate located in middle latitudes. The seasonal mean air temperature in these regions is close to freezing (-5°C to +5°C). The study notes that due to the non-linear relationship between the duration of snow season and the rate of snow accumulation in various elevations, the impact of increasing temperature and precipitation on SCD of mountainous regions is complex.

In addition to the changes in the onset and disappearance time of snow season, due to the decline in SCA in the Northern Hemisphere, month of maximum SCA has moved from February to January, and annual mean SCA has reduced significantly (IPCC, 2007).

In **North America**, snow cover has declined in the second half of the 20$^{th}$ century with the greatest changes observed in western United States. Furthermore, earlier spring thaw has been observed in west central Canada (Burn, 1994), northern British Columbia and the Yukon Territory (Zhang et al., 2001), as well as northern Alaska (Stone et al., 2002). Pederson et al. (2011) investigated snowpack reduction in western North America, in Colorado, Columbia and Missouri River drainages. These regions are the key contributors to snowmelt run-off. Using tree-ring chronology, the snowpack trends are constructed for the past millennium. The study reveals that the observed reduction in the north of Rocky Mountains, during the latter half of the 20$^{th}$ century, is unique. According to the observed data, mean April 1 SWE anomalies are negative during the time period of 1980-2006 in the study area.

In **Eurasia**, depending on the region and altitude, various trends of snow cover are observed: Falarz (2004) studied time series of number of days with snow cover larger than 1 cm depth as well as seasonal maximum depth of snow cover for the time periods of 1948-1997 and 1895-2002 in Poland. Snow cover has decreased slightly during the time period of 1948-1997 in most parts of Poland except in northern Poland and mountainous regions where increasing trends are observed in the depth and duration of snow cover. Despite the observed trends in the second half of the 20$^{th}$ century, time series of the 1895-2002 period do not show a significant decreasing trend. IPCC (2007) summarizes the observed trends as follows: reductions in snow cover have been observed in the mountains of Slovakia and Switzerland low-land regions of central Europe, whereas, no significant trend was detected in Bulgaria in the time period of 1931-2000. In Finland, in the Tibetan Plateau, and the former Soviet Union increasing trends have been observed in the maximum depth of snow; however, the snow season has shortened. No significant trend in the depth or extent of snow cover has been observed in western China in the latter half of the 20$^{th}$ century.

#### 2.2.1.2 River and Lake Ice

River and lake ice have significant impacts on human activities. Ice also influences the biological productivity through controlling the interaction between atmosphere and aquatic systems (Prowse et al., 2007). Similar to snow season, the duration of river and lake ice has undergone changes due to warmer climate that leads to decreased ice thickness. In addition to warmer temperatures, specified reductions in snow cover greatly influence the thickness of ice since snow has a significant insulating effect that reflects most of the radiative

energy back to space (Duguay et al., 2003). In addition to the composition and duration of ice coverage, the extent of ice coverage is changing. These changes, particularly in cold regions where ice has a great impact on hydrological processes, have significant hydrological consequences such as ice jams and flood events. Most studies (some of which are cited in this section) focus on detecting and analysing the trends of the duration, timing, etc. of ice-related events and associating the trends with air temperature. Besides the efforts to assess the past trends and project future changes in water resources, it is of critical importance to understand the relationship between climate and the dynamics of processes controlling ice-related events. The study by Beltaos and Prowse (2009) describes how climate change leads to the observed trends and their consequences such as ice jams and flood events by providing detailed information on the processes involved in freeze-up, ice growth, and breakup.

Magnuson et al. (2000) define the 'freeze date' as the time when the water body is covered with ice for the first time in the corresponding year. The last observed breakup marks the 'breakup date'. Studying 39 rivers and lakes located all over the Northern Hemisphere, during the time period of 1846-1995, Magnuson et al. (2000) reported later freeze dates and earlier breakup dates. Furthermore, the rates of interannual variabilities have increased since 1950. Looking at the smaller picture, Zhang et al. (2001) examined streamflow data of a larger number of Canadian rivers (compared to Magnuson et al. (2000)) with the records from the last 30 to 50 years. Although substantial variability is observed in the breakup and freeze dates, generally, freeze dates (especially in eastern Canada) and breakup dates (particularly in British Columbia) have shifted to earlier time. Analysing the trends of the time period of 1951-2000, Duguay et al. (2006) reported earlier breakup dates, particularly in western Canada, whereas no general trend was observed in the freeze dates. The analysis of the recent records of Russian rivers reveals that the freeze dates of the western Russian rivers have shifted towards earlier time, whereas the eastern Siberian rivers exhibit trends toward later freeze-up. Breakup dates do not show statistically significant trends (IPCC, 2007).

The analysis of the ice breakup events in the above-indicated studies is based on ice cover dates. However, more precise results could be obtained using the water level charts. In order to study the spring breakup timing and duration as well as their spatial aspects in the Mackenzie River Basin during 1913-2002, de Rham et al. (2008) analysed two hydrometric variables from water level charts: breakup initiation time and maximum water level during breakup. The study also includes the assessment of the commonly used 'last

B date' (last day of ice effects) indicator. Results reveal earlier occurrence of all the events represented by the aforementioned variables; in the upstream regions of the major tributaries, spring breakup dates have moved to earlier time with the average rate of 1 day per decade over the time period of 1970-2002.

To study how climate change influences the severity and timing of the breakup flooding events, it is required to investigate the controlling hydroclimatic measures. The analysis of these factors leads to a better understanding of how warming climate causes the observed spatial and temporal changes and yields better explanations than considering simple relationships between air temperature and timing of breakup. Goulding et al. (2009) investigated some of the hydroclimatic factors in the Mackenzie Delta during 1974-2006. The study analyses both the upstream driving force (peak discharge and rate of rise in discharge) and downstream resistance force (downstream ice conditions and the balance between upstream and downstream ice melt). Results reveal positive trends in pre-breakup melt interval and freeze-up stage, whereas negative trends are observed in peak discharge, rate of rise in discharge, and ice thickness.

In addition to spring breakup described above, changes in winter temperature can have a significant impact on mid-winter breakup and ice jams, especially in middle latitudes with mild winters. For instance, three mid-winter breakup events occurred in the Saint John River (located in the boundary of New Brunswick, Canada and Maine, USA) during 1995 and 1996 (Beltaos, 2002). As indicated in Section 2.2.1.1.2, due to increases in winter temperature, more precipitation falls as rain instead of snow. A few days of mild temperature, particularly if it is accompanied by precipitation in the form of rain, can cause quick rises in river flow and rapid runoff. The hydrodynamic forces associated with the rapid runoff initiate river ice breakup. The mid-winter breakup and ice jams increase the risk of flood events. For example, if a breakup event occurs in the upstream of a river, and the downstream of the river is still frozen, the downstream part can form an ice dam that leads to flooding of the upstream region of the river. Besides increasing risk of flood events, other impacts associated with mid-winter ice breakups include problems created in hydropower generation, navigation, and the aquatic ecosystem (Beltaos, 2002; Prowse and Beltaos, 2002).

To analyse the impact of climate change on river ice characteristics in the future, Prowse et al. (2010) analysed the temporal and spatial changes of spring 0°C isotherm (Bonsal and Prowse, 2003) in the main-stem reaches of four large northward flowing Arctic rivers:

Lena, Mackenzie, Ob, and Yenisey. The study focuses on the regions within 2000 km from the headwaters. Since spring 0°C isotherm could be used as the indicator of spring breakup dates, the study compares the contemporary mean spring isotherm (1979-2008) to the future conditions during two time periods of 2041-2070 and 2071-2100. The results show that mean spring isotherm (obtained from the four models used in the study) occurs earlier by 7.5-16.5 (13.6-25.5) days in the 2050s (2080s) decades. The study notes that lower temperatures in the river mouths at the time when the temperatures of the headwaters are approximately 0°C increase the risk and severity of ice jam floods.

Dibike et al. (2011a) analysed the influence of climate change on lake ice characteristics in the cold-region portion of North America (40°N-75°N) using 'Multi-year simulation model for Lake thermo- and phytoplankton dynamics' (MyLake). Mean breakup and freeze-up dates over the time period of 2041-2070 are obtained by simulating the lake-ice phenology. The simulation results indicate that the predicted warming causes ice breakup to occur 10-20 days earlier compared to the base period of 1961-1990. Furthermore, later freeze-up dates (5-15 days) are forecast. This indicates that the lake ice durations would be shorter by 15-35 days. Moreover, the ice thickness would decrease by 10-30 cm. The study reveals that freeze-up timing and maximum ice thickness are influenced by lake depth. A similar analysis was conducted by Dibike et al. (2011b) in the Northern Hemisphere (40°N-75°N) for the time period of 2040-2079 with the base period of 1960-1999. The study reports earlier breakup dates by 10-30 days and later freeze-up dates by 5-20 days. Therefore, a decline in the lake ice duration by 15-20 days is expected. The study indicates a reduction in ice thickness (10-15 cm) as well.

#### 2.2.1.3 Glaciers

Included among the indicators of climate change are glaciers and ice caps. Climate determines the mass balance at the surface of a glacier; that is, how much snow and ice is gained and lost, and during hydrological cycles, what the net change in the size of the glacier is. In the middle to high latitudes, the hydrological cycle is defined as accumulation in winter and consumption (oblation) in spring and summer. As discussed earlier, due to recent changes in climate, the duration of cold season is subject to change. So is the mass balance season for glaciers as well as the net accumulation. However, changes in glaciers lag by a few years in the tropical mountains and a few centuries in the large glaciers on gentle slopes (IPCC, 2007). Glacier thaws cause a significant sea level rise. This especially

threatens low-lying areas such as Mackenzie Delta with an inundation risk which has a significant impact on the hydrological and biological systems (Prowse and Ommanney, 1990). To understand and forecast future changes in sea level, it is important to have a global-scale estimate of ice volume. Using a statistical method, Radic and Hock (2010) evaluated the estimates of the volumetric magnitude of glacier systems and ice caps as well as their sea level equivalent (SLE) on the global scale. The study reports total ice volume of $241 \times 10^3 \pm 29 \times 10^3$ km$^3$. This ice volume is the equivalent of $0.60 \pm 0.07$ m SLE. 32% of the estimated volume belongs to glaciers in Greenland and Antarctica.

The addition of fresh water from glaciers to the oceans may cause changes in the ocean ecosystem. The changes in the size of glaciers lead to temporal and spatial changes in the gravitational field, ellipticity, and rate of rotation of the earth (Dyurgerov and Meier, 2005). Moore et al. (2009) investigated the glaciers of Alaska and western Canada. The study refers to the effects of glacier retreat. The variations in the size of glaciers may be hazardous through the changes they cause in landform. For instance, glacial lake outburst floods may occur due to thawing glaciers in moraine-dammed lakes. Another geomorphic hazard is the plucked off glacial debris from valley walls. In addition to geomorphic hazards, thawing glaciers change the temperature of streams (which particularly influences hydroecology), concentration of suspended sediments in streams, and aquatic chemistry.

The mass balance at the surface of a glacier is influenced by the mixed effects of precipitation (particularly snow), fluxes of radiative energy, and ambient air temperature. In the Northern Hemisphere, the air temperature has a positive correlation with spring and summer freshet, whereas mean specific mass balance (mass balance averaged over the surface area) and winter accumulation correlate negatively with the air temperature (Greene, 2005). The study by Dyurgerov and Meier (2005) reveals that significant negative mean specific mass balances exist in northwest of USA, southwest of Canada, and Alaska. The rate of change is large in Alaska after the mid-1990s. The mean specific mass balance observed in Europe is almost zero due to significant losses and gains in the Alps and maritime Scandinavia (northern Europe), respectively. Changes in glaciers have been observed in the high mountainous regions of Asia as well. The fluctuation in the size of the glaciers is highly correlated with air temperature (Greene, 2005).

Casassa et al. (2009) investigated run-off and discharge peaks in mountain basins caused by melting of glaciers. The study indicates that run-off has reduced in some regions like southern and central British Columbia, the central Andes in Chile, and low-middle eleva-

tions in the Alps. The reason is the decreased snow cover and/or the great glacial mass loss that have occurred in the past. In other regions such as northwest of British Columbia, southwest of Yukon, high elevations in the Swiss and Austrian Alps, the Tianshan Mountains, and Tibet, records show increased run-off. Under the projected warming conditions, run-off in these regions would eventually decline. Similar trends as the above-indicated trends in run-off are reported by Moore et al. (2009) for the glaciers of Alaska and western Canada.

#### 2.2.1.4 Permafrost

Prowse and Ommanney (1990) define permafrost as "*the ground that is continuously below* $0°C$ *for two years or more*". 25% of the land surface in the world is covered with permafrost (Prowse and Ommanney, 1990). The presence of permafrost influences the streamflow generation, catchment hydrology, as well as water drainage and storage patterns. Moreover, the dynamics of permafrost soil is radically different from that of the soil in the above-zero region. Therefore, it has significant impacts on land cover and all aspects of the hydrological cycle: surface water, subsurface water, and atmosphere.

##### 2.2.1.4.1 Permafrost Hydrology

All permafrost regions have the following characteristics despite the physically diverse environment (IPCC, 2007):

- Permafrost acts as a low permeability layer similar to aquiclude.
- In the permafrost region, most of the hydrological processes are taking place in the layer above the impermeable bed of permafrost. This layer thaws and freezes seasonally and is called the 'active layer'.
- Most of the hydrological processes on the surface of permafrost are inactive during long and cold winters.
- The spring freshet and seasonal thawing of the active layer have a significant impact on the surface and subsurface water system. Furthermore, it could lead to severe flooding and erosion (Woo et al., 2008).

#### 2.2.1.4.2 Climate Change Impacts on Permafrost

Temperatures in the permafrost regions are increasing due to climate change. This leads to thawing of permafrost (or thickening of the active layer) and even permanent disappearance of permafrost in some regions, specifically in the areas with discontinuous and sporadic permafrost. Syed et al. (2007) reported that permafrost degradation has accelerated recently. Thawing permafrost alters the moisture and energy balance of the ground and causes pronounced changes in hydrological processes from subsurface to the atmosphere. This consequently leads to changes in the biological and social systems (e.g. human subsystems) that should adapt to new conditions (Hinzman et al., 2005).

Warming of the continuous permafrost in the Northern Hemisphere has resulted in thinning of the permafrost, and the southern boundary of the continuous permafrost has moved northward. Kwong and Gan (1994) examined the distribution of permafrost along the Mackenzie Highway located at the south of Great Slave Lake using hand augering and measurement of soil temperature. They conducted the field investigation in 1988 and compared the results to the field survey that had been conducted by Brown (1964) 26 years earlier in 1962. The study reveals that the southern boundary of sporadic discontinuous permafrost has moved northward in 26 years (120 km). Studying the mean annual air temperature, they associated the detected change in the southern limit of permafrost with the climate warming. Using three general circulation models with the assumption of 2°C warming, Anisimov and Nelson (1996) predicted 25-44% contraction in equilibrium permafrost in the Northern Hemisphere. According to the results from these models, the continuous permafrost zone is expected to be more severely affected (29-67% reduction). Anisimov and Nelson (1997) created maps of permafrost zonation in the mid-21$^{st}$ century, in the Northern Hemisphere using three transient general circulation models as well as 'frost index' (dimensionless number to predict spatial distribution of permafrost). Models with the assumption of doubled $CO_2$ concentrations reveal significant reduction in equilibrium permafrost. Stendel and Christensen (2002) used coupled atmosphere-ocean general circulation model ECHAM4/OPYC3 to analyse the changes in the conditions of Arctic permafrost by the end of the 21$^{st}$ century. Their results indicate that there would be an increase of 30-40% in the thickness of the active layer in the Northern Hemisphere, and more severe changes are predicted for the northernmost locations.

Georgiadi et al. (2010) investigated the changes in run-off in the basin of one of the Arctic rivers, Lena River, caused by warming permafrost. The study reveals an increase

in run-off over the last 15-20 years; however, the magnitude of this increase varies across the basin. The projection of future changes using two atmosphere-ocean global circulation models, ECHAM4/OPY3 and GFDL-R30, indicates that more significant changes in run-off in the basin of Lena River are expected in the 21$^{st}$ century compared to the 20$^{th}$ century.

It should be noted that the changes in the thickness of active layer have been subject to wide experimentation. As indicated, most researchers believe that changes in permafrost are significantly associated with the increase in temperatures. More experiments should be conducted to accept this hypothesis; permafrost thawing is mostly influenced by summer temperatures, whereas the recent warming is more profound in winter and spring temperatures. On the other hand, the high albedo of snow and its insulating properties play an important role in the heat exchange and energy balance of the permafrost zone. Therefore, changes in the patterns of precipitation and snow cover should be taken into account when investigating the effects of climate change on permafrost (Zhang et al., 2005).

The hydrological and atmospheric consequences of deepening of the active layer are summarized below:

- It causes an increase or decrease in the size of thermokarst lakes. As permafrost thaws, the size of thaw lakes increases. However, complete degradation of permafrost causes the lakes to drain into the ground, and the water bodies disappear. In short, thawing permafrost has a great impact on thermokarst activities (IPCC, 2007).

- It changes the drainage patterns, intensifies flowpaths in the subsurface, leads to greater discharges or recharges, and in short, influences the groundwater system. Previously, not many studies were devoted to the behaviour of groundwater in permafrost; however, due to permafrost thaw and disappearance of this impermeable layer, which emerges as a serious problem, researchers are more concerned about the patterns and consequences of permafrost degradation (Smith et al., 2007; Walvoord and Striegl, 2007; Jacques and Sauchyn, 2009).

- In permafrost regions, ground levels or domes that are seasonally created due to ice formation in the subsurface collapse as the active layer or permafrost thaws. This is one of the processes that causes the increase of sediments in rivers and lakes. This consequently results in declining stability of rivers and lakes (IPCC, 2007).

- The degradation of the near-surface permafrost in the circumpolar Arctic, particularly in the south of 70°N, has a significant impact on the hydrology and ecology of Arctic. Thawing permafrost influences the concentrations of organic and inorganic matters as well as major ions transported to Arctic. It is uncertain how the concentrations of organic and inorganic matters would change; however, increases are predicted for the concentrations of major ions, most commonly phosphate and silicate. All the above-indicated consequences such as changes in topography and land cover, possibility of complete degradation of permafrost, groundwater-dominated aquatic system, and thermokarst activities are likely to occur (Frey and McClelland, 2009).

- Boreal forests and wetlands are important features of permafrost regions. Most of these wetlands are formed on the impermeable and permanently frozen layer in the subsurface. Permafrost degradation increases the available water in wetlands. On the other hand, complete thawing of the impervious strata leads to drying and drainage of these wetlands. Both phenomena endanger the habitat of a lot of species (Prowse and Ommanney, 1990).

- Wetlands play a key role in the carbon cycle. They are the largest contributors of Methane to the atmosphere (Mungall and McLaren, 1990). As indicated earlier, Methane is one of the GHGs causing the climate change. Therefore, in addition to the impacts of wetlands on the wildlife, they indirectly influence the issue of global warming. On the other hand, if wetlands dry and drain into the ground, the oxidation of the organic materials will emit Carbon Dioxide which is a GHG as well (Prowse and Ommanney, 1990).

### 2.2.2 Impacts of Climate Change on Engineering

Engineers are mostly concerned with the potential impacts of climate change on environmental conditions that in turn influence the design of infrastructure such as buildings and industrial facilities in the permafrost and coastal zones, oil, gas, and mining industry, landfills, etc. Rising engineering issues could be listed as follows:

- The reasons for and consequences of increasing temperature in the permafrost regions are indicated in Section 2.2.1.4. The physical properties of the soil in the permafrost regions are highly dependent on temperature. Camill (2005) predicts the $1.4 - 5.8$°C

increase of the mean annual temperature by 2100. As a result of this warming, the mean annual air and ground temperature would rise above 0°C in the sporadic and discontinuous permafrost zones over the Northern Hemisphere causing permafrost thaw. Degradation of permafrost causes deformation characteristics and threatens human beings with the possibility of foundation failure. Due to erosion, engineered structures on slopes face a higher risk of subsidence. Currently, the effects of warming permafrost on engineering are more profound and evident in the sporadic and discontinuous permafrost regions than the continuous permafrost zone since permafrost is warmer and closer to the melting point of ice (0°C) in the former (Nelson et al., 2001; Instanes, 2006).

- Thawing ice caps and glaciers as well as expanded water due to the increased temperature cause sea level rise. Increased water volumes lead to more erosion in coastal zones since stronger wave currents hit the coast. Moreover, models predict more intense and stronger atmospheric storms and winds. This would lead to stronger and higher waves as well as intense and more frequent rainfalls; hence, even more erosion and sediment movements would occur. These severe erosion events have significant impacts on coastal villages, towns, industries, etc. (Instanes, 2006). The increase in sea level and more intense storms increase the risk of inundation in low-lying coastal regions like New York (SWIPA, 2011).

- Increased icebergs due to warmer temperatures in Arctic influence the oil and gas exploration and extraction processes. In the mining operations in Arctic coastal regions, transportation conditions greatly impact this industry. Global warming would cause high costs of maintenance of roads, railroads, etc. which are built on the permafrost zone (Humlum et al., 2003; Instanes, 2006).

- Thawing permafrost or the phase change of water (expansion and contraction of water) may break the liners in the landfills. Consequently, the underground water would be exposed to the leachate from the landfills and contaminated (Instanes, 2006).

- The advancement of industry and increasing population in some regions of Arctic in Canada (Nunavut and Northwest Territories) increase the demand for electricity. Furgal and Prowse (2008) indicate that the reduction in SCA and increase in snow-free period influence hydroelectric power generation in this zone and could have

short-term advantages. In middle latitudes with seasonal snow cover, warmer winters and decreased snow cover and snow duration would reduce the cost of ice and snow management. Furthermore, the cost of the maintenance of roads and bridges due to the adverse impacts of salt and chemicals (used to control snow and ice) would decline (NRC, 2008).

### 2.2.3 Large-scale Atmospheric and Oceanic Oscillations

The objective of this section is to investigate large-scale atmospheric and oceanic oscillation patterns. It attempts to identify the links between changes in patterns of these oscillations and the recent climate change.

The distribution of thermal energy on the earth surface is influenced by large-scale air circulations and ocean circulations (in a smaller scale). Some of these large-scale circulation patterns could be listed as El Nino-Southern Oscillation (ENSO), Pacific Decadal Oscillation (PDO), and North Atlantic Oscillations (NAO). There is no doubt that these patterns significantly influence the earth climate on the annual to decadal time scale; however, the links between recent climate change and these patterns are not clear. For example, since 1970 (during the period of high global warming), the frequency of warm-ENSO events (El Nino) has increased. It is speculated that extreme ENSO events are caused by changing climate; however, it may be equally true that a lower periodicity of warm-ENSO events triggered global warming. Recent research provides an explanation for the higher incidence of ENSO events considering the relationship between SO and PDO. When both PDO and SO are in a warm or cold phase, more intense SO events occur, whereas the SO events are dampened if PDO and SO are not in phase. PDO experienced a phase shift in the early 1970s and stayed in the positive phase until the winters of 1997-1998. During this period, a high frequency of intense ENSO events was observed. Considering the high thermal capacity of oceans as well as their slow response to changes, it seems only a matter of time before the relationship between any of these large-scale circulations and climate change is clarified (Rohli and Vega, 2008).

Using the data of atmospheric variables (monthly mean temperature, geopotential height, and corresponding geostrophic wind at the pressure levels of 200, 300, 500, and 700 (hPa)), snow cover, and sea surface temperature (SST), Watanabe and Nitta (1999) studied the changes in winter climate, after 1989, in the middle to high latitudes of the

Northern Hemisphere on the decadal time scale. The observed changes are as follows:

Geopotential height data reveal a dipole pattern with middle latitudes and polar regions on the poles. The temperature of the middle troposphere is increasing in the middle latitudes and decreasing in polar regions. The statistical analysis of the geopotential height data at 500 hPa is the indicator of a regime shift in 1989 over the entire Northern Hemisphere. Further investigations relate the observed structure to the linear combination of Pacific North American (PNA) and Eurasian patterns as well as NAO. The sudden shifts of 1977 and 1989 are explained by the simultaneous occurrence of phase shifts of NAO and PNA patterns.

Comiso (2003) examined the satellite thermal infrared surface temperature data of the pan-Arctic. The data are recorded during the cloud free conditions and span the 1981-2001 period. The study reports positive mean temperature trends over sea ice, in the Northern Hemisphere. On the seasonal scale, except winter, positive temperature trends are dominant in all of the seasons. Comiso (2003) related the recent changes in climate to the phase change of Arctic Oscillations (AO) which is believed to be caused by the increasing GHGs.

In their study of trends in spring and autumn 0°C isotherm dates over Canada, Bonsal and Prowse (2003) investigated the relationship between the observed trends and large-scale oscillations over Pacific and Atlantic oceans. Results reveal that majority of stations are not in phase with the large-scale oscillations. Furthermore, no evidence of an abrupt change in the large-scale oscillations over Pacific is found to explain the observed shift toward earlier spring 0°C isotherm dates in the west of Canada. The study concludes that although the large-scale oscillations have some impacts on the observed trends, they cannot provide adequate explanation. One plausible explanation is that climatic warming has caused the trends; however, Bonsal and Prowse (2003) note that in the two cases of later spring isotherm dates in northeastern areas and insignificant trends during autumn, it is not clear whether they have been caused by climatic warming. If it is assumed that climate change has some impact on large-scale circulations, the observed trends could be explained by ENSO and NAO and hence be indirectly related to global warming.

The following studies indicate mid-1970s, late 1980s and 1990s as the shift time for a number of large-scale atmospheric patterns. On the other hand, temperature shifts of the mid-1970s and late 1980s have been reported in numerous studies (e.g., Polyakov et al., 2003; Belkin, 2009; Lo and Hsu, 2010; Powell and Xu, 2011). The synchronization of the

observed shifts in teleconnection patterns and climate anomalies supports the idea of the existence of a strong link between them.

To study the correlation between the abundance of Pacific saury and recent climatic changes, Tiana et al. (2004) conducted the principal component analysis (PCA) and correlation analysis on climatic and oceanographic indices as well as the abundance and biological indices of Pacific saury in the subtropical Pacific. The climatic variables include SST, air temperature, and wind velocity. North Pacific (NP) index, AO index, and PDO index are some of the oceanographic indices used in the analysis. The analysis of teleconnections reveals significant regime shifts in 1987-1988 and possibly 1997-1998, in the Kuroshio region. The analysis of the abundance and biological indices of saury not only signifies the response of Pacific saury to the detected regime shifts, but verifies the results obtained using the above-mentioned atmospheric indices. Furthermore, it could be inferred from this study that these large-scale patterns are responding to the recent climate change.

Rodionov and Overland (2005) applied the sequential t-test algorithm (Rodionov, 2004, 2006) to detect regime shifts of some of the large-scale patterns. 1943 and 1976-1977 were the strongest shifts observed in PDO. Aleutian Low Pressure index, NP index, and PNA index exhibit the most significant shift as 1976-1977. The regime shift of 1989 was mostly conspicuous in AO index. The analysis of NP index from the Climate Prediction Center and East Pacific index reveals that the most significant shift has occurred in 1998.

Ivanov and Evtimov (2010) investigated the following annual surface temperature anomalies of the Northern Hemisphere: marine data, land air data, and combined land and marine data. To support the results obtained from the analysis of these time series, a number of climate indices were investigated in addition to the surface temperatures in the Northern Hemisphere: North American index, SO index, PNA index, Atlantic Multidecadal Oscillation index, and PDO index. Over a large region like the Northern Hemisphere, the polarities of the above-mentioned index series are in association with the leading patterns of temperature anomalies.

Lo and Hsu (2010) related the synchronization of abrupt temperature changes in different locations of the Northern Hemisphere, in the late 1980s to the large-scale patterns. They found a resemblance between the first empirical orthogonal function (EOF1) of the land and sea surface temperature, in the Northern Hemisphere and the temperature fluctuations associated with AO. That is, EOF1 reveals the AO-like pattern. On the other hand, EOF2 exhibits the PDO-like pattern. According to this study, the correlation between

EOF2 (EOF1) and the mean temperature in the Northern Hemisphere is high (low) before the 1980s, whereas the correlation between EOF1 (EOF2) and the mean temperature in the Northern Hemisphere is high (low) after the 1980s. Therefore, the mean temperature in the Northern Hemisphere exhibits the PDO-like pattern before the 1980s; however, the AO-like pattern becomes more dominant after the 1980s.

## 2.3 Detection of Climate Change

Temperature is among the primary indicators of climate change. There is no doubt that examining temperature data is the most important guide to climate induced changes. In addition to studies which directly analyse temperature data (e.g., Zhang et al., 2000; Bonsal and Prowse, 2003; Ivanov and Evtimov, 2010; Prowse et al., 2010), many studies associate the observed trends in other variables (e.g., snowmelt run-off pulse) with changes in temperature (e.g., Burn, 1994; Zhang et al., 2001; Cayan et al., 2001; Dye, 2002; Stewart, 2009). The focus of this section is on introducing the techniques that could be used for the statistical analysis and modelling of temperature regimes as well as examining regime shift points. These rigorous statistical tools are then used to locate grid cells in the Northern Hemisphere whose temperature has permanently risen above 0°C during the time period of 1901-2009 (Chapters 4 and 5).

### 2.3.1 Trend Detection

Trend analysis is one of the techniques used to examine the underlying patterns of time series under study. To test whether the detected trends are significant, several statistical tests exist. These tests fall under two main categories: parametric and non-parametric. Kundzewicz and Robson (2004) classify the most frequently used statistical tests in the trend analysis as follows: i) Spearman's rho test, ii) Kendall's tau and Mann-Kendall test, iii) seasonal Kendall test, iv) linear regression, v) other robust regression tests: least absolute deviation regression, M-estimate of regression, and trimmed regression.

In the analysis of the environmental data, non-parametric tests are usually preferred over parametric techniques. The reason is that the non-parametric tests do not require any assumption regarding the underlying distribution of the population from which data

are obtained. Moreover, using non-parametric techniques, it is much easier to analyse the data with missing values, tied values, serial correlation, and censored values (which are very common in the climatic and hydrological data). Using Monte Carlo simulation, Yue and Pilon (2004) concluded that the power of the rank-based non-parametric tests is higher than the slope-based parametric techniques in detecting the trends of non-normally distributed data.

As indicated, one of the frequently used non-parametric tests is the Mann-Kendall (MK) test (Mann, 1945; Kendall, 1975; Hirsch et al., 1982). In the MK test, the null hypothesis is the independence and randomness of data. If data are serially correlated, the probability of type I error increases. This implies that the probability of detecting a trend when there is no significant trend increases. This is due to the fact that the presence of a positive serial correlation can increase the test statistic and complicate the process of trend detection (Helsel and Hirsch, 2002).

One approach to modify the statistical tests used to detect monotonic trends in the presence of autocorrelation is to pre-whiten or deserialize data. The procedure involves modelling the time series with an autoregressive process. One drawback of this technique is that sometimes, although the underlying model is deterministic, a large lag-1 serial correlation coefficient is obtained. This is particularly more likely if the temporal resolution of the data is not very high (e.g., annual). Using Monte Carlo simulation, Fleming and Clarke (2002) concluded that the pre-whitening procedure had the potential to yield inaccurate results; the technique introduces a positive bias in the estimation of slope. Furthermore, the power of the test decreases using pre-whitening. Based on this conclusion, they suggested not to use this method unless there is external evidence supporting the assumption of autoregressive noise.

Yue et al. (2002) and Yue and Pilon (2003) examined cases where both deterministic and stochastic parameters are present in time series. Their studies are particularly focused on the cases where a linear trend is present as well as the lag-1 autoregressive process. Monte Carlo simulation demonstrates that there is an interaction between the serial correlation and linear trend; the estimation of the magnitude of the serial correlation is influenced by the existence of a trend. On the other hand, the variance of the estimated MK test statistics is affected by the presence of the serial correlation. They found that if the positive serial correlation is removed from a time series (pre-whitening), a negative bias would be introduced into the estimates of the existing trend; however, the impact of the

existing trend on the serial correlation could be removed if the underlying deterministic trend is eliminated before pre-whitening. The results of the analysis reveal that following this procedure, the evaluated value of the lag-1 autoregressive coefficient does not differ significantly from the true value. Following these results, Yue and Pilon (2003) developed the trend-free pre-whitening (TFPW) approach. The TFPW technique first estimates the monotonic trend of the time series under study and eliminates the trend. Then, pre-whitening is applied to the trend-free time series. Yue and Pilon (2003) also emphasized the importance of the bootstrap technique to test the global significance of the trends since in some cases, locally significant trends do not exhibit globally significant trends.

Burn et al. (2004) applied the MK test to study the trends of several hydrological variables in the Liard River basin, in northern Canada. A slightly modified TFPW approach developed by Yue and Pilon (2003) was used (refer to Section 3.5.2 for more details). They also applied the bootstrapping technique to examine the cross-correlation between the time series of the variables and test the global significance of the trends.

Following Burn et al. (2004), the modified MK test is selected to investigate the existence and quality of the temperature-time trends in this thesis. This method is preferred over the other techniques since

- it is a rank-based non-parametric technique. No assumption is required regarding the underlying population of the time series. Moreover, it could easily be applied to the cases with missing, tied, or seasonal values as well as serially correlated data.
- as recommended by Kundzewicz and Robson (2004), distribution-free techniques like resampling methods are among the most suitable techniques to analyse the environmental time series. The distribution of the test statistics in the MK test is obtained using the permutation approach, which falls under the category of the resampling methods.
- as is inferred from the sequence of the modifications applied to the original MK test, this technique is the most improved method among the ones indicated in this section.

### 2.3.2 Detecting Changes in the Means of Time Series

With increasing concern regarding the consequences of anthropogenically induced global warming, numerous studies have been devoted to analysing the changes introduced in cli-

matic variables and modelling the natural climate variability. The extent and particularly the quality of the historical climate time series play a critical role in such studies.

The first step in analysing any climate time series for the change detection and modelling purposes is to homogenize data. Conrad and Pollak (1962) described the homogeneous time series as the series with the embedded variability only caused by climate. Bradley and Jones (1985) categorized the inhomogeneities in the climate data as natural (caused by abrupt climate changes) and artificial. The significant causes of artificial inhomogeneities could be classified as follows: i) changes in instrumentation and measurement techniques, ii) changes in the position or elevation of stations, iii) changes in observation times, e.g., from morning to evening, iv) changes in the techniques of mean calculation, modelling, and data analysis over time (Barnston and Livezey, 1987; Lambert, 1990), v) urbanization which often introduces positive bias (refer to Section 4.2.2 for detailed description of the potential causes of inhomogeneities).

Bradley and Jones (1985) discussed the data homogenization techniques as well; however, the inhomogeneities like urbanization, which occur gradually over time, are really difficult to remove from time series following these techniques. Based on the assessment of gridded temperature data from the Northern Hemisphere, Jones et al. (1986) indicated that in the analysis of temperature trends over such a large region, the inhomogeneities introduced by urbanization could be ignored. It should be noted that the data collected using satellites may exhibit inhomogeneities as well. For example, different satellites have different crossing times as well as spectral windows. These factors cause discontinuities in the recorded infrared radiation by satellites (Chelliah and Arkin, 1992).

Since discontinuities are not distinct features of available data, they are very difficult to detect. Historical climate time series that span a rather long time are not usually homogeneous. To eliminate the artificial inhomogeneities, the investigation of the accompanying metadata such as station histories may be useful; however, historically, not all the changes in a station that eventually affect the statistical behaviour of the time series have been recorded. Motivated by this, a number of techniques have been developed to detect the discontinuities (artificial and natural) that have not been reported. These techniques may be categorized as methods using reference series and techniques independent from reference series. It should be noted that the techniques described here are suitable for detecting sharp changes in the means of time series rather than trend inhomogeneities.

#### 2.3.2.1 Techniques Using Reference Series

These techniques are based on the comparison of target stations against the corresponding reference series. Some of the studies focused on these methods could be listed as Kohler (1949), Alexandersson (1986), Portman (1993), Rhoades and Salinger (1993), Hanssen-Bauer and Forland (1994), and Peterson and Easterling (1994). More advanced methods dependent on reference series have also been developed such as the regression-based techniques (e.g., Gullet et al., 1991; Easterling and Peterson, 1995).

The necessity of comparison to reference stations is one of the drawbacks of these methods since i) in the case of global changes such as global warming, all the neighbouring stations are affected as well, ii) in some situations, there are no data available from the neighbouring stations, or there is no station within a reasonable distance from the target station, iii) using reference series introduces another source of uncertainty into the analysis, and the results of the analysis change as the underlying assumptions in constructing reference series change.

#### 2.3.2.2 Techniques Independent from Reference Series

Based on the above discussion, the techniques that are based on reference series cannot be applied to detect natural climatic discontinuities since the neighbouring stations are usually influenced by the same changes, and the usage of metadata is inapplicable. These techniques are mostly suitable for the cases in which changes in instrumentation, calibration, and time of observation lead to inhomogeneities in time series.

Lanzante (1996) proposed a method (the L method) that is independent of the external data such as reference data and metadata, and hence, applicable to climate shift detection. The technique uses an iterative algorithm to detect multiple discontinuities in time series. Moreover, no assumption regarding the timing of the shifts is required. Since the technique is a rank-based technique, it could easily be applied to cases with outliers and non-normal distributions. Moreover, due to the iterative nature of the method, it is suitable for detecting subtle changes. Comparing the L method to the method developed by Easterling and Peterson (1995) (the EP method), Lanzante (1996) concluded that the two methods generate comparable results.

Lanzante (1996) noted several principles that should be considered in interpreting the results of the L method. These points are important in distinguishing between artificial

and natural discontinuities:

- if the observed discontinuities are not detected in the neighbouring stations, this implies that the inhomogeneities have been caused by artificial rather than natural climatic factors.
- if similar changes are detected in the neighbouring stations in the same country as that of the target station, however not in the surrounding stations located across the border, the observed discontinuities may be artificial.

The main disadvantage of the L method is that to achieve a high degree of confidence in detecting the points of discontinuity, at least 10 points of data are required. Therefore, the uncertainty of the estimations increases close to both ends of time series. This also implies that the technique is not suitable to detect the most recent changes since at least 10 years should pass before the change is detected. By the time that this change is discovered, the time series may be experiencing another shift.

The inability to detect changes close to the ends of time series is common in most of the regime shift detection techniques. The proposed sequential algorithm by Rodionov (2004) is capable of estimating the probability of the potential discontinuity soon after it occurs, and it continues to monitor this probability as new points are included in the time series. Since this technique detects any change with a minimum delay, it is able to discover discontinuities that occur close to the ends of time series. Further advantages of this technique are as follows:

- It is capable of detecting multiple shifts.
- As indicated earlier, it could easily be automated and used in the analysis of large data sets.
- It can analyse the original data directly, and the technique does not necessitate the use of anomalies. The conversion of the original data requires the determination of a base period. By using the original data, the ambiguity regarding the definition of a base period is avoided.
- Similar to the methods developed by Gullet et al. (1991), Easterling and Peterson (1995), and Lanzante (1996), *a priori* assumptions regarding the timing of the shifts are not required.

- With most of the regime shift detecting techniques, if a trend exists in the time series, it leads to false conclusions since the technique would identify the center of the time series as the potential discontinuity. The algorithm developed by Rodionov (2004) is robust against this problem. Having compared this technique with the L method, Rodionov (2004) concluded that the results generated by both methods resemble each other when no trend exists in time series; however, if inhomogeneities are superimposed on existing trends, Rodionov's (2004) method generates more consistent results.

The first sequential algorithm developed by Rodionov (2004) assumes that observations are not correlated. Stationary red noise processes can create long intervals during which the data are larger or smaller than the overall mean value of the process. To avoid false identification of these intervals as climatic regimes, Rodionov (2006) proposed a procedure of red noise removal; i.e., a pre-whitening process was added to the previously proposed algorithm (Rodionov, 2004). The goal of pre-whitening is to examine whether the climate regimes can be more than just a red noise. Two key features of the procedure are i) subsampling, ii) bias correction of the least square estimate of the serial correlation coefficient. Rodionov (2006) developed a new method to correct the bias of the estimated autoregressive parameter (more details can be found in Section 3.2.2). In this thesis, the combination of the above-indicated two procedures, sequential algorithm and pre-whitening (Rodionov, 2004, 2006), is referred to as the R method.

Due to the aforementioned advantages of the R method, it has been selected as one of the techniques to analyse the data in this study.

### 2.3.3 Regression Modelling

The behaviour of climate data over time could be modelled using the piecewise polynomial fitting procedure. The basic idea of piecewise fitting is to approximate the true underlying function by several simple (low order) parametric functions each modelling a subsection of the entire data set. If climate time series are modelled using linear segments, based on the changes in slope, inferences could be made about the time of climatic changes.

#### 2.3.3.1 Global Parametric Modelling

Parametric modelling requires *a priori* assumption of the true underlying function (usually a simple function) to fit to data. The method of least squares is often used to calculate the model parameters. Although it is possible to model even a few data points (if a simple model is assumed), this type of modelling is of limited flexibility; only when the behaviour of the data is close to the pre-assumed model is it likely to generate accurate approximations.

#### 2.3.3.2 Non-parametric Regression

In non-parametric regression, it is usually assumed that the function representing the data is continuous and smooth. *A priori* assumption of the form of this function is not required; i.e., there is no parameter to estimate, and the function is derived directly from the data under study. In low dimensional settings ($n \leq 2$, $n$ = number of independent variables), there are three related concepts that generalize the global parametric modelling to non-parametric regression: piecewise parametric fitting, local parametric fitting, and roughness penalty methods (Friedman, 1991). Spline is the most commonly used piecewise polynomial fitting technique. This method is used to model a set of data when the data cannot be approximated using a single polynomial. In this case, polynomials of degree $q$ with the first continuous derivative model the data (De Boor, 2001).

#### 2.3.3.3 Adaptive Computation

The adaptive technique, which is a subset of the non-parametric modelling, adjusts its strategy dynamically to allow approximating the behaviour of the data set under study. Recursive partitioning (Morgan and Sonquist, 1963) is one of the adaptive algorithms developed for approximating the true underlying function.

Morgan and Sonquist (1963) referred to the difficulties regarding data analysis when there is an interaction between independent variables; however, their proposed approach does not impose any restriction on interaction effects. The goal of their study is to develop a technique that is capable of following the data set behaviour adaptively and improving the approximated function step by step. The proposed model (recursive partitioning regression model) simultaneously estimates an optimal set of subsections as well as parameters of the

functions approximating the behaviour of data in each sub-region. First, it selects the entire domain as the starting section. At each step, the previously existing sections are optimally partitioned into two subsections. The functions used to model the sub-regions are generally of low degree. For example, Morgan and Sonquist (1963) and Breiman and Friedman (1985) used constant functions.

Breiman and Meisel (1976) and Friedman (1979) presented algorithms similar to the technique proposed by Morgan and Sonquist (1963). The algorithms are based on adaptive (data-directed and dynamic) partitioning; however, the underlying function of each subsection is approximated using linear regression.

The recursive partitioning regression is a powerful technique. If the piecewise constant approximation (Morgan and Sonquist, 1963; Breiman and Friedman, 1985) is used, the recursive nature of the algorithm enables the model to include the independent variables that are influential in the local level but insignificant when the entire data set is modelled as one region. This leads to more precise study of the independent variables impacting the response variable. As the entire domain is partitioned into more sections, the model becomes more local. It should be noted that the recursive partitioning algorithm that is based on piecewise linear approximation (Breiman and Meisel, 1976; Friedman, 1979) lacks the ability to select the influential subset of local variables; hence, it has limited power and applicability (Friedman, 1991).

In summary, the following restrictions limit the applicability and accuracy of the recursive regression partitioning (Friedman, 1991):

- One of the most important restrictions is the discontinuities in the sub-region boundaries. Boundary discontinuities limit the approximation precision, particularly if the true underlying function is continuous.
- There is a limitation regarding the complexity of the functions modelling the sub-regions. For example, as the number of coefficients of linear functions or variables of additive functions increases, it becomes more difficult to estimate model parameters.
- The model that is eventually represented does not clarify whether the independent variables are interacting or the model is an additive model.

#### 2.3.3.4 Adaptive Regression Splines

Friedman (1991) developed the multivariate adaptive regression spline (MARS) algorithm to overcome some of the limitations associated with the existing methodology outlined in Section 2.3.3.3. Indeed, the MARS technique is an improved and generalized version of the recursive partitioning algorithm originally developed by Morgan and Sonquist (1963) and Breiman and Friedman (1985). Some of the unique features of the algorithm are as follows:

- It is powerful, accurate, and applicable to cases with the sample size ($N$) of $50 \leq N \leq 100$ and dimension of $3 \leq n \leq 20$.
- The recursive partitioning algorithm is also known as the stepwise regression technique. It should be noted that the only feature of the recursive partitioning algorithm that introduces boundary discontinuities is the step functions included in the algorithm. To solve this problem, the step functions have been replaced by continuous functions whose first derivatives are continuous as well (Algorithm 1 of Friedman (1991)).
- MARS is capable of handling missing values and categorical variables (e.g., gender: male and female).
- It has a higher power in modelling the additive behaviour of data compared to the recursive regression. It also generates more precise results if there are interactions between a few independent variables. Furthermore, the final presentation of the model clearly specifies which terms are additive, and which independent variables are interacting.

Nicholas J. Gralewicz (personal communication) performed a preliminary analysis on the climate time series using MARS. Motivated by his study and the unique characteristics of MARS, this technique is used to model the time series of this thesis.

### 2.3.4 Testing Trend shifts

As indicated earlier, examining temperature data provides useful and important information about climate induced changes. The time series of annual mean anomalies of the air

temperature in the Northern Hemisphere seem to be non-stationary during the $20^{th}$ century. In the literature, the long-term changes are referred to as climatic changes and the short-term changes are indeed climatic noises (Ivanov and Evtimov, 2010). A number of studies have been devoted to analysing the nature of this non-stationary process; the goal is to understand whether it is a trend-stationary process or a unit root process (Ivanov and Evtimov, 2010). Perron (1989) and Hamilton (1994) discussed the hypothesis tests of trend-stationarity versus unit root. If a time series tends to go back to the original long-term mean after facing a change or shock, the process is trend-stationary. However, if the series is permanently affected by the shock (e.g., moves to a new mean level), it is a unit root process. Ivanov and Evtimov (2010) noted that the results of the hypothesis tests of trend-stationarity versus unit root are strongly dependent on *a priori* assumption of the deterministic trend. To avoid this problem, they applied the unit root test developed by Kim and Perron (2009) in their analysis. Their analysis reveals that the nature of the above-mentioned non-stationary process in the Northern Hemisphere is trend-stationary.

A lot of abrupt, significant, and large-scale climate changes have been recorded in the past. Abrupt climate changes could occur due to many reasons; however, there is no doubt that anthropogenic impacts are among the key factors increasing the likelihood of the future abrupt changes in the climate (Alley et al., 2003). Numerous studies have referred to the widespread and sudden climate change in the late 1980s (Kerr, 1992; Hare and Mantua, 2000; Rodionov and Overland, 2005; Lo and Hsu, 2010). Since climate can experience abrupt shifts in addition to gradual changes, statistical tests developed to detect breaks in the structure of time series can be applied to the problem of finding break points in the trend function of climate time series (Ivanov and Evtimov, 2010).

In detecting structural breaks, it is of practical importance to have a test that does not require *a priori* assumption on whether the noise component of a process is stationary or contains an autoregressive unit root. On the other hand, to understand the nature of the noise component, information about the existence of a structural break (at least at unknown time) is required (Perron and Yabu, 2009b).

Perron (1989) developed a technique that was an improvement over the existing standard tests at the time. The null hypothesis of the procedure is unit root process, and the alternative assumes that the process is trend-stationary. The test allows the existence of a one-time structural break in the slope or level of the trend function. However, the break in the test is known and selected based on some external knowledge, completely independent

of data. This implies that Perron's (1989) test is powerful in distinguishing the hypotheses only if a break is present and known.

Zivot and Andrews (1992) and Vogelsang and Perron (1998) modified Perron's (1989) test. In their procedure, the break time is unknown and should be estimated based on data. This implies that the estimation of the break point is 'endogenized'. Similar to Perron (1989), these techniques test the structural breaks in intercept, in slope, and in both intercept and slope. The models are termed 'crash model', 'changing growth model', and 'crash and changing growth model', respectively by Perron (1989). If there exists a change in trend, both the size and power of these tests (Vogelsang and Perron, 1998; Zivot and Andrews, 1992) can be affected by changes in slope or intercept.

Perron and Yabu (2009b) noted the necessity of developing tests of structural change in level and/or slope that are valid regardless of the non-stationary nature of the process. Their solution is based on their earlier work; i.e., Perron and Yabu (2009a). The study by Perron and Yabu (2009a) is focused on determining and testing the significance of the slope coefficient of a linear trend model without *a priori* knowledge of whether the noise component is stationary ($I(0)$) or has a unit root ($I(1)$). Perron and Yabu (2009b) extended the analysis of Perron and Yabu (2009a) to the case of testing for changes in level or slope of the trend function of a univariate time series. The goal is to develop a test that has the same size in both cases of $I(0)$ and $I(1)$. Perron and Yabu (2009b) compared their test to Vogelsang's (1999) test (the only test available that was valid in both cases of $I(0)$ and $I(1)$). The result of the comparison reveals that Perron and Yabu's (2009b) test has a higher power. If the result of Perron and Yabu's (2009b) test indicates that there exists a break, the time of the break can be approximated using the procedure described by Kim and Perron (2009).

According to the sequence of the statistical tools on trend shift detection, Perron and Yabu's (2009b) method for testing structural breaks along with Kim and Perron's (2009) technique for determining the time of breaks have the potential to generate very interesting results. Hence, in addition to the R method (Rodionov, 2004, 2006) and the MARS algorithm (Friedman, 1991), the temperature time series in this thesis are analysed using the above techniques.

# Chapter 3

# Methodology

## 3.1 Procedure Overview

The analysis of the temperature time series in this document consists of the following steps. The selection criteria are indicated in Section 4.3.

1. The time series are analysed using the methods indicated below, and all the shifts and break points of interest are identified.
    - R method (Section 3.2)
    - MARS algorithm (Section 3.3)
    - trend break detection technique (Section 3.4)
2. The modified MK test (Section 3.5.1) is applied to test the significance of trends in the sections of interest. What the section of interest is and the procedure of selecting it are described in detail in Section 4.4.
3. To test the global significance of the trends, a bootstrap algorithm (Section 3.5.3) is used.
4. Two non-parametric tests are employed to examine how the results vary from one methodology to another (Section 3.6).

## 3.2 R Method

The key features of the technique and the reasons for the inclusion of this method in the analysis are described in Section 2.3.2.2. There are two main procedures involved in the R method: i) sequential algorithm (Rodionov, 2004), ii) pre-whitening (Rodionov, 2006). These steps are summarized in the following sections, and more details can be found in the original studies.

**Note:** The R method is suitable for detecting abrupt shifts, and gradual shifts may not be detected.

### 3.2.1 Sequential Algorithm (Sequential t-test)

The steps involved in detecting regime shifts are as follows:

1. The cut-off length ($l$) of the climate regimes is determined for the time series ($X_t$). $l$ denotes the minimum length of regimes; i.e., once a shift is detected, the magnitude of the shift does not change for the minimum period of length $l$.

2. The difference (*diff*) between mean values of two subsequent regimes is calculated.

$$diff = t\sqrt{\frac{2\sigma_l^2}{l}} \tag{3.1}$$

   where

   $t$ is the value of the Student's t-distribution with the degree of freedom equal to $2l-2$ and at the pre-specified significance level. $\sigma_l^2$ is a constant variance evaluated as the average of the variances calculated for each section of length $l$.

3. $\overline{x}_{R1}$ is the average of the first $l$ values of the climate time series under study. $\overline{x}'_{R2}$ is the expected minimum average of the next $l$ values constructing the next climate regime and is calculated as follows:

$$\overline{x}'_{R2} = \overline{x}_{R1} \pm diff \tag{3.2}$$

   The above statement means that if the value of the $(l+1)^{\text{th}}$ observation (or point $j$) exceeds $\overline{x}'_{R2}$, that point is identified as the time of a potential shift, and the algorithm

proceeds with Step 4; however, if it falls within the boundaries indicated by Equation 3.2, the algorithm updates $\overline{x}_{R1}$ including the $j^{\text{th}}$ observation. $\overline{x}'_{R2}$ is then recalculated, and the procedure continues.

4. If the climate shift takes the data to a higher level, $x_i^* = x_i - \overline{x}'_{R2}$, where $x_i$ is the observation at point $i \geq j$; otherwise, $x_i^* = \overline{x}'_{R2} - x_i$. If these differences have the same sign as the differences obtained at the time of the potential shift ($x_j - \overline{x}'_{R2}$ and $\overline{x}'_{R2} - x_j$, respectively), the statistical confidence of identifying $j$ as the time of shift increases. The regime shift index (RSI) is a variable that keeps track of changes in the confidence level:

$$RSI_{i,j} = \sum_{i=j}^{j+w} \frac{x_i^*}{l\sigma_l}, \quad w = 0, 1, ..., l-1 \tag{3.3}$$

If during the entire time period of $j+1$ to $j+l-1$ the value of $RSI$ remains positive, this implies that the shift at point $j$ is significant at the significance level determined for the t-statistic in Step 2. At this point, $\overline{x}_{R1}$ is updated by calculating the actual average of the identified regime. The calculations continue starting from the observation at point $i = j+1$, and the above steps are repeated. If the sign of $RSI$ changes to negative, $\overline{x}_{R1}$ is updated including the observation at point $j$, and the analysis starts again from Step 3.

Steps 3 and 4 are repeated until all the observations are processed. Based on the steps involved in the analysis, it is inferred that the smaller the value of $l$ is, the more precise the results will be since a small value of $l$ makes it possible to detect short regimes. However, this interpretation is not always correct. The reason is that as $l$ decreases, the degree of freedom $(2l-2)$ decreases as well. At a given significance level, this causes the value of t-statistic to increase, and a large critical value may prevent regime detection.

### 3.2.2 Pre-whitening

So far, in the sequential algorithm, it has been assumed that observations are not correlated. If data are correlated, the time series may be approximated as a stationary red noise process using a first-order autoregressive (AR(1)) model. Red noise processes can create long intervals (runs) during which the data are larger or smaller than the overall mean value

of the process. If the Student's t-test is used to test the significance of the shifts at the change points of these runs, the test favours significant shifts. To avoid false identification of these intervals as climatic regimes, Rodionov (2006) proposed a procedure of red noise removal. This procedure is described in this section. After 'pre-whitening', the sequential algorithm can be used to find climatic regimes.

As described above, a stationary red noise process can be approximated by an AR(1) process:

$$(X_t - \mu) = \rho(X_{t-1} - \mu) + \varepsilon_t \xrightarrow{\mu'=(1-\rho)\mu} X_t = \rho X_{t-1} + \mu' + \varepsilon_t \tag{3.4}$$

where
$X_t$ represents the value of the variable under study at time $t$.
$\mu$ is the population mean.
$\rho$ denotes an autoregressive parameter.
$\varepsilon : N(0, \sigma^2)$ is the independent and identically distributed (i.i.d.) noise component.

if $|\rho| < 1$, the process is stationary and one of the following cases:

- $0 < \rho < 1 \rightarrow$ red noise process
- $-1 < \rho < 0 \rightarrow$ violet noise process
- $\rho = 0 \rightarrow$ white noise process
- $\rho = 1 \rightarrow$ random walk process

If regime shifts exist in addition to red noise, the time series should be approximated by a more complex model as indicated below:

$$X_t = \rho X_{t-1} + f'_t + \varepsilon_t \tag{3.5}$$

where $f_t$ is the trend function at time $t$ and $f'_t = f_t - \rho f_{t-1}$.

In order to avoid incorrectly detecting the extended intervals of red noise processes as regime shifts, one of the following two approaches could be adopted:

**Approach 1** In testing the significance of regime shifts using Student's t-test, significance levels are calculated considering the serial correlation of data. The method of 'equivalent sample size' for the t-test (Storch and Zwiers, 1999) could be used in this case.

**Approach 2** The process is pre-whitened, and the red noise is removed using $X_t - \hat{\rho}X_{t-1}$. In order to calculate the lag-1 autoregressive coefficient ($\hat{\rho}$) as precisely as possible, Rodionov (2006) developed a subsampling technique. The goal of subsampling is to avoid the uncertainty caused by using the entire data set to estimate $\rho$. The subsampling technique discussed here divides the entire data set into subsamples of size $m$ where $m \leq \frac{l+1}{3}$. $\hat{\rho}$ is selected as the median of the obtained $\hat{\rho}$'s for subsamples.

Furthermore, common techniques, such as maximum likelihood estimators or the OLS technique provide biased estimations of $\rho$. The bias is larger for a sample of small size. According to Rodionov (2006), the following techniques are more suitable to correct the bias of the OLS estimate of $\rho$ for small samples:

1. MPK method (after Marriott, Pope, and Kendall):

$$\hat{\rho}^c = \frac{(m-1)\hat{\rho}+1}{m-4} \tag{3.6}$$

2. IP4 method (Inverse Proportionality with 4 corrections):

$$\hat{\rho}^{c,1} = \hat{\rho} + \frac{1}{m} \tag{3.7}$$

$$\hat{\rho}^{c,k} = \hat{\rho}^{c,k-1} + \frac{|\hat{\rho}^{c,k-1}|}{m} \quad k = 2^{\text{nd}}, 3^{\text{d}}, 4^{\text{th}} \text{ correction} \tag{3.8}$$

Using Monte Carlo simulations and examining the plots of rejection rate of $H_0$ : no regime shift versus lag-1 autoregressive coefficient, the study concludes that the results of the above-mentioned correction techniques are very close if $m \leq 10$; however, for large samples, the IP4 method yields more precise estimates (i.e., with less bias and variance). Furthermore, Approach 1 has a smaller rejection rate compared to that of the case which does not consider the serial correlation of data. However, it is not a significant improvement over the latter.

## 3.3 MARS

In Section 2.3.3.4, the merits of this technique are discussed. As indicated earlier, MARS produces smooth curves and surfaces, not the step functions of e.g., the CART method

(Steinberg and Colla, 1995). The nature of the modification is essentially replacing the piecewise constant approach with the piecewise linear (or higher order) approach and removing the points of discontinuity. Nicholas J. Gralewicz (personal communication) noted that if climate time series are modelled using linear segments, based on the changes in slope, inferences could be made about the time of regime shifts.

The key feature of MARS is its capability of finding the right transformation points of input variables. All input variables are scanned one at a time across their entire ranges of values. Then, MARS uses e.g., the piecewise linear spline approach in order to identify best possible non-linear transformations. Moreover, MARS has the capability to detect interactions. There are some measures to protect models against over-fitting and identify optimal models. MARS uses an approach based on 'generalized cross validation' (GCV) which is essentially the framework where the entire data set is used for modelling and identifying optimal model structure and size.

In every modelling problem, it is of key importance to approximate the dependent variable ($y$) as precisely as possible given some independent variables like $x_1, \ldots, x_n$. The problem could be formulated as follows:

$$y = f(x_1, \ldots, x_n) + \varepsilon \tag{3.9}$$

Classical approaches, such as parametric modelling, require the analyst to search for a model that best suits the data under study. Then, the problem turns into the problem of trial and error, which involves steps such as model specification, diagnostic checks, performance assessment, etc. Furthermore, it is not feasible to automate these techniques to analyse large data sets.

In contrast to conventional approaches, modern algorithms are developed such that they derive the underlying pattern of data based on the information acquired from the data set itself. Among these methods, some require the modeller to input variables; then, the function approximating the underlying structure is found by the model. Generalized additive models (Hastie and Tibshirani, 1986) are examples that fall under this category. Some techniques, such as MARS, on the other hand, operate independently in both variable selection and finding the most appropriate function.

### 3.3.1 Algorithm Description

The main goal of the MARS algorithm was to improve and overcome some of the limitations of recursive partitioning regression. Therefore, to explain the MARS algorithm, first, the modifications applied in generalization of the recursive partitioning regression to MARS are described. Then, a summary of the steps carried out in MARS is presented. More details are available in Section 3 of Friedman (1991).

1. **Generalization of Recursive Partitioning Regression:** As discussed in Section 2.3.3.4, MARS is an improved and generalized version of the recursive partitioning algorithm originally developed by Morgan and Sonquist (1963) and Breiman and Friedman (1985). Equations 3.10 and 3.11 represent the recursive partitioning approximation of the function $f$ indicated in Equation 3.9:

$$\text{if } \mathbf{x} \in R_m \Longrightarrow \hat{f}(\mathbf{x}) = g_m(\mathbf{x}|\{a_j\}_1^p) \tag{3.10}$$

   $\{R_m\}_1^M$ represents the discontinuous sub-regions obtained from partitioning the entire domain $D$ into $M$ sections. $g_m$ is the function used to model sub-regions. As indicated earlier, $g_m$ could be as simple as follows ($a_m$ is a constant function):

$$g_m(\mathbf{x}|a_m) = a_m \tag{3.11}$$

   The MARS algorithm changes the concept of sub-regions ($g_m$) to the concept of basis functions (BF). This implies that Equations 3.10 and 3.11 take the forms illustrated by Equations 3.12 and 3.13.

$$\hat{f}(\mathbf{x}) = \sum_{m=1}^{M} a_m B_m(\mathbf{x}) \tag{3.12}$$

$$B_m(\mathbf{x}) = I[\mathbf{x} \in R_m] \tag{3.13}$$

   where $B_m$ denotes basis functions defined as indicator functions ($I$) which take binary values: 0 (false argument) and 1 (true argument). $\{a_m\}_1^M$ are coefficients to be estimated by the algorithm.

2. **Correction of Recursive Partitioning for Boundary Discontinuities:** As indicated earlier, MARS solved the problem of discontinuity in the boundaries of sub-regions. The algorithm of recursive partitioning ('Algorithm 1' in Friedman (1991))

includes a step function that leads to disjoint sub-regions. In fact, this step function is a spline BF with the order of zero. In order to adjust Algorithm 1 for discontinuity, this spline function of zero order is generalized to higher dimensions (multivariate spline BF's). The degree of continuity is discussed in the study, and it suggests that only the continuity of the approximating function as well as its first derivative at each node is necessary; node indicates where one sub-region starts another sub-region. These two constraints dramatically reduce the number of free parameters that should be estimated for each sub-region.

3. **Further Generalization of Recursive Partitioning Regression:** The recursive partitioning algorithm lacks the ability to precisely estimate the parameters of a simple class of functions: functions with no interactions or only a few interacting independent variables. An example of this type is additive functions. To solve this problem, it is important to derive a good set of BF's. The recursive partitioning, unless there is only one independent variable, includes the BF's with several independent variables that lead to high-order interactions. The algorithm is designed such that during the process the interaction order increases. As indicated, recursive partitioning is a spline BF with the order of zero. This implies that the algorithm only selects a small subset from the large set of BF's that are tensor products of univariate spline functions. MARS generalizes the algorithm of recursive partitioning by including all these spline functions in the analysis. This modification results in an algorithm with no constraint on the existing BF's and hence, capable of producing models with low or high degrees of interaction.

The major modifications to the recursive partitioning regression are explained above. Including those steps, the MARS algorithm is described below:

1. As discussed earlier, the underlying model in MARS is basically a hybrid of the classical spline approach and a modern way of partitioning data into sub-regions. Therefore, the overall model can be relatively easily described in terms of conventional analytics. In short, the idea is that instead of writing a single regression, as many regressions as different segments are written. Then, they are combined into one single expression that represents all these individual segments.

2. Knots are predetermined in the classical spline approach. Instead of trying to determine knots in a kind of deterministic uniform way before running the actual process,

MARS identifies best knot placements automatically. Only significant knots are detected by the algorithm; for example, if a single line is the best fit, no interior knot placement would occur. The search algorithm for the best knots is as follows:

To increase the computational efficiency, knots are always selected from the existing data points and not permissible values in between. If there is only one independent variable, and the goal is to select one knot, every data point has the potential to be selected as this knot. Every time, after selecting a knot, the sum of squared errors (SSE) is calculated, and eventually, a knot which yields the minimum SSE is selected. It should be noted that due to the restriction on the number of data points required at each step for modelling, this search algorithm may prevent knot placement close to the end of series.

As could be inferred from the above explanation, the analysis becomes very complicated if the goal is finding more than one interior knot simultaneously. In this case, instead of looking at all possible combinations, at each step, the algorithm looks for the strongest and best knot placement given the configuration at that stage. As described above, the complexity of searching for a single knot is linear in the data set size. However, if it is desired to place two simultaneous knots, the complexity of that operation is quadratic in size, and that is already unacceptable by all algorithmic requirements. Hence, to avoid this complexity, MARS adopts a sequential algorithm. This implies that it always places one knot at a time based on the most updated configuration. The procedure described in this step is called 'forward knot placement'.

3. The forward knot placement strategy is capable of recovering the true knots; however, it also carries over a large number of knots that look important initially, but they are not really needed. Therefore, the algorithm does not stop at a point where all of these knots are introduced. Forward knot placement is the beginning of the next step which is 'backward cleaning'. The backward cleaning step revisits all the knots the process identifies in the forward fashion and sequentially removes the knots that are not required.

4. If there is more than one independent variable, the process of knot selection indicated above becomes very difficult to manage. Furthermore, it is not feasible to represent interactions with the above-mentioned knot selection strategy. These are the reasons that explain the necessity of having BF's as formulated by Equations 3.12 and 3.13.

To clarify more on the idea of using BF's in MARS, the following two expressions are presented. These two types of BF's could be used multiple times with a single independent variable ($x$).

- Direct BF: $max\ (0, x - c)$
- Mirror image BF: $max\ (0, c - x)$

where $c$ is a threshold, and it is taken within a certain variable range. MARS considers constructing such BF's with all permissible data points taken as $c$. Basically, $c$ stands for knot locations. Thus, as $c$ varies over the range of $x$, a knot itself moves around. The reason for having a mirror image BF is that a direct BF function generates a zero slope for values less than the knot. Therefore, MARS creates BF's in pairs in order to complete the forward knot placement process for the flat top function. In addition to improving the knot placement strategy, BF's make the mathematical and computational implementation of MARS much easier. For example, two variables could easily be interacted by multiplying the BF's of them. Furthermore, the analysis of categorical variables and missing or censored values is only possible through BF's.

In summary, first, an over-fit model is deliberately developed by adding pairs of BF's where each pair relates to an individual knot. Then, the model is pruned back, which is the knot cleaning step. The backward step always removes the BF's one at a time. This means that once MARS moves to the pruning step, it is no longer required to keep BF's in pairs. In fact, having pairs would decrease the model performance if flat segments are desired. Therefore, in the forward step both BF's are kept, and in the backward step, those BF's are investigated one at a time to see which ones are more important and more influential than the others.

It should be noted that MARS is in fact an additive model since BF's are added one at a time and in an additive form. Furthermore, each BF uses one variable at a time. Therefore, by definition, it is a generalized additive model at this point. When interactions are allowed, MARS tests the performance of the model when a new BF pair is added to the model independently and when the same pair interacts with an already existing single BF. Then, the algorithm selects the best performance. In fact, the model effectively penalizes variables when they are not yet part of the model. This has a tendency to shift focus to a smaller subset of variables, but it may also generate models that are overly difficult to understand. This is due to the fact that all the variables that are part of the model

would be explored in terms of all potential correlations with all the variables that have not been selected as part of the model, and in some cases, it may produce somewhat confusing models.

In practice, the analyst specifies an upper limit for the number of knots (more precisely, the number of BF's) to be generated in the forward step. That limit should be large enough to ensure that the data structure is captured; however, it cannot be very large. If the algorithm attempts to build a large number of BF's, that is an equivalent of trying to fit a multiple linear regression with a large number of terms. This is likely to cause computational, time, and memory difficulties. It should be noted that in the forward step, MARS does not always come back with the prespecified number of BF's. Since BF's are always entered in pairs, at some point, mirror image BF's become redundant. In this case, MARS automatically identifies some of the BF's as linearly dependent and eliminates those.

There are several points to note about the MARS algorithm:

- GCV which is a penalized version of mean squared error is used for optimal model selection.
- MARS has no intuition of its own, and it simply follows the rules of its algorithmic structure. In some cases, it may be necessary that a modeller uses their own judgement in selecting the final model. For example, if the analyst believes that the model is over-fitting the data under study, one simple approach to avoid this problem is to select a model with a smaller number of BF's. However, with this approach, a sequence of naturally generated MARS models is obtained. It is never guaranteed that the previously existing BF's, which led to over-fitting, would be eliminated in the order the analyst wishes. Therefore, to eliminate specific BF's, the modeller themselves should identify the BF's that are responsible for the observed undesirable local anomalies.

## 3.4 Trend Shift Detection

According to Section 2.3.4, another interesting technique to be applied to the data in this study is the trend shift detection method developed by Perron and Yabu (2009b). The

method is introduced briefly, and further details can be found in the original paper.

The data generating process is assumed to be the following regression:

$$y_t = x_t'\Psi + u_t \tag{3.14}$$

Below, the noise component is assumed to be an AR(1) process; however, it could be generalized to a higher order ($p$) as described later in this section.

$$u_t = \varrho u_{t-1} + v_t \tag{3.15}$$

$$v_t = d(L)e_t \tag{3.16}$$

$$d(L) = \sum_{i=0}^{\infty} d_i L^i, \quad \sum_{i=0}^{\infty} i|d_i| < \infty, \quad d(1) \neq 0 \tag{3.17}$$

where $t = 1, \ldots, T$; $T$ is the number of years. $e_t$ is the i.i.d. noise component with the mean and variance of 0 and $\sigma^2$, respectively. $r$ is the number of unknown parameters. $\Psi$ with the size of $(r \times 1)$ contains the model parameters to be estimated. $x_t$ contains the deterministic components and is a matrix of size $(r \times 1)$. $x_t'$ is the transpose matrix of $x_t$.

This method is based on the quasi-feasible generalized least squares (quasi-FGLS) approach. $\varrho$ is the sum of the autoregressive coefficients estimated using the detrended data and following the OLS approach. $-1 < \varrho \leq 1$; hence, the noise component could be either stationary or integrated. A super-efficient estimate of $\varrho$ is used if $\varrho = 1$.

The null hypothesis of the test is $R\Psi = \gamma$. $R$ is a full-rank matrix with the size of $(q \times r)$. $\gamma$ is the vector of restrictions with the size of $(q \times 1)$. This implies that $q = 1$ when the technique tests for a structural break in intercept or slope; however, $q = 2$ if the simultaneous break in slope and intercept is tested. The reader is referred to Equations 3.18 to 3.20 for more details. Throughout this section, the break date for a given $\lambda_1 \in (0, 1)$ is determined as $T_1 = \lambda_1 T$, and $1(.)$ is an indicator matrix.

As indicated in Section 2.3.4, the technique tests for 3 types of structural breaks: i) structural break in the level (intercept) of the trend function (Model 1), ii) structural break in the slope of the trend function (Model 2), iii) simultaneous structural break in the intercept and slope of the trend function (Model 3). Each model is explained below:

- **Model 1**

$$\left.\begin{aligned} x_t &= (1, DU_t, t)' \\ \Psi &= (\mu_0, \mu_0, \beta_1)' \\ DU_t &= 1(t > T_1) \end{aligned}\right\} \implies y_t = \mu_0 + \mu_1 DU_t + \beta_0 t + u_t \tag{3.18}$$

  $R = [0\ 0\ 1]$. Therefore, the null hypothesis of interest is $\mu_1 = 0$.

- **Model 2**

$$\left.\begin{aligned} x_t &= (1, t, DT_t)' \\ \Psi &= (\mu_0, \beta_0, \beta_1)' \\ DT_t &= 1(t > T_1)(t - T_1) \end{aligned}\right\} \implies y_t = \mu_0 + \beta_0 t + \beta_1 DT_t + u_t \tag{3.19}$$

  $R = [0\ 0\ 1]$, and the null hypothesis of interest is $\beta_1 = 0$. As could be inferred from Equation 3.19, there is a shift only in the slope of the trend function; hence, the trend function is continuous at the break time.

- **Model 3**

$$\left.\begin{aligned} x_t &= (1, DU_t, t, DT_t)' \\ \Psi &= (\mu_0, \mu_1, \beta_0, \beta_1)' \end{aligned}\right\} \implies y_t = \mu_0 + \mu_1 DU_t + \beta_0 t + \beta_1 DT_t + u_t \tag{3.20}$$

  $R = \begin{bmatrix} 0 & 1 & 0 & 0 \\ 0 & 0 & 0 & 1 \end{bmatrix}$, and the null hypothesis is $\mu_1 = \beta_1 = 0$.

After clarifying the data generating process, the rest of this section focuses on the steps involved in the analysis:

1. $\varrho$ is calculated following Equation 3.21 which is a truncated autoregression of order $k$:

$$\hat{u}_t = \varrho \hat{u}_{t-1} + \sum_{i=1}^{k} \xi_i \Delta \hat{u}_{t-i} + e_{tk} \tag{3.21}$$

   where $\hat{u}_t$ is the estimate of the residuals computed using the regression of $y$ on $x$ (Equation 3.14). An information criterion, such as Bayesian information criterion (BIC) or Akaike information criterion (AIC) is used to estimate $k$, and $k$ should be in the range of $\left[0, 12\left(T/100\right)^{1/4}\right]$. Therefore,

$$k_{max} = 12\left(\frac{T}{100}\right)^{1/4} \tag{3.22}$$

2. Matrices of regressors for OLS are constructed as follows:

**Model 1**

$$X = \left[ones(T,1) \;\; [1:1:T]' \;\; DU_i\right] \tag{3.23}$$

**Model 2**

$$X = \left[ones(T,1) \;\; [1:1:T]' \;\; DT_i\right] \tag{3.24}$$

**Model 3**

$$X = \left[ones(T,1) \;\; DU_i \;\; [1:1:T]' \;\; DT_i\right] \tag{3.25}$$

3. Since the OLS estimate of $\varrho$ is biased, the bias is corrected using Equation 3.26:

$$\hat{\varrho}_M = \hat{\varrho} + C(\hat{\tau})\hat{\sigma}_{\varrho} \tag{3.26}$$

where

$$\hat{\tau} = \frac{\hat{\varrho} - 1}{\hat{\sigma}_{\varrho}} \tag{3.27}$$

$$C(\hat{\tau}) = \begin{cases} -\hat{\tau} & \text{if} \quad \hat{\tau} > \tau_{pct} \\ I_p T^{-1}\hat{\tau} - (1+r)\left[\hat{\tau} + c_2(\hat{\tau}+a)\right]^{-1} & \text{if} \quad -a < \hat{\tau} \leq \tau_{pct} \\ I_p T^{-1}\hat{\tau} - (1+r)\hat{\tau}^{-1} & \text{if} \quad -c_1^{1/2} < \hat{\tau} \leq -a \\ 0 & \text{if} \quad \hat{\tau} \leq -c_1^{1/2} \end{cases} \tag{3.28}$$

$$c_1 = (1+r)T \tag{3.29}$$

$$c_2 = \left[(1+r)T - \tau_{pct}^2(I_p + T)\right]\left[\tau_{pct}(a+\tau_{pct})(I_p+T)\right]^{-1} \tag{3.30}$$

$$I_p = \frac{p+1}{2} \tag{3.31}$$

$\hat{\sigma}_{\varrho}$ is the standard deviation of $\hat{\varrho}$. $\tau_{pct}$ represents a percentile of the limit distribution of $\hat{\tau}$, and the study uses $\tau_{0.99}$ for the unknown break dates. The values for $\tau_{0.99}$ could be found in Tables IV to VI of Perron (1989). $p$ refers to the order of the autoregression of the noise component, which is specified to be 1 above and could be a larger value. Based on simulation results, $a = 10$.

4. Truncation is applied:

$$\hat{\varrho}_{MS} = \begin{cases} \hat{\varrho}_M & \text{if} \quad |\hat{\varrho}_M - 1| > T^{-1/2} \\ \\ 1 & \text{if} \quad |\hat{\varrho}_M - 1| \leq T^{-1/2} \end{cases} \tag{3.32}$$

The above equation implies that if the distance of $\hat{\varrho}_M$ from 1 is less than $T^{-\delta}$ ($\delta$ is determined to be 1/2 by simulation analysis), it is assigned a value of 1.

5. The test statistic is computed. Based on the nature of the error component ($I(0)$ or $I(1)$) and the type of the model selected (Model 1, 2, or 3), the form of the Wald statistic (Andrews and Ploberger, 1994) changes.

- **I(0) noise component**
  For all models, the Wald statistic ($W_{RQF}$) is calculated by Equation 3.33. RQF stands for robust quasi-feasible GLS.

$$W_{RQF}(\lambda_1) = \big[R(\widetilde{\Psi} - \Psi)\big]' \big[\hat{h_v} R(X'X)^{-1} R'\big]^{-1} \big[R(\widetilde{\Psi} - \Psi)\big] \tag{3.33}$$

  where $\widetilde{\Psi}$ is estimated by applying the quasi-FGLS approach to Equation 3.14 assuming that the error component is an AR(1) process. In other words, $\widetilde{\Psi}$ is computed using the OLS approach in the following regression:

$$(1 - \widetilde{\varrho}_{MS}\, L) y_t = (1 - \widetilde{\varrho}_{MS}\, L) x_t' \Psi + (1 - \widetilde{\varrho}_{MS}\, L) u_t \tag{3.34}$$

  $\hat{h_v}$ is obtained from Equation 3.35.

$$\hat{h}_v = (T - k)^{-1} \sum_{t=k+1}^{T} \hat{e}_{tk}^2 \tag{3.35}$$

  $\hat{e_{tk}}$ denotes the OLS residuals estimated using the following regression:

$$y_t - \widetilde{\varrho}_{MS}\, y_{t-1} = x_t' \Psi^* + \sum_{i=1}^{k} \rho_i \Delta y_{t-i} + e_{tk} \tag{3.36}$$

  where $\Psi^*$ replaces $\Psi$ as a result of a number of modifications indicated in the original study.

- **I(1) noise component**

**Model 2**

For Model 2, $W_{RQF}(\lambda_1)$ is calculated by Equation 3.33 with the difference that $\hat{h}_v$ is computed as follows:

$$\hat{v}_t = \sum_{i=1}^{k} \xi_i \hat{v}_{t-i} + e_{tk}, \quad \hat{\xi}(L) = (1 - \hat{\xi}_1 L - \ldots - \hat{\xi}_k L^k) \tag{3.37}$$

$$\hat{h}_v = \frac{(T-k)^{-1} \sum_{t=k+1}^{T} \hat{e}_{tk}^2}{\hat{\xi}(1)^2} \tag{3.38}$$

**Models 1 and 3**

In this case, $\widetilde{\Psi}$ has been modified to $\widetilde{\Psi}^*$. The reader is referred to the original paper for the details and reasons of this change.

$$W^*_{RQF}(\lambda_1) = \big[R(\widetilde{\Psi}^* - \Psi)\big]' \big[\hat{h_v} R(X'X)^{-1} R'\big]^{-1} \big[R(\widetilde{\Psi}^* - \Psi)\big] \tag{3.39}$$

Whether the test statistic of $I(0)$ or $I(1)$ should be used depends on the value of $\widetilde{\varrho}_{MS}$.

6. If the break time is unknown, the test statistic should be computed for all the break date candidates $(\epsilon T, \ldots, (1-\epsilon)T)$. According to Table 2 of Perron and Yabu (2009b), $\epsilon$ could take one of the values in [0.01, 0.05, 0.1, 0.15, 0.25].

7. Three functionals of the Wald test are available: mean, exp, and sup. However, in the case of unknown break dates, only the exp functional of the Wald test leads to almost equal limit distributions for both cases of $I(0)$ and $I(1)$. The exp functional is calculated by Equation 3.40.

$$Exp{-}Wald = \log\big[T^{-1} \sum \exp\big(1/2\, W(\lambda_1')\big)\big] \tag{3.40}$$

where $W(\lambda_1')$ denotes the test statistic computed as described in Step 5 using one of the permissible break dates. The sum is obtained by repeating this calculation across all the break dates.

8. The value of the test statistic is compared to the critical values in Table 1 of Perron and Yabu (2009b) to see whether the break in the trend function is significant.

The break time is approximated using the procedure described by Kim and Perron (2009). The break date is estimated by minimizing the sum of squared residuals of Regression 5 (additive outlier (Aout) models) or Regression 7 (innovational outlier (IO) models) considering all permissible break dates. Regression 5 and Regression 7 can be found in Kim and Perron (2009). Using IO models requires fixing the range of the transition period. Starting from 1, the transition period is increased until the estimates of break date and model parameters become stable. The transition period of interest is the smallest value after which the estimates do not change significantly. In the case of AO models, the transition period is assumed to be 0.

**Note:** Throughout this thesis, the trend shift detection technique, described in this section, is referred to as the 'KPY' method after Kim, Perron, and Yabu (Kim and Perron, 2009; Perron and Yabu, 2009b).

## 3.5 Trend Analysis

It is explained in Section 2.3.1 why it is preferred to base the trend analysis on the non-parametric MK test in this study. In this section, first, the original MK test is described. The reader is referred to Helsel and Hirsch (2002) for more details. Then, the modifications applied to the MK test including the TFPW approach are explained according to Burn et al. (2004). As indicated earlier, trends detected locally may not be significant globally. Therefore, the rest of this section focuses on a bootstrap technique to test the global significance of the trends.

### 3.5.1 Non-parametric Mann-Kendall Test

In order to measure the monotonic (linear and non-linear) correlation between independent ($x$) and dependent ($y$) variables, the two-sided hypothesis test shown below is conducted. $\tau$ represents Kendall's tau, which measures the strength of the monotonic relationship. $\tau$ is a rank-based parameter; hence, it is resistant against outliers, non-normally distributed

values, and censored data points. Furthermore, P-values estimated based on the large-sample approximations of $\tau$ are very close to the true P-values even if the sample size is small (Helsel and Hirsch, 2002).

$$\begin{cases} \mathrm{H}_0 : \text{There is no correlation between } x \text{ and } y \ (\tau = 0) \\ \mathrm{H}_1 : x \text{ and } y \text{ are correlated } (\tau \neq 0) \end{cases}$$

$\tau$ is computed as follows:

$$\tau = \frac{S}{n(n-1)/2} \tag{3.41}$$

where $n$ is the number of observations. $S$ is calculated using the following formula:

$$S = P - M \tag{3.42}$$

In order to compute $S$, $(x, y)$ pairs are arranged in ascending order of $x$. $P$ represents the number of $(x, y)$ pairs where $y$ increases as $x$ increases ('concordant pairs'), and $M$ is the number of $(x, y)$ pairs with increasing $x$ while $y$ decreases ('discordant pairs').

Equations 3.41 and 3.42 explain the above-indicated null hypothesis. If $x$ and $y$ are independent, the number of concordant pairs is almost the same as that of discordant pairs (i.e., $\tau = 0$). If there exists a negative correlation between $x$ and $y$, the number of concordant pairs is expected to be less than discordant pairs ($\tau < 0$), and vice versa.

To test the significance of $\tau$, the permutation approach is adopted in this study for $n \leq 10$. The distribution of the test statistics under the null hypothesis is obtained by calculating all possible values of $S$ with a given number of $(x, y)$ pairs for $n \leq 10$. For the values of $n > 10$, the distribution of the test statistics could be approximated by a normal distribution. The test statistic for a large sample is computed as follows:

$$Z_s = \begin{cases} \dfrac{S-1}{\sigma_s} & \text{if } S > 0 \\ 0 & \text{if } S = 0 \\ \dfrac{S+1}{\sigma_s} & \text{if } S < 0 \end{cases} \tag{3.43}$$

where

$$\sigma_s = \sqrt{(n/18)(n-1)(2n+5)} \tag{3.44}$$

If the value of $Z_s$ falls within the rejection range of the standard normal distribution considering the significance level of $\alpha$ (i.e., $|Z_s| > Z_{critical}$), the null hypothesis of $\tau = 0$ is rejected, and it is concluded that $x$ and $y$ are correlated.

In the case of large sample approximation, if there are tied $x$ or $y$ values, the value of $\sigma_s$ should be modified as follow:

$$\sigma_s = \sqrt{\frac{n(n-1)(2n+5) - \sum_{i=1}^{n} k_i(i)(i-1)(2i+5)}{18}} \tag{3.45}$$

where $i$ is the extent of ties. $k_i$ is the number of ties with the extent of $i$ in the entire data set.

Mann (1945) used Kendall's $\tau$ to test the significance of the monotonic trend when the independent variable is time. As indicated earlier in Section 2.3.1, in order to obtain correct P-values, the data should not be serially correlated.

If it is assumed that the monotonic relationship between $y$ and $x$ is linear, a robust non-parametric line could be used to represent this relationship. In contrast to the OLS regression, the significance of the linear dependence between $x$ and $y$ (i.e., whether the slope is significantly different from 0) is not affected by the non-normal behaviour of residuals or the presence of outliers. To estimate the slope of this non-parametric line, Theil's approach is applied here:

$$\hat{y} = \hat{b}_0 + \hat{b}_1 x \tag{3.46}$$

where

$$\hat{b}_1 = \text{median } \frac{(y_j - y_i)}{(x_j - x_i)} \quad \text{for all } i < j \tag{3.47}$$

$$i = 1, \ldots, (n-1) \text{ and } j = 2, \ldots, n$$

and

$$\hat{b}_0 = y_{med} - (\hat{b}_1)(x_{med}) \tag{3.48}$$

where $y_{med}$ and $x_{med}$ are the medians of $y$ and $x$ data sets, respectively.

### 3.5.2 Modified TFPW Approach

As indicated, one of the key assumptions of the MK test is zero serial correlation. However, most of the temporal observations are serially correlated. Based on the sequence of studies devoted to solving this problem (described in Section 2.3.1), a modified version of the TFPW technique developed by Yue and Pilon (2003) is used in this study. The steps involved in this approach are as follows (more details can be found in Burn et al. (2004)):

1. The monotonic trend of data is removed using the following formula:

$$f_t = y_t - \hat{b}_1 t \tag{3.49}$$

   where $y$ is the response variable at time $t$, and $f_t$ represents detrended observations.

2. The lag-1 serial correlation coefficient ($\rho_1$) for the detrended data is computed. If the serial correlation is insignificant at the significance level of $\alpha$, the procedure described in the previous section (Section 3.5.1) is applied to test the trend significance and evaluate slope. However, if $\rho_1$ is significant, the algorithm proceeds with the pre-whitening step:

$$f'_t = f_t - \rho_1 f_{t-1} \tag{3.50}$$

3. The monotonic trend removed in Step 1 is added back to the detrended and pre-whitened series ($f'_t$):

$$f''_t = f'_t + \hat{b}_1 t \tag{3.51}$$

4. The MK test explained in Section 3.5.1 is applied to $f''_t$.

### 3.5.3 Field Significance

To investigate whether the percentage of observed locally significant trends is high enough to consider them globally significant, a field significance test is used in this study. To determine the critical values for the distribution of the percentage of the MK tests that are expected to reveal significant trends at the local significance level of $\alpha$, a bootstrap algorithm is applied here. The analysis steps are summarized below, and the detailed description of the algorithm can be found in Cunderlik and Burn (2002), Burn and Hag Elnur (2002), and Burn et al. (2004).

1. A random vector of years is constructed. The size of this vector is equal to the total number of years the data span. The years are selected from the range permissible in the study, and repeated entries are allowed.

2. A station-year matrix is constructed. Each column of this matrix includes all station values that correspond to a year from the above vector. Columns are entered into this matrix in the order specified in the above vector. If no information is available for a station, it is left blank (NaN).

   **Note:** The random selection of years in Step 1 eliminates any temporal trend in the data set; however, since the information of all stations is included for a given year, the cross correlations between stations remain intact. Therefore, the percentage distribution found following this procedure is influenced by existing cross-correlations.

3. Using the MK test specified in Section 3.5.1, the trend significance of each station is tested at the local significance level of $\alpha$; this implies that the MK test is applied to each row of the big matrix constructed in Step 2 excluding all NaN values. Then, the percentage of stations that exhibit locally significant trend is recorded. It should be noted that if the number of remaining data points after removing NaN values is less than 3, the MK test is not applicable. In this case, these stations are excluded, and the total number of stations is adjusted accordingly.

4. Steps 1 to 3 are repeated NS times. NS is a number which is specified by the analyst. In this study, it is equal to 10,000. By repeating the above-indicated steps NS times, the distribution of the percentage of tests that result in locally significant trends at the significance level of $\alpha$ is obtained.

5. The test statistic is the percentage of the stations with significant trends in the study area. If this value falls in the rejection region of the distribution found above, it is concluded that the number of locally significant trends is so high that it could not have occurred by chance.

In order to find the distribution and critical values of the percentage of stations showing significant increasing or decreasing trends, some additional steps are required. In Step 3, in addition to testing the significance of trends, Theil's slope estimates are computed, and the percentage of locations with significant trends and positive or negative slopes is

obtained. In Step 4, the distribution and critical values for the percentage of locations with significant increasing or decreasing trends are found.

## 3.6 Non-parametric Comparison Techniques

As explained in the beginning of this chapter, there are 3 different techniques employed to examine the time series in this study. These methods follow different algorithms, and the question arises as to how the results of them can be compared. Classical tests, such as t-test and F-test, are parametric techniques that assume that data are random and normally distributed. In practice and particularly with environmental data, it is really difficult to justify the assumptions of parametric methods; hence, non-parametric or distribution-free techniques are preferred, which require no assumption regarding the underlying distribution of data. Among non-parametric tests, 'Wilcoxon signed-rank test for paired observations' and 'Wilcoxon rank-sum test' are the most compatible methods with the comparison goals of this study. The methodologies are described in this section (for more details, refer to Miller (1986), Glantz (2002), Gibbons and Chakraborti (2003), and Montgomery and Runger (2003)); however, the clarification on why these techniques are the most suitable ones is presented in Chapter 5, after describing the study area and obtaining analysis results.

### 3.6.1 Wilcoxon Signed-Rank Test for Paired Observations

Let $Y_{i1}$ and $Y_{i2}$ ($i = 1, \ldots, n$ and $n$ is the number of paired observations) be a collection of paired observations, and $D_i = Y_{i1} - Y_{i2}$. $D_i$ is the difference between the results of two models at the corresponding station $i$. $\mu_1$ and $\mu_2$ are the population means of $Y_1$ and $Y_2$, respectively. The one-sided and two-sided hypothesis tests are as follows:

$$\begin{cases} \mathrm{H}_0 : \mu_1 = \mu_2 \quad \mu_D = 0 \\ \mathrm{H}_1 : \mu_1 \neq \mu_2 \quad \mu_D \neq 0 \\ \text{or} \\ \mathrm{H}_1 : \mu_1 > \mu_2 \quad \mu_D > 0 \\ \text{or} \\ \mathrm{H}_1 : \mu_1 < \mu_2 \quad \mu_D < 0 \end{cases}$$

The assumptions of the Wilcoxon signed-rank test are as follows:

1. This technique is based on ranks. Therefore, there is no restriction on the nature of the underlying population of $Y_1$ and $Y_2$ except that the distributions should be continuous and should differ only with respect to their means; i.e., the distributions have similar shapes. The latter is required since it guarantees that the distribution of $D_i$ is symmetric. In the Wilcoxon signed-rank test, the input sample to the test (the sample which is ranked and receives signs) should always be from a continuous and symmetric population.

   **Note:** Since it is assumed that the input population is symmetric, no tie is expected. However, ties do occur in practice, and how to handle ties is discussed in Section 3.6.1.1.

2. The observations within each group are independent. This means that each pair (and subsequently the difference between the paired observations) is independent of the other pairs.

3. The level of measurement should at least be ordinal. This implies that phrases such as 'less than' should be meaningful in the scale of measurement.

The steps in the analysis are as described below:

1. $D_i$'s are computed.

2. The absolute values of these differences are ranked in ascending order (refer to Section 3.6.1.1 for the discussion on how to rank the ties).

3. The sign of the corresponding difference is attached to each rank.

4. The signed ranks are summed to obtain the test statistic $W_1$. If $Y_1$ and $Y_2$ are not statistically different, $W_1$ should be close to zero. This implies that the sum of the positive ranks is similar to the sum of the negative ranks.

5. The distribution of $W_1$ is found by the permutation approach applied to signed ranks. This implies that all possible values of $W_1$ are computed by considering all the combinations of signed ranks for the given ranks and sample size.

If the sample size is larger than 20, the distribution of $W_1$ can be closely approximated with a normal distribution:

$$z_{W_1} = \frac{(W_1 - \mu_{W_1}) \pm 0.5}{\sigma_{W_1}} \tag{3.52}$$

where $\mu_{W_1} = 0$, and $\sigma_{W_1}$ could be calculated following Glantz (2002):

$$\sigma_{W_1} = \sqrt{\frac{(n)(n+1)(2n+1)}{6} - \sum_i \frac{(k_i - 1)(k_i)(k_i + 1)}{12}} \tag{3.53}$$

In Equation 3.53, $k_i$ is the number of ties with the extent of $i$ within the entire data set. $\pm 0.5$ in Equation 3.52 is for the continuity correction. Since $W_1$ (a discrete value) is approximated using a continuous distribution (normal distribution), the continuity correction should apply: $-0.5$ if $W_1 > \mu_{W_1}$ and $+0.5$ if $W_1 < \mu_{W_1}$.

6. The probability of obtaining a test statistic equal to or larger than $W_1$ associated with the sample under study is calculated. This probability is then compared to the probability of the critical region. If it is equal to or less than the probability of the rejection region, the null hypothesis is rejected.

**Note:** $W_1$ could also be calculated as the sum of positive or negative signed ranks. One should be cautious to select a correct distribution and critical values for $W_1$ in each case.

#### 3.6.1.1 Ties in the Wilcoxon Signed-Rank Test

There are two types of ties (Miller, 1986):

1. $D_i$'s are tied in absolute values.
2. The values of $Y_{1i}$ and $Y_{2i}$ in the specified pair $i$ are exactly the same. Therefore, $D_i = 0$.

Below, each of the above cases is discussed in detail:

1. If the observations are tied in absolute values, the average of the ranks is assigned to each of the differences with the same absolute magnitude. This means that the ranks that would be assigned to differences if they were slightly different from each other are averaged, and each of these ties receives the average rank. Pratt (1959) calls this method 'average rank procedure'. The study emphasizes that in this case, the distribution of the test statistics changes; i.e., one cannot use the ordinary Wilcoxon critical values when using the average rank procedure, and the permutation approach should be based on the averaged ranks.

2. Traditionally, the way to handle 0's is to drop them from the analysis and adjust the sample size. Pratt (1959) calls this approach 'reduced sample procedure'. This is due to the fact that 0's provide no information about whether the variable under study has increased or decreased. Miller (1986) calls this approach 'conditional approach' since 0's are excluded, and the question of $P\big[(D_i > 0 \,|\, D_i \neq 0)$ or $(D_i < 0 \,|\, D_i \neq 0)\big]$ is considered. Miller (1986) also emphasizes that this could be a worthless question to ask if the number of 0's is large compared to the sample size. If the large proportion of 0's occurs, the difference between $Y_1$ and $Y_2$ may be unimportant.

   A more conservative approach is proposed by Pratt (1959) to handle 0's. The procedure is described below:

   (a) The absolute values of all observations including 0's are ranked in ascending order.

   (b) The ranks of 0's are dropped without changing the rest of the ranks, and the sample size is adjusted.

   (c) The remaining ranks receive the corresponding signs.

   (d) $W_1$ is calculated using the signed ranks.

   **Note:** In the permutation approach, all possible signed-rank combinations of the remaining ranks are considered, and the total number of observations is equal to the number of observations after dropping 0's.

#### 3.6.1.2 Notes on Using the Wilcoxon Signed-Rank Test

Modarres et al. (2005) refer to several cautionary notes on the use of the Wilcoxon signed-rank test to analyse the environmental data:

- As indicated above, the null hypothesis tests whether the means of $Y_1$ and $Y_2$ are the same. In reality, however, it tests whether the PDF's of them are the same. This clarifies the necessity of Assumption 1 of the test. If the PDF's differ in any parameter other than location, the use of the Wilcoxon signed-rank test to check the equality of means may not generate correct results. This is due to the fact that even in the case of equal means, the test would detect differences between other parameters, such as skewnesses, variances, etc.
- When the observations within each group are correlated, the Wilcoxon signed-rank test becomes very conservative in rejecting the null hypothesis.

### 3.6.2 Wilcoxon Rank-Sum Test

Let $Y_1$ and $Y_2$ be two independent continuous populations with means $\mu_1$ and $\mu_2$, respectively. The populations of $Y_1$ and $Y_2$ should have the same shapes and parameters and should only differ in their means. Now, assume $Y_{11}, Y_{12}, ..., Y_{1n_1}$ and $Y_{21}, Y_{22}, ..., Y_{2n_2}$ are random samples selected from $Y_1$ and $Y_2$, respectively, with sizes $n_1 \leq n_2$. The hypothesis test is the same as that of the Wilcoxon signed-rank test. In order to perform the hypothesis testing, the steps below are followed:

1. All $n_1 + n_2$ observations are ranked in ascending order. Ties receive the average of the ranks that they would have if they were slightly different.
2. The test statistic ($W_2$) is the sum of the ranks of the group with smaller size. If $n_1 = n_2$, the sum of the ranks of either of two samples can be selected as the test statistic.
3. In order to find the distribution of the test statistics, all possible combinations of the ranks of the smaller group are considered.
4. If the size of the small sample is larger than 8, the distribution of the test statistics is very similar to the normal distribution with mean

$$\mu_{W_2} = \frac{n_S(n_S + n_B + 1)}{2} \tag{3.54}$$

and standard deviation

$$\sigma_{W_2} = \sqrt{\frac{n_S n_B (n_S + n_B + 1)}{12}} \tag{3.55}$$

where $n_S$ is the size of the smaller sample, and $n_B$ stands for the size of the larger sample.

**Note:** When there are identical observations, $\sigma_{W_2}$ should be adjusted for the ties:

$$\sigma_{W_2} = \sqrt{\frac{n_S n_B (N+1)}{12} - \frac{n_S n_B}{12N(N-1)} \sum_i (k_i - 1)(k_i)(k_i + 1)} \tag{3.56}$$

where $N = n_S + n_B$, and $k_i$ denotes the number of ties with the extent of $i$ within the entire data set.

Finally, the test statistic for the normal distribution is evaluated as follows:

$$z_{W_2} = \frac{W_2 - \mu_{W_2}}{\sigma_{W_2}} \tag{3.57}$$

Similar to Equation 3.52, Equation 3.57 should be corrected for continuity:

$$z_{W_2} = \frac{|W_2 - \mu_{W_2}| - 0.5}{\sigma_{W_2}} \tag{3.58}$$

5. If the test statistic falls in the rejection area of the distribution of rank sums, it is concluded that the two samples are statistically different.

# Chapter 4

# Study Area and Data Description

## 4.1 Introduction

Like all research projects, the matters of greatest importance are the data required to answer the proposed questions as well as the sources of such data. Therefore, prior to presenting the analysis results, Chapter 4 is devoted to introducing the data used for the study and giving an overview of the steps followed in the assessment of the final database to fulfil the research goals. Section 4.2 describes how the data are collected, homogenized and adjusted to be the indicators of the monthly climate variations. In Section 4.3, it is explained which temporal and spatial subset of the large data set, introduced in Section 4.2, best suits the objectives of this research. An overview of the procedure of the data analysis is given in Section 4.4.

## 4.2 Data Description

### 4.2.1 Data Sources

Data are obtained from the Climate Research Unit (CRU), at the University of East Anglia (University of East Anglia Climate Research Unit, 2011). In this study, the gridded CRU TS 3.1 data set is used. This data set includes month-by-month variation in nine climate

variables that span the 1901-2009 period. The spatial resolution of the data is 0.5° × 0.5° (latitude × longitude), and the data set covers the land surface throughout the entire globe except Antarctic; i.e. 179.75° W to 179.75° E and 89.75° S to 89.75° N. This spatial resolution of data may be unsuitable for small regions; however, for a large region under study like the Northern Hemisphere or the entire globe, it provides sufficient information. In this project, 'tmp' (Monthly Average of the Daily Mean Temperature) from the CRU TS 3.1 data set is used to achieve the analysis goals. Prior to proceeding to describe the data processing methodology, it should be noted that at the time of writing this thesis, the paper on the CRU TS 3.0 data set (and CRU TS 3.1 data set which entirely supersedes CRU TS 3.0) is in preparation; however, according to BADC (2011):

*"For CRU TS 3.0: In preparation. But in the meantime, Mitchell and Jones, 2005 can be used as background information for TS 3.0. The major difference between the CRU TS 2.1 and CRU TS 3.0 processes is that no new homogenization is explicitly performed in the latter. Existing homogenizations in the underlying data sets, and homogenizations performed by national meteorological agencies prior to releasing their station data, are incorporated."*

Based on the above quote, this thesis refers to Mitchell and Jones (2005) to understand underlying techniques adopted in data processing.

More than 4000 weather stations distributed around the world have contributed to the construction of the CRU TS 3.1 gridded data set. It should be noted that the number of stations has increased over time; the earlier years of the records included fewer stations. Therefore, the gridded estimates for the early parts of the records are more uncertain than those for the later parts. The data have been obtained and updated from global network of meteorological stations rather than satellites due to the following two reasons (Mitchell and Jones, 2005):

- There are no satellite data available prior to 1970.
- The focus of the study is on the data at the surface rather than the data measured through the depth of the atmosphere by satellites.

To extend the spatial and temporal coverage of data, information from several sources is merged into a single database. Since consistently new information is added to this

database, and the number of sources increases by time, quality assurance (QA) checks should always be performed to maintain the quality of data.

QA checks are performed on each of the data sources. The QA procedure checks for problems in the data sets such as simultaneous zeros, impossible values, duplication of data, etc. The complete list of 'Data Problems' and the 'Description of Checks' can be found in Menne et al. (2009). After different data sources are merged into a single database, as indicated in Menne et al. (2009), additional climatological and spatial QA checks are performed.

Although the CRU TS 3.1 date set includes several variables, only the temperature data as a subset of CRU TS 3.1 are analysed in this study. The primary source for temperature is Jones and Moberg (2003). As indicated in Mitchell and Jones (2005), the sources are incorporated into the database in the order presented in Table 4.1 . This implies that the sources with higher reliability should be merged in priority order.

### 4.2.2 Data Homogenization

As described in Section 2.3.2, factors such as changes in the time of observation, minor station relocations, and changes in instrumentation introduce artificial inhomogeneities to time series. The purpose of the homogenization process is to remove all the artificial discontinuities indicated above. The investigation of the potential causes of inhomogeneities is discussed in detail in Menne et al. (2009) and is summarized below:

1. **Inhomogeneities caused by the variation in the daily recording schedule of observations:**

   The time of observation for most of the stations in the United States, for example, has switched from sunset to morning in mid $20^{\text{th}}$ century. This has led to a slight positive bias in the data from the first half of the $20^{\text{th}}$ century. To adjust the time of observation bias, documentation and metadata of changes are required. Karl et al. (1986) propose a technique for the adjustment of time of observation bias. The effect of the adjustment of the time of observation bias on the data is calculated by constructing a difference series as indicated below. For more details, refer to Menne et al. (2009).

**Table 4.1:** Data sources integrated into the CRU TS database selected for this study. The primary source for temperature is Jones and Moberg (2003). The sources are incorporated into the database in the order presented in the table (Mitchell and Jones, 2005).

| Reference | Period |
|---|---|
| Jones and Moberg (2003) | 1701 - 2002 |
| Peterson et al. (1998) | 1702 - 2001 |
| New et al. (2000) | 1901 - 1999 |
| Hahn and Warren (1999) | 1971 - 1996 |
| William Angel, Personal Communication with Mitchell and Jones (2005) | 1990 - 2002 |
| UK Met Office, Personal Communication with Mitchell and Jones (2005) | 1994 - 2002 |

The anomaly of the adjusted monthly temperature of each station from its 1961-1990 average is calculated. The anomalies are then interpolated to obtain the desired resolution of the latitude-longitude grids. Following this step, the area weighted average of anomalies of each year in a given month is calculated for the entire region. The same process applies to the unadjusted data. Finally, the difference series is calculated as the difference between the anomalies from adjusted and unadjusted data. The change in the mean yearly temperature relative to the raw values reported during the change in the recording schedule could be inferred from the difference series. This helps understand whether the adjustment of the time of observation bias has increased or decreased the overall trend.

2. **Inhomogeneities caused by other changes in data collection:**

   As indicated above, there are other sources of artificial shifts in the climate time series such as relocating stations or changes in instrumentation. To adjust the bias associated with these changes, one traditionally used procedure is the investigation of the documented changes in the station history (Karl and Williams Jr., 1987).

The drawback of this method is that it is unable to detect the undocumented discontinuities. There is another method for homogenization proposed by Menne and Williams Jr. (2009). This method is based on the pairwise comparison of time series, hence, is capable of detecting both documented and undocumented inhomogeneities. The approach compares all possible (or numerous) combinations of time series in the region. As a result of this comparison, abrupt changes (inhomogeneities) in one station are detected compared to many other stations. The technique generates much more reliable results when there are a lot of neighbouring stations available for a target station to be compared to.

Mitchell and Jones (2005) apply a slightly modified version of the above-indicated homogenization technique (Menne and Williams Jr., 2009) to CRU TS database. The methodology used in Mitchell and Jones (2005) is summarized here. The reader is referred to Mitchell and Jones (2005) for the detailed description of the method and the differences between steps followed in Mitchell and Jones (2005) and Menne and Williams Jr. (2009).

The homogenization is performed by comparing a candidate series to a reference series constructed by examining the neighbouring series and using the correlation method. It is worth noting that the algorithm is capable of detecting both abrupt and gradual discontinuities; however, inhomogeneities such as urbanization, which are widespread and have led to the gradual change in the historical data of stations, are not eliminated. The detection of these embedded inhomogeneities is not critical. This is due to the fact that the data are supposed to exhibit long-term monthly or yearly changes in temperature at the earth's surface, not changes experienced only due to GHG emissions. Below, the iterative algorithm of homogenization is explained:

**Step 1** All the stations could be used to construct reference series for the detection of inhomogeneities. Reference series should be created for each month, rather than the entire year. The reason is that some of the discontinuities could be cancelled out in the annual mean since they have opposite effects during different seasons. The attempt is to create a reference series for a given candidate using the records from several stations (parallels); using more than one station to build a reference series for a target station has the advantage of reducing the effect of existing discontinuities in each of the parallels, on the final reference series. Mitchell and Jones (2005) set the minimum and maximum number of parallels to

2 and 5, respectively, and each calendar month could have a different number of parallels. The lengths of data records vary among stations; therefore, to identify neighbours to be used as parallels, the first task is to replace any missing value in the historical records of the surrounding stations. The process of finding best estimates for missing values is described in detail by Mitchell and Jones (2005). Filling in any gap is necessary since difference series are used in the next step to calculate the correlation between each candidate and the corresponding reference series. A difference series is the year to year change in temperature ($\frac{dT}{dt}$). The reason for working with difference series instead of absolute values is that in the correlation calculation, the effect of any discontinuity in original series is shown as the inhomogeneity occurred instantaneously, in one year. When using difference series, missing values will be detected as discontinuities. Therefore, missing values should be replaced prior to the next step. Furthermore, it should be emphasized that the treatment of missing values in this step is for the sole reason of creating reference series.

**Step 2** The correlation coefficient between the difference series of a candidate station and each of its neighbouring difference series is calculated. If it is at least 0.4, the neighbouring difference series is selected as one of the candidates to be selected as a parallel in Step 3. Due to the large size of data and insignificant effect of remote stations on a given candidate station, each target station is compared to only the closest 100 stations located within the correlation decay distance (1200 km) from it. The weight attached to each neighbouring station is the square of its correlation coefficient with the candidate station.

**Step 3** To select a set of neighbours to create a reference series, an iterative algorithm is adopted. The algorithm is depicted as two flowcharts in Mitchell and Jones (2005). After the parallels are selected for a given station and month, they are averaged into a single reference series using their weights.

**Step 4** To detect the discontinuities of each candidate station, the difference between the time series of the candidate station and the corresponding reference series is calculated. For each station, 12 time series of differences, one for each month, should be obtained. The residual sum of squares (RSS) technique is used to detect the most probable year as the time of break among all 12 months. The reader is referred to Easterling and Peterson (1995) and Mitchell and Jones

(2005) for more details on the RSS technique. After the discontinuity is confirmed for a given station, a correction factor is calculated to eliminate the discontinuities of all months.

**Step 5** After the data of a station is adjusted for the detected inhomogeneity, that station is integrated into the final database. When merging one station into the final database, if there is already a record associated with the station, two records should be compared to make certain that the longest possible record is provided for that station, and there is no duplication of data.

Steps 1 to 5 are repeated for all stations. Each time, to construct the reference series for a station, any station with the following characteristics is allowed to be included in the set of potential parallels:

- It has been corrected for inhomogeneities and added to the final data base.
- No inhomogeneity is detected in the previous iterations.
- The record associated with the station could be divided into independent sections using the time of potential shifts in the time series.

Mitchell and Jones (2005) name these stations 'trusted' stations. Following steps 1 to 5 and using trusted stations, the construction of reference series and the subsequent comparisons to candidate stations continue until no more reference series could be created. At this point, the 'omissions criterion' ($\lambda$) which was set to zero for the first iteration is increased (5 years at each iteration). $\lambda$ is defined as the number of years of the candidate station for which there is no value in the corresponding reference series. The process ends when $\lambda$ is larger than the length of the longest station that remains unchecked, and all the remaining unchecked stations are added to the final database. There are two reasons for not excluding these unchecked stations:

- As could be inferred from steps 1 to 5, homogenization requires relatively long records. Therefore, all the recent stations, specially the ones from William Angel and UK Met Office (refer to Table 4.1), are added to the final database without any homogenization.
- According to Mitchell and Jones (2005), most of the unchecked stations are from the areas or time intervals with low density of information. Therefore, for the

purpose of gridding, including these unhomogenized stations is preferred to not having any information at all.

### 4.2.3 Data Grids

The data from stations should be interpolated onto a continuous surface; this continuous surface is divided into boxes with the resolution that suits the research objectives or the extent of the region under study. For data gridding, first, the time series of the stations are converted into anomalies from a base period (in this case, 1961-1990). These anomalies (instead of absolute values) are interpolated to create grids of information. Normals are gridded in the same way. The anomaly associated with a specific grid is converted to an absolute value by combining it with the normal associated with that grid. For more details on the interpolation techniques, refer to New et al. (2000) and Mitchell and Jones (2005). Stations with some missing values are included in the process as well; the missing values of these stations are estimated by interpolating the anomalies (not the absolute values) of the adjacent stations. There are two further steps to take prior to interpolating anomalies onto a continuous surface:

1. Extreme values (i.e., data that are larger than three standard deviations from the mean of the series) are excluded from the time series.
2. All the stations located within 8 (km) from a given station are integrated into a single station. This task is mainly performed to prevent using duplicate values in the interpolation process.

It should be noted that since normals affect all the values in the time series, they should be calculated accurately. In the study by Jones and Moberg (2003), any station with more than 25% of the values missing in the base period (1961-1990) is excluded, and the normal of that station is not used in creating grids. To avoid the loss of information imposed by this procedure, Mitchell and Jones (2005) build reference series for such stations (similar to the homogenization method); the 1961-1990 means of the reference series are used as the normals for the corresponding target stations.

## 4.3 Study Area

As indicated in Section 1.1, the goal of this study is to find locations whose temperature has permanently changed sign and become positive in the time period of 1901-2009 during JFM or MAM.

As mentioned earlier in Section 4.2.1, the CRU TS 3.1 data set includes month-by-month variation in nine climate variables which span the 1901-2009 period. Due to the specific objective of this thesis, 'tmp' (Monthly Average of the Daily Mean Temperature) is the only variable selected from the data set for the analysis. The CRU TS 3.1 data set covers the land surface throughout the entire globe except Antarctic at relatively high resolution: $0.5^\circ \times 0.5^\circ$ (refer to Section 4.2.1 for more details). It is worth noting again that the number of weather stations contributing to the construction of the CRU TS 3.1 data set has increased over time; the earlier years of the records included fewer stations. Therefore, the gridded estimates for the early parts of the records are more uncertain than those for the later parts. This thesis only investigates the grid cells located in the extra-tropical Northern Hemisphere. The study area spans from 20.25°N to 89.75°N and 179.75°E to 179.75°W and includes a total of 46,224 grid cells. The following steps are employed to construct the final database for this study:

1. The winter temperature for each location is evaluated as the average temperature of the three months of January, February, and March in the corresponding year. The spring temperature is computed as the mean temperature of March, April, and May.

2. The area that comprises grid cells whose temperature changes sign and permanently moves above 0°C is referred to as '*transition area*'. To identify the *transition area*, the first step is to exclude all locations where the original temperature data do not change sign during the entire time period of 1901-2009 (Rule 1 of *transition area*). If the original data points of a time series are all above or below 0°C, this implies that using any modelling technique, the modelled series would not cross the 0°C line. Therefore, Rule 1 of *transition area* ensures that only locations are kept that have at least one sign change in temperature over 109 years. Following this step, the number of grid cells reduces to 6206 for winter (JFM) and 9842 for spring (MAM).

3. As indicated, from the above set, the study is concerned only with the locations that cross the 0°C line in the positive direction (i.e., from below freezing to above freezing)

and remain above it. To fulfill the above requirements, Rule 2 of *transition area* is defined as follows: the database constructed as the result of Rule 1 of *transition area* (indicated in Step 2) is filtered to only return locations whose modelled time series, using any modelling method, have at least one positive zero crossing, and the last temperature (at 2009) calculated by the model is positive. Based on Rule 2 of *transition area*, the final databases for winter (JFM) and spring (MAM) are obtained. The number of grid cells generated as the output of this step differs for the three techniques employed in this thesis (i.e., the R method (Section 3.2), MARS (Section 3.3), and the KPY method (Section 3.4)). The detailed numbers of each method are tabulated in Chapter 5.

## 4.4 Data Analysis: Overview

After selecting the locations of interest following Rules 1 and 2 of *transition area*, the procedure of data analysis involves the following steps:

1. Any modelling technique applied in this research (the R method, MARS, or the KPY method) divides the entire time series into sub-regions that are polynomials of degree zero or one. The 'year of 0°C crossing' ($y_0$) is determined as the time when the model approximating the time series rises above 0°C.

   In the study by Bonsal and Prowse (2003), in order to find the time when the mean daily temperature moves above or below 0°C (0°C isotherms), a 31-day running mean is used. The reason is that time series of mean daily temperature fluctuate and may cross the 0°C line several times; hence, if the time series are smoothed with a 31-day running mean, there would be only one 0°C crossing. In this study, some of the modelled time series cross the 0°C line in the positive direction more than once. There are several rules set to determine $y_0$ in these cases. These rules depend on the characteristics of each model; thus, each technique has its own set of rules, which is indicated in Chapter 5.

2. Once $y_0$ is determined, the segment within which this point falls is termed the 'segment of interest' ($S_{interest}$). This definition is modified in the context of the R method by virtue of its characteristics (refer to Section 5.6).

3. In addition to $y_0$, this study is concerned with the determination of the onset of warming that causes the JFM or MAM temperature to rise above zero permanently. The 'start year of warming' ($y_w$) is defined as the beginning year of $S_{interest}$.

4. To examine whether the warming that moves the JFM or MAM temperature above 0°C is significant, the MK test is applied to the original temperature data within $S_{interest}$. If the sections following $S_{interest}$ have positive slopes, this implies that the increase in temperature has not stopped after crossing the 0°C line. In this thesis, the region that starts at $y_w$ and consists of these consecutive segments with positive slopes is referred to as 'section of total warming' ($S_{W_{total}}$); the warming that occurs during $S_{W_{total}}$ is called 'total warming' ($W_{total}$). Therefore, in addition to testing the significance of the trend in $S_{interest}$, the MK test is performed to examine the significance of the trend in $S_{W_{total}}$ using the original data. Furthermore, the MK test is applied to the original data from $y_w$ to $y_0$ to test whether a significant temperature increase has occurred during this time period.

   **Note:** $S_{W_{total}}$ is the same as $S_{interest}$ if the slope of the segment after $S_{interest}$ turns negative.

5. To investigate whether the percentage of locally significant trends is high enough to consider them globally significant, the field significance test described in Section 3.5.3 is applied to each technique.

**Note:** The original time series are used for modelling. The algorithms of the methods applied in this study do not require the use of anomalies. In the case of the R method and the KPY method, these techniques are capable of detecting shifts in the original data and trend functions of time series, respectively. Therefore, no smoothing is performed either. In the case of MARS, it is possible to use the results of running-average smoothing for modelling. Nicholas J. Gralewicz (personal communication) compared the results obtained from modelling the 10-year and 30-year running averages to that of the original data. The analysis indicates that the original data yield better approximations, particularly if the objective is to determine $y_w$ and $y_0$.

# Chapter 5

# Results

## 5.1 Introduction

In the previous chapter, the *transition area* was described. This chapter first focuses on introducing the variables that are analysed in the *transition area* (Section 5.2) followed by Section 5.3, which explains the common features of all the tables, histograms, and maps of this chapter. The details of the different techniques including input parameters, $y_w$ and $y_0$ determination rules, and results are provided in Sections 5.4, 5.5, and 5.6 for trend shift detection method, MARS, and R method, respectively. To examine the global significance of the observed trends, Section 5.7 presents the bootstrapping results. Finally, Section 5.8 concludes this chapter with the discussion on the differences between various methods, results, best model selection, and cryospheric evidence for observed trends.

## 5.2 Introduction to Variables

This section describes the variables evaluated in this study. The following variables are analysed, and detailed tables, histograms, and descriptive maps are provided to present the results. It should be noted that due to special characteristics of the R method (indicated in Sections 3.2, 5.6, and 5.8.1.1), the definitions of these variables are modified slightly (refer to Section 5.6.1):

1. $\mathbf{y_w}$: Described in Section 4.4

2. $\mathbf{y_0}$: Described in Section 4.4

3. **Slope (1)** or slope of the segment of interest ($S_{interest}$, described in Section 4.4): This is the slope of the line modelling the data within $S_{interest}$.

4. **Slope (2)** or slope of the section of total warming ($S_{W_{total}}$, described in Section 4.4): This slope is calculated using Equation 5.1.

$$Intensity = \frac{T_2 - T_1}{y_2 - y_1} \tag{5.1}$$

   where, $T_2$ is the temperature of the last year of $S_{W_{total}}$ ($y_2$) which is approximated by the model. $T_1$ is the temperature evaluated by the model at $y_w$ ($y_1$). The goal of evaluating Slope (2) is to find the rate of increase in temperature over $S_{W_{total}}$. If warming stops at the end of $S_{interest}$ (i.e., if the slope of the segment following $S_{interest}$ turns negative), $S_{W_{total}}$ is the same as $S_{interest}$; hence, Slope (1) is equal to Slope (2). However, if $S_{W_{total}}$ consists of more than one segment, Slope (2) yields an estimate of the rate of the overall warming during $S_{W_{total}}$. It should be noted that in the case of trend shift detection (the KPY method), the entire time series is divided into two sub-regions. Therefore, the maximum number of segments forming $S_{W_{total}}$ is two, provided that the first segment is $S_{interest}$, and the following segment has a positive slope. Using the other two techniques (MARS and the R method), there may be more than 2 segments forming $S_{W_{total}}$ since these methods may split the entire domain into more than 2 parts.

5. **Accumulation**: Accumulation over any sub-region of a time series is evaluated by subtracting the first modelled temperature from the last modelled temperature in that sub-region.

6. **Duration**: The number of years spanned by a sub-region of a time series is called the duration of that sub-region.

7. **H**: H indicates the result of the MK test. If H = 1, it implies that a significant temperature-time trend exists, whereas H = 0 is indicative of an insignificant relationship between temperature and time. As indicated in Section 4.4, the MK test is performed over three time periods in this study which are as follows:

(a) From $y_w$ to $y_0$

(b) During the segment of interest (i.e., from $y_w$ to the end of $S_{interest}$)

(c) During warming starting from $y_w$ (i.e., from $y_w$ to the end of $S_{W_{total}}$)

**Note:**

- As mentioned in Section 4.4, the MK test applies to the original temperature data during the above-indicated time periods.
- In this study, all the significant temperature-time trends (H = 1) are positive.

8. **Theil Slope**: In order to compare the distribution of Theil slope with those of Slope (1) and Slope (2), Theil slope (Equation 3.47) is evaluated for the period of $y_w - y_0$, $S_{interest}$, and $S_{W_{total}}$.

9. ***α***: This is the local significance level for detecting trends using the MK test. Throughout this document, $\alpha = 0.05$.

## 5.3 Introduction to Tables, Histograms, and Maps

The goal of this section is to explain the common features of all the tables, histograms, and maps of this chapter. Each technique may include some additional concepts that are described later in the corresponding section.

### 5.3.1 Tables

Tables provide detailed information on the number of grid cells selected in each step involved in the preparation of the final database (refer to Section 4.3 for more details on the final database). Moreover, they include the number of locations with $y_w = 1901$. The only exception is the table created for the R method (Table 5.4) since $y_w$ is not defined for this technique (refer to Section 5.6.2). Time series are truncated at 1901. Hence, $y_w = 1901$ may in fact refer to the warming that was initiated prior to 1901. Furthermore, the approximation of temperature in early years of the $20^{th}$ century would be more precise if more data points were available prior to 1901. Due to these reasons, it is of interest to count locations with $y_w = 1901$.

When there is more than one positive 0°C crossing, the $y_w$ and $y_0$ determination rules for each technique (KPY method: Rule 2a, MARS: Rule 2a) are set such that they avoid incorrectly selecting the first segment as $S_{interest}$ if the warming over the first segment is insignificant. Based on the method used, $y_w = 1901$ could be interpreted as follows. Note that to clarify more on $y_w$ and $y_0$ determination rules and how time series are modelled, Appendix A provides sample plots for each technique.

- **the KPY method:** This thesis only focuses on two types of models from this category: Model 2 and Model 3 (Section 3.4).
  - **Model 2:** As indicated in Section 3.4, Model 2 divides the entire time series into two sub-regions, and the boundary of the two segments is determined by the break date. Model 2 is continuous at the break point; hence, only one positive 0°C crossing could occur (Sample plots can be found in Section A.1). All the locations with $y_w = 1901$ are the grid cells whose $y_w$ and $y_0$ are determined following Rule 1a (Section 5.4.2). This implies that the only positive 0°C crossing occurs at $y_0$ which moves the time series above 0°C. According to Rule 2 of *transition area* (Section 4.3), the approximated final temperature by the model (at 2009) should be positive. Based on the above-indicated rules, in the case of Model 2, $y_w = 1901$ implies that the increase in temperature starts in 1901 (or probably some time prior to 1901). As a result of this warming, the time series moves above 0°C and stays above the 0°C line.
  - **Model 3:** As with Model 2, the entire domain of a time series is split into two segments using Model 3. However, since the break date marks the time when both the intercept and slope of the trend function change, the model is not continuous at the break time (refer to sample plots of Section A.2). Due to the discontinuous boundary, more than one positive 0°C crossing is possible, and Rule 2 of $y_0$ and $y_w$ determination (Section 5.4.2) applies to these cases. In this case, $y_w = 1901$ refers to one of the following two cases:
    1. There is only one positive 0°C crossing which falls within the first segment (refer to Figure A.4 as an example). In this case, due to Rule 2 of *transition area*, the second segment is certainly above the 0°C line. This implies that the warming that may have initiated prior to 1901 causes the time series to rise above 0°C, and despite the structural change in both intercept and slope at the time of break, temperature remains positive.

2. Both segments cross the 0°C line in the positive direction (Figure A.7). Rule 2a indicated in Section 5.4.2 applies to this case. If as a result of following this rule, the first segment is still selected as $S_{interest}$, it could be concluded that a significant increase in temperature has occurred during $S_{interest}$. This warming leads to the change of temperature sign. Although there is a break in the intercept and slope of the trend function, the warming resumes, and the temperature goes back above 0°C after the break time.

- **MARS:** Similar to Model 3, $y_w = 1901$ could be interpreted in two ways:

1. The first segment is the only segment that crosses 0°C in the positive direction. Figures A.9 to A.11 provide examples for this case. Most of the cases with $y_w = 1901$ fall under this category, particularly during MAM. Due to the warming that starts in 1901 (or some time prior to 1901), temperature turns positive. Although temperature fluctuates afterwards, based on Rule 2 of *transition area*, it stays above the 0°C line.
2. There is more than one positive 0°C crossing, and the first segment is selected as $S_{interest}$ since it has the maximum slope and cumulative warming (Figure A.15). This case includes very small subsets of JFM and MAM data sets. The most commonly observed model behaviour is a significant warming in the beginning of the time series that causes a 0°C crossing. The segment is followed by some fluctuations and a short period of negative temperature after which temperature turns positive again and continues to increase.

The tables also reveal the number of locations with short periods of $y_w - y_0$. The algorithm of the MK test is such that it is not applicable to the sets with less than 3 data points. As is shown later in this document (Tables 5.1 to 5.4), in both cases of JFM and MAM, only small subsets of the *transition area* fall under this category. The MK test is applied to the time period of $y_w - y_0$ to investigate whether significant warming takes place from $y_w$ until the time series crosses 0°C. This time period is usually short, and the analysis results (Figures 5.4, 5.8, 5.50, 5.55, 5.98, and 5.103) show that the increase in temperature during this period is insignificant; however, significant warming is often observed during $S_{interest}$.

### 5.3.2 Histograms

In order to have an impression of the distributions of the results and understand the most frequently occurring values among grid cells, histograms are provided for the variables introduced in Section 5.2: $y_w$, $y_0$, break date, accumulation, duration, Slope (1), Slope (2), Theil slope, and H. Some of these variables are excluded in the case of the R method (refer to Section 5.6.1).

### 5.3.3 Maps

Maps illustrate the spatial distributions of the variables introduced in Section 5.2. For each variable, the map of the entire Northern Hemisphere is provided followed by more detailed figures focussing on specific regions (e.g. North America).

As is observed in the histogram plots of $y_0$, Slope (1), and Slope (2) (e.g., Figures 5.1 and 5.3), these histograms are denser on one end (on the left end for Slope (1) and Slope (2) and on the right end for $y_0$). Therefore, if the color bars of the maps of these variables were linearly spaced, much of the interesting information on the maps would be lost. Therefore, the following non-linear transformations are used to map the data. As a result of these transformations, the color bars are not linearly spaced.

- **Slope (1) and Slope (2)**
  Equation 5.2 is adopted from Carlson (1986).

$$Z = \frac{(sgn\ x)\ ln(1 + \mu|x|)}{ln(1 + \mu)}, \quad |x| <= 1 \tag{5.2}$$

  where $Z$ denotes the transformed form of $x$, and $\mu$ should be set to a large number (e.g., 100, 200), which leads to a better display of the colors and variations on the map.

- **$y_0$**

$$Z = \frac{exp(\tau|x|) - 1}{exp(\tau) - 1}, \quad |x| <= 1 \tag{5.3}$$

  where $Z$ is the transformed form of $x$, and $\tau$ should be set to a small number (e.g., 2, 3), which displays variations in more details on the map.

## 5.4 Trend Shift Detection

In this section, following the KPY method (Kim and Perron, 2009; Perron and Yabu, 2009b) described in Section 3.4, the JFM and MAM time series are tested for structural changes in the trend functions. As indicated earlier, the focus of this study is only on Model 2 and Model 3 (Section 3.4) from this category.

It should be noted that the KPY method first tests for a significant structural break in the trend function of a time series. If the test favours a significant break, the time of this shift is evaluated. This implies that the significance test applies to all the grid cells selected as a result of Rule 1 of *transition area* (Step 2 in Section 4.3). Using the locations with significant break dates, the analysis then continues with Rule 2 of *transition area* (Step 3 in Section 4.3) to select locations eligible for the $y_w$ and $y_0$ analysis. The results (not shown here) reveal that if this procedure is followed, the number of acceptable locations for the $y_w$ and $y_0$ analysis decreases drastically. Particularly over North America, only few grid cells exhibit significant shifts which could not be used for the $y_w$ and $y_0$ analysis according to Rule 2 of *transition area*. This implies that if only locations with significant breaks were considered, no grid cell experiencing a positive sign change would eventually be selected in North America. To be consistent with the other two methods (MARS and the R method), this research skips the break significance testing procedure, and break times of all the locations selected based on Rule 1 of *transition area* are evaluated and assumed to be valid. Then, Rule 2 of *transition area* applies to these grid cells. The aforementioned assumption is logical since the algorithms of MARS and the R method do not test the statistical significance of shift points either.

### 5.4.1 Input parameters

As with other modelling techniques, there are several parameters that should be set by the analyst:

- **$\epsilon$**
  As indicated in Section 3.4, if the break time is unknown, the permissible range of break date candidates is $(\epsilon T, \ldots, (1-\epsilon)T)$. Therefore, the smaller $\epsilon$ is, the larger the range is. According to Table 2 of Perron and Yabu (2009b), $\epsilon$ could take one of the values in [0.01, 0.05, 0.1, 0.15, 0.25]. $\epsilon$ is selected to be 0.05 in this study since

it is small enough to allow a large range (∼1906-2004) to be examined in the break date evaluation and is large enough not to include the points too close to both ends of time series as candidates for shift times.

- **Information Criterion**
  Bayesian information criterion (BIC)

- **Break Date Estimation Models (IO or Aout Models)**
  As described in Section 3.4, the break time is the candidate that minimizes the sum of squared residuals of Regression 5 (Aout models) or Regression 7 (IO models) of Kim and Perron (2009). In the assessment of climate data, IO models are more suitable since the trend shifts of climate data usually do not occur instantly as in the case of Aout models (Ivanov and Evtimov, 2010). However, due to the following two reasons, Aout models are used in this study:

  1. Model 2 of IO type requires the assumption of no break under the null hypothesis. This is contrary to the null hypothesis of Kim and Perron (2009), which allows for a break.
  2. Using IO models requires fixing the length of the transition period. Starting from 1, the transition period is increased until the estimates of break date and model parameters become stable. The transition period of interest is the smallest value after which the estimates do not change significantly. In this thesis, a large number of time series are analysed, and there are a considerable number of grid cells whose break dates and model parameter estimates do not stabilize by increasing the length of transition period. Therefore, Model 3 of Aout type with no transition period is used to analyse all the JFM (6206 grid cells) and MAM (9842 grid cells) time series.
  3. Model 2 or Model 3 of Aout type are more compatible with the other two models since in the case of MARS and the R method shifts take place instantly as well. This leads to simpler comparisons between different techniques.

### 5.4.2 $y_0$ and $y_w$ Determination Rules

In the case of Model 2 and Model 3, the following rules define $y_0$ and consequently $y_w$ and $S_{interest}$:

1. **One positive 0°C crossing**

   (a) First segment crosses 0°C

   - $\mathbf{y_0}$ : year of 0°C crossing
   - $\mathbf{y_w}$ : start year of the first segment (i.e., 1901)

   Sample plots: Figure A.1 (Model 2), Figure A.4 (Model 3)

   (b) Second segment crosses 0°C

   - $\mathbf{y_0}$ : year of 0°C crossing
   - $\mathbf{y_w}$ : start year of the second segment (i.e., break time)

   Sample plots: Figures A.2 and A.3 (Model 2), Figure A.5 (Model 3)

2. **Two positive 0°C crossings**
   The rules below are only applicable to Model 3. Model 3 tests for simultaneous breaks in intercept and slope and approximates a time series with two disjoint segments. Therefore, it is possible to have two positive 0°C crossings. Model 2, on the other hand, is continuous at the break point since it only exhibits the shift in the slope of the trend function of a time series; hence, there can be only one positive 0°C crossing (refer to Section 3.4 for more details).

   (a) The first line has the maximum slope

   - $\mathbf{y_0}$ : 0°C crossing year of the line with the greatest cumulative warming (Cumulative warming is evaluated by subtracting the modelled temperature in the beginning of the line from the approximated temperature at the end of the line.)
   - $\mathbf{y_w}$ : start year of the line with the greatest cumulative warming

   Rule 2a is set to avoid having $y_w = 1901$ if significant warming has not occurred during the period of the first segment. As illustrated by Figure A.6, sometimes when there are two 0°C crossings, the slope of the first segment is larger than the second segment. However, the period over which this warming takes place is shorter, and the magnitude of cumulative warming is smaller. On the other hand, despite its smaller slope, the second segment exhibits a larger increase in temperature over a longer period which causes the time series to rise above 0°C. Furthermore, the approximation of temperature in early years of the $20^{\text{th}}$

century would be more precise if more data points were available prior to 1901. Therefore, since the magnitude of warming is larger over the second segment, and more data points are involved in determining the model parameters (e.g., slope) of the second segment, it seems more logical to select the second 0°C crossing as $y_0$. If the first segment has the maximum slope and magnitude of cumulative warming, as depicted by Figure A.7, it could be inferred that the major warming that moves the time series above 0°C has occurred during the first segment. Hence, $y_0$ is determined as the year of 0°C crossing of the first segment. Although the first line is followed by a break in the intercept and slope of the trend function, the warming resumes, and the temperature goes back above 0°C after the break time.

(b) The second line has the maximum slope

- $\mathbf{y_0}$ : 0°C crossing year of the second line
- $\mathbf{y_w}$ : start year of the second line (i.e., break time)

Sample plot: Figure A.8

As indicated in Section 4.4, $S_{interest}$ is the segment that includes $y_0$.

### 5.4.3 Model 2 Results

The results of the analysis of the temperature time series using Model 2 are presented in this section. First, the detailed table (Table 5.1) and histograms for the JFM and MAM time series are provided (JFM: Figures 5.1 to 5.4, MAM: Figures 5.5 to 5.8). Then, the descriptive maps of the Northern Hemisphere (JFM: Figures 5.9 to 5.27, MAM: Figures 5.28 to 5.46) are presented to better understand the spatial distribution of the variables. The reader is referred to Sections 5.8.3 (tables and histograms) and 5.8.4 (maps) for the comprehensive description and discussion of the results.

**Table 5.1:** Based on the analysis of the JFM and MAM time series using **Model 2**, the table provides some information on the numbers of grid cells with specific characteristics described in the left column. The input parameters are as indicated in Section 5.4.1. The reader is referred to Section 5.3 for more details on the cases presented below.

| **Characteristic** | **Number** | |
|---|---|---|
| | **JFM** | **MAM** |
| Selected for study (following Rule 1 of *transition area*, described in Section 4.3) | 6206/46224 | 9842/46224 |
| Last modelled temperature positive (based on Rule 2 of *transition area*, described in Section 4.3) | 3644/6206 | 6365/9842 |
| Final database: selected for the $y_w$ and $y_0$ analysis (based on Rules 1 and 2 of *transition area*) | **1668/3644** | **2702/6365** |
| $y_w = 1901$ | 157/1668 | 769/2702 |
| Duration of $y_w$ to $y_0$ less than 3 years, MK test N/A | 79/1668 | 125/2702 |
| $S_{W_{total}}$ is the same as $S_{interest}$ | 1541/1668 | 2145/2702 |

#### 5.4.3.1 Histograms

##### 5.4.3.1.1 JFM

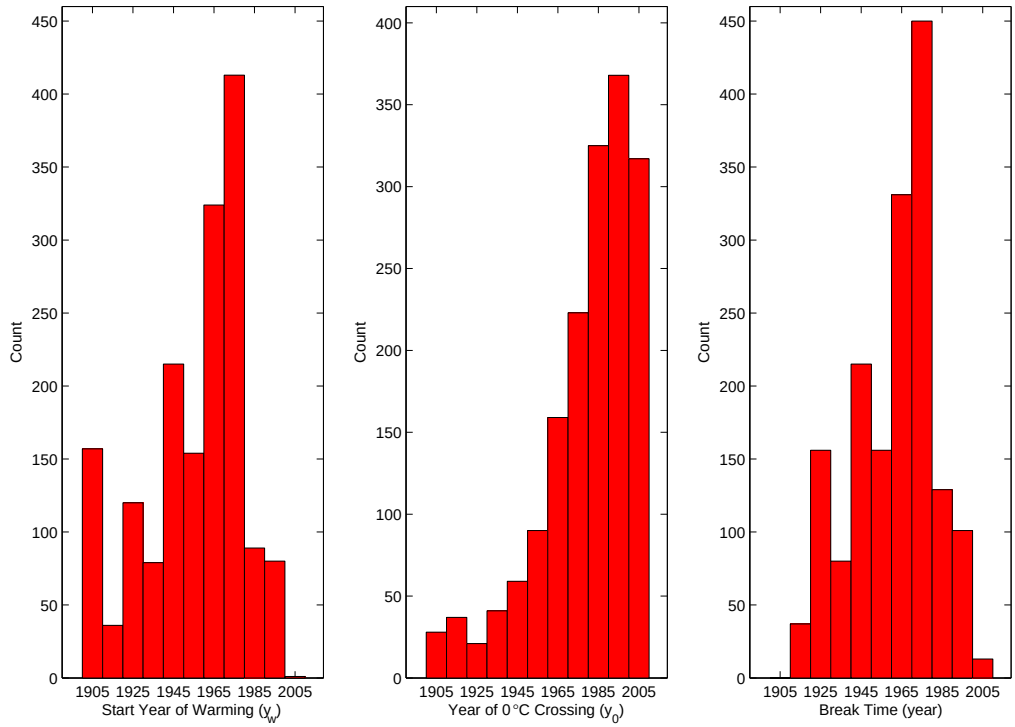


**Figure 5.1:** The histograms exhibit the temporal distributions of $y_w$, $y_0$, and break date during **JFM**. The results are obtained using **Model 2**, and the input parameters are as indicated in Section 5.4.1.

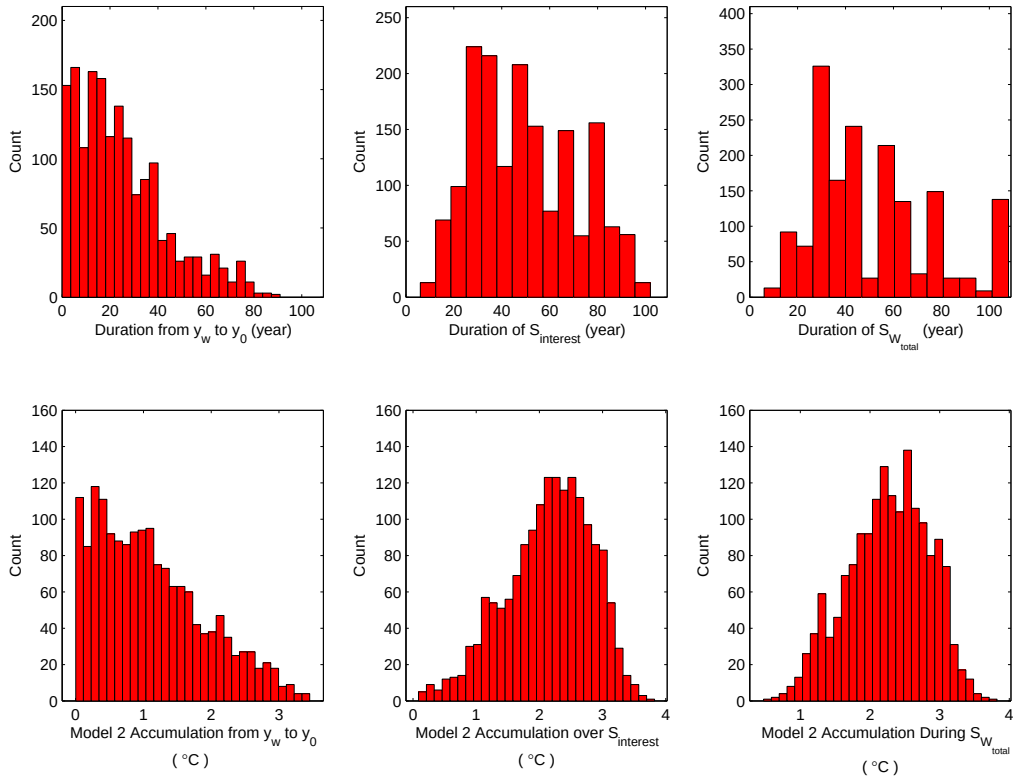


**Figure 5.2:** The histograms exhibit the distributions of duration and temperature accumulation during $y_w - y_0$, $S_{interest}$, and $S_{W_{total}}$ for **JFM**. The results are obtained using **Model 2**, and the input parameters are as indicated in Section 5.4.1. The reader is referred to Section 5.2 for details on the variables used above.

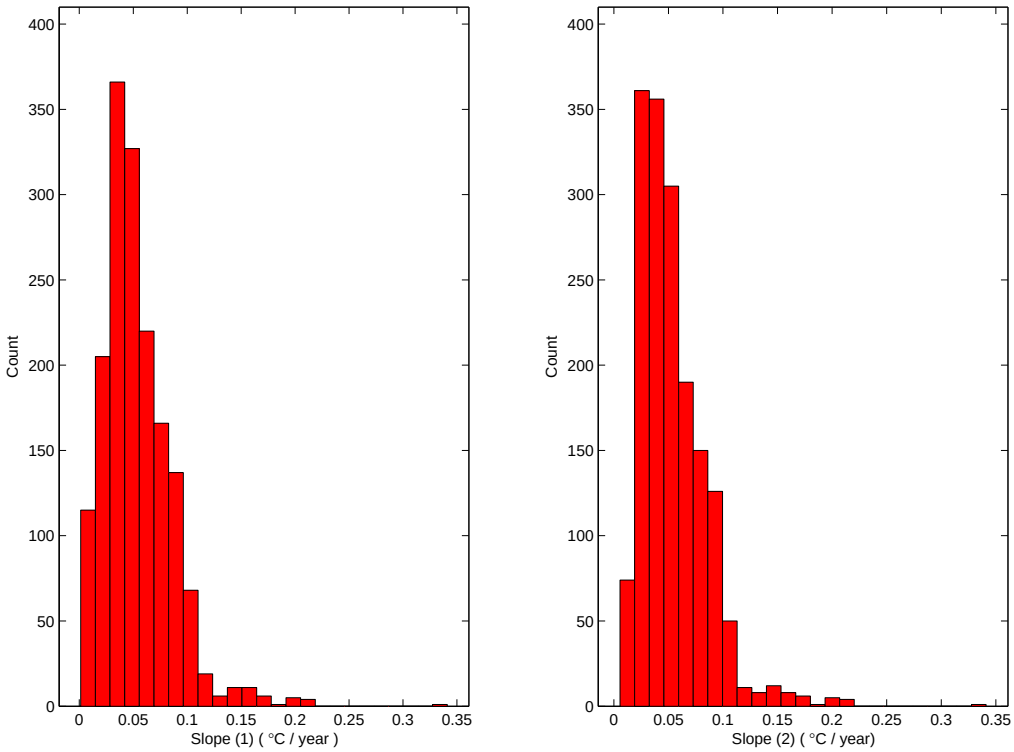


**Figure 5.3:** The histograms exhibit the distributions of Slope (1) and Slope (2) for **JFM**. The results are obtained using **Model 2**, and the input parameters are as indicated in Section 5.4.1. The reader is referred to Section 5.2 for details on the variables used above.

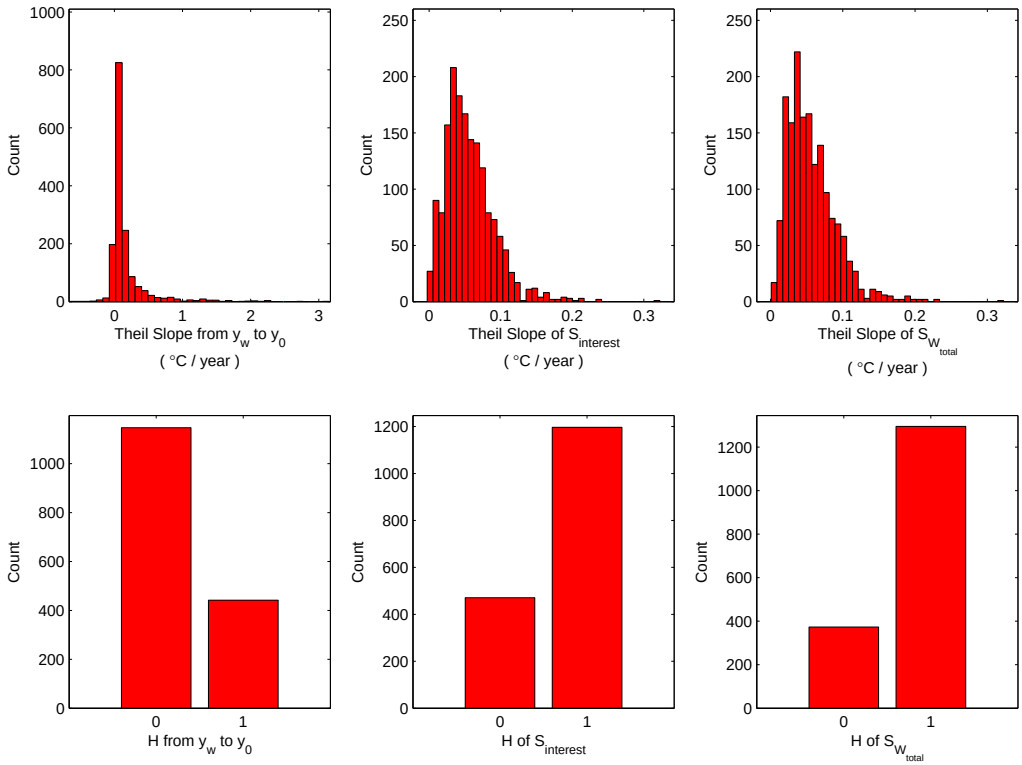


**Figure 5.4:** The histograms exhibit the distributions of Theil slope and H during $y_w - y_0$, $S_{interest}$, and $S_{W_{total}}$ for **JFM**. The results are obtained using **Model 2**, and the input parameters are as indicated in Section 5.4.1. The reader is referred to Section 5.2 for details on the variables used above.

#### 5.4.3.1.2 MAM

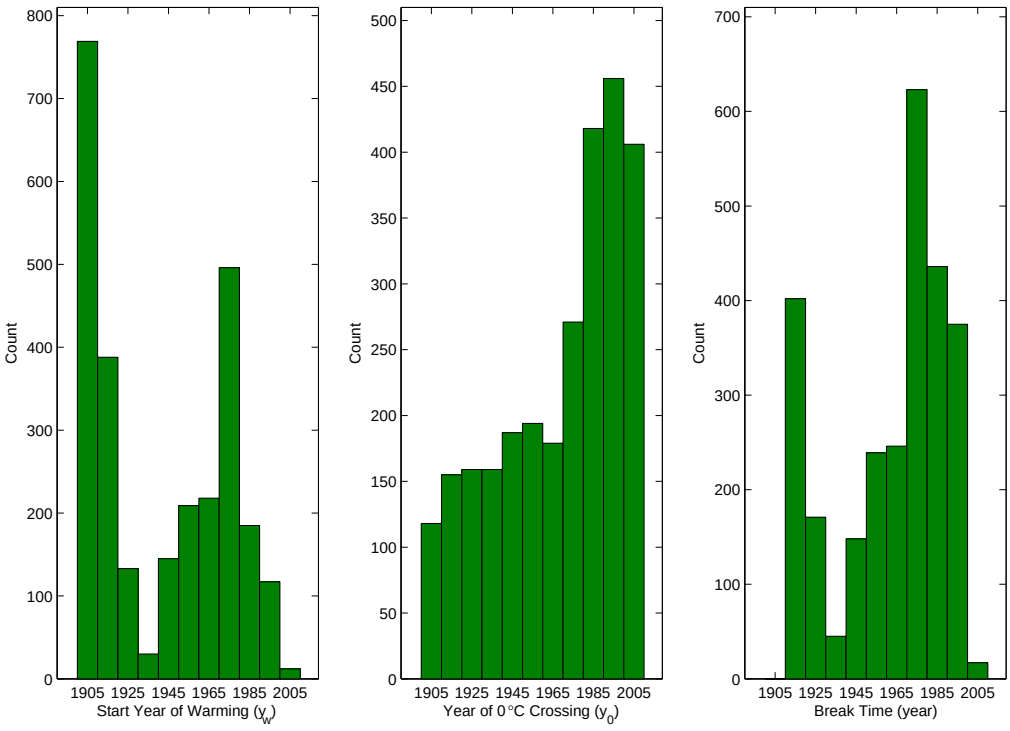


**Figure 5.5:** The histograms exhibit the temporal distributions of $y_w$, $y_0$, and break date during **MAM**. The results are obtained using **Model 2**, and the input parameters are as indicated in Section 5.4.1.

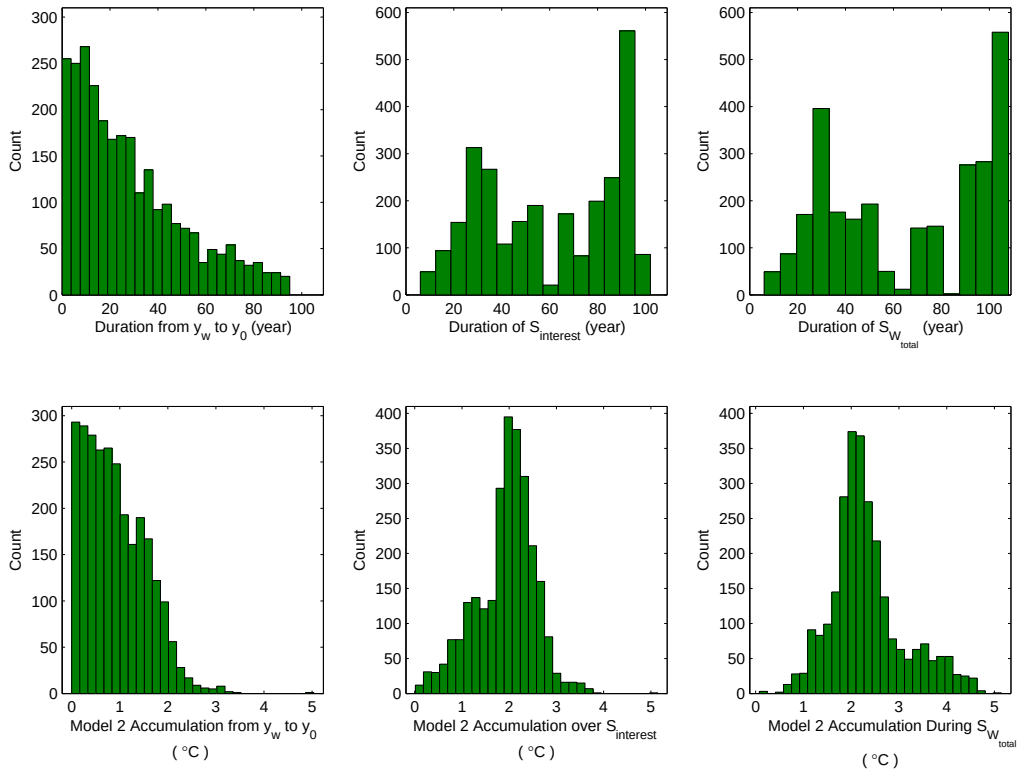


**Figure 5.6:** The histograms exhibit the distributions of duration and temperature accumulation during $y_w - y_0$, $S_{interest}$, and $S_{W_{total}}$ for **MAM**. The results are obtained using **Model 2**, and the input parameters are as indicated in Section 5.4.1. The reader is referred to Section 5.2 for details on the variables used above.

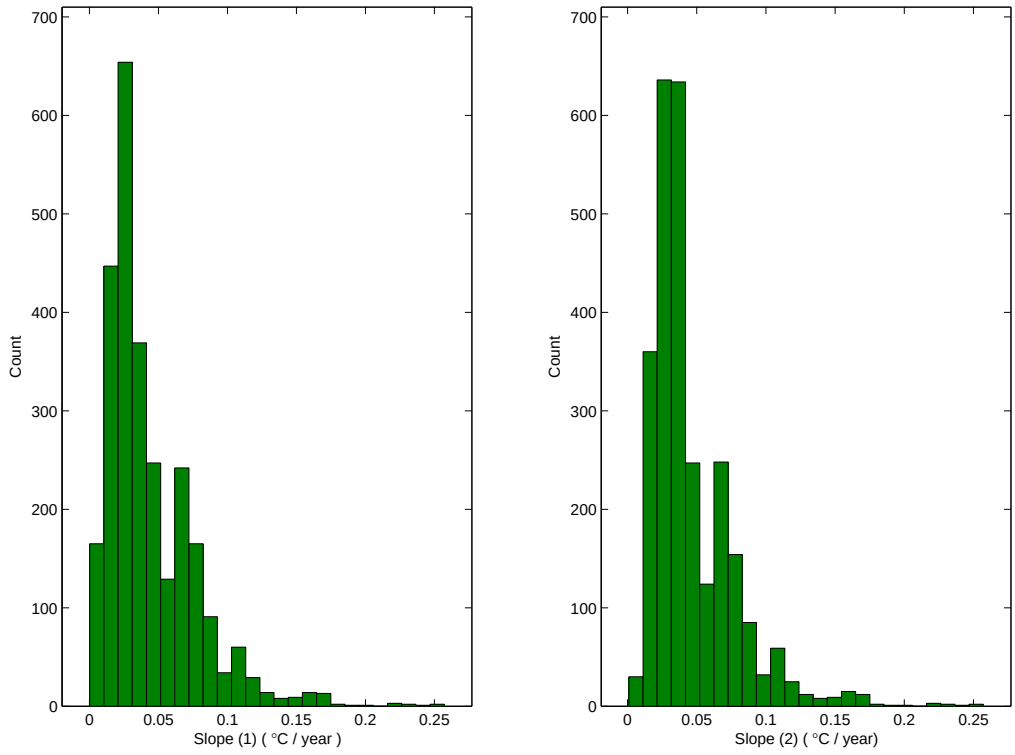


**Figure 5.7:** The histograms exhibit the distributions of Slope (1) and Slope (2) for **MAM**. The results are obtained using **Model 2**, and the input parameters are as indicated in Section 5.4.1. The reader is referred to Section 5.2 for details on the variables used above.

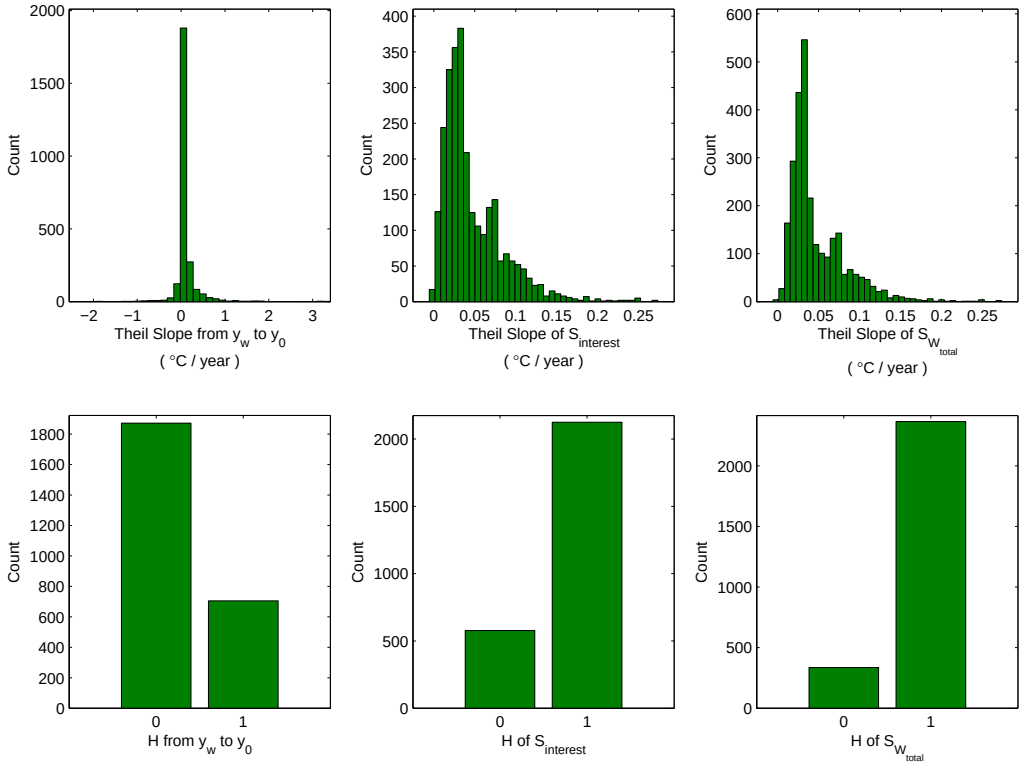


**Figure 5.8:** The histograms exhibit the distributions of Theil slope and H during $y_w - y_0$, $S_{interest}$, and $S_{W_{total}}$ for **MAM**. The results are obtained using **Model 2**, and the input parameters are as indicated in Section 5.4.1. The reader is referred to Section 5.2 for details on the variables used above.

#### 5.4.3.2 Maps of Model 2 for JFM

##### 5.4.3.2.1 $y_w$

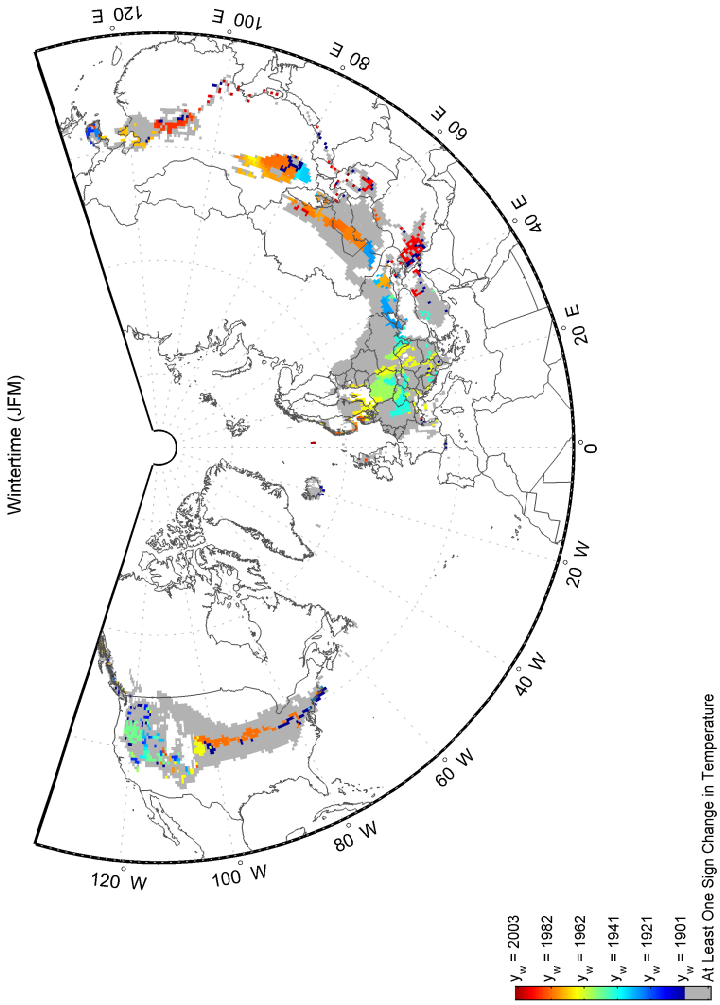


**Figure 5.9:** The map depicts the spatial distribution of $y_w$ in the Northern Hemisphere during **JFM**. The results are obtained using **Model 2**, and the input parameters are as indicated in Section 5.4.1.

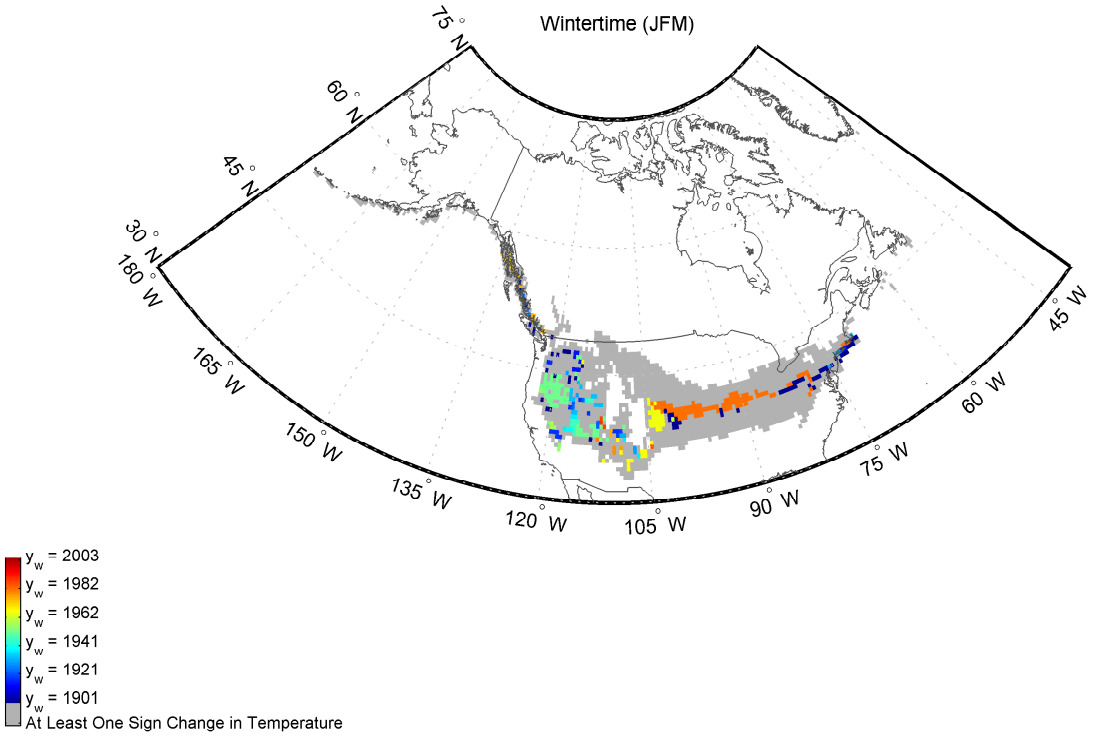


**Figure 5.10:** The same as Figure 5.9: zoomed in view of North America

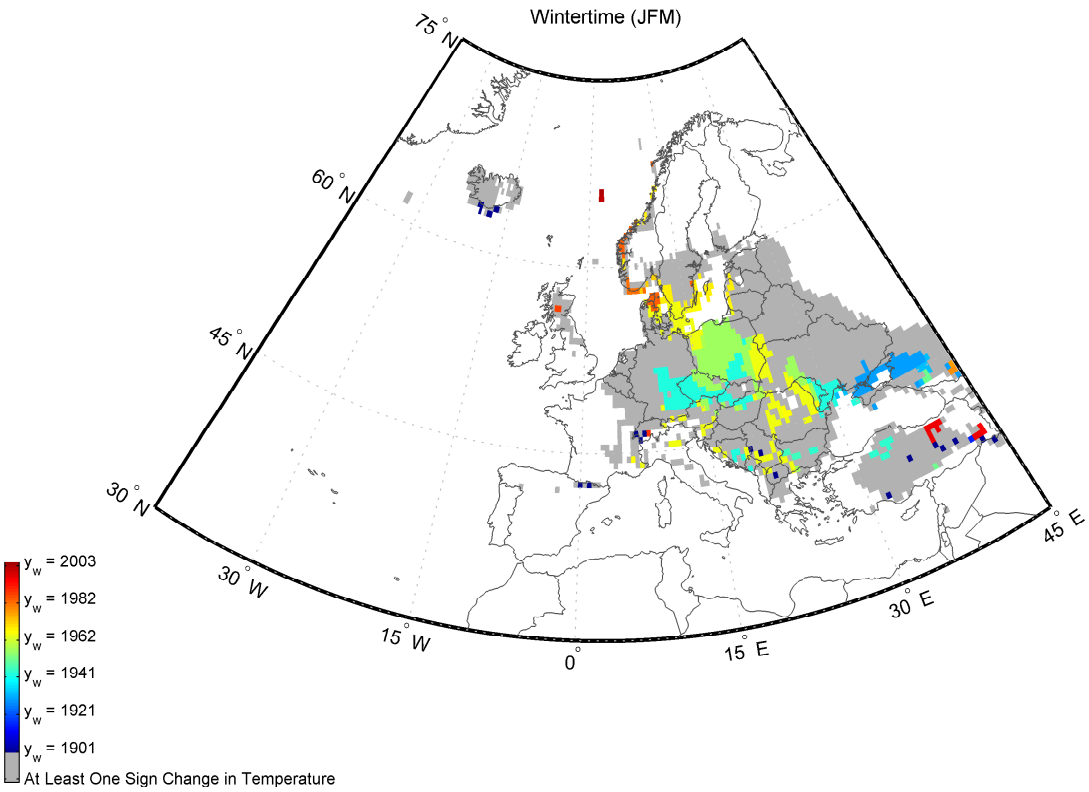


**Figure 5.11:** The same as Figure 5.9: zoomed in view of Europe

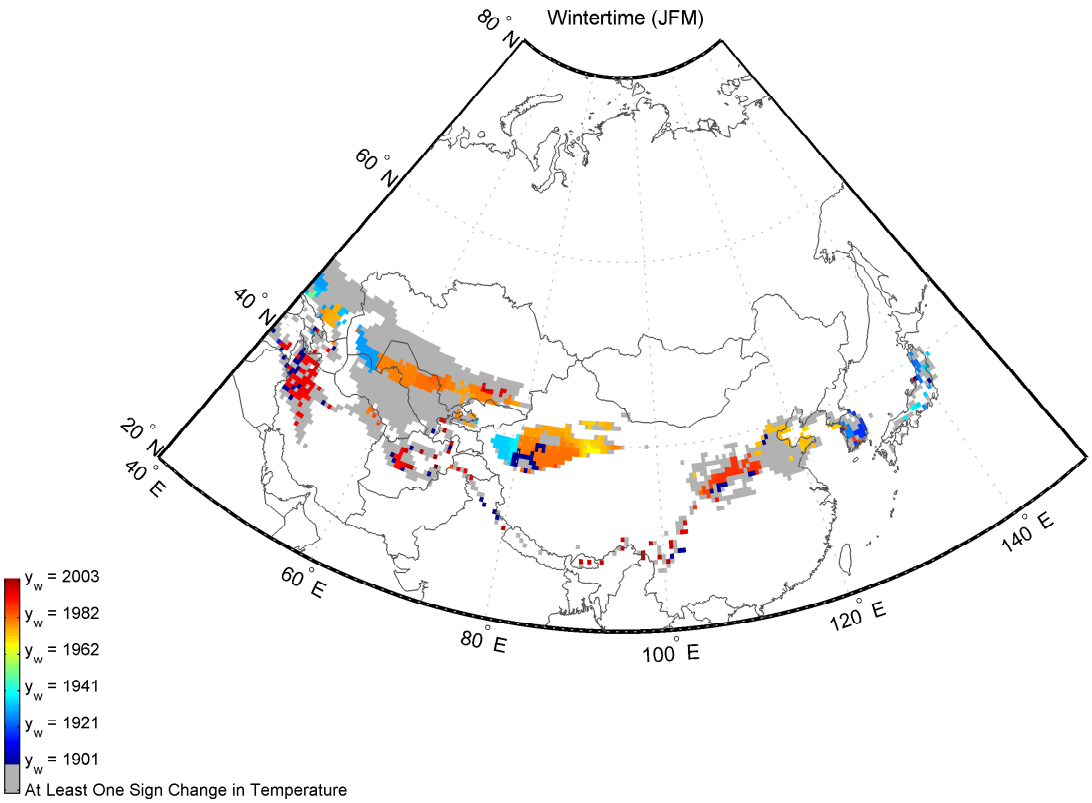


**Figure 5.12:** The same as Figure 5.9: zoomed in view of Asia

#### 5.4.3.2.2 $y_0$

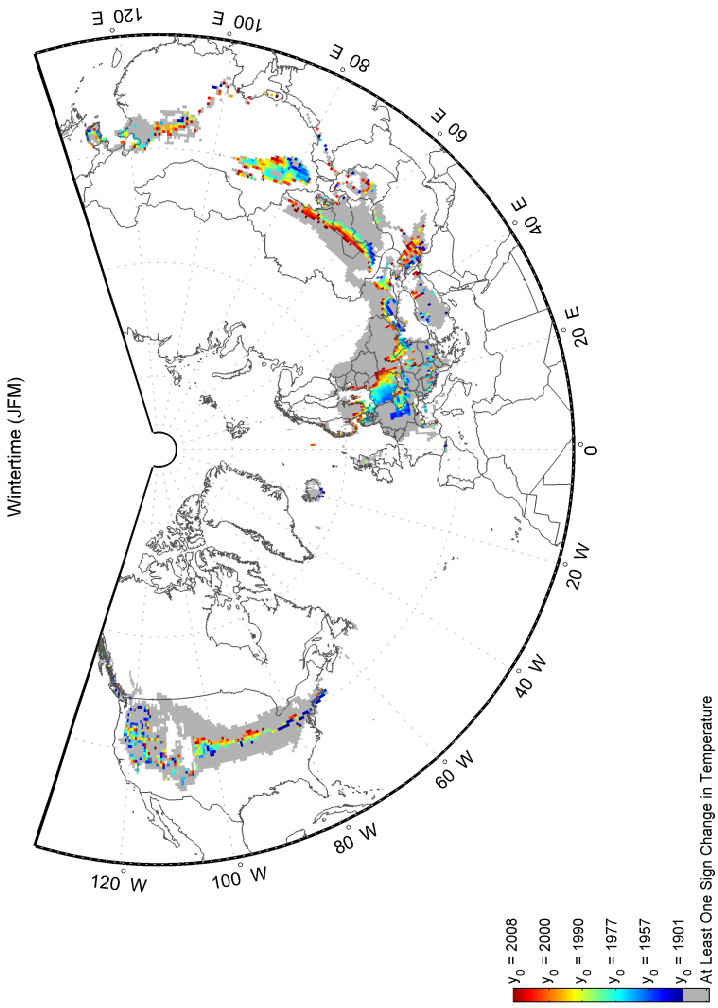


**Figure 5.13:** The map depicts the spatial distribution of $y_0$ in the Northern Hemisphere during **JFM**. The results are obtained using **Model 2**, and the input parameters are as indicated in Section 5.4.1.

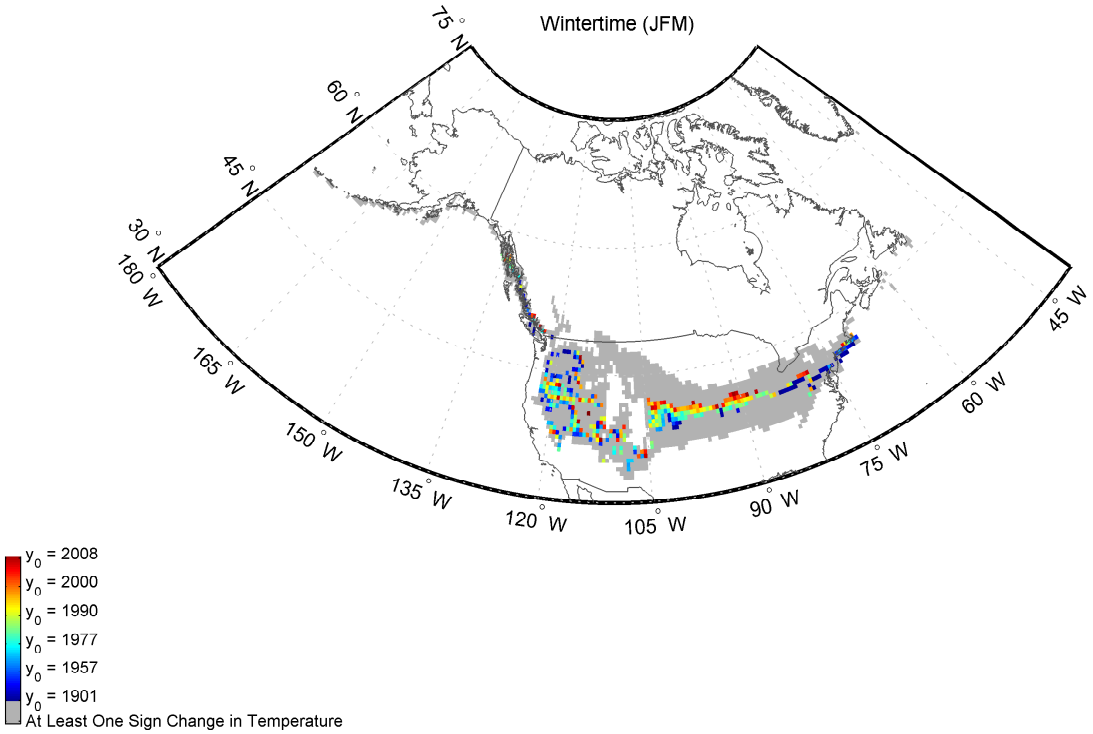


**Figure 5.14:** The same as Figure 5.13: zoomed in view of North America

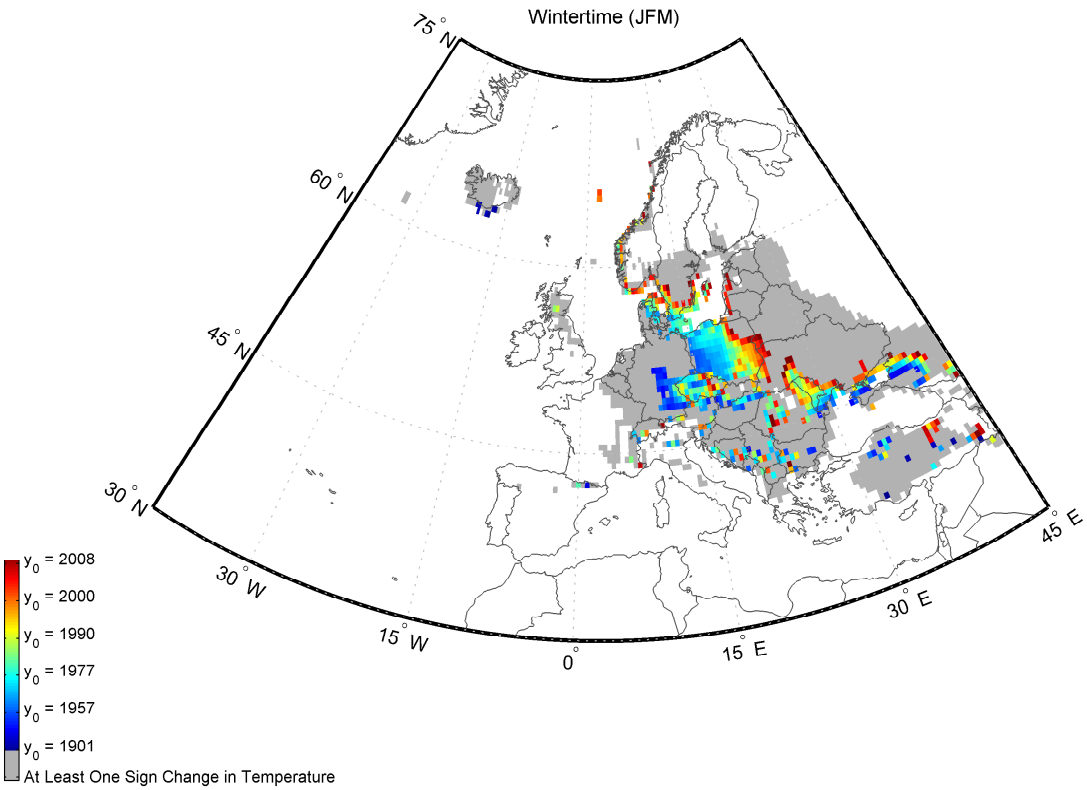


**Figure 5.15:** The same as Figure 5.13: zoomed in view of Europe

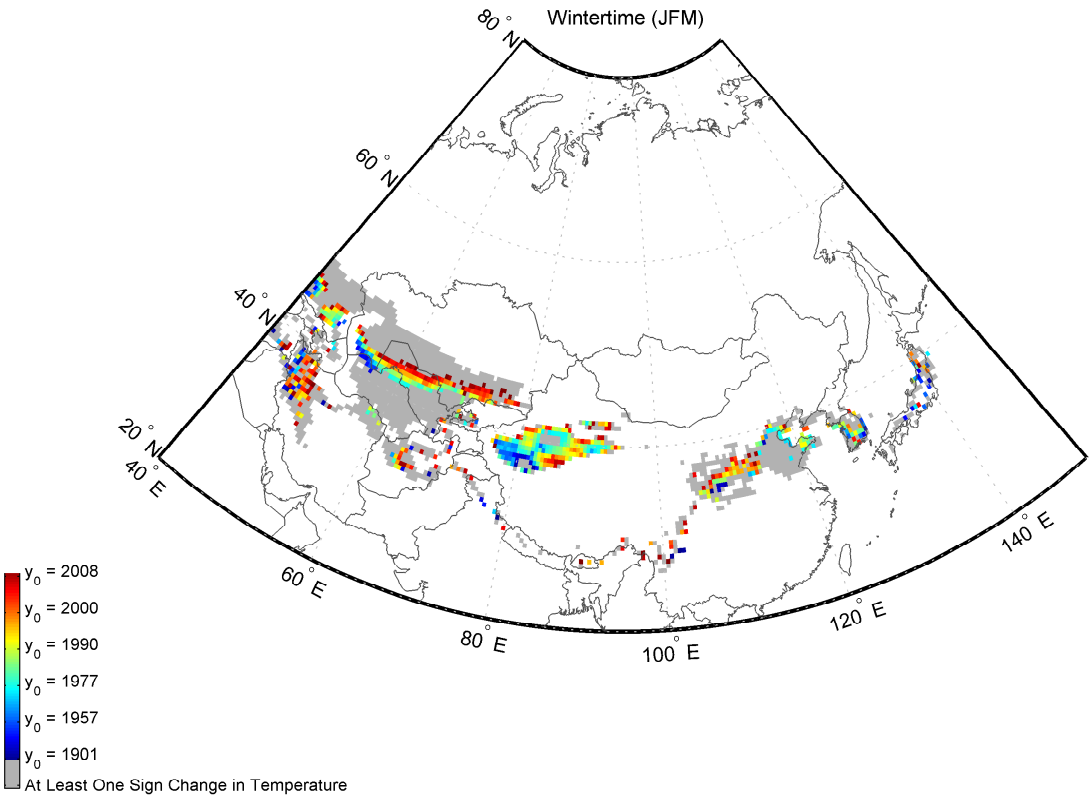


**Figure 5.16:** The same as Figure 5.13: zoomed in view of Asia

#### 5.4.3.2.3 Slope (1)

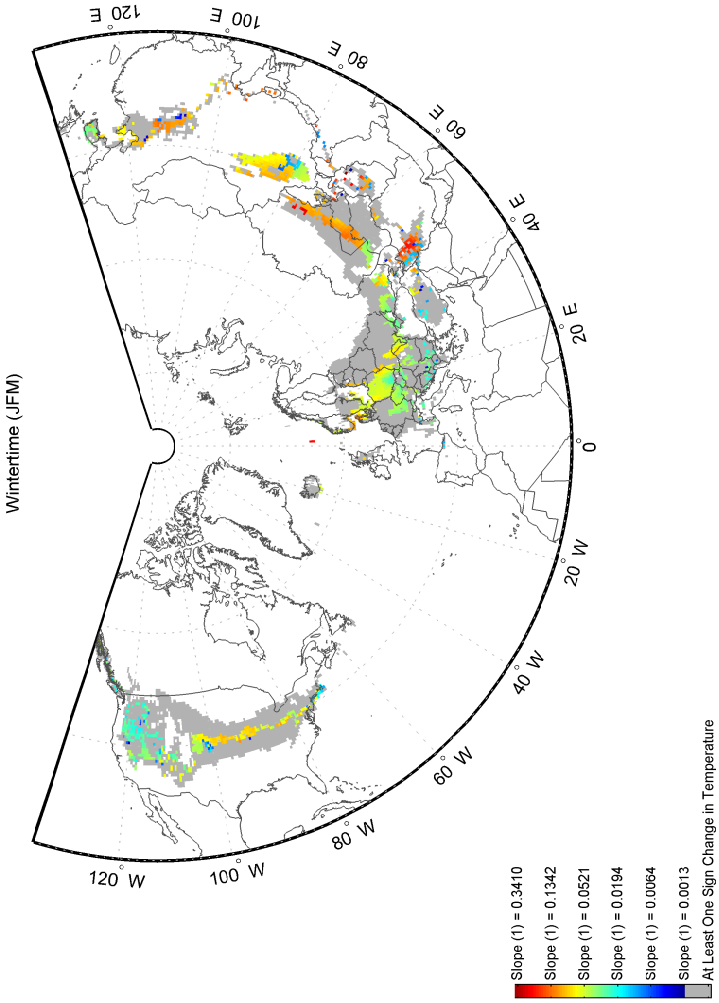


**Figure 5.17:** The map depicts the spatial distribution of Slope (1) in the Northern Hemisphere during **JFM**. The results are obtained using **Model 2**, and the input parameters are as indicated in Section 5.4.1. Refer to Section 5.2 for the definition of 'Slope (1)'.

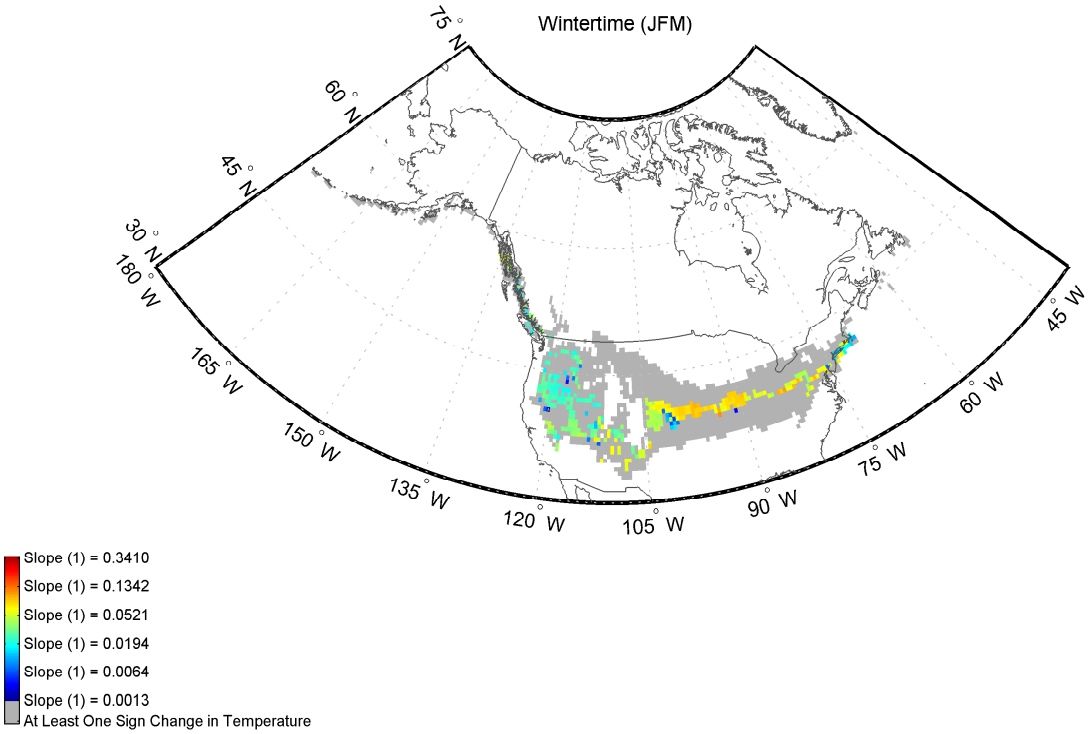


**Figure 5.18:** The same as Figure 5.17: zoomed in view of North America

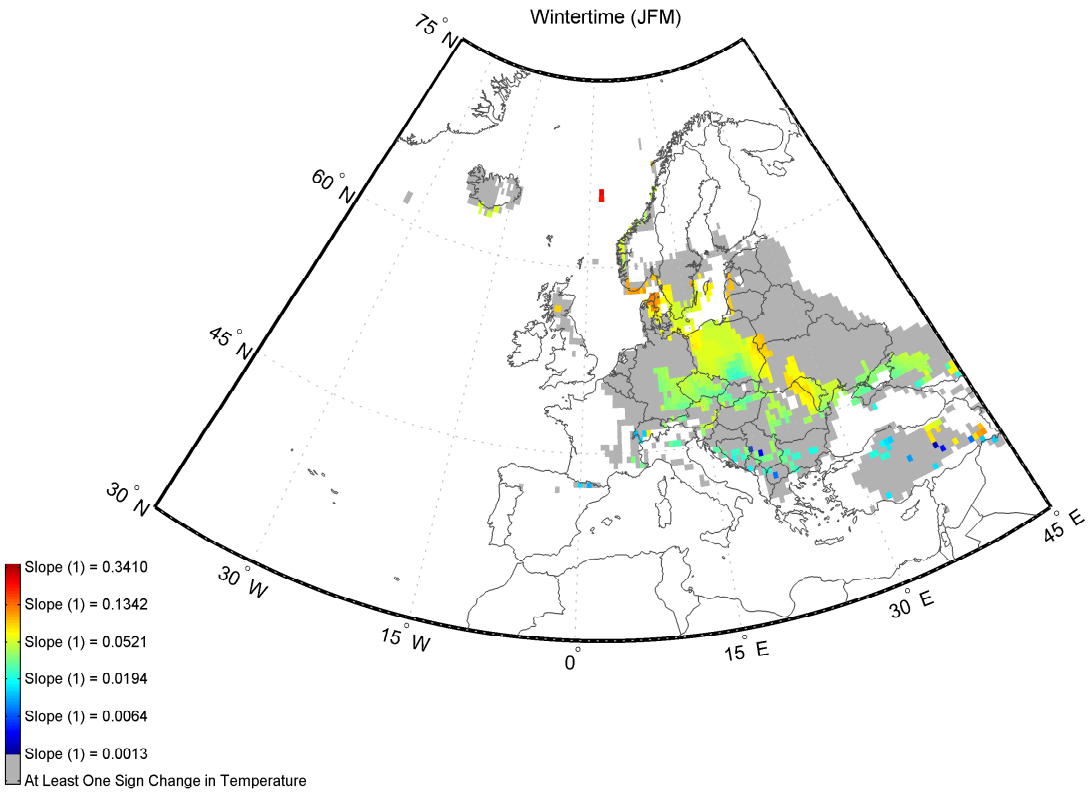


**Figure 5.19:** The same as Figure 5.17: zoomed in view of Europe

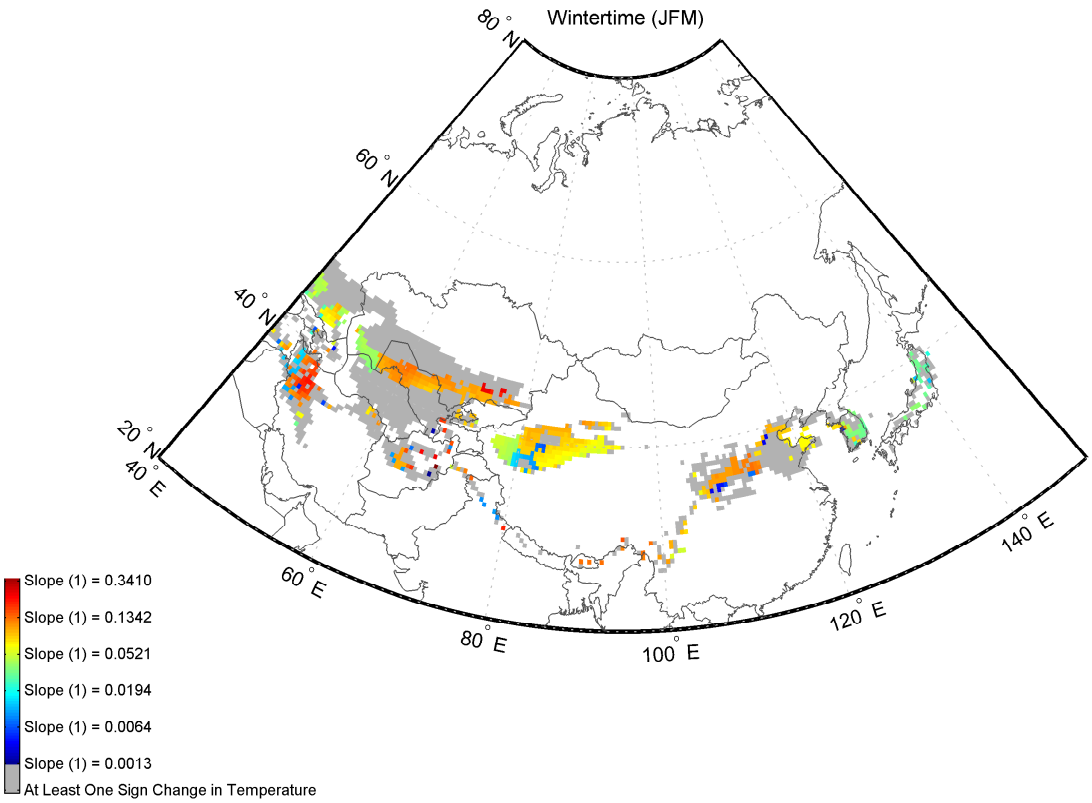


**Figure 5.20:** The same as Figure 5.17: zoomed in view of Asia

#### 5.4.3.2.4 Slope (2)

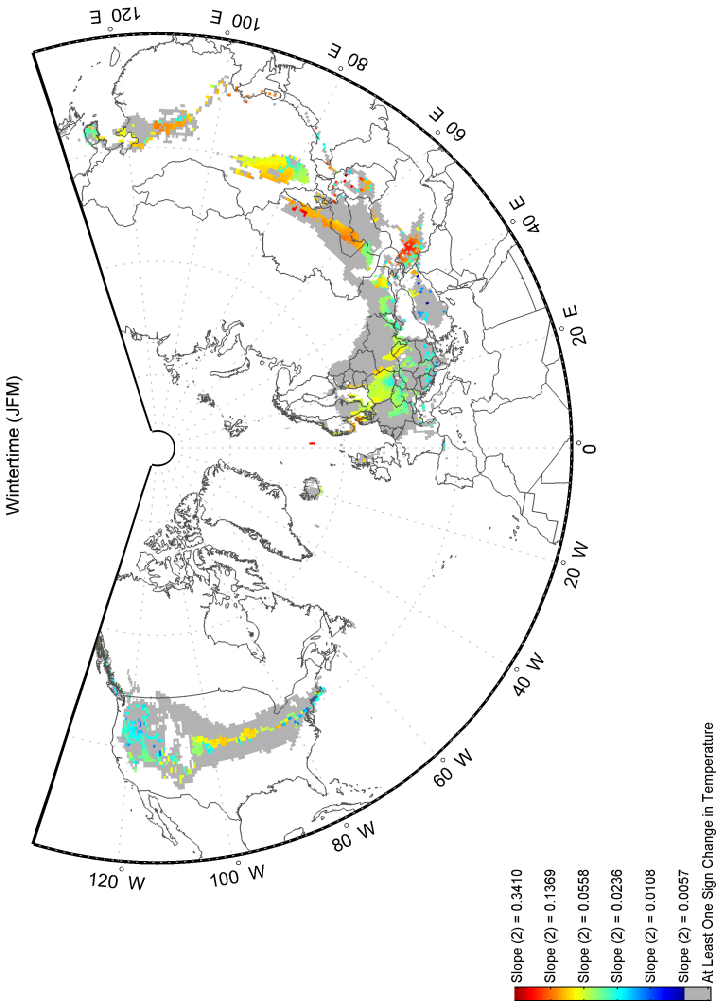


**Figure 5.21:** The map depicts the spatial distribution of Slope (2) in the Northern Hemisphere during **JFM**. The results are obtained using **Model 2**, and the input parameters are as indicated in Section 5.4.1. Refer to Section 5.2 for the definition of 'Slope (2)'.

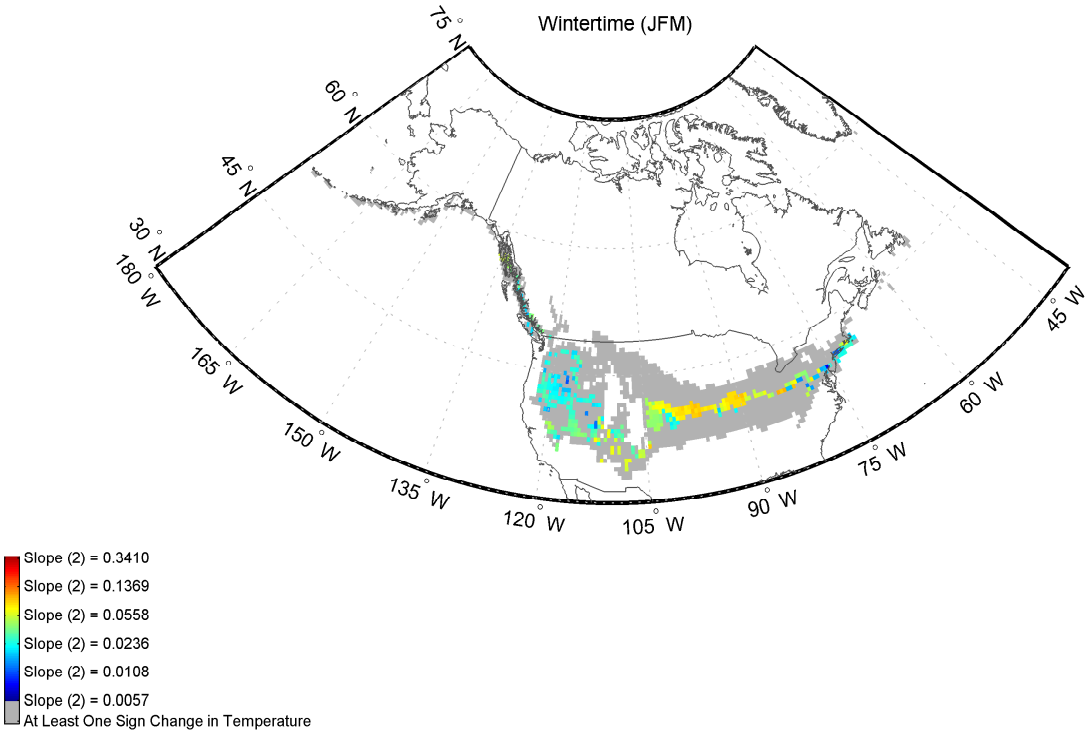


**Figure 5.22:** The same as Figure 5.21: zoomed in view of North America

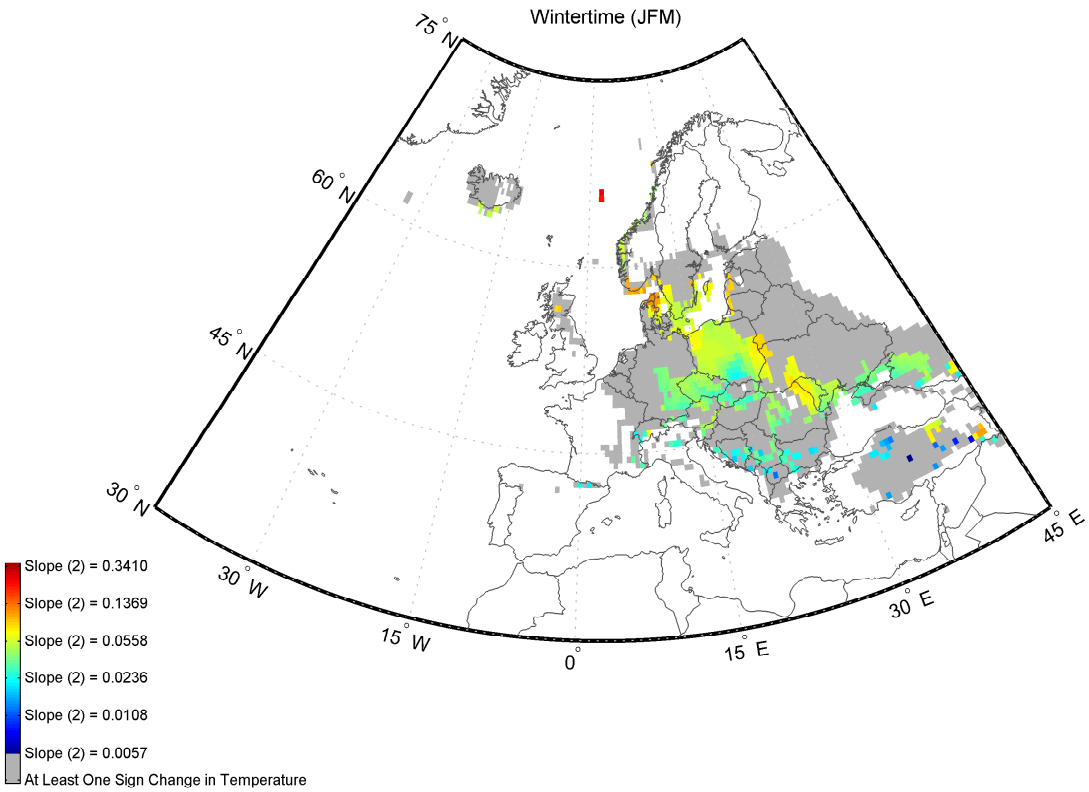


**Figure 5.23:** The same as Figure 5.21: zoomed in view of Europe

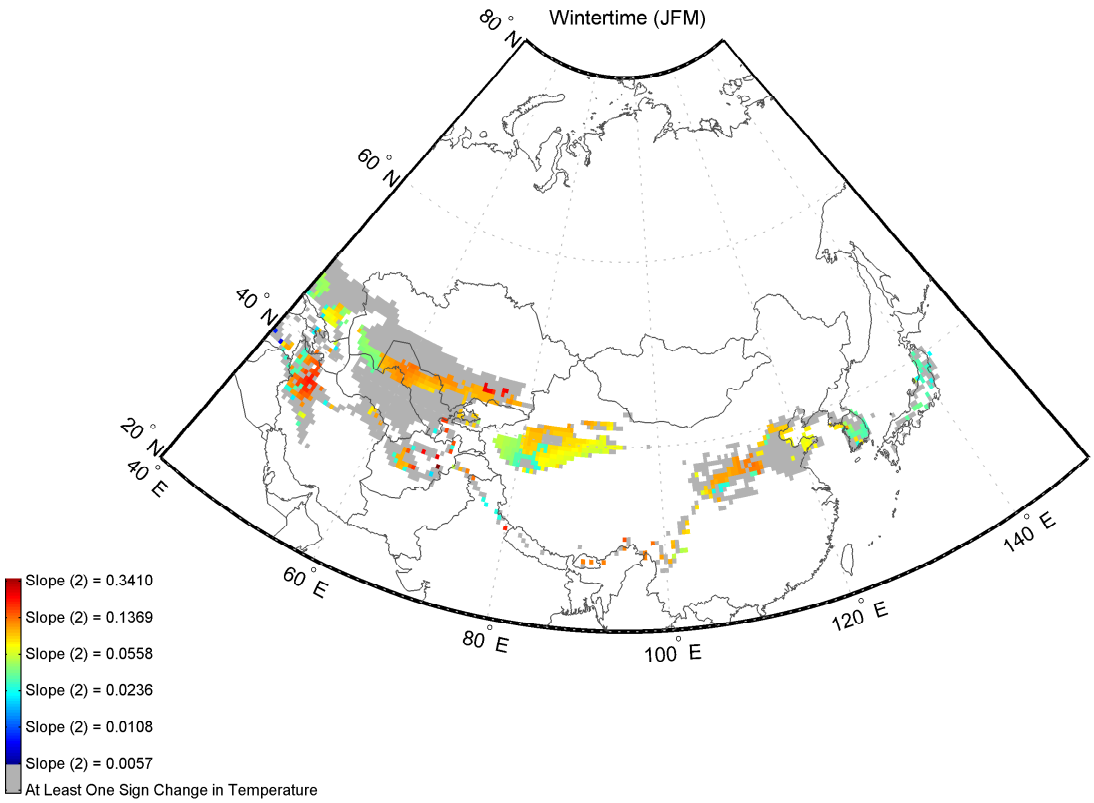


**Figure 5.24:** The same as Figure 5.21: zoomed in view of Asia

#### 5.4.3.2.5 H from $y_w$ to $y_0$

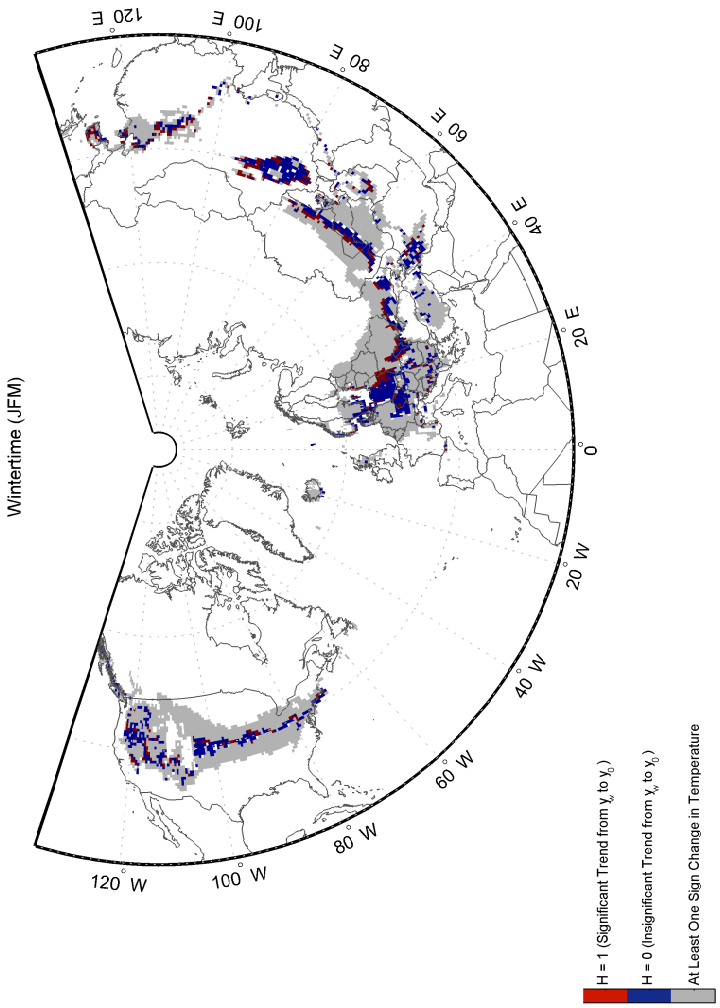


**Figure 5.25:** The map depicts the spatial distribution of H from $y_w$ to $y_0$ in the Northern Hemisphere during **JFM**. The results are obtained using **Model 2**, and the input parameters are as indicated in Section 5.4.1.

#### 5.4.3.2.6 H of $S_{interest}$

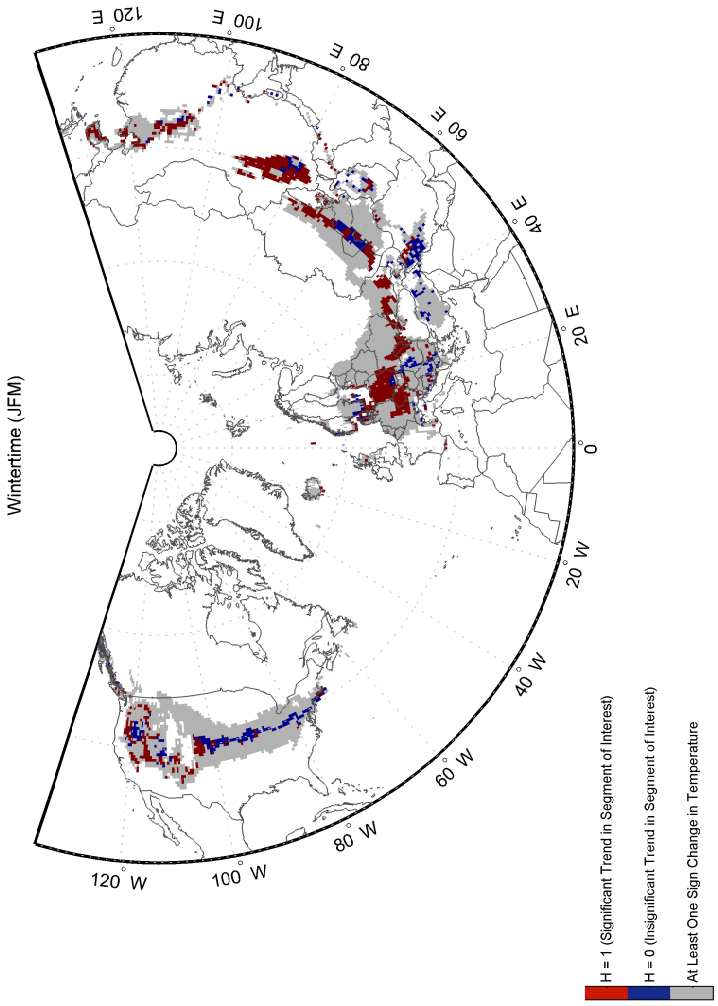


**Figure 5.26:** The map depicts the spatial distribution of H of $S_{interest}$ in the Northern Hemisphere during **JFM**. The results are obtained using **Model 2**, and the input parameters are as indicated in Section 5.4.1.

#### 5.4.3.2.7 H of $Sw_{total}$

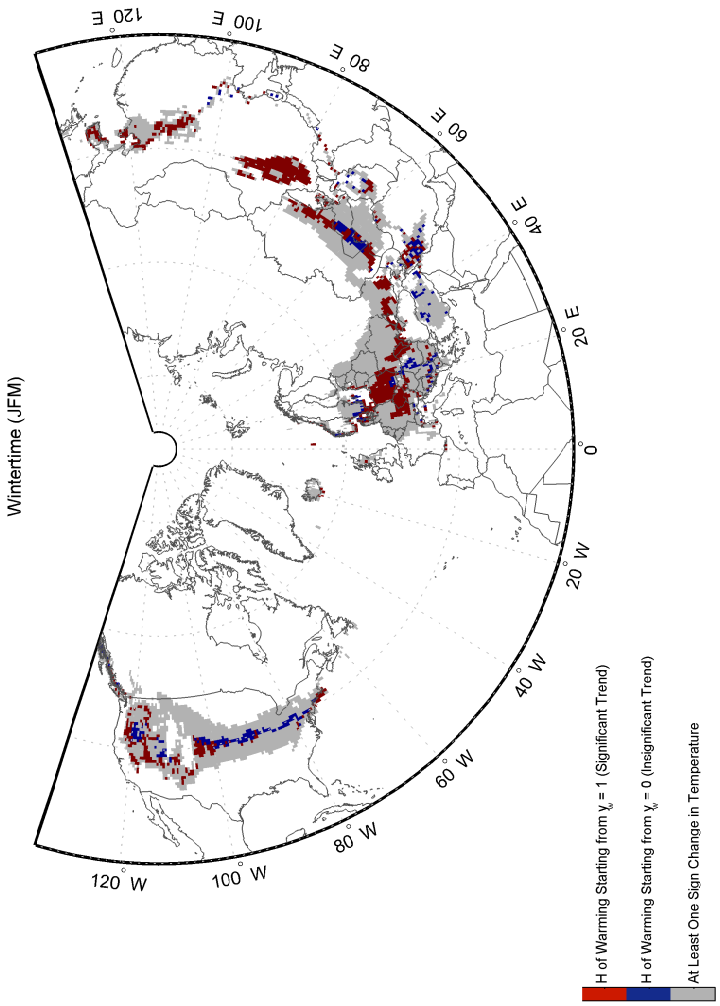


**Figure 5.27:** The map depicts the spatial distribution of H of $Sw_{total}$ in the Northern Hemisphere during **JFM**. The results are obtained using **Model 2**, and the input parameters are as indicated in Section 5.4.1.

#### 5.4.3.3 Maps of Model 2 for MAM

##### 5.4.3.3.1 $y_w$

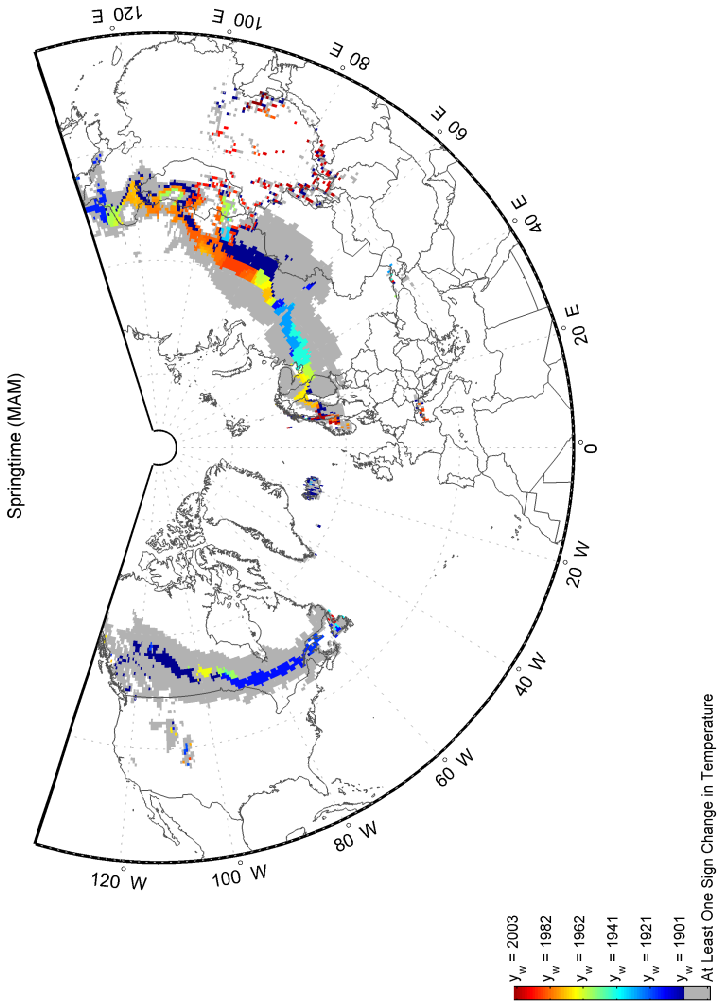


**Figure 5.28:** The map depicts the spatial distribution of $y_w$ in the Northern Hemisphere during **MAM**. The results are obtained using **Model 2**, and the input parameters are as indicated in Section 5.4.1.

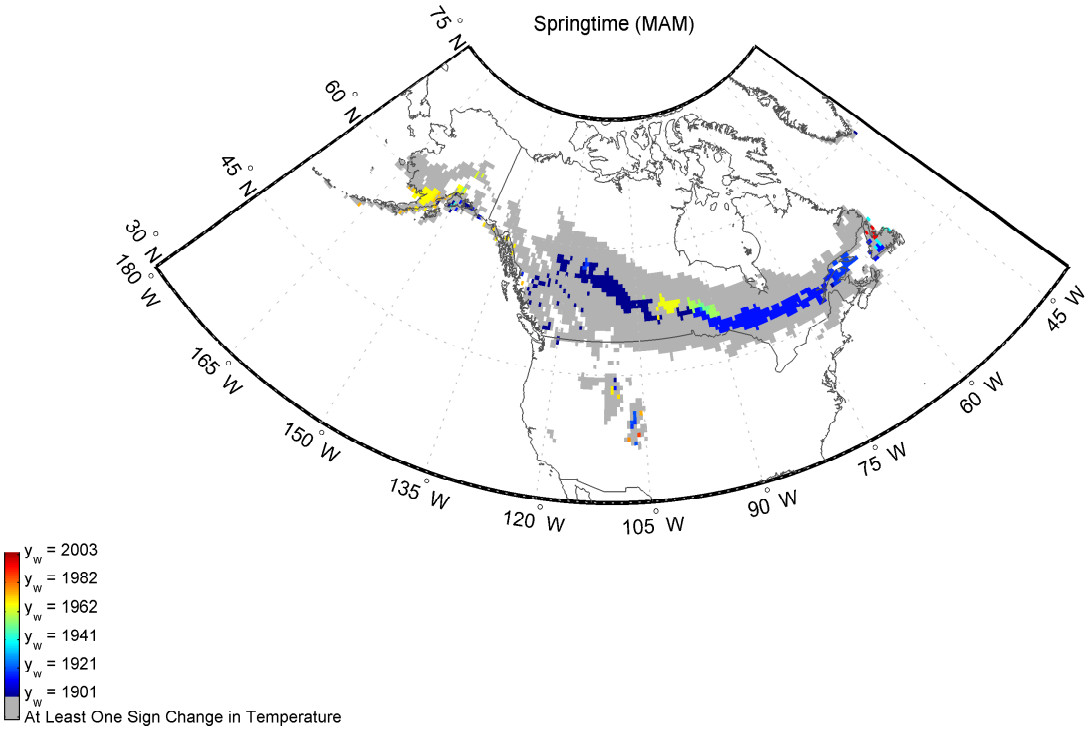


**Figure 5.29:** The same as Figure 5.28: zoomed in view of North America

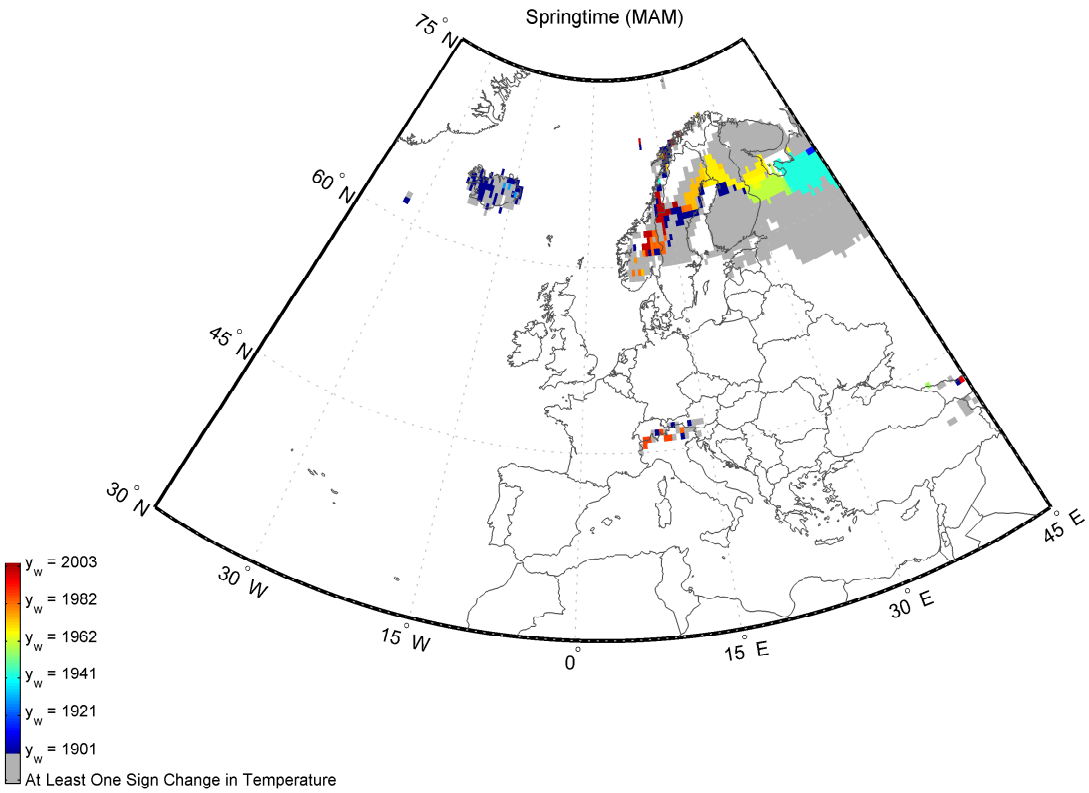


**Figure 5.30:** The same as Figure 5.28: zoomed in view of Europe

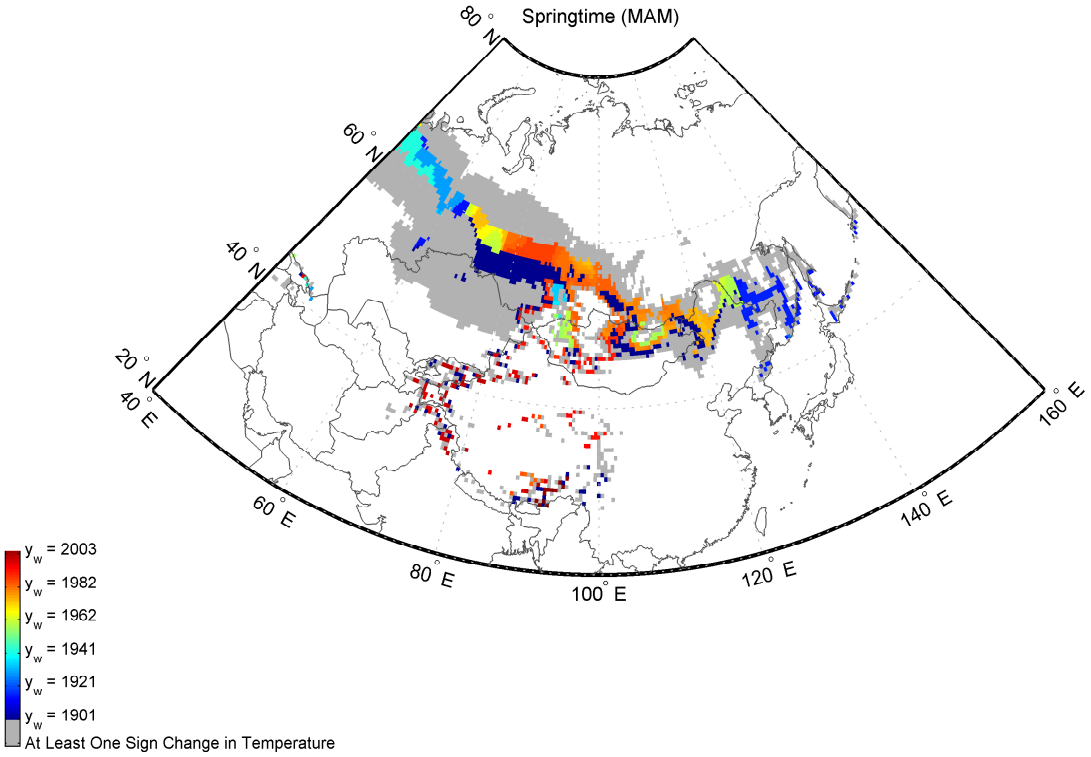


**Figure 5.31:** The same as Figure 5.28: zoomed in view of Asia

#### 5.4.3.3.2 $y_0$

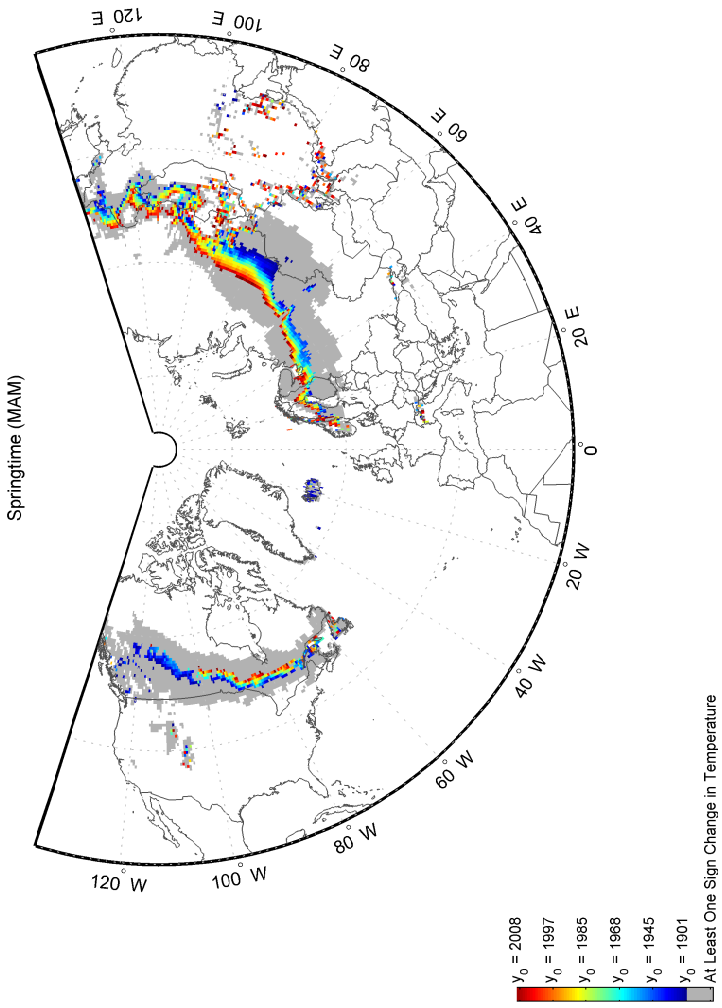


**Figure 5.32:** The map depicts the spatial distribution of $y_0$ in the Northern Hemisphere during **MAM**. The results are obtained using **Model 2**, and the input parameters are as indicated in Section 5.4.1.

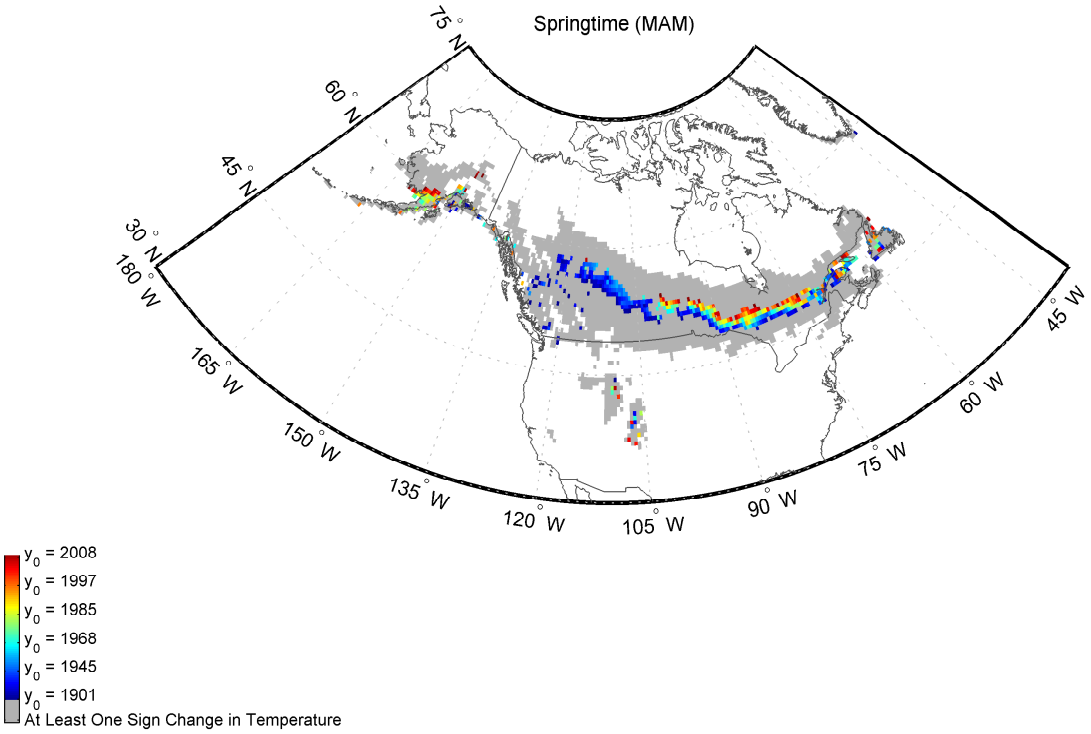


**Figure 5.33:** The same as Figure 5.32: zoomed in view of North America

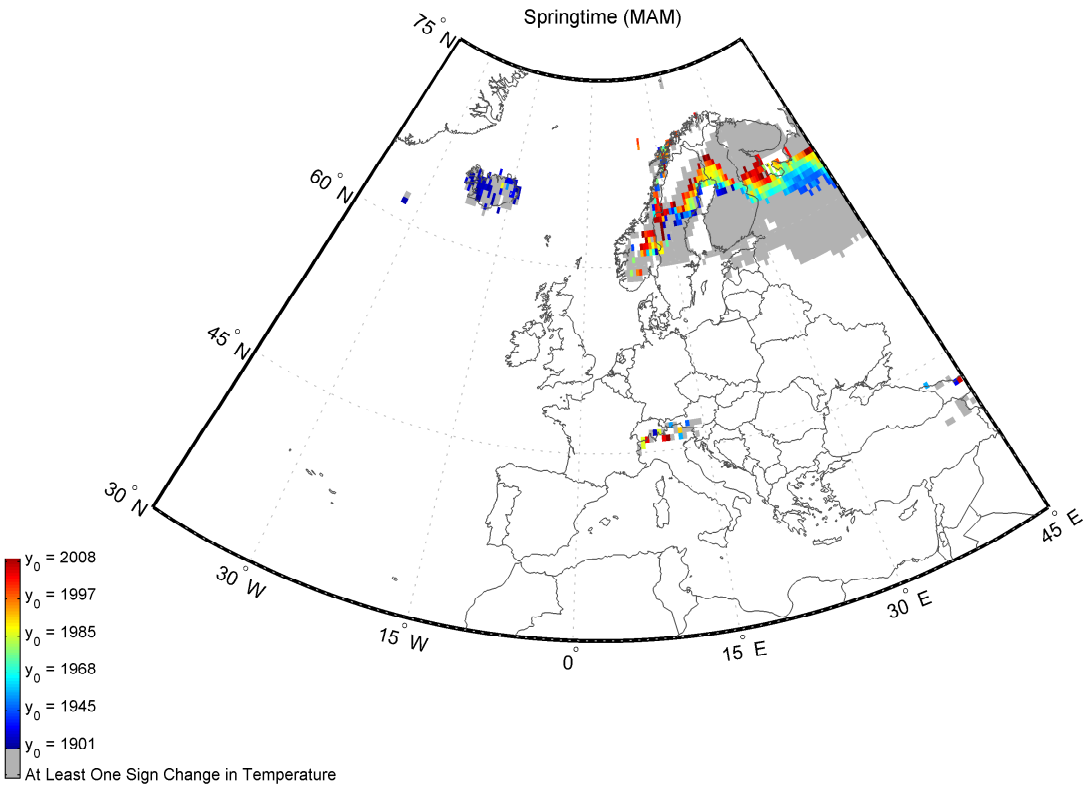


**Figure 5.34:** The same as Figure 5.32: zoomed in view of Europe

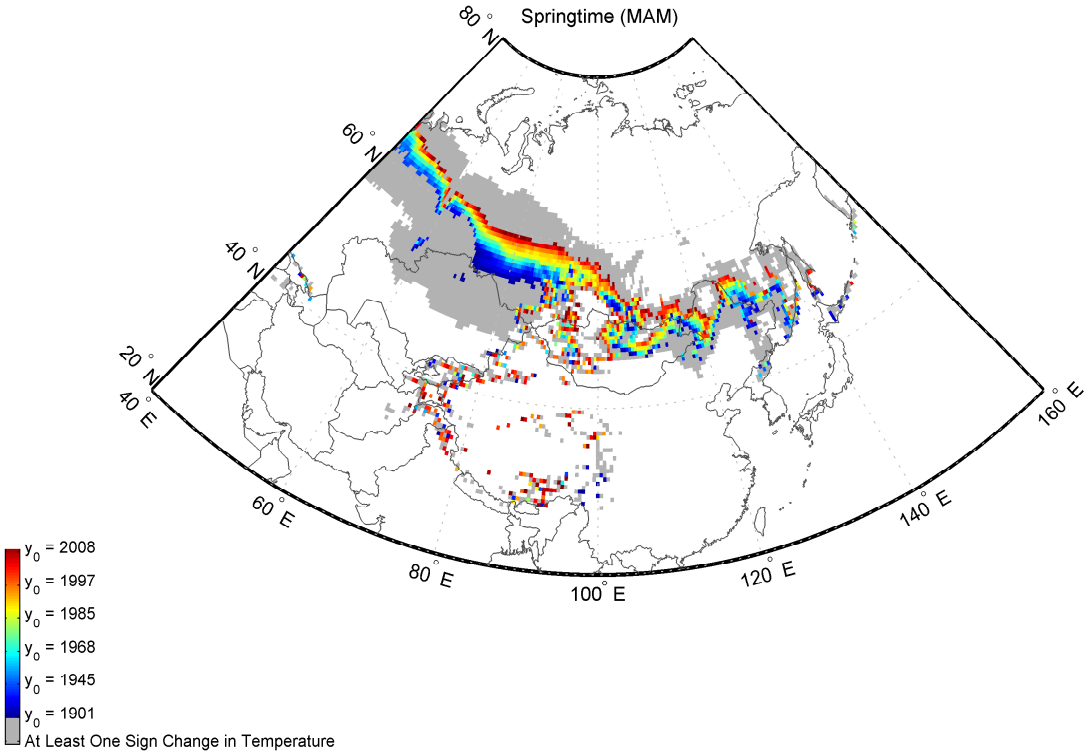


**Figure 5.35:** The same as Figure 5.32: zoomed in view of Asia

#### 5.4.3.3.3 Slope (1)

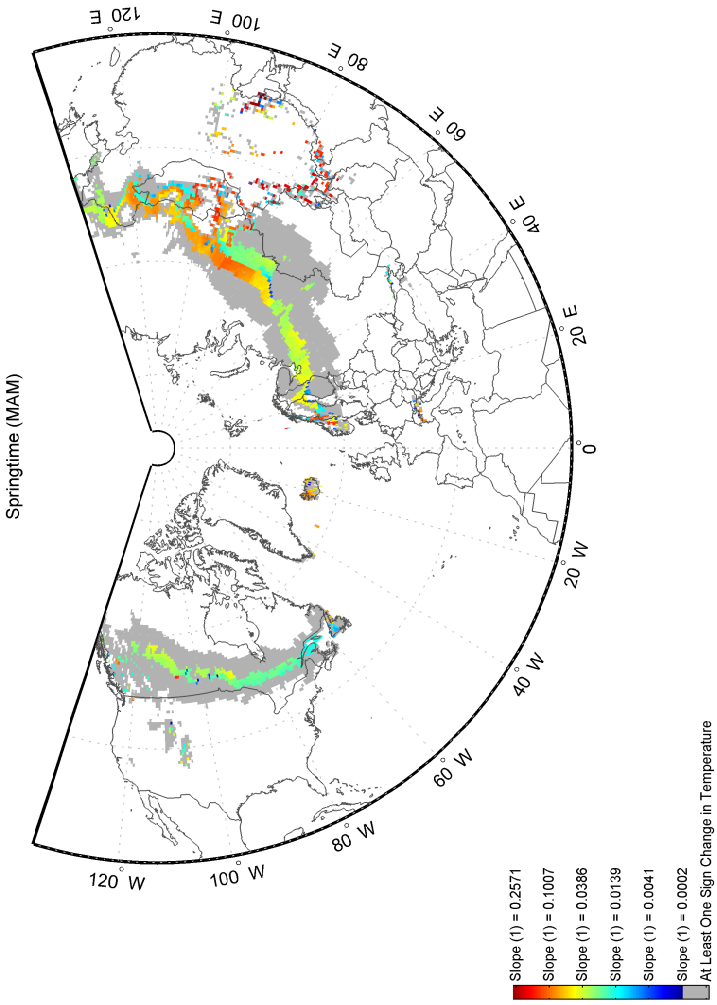


**Figure 5.36:** The map depicts the spatial distribution of Slope (1) in the Northern Hemisphere during **MAM**. The results are obtained using **Model 2**, and the input parameters are as indicated in Section 5.4.1. Refer to Section 5.2 for the definition of 'Slope (1)'.

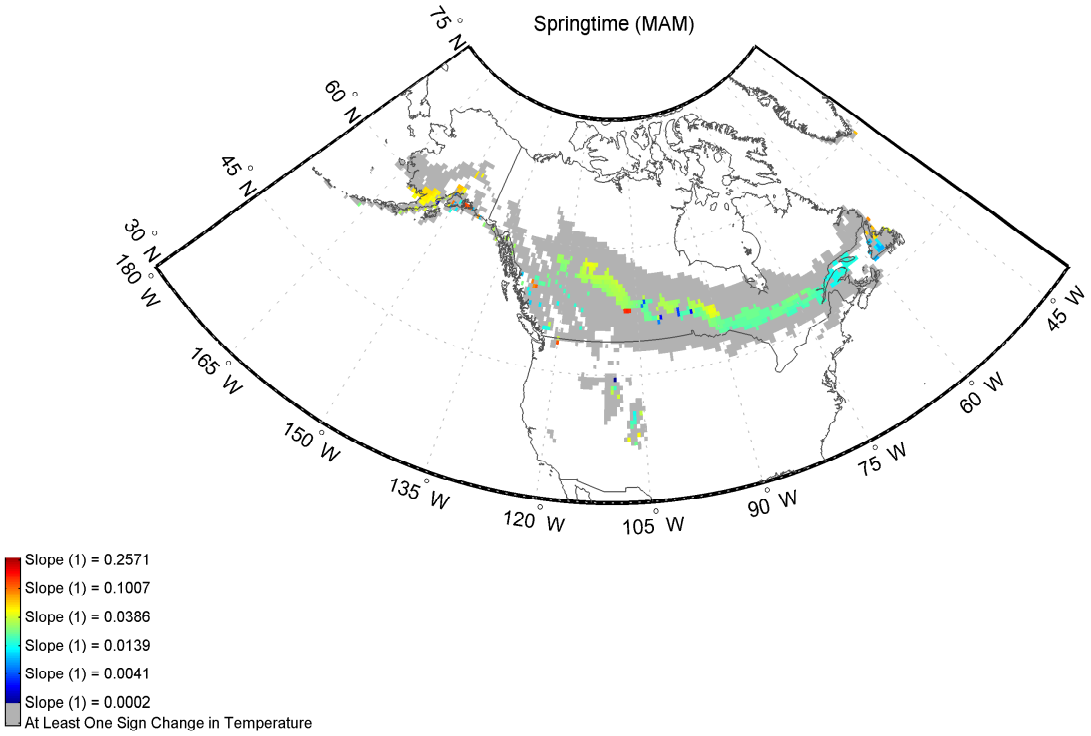


**Figure 5.37:** The same as Figure 5.36: zoomed in view of North America

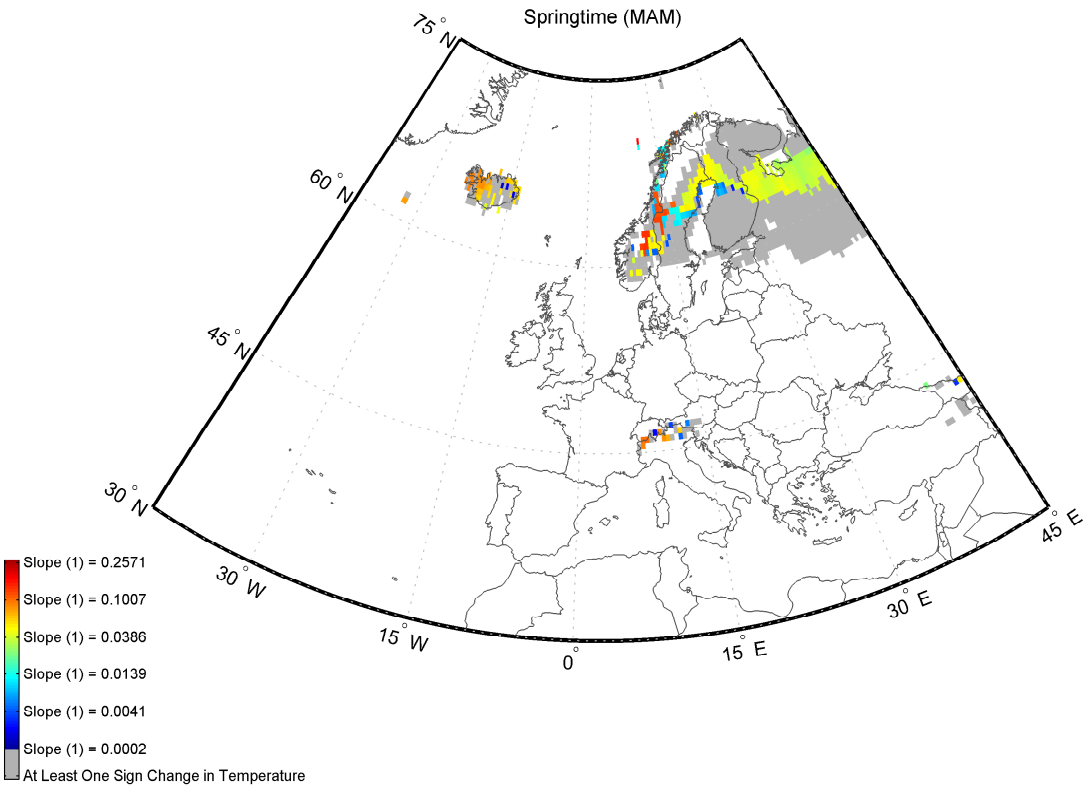


**Figure 5.38:** The same as Figure 5.36: zoomed in view of Europe

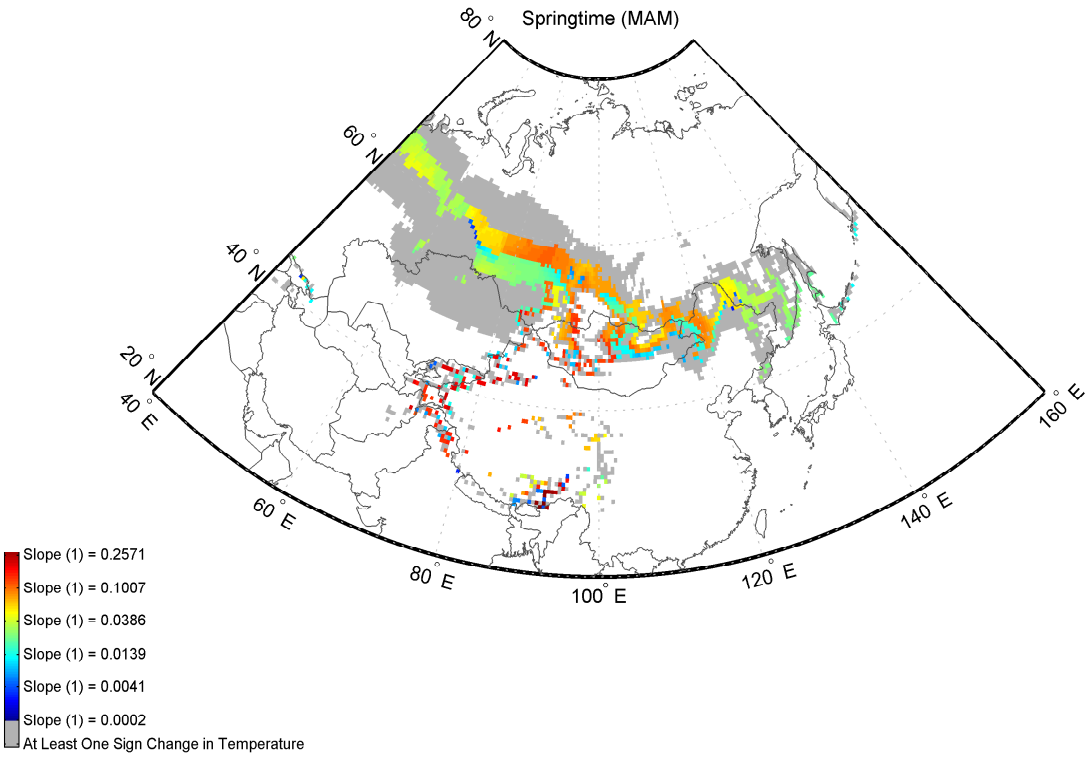


**Figure 5.39:** The same as Figure 5.36: zoomed in view of Asia

#### 5.4.3.3.4 Slope (2)

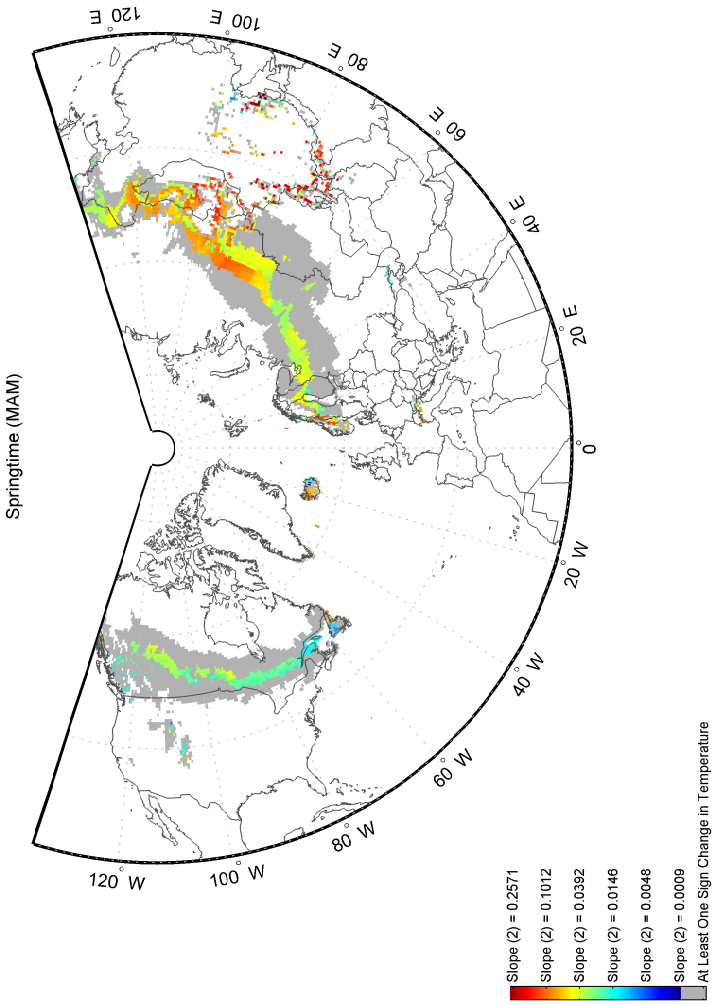


**Figure 5.40:** The map depicts the spatial distribution of Slope (2) in the Northern Hemisphere during **MAM**. The results are obtained using **Model 2**, and the input parameters are as indicated in Section 5.4.1. Refer to Section 5.2 for the definition of 'Slope (2)'.

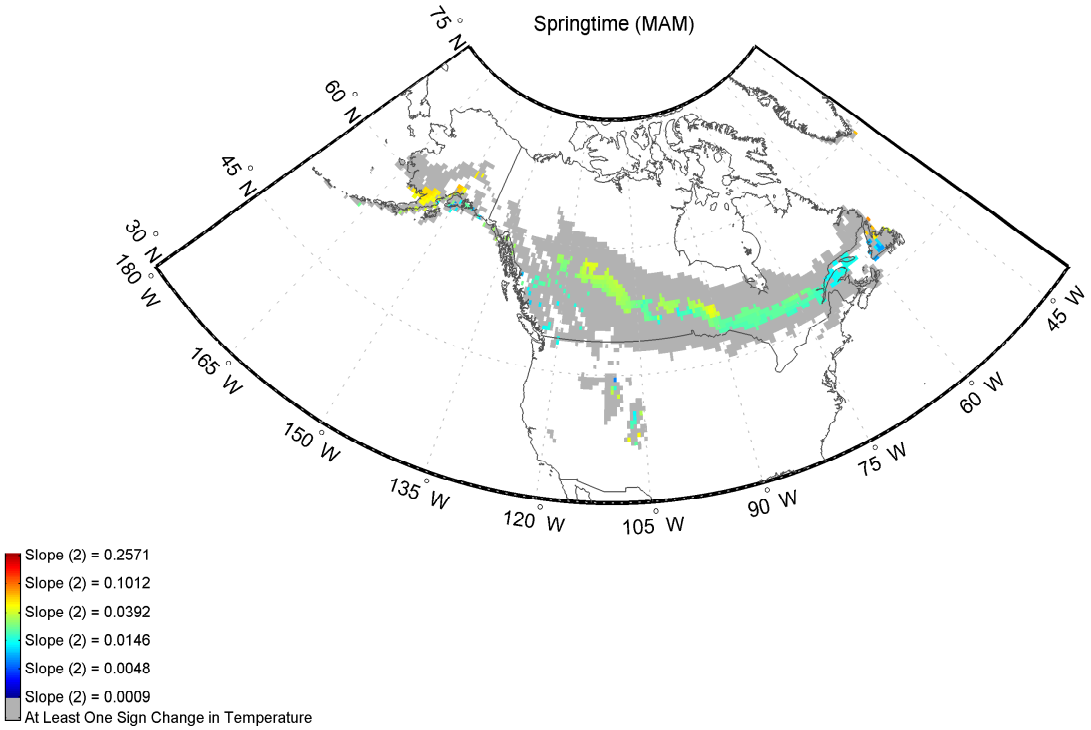


**Figure 5.41:** The same as Figure 5.40: zoomed in view of North America

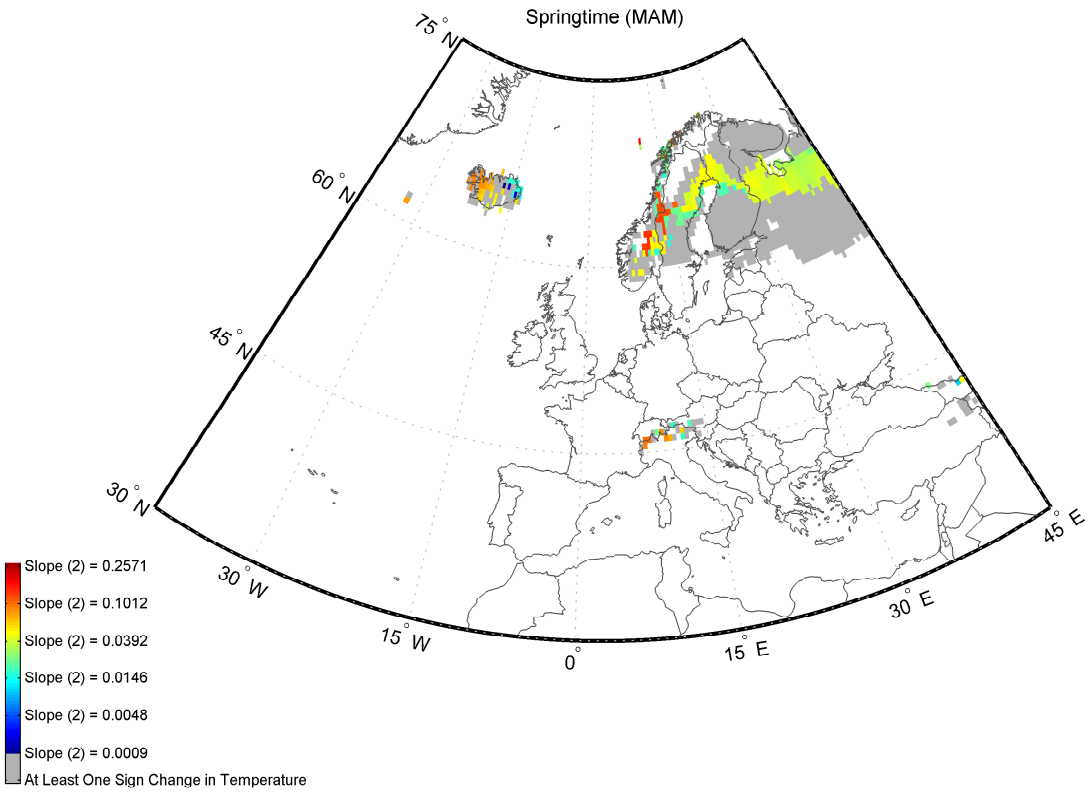


**Figure 5.42:** The same as Figure 5.40: zoomed in view of Europe

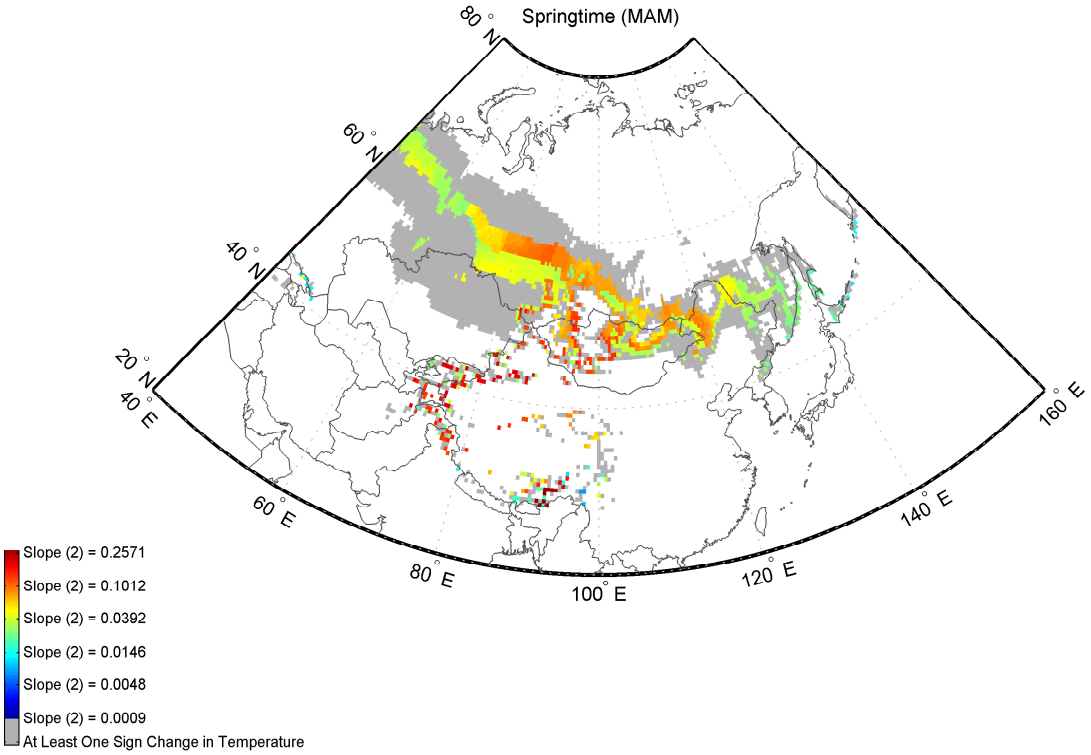


**Figure 5.43:** The same as Figure 5.40: zoomed in view of Asia

#### 5.4.3.3.5 H from $y_w$ to $y_0$

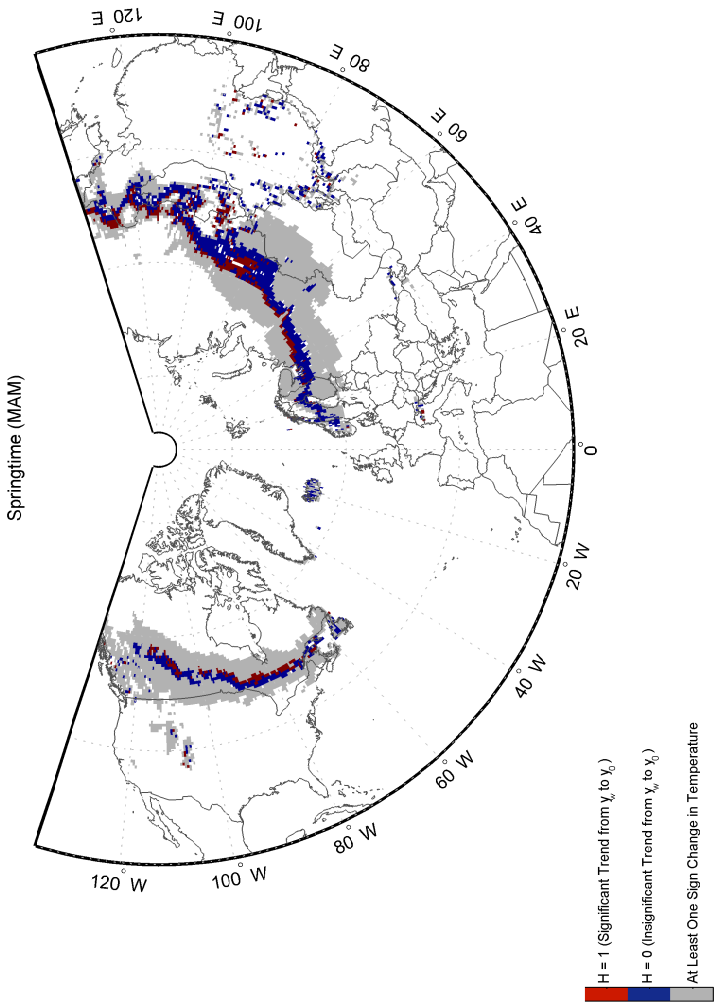


**Figure 5.44:** The map depicts the spatial distribution of H from $y_w$ to $y_0$ in the Northern Hemisphere during **MAM**. The results are obtained using **Model 2**, and the input parameters are as indicated in Section 5.4.1.

#### 5.4.3.3.6 H of $S_{interest}$

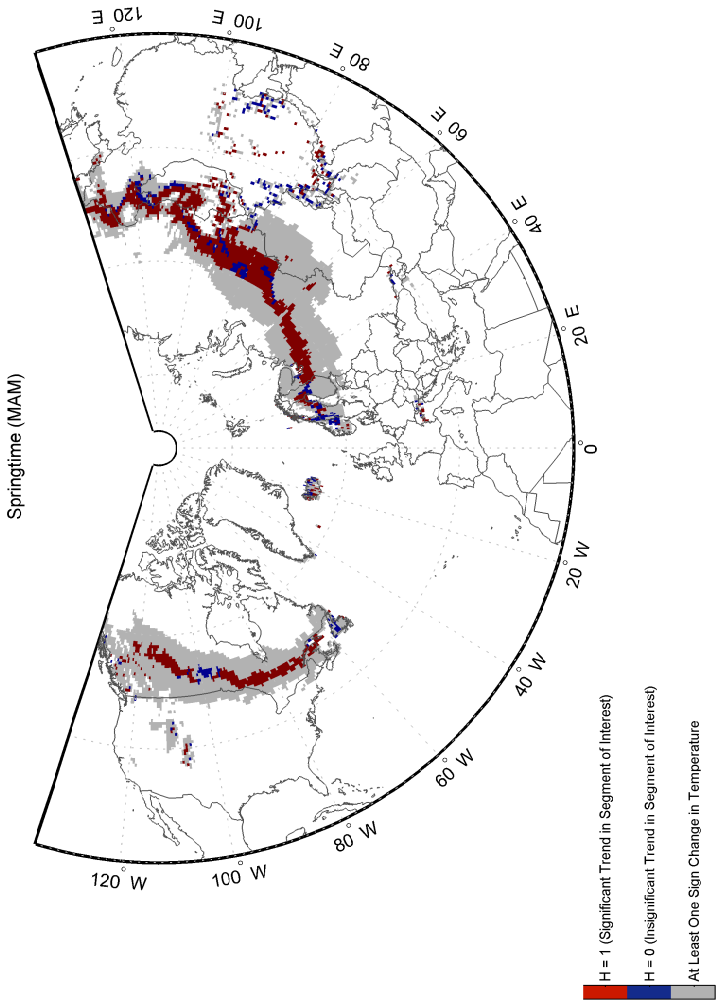


**Figure 5.45:** The map depicts the spatial distribution of H of $S_{interest}$ in the Northern Hemisphere during **MAM**. The results are obtained using **Model 2**, and the input parameters are as indicated in Section 5.4.1.

#### 5.4.3.3.7 H of $Sw_{total}$

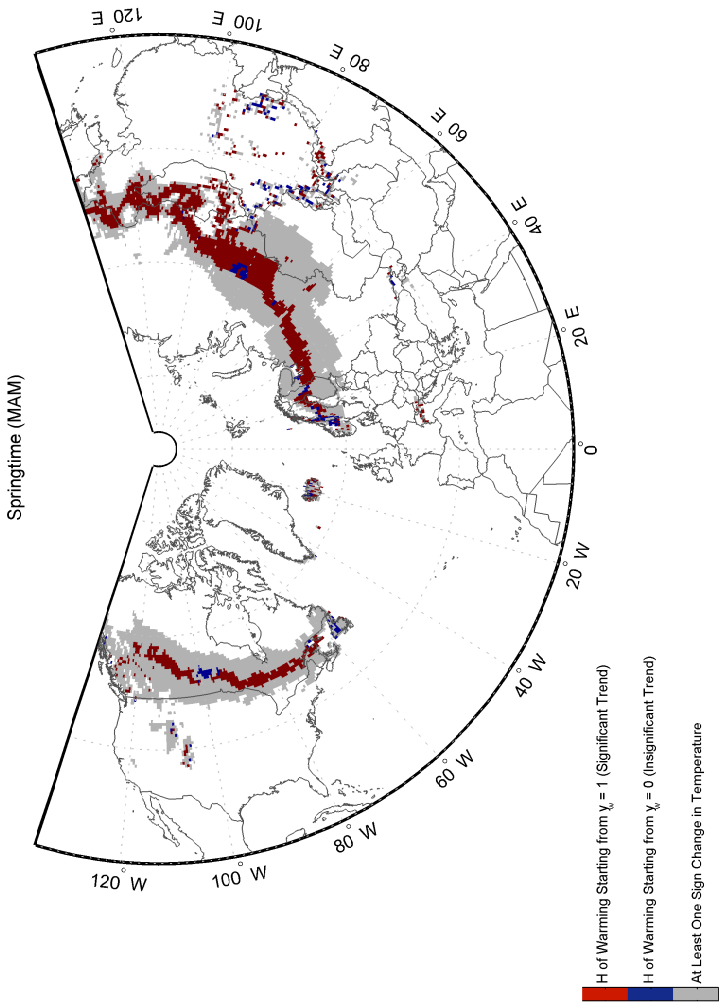


**Figure 5.46:** The map depicts the spatial distribution of H of $Sw_{total}$ in the Northern Hemisphere during **MAM**. The results are obtained using **Model 2**, and the input parameters are as indicated in Section 5.4.1.

### 5.4.4 Model 3 Results

As with Model 2, the results are presented in the form of a descriptive table (Table 5.2), histograms (JFM: Figures 5.47 to 5.51, MAM: Figures 5.52 to 5.56), and maps (JFM: Figures 5.57 to 5.75, MAM: Figures 5.76 to 5.94). The results are thoroughly explained and discussed in Sections 5.8.3 (tables and histograms) and 5.8.4 (maps).

**Table 5.2:** Based on the analysis of the JFM and MAM time series using **Model 3**, the table provides some information on the numbers of grid cells with specific characteristics described in the left column. The input parameters are as indicated in Section 5.4.1. The reader is referred to Section 5.3 for more details on the cases presented below.

| **Characteristic** | **Number** | |
|---|---|---|
| | **JFM** | **MAM** |
| Selected for study (following Rule 1 of *transition area*, described in Section 4.3) | 6206/46224 | 9842/46224 |
| Last modelled temperature positive (based on Rule 2 of *transition area*, described in Section 4.3) | 3481/6206 | 6147/9842 |
| Final database: selected for the $y_w$ and $y_0$ analysis (based on Rules 1 and 2 of *transition area*) | **1471/3481** | **2233/6147** |
| Two positive 0°C crossings: The first segment crosses 0°C and has the maximum slope; i.e., Rule 2a of $y_w$ and $y_0$ determination applies (Section 5.4.2) | 148/1471 | 114/2233 |
| $y_w = 1901$ | 105/1471 | 523/2233 |
| Duration of $y_w$ to $y_0$ less than 3 years, MK test N/A | 41/1471 | 94/2233 |
| $S_{W_{total}}$ is the same as $S_{interest}$ | 1410/1471 | 1898/2233 |

#### 5.4.4.1 Histograms

##### 5.4.4.1.1 JFM

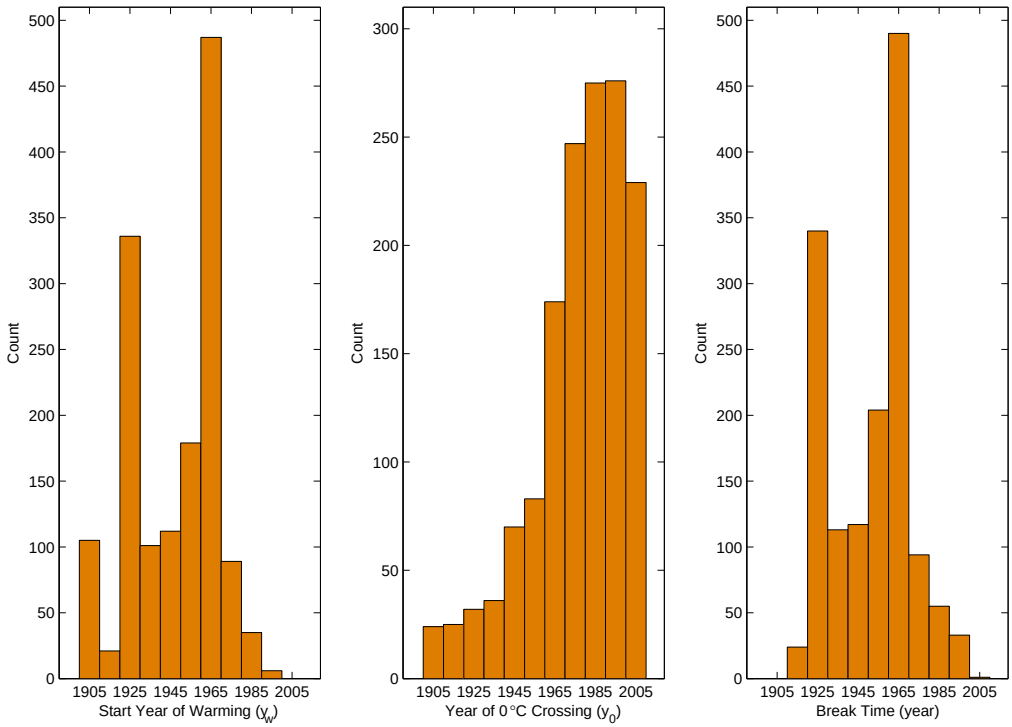


**Figure 5.47:** The histograms exhibit the temporal distributions of $y_w$, $y_0$, and break date during **JFM**. The results are obtained using **Model 3**, and the input parameters are as indicated in Section 5.4.1.

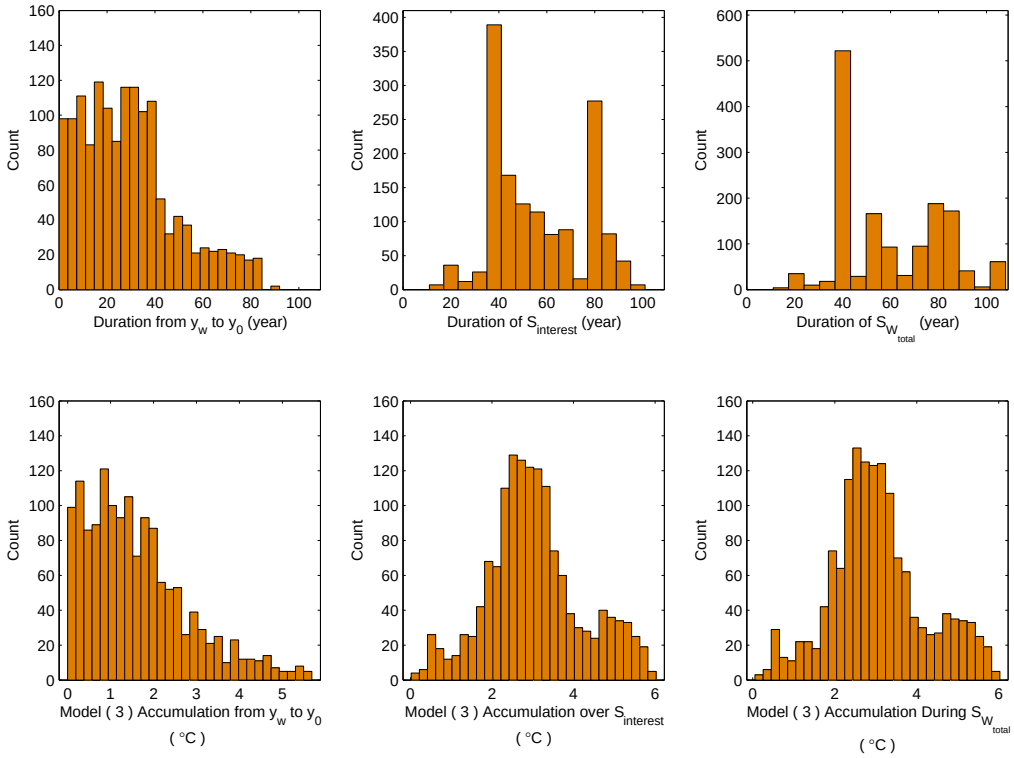


**Figure 5.48:** The histograms exhibit the distributions of duration and temperature accumulation during $y_w - y_0$, $S_{interest}$, and $S_{W_{total}}$ for **JFM**. The results are obtained using **Model 3**, and the input parameters are as indicated in Section 5.4.1. The reader is referred to Section 5.2 for details on the variables used above.

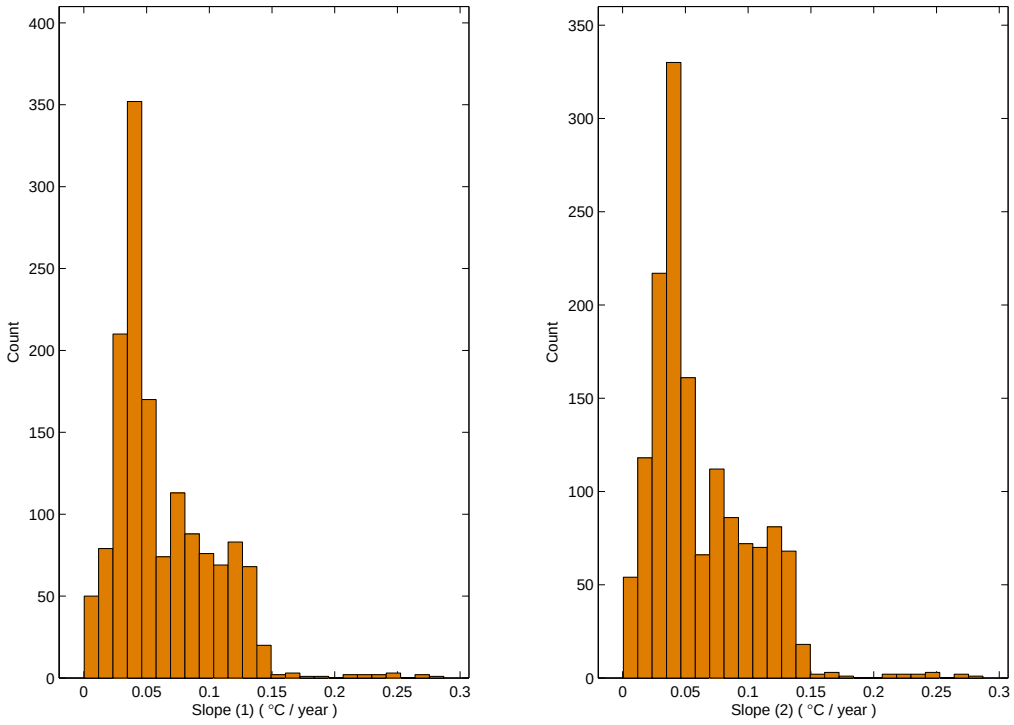


**Figure 5.49:** The histograms exhibit the distributions of Slope (1) and Slope (2) for **JFM**. The results are obtained using **Model 3**, and the input parameters are as indicated in Section 5.4.1. The reader is referred to Section 5.2 for details on the variables used above.

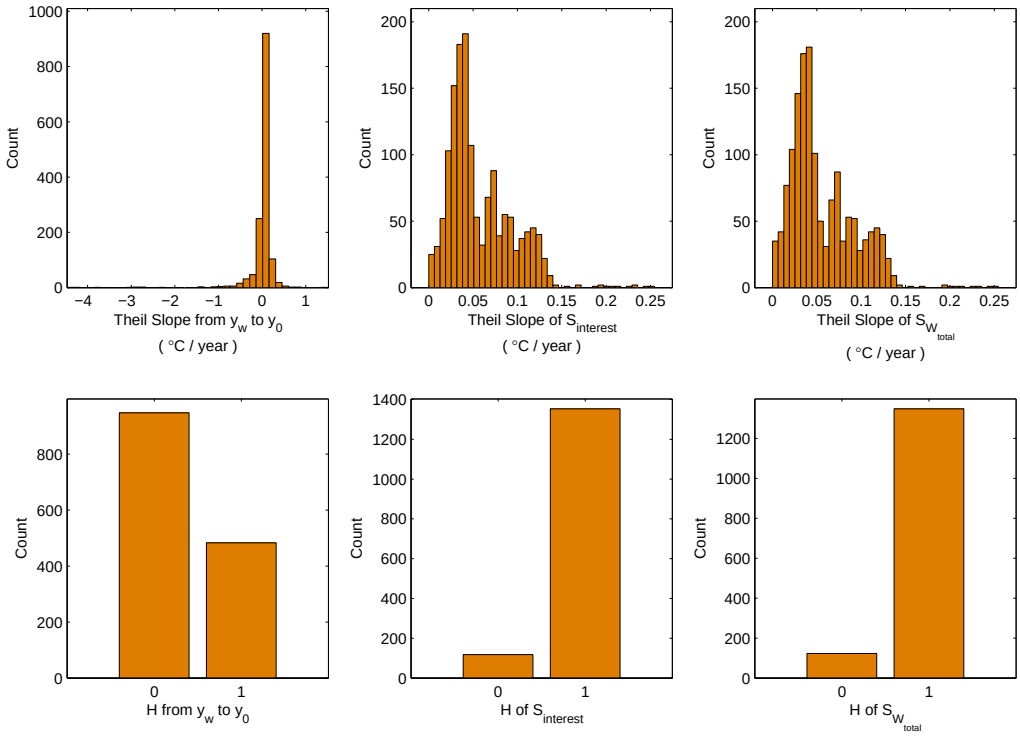


**Figure 5.50:** The histograms exhibit the distributions of Theil slope and H during $y_w - y_0$, $S_{interest}$, and $S_{W_{total}}$ for **JFM**. The results are obtained using **Model 3**, and the input parameters are as indicated in Section 5.4.1. The reader is referred to Section 5.2 for details on the variables used above.

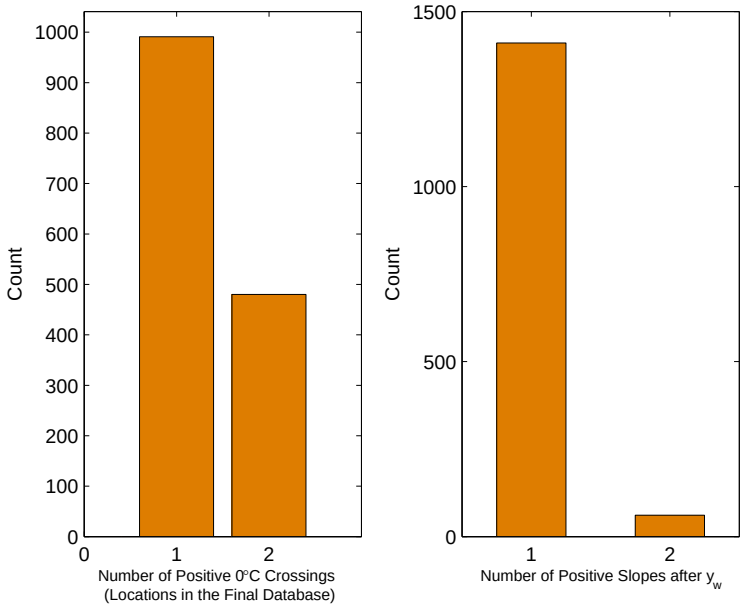


**Figure 5.51:** The histograms exhibit the distributions of number of positive 0°C crossings and positive slopes after $y_w$ for **JFM**. The results are obtained using **Model 3**, and the input parameters are as indicated in Section 5.4.1.

#### 5.4.4.1.2 MAM

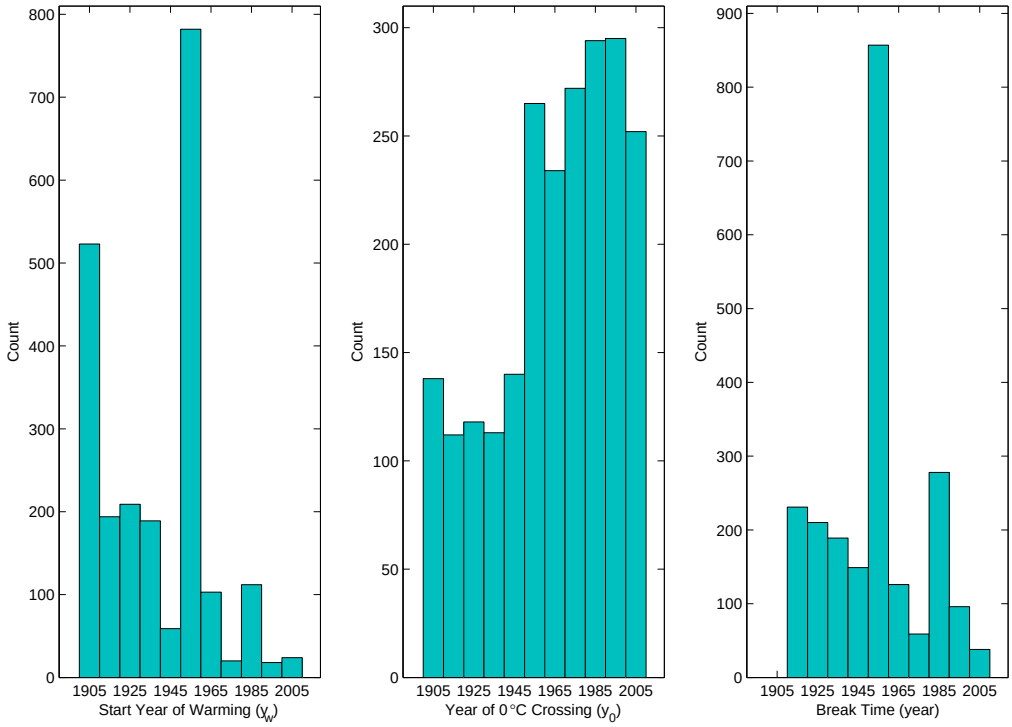


**Figure 5.52:** The histograms exhibit the temporal distributions of $y_w$, $y_0$, and break date during **MAM**. The results are obtained using **Model 3**, and the input parameters are as indicated in Section 5.4.1.

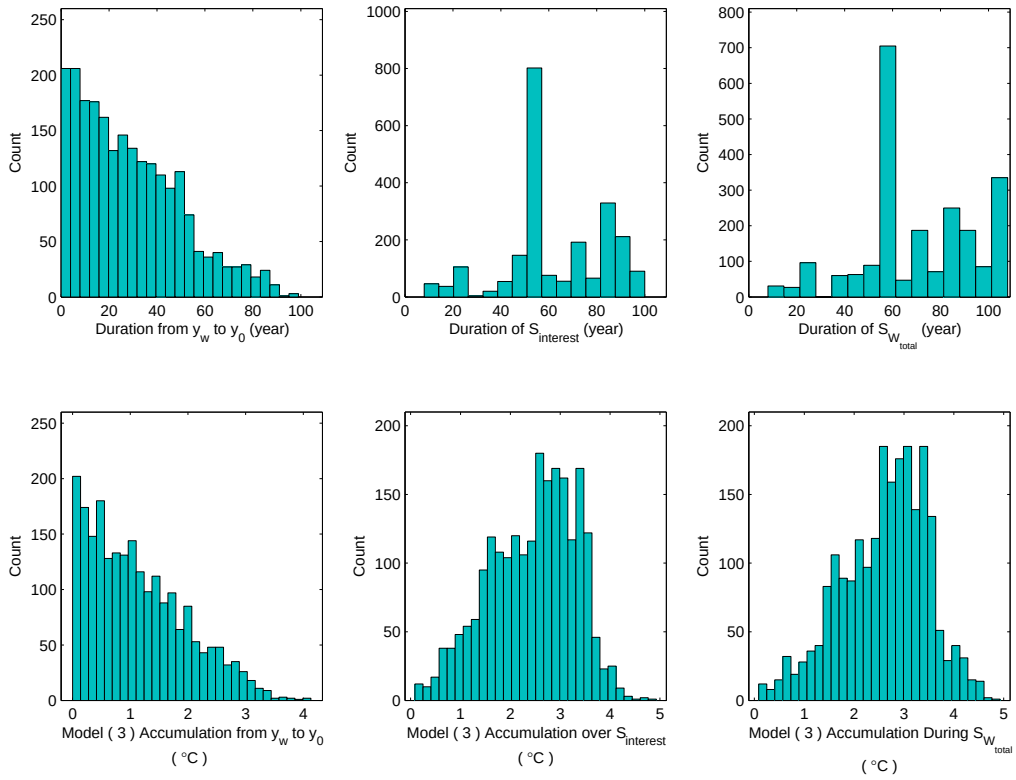


**Figure 5.53:** The histograms exhibit the distributions of duration and temperature accumulation during $y_w - y_0$, $S_{interest}$, and $S_{W_{total}}$ for **MAM**. The results are obtained using **Model 3**, and the input parameters are as indicated in Section 5.4.1. The reader is referred to Section 5.2 for details on the variables used above.

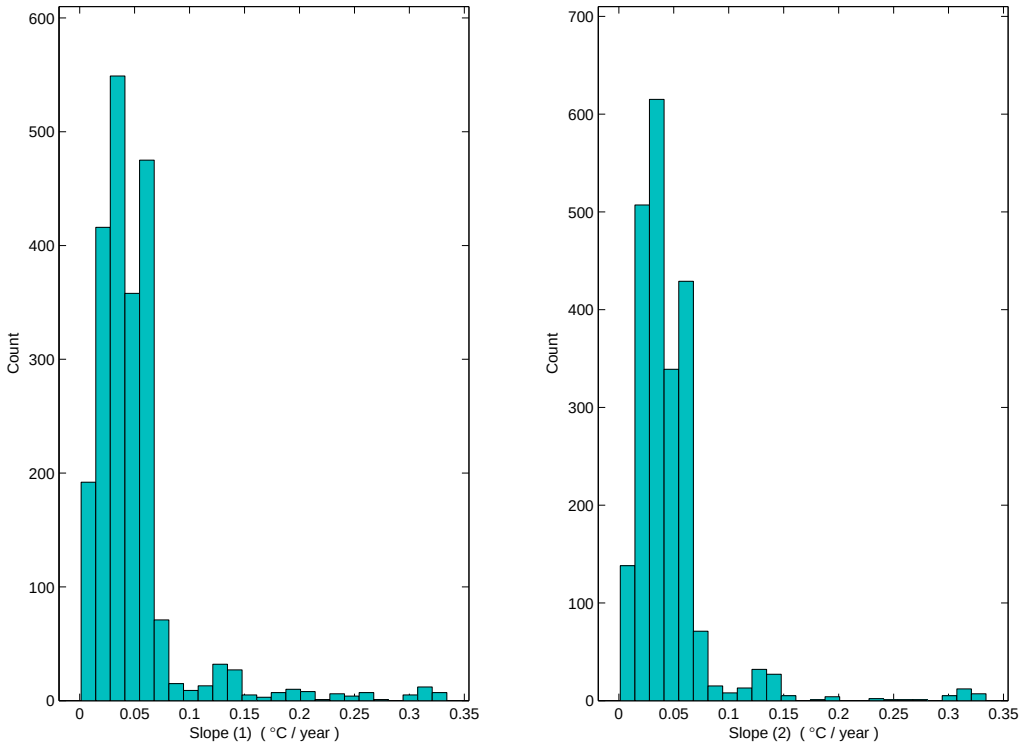


**Figure 5.54:** The histograms exhibit the distributions of Slope (1) and Slope (2) for **MAM**. The results are obtained using **Model 3**, and the input parameters are as indicated in Section 5.4.1. The reader is referred to Section 5.2 for details on the variables used above.

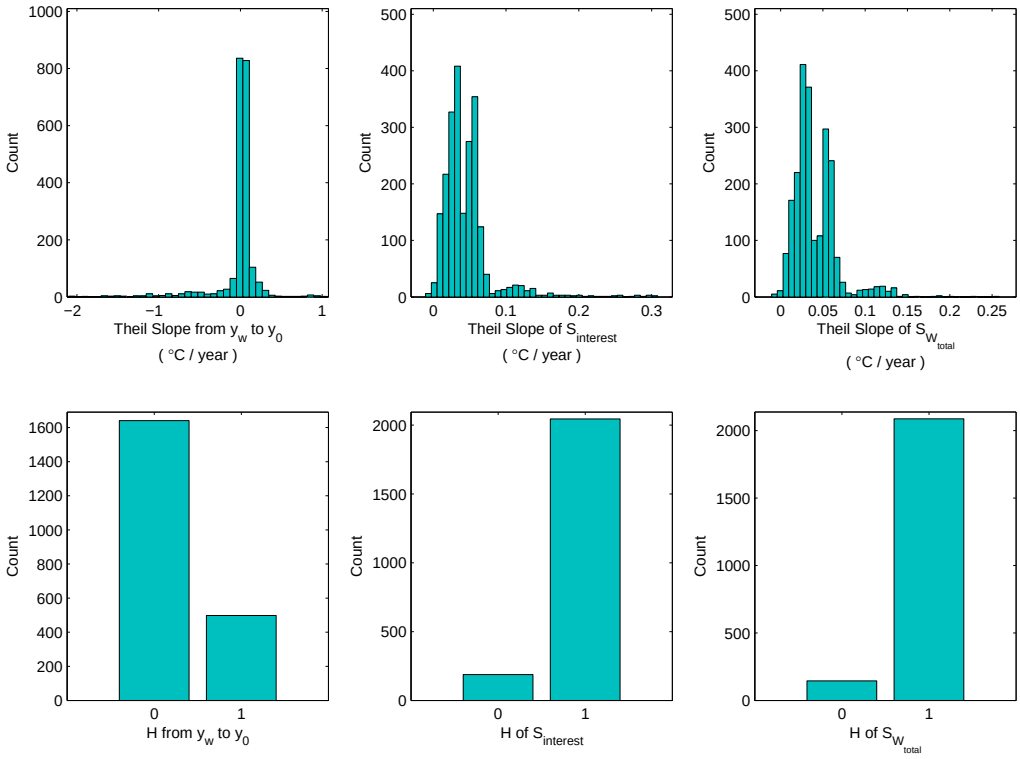


**Figure 5.55:** The histograms exhibit the distributions of Theil slope and H during $y_w - y_0$, $S_{interest}$, and $S_{W_{total}}$ for **MAM**. The results are obtained using **Model 3**, and the input parameters are as indicated in Section 5.4.1. The reader is referred to Section 5.2 for details on the variables used above.

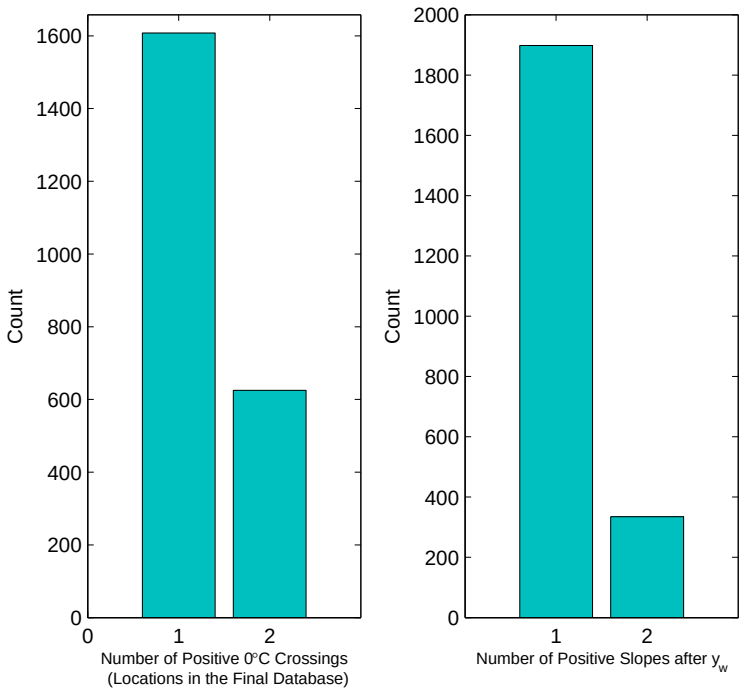


**Figure 5.56:** The histograms exhibit the distributions of number of positive 0°C crossings and positive slopes after $y_w$ for **MAM**. The results are obtained using **Model 3**, and the input parameters are as indicated in Section 5.4.1.

#### 5.4.4.2 Maps of Model 3 for JFM

##### 5.4.4.2.1 $y_w$

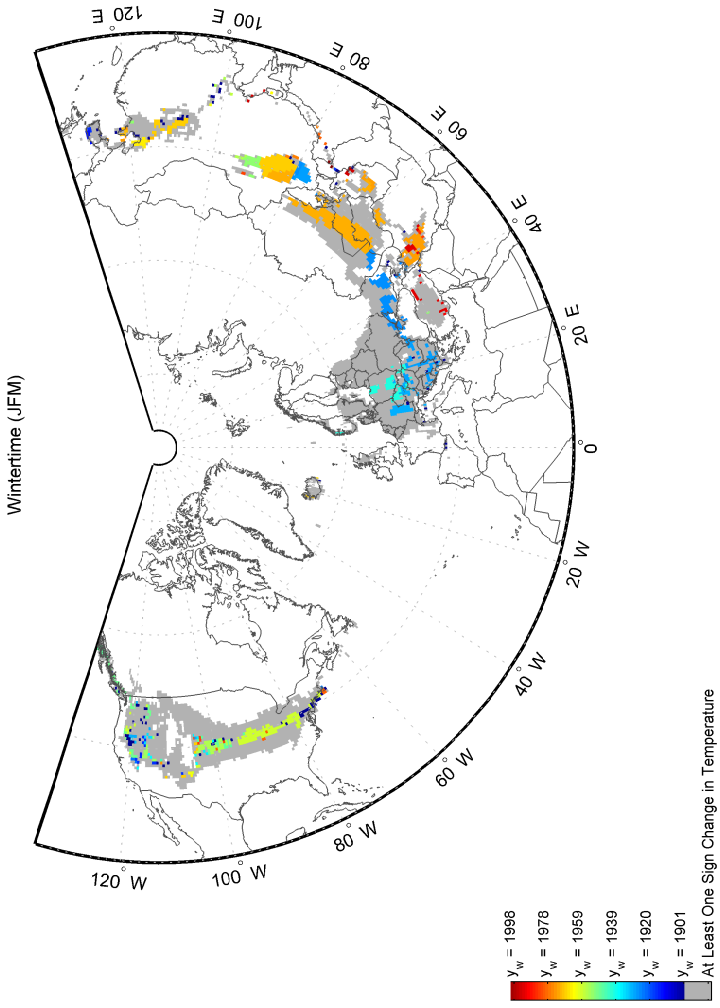


**Figure 5.57:** The map depicts the spatial distribution of $y_w$ in the Northern Hemisphere during **JFM**. The results are obtained using **Model 3**, and the input parameters are as indicated in Section 5.4.1.

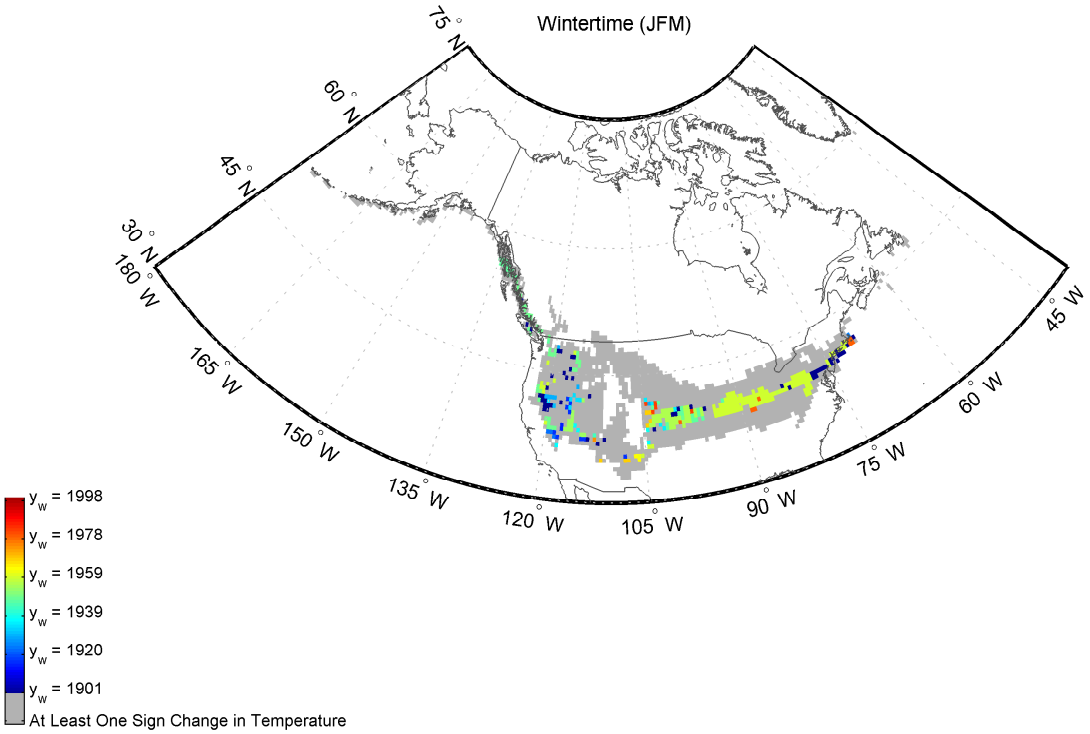


**Figure 5.58:** The same as Figure 5.57: zoomed in view of North America

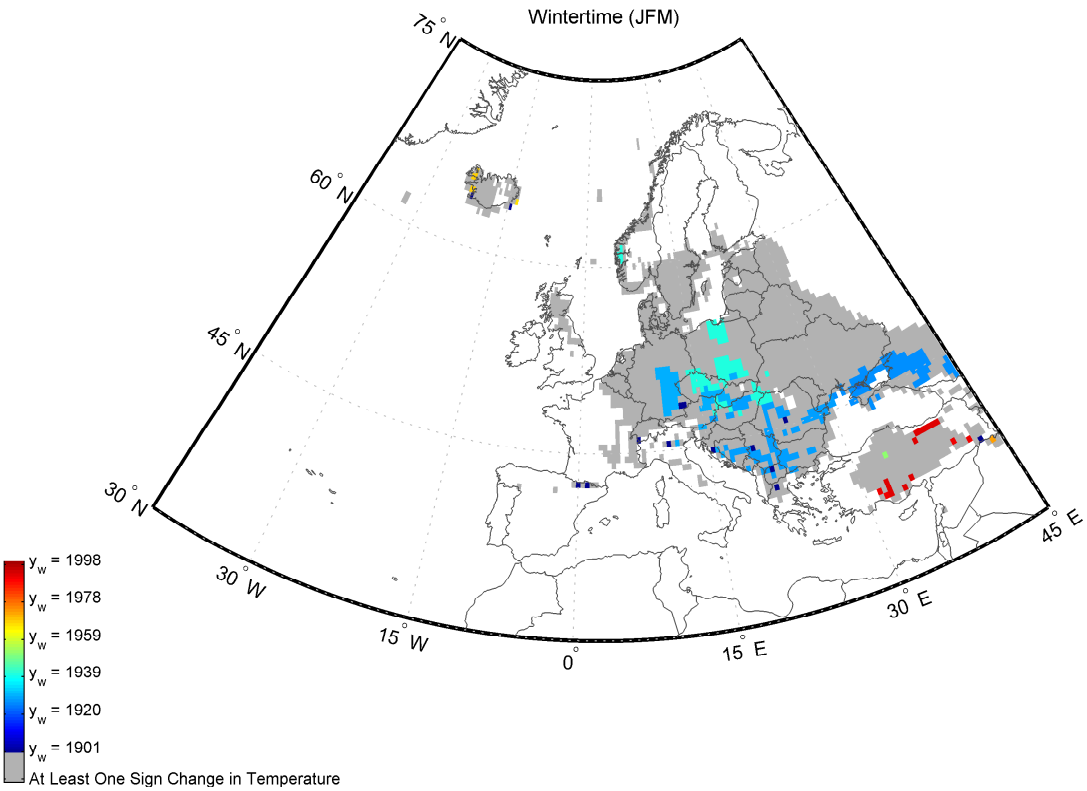


**Figure 5.59:** The same as Figure 5.57: zoomed in view of Europe

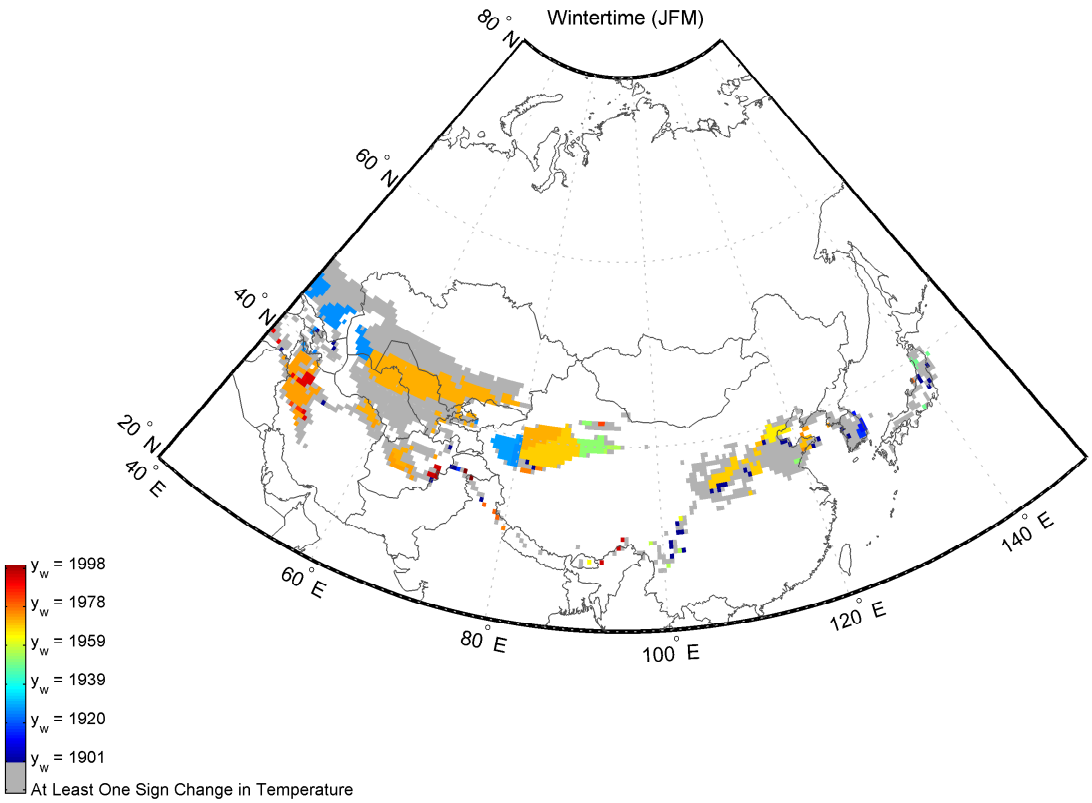


**Figure 5.60:** The same as Figure 5.57: zoomed in view of Asia

#### 5.4.4.2.2 $y_0$

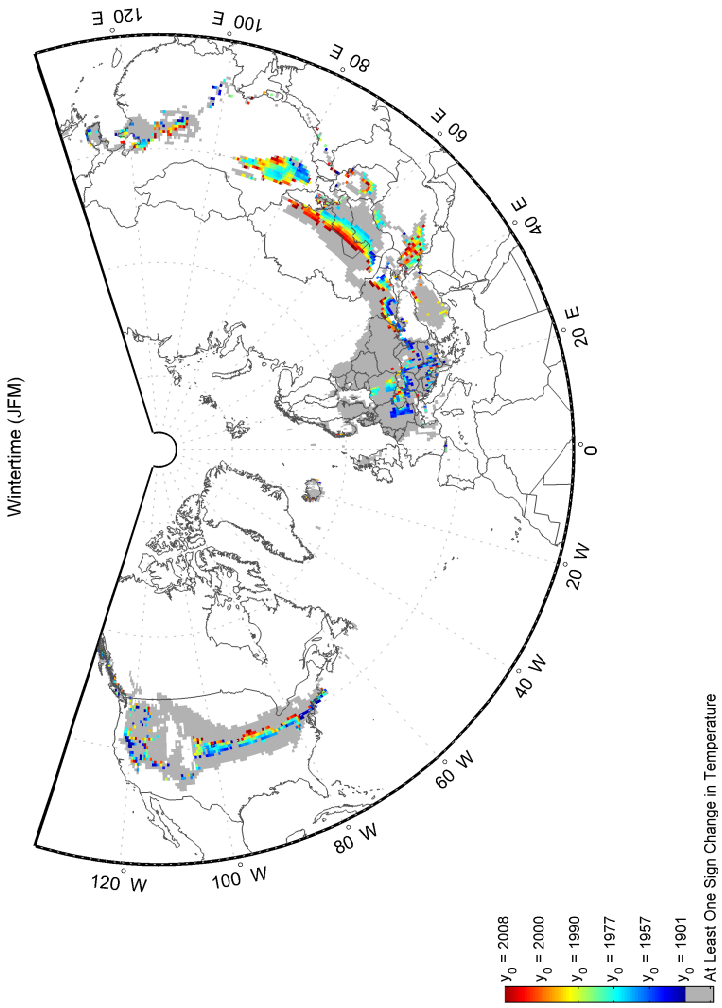


**Figure 5.61:** The map depicts the spatial distribution of $y_0$ in the Northern Hemisphere during **JFM**. The results are obtained using **Model 3**, and the input parameters are as indicated in Section 5.4.1.

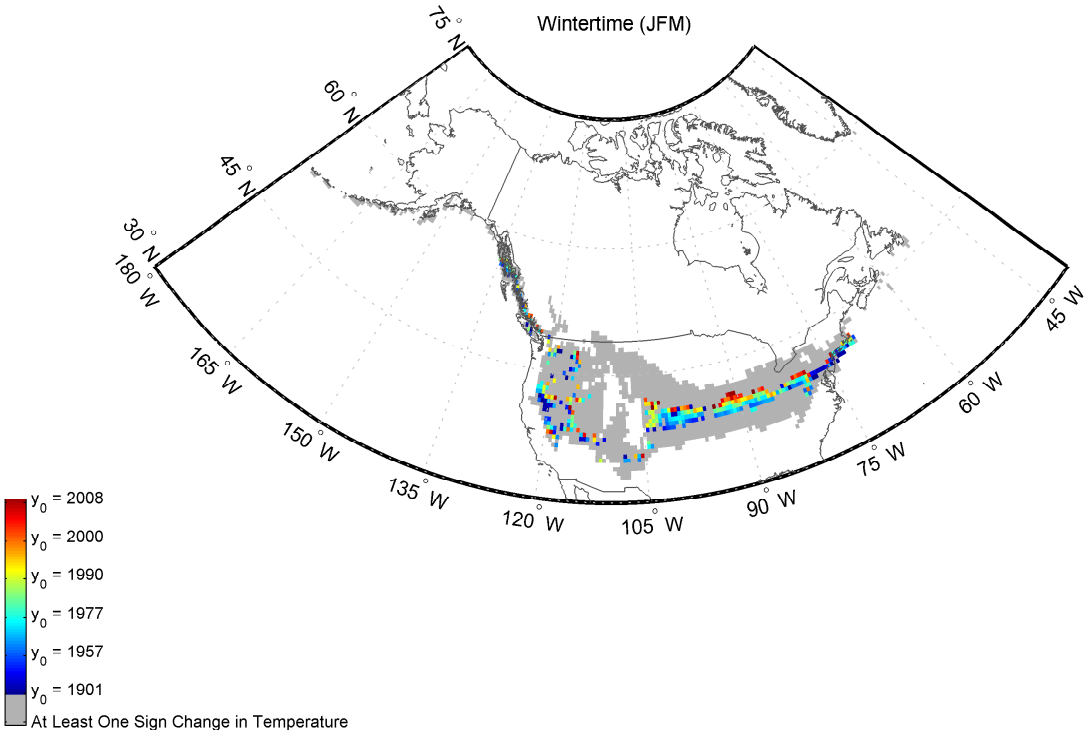


**Figure 5.62:** The same as Figure 5.61: zoomed in view of North America

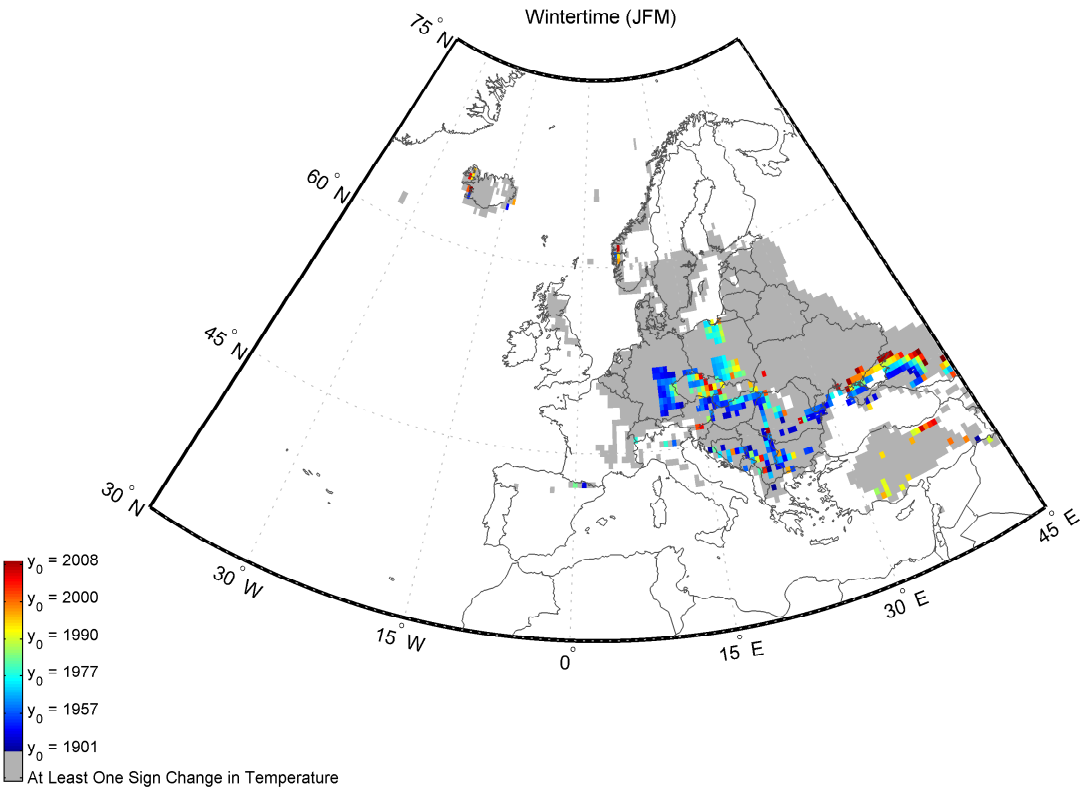


**Figure 5.63:** The same as Figure 5.61: zoomed in view of Europe

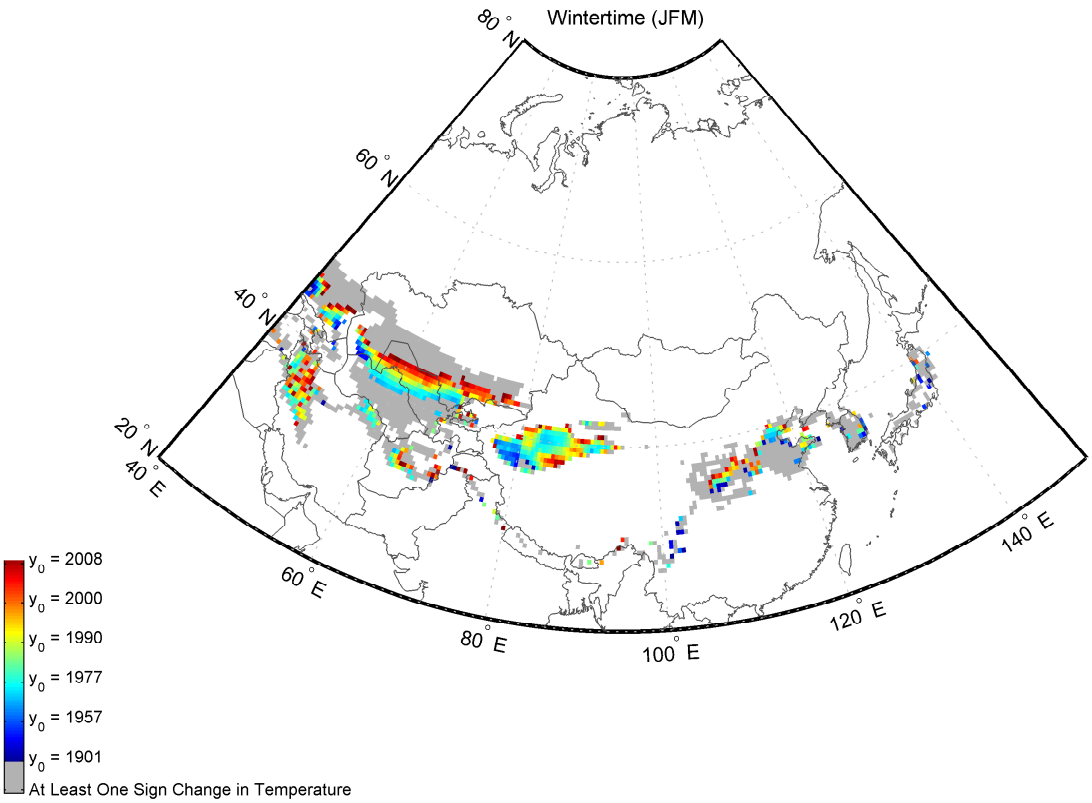


**Figure 5.64:** The same as Figure 5.61: zoomed in view of Asia

#### 5.4.4.2.3 Slope (1)

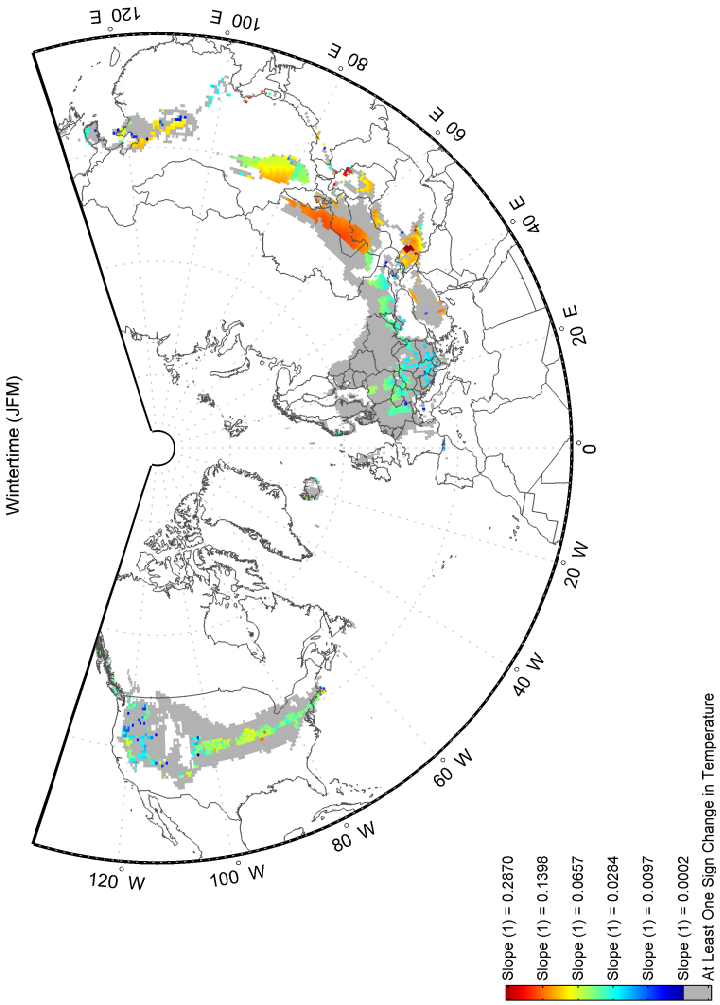


**Figure 5.65:** The map depicts the spatial distribution of Slope (1) in the Northern Hemisphere during **JFM**. The results are obtained using **Model 3**, and the input parameters are as indicated in Section 5.4.1. Refer to Section 5.2 for the definition of 'Slope (1)'.

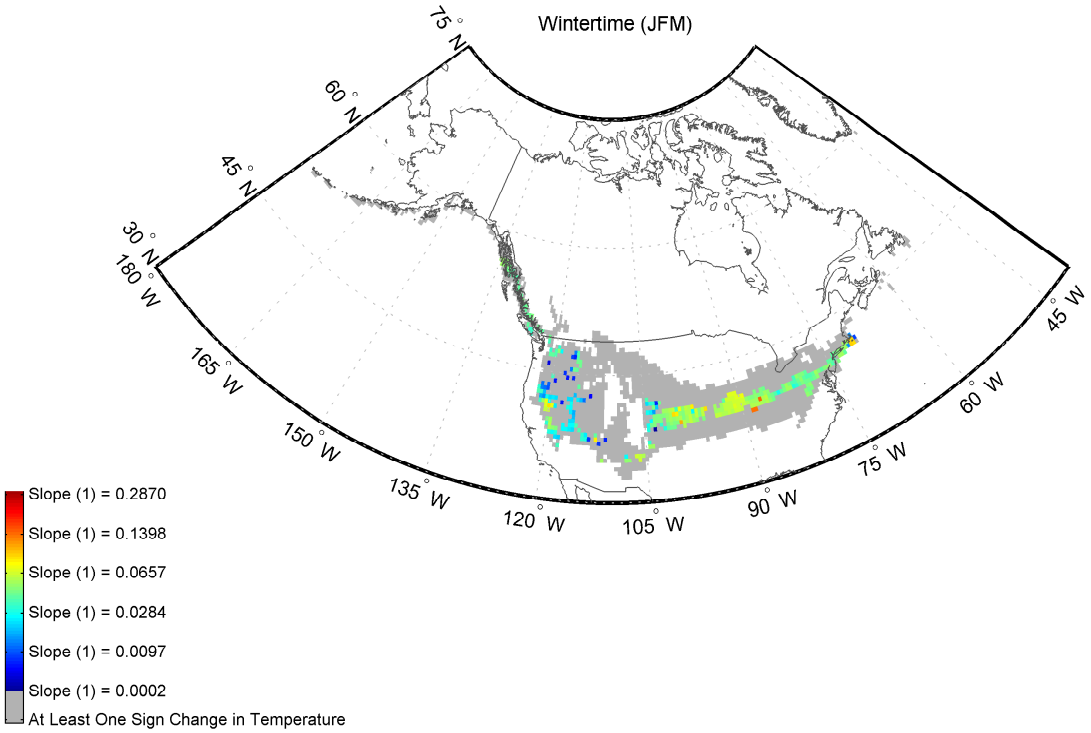


**Figure 5.66:** The same as Figure 5.65: zoomed in view of North America

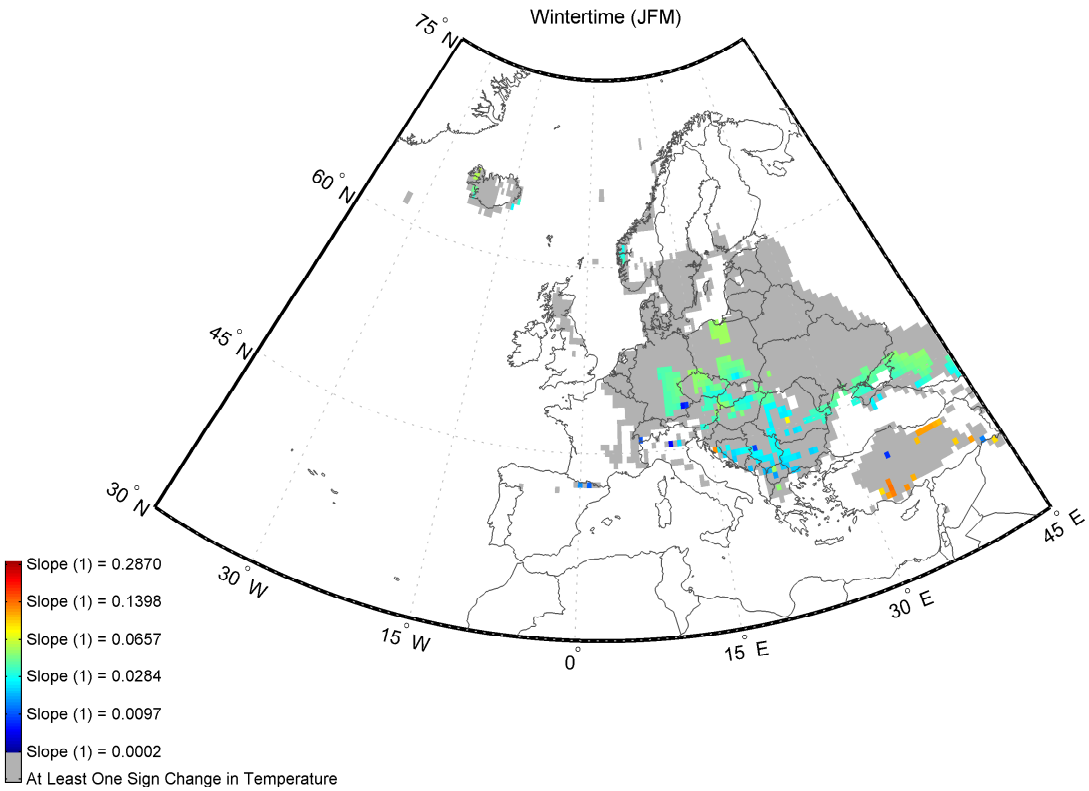


**Figure 5.67:** The same as Figure 5.65: zoomed in view of Europe

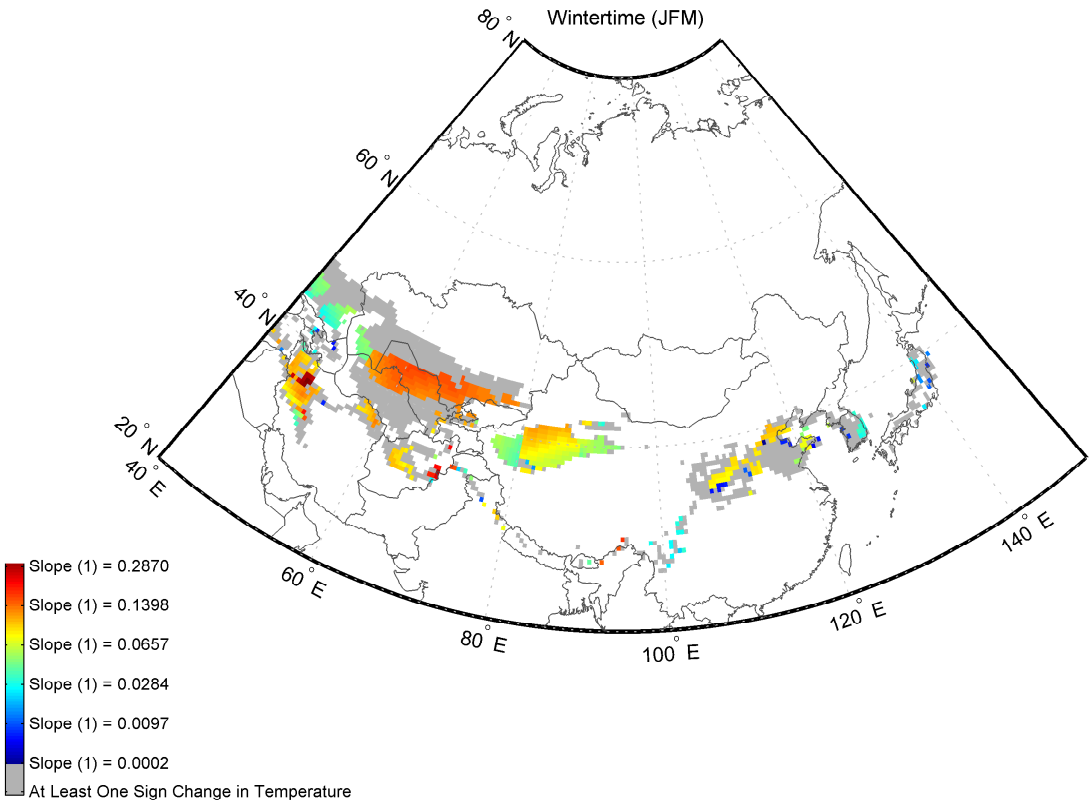


**Figure 5.68:** The same as Figure 5.65: zoomed in view of Asia

#### 5.4.4.2.4 Slope (2)

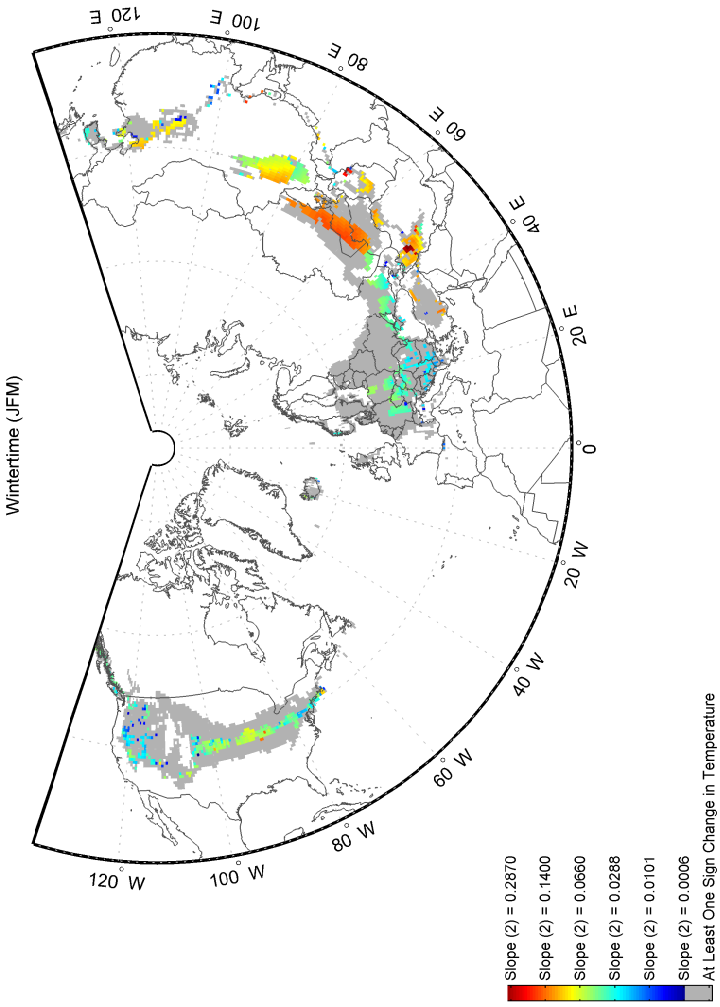


**Figure 5.69:** The map depicts the spatial distribution of Slope (2) in the Northern Hemisphere during **JFM**. The results are obtained using **Model 3**, and the input parameters are as indicated in Section 5.4.1. Refer to Section 5.2 for the definition of 'Slope (2)'.

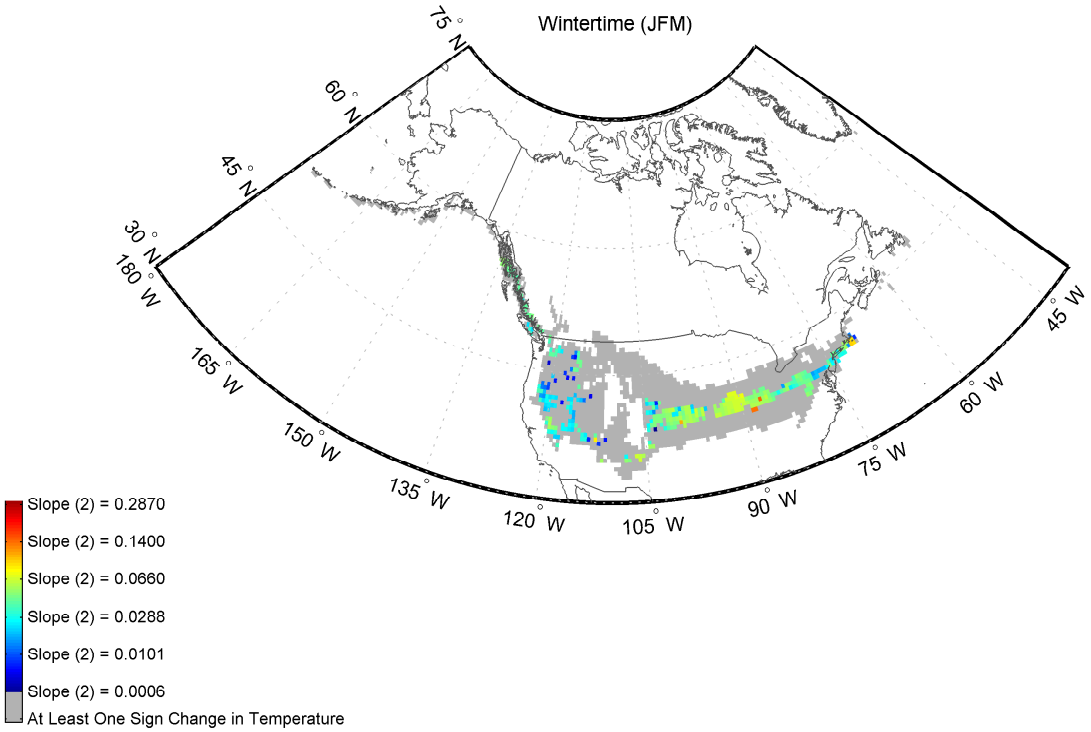


**Figure 5.70:** The same as Figure 5.69: zoomed in view of North America

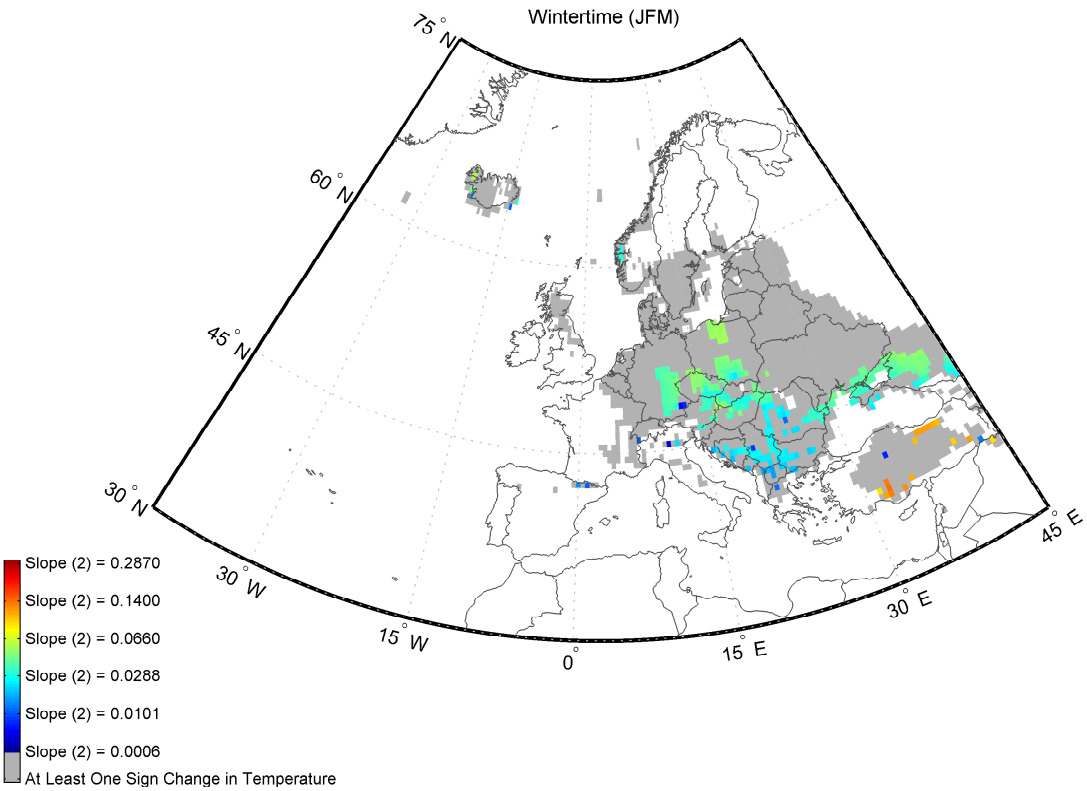


**Figure 5.71:** The same as Figure 5.69: zoomed in view of Europe

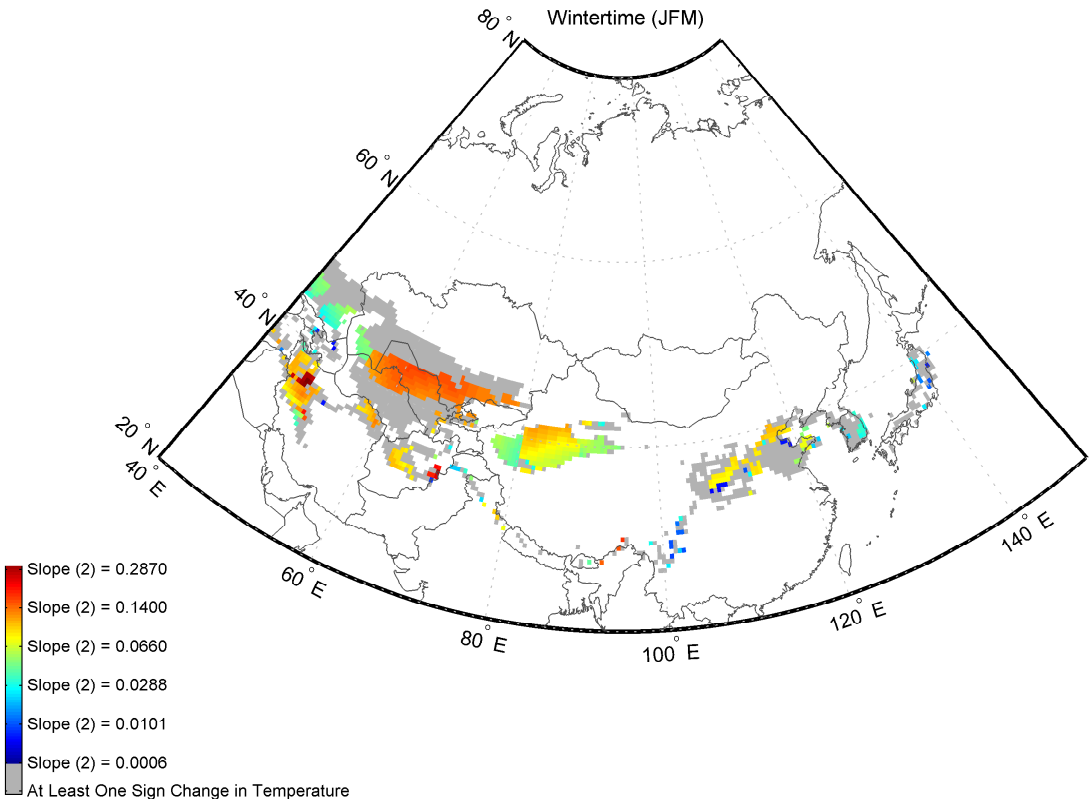


**Figure 5.72:** The same as Figure 5.69: zoomed in view of Asia

#### 5.4.4.2.5 H from $y_w$ to $y_0$

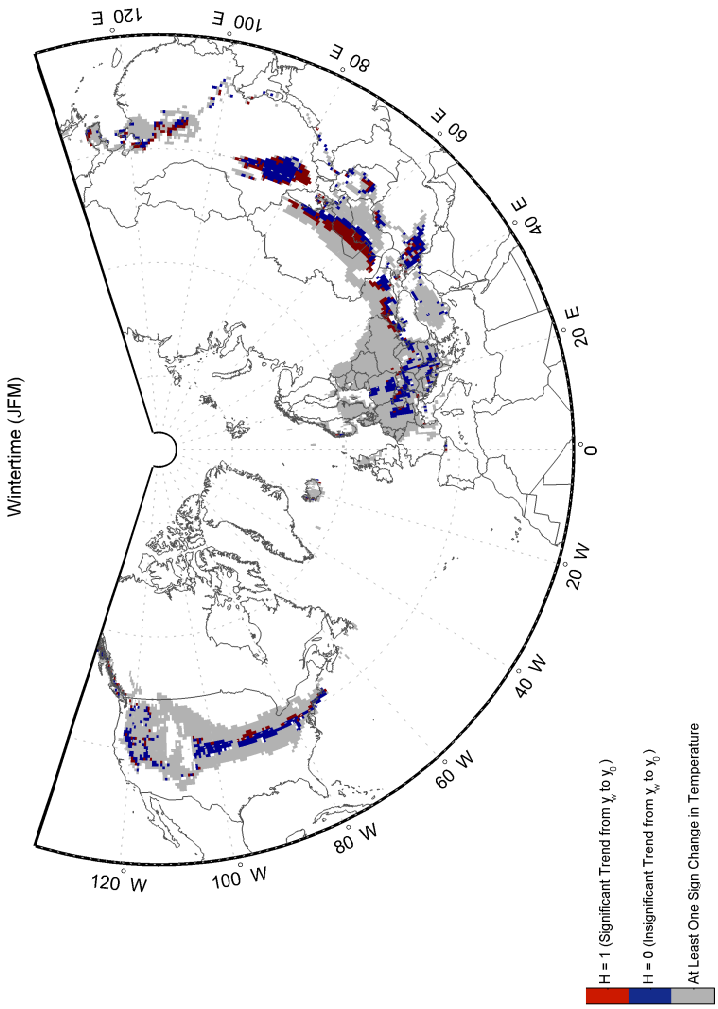


**Figure 5.73:** The map depicts the spatial distribution of H from $y_w$ to $y_0$ in the Northern Hemisphere during **JFM**. The results are obtained using **Model 3**, and the input parameters are as indicated in Section 5.4.1.

#### 5.4.4.2.6 H of $S_{interest}$

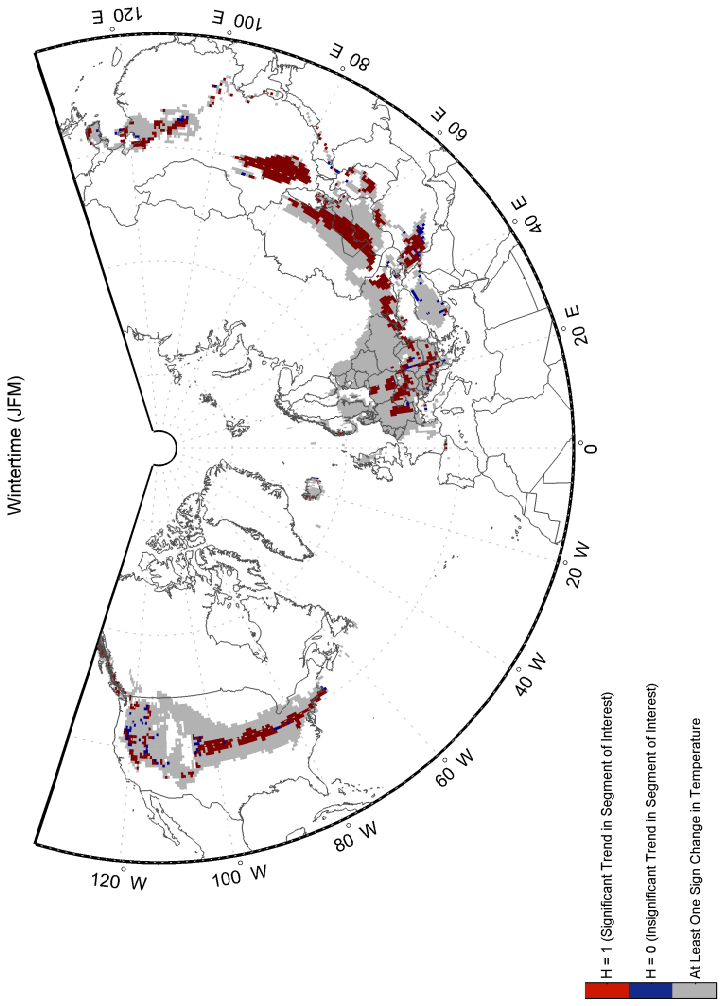


**Figure 5.74:** The map depicts the spatial distribution of H of $S_{interest}$ in the Northern Hemisphere during **JFM**. The results are obtained using **Model 3**, and the input parameters are as indicated in Section 5.4.1.

#### 5.4.4.2.7 H of $Sw_{total}$

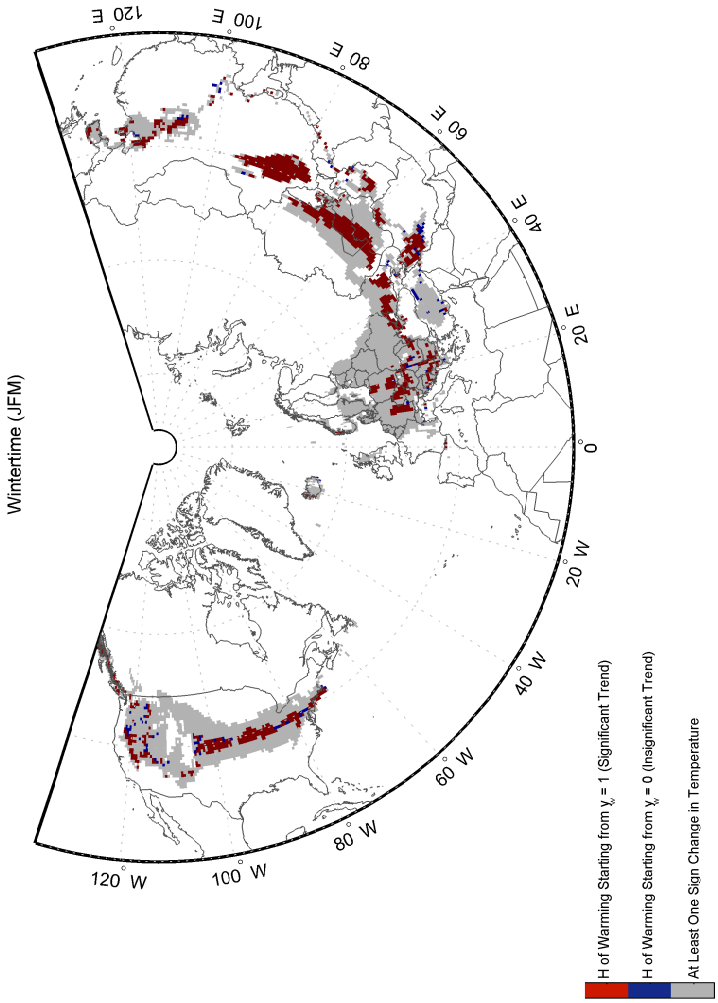


**Figure 5.75:** The map depicts the spatial distribution of H of $Sw_{total}$ in the Northern Hemisphere during **JFM**. The results are obtained using **Model 3**, and the input parameters are as indicated in Section 5.4.1.

#### 5.4.4.3 Maps of Model 3 for MAM

##### 5.4.4.3.1 $y_w$

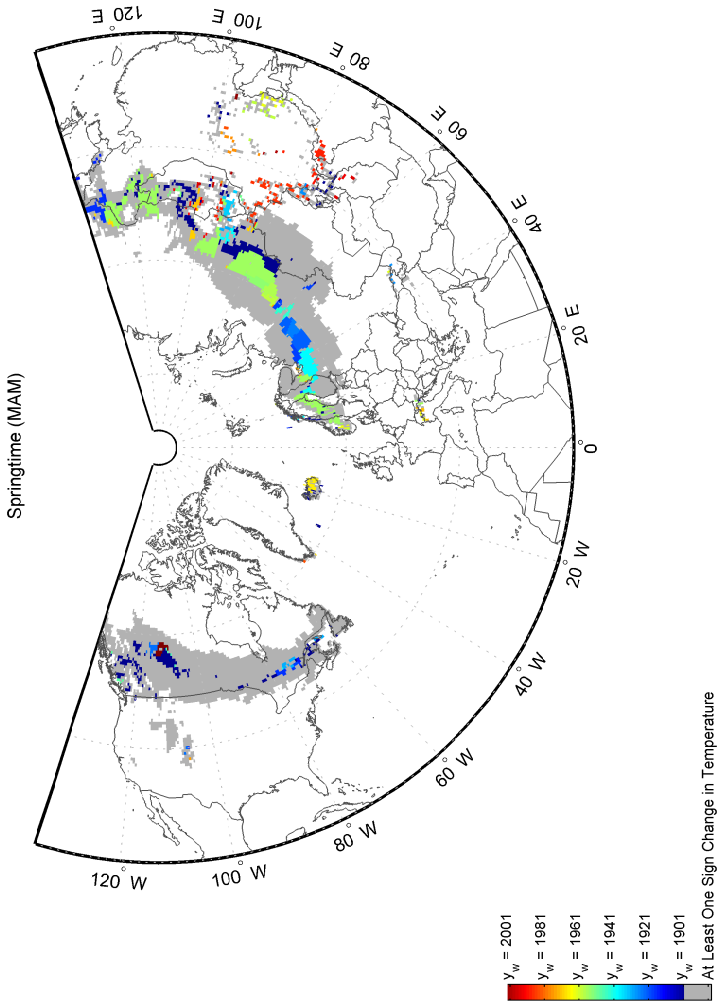


**Figure 5.76:** The map depicts the spatial distribution of $y_w$ in the Northern Hemisphere during **MAM**. The results are obtained using **Model 3**, and the input parameters are as indicated in Section 5.4.1.

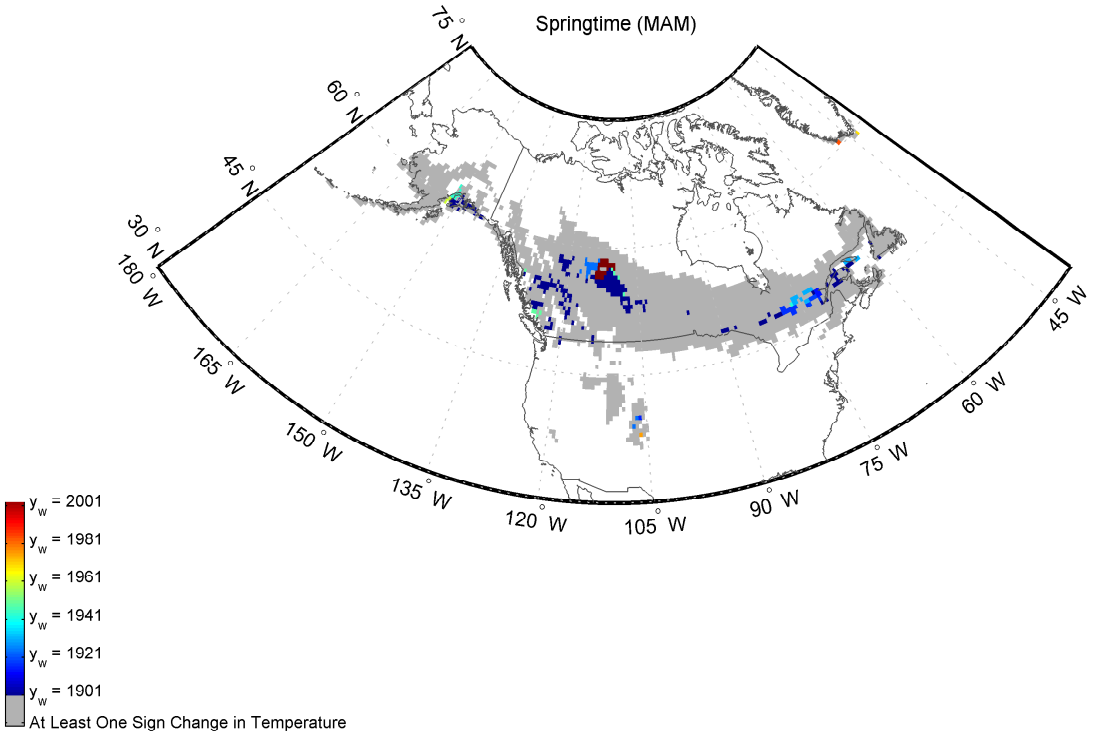


**Figure 5.77:** The same as Figure 5.76: zoomed in view of North America

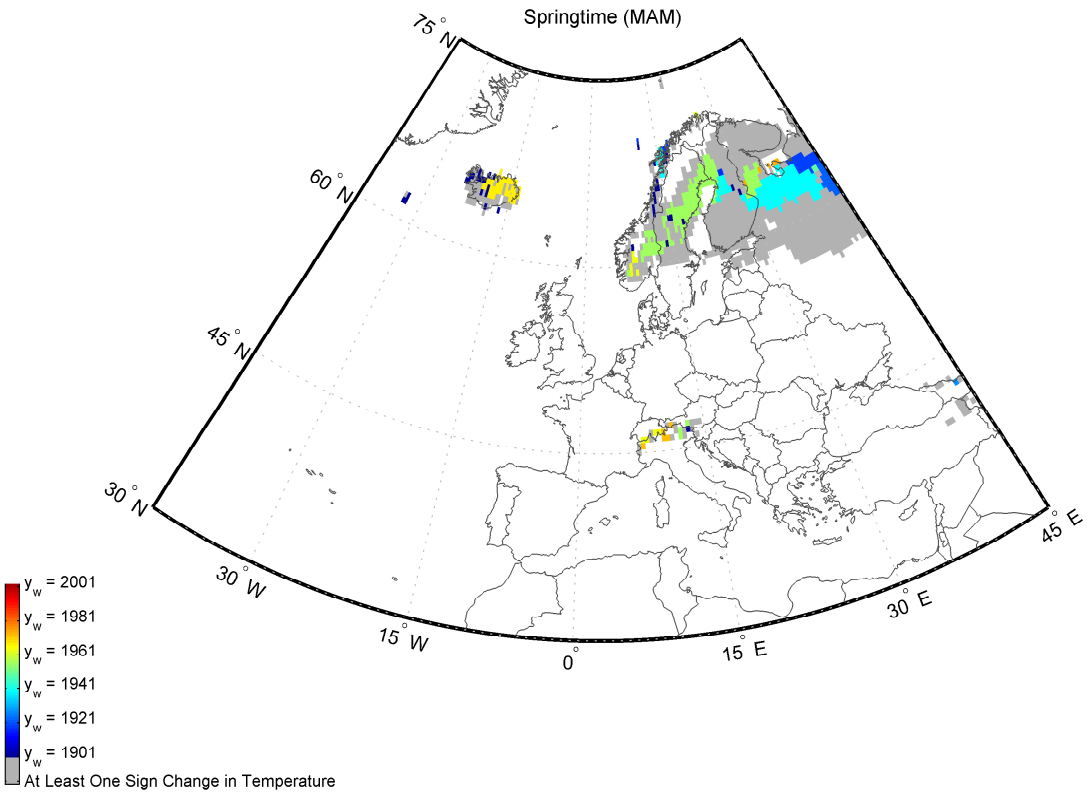


**Figure 5.78:** The same as Figure 5.76: zoomed in view of Europe

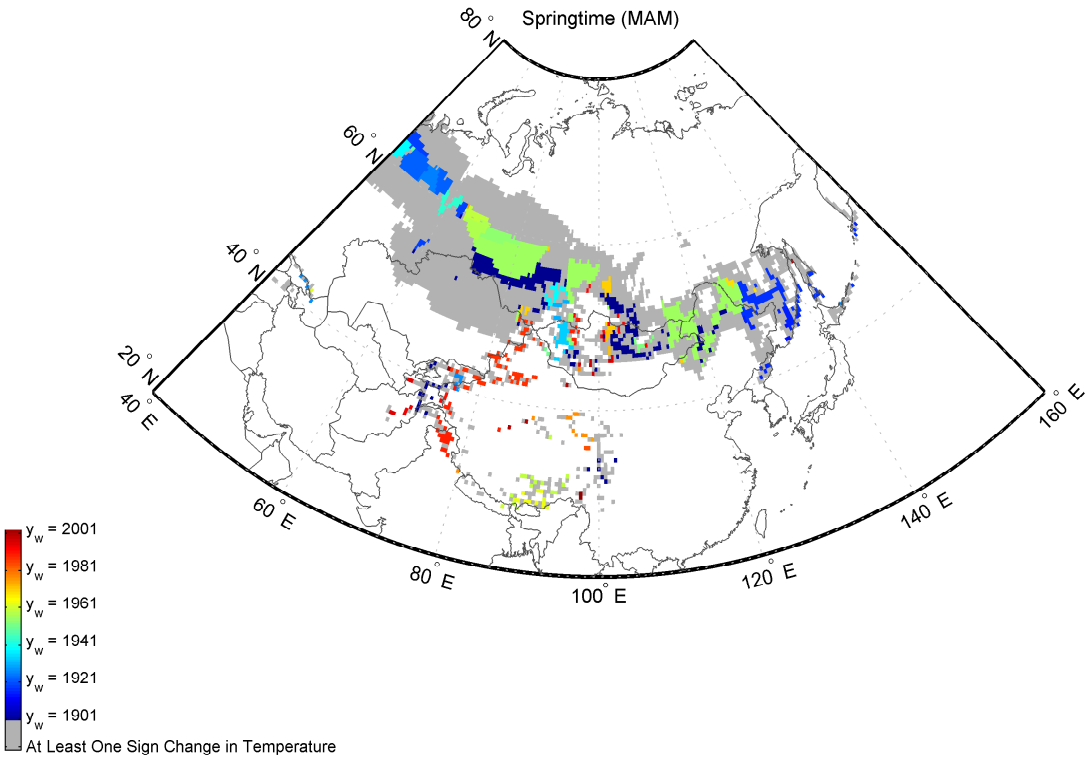


**Figure 5.79:** The same as Figure 5.76: zoomed in view of Asia

#### 5.4.4.3.2 $y_0$

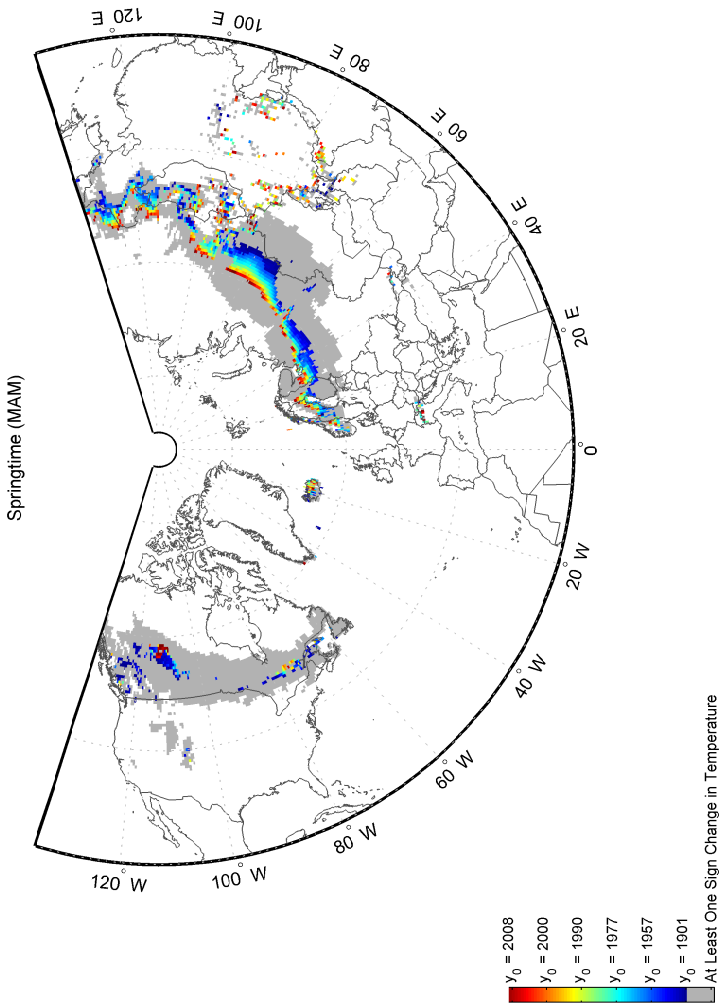


**Figure 5.80:** The map depicts the spatial distribution of $y_0$ in the Northern Hemisphere during **MAM**. The results are obtained using **Model 3**, and the input parameters are as indicated in Section 5.4.1.

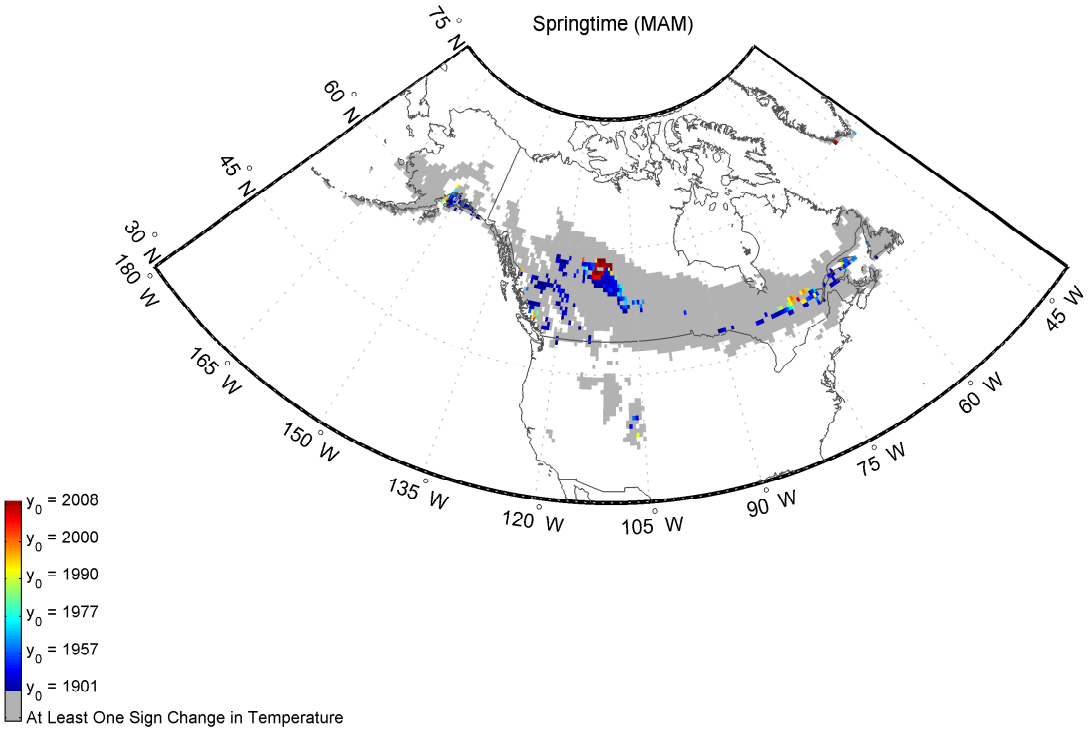


**Figure 5.81:** The same as Figure 5.80: zoomed in view of North America

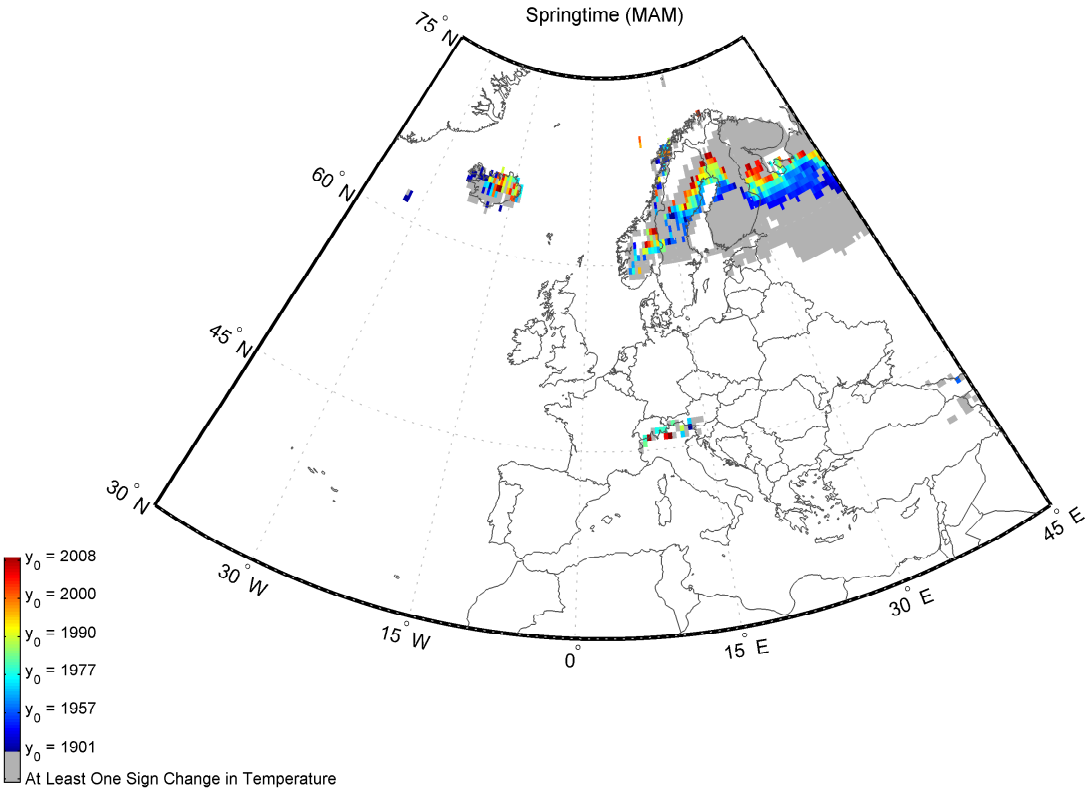


**Figure 5.82:** The same as Figure 5.80: zoomed in view of Europe

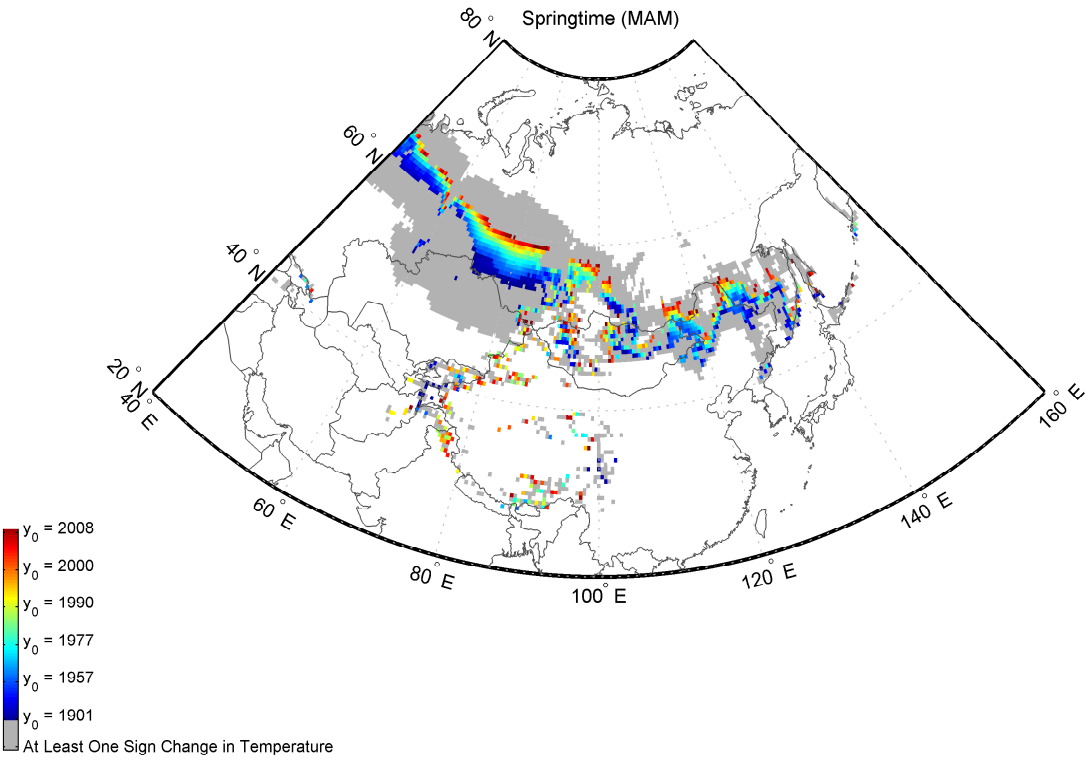


**Figure 5.83:** The same as Figure 5.80: zoomed in view of Asia

#### 5.4.4.3.3 Slope (1)

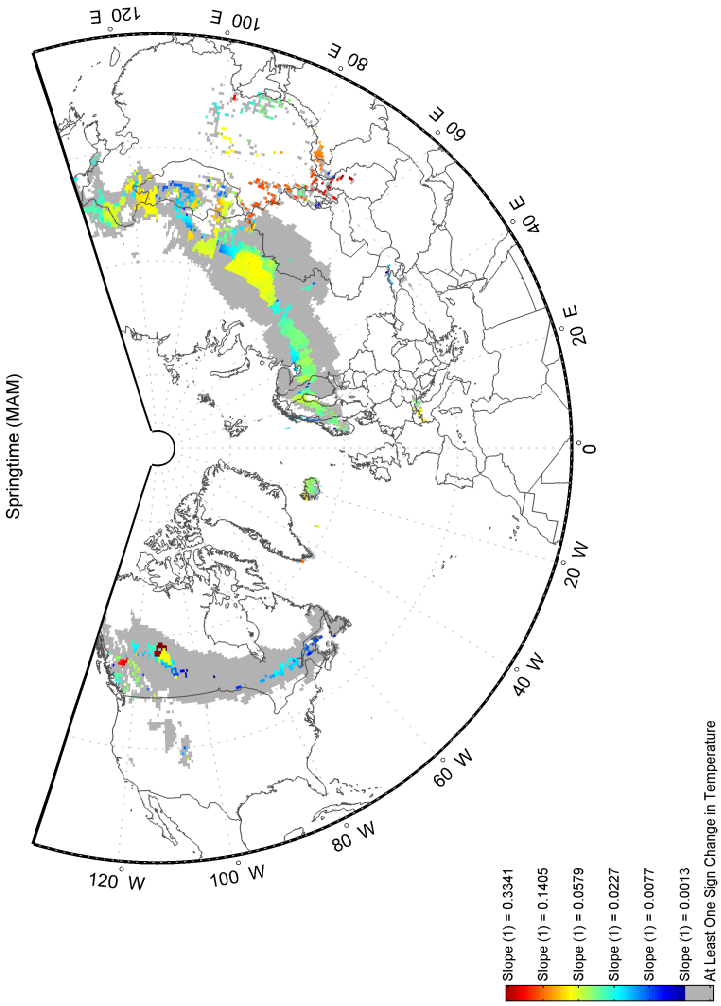


**Figure 5.84:** The map depicts the spatial distribution of Slope (1) in the Northern Hemisphere during **MAM**. The results are obtained using **Model 3**, and the input parameters are as indicated in Section 5.4.1. Refer to Section 5.2 for the definition of 'Slope (1)'.

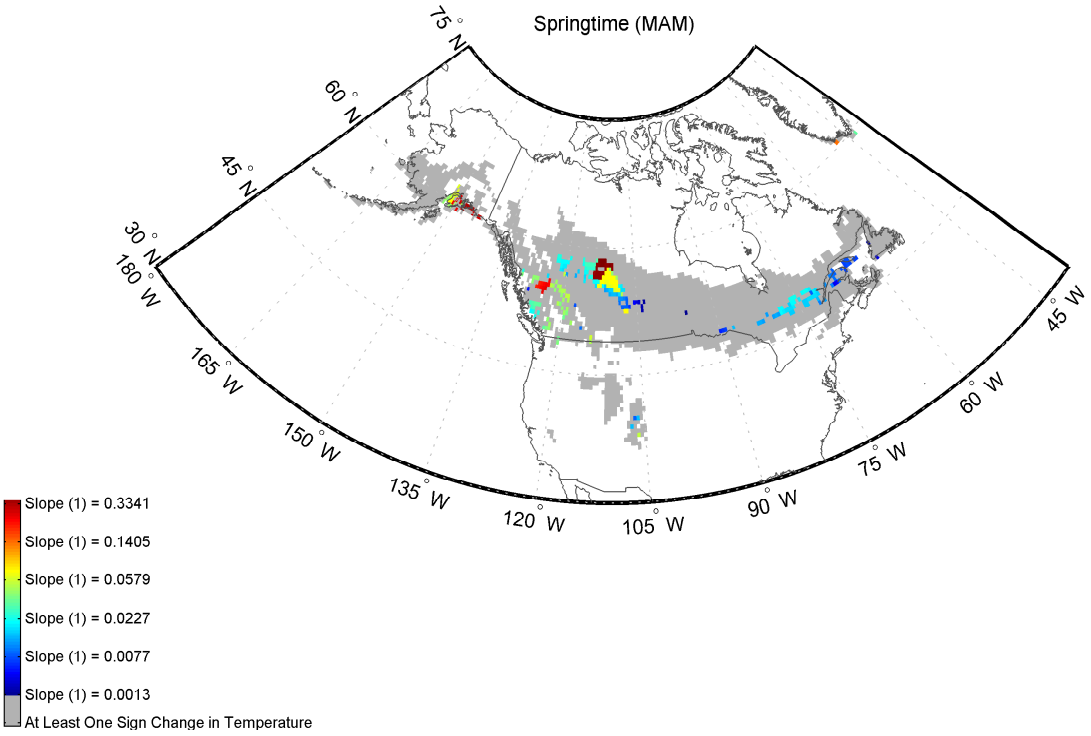


**Figure 5.85:** The same as Figure 5.84: zoomed in view of North America

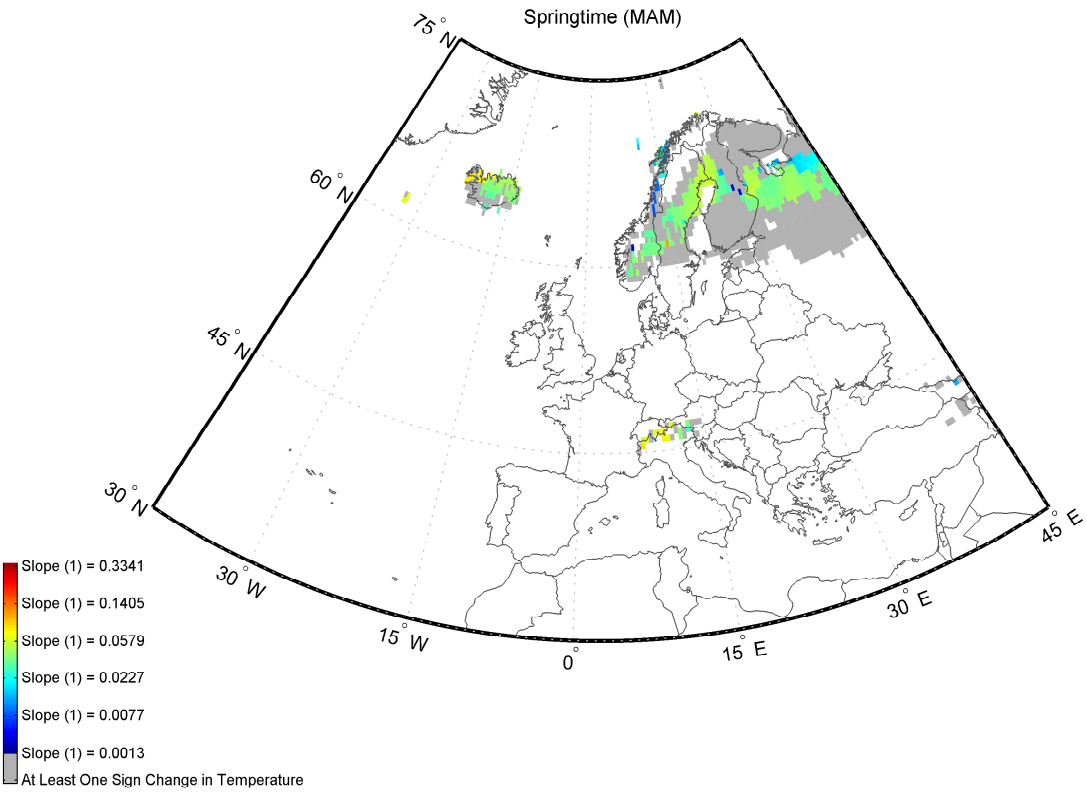


**Figure 5.86:** The same as Figure 5.84: zoomed in view of Europe

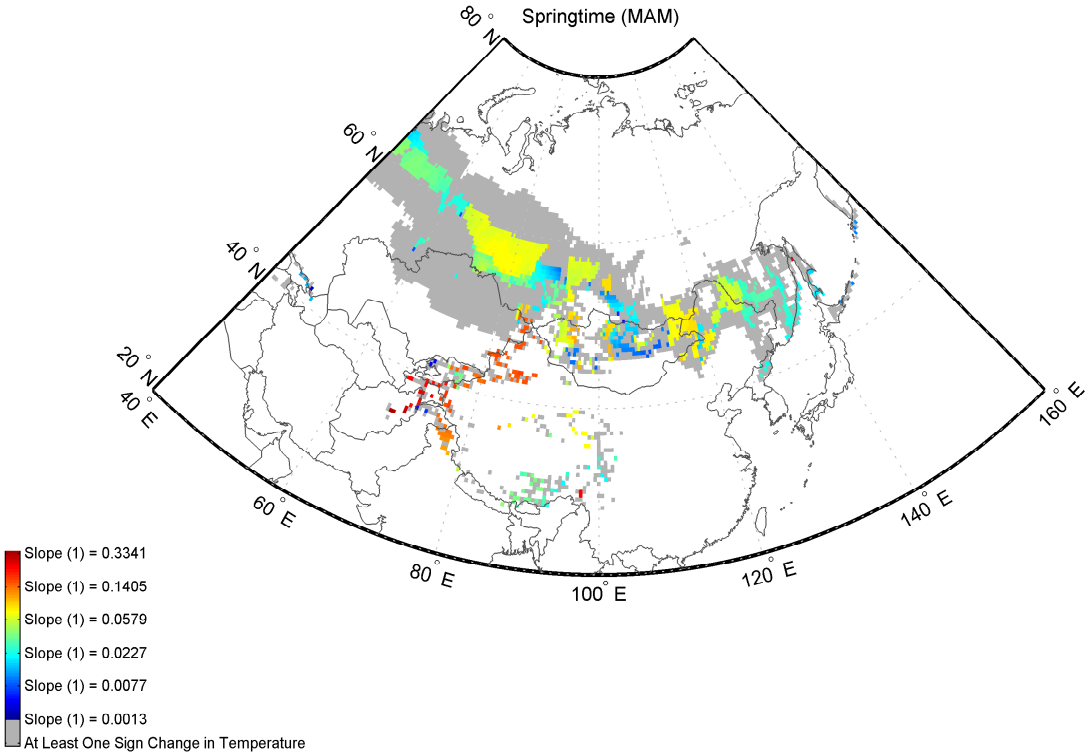


**Figure 5.87:** The same as Figure 5.84: zoomed in view of Asia

#### 5.4.4.3.4 Slope (2)

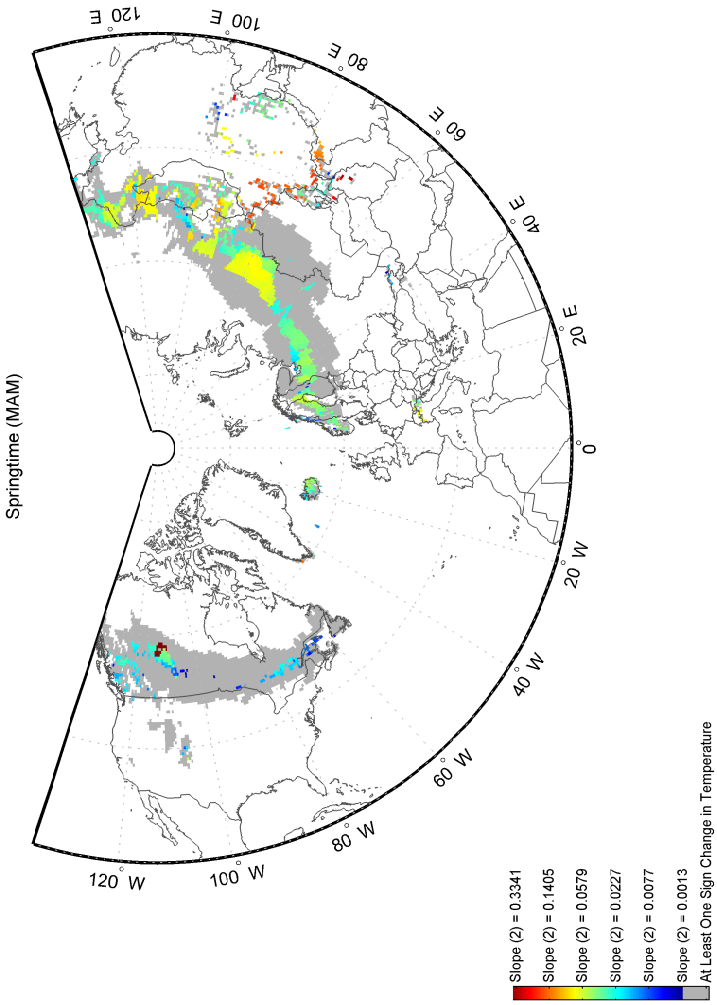


**Figure 5.88:** The map depicts the spatial distribution of Slope (2) in the Northern Hemisphere during **MAM**. The results are obtained using **Model 3**, and the input parameters are as indicated in Section 5.4.1. Refer to Section 5.2 for the definition of 'Slope (2)'.

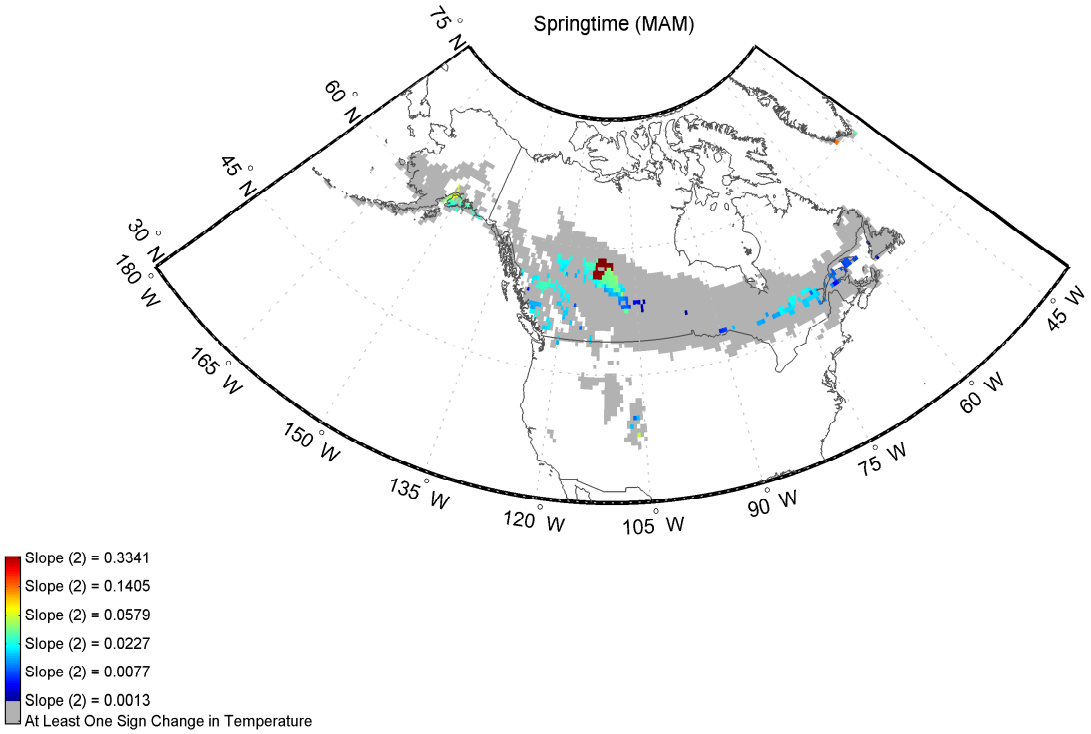


**Figure 5.89:** The same as Figure 5.88: zoomed in view of North America

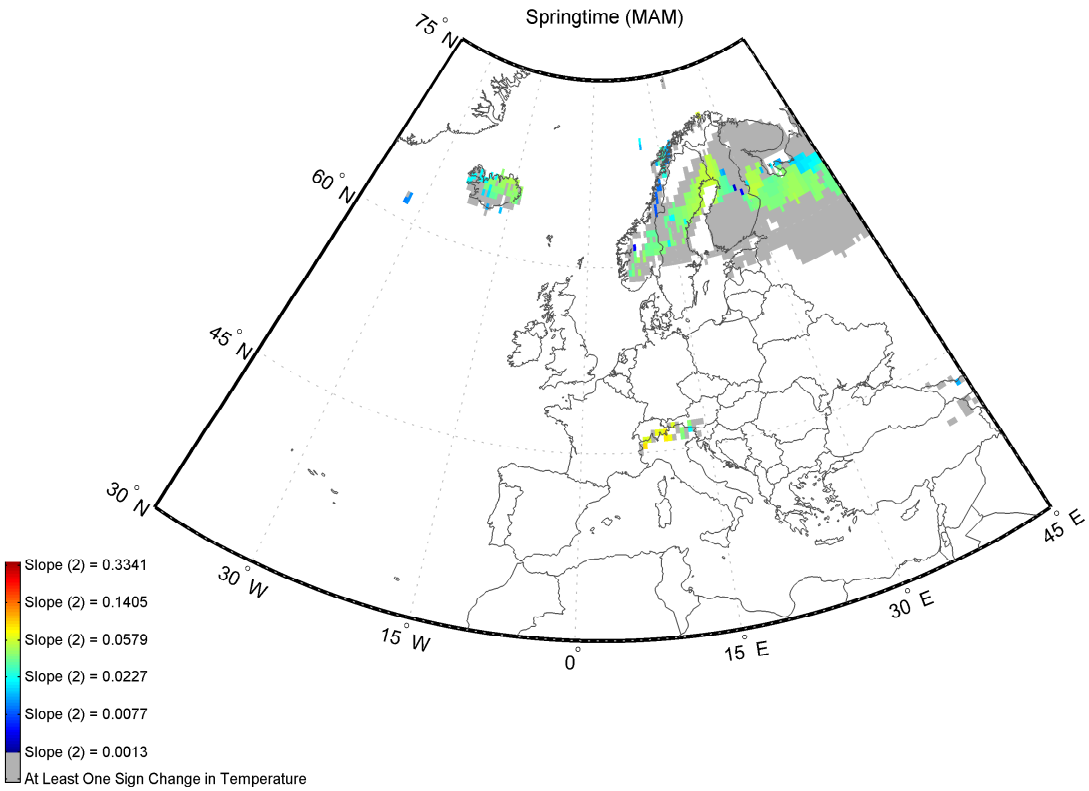


**Figure 5.90:** The same as Figure 5.88: zoomed in view of Europe

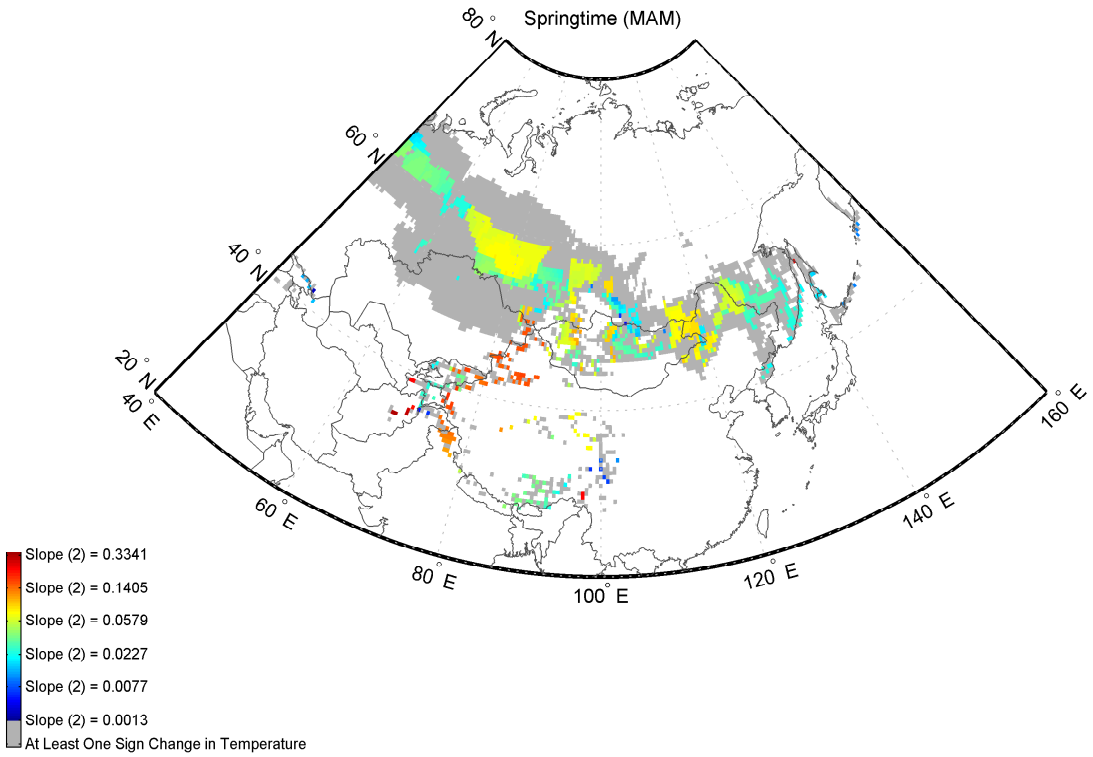


**Figure 5.91:** The same as Figure 5.88: zoomed in view of Asia

#### 5.4.4.3.5 H from $y_w$ to $y_0$

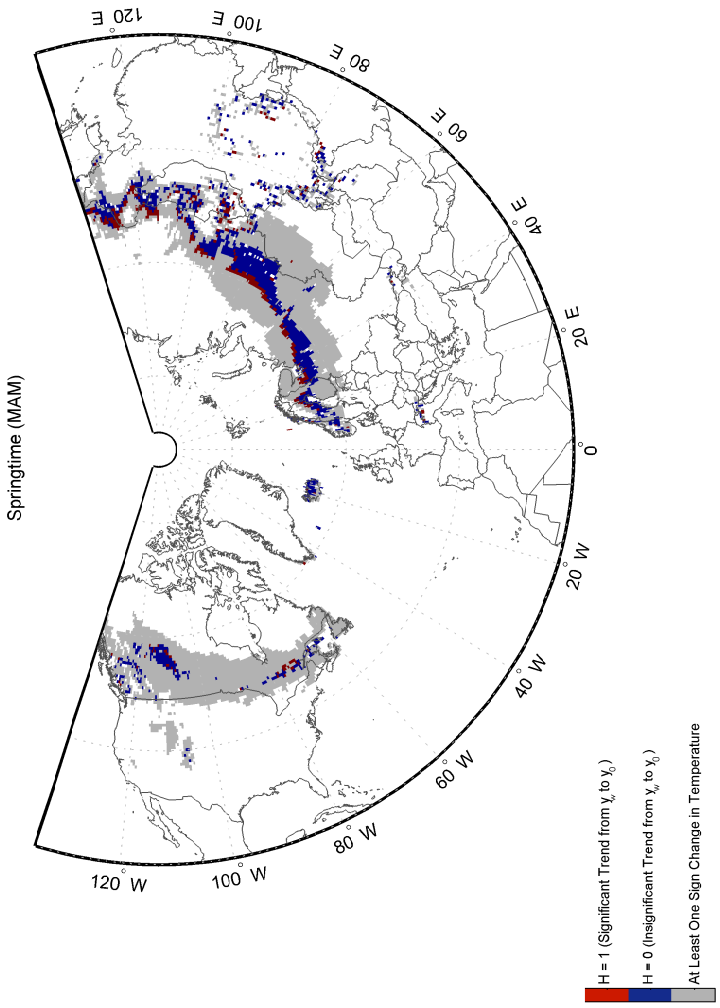


**Figure 5.92:** The map depicts the spatial distribution of H from $y_w$ to $y_0$ in the Northern Hemisphere during **MAM**. The results are obtained using **Model 3**, and the input parameters are as indicated in Section 5.4.1.

#### 5.4.4.3.6 H of $S_{interest}$

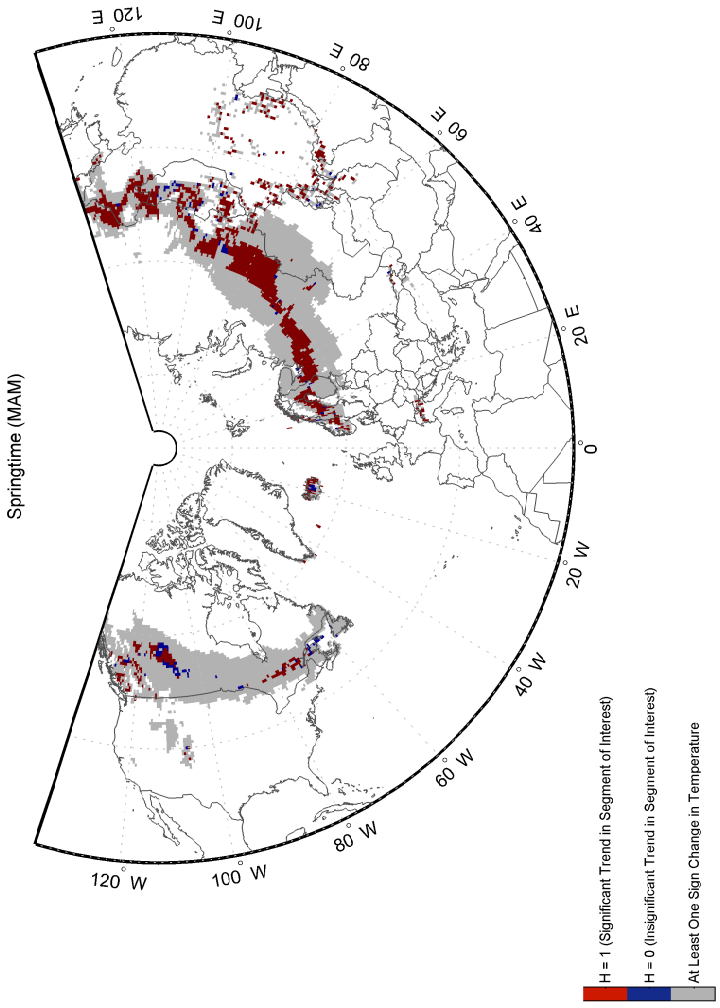


**Figure 5.93:** The map depicts the spatial distribution of H of $S_{interest}$ in the Northern Hemisphere during **MAM**. The results are obtained using **Model 3**, and the input parameters are as indicated in Section 5.4.1.

#### 5.4.4.3.7 H of $Sw_{total}$

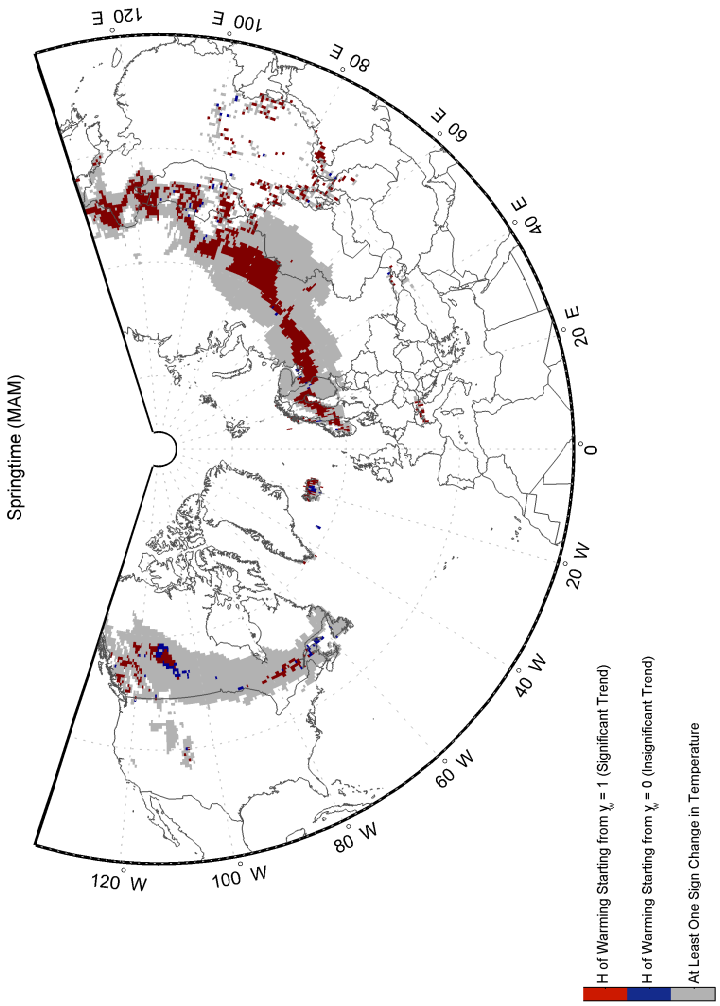


**Figure 5.94:** The map depicts the spatial distribution of H of $Sw_{total}$ in the Northern Hemisphere during **MAM**. The results are obtained using **Model 3**, and the input parameters are as indicated in Section 5.4.1.

## 5.5 MARS

This section includes all the details regarding the application of the MARS algorithm to the time series in this study. First the input parameters of the algorithm are introduced (Section 5.5.1). Then, $y_w$ and $y_0$ determination rules are described (Section 5.5.2). Finally, Section 5.5.3 presents the descriptive table, histograms, and maps.

### 5.5.1 Input Parameters

A MATLAB® toolbox provided by ARESLab (Jekabsons, 2010) is used for building MARS models in this study. Based on practical examples and runs, it seems that the input arguments are open to experimentation. Therefore, for every new model and situation, it may be necessary to study the difference that it takes to run the model with different values of the input arguments and examine which of the possibilities yields the best performance and the best result. Due to the large number of locations under study in this thesis, it is not feasible to investigate each case separately. On the other hand, setting the input parameters to the most conservative values may lead to over-fitted models. Unfortunately, it is not very helpful to test the performance of the models, generated by different sets of input arguments, using the Leave-One-Out cross validation or k-fold cross validation since the results of the tests are very close.

To mitigate this problem, three different sets of input parameters are used with the first set including the most suitable values. The three sets of input parameters act as filters. The output of the first filter (set of input parameters) is the locations with one MARS segment. This implies that the model consists of only the intercept term, and the entire time series is approximated by one polynomial of degree zero. The output from each set is used as an input to the next set. The parameters are set based on the manual examination of over 50 cases by the author and Nicholas J. Gralewicz (personal communication). These three input sets differ in the maximum number of BF's in the forward pass, usage of End Span, and maximum number of BF's in the pruned model (maximum final functions). The input parameters are briefly explained below:

- **Maximum number of BF's in the forward pass**
  To have the best possible small model, it is preferable to build a big set of BF's in the

forward pass (a large Maximum Number of BF's) and prune them in the backward phase. This technique is recommended since the forward phase only looks at one step ahead, whereas the backward phase considers all the model terms before removing any.

Usually the default value of 21 is assigned to this parameter. However, in order to have a higher degrees of freedom to increase the ability of the procedure to approximate more complex functions (Friedman, 1991), the first and second sets of input parameters attribute the value of 50 to this parameter. The third set assigns the value of 100 to this input argument.

- **Generalized Cross-Validation (GCV) penalty per knot**
  As described in Section 3.3, GCV is essentially the penalized version of mean squared error and is used for the optimal model selection. The larger the value of GCV is, the simpler the generated final model is. A value from the range of 2-4 is suggested for this parameter. In the case of additive model like this study, the value of 2 is often used.

- **Maximum final functions**
  This parameter sets the maximum number of segments allowed in the final model. To avoid over-fitted models and models that are too sensitive to local variances, the first and second groups of input parameters set this value to 4, which means maximum 5 MARS segments are allowed. The third group sets this value to 5.

- **Minimum Span**
  Minimum Span is used to prevent the algorithm from generating a model with drastic or abrupt changes. After selecting each knot in the forward pass, the search for the next potential knot starts after the Minimum Span interval. This argument is set to the automatic mode, which allows the algorithm to decide on the next knot placement.

- **End Span**
  End Span does not allow the algorithm to consider the last End Span number of data cases for the knot placement. This makes the technique resistant to the local variances close to the ends of data. The End Span is disabled in the first group of input parameters to consider the data close to the ends of series for the knot

placement; however, the second and third classes of input are set to the automatic mode.

- **Threshold**
  This is one of the criteria that indicate when to quit the forward pass. The larger this value is, the simpler the resulting model is. This is set to $10^{-4}$ for all input sets.

- **Maximum Interaction**
  As discussed in Section 3.3, BF's are added one at a time and in an additive fashion. Therefore, the model is additive. Moreover, there is only one independent variable. Thus, this parameter is set to 1, which refers to an additive model.

- **Self Interaction**
  No self interaction is allowed in this application.

- **Pruning Method**
  Model is set to be pruned in the backward phase.

### 5.5.2 $y_0$ and $y_w$ Determination Rules

1. **One positive 0°C crossing**

   (a) The first segment crosses 0°C

   - $\mathbf{y_0}$ : year of 0°C crossing
   - $\mathbf{y_w}$ : start year of the first segment (i.e., 1901)

   Sample plots: Figures A.9 to A.11

   (b) The first segment does not cross 0°C

   - $\mathbf{y_0}$ : year of 0°C crossing
   - $\mathbf{y_w}$ : start year of the segment which includes $y_0$

   Sample plots: Figures A.12 to A.14

2. **More than one positive 0°C crossing**

   (a) The first segment crosses 0°C and has the maximum slope

- $\mathbf{y_0}$ : 0°C crossing year of the line with the greatest cumulative warming (among the lines that cross 0°C in the positive direction)
- $\mathbf{y_w}$ : start year of the line with the greatest cumulative warming

In some cases, the slope of the first segment is large due to a very short period of warming and not a significant magnitude of warming. This segment is often followed by some temperature fluctuations; eventually, a significant warming takes place over a long period and moves the time series above 0°C. Rule 2a is set to prevent incorrect selection of the first segment as $S_{interest}$ in such cases. Figure A.16 provides an example for this case. If both the maximum cumulative warming and slope occur during the first segment, then the 0°C crossing of the first segment is accepted as $y_0$ (Figure A.15). The reader is referred to Section 5.3 for the detailed explanation of the latter case. It should be noted that Rule 2a applies to a small number of the time series from the final database (Table 5.3).

(b) The first segment does not either cross 0°C or have the maximum slope

- $\mathbf{y_0}$ : 0°C crossing year of the segment with the largest slope
- $\mathbf{y_w}$ : start year of the segment with the largest slope

Sample plot: Figure A.17

### 5.5.3 MARS Results

In this section, Table 5.3, histograms (JFM: Figures 5.95 to 5.99, MAM: Figures 5.100 to 5.104), and maps (JFM: Figures 5.105 to 5.123, MAM: Figures 5.124 to 5.142) present the results of the analysis of the time series using MARS. The variables under study are all introduced in Section 5.2. The reader is also referred to Section 5.3 for some notes on the table, histograms, and maps. The results are thoroughly explained and discussed in Sections 5.8.3 (tables and histograms) and 5.8.4 (maps).

**Table 5.3:** Based on the analysis of the JFM and MAM time series using **MARS**, the table provides some information on the numbers of grid cells with specific characteristics described in the left column. The input parameters are as indicated in Section 5.5.1. The reader is referred to Section 5.3 for more details on the cases presented below.

| **Characteristic** | **Number** | |
|---|---|---|
| | **JFM** | **MAM** |
| Selected for study (following Rule 1 of *transition area*, described in Section 4.3) | 6206/46224 | 9842/46224 |
| At least one positive 0°C crossing (based on Rule 2 of *transition area*, described in Section 4.3) | 1559/6206 | 2637/9842 |
| Final database: selected for the $y_w$ and $y_0$ analysis (based on Rules 1 and 2 of *transition area*) | **1498/1559** | **2520/2637** |
| More than one positive 0°C crossing: The first segment crosses 0°C and has the maximum slope; i.e., Rule 2a of $y_w$ and $y_0$ determination applies (Section 5.5.2) | 20/1498 | 16/2520 |
| $y_w = 1901$ | 88/1498 | 439/2520 |
| Duration of $y_w$ to $y_0$ less than 3 years, MK test N/A | 60/1498 | 100/2520 |
| $S_{W_{total}}$ is the same as $S_{interest}$ | 1412/1498 | 2394/2520 |

#### 5.5.3.1 Histograms

##### 5.5.3.1.1 JFM

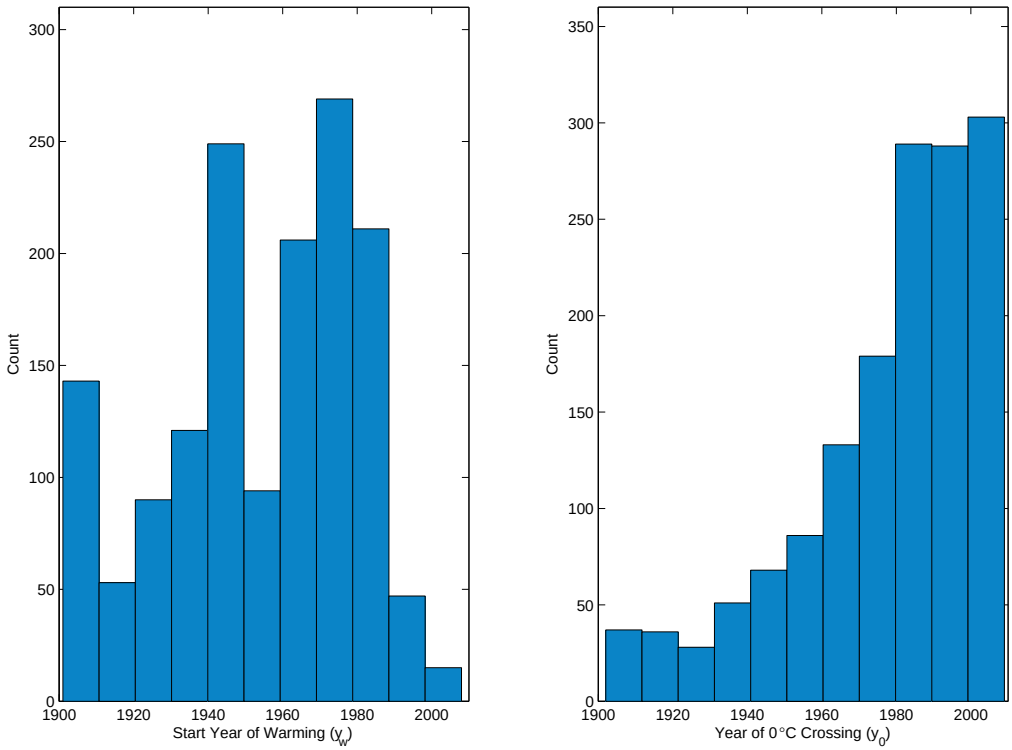


**Figure 5.95:** The histograms exhibit the temporal distributions of $y_w$ and $y_0$ during **JFM**. The results are obtained using **MARS**, and the input parameters are as indicated in Section 5.5.1.

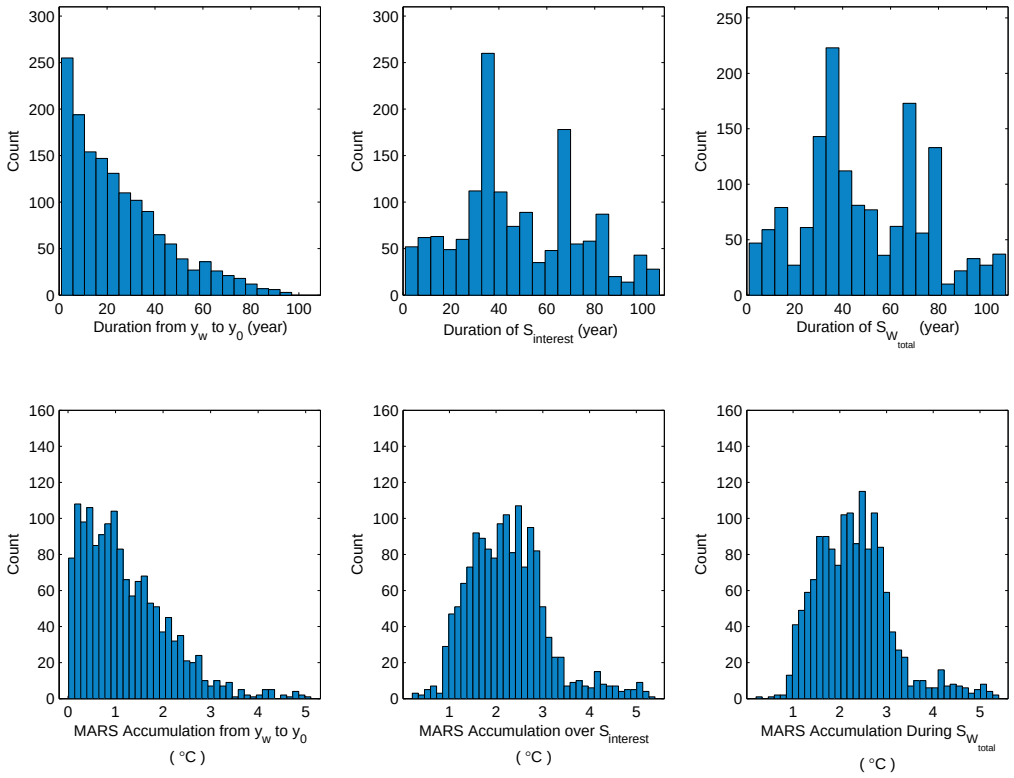


**Figure 5.96:** The histograms exhibit the distributions of duration and temperature accumulation during $y_w - y_0$, $S_{interest}$, and $S_{W_{total}}$ for **JFM**. The results are obtained using **MARS**, and the input parameters are as indicated in Section 5.5.1. The reader is referred to Section 5.2 for details on the variables used above.

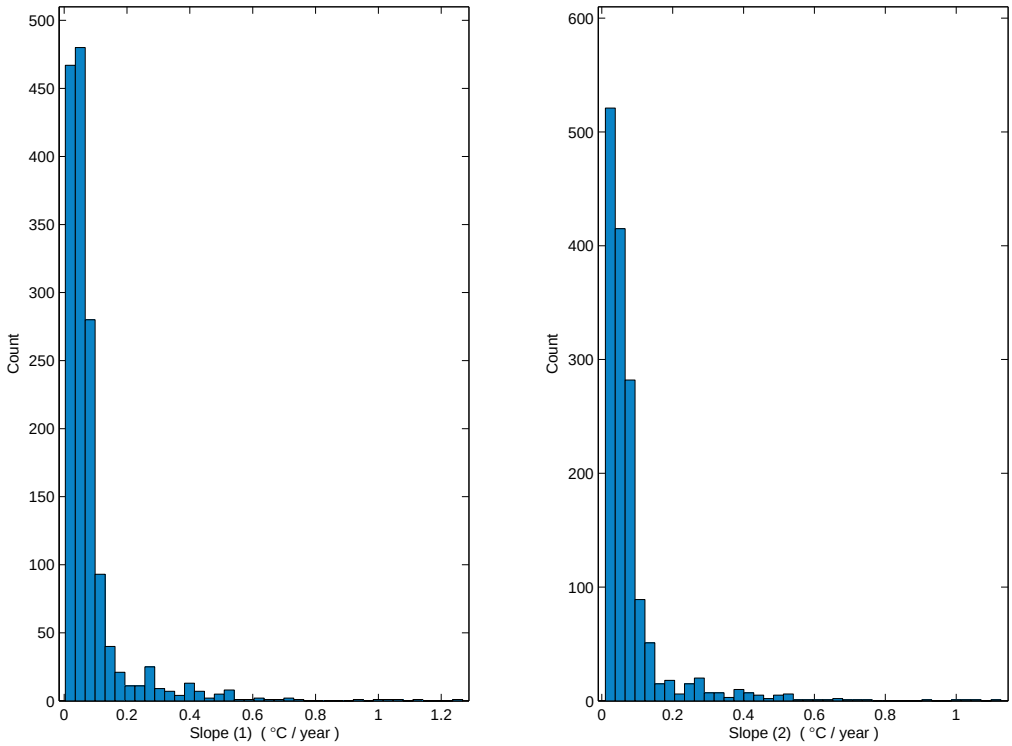


**Figure 5.97:** The histograms exhibit the distributions of Slope (1) and Slope (2) for **JFM**. The results are obtained using **MARS**, and the input parameters are as indicated in Section 5.5.1. The reader is referred to Section 5.2 for details on the variables used above.

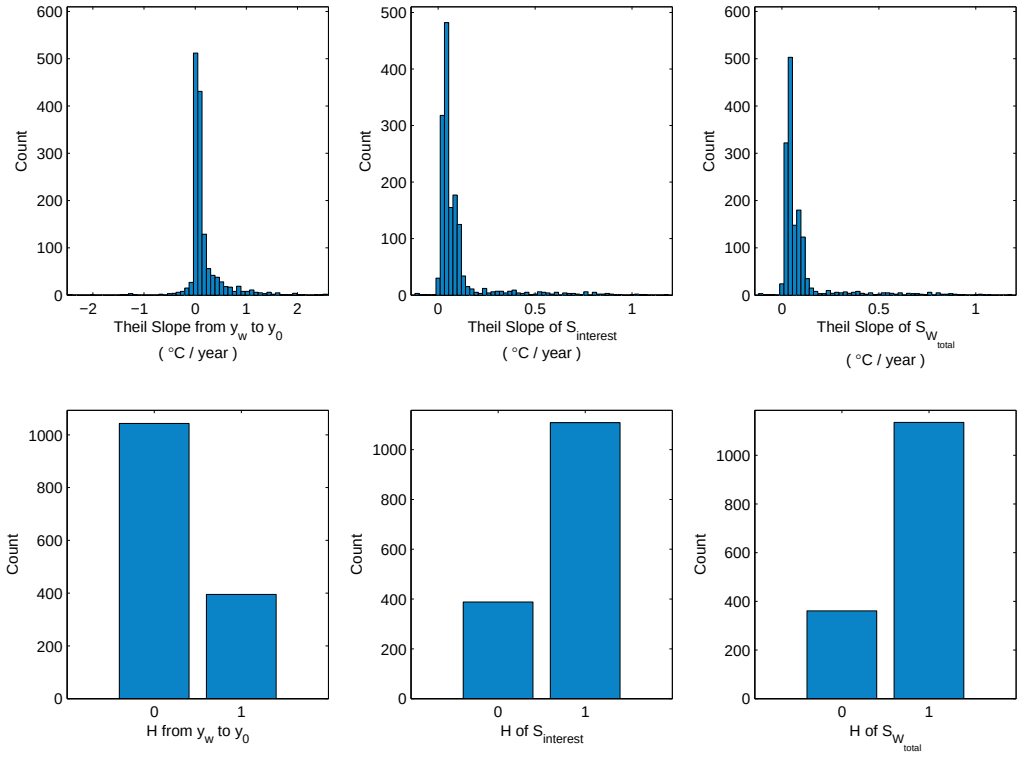


**Figure 5.98:** The histograms exhibit the distributions of Theil slope and H during $y_w - y_0$, $S_{interest}$, and $S_{W_{total}}$ for **JFM**. The results are obtained using **MARS**, and the input parameters are as indicated in Section 5.5.1. The reader is referred to Section 5.2 for details on the variables used above.

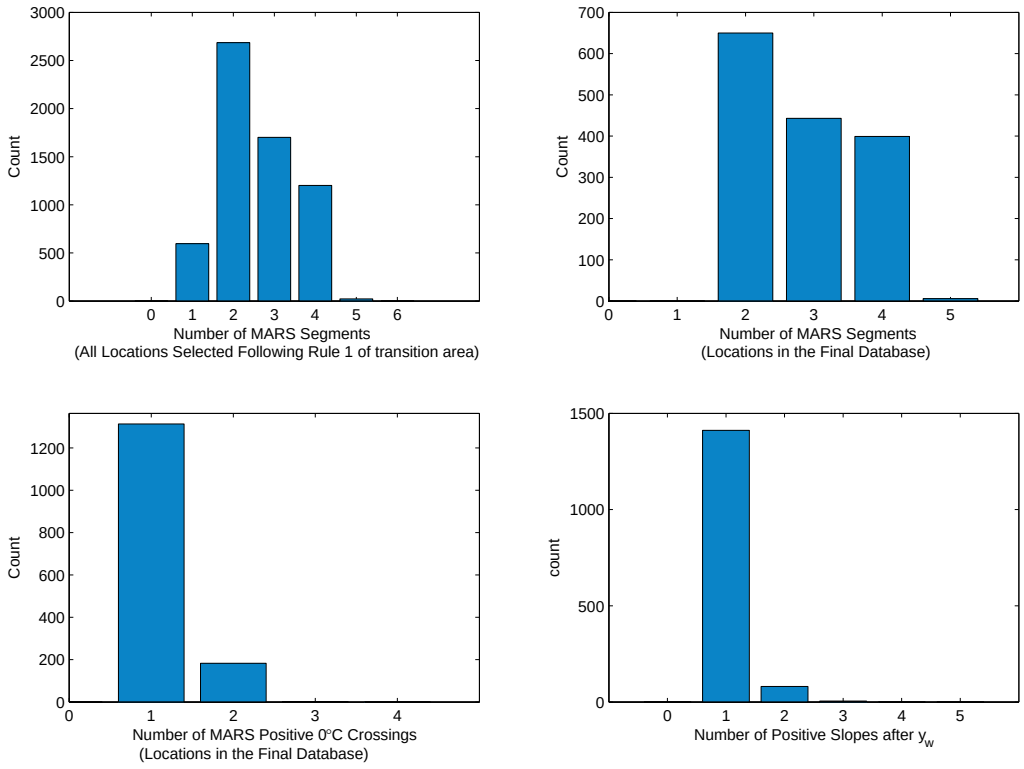


**Figure 5.99:** The histograms exhibit the **JFM** distributions of number of MARS segments under different categories, positive 0°C crossings, and positive slopes after $y_w$. The results are obtained using **MARS**, and the input parameters are as indicated in Section 5.5.1.

#### 5.5.3.1.2 MAM

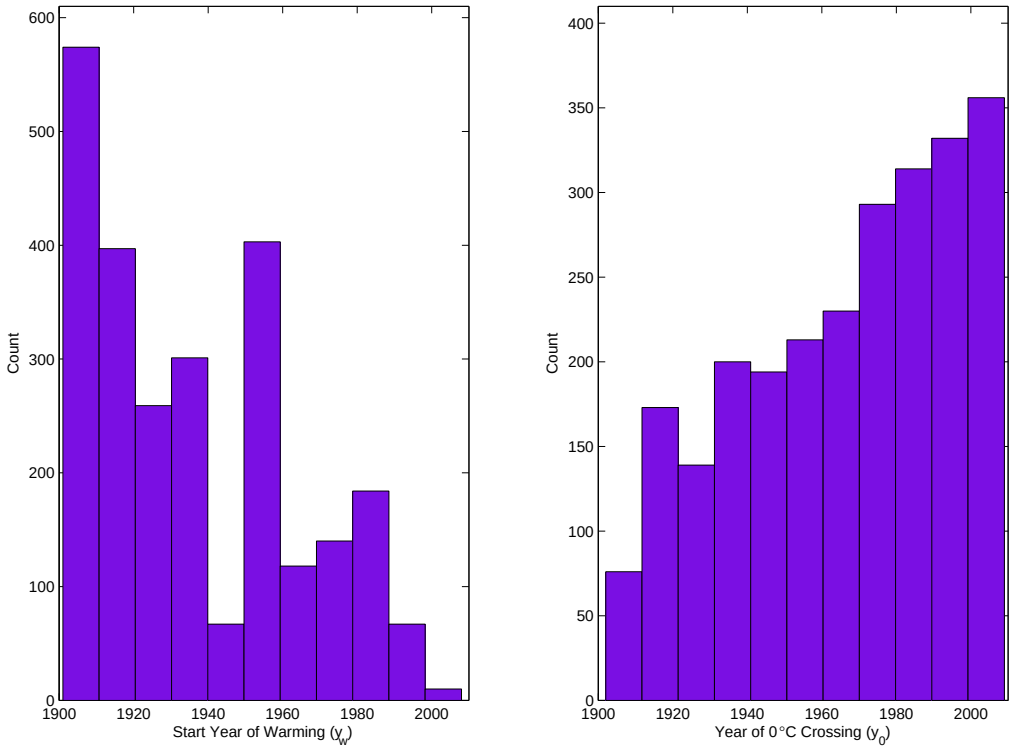


**Figure 5.100:** The histograms exhibit the temporal distributions of $y_w$ and $y_0$ during **MAM**. The results are obtained using **MARS**, and the input parameters are as indicated in Section 5.5.1.

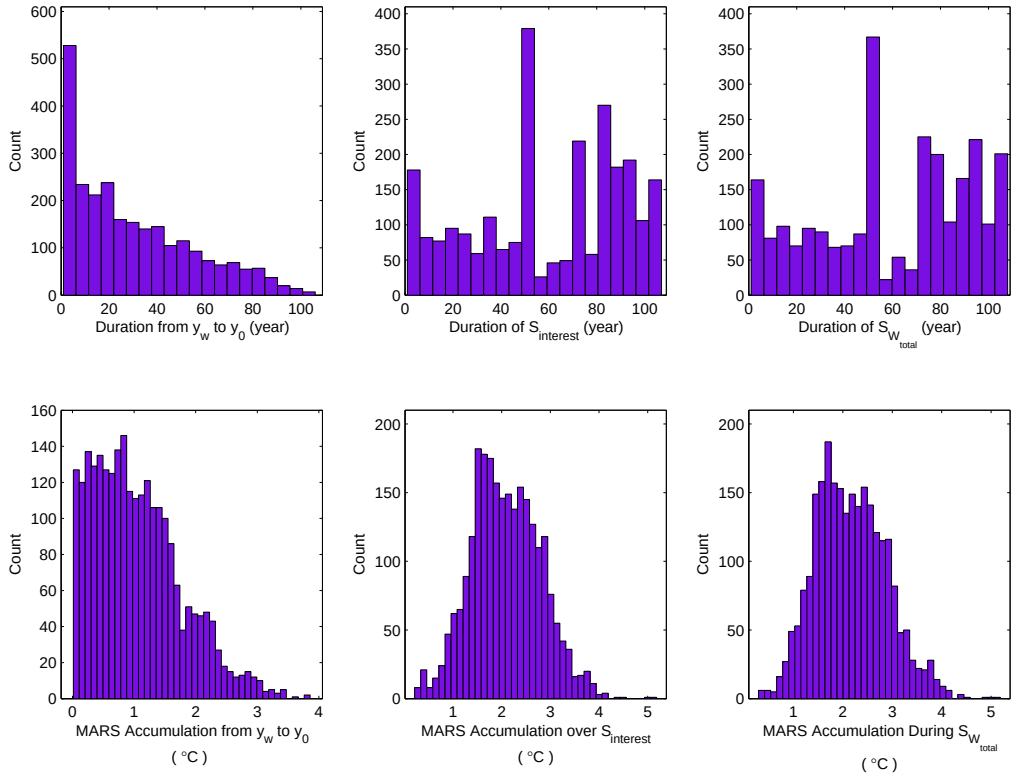


**Figure 5.101:** The histograms exhibit the distributions of duration and temperature accumulation during $y_w - y_0$, $S_{interest}$, and $S_{W_{total}}$ for **MAM**. The results are obtained using **MARS**, and the input parameters are as indicated in Section 5.5.1. The reader is referred to Section 5.2 for details on the variables used above.

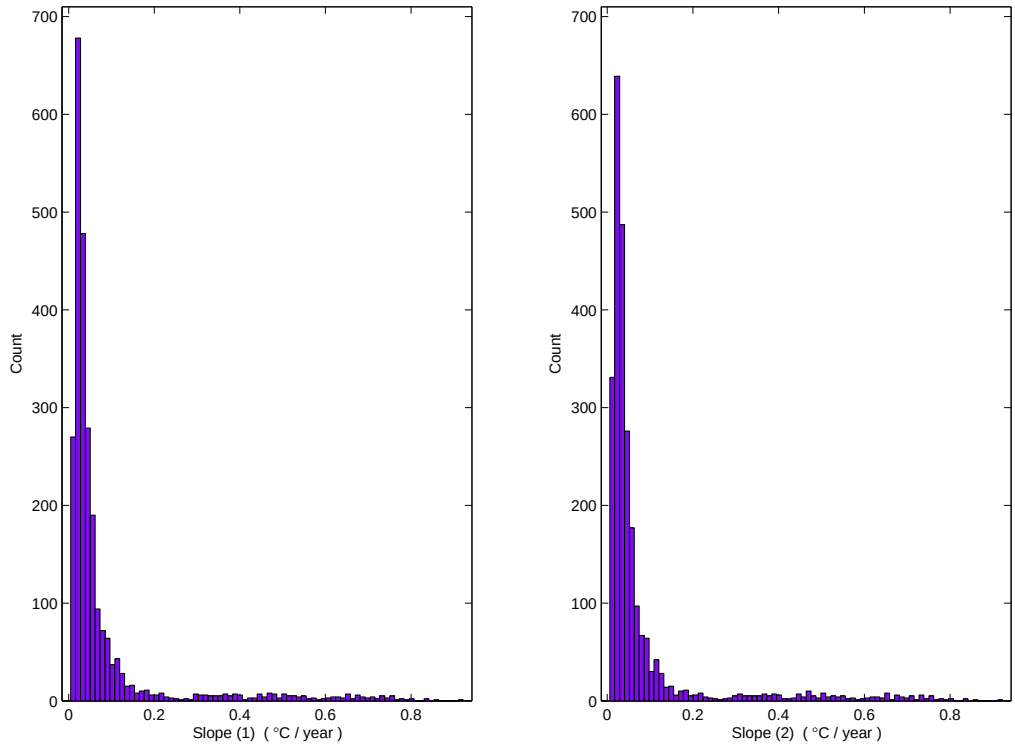


**Figure 5.102:** The histograms exhibit the distributions of Slope (1) and Slope (2) for **MAM**. The results are obtained using **MARS**, and the input parameters are as indicated in Section 5.5.1. The reader is referred to Section 5.2 for details on the variables used above.

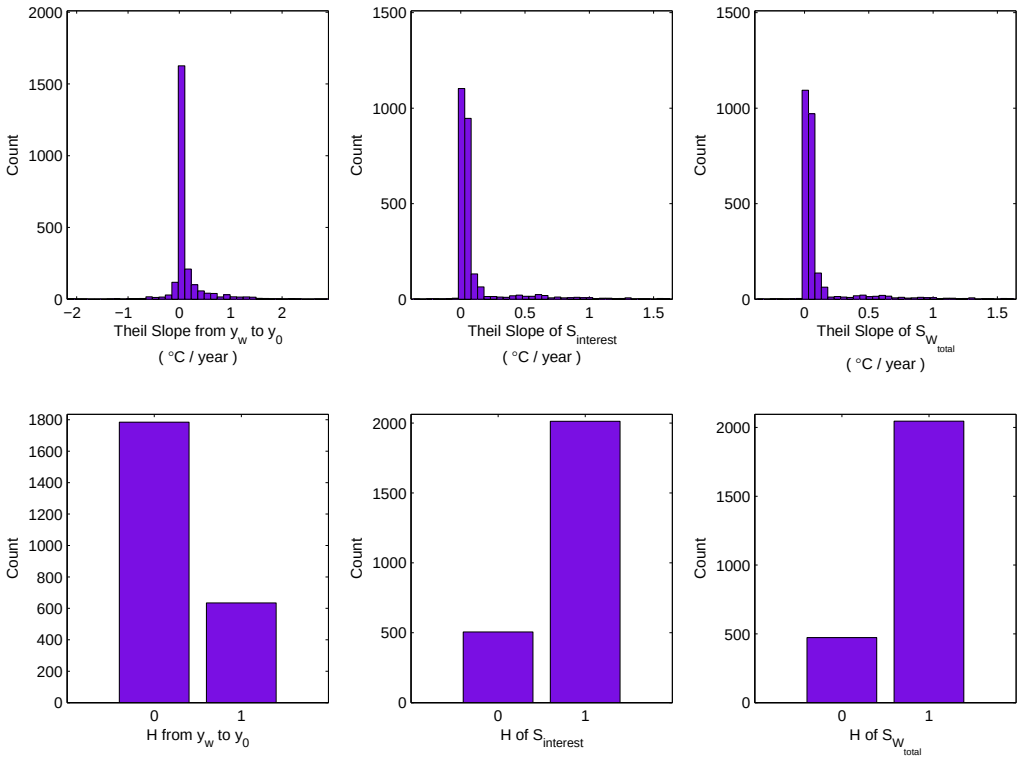


**Figure 5.103:** The histograms exhibit the distributions of Theil slope and H during $y_w - y_0$, $S_{interest}$, and $S_{W_{total}}$ for **MAM**. The results are obtained using **MARS**, and the input parameters are as indicated in Section 5.5.1. The reader is referred to Section 5.2 for details on the variables used above.

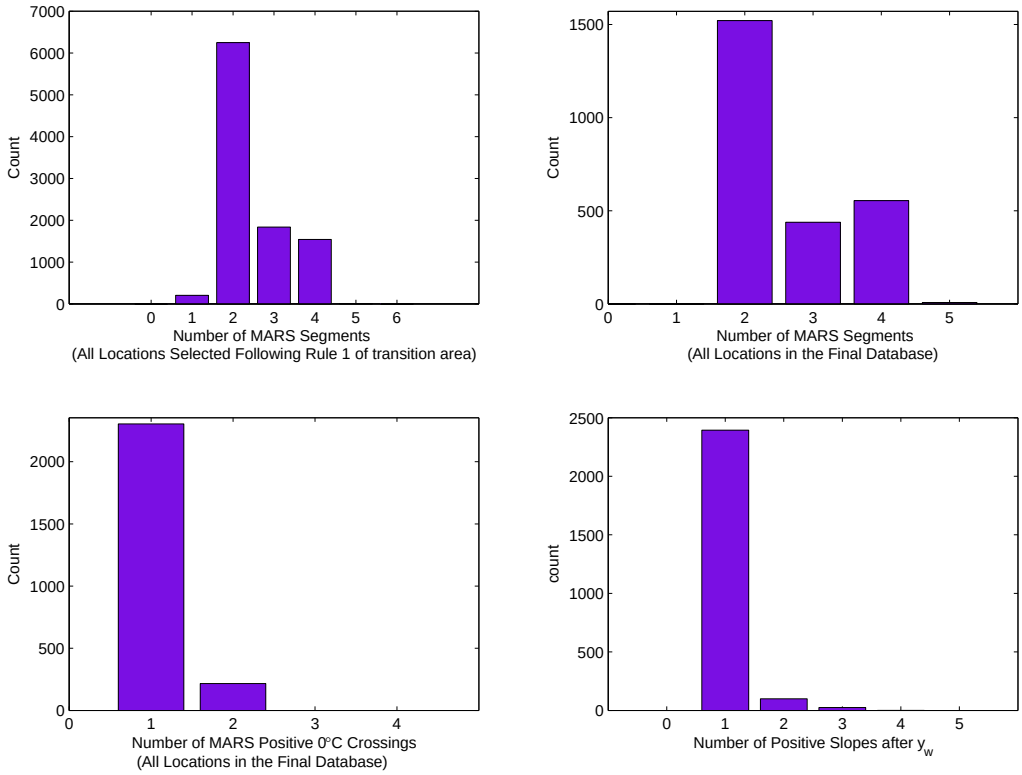


**Figure 5.104:** The histograms exhibit the distributions of number of MARS segments under different categories, positive 0°C crossings, and positive slopes after $y_w$ for **MAM**. The results are obtained using **MARS**, and the input parameters are as indicated in Section 5.5.1.

#### 5.5.3.2 Maps of MARS for JFM

##### 5.5.3.2.1 $y_w$

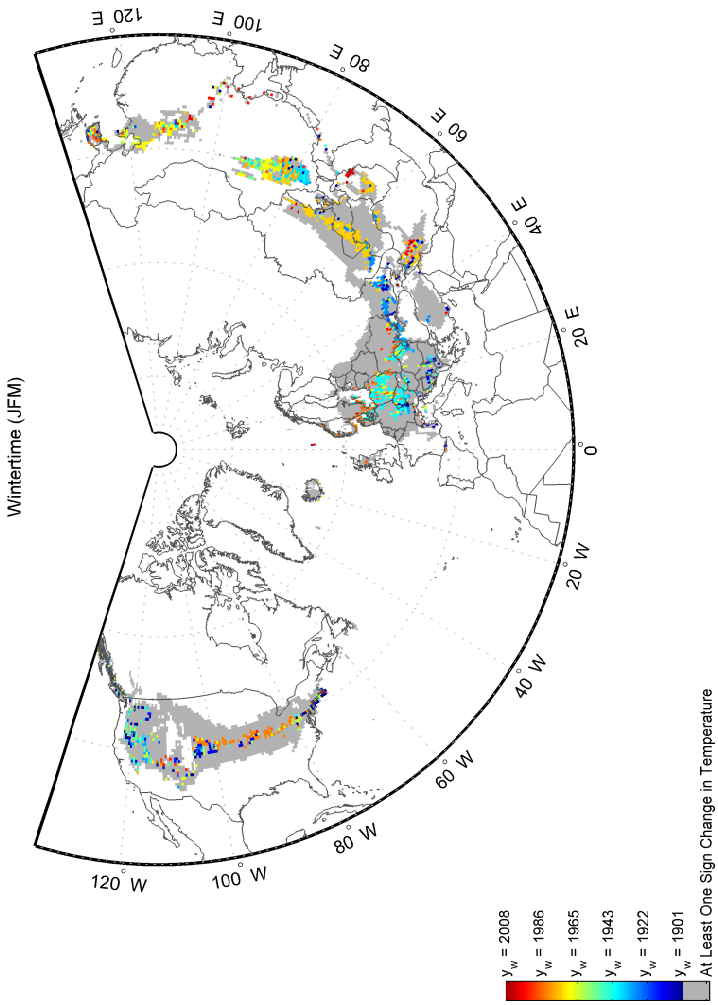


**Figure 5.105:** The map depicts the spatial distribution of $y_w$ in the Northern Hemisphere during **JFM**. The results are obtained using **MARS**, and the input parameters are as indicated in Section 5.5.1.

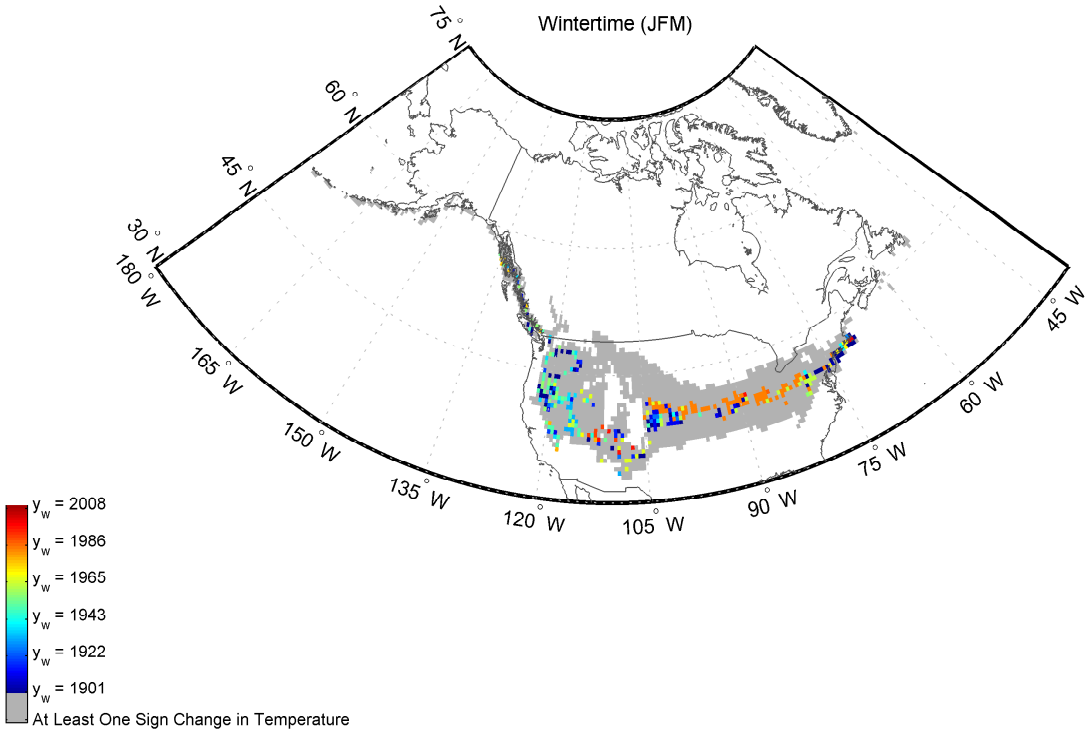


**Figure 5.106:** The same as Figure 5.105: zoomed in view of North America

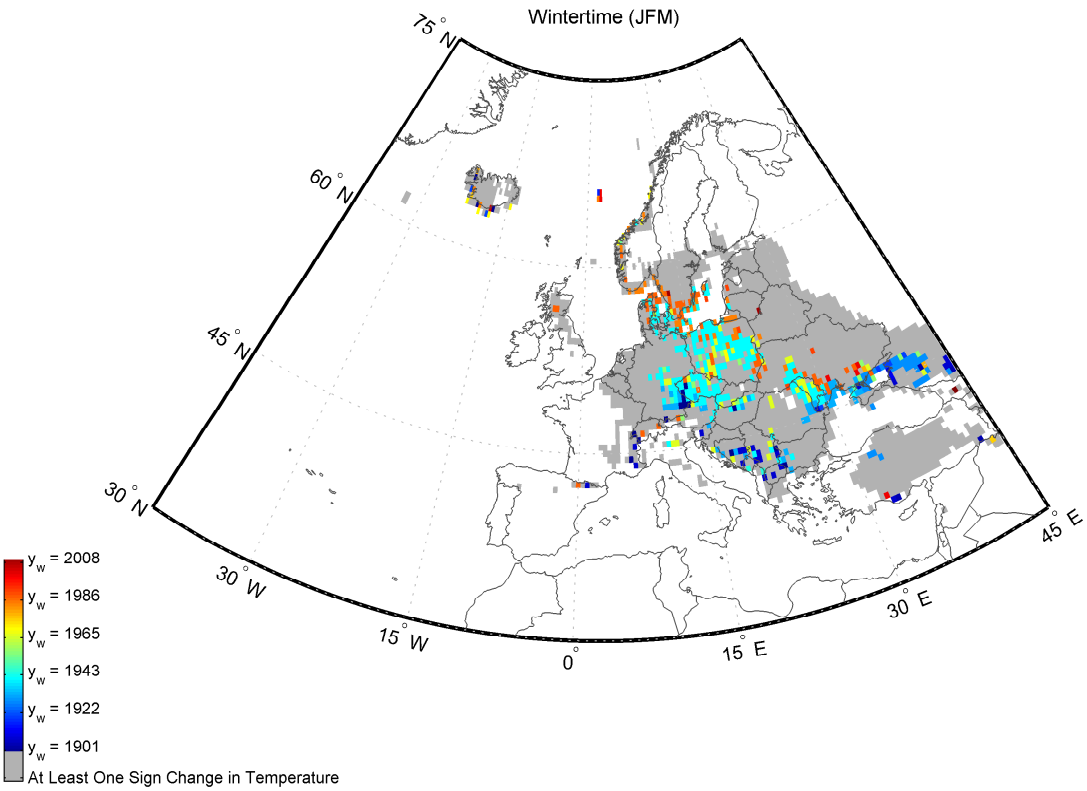


**Figure 5.107:** The same as Figure 5.105: zoomed in view of Europe

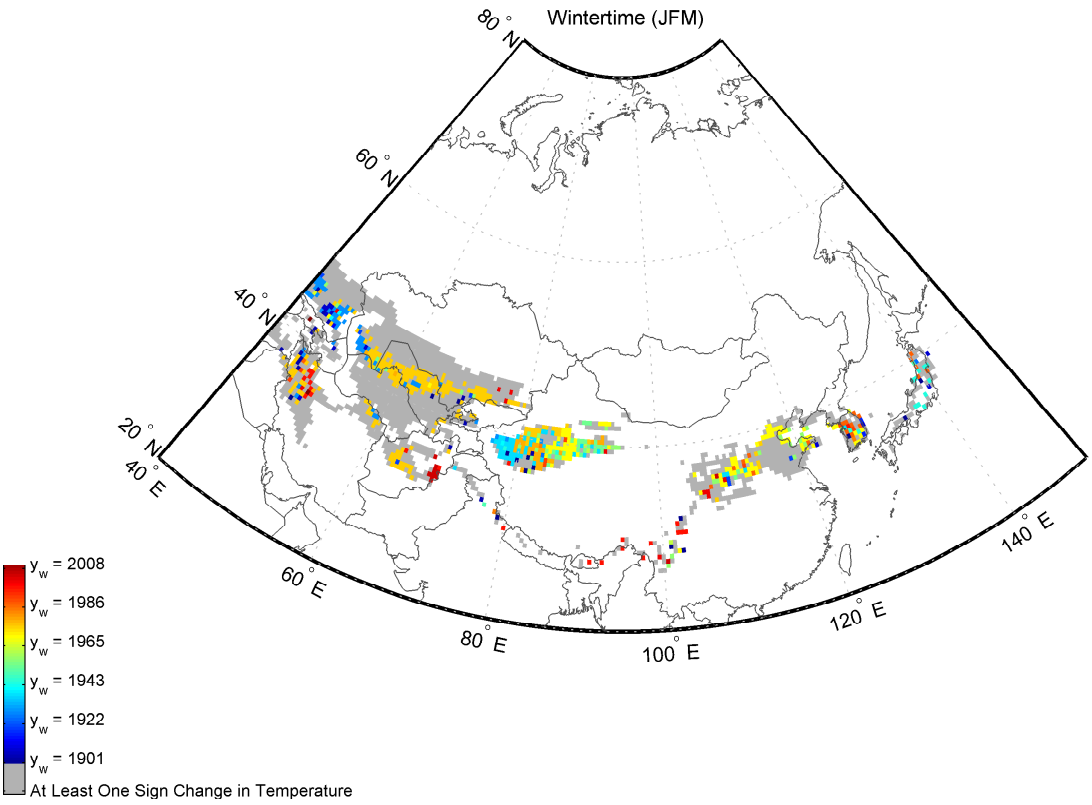


**Figure 5.108:** The same as Figure 5.105: zoomed in view of Asia

#### 5.5.3.2.2 $y_0$

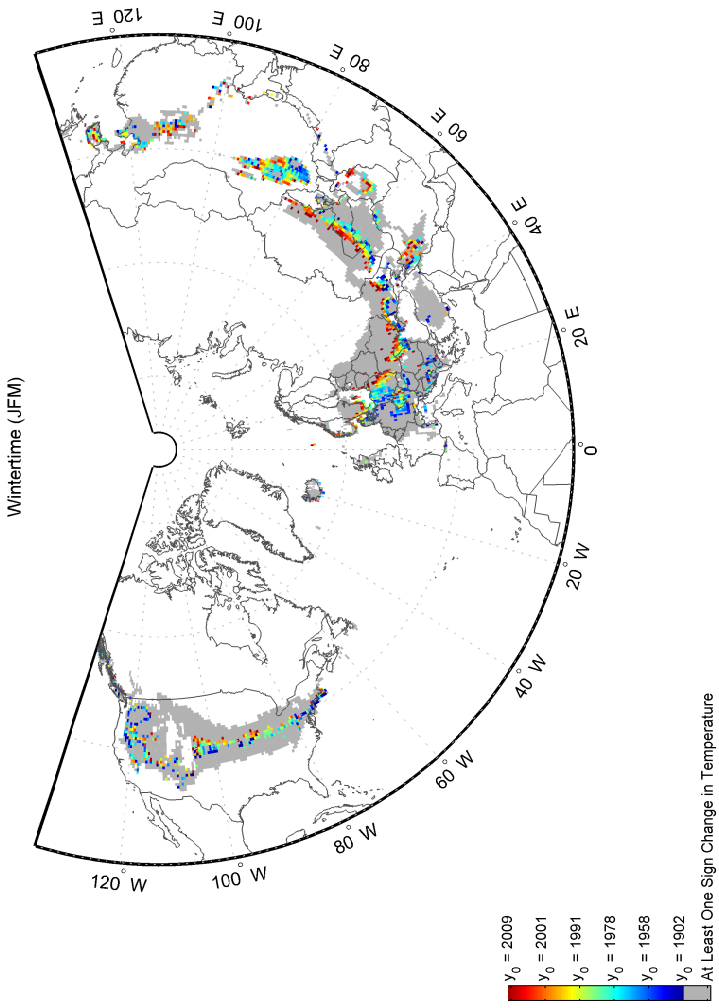


**Figure 5.109:** The map depicts the spatial distribution of $y_0$ in the Northern Hemisphere during **JFM**. The results are obtained using **MARS**, and the input parameters are as indicated in Section 5.5.1.

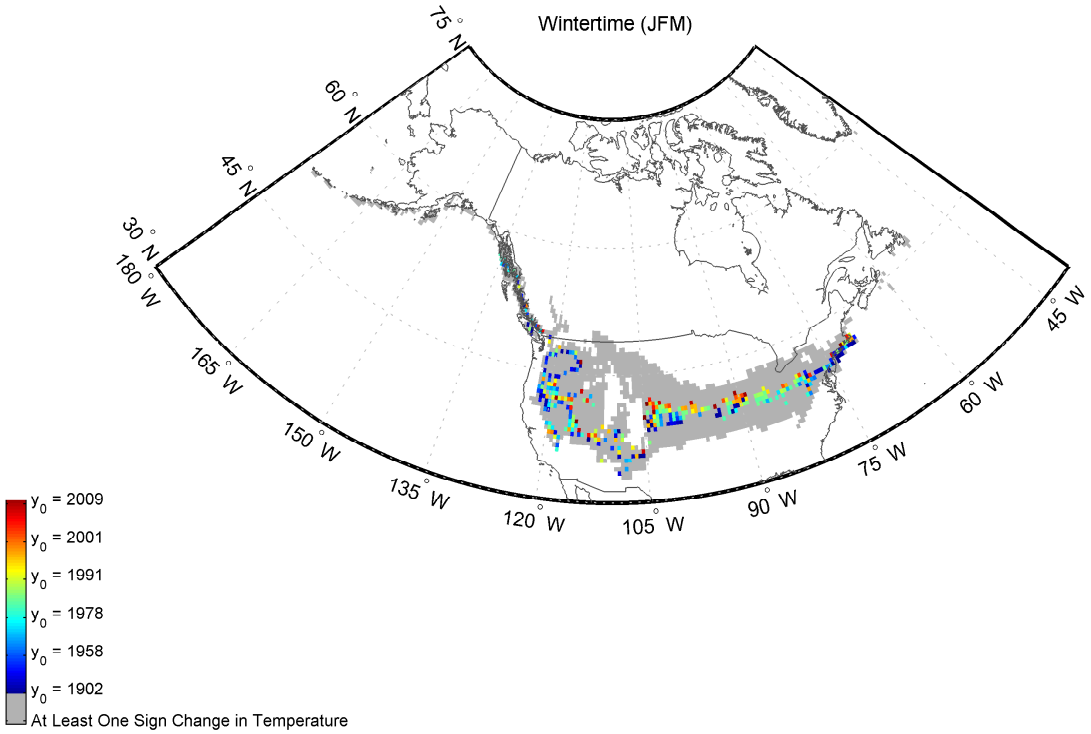


**Figure 5.110:** The same as Figure 5.109: zoomed in view of North America

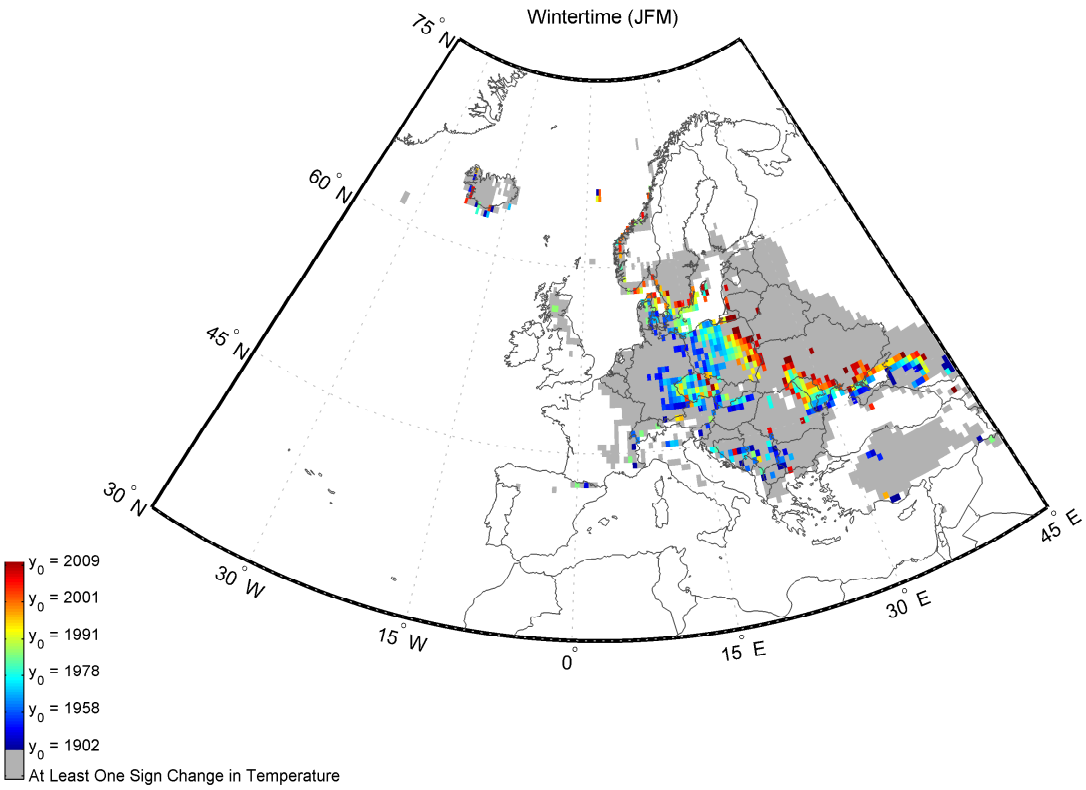


**Figure 5.111:** The same as Figure 5.109: zoomed in view of Europe

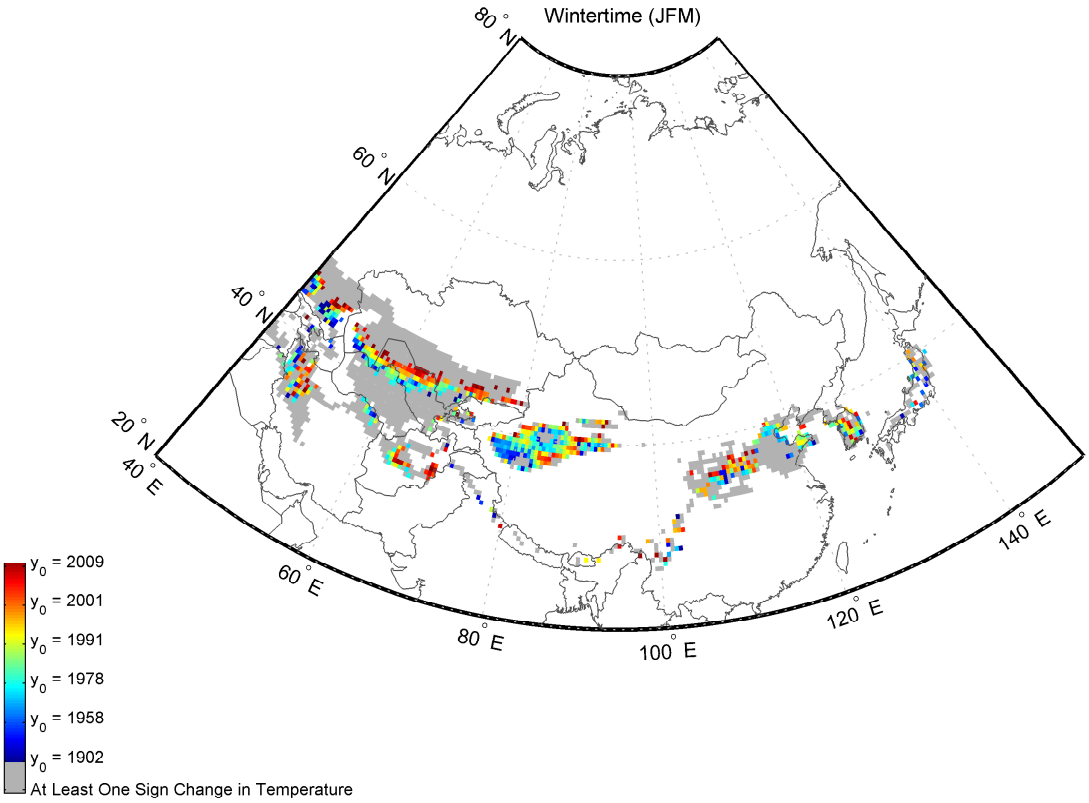


**Figure 5.112:** The same as Figure 5.109: zoomed in view of Asia

#### 5.5.3.2.3 Slope (1)

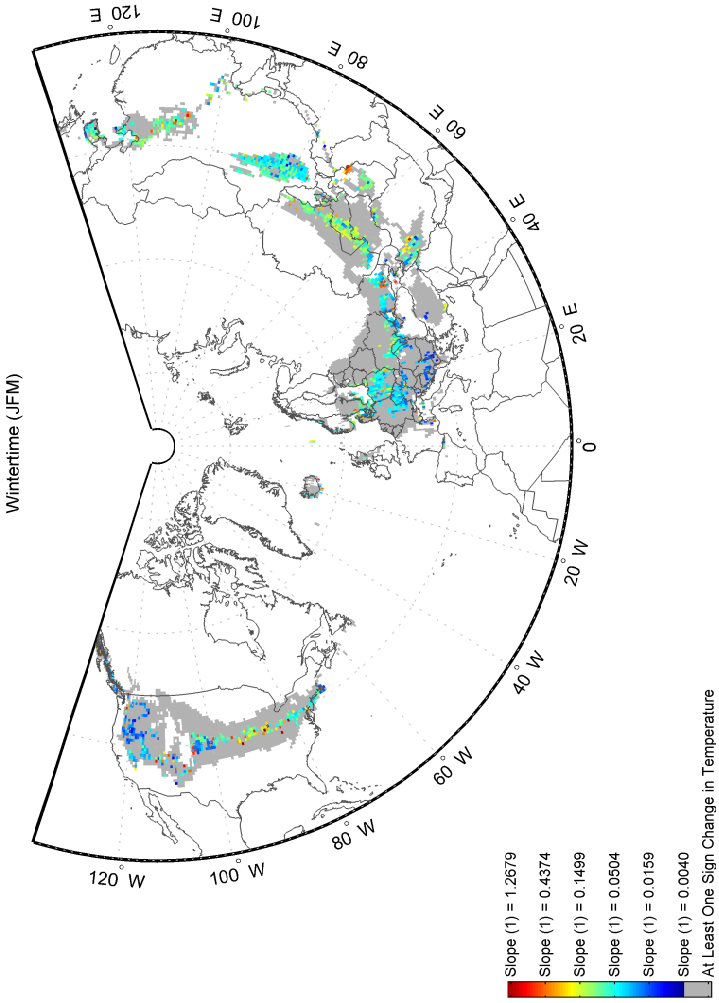


**Figure 5.113:** The map depicts the spatial distribution of Slope (1) in the Northern Hemisphere during **JFM**. The results are obtained using **MARS**, and the input parameters are as indicated in Section 5.5.1. Refer to Section 5.2 for the definition of 'Slope (1)'.

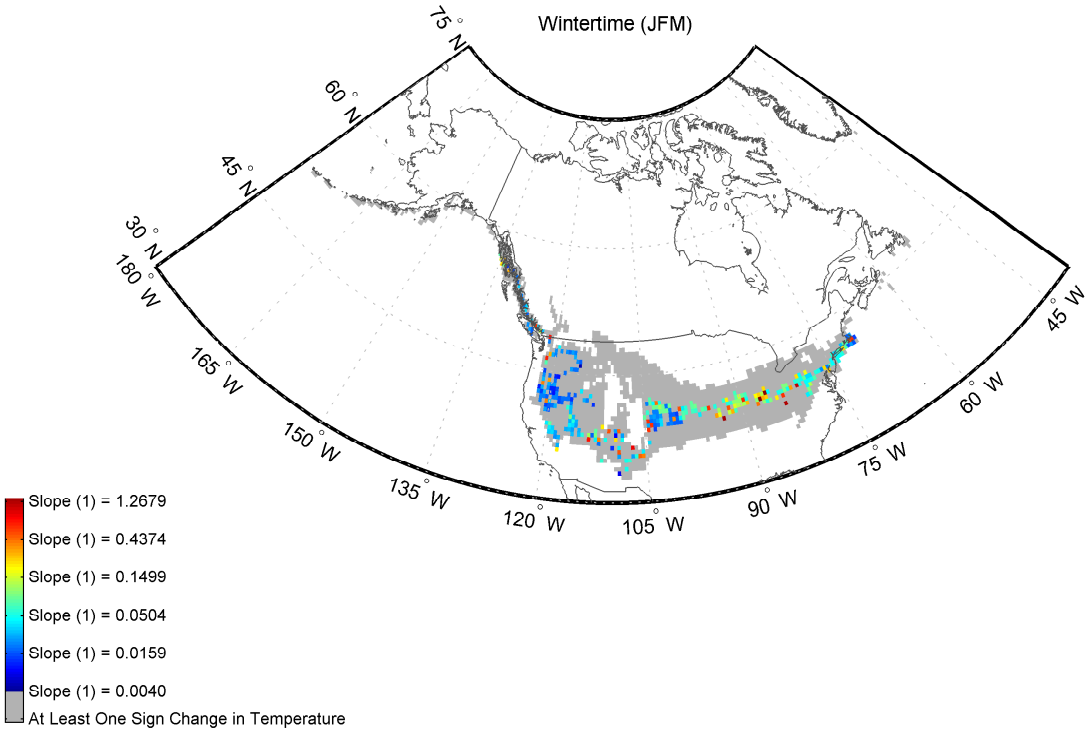


**Figure 5.114:** The same as Figure 5.113: zoomed in view of North America

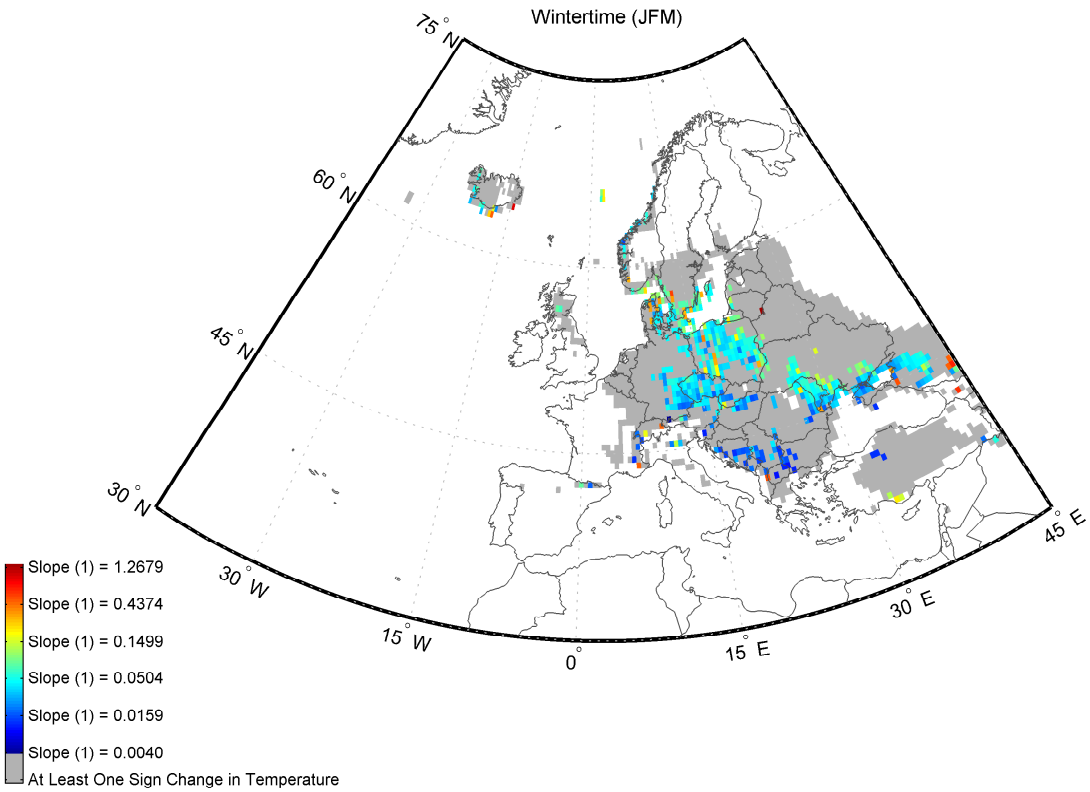


**Figure 5.115:** The same as Figure 5.113: zoomed in view of Europe

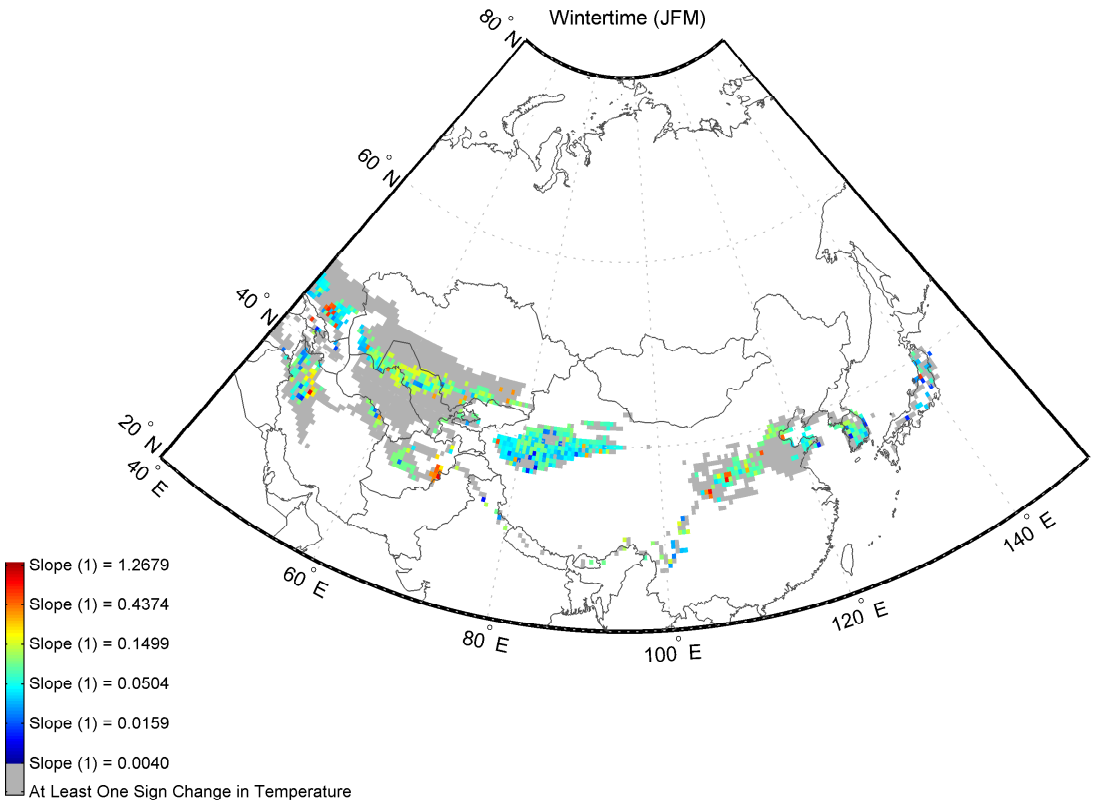


**Figure 5.116:** The same as Figure 5.113: zoomed in view of Asia

#### 5.5.3.2.4 Slope (2)

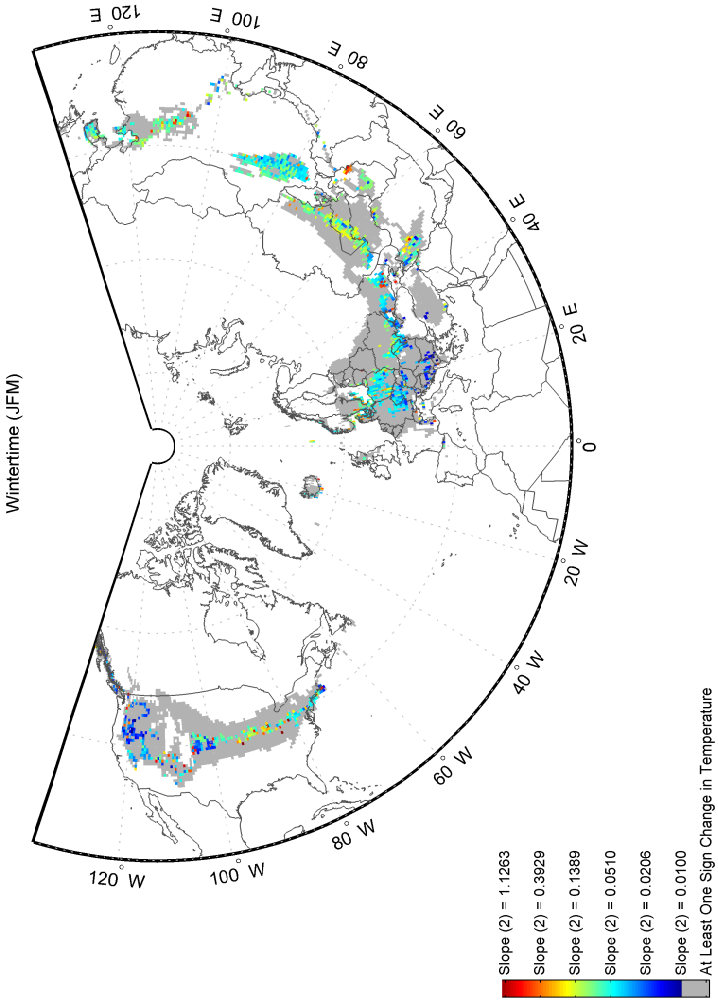


**Figure 5.117:** The map depicts the spatial distribution of Slope (2) in the Northern Hemisphere during **JFM**. The results are obtained using **MARS**, and the input parameters are as indicated in Section 5.5.1. Refer to Section 5.2 for the definition of 'Slope (2)'.

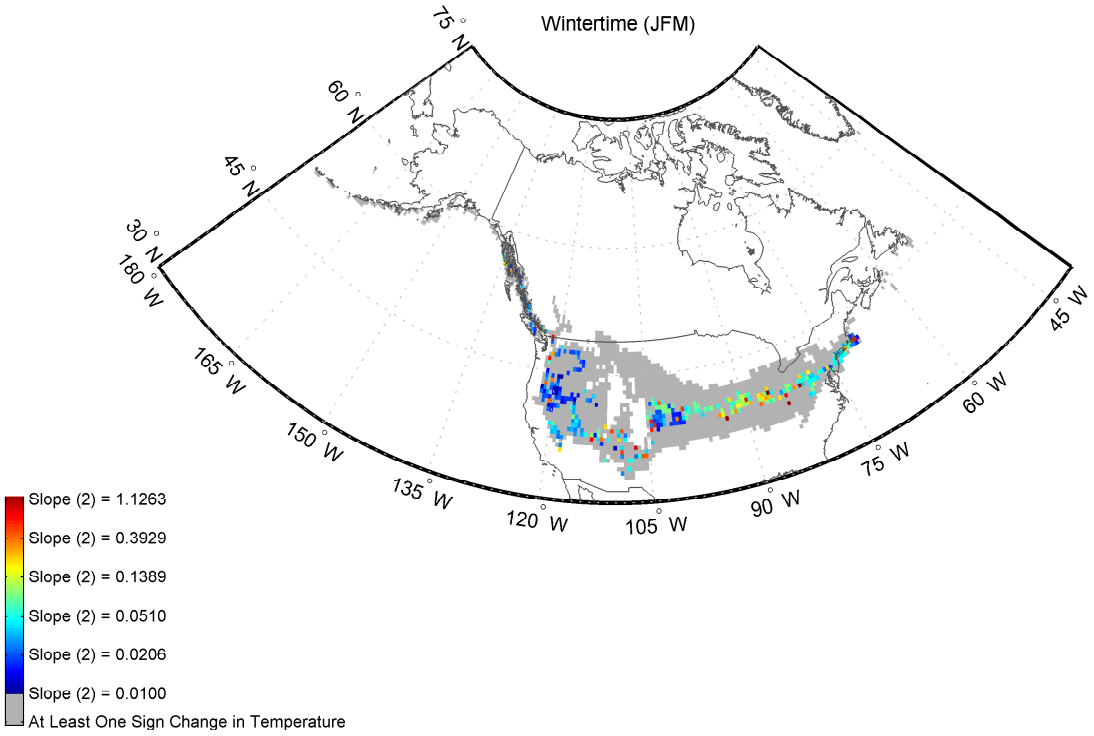


**Figure 5.118:** The same as Figure 5.117: zoomed in view of North America

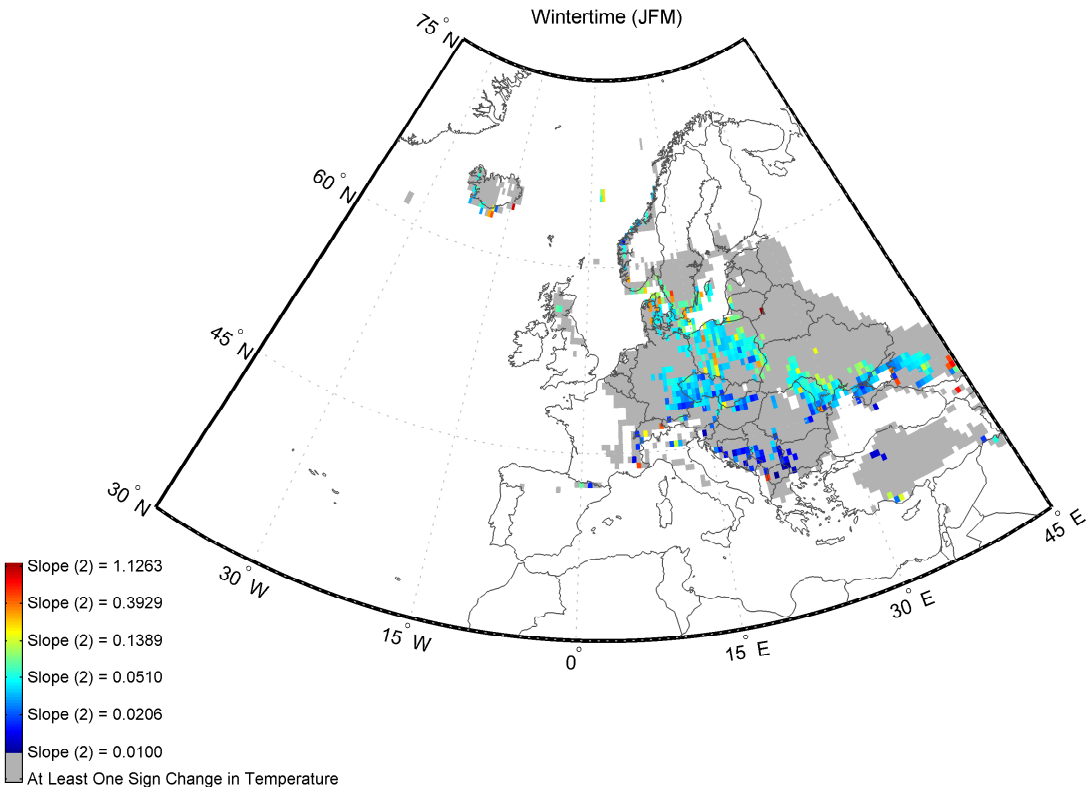


**Figure 5.119:** The same as Figure 5.117: zoomed in view of Europe

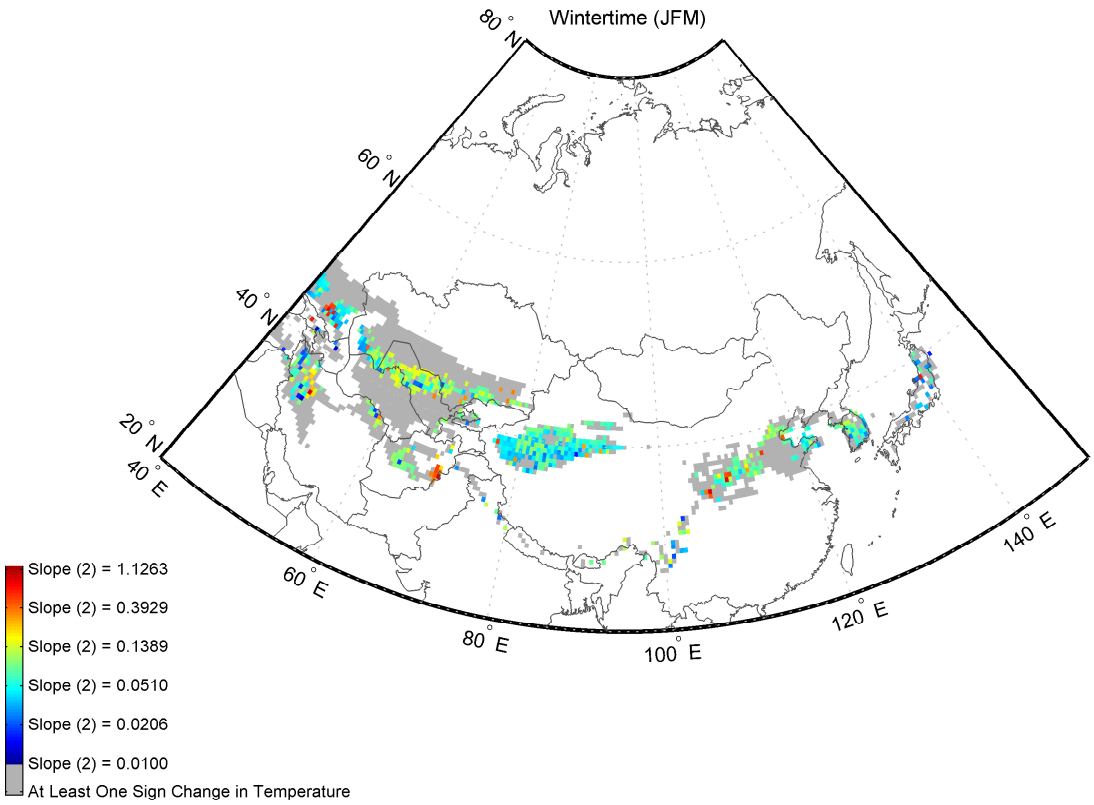


**Figure 5.120:** The same as Figure 5.117: zoomed in view of Asia

#### 5.5.3.2.5 H from $y_w$ to $y_0$

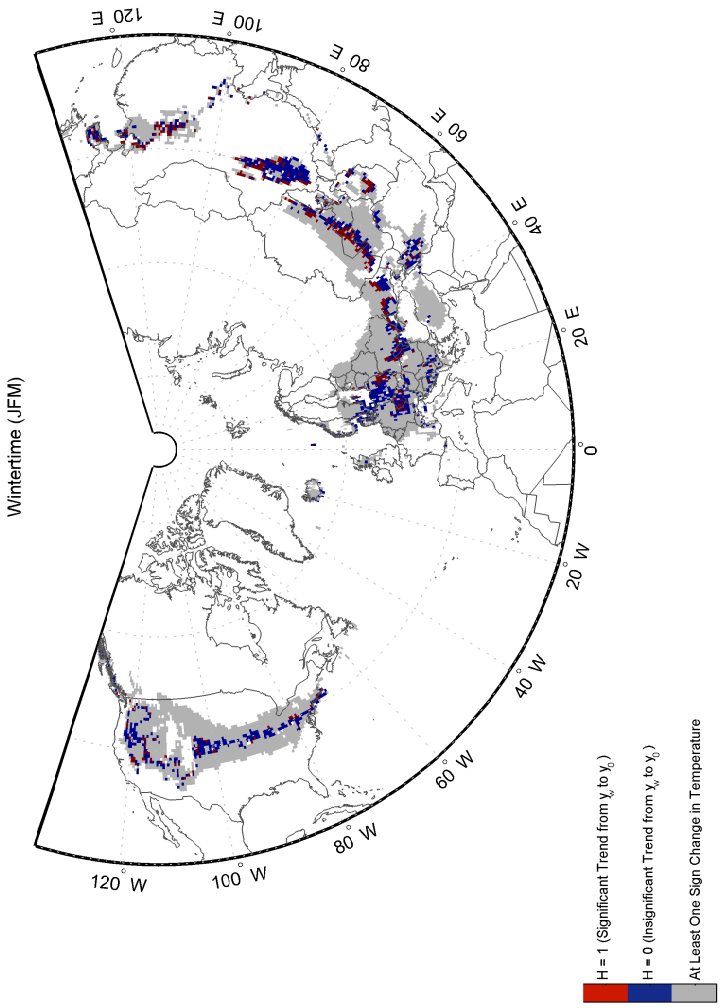


**Figure 5.121:** The map depicts the spatial distribution of H from $y_w$ to $y_0$ in the Northern Hemisphere during **JFM**. The results are obtained using **MARS**, and the input parameters are as indicated in Section 5.5.1.

#### 5.5.3.2.6 H of $S_{interest}$

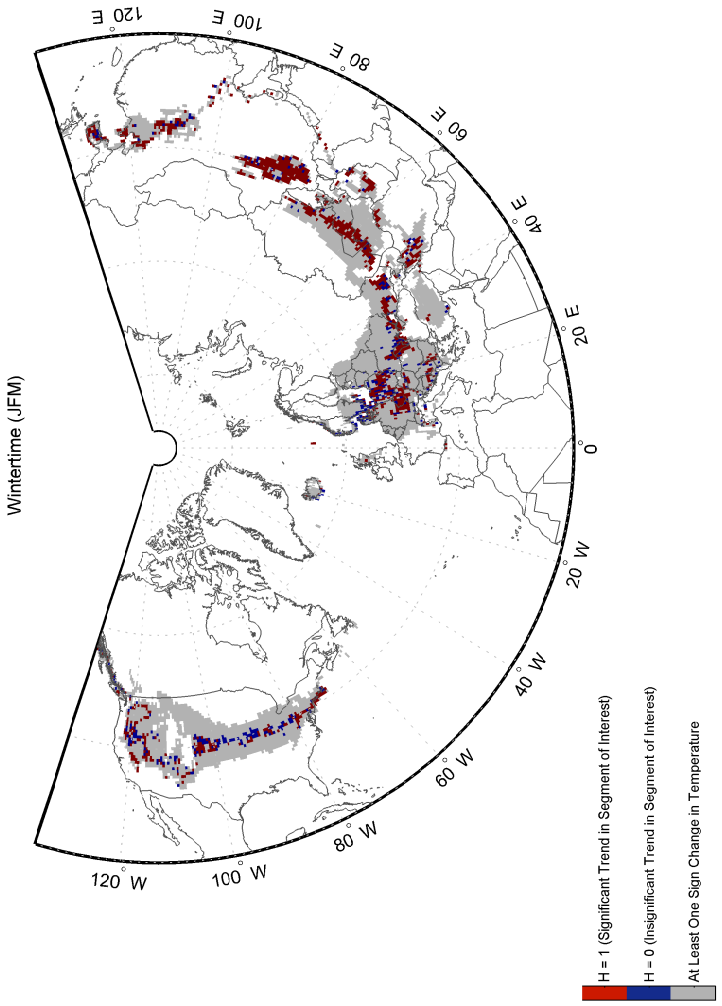


**Figure 5.122:** The map depicts the spatial distribution of H of $S_{interest}$ in the Northern Hemisphere during **JFM**. The results are obtained using **MARS**, and the input parameters are as indicated in Section 5.5.1.

#### 5.5.3.2.7 H of $Sw_{total}$

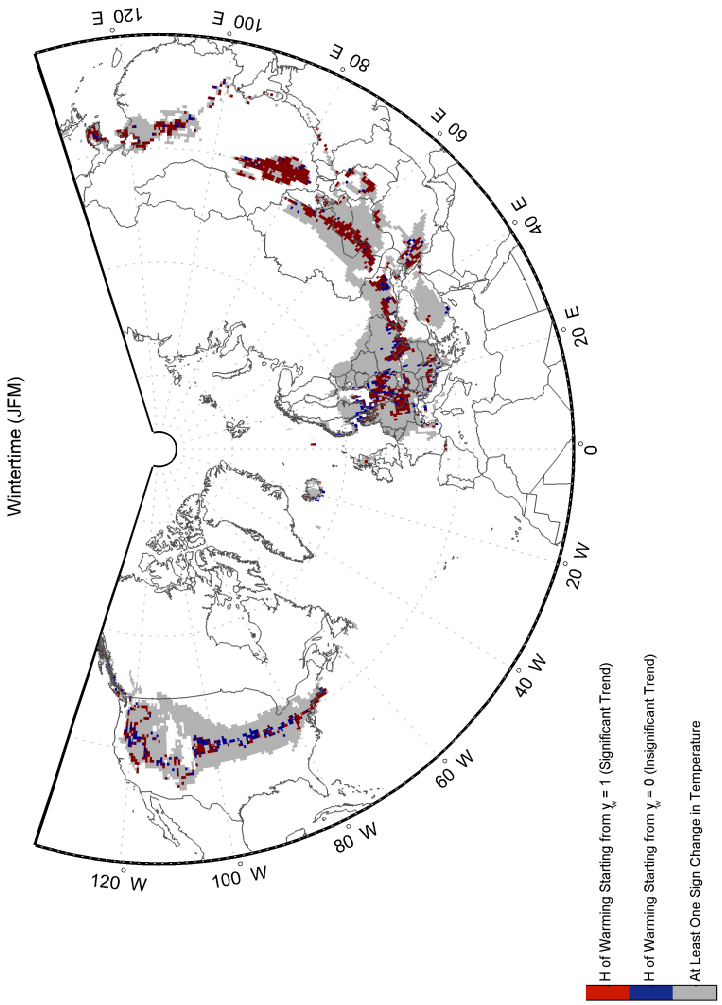


**Figure 5.123:** The map depicts the spatial distribution of H of $Sw_{total}$ in the Northern Hemisphere during **JFM**. The results are obtained using **MARS**, and the input parameters are as indicated in Section 5.5.1.

#### 5.5.3.3 Maps of MARS for MAM

##### 5.5.3.3.1 $y_w$

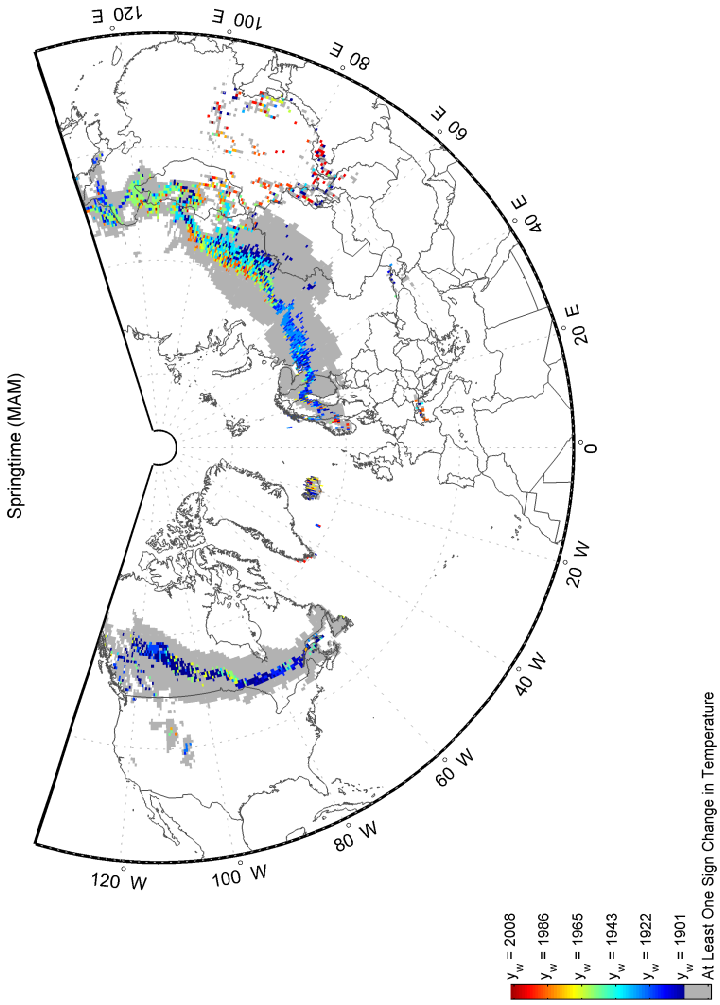


**Figure 5.124:** The map depicts the spatial distribution of $y_w$ in the Northern Hemisphere during **MAM**. The results are obtained using **MARS**, and the input parameters are as indicated in Section 5.5.1.

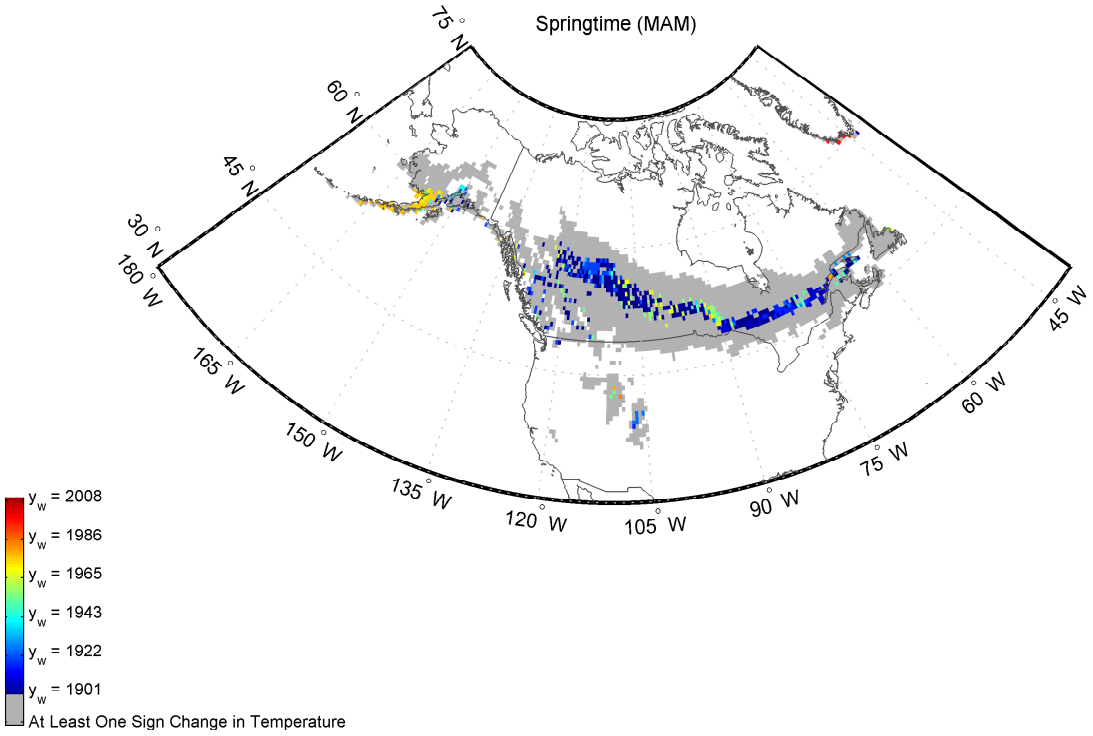


**Figure 5.125:** The same as Figure 5.124: zoomed in view of North America

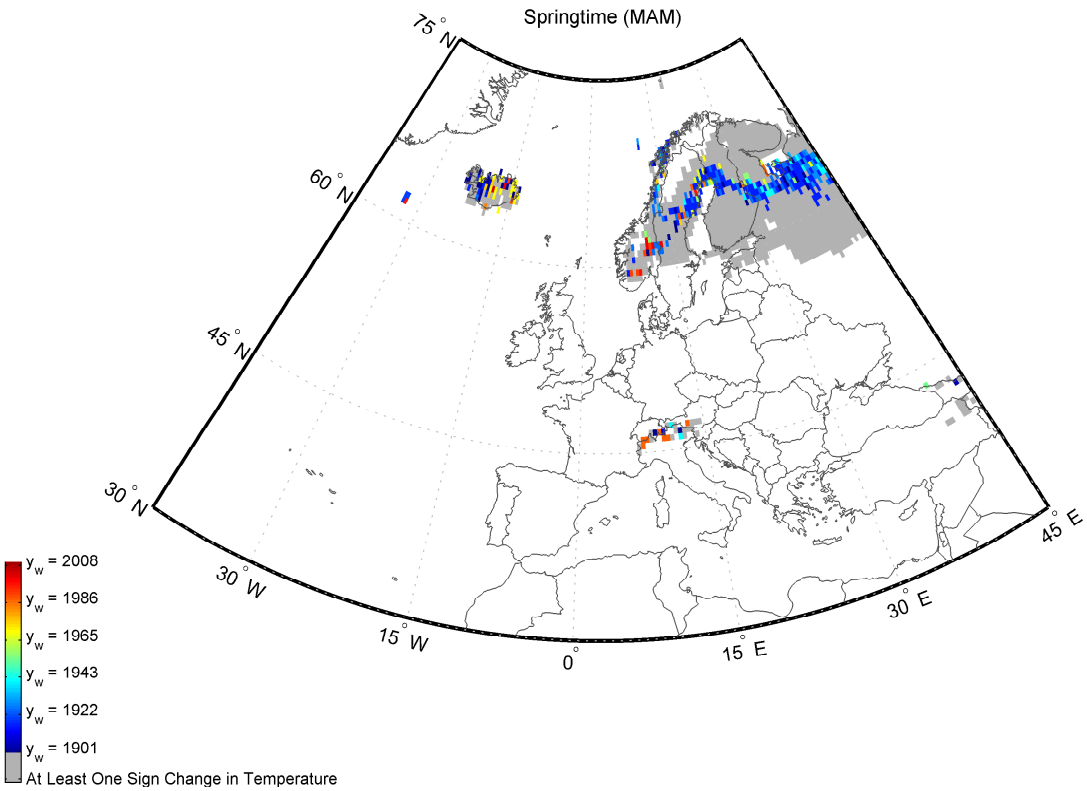


**Figure 5.126:** The same as Figure 5.124: zoomed in view of Europe

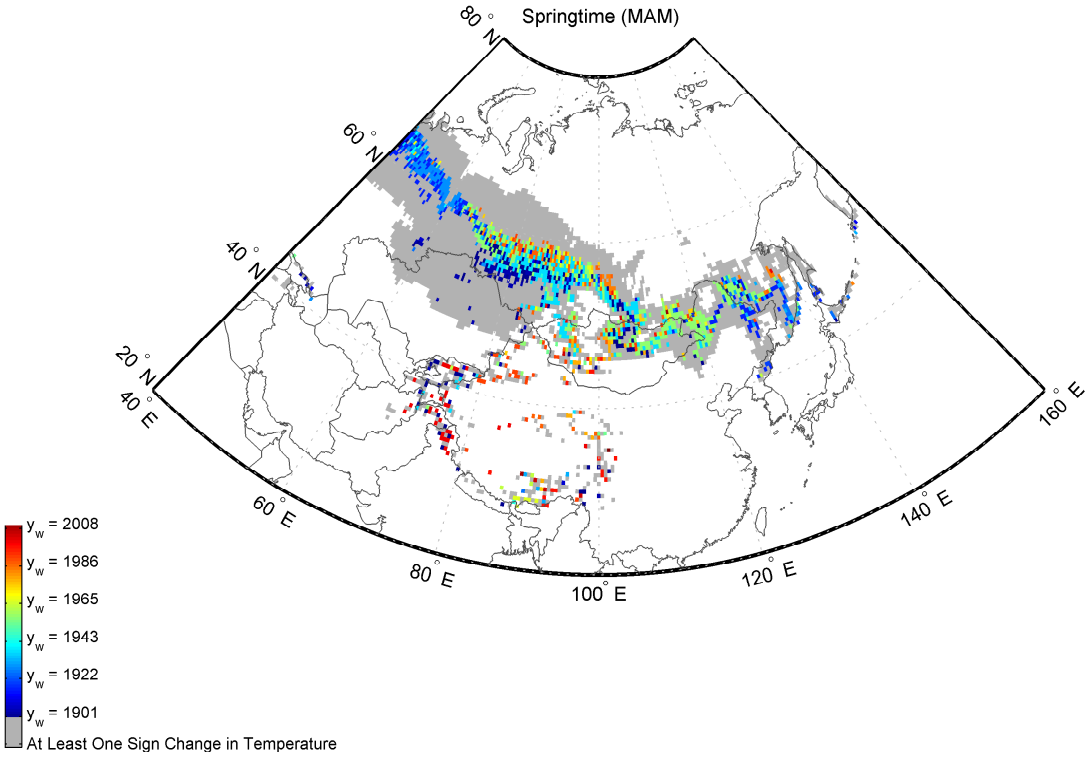


**Figure 5.127:** The same as Figure 5.124: zoomed in view of Asia

#### 5.5.3.3.2 $y_0$

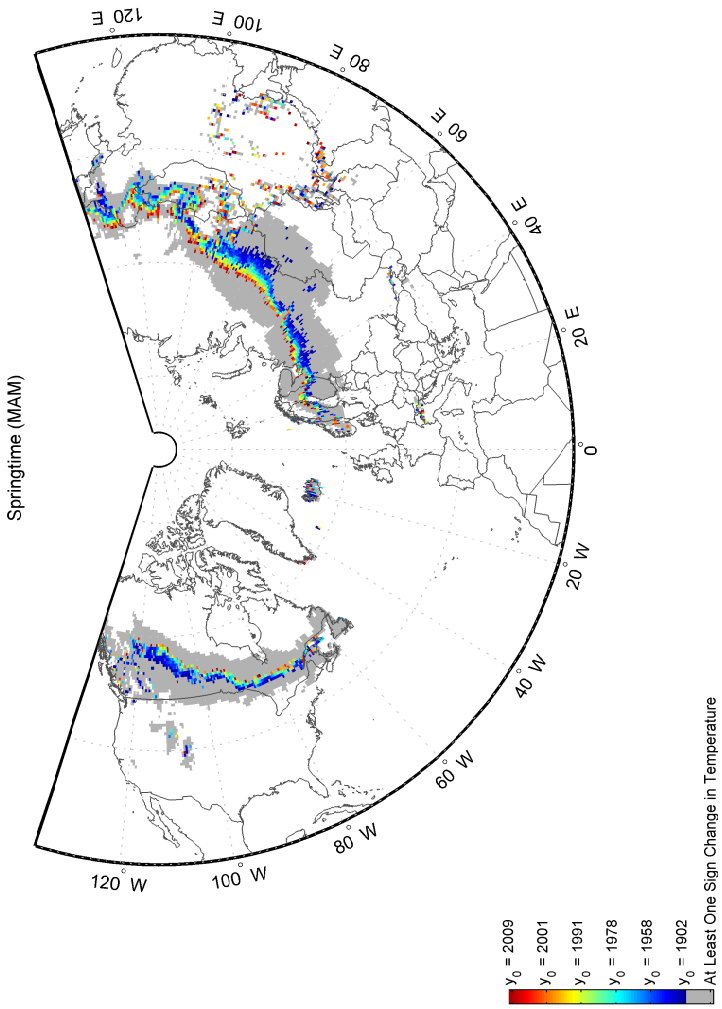


**Figure 5.128:** The map depicts the spatial distribution of $y_0$ in the Northern Hemisphere during **MAM**. The results are obtained using **MARS**, and the input parameters are as indicated in Section 5.5.1.

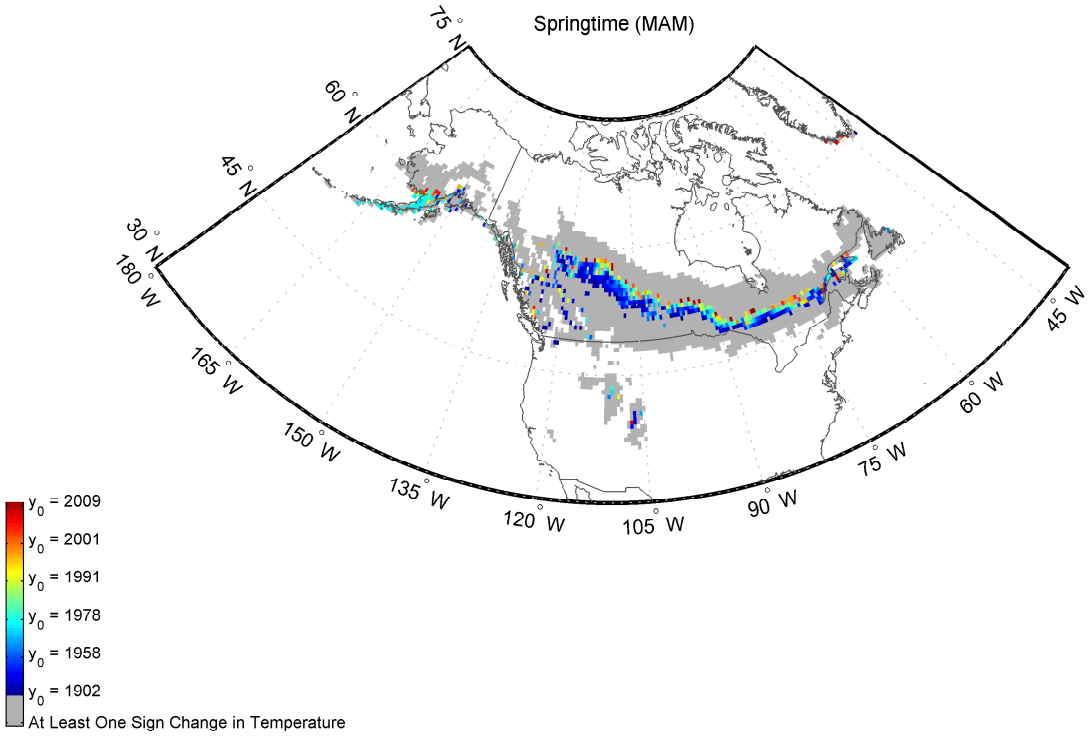


**Figure 5.129:** The same as Figure 5.128: zoomed in view of North America

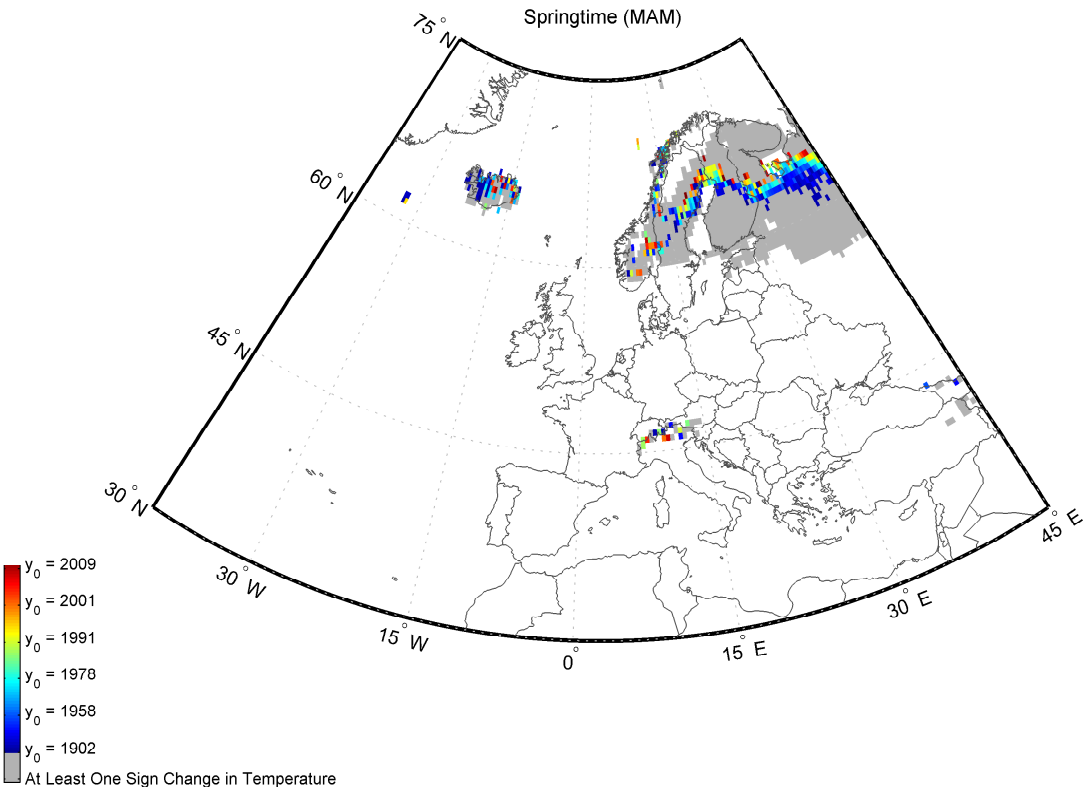


**Figure 5.130:** The same as Figure 5.128: zoomed in view of Europe

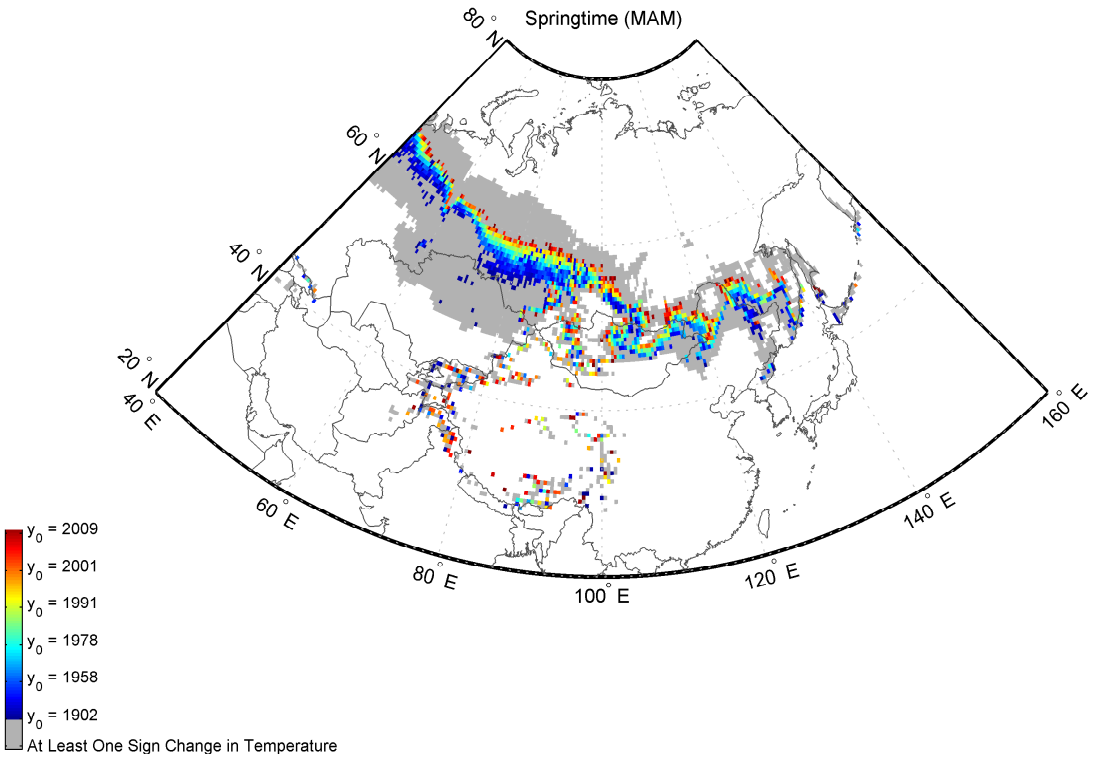


**Figure 5.131:** The same as Figure 5.128: zoomed in view of Asia

#### 5.5.3.3.3 Slope (1)

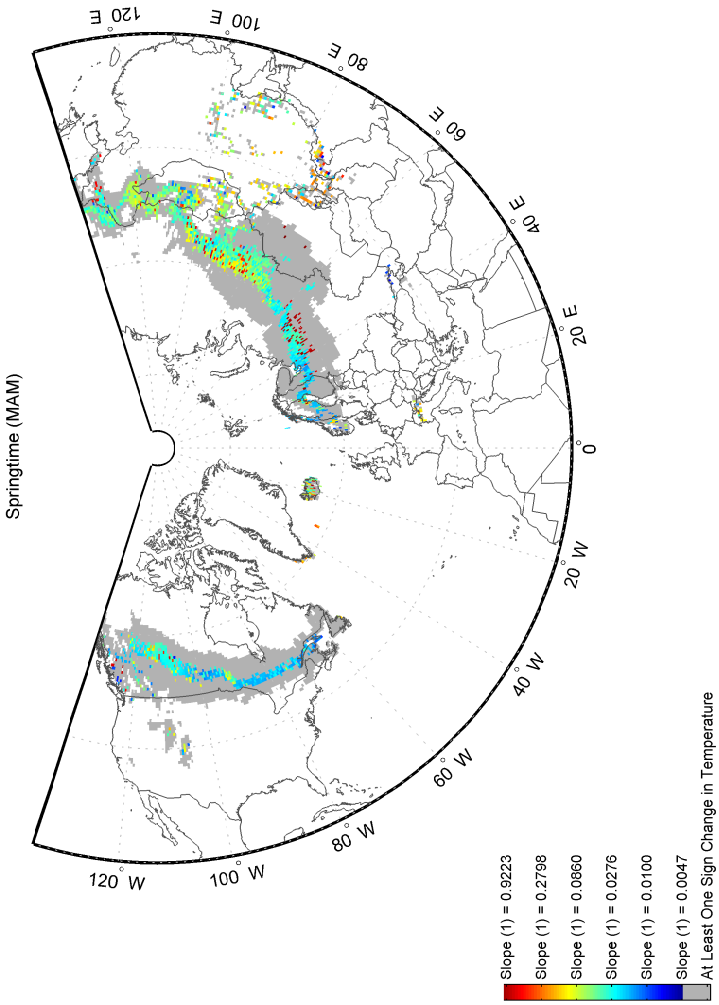


**Figure 5.132:** The map depicts the spatial distribution of Slope (1) in the Northern Hemisphere during **MAM**. The results are obtained using **MARS**, and the input parameters are as indicated in Section 5.5.1. Refer to Section 5.2 for the definition of 'Slope (1)'.

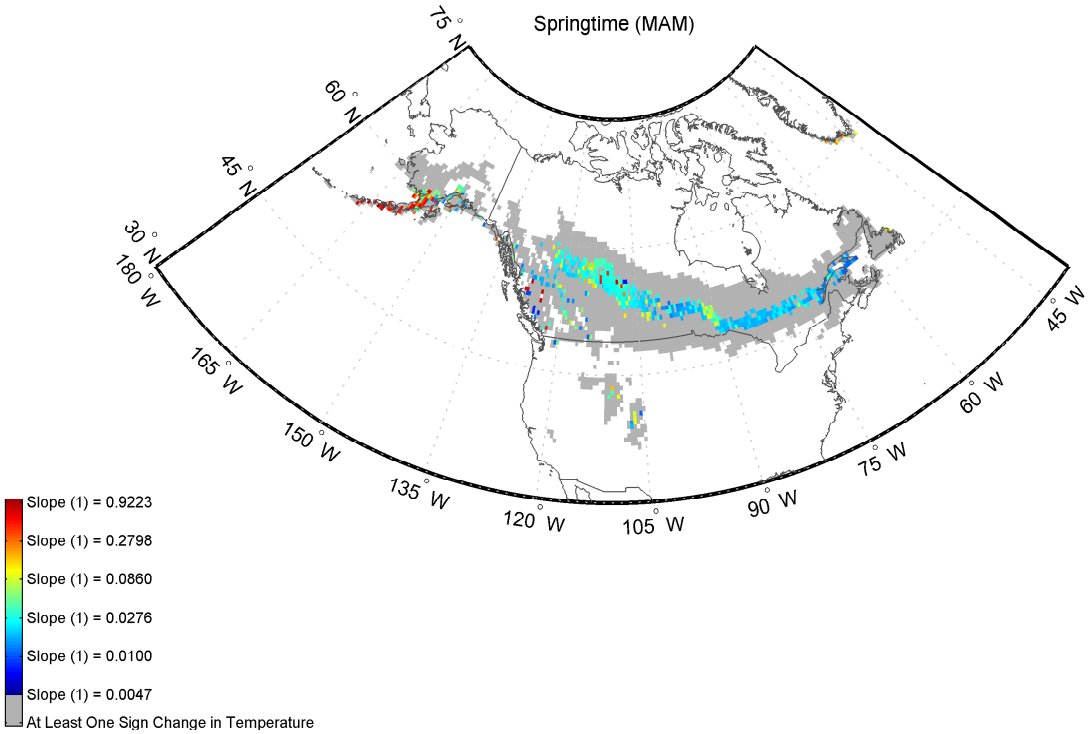


**Figure 5.133:** The same as Figure 5.132: zoomed in view of North America

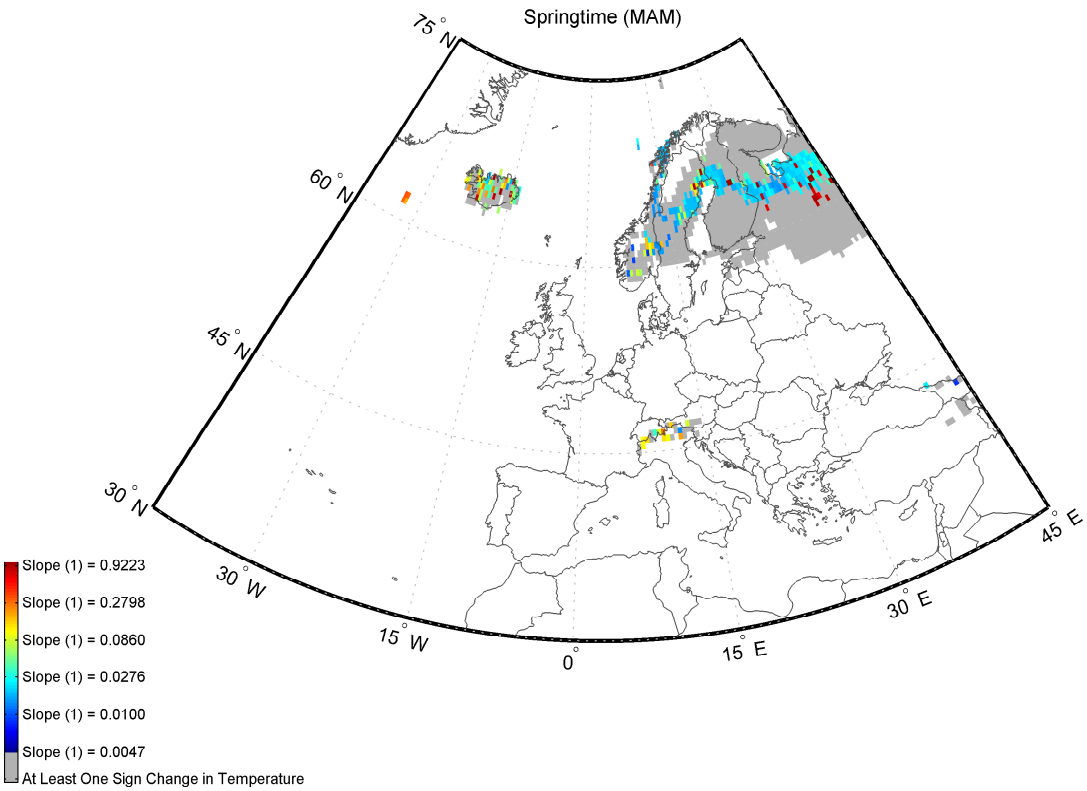


**Figure 5.134:** The same as Figure 5.132: zoomed in view of Europe

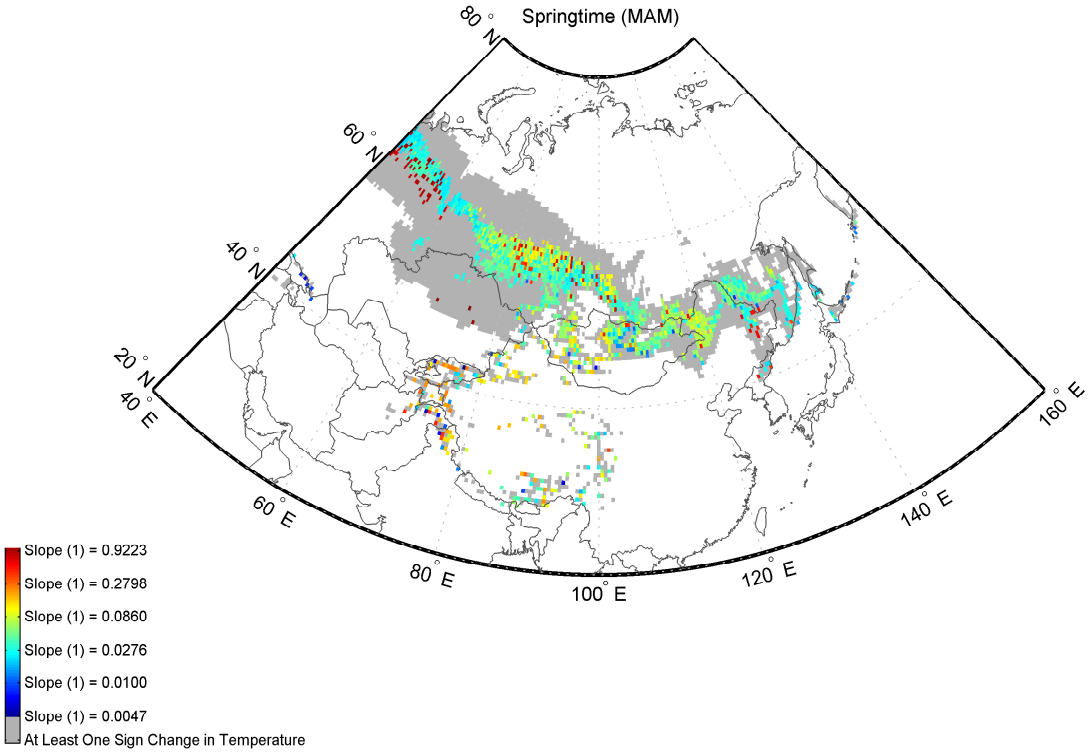


**Figure 5.135:** The same as Figure 5.132: zoomed in view of Asia

#### 5.5.3.3.4 Slope (2)

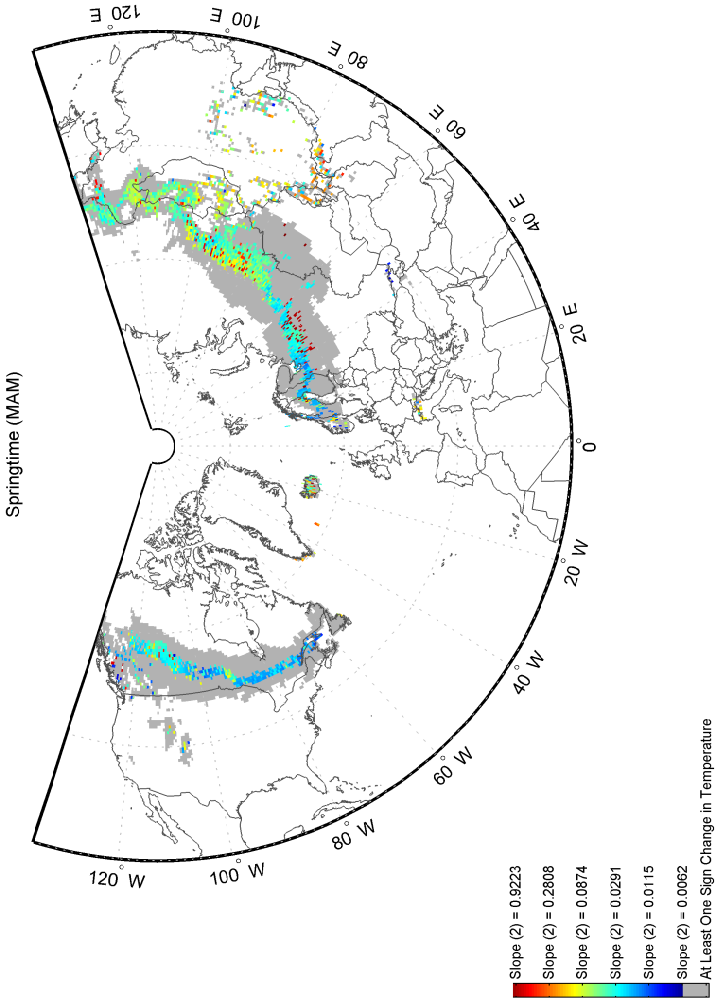


**Figure 5.136:** The map depicts the spatial distribution of Slope (2) in the Northern Hemisphere during **MAM**. The results are obtained using **MARS**, and the input parameters are as indicated in Section 5.5.1. Refer to Section 5.2 for the definition of 'Slope (2)'.

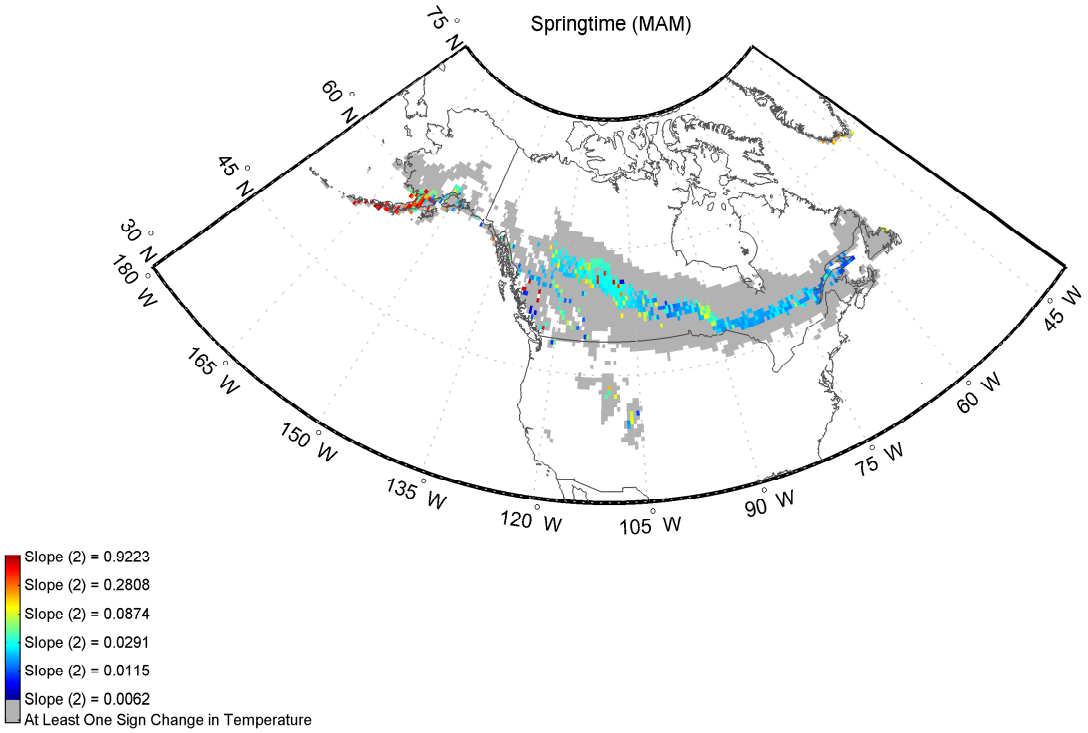


**Figure 5.137:** The same as Figure 5.136: zoomed in view of North America

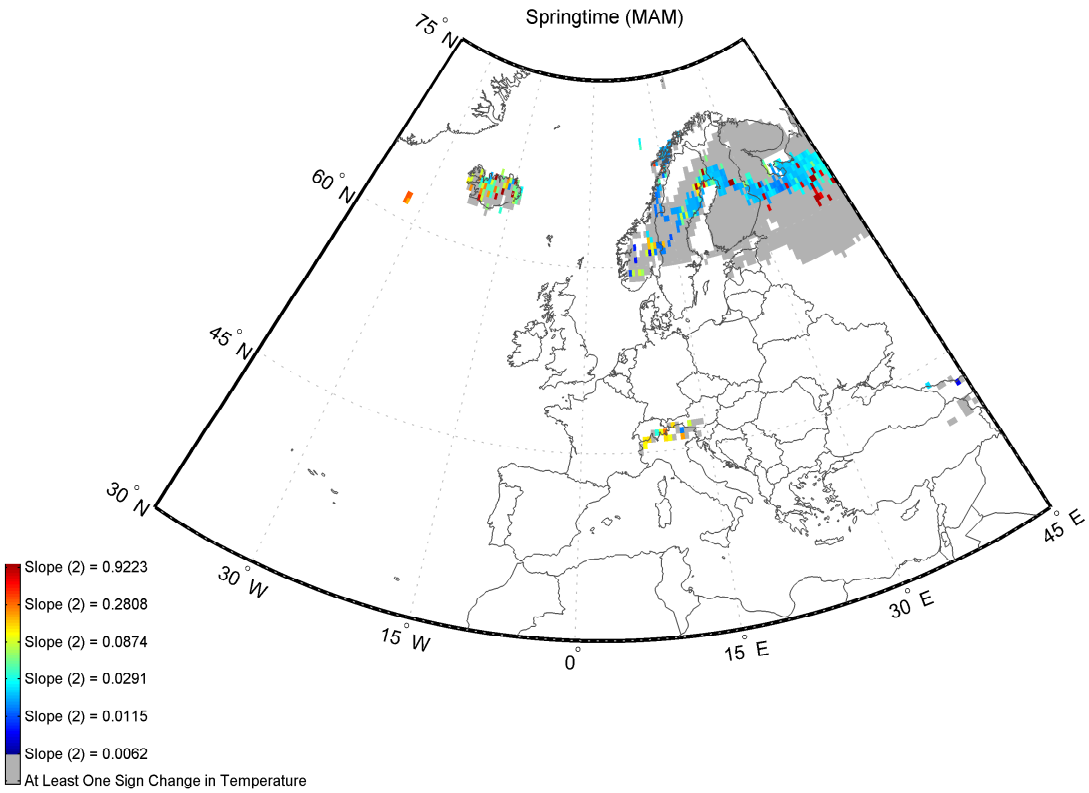


**Figure 5.138:** The same as Figure 5.136: zoomed in view of Europe

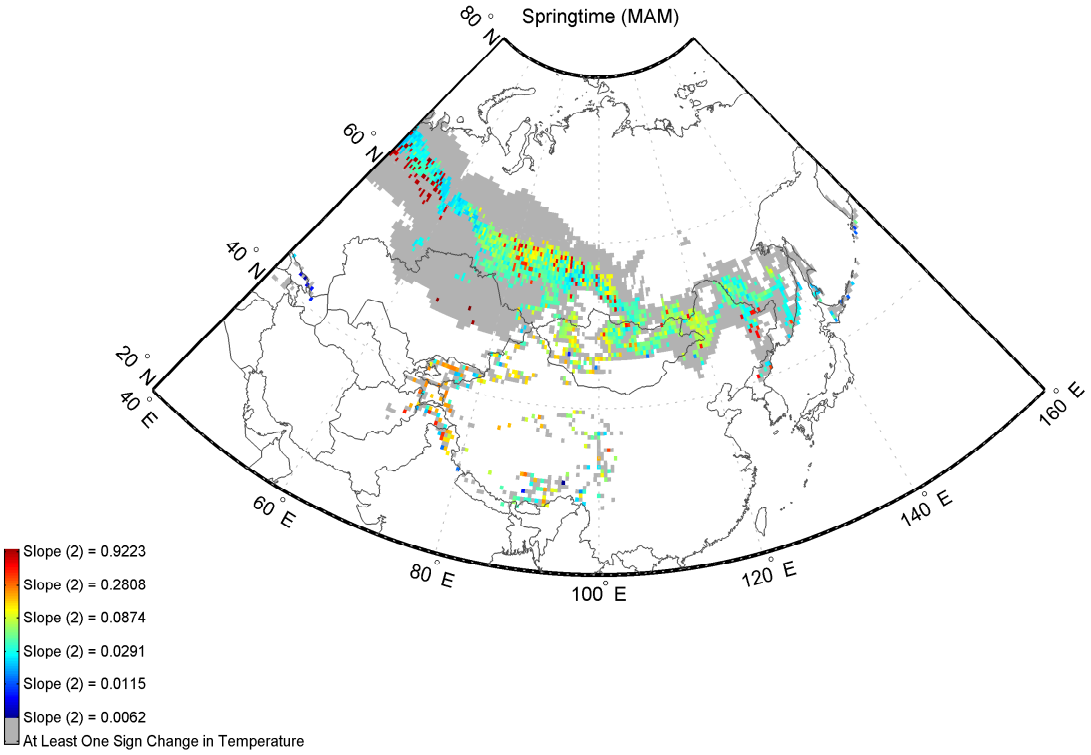


**Figure 5.139:** The same as Figure 5.136: zoomed in view of Asia

#### 5.5.3.3.5 H from $y_w$ to $y_0$

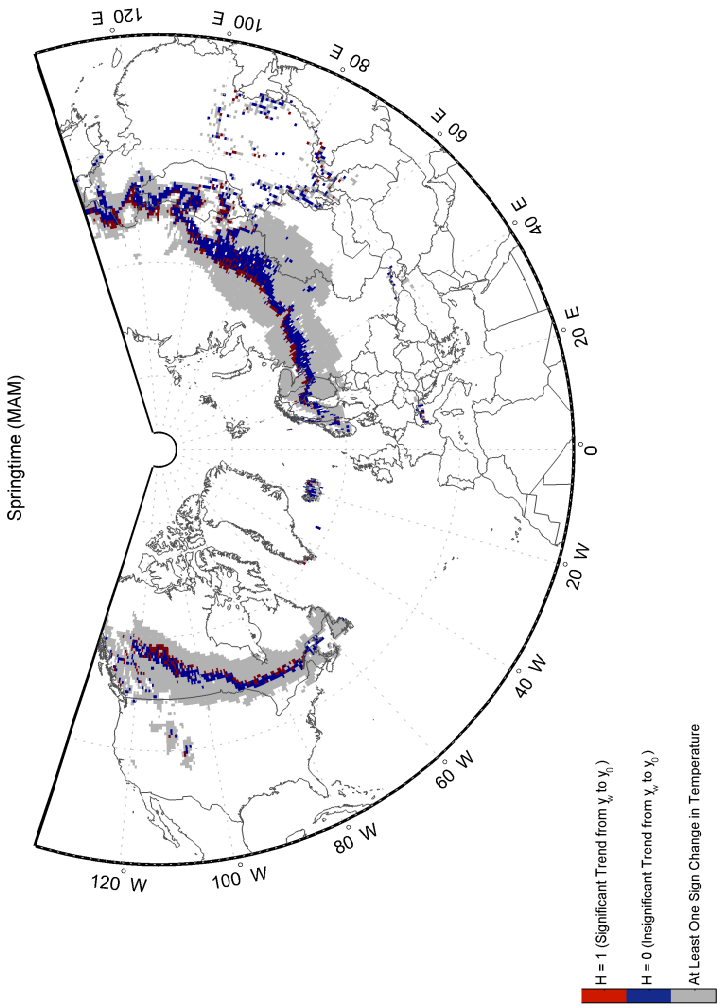


**Figure 5.140:** The map depicts the spatial distribution of H from $y_w$ to $y_0$ in the Northern Hemisphere during **MAM**. The results are obtained using **MARS**, and the input parameters are as indicated in Section 5.5.1.

#### 5.5.3.3.6 H of $S_{interest}$

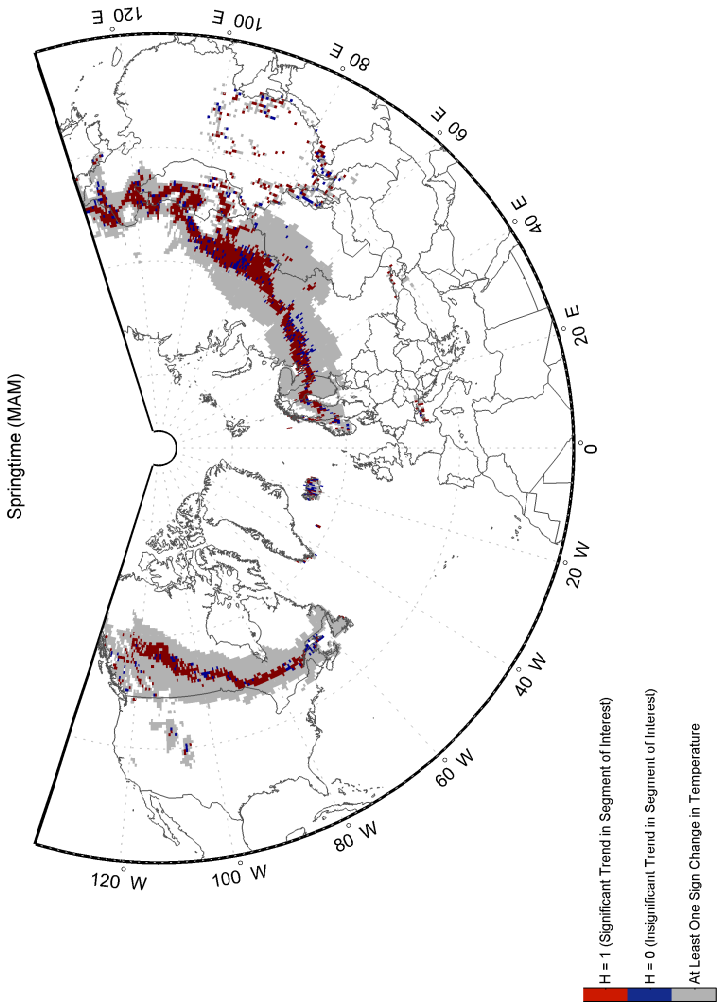


**Figure 5.141:** The map depicts the spatial distribution of H of $S_{interest}$ in the Northern Hemisphere during **MAM**. The results are obtained using **MARS**, and the input parameters are as indicated in Section 5.5.1.

#### 5.5.3.3.7 H of $Sw_{total}$

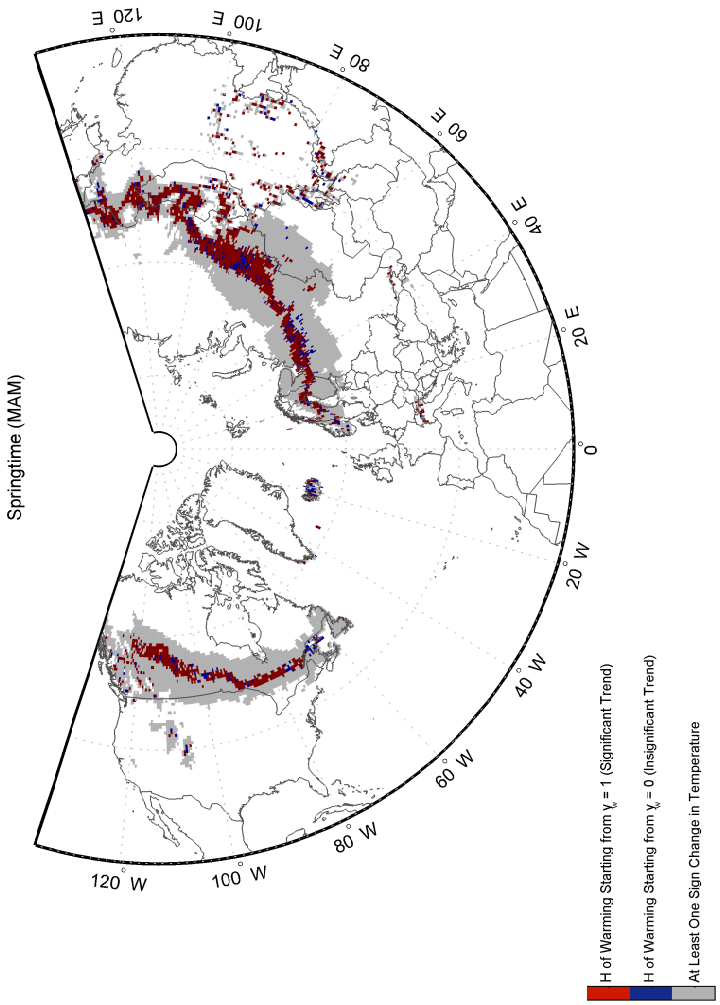


**Figure 5.142:** The map depicts the spatial distribution of H of $Sw_{total}$ in the Northern Hemisphere during **MAM**. The results are obtained using **MARS**, and the input parameters are as indicated in Section 5.5.1.

## 5.6 R Method

The R method is the last technique applied in this research to analyse the temperature data. As described in Section 3.2, it is a technique that detects the significant shifts in the mean level of temperature fluctuations; hence, all the segments are polynomials of degree zero (i.e., lines of zero slope). Due to this reason, the definitions of the variables introduced in Sections 4.4 and 5.2 are modified. These definitions are presented in Sections 5.6.1 and 5.6.2. Similar to the other techniques, the values assigned to input arguments are provided (Section 5.6.3) followed by the results (Section 5.6.4).

### 5.6.1 Definitions of the Terms Used in the R Method

1. **Year of Positive 0°C Crossing**: 'Year of Positive 0°C Crossing' is defined as the time when a negative mean level modelling the original data turns positive. Before determining the positive 0°C crossing of interest ($y_0$), there are several other terms that should be defined:

2. **Duration:** 'Duration' is defined as the sum of the durations of the two mean levels before and after the time of positive 0°C crossing (Figure 5.143).

3. **Total Duration** 'Total Duration' is the time that elapses from the beginning of the first negative mean level before the year of 0°C crossing to the beginning of the first negative mean level after the year of 0°C crossing. If no negative mean level follows the positive 0°C crossing, 'Total Duration' ends in the final year of the time series (Figure 5.143).

4. **Accumulation:** 'Accumulation' is the difference between the mean levels before and after the year of 0°C crossing (Figure 5.143).

5. **Total Accumulation:** 'Total Accumulation' is determined as the difference between the last positive mean level in the series of consecutive positive means after the year of 0°C crossing and the first negative mean level before the year of 0°C crossing (Figure 5.143).

6. **Slope (1):** 'Slope (1)' is obtained by dividing 'Accumulation' by 'Duration'.

7. **Slope (2):** 'Slope (2)' is evaluated by dividing 'Total Accumulation' by 'Total Duration'.

**Note:** Throughout Section 5.6, '(1)' or '(2)' following any variable implies that the variable is evaluated over the period defined as 'Duration' or 'Total Duration', respectively.

### 5.6.2 $y_0$ Determination Rules

1. If there is only one positive 0°C crossing, $y_0$ is defined as the time of this 0°C crossing (Figure A.18).

2. If there is more than one positive 0°C crossing, the 0°C crossing with the greatest 'Slope (1)' is selected as $y_0$ (Figure A.19). It should be noted that Rule 2 applies to a small subset of the final database (JFM: 20/1324, MAM: 38/1866).

**Notes:**

- Time series are modelled by lines of zero slope. Each segment represents the mean level during the length of the corresponding constant line, and all of these segments are discontinuous at the boundaries. Due to the characteristics of this technique, the definition of $y_w$ as the starting year of the time period termed as 'Duration' results in $y_w = 1901$ for most of the locations in the final database. Therefore, from the hydrological point of view, the concept of $y_w$ as indicated above is not acceptable, and $y_w$ is omitted from the list of variables to be determined.

- $S_{interest}$ and $S_{W_{total}}$ are the sections that determine 'Duration' and 'Total Duration', respectively, and include $y_0$ (Figures A.18 and A.19).

### 5.6.3 Input Parameters

The R method is thoroughly explained in Section 3.2. In this research, the latest version of the code written in Visual Basic® for Applications (VBA) is used (Rodionov, 2007). As indicated in Section 3.2, there are several parameters that should be set by the analyst.

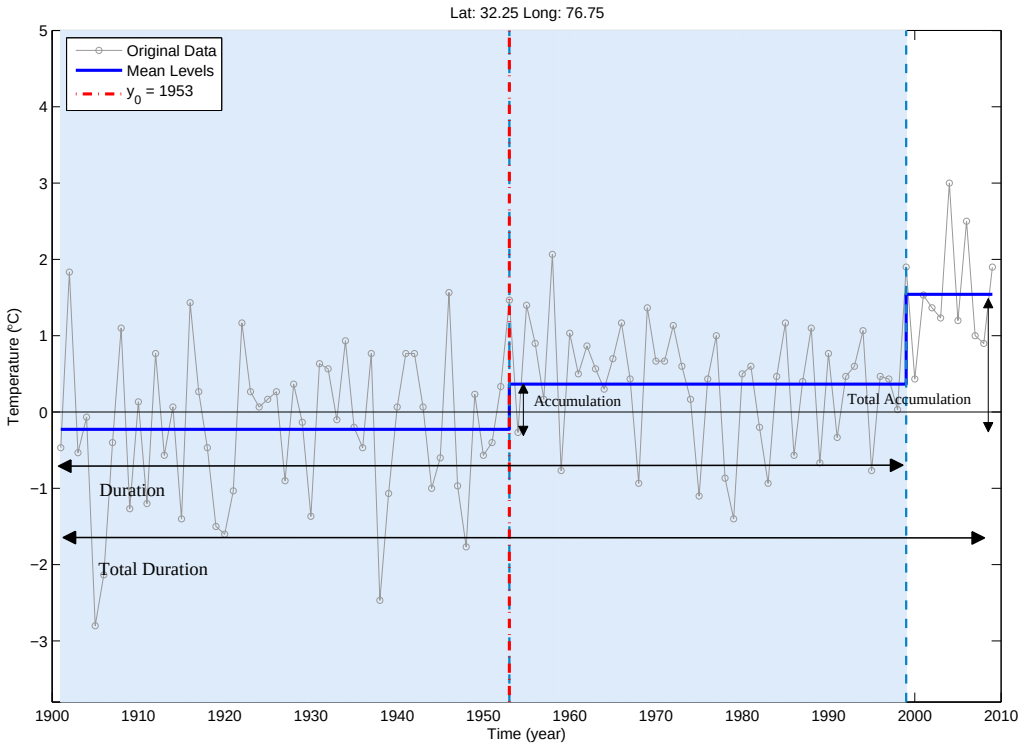


**Figure 5.143:** The above **JFM** time series is approximated using the **R method**. The boundaries are the dashed blue lines, and the time series is modelled by three segments with disjoint boundaries. The plot graphically depicts the terms defined in Section 5.6.1.

Except the Huber's Weight Parameter (explained below), the detailed description of all the variables can be found in Section 3.2. This research attributes the following values to the input parameters:

- **Cut-Off length**
  Based on the results of some experimentations with the cut-off length ($l$), this parameter is set to be 20.
- **Subsample size**: The subsample size ($m$) is set to be 7 since $m \leq \dfrac{l+1}{3}$.

- **Bias correction method**
  The IP4 method is selected. Since $m = 7$, the MPK method could be used as well. However, with the value of $m$ larger than 10, IP4 leads to a more precise estimation of the lag-1 autoregressive coefficient (Section 3.2).

- **Approach**
  Approach 2 (pre-whitening) is applied in this research to have a process that is robust against the existence of trends and to avoid detecting false regime shifts.

- **Huber's weight parameter**
  In the calculation of mean levels, the algorithm described in Section 3.2 assigns the equal weight of 1 to all data points. To eliminate the influence of outliers on the calculation of the mean levels of climate regimes, smaller weights should be assigned to outliers. Huber's weight function (Huber, 2005) is used in the VBA code to handle outliers:

$$\text{weight} = \min\left(1, \frac{\text{parameter}}{|\text{anomaly}|}\right) \tag{5.4}$$

  where anomaly is determined as the difference between each value and the expected mean level of the corresponding new regime that is normalized by $\sigma_l$ (Section 3.2). The parameter is set to be 2 in this study.

### 5.6.4 Results of the R Method

As with all the other techniques used in this research, the numbers of locations with specific characteristics are presented in Table 5.4 followed by histograms that provide better understanding of the distribution of the results (JFM: Figures 5.144 to 5.148, MAM: Figures 5.149 to 5.153). Finally, maps depict the spatial distribution of the results (JFM: Figures 5.154 to 5.167, MAM: Figures 5.168 to 5.181). The results are thoroughly explained and discussed in Sections 5.8.3 (tables and histograms) and 5.8.4 (maps).

**Table 5.4:** Based on the analysis of the JFM and MAM time series using **the R method**, the table provides some information on the numbers of grid cells with specific characteristics described in the left column. The variables are as indicated in Section 5.6.1. The reader is referred to Section 5.3 for more details on the cases presented below.

| **Characteristic** | **Number** | |
|---|---|---|
| | **JFM** | **MAM** |
| Selected for study (following Rule 1 of *transition area*, described in Section 4.3) | 6206/46224 | 9842/46224 |
| Last segment (mean level) is positive (based on Rule 2 of *transition area*, described in Section 4.3) | 3594/6206 | 5880/9842 |
| Final database: selected for the $y_0$ analysis (based on Rules 1 and 2 of *transition area*) | **1324/3594** | **1866/5880** |
| Duration or Total Duration less than 3 years, MK test N/A | 0/1324 | 0/1866 |
| $S_{W_{total}}$ is the same as $S_{interest}$ | 1027/1324 | 1303/1866 |

#### 5.6.4.1 Histograms

##### 5.6.4.1.1 JFM

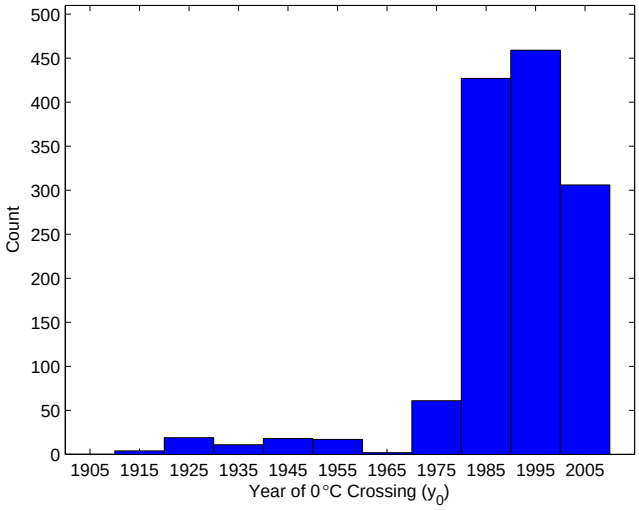


**Figure 5.144:** The histogram exhibits the temporal distribution of $y_0$ during **JFM**. The result is obtained using the **R method**, and the input parameters are as indicated in Section 5.6.3.

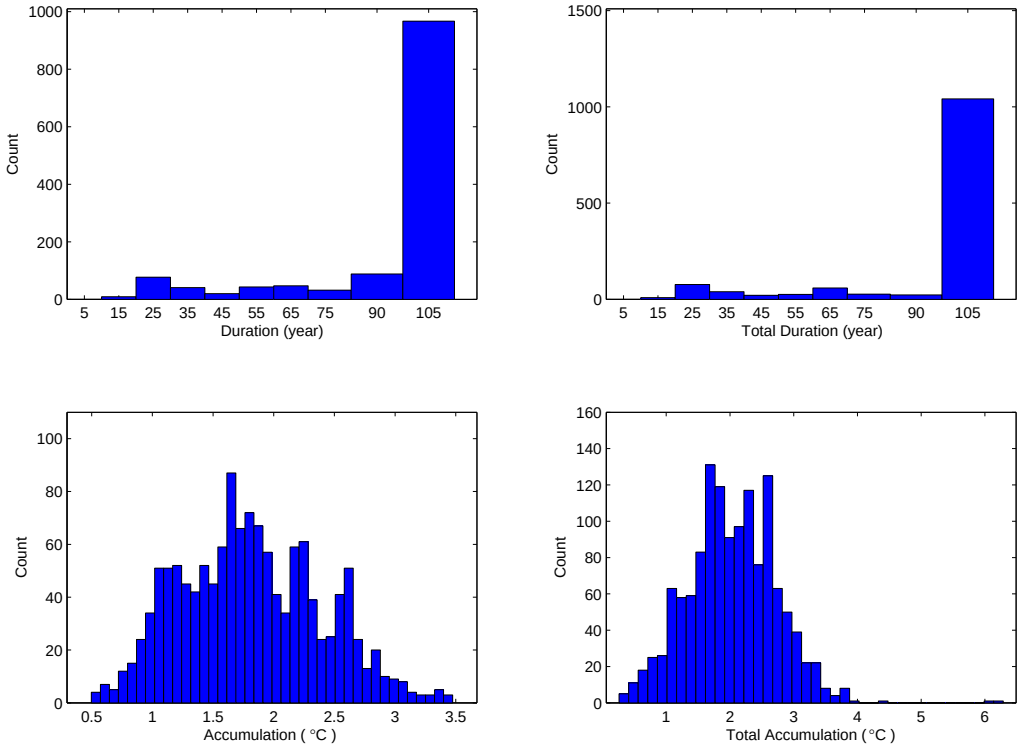


**Figure 5.145:** The histograms exhibit the distributions of Duration, Total Duration, Accumulation, and Total Accumulation for **JFM**. The results are obtained using the **R method**, and the input parameters are as indicated in Section 5.6.3. The reader is referred to Section 5.6.1 for details on the variables used above.

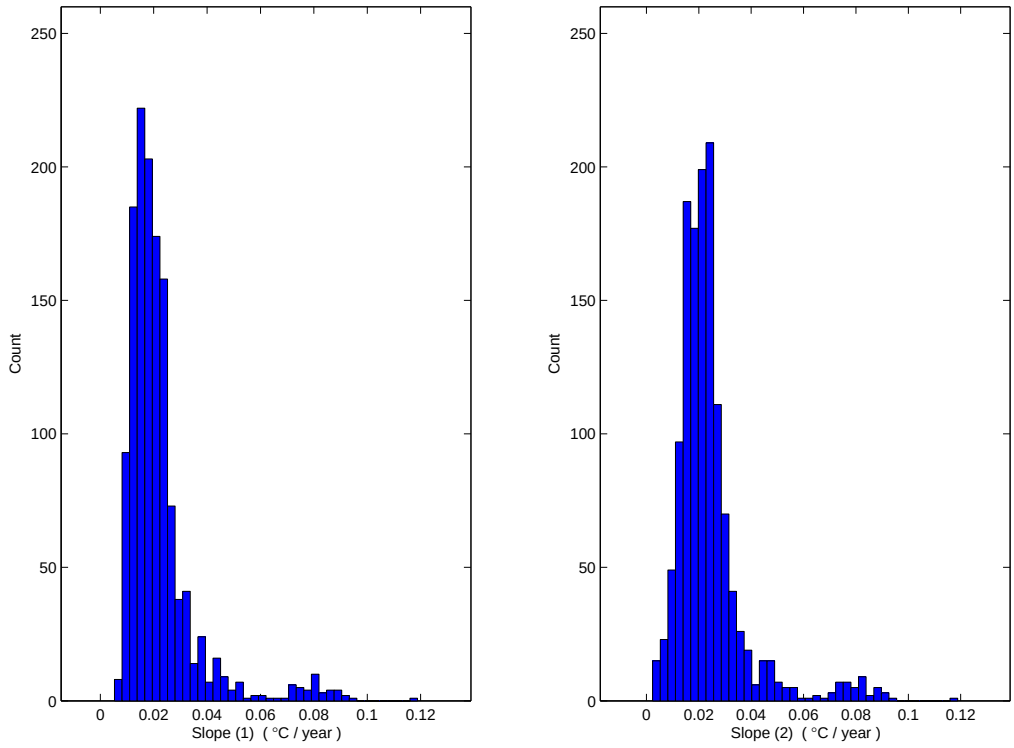


**Figure 5.146:** The histograms exhibit the distributions of Slope (1) and Slope (2) for **JFM**. The results are obtained using the **R method**, and the input parameters are as indicated in Section 5.6.3. The reader is referred to Section 5.6.1 for details on the variables used above.

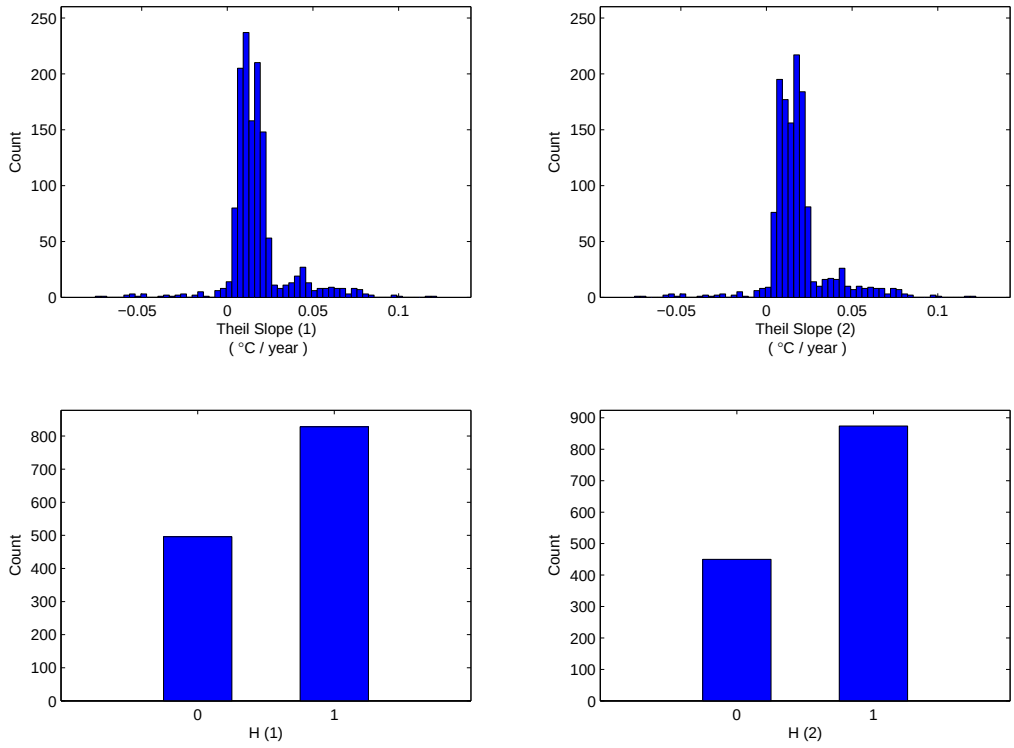


**Figure 5.147:** The histograms exhibit the distributions of Theil slope (1), Theil slope (2), H(1), and H (2) for **JFM**. The results are obtained using the **R method**, and the input parameters are as indicated in Section 5.6.3. The reader is referred to Section 5.6.1 for details on the variables used above.

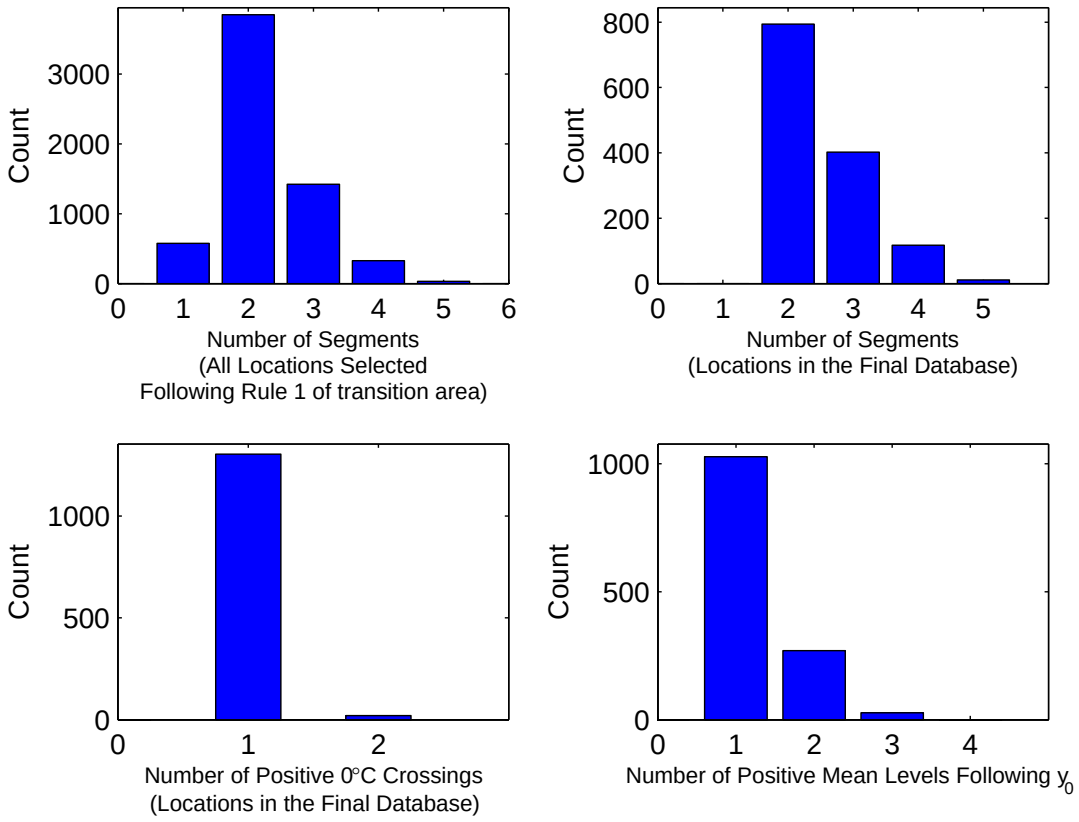


**Figure 5.148:** The histograms exhibit the **JFM** distributions of number of segments under different categories, positive 0°C crossings, and positive mean levels after $y_0$. The results are obtained using the **R method**, and the input parameters are as indicated in Section 5.6.3.

#### 5.6.4.1.2 MAM

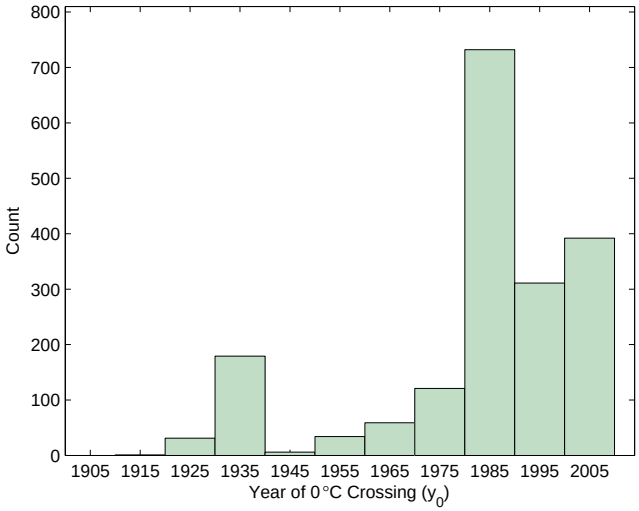


**Figure 5.149:** The histogram exhibits the temporal distribution of $y_0$ during **MAM**. The result is obtained using the **R method**, and the input parameters are as indicated in Section 5.6.3.

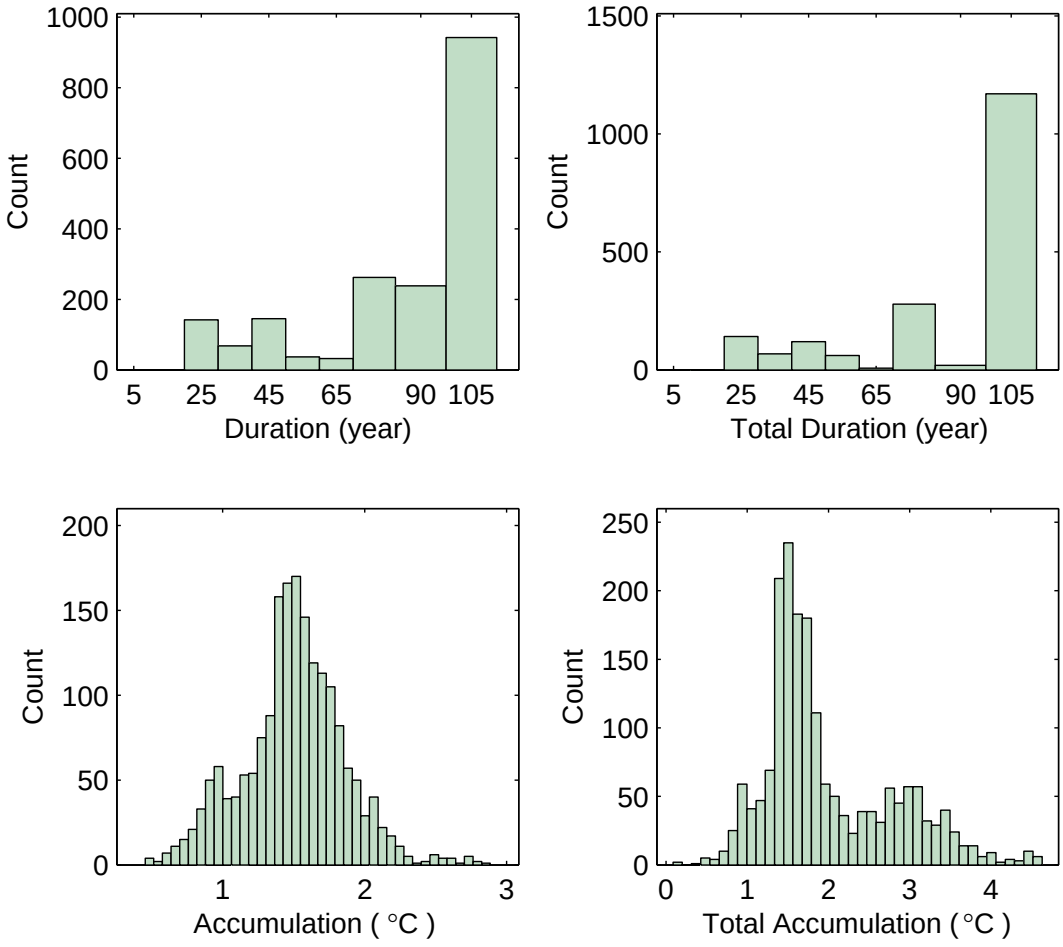


**Figure 5.150:** The histograms exhibit the distributions of Duration, Total Duration, Accumulation, and Total Accumulation for **MAM**. The results are obtained using the **R method**, and the input parameters are as indicated in Section 5.6.3. The reader is referred to Section 5.6.1 for details on the variables used above.

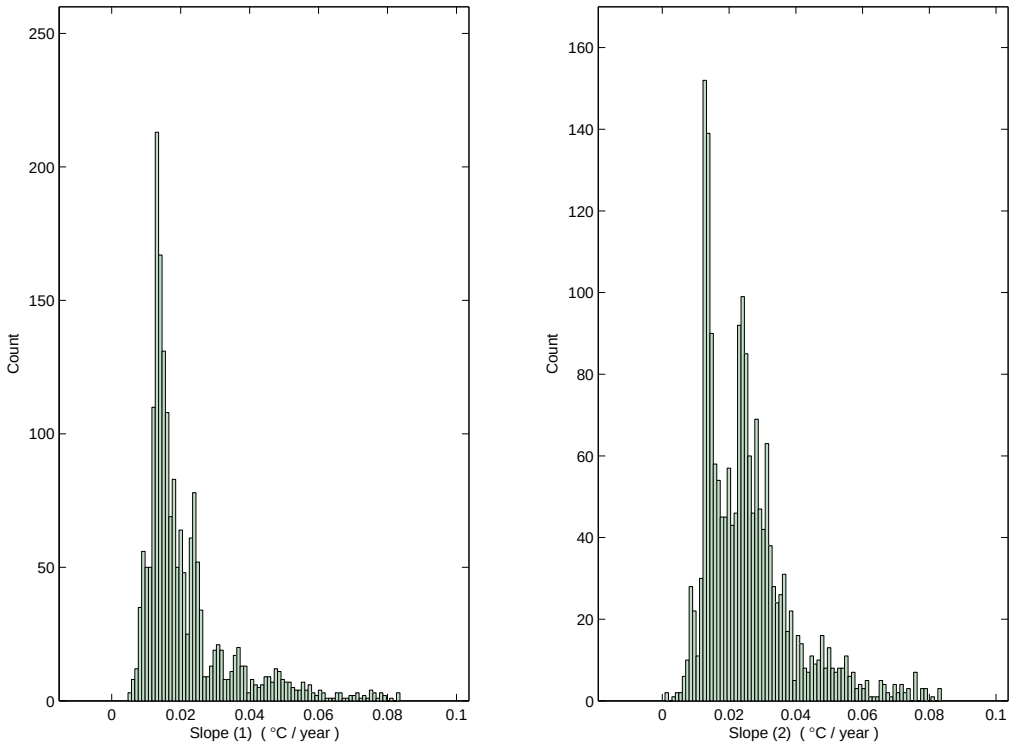


**Figure 5.151:** The histograms exhibit the distributions of Slope (1) and Slope (2) for **MAM**. The results are obtained using the **R method**, and the input parameters are as indicated in Section 5.6.3. The reader is referred to Section 5.6.1 for details on the variables used above.

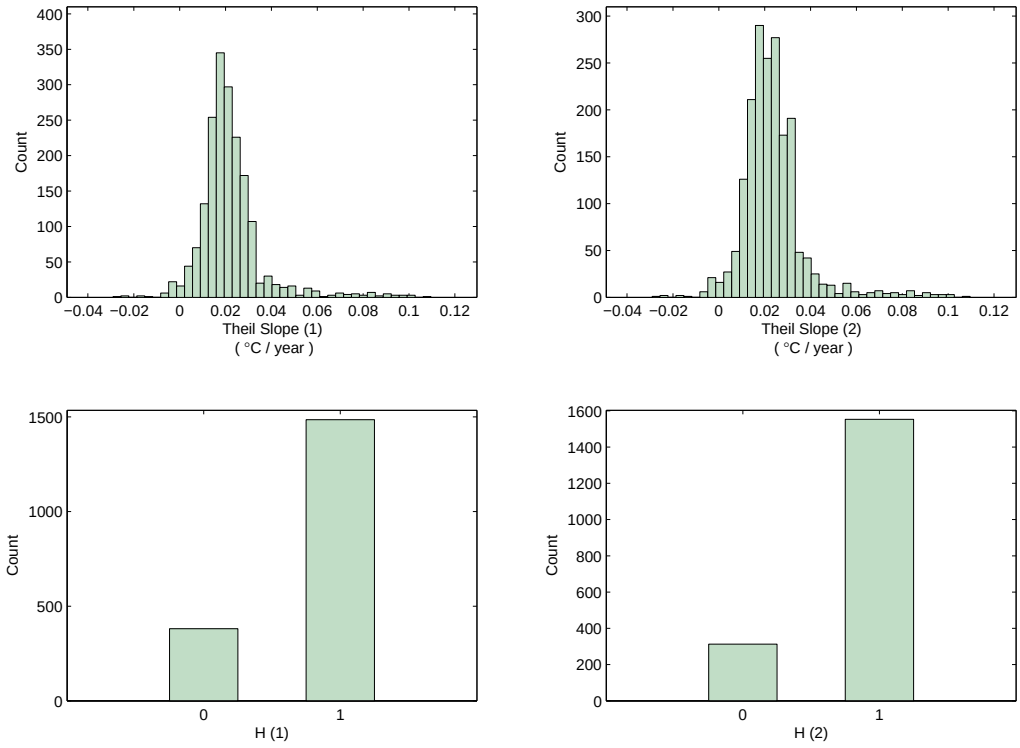


**Figure 5.152:** The histograms exhibit the distributions of Theil slope (1), Theil slope (2), H(1), and H (2) for **MAM**. The results are obtained using the **R method**, and the input parameters are as indicated in Section 5.6.3. The reader is referred to Section 5.6.1 for details on the variables used above.

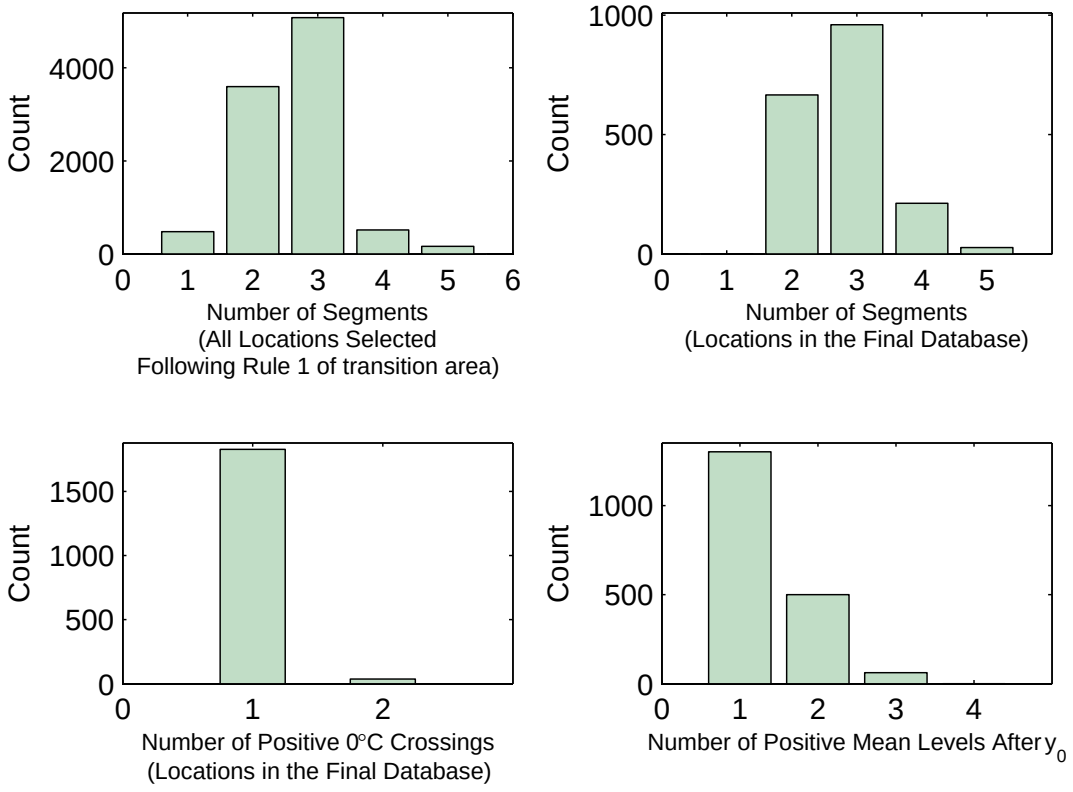


**Figure 5.153:** The histograms exhibit the **MAM** distributions of number of segments under different categories, positive 0°C crossings, and positive mean levels after $y_0$. The results are obtained using the **R method**, and the input parameters are as indicated in Section 5.6.3.

#### 5.6.4.2 Maps of the R Method for JFM

##### 5.6.4.2.1 $y_0$

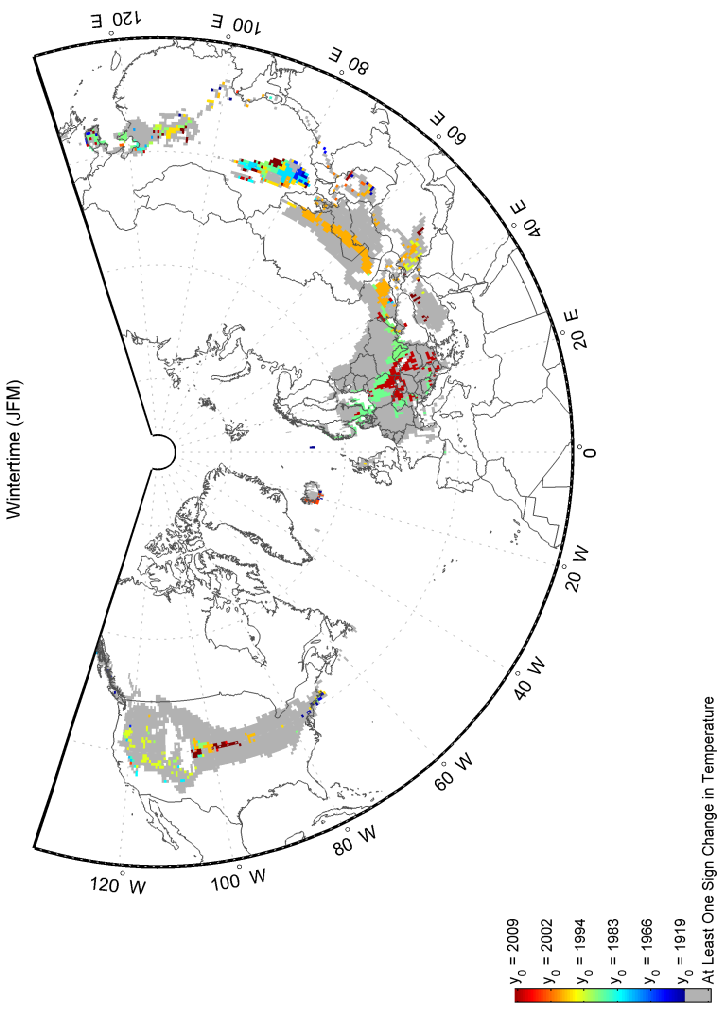


**Figure 5.154:** The map depicts the spatial distribution of $y_0$ in the Northern Hemisphere during **JFM**. The results are obtained using the **R method**, and the input parameters are as indicated in Section 5.6.3.

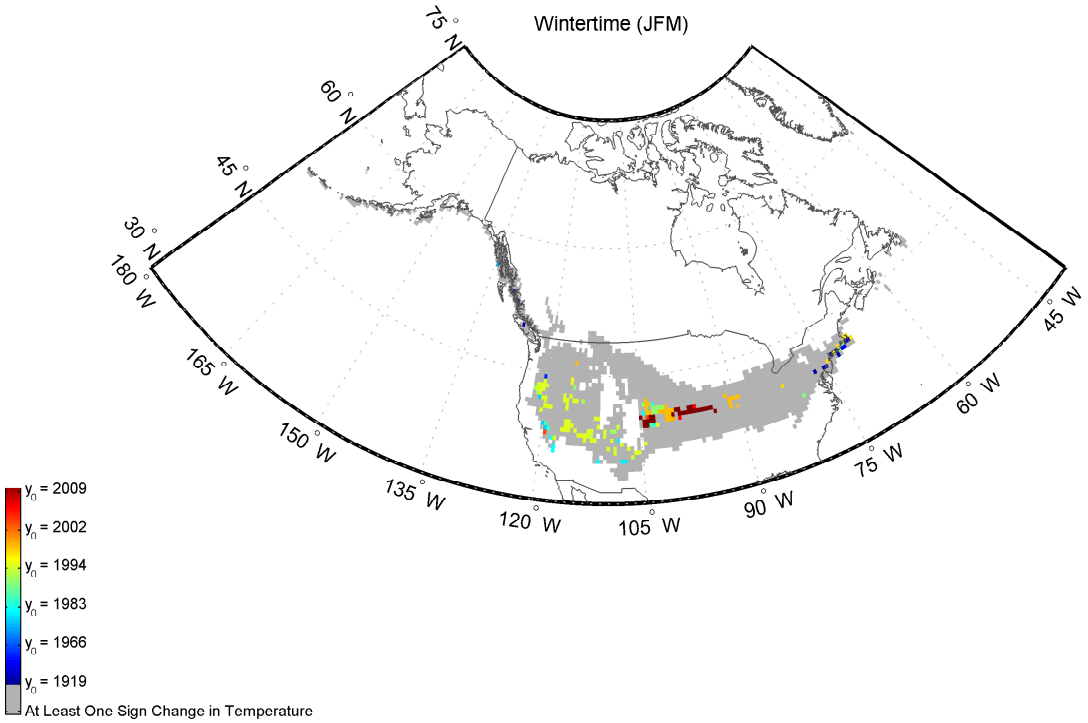


**Figure 5.155:** The same as Figure 5.154: zoomed in view of North America

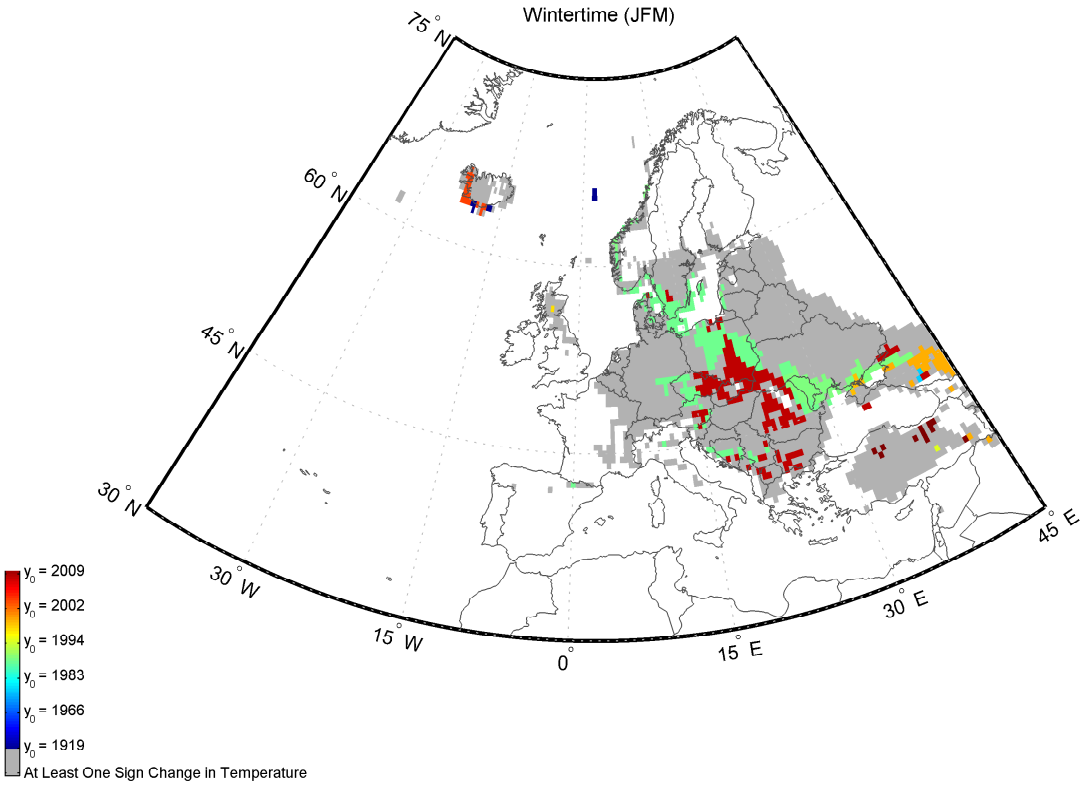


**Figure 5.156:** The same as Figure 5.154: zoomed in view of Europe

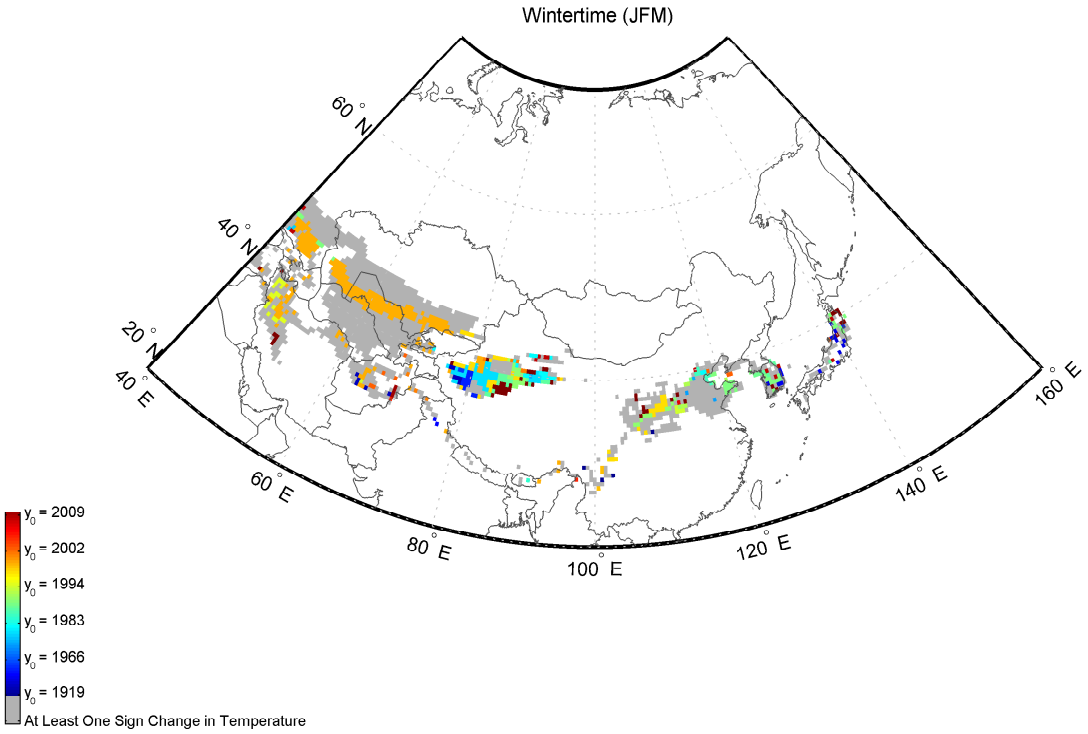


**Figure 5.157:** The same as Figure 5.154: zoomed in view of Asia

#### 5.6.4.2.2 Slope (1)

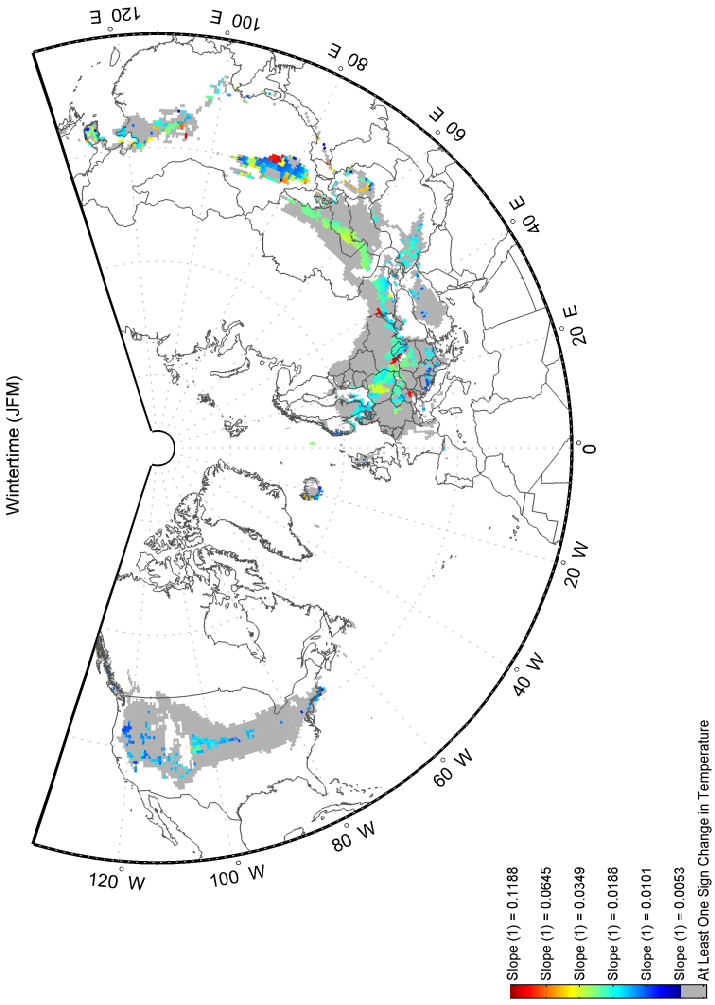


**Figure 5.158:** The map depicts the spatial distribution of Slope (1) in the Northern Hemisphere during **JFM**. The results are obtained using the **R method**, and the input parameters are as indicated in Section 5.6.3. The reader is referred to Section 5.6.1 for the definition of 'Slope (1)'.

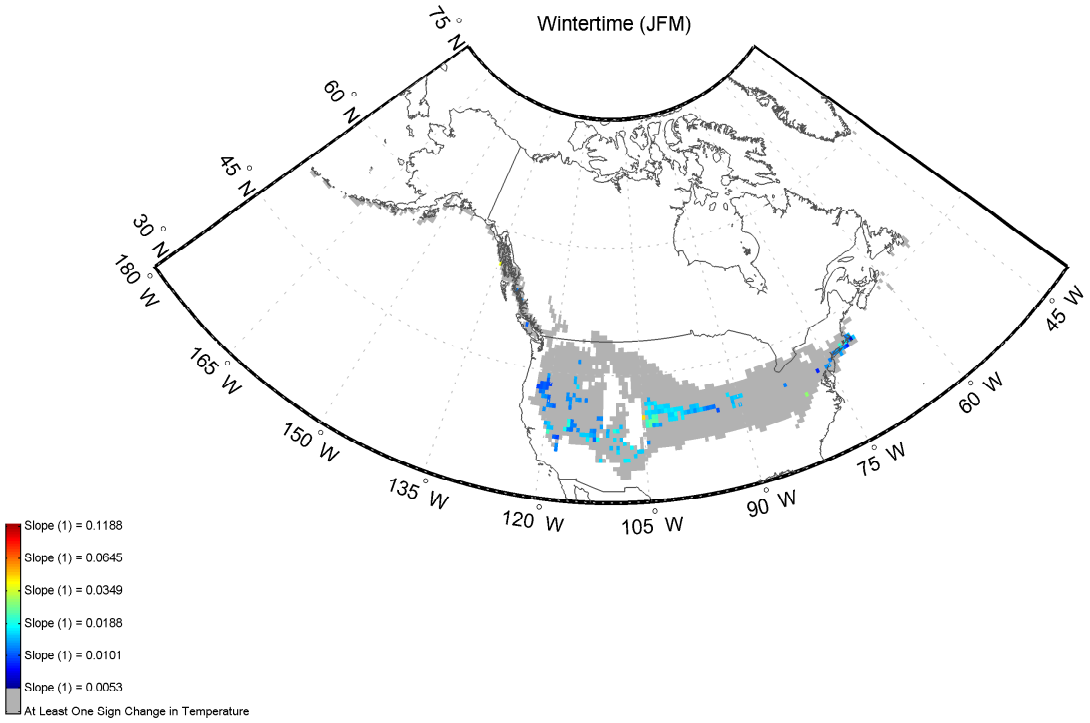


**Figure 5.159:** The same as Figure 5.158: zoomed in view of North America

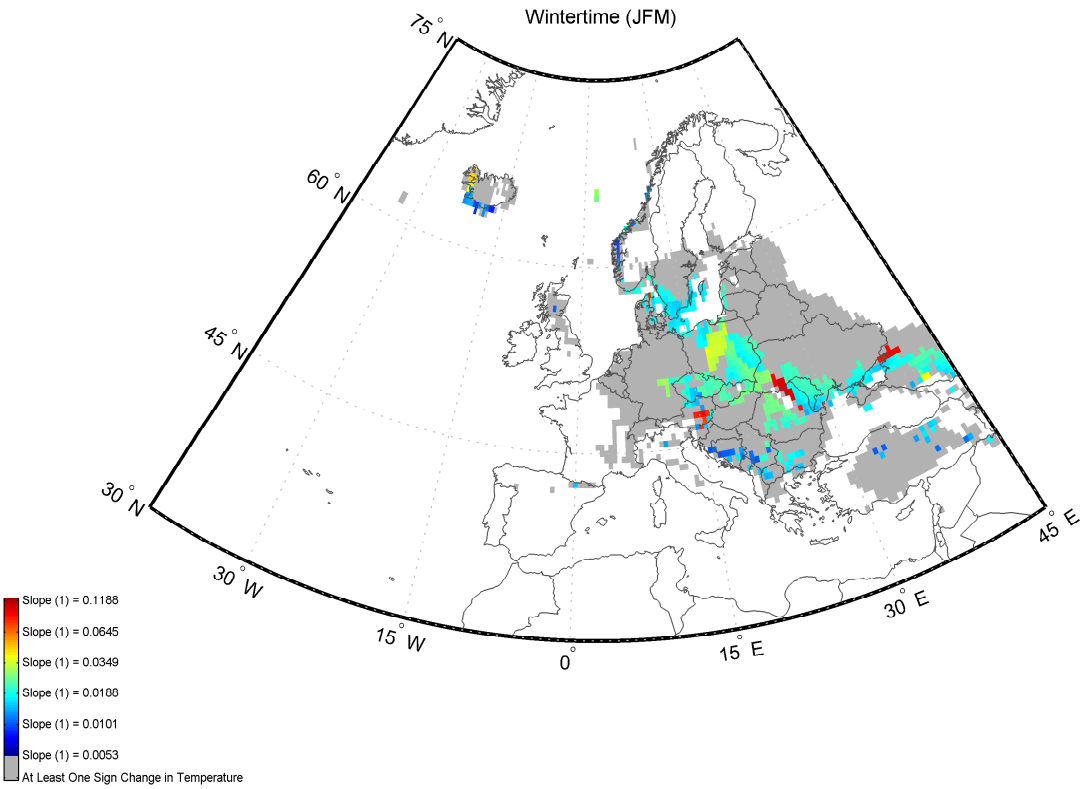


**Figure 5.160:** The same as Figure 5.158: zoomed in view of Europe

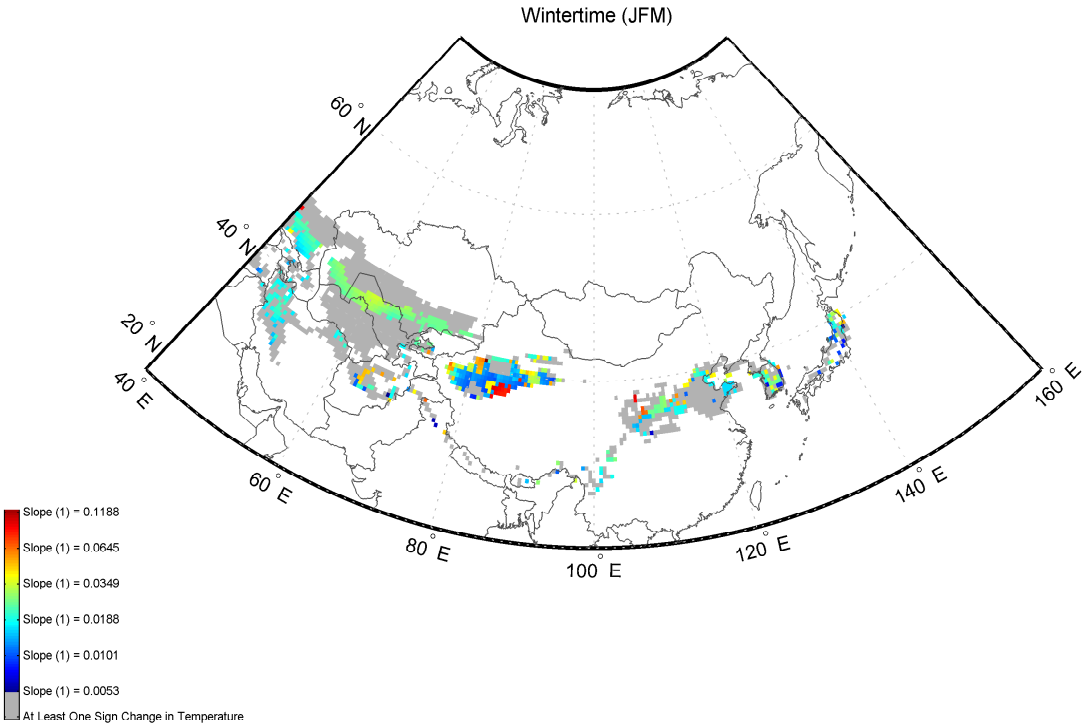


**Figure 5.161:** The same as Figure 5.158: zoomed in view of Asia

#### 5.6.4.2.3 Slope (2)

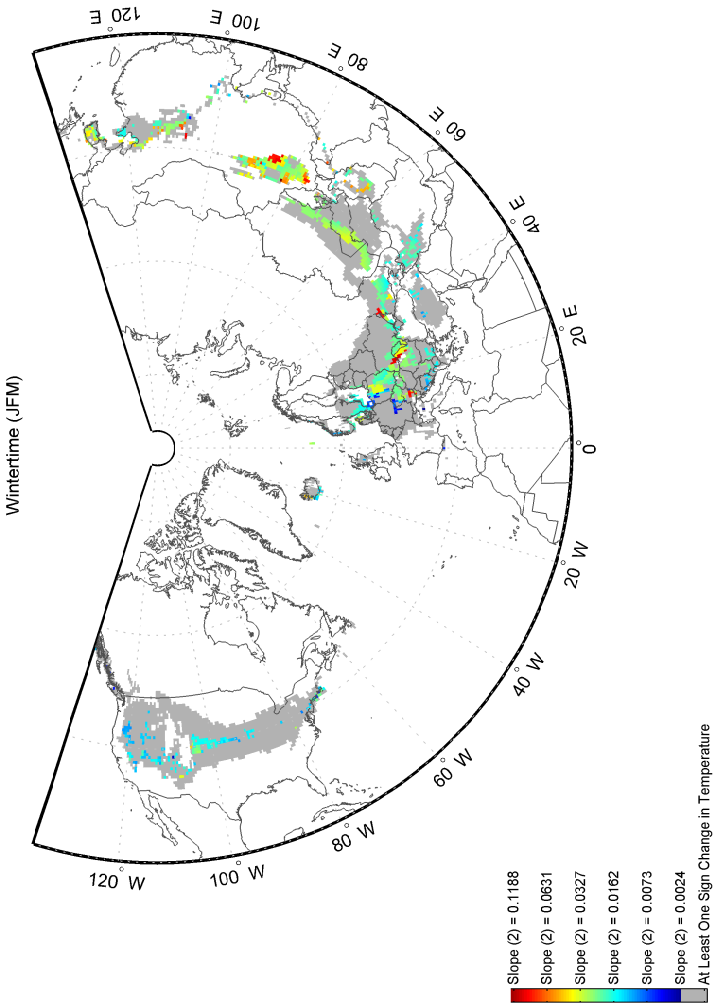


**Figure 5.162:** The map depicts the spatial distribution of Slope (2) in the Northern Hemisphere during **JFM**. The results are obtained using the **R method**, and the input parameters are as indicated in Section 5.6.3. The reader is referred to Section 5.6.1 for the definition of 'Slope (2)'.

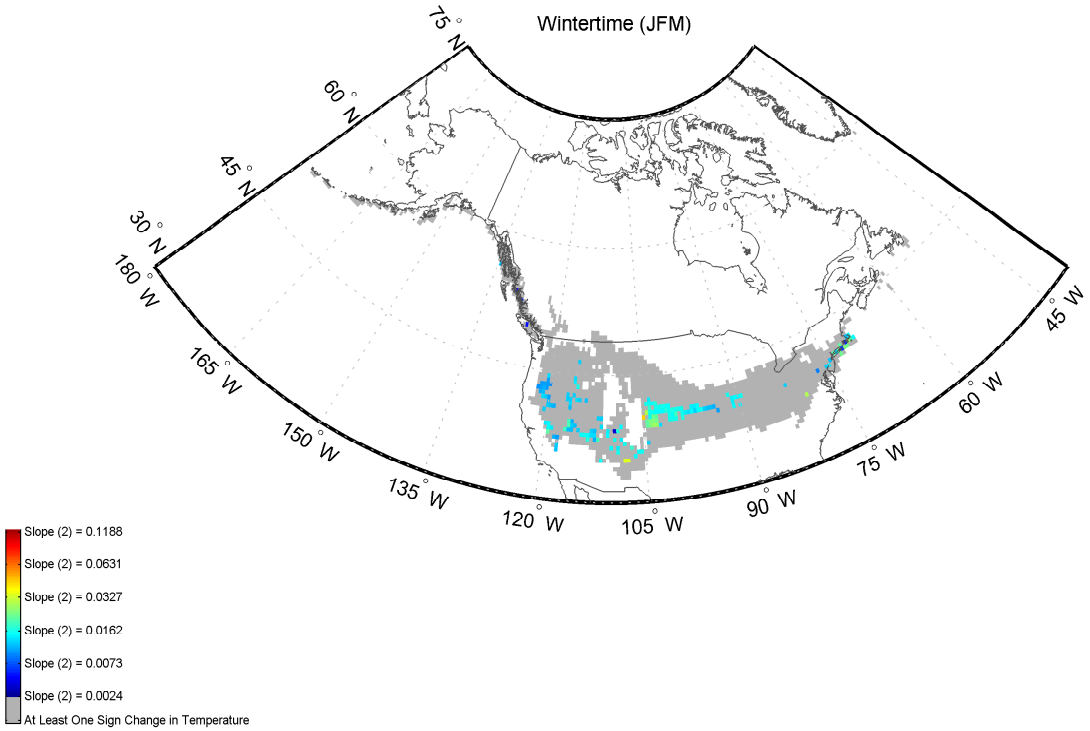


**Figure 5.163:** The same as Figure 5.162: zoomed in view of North America

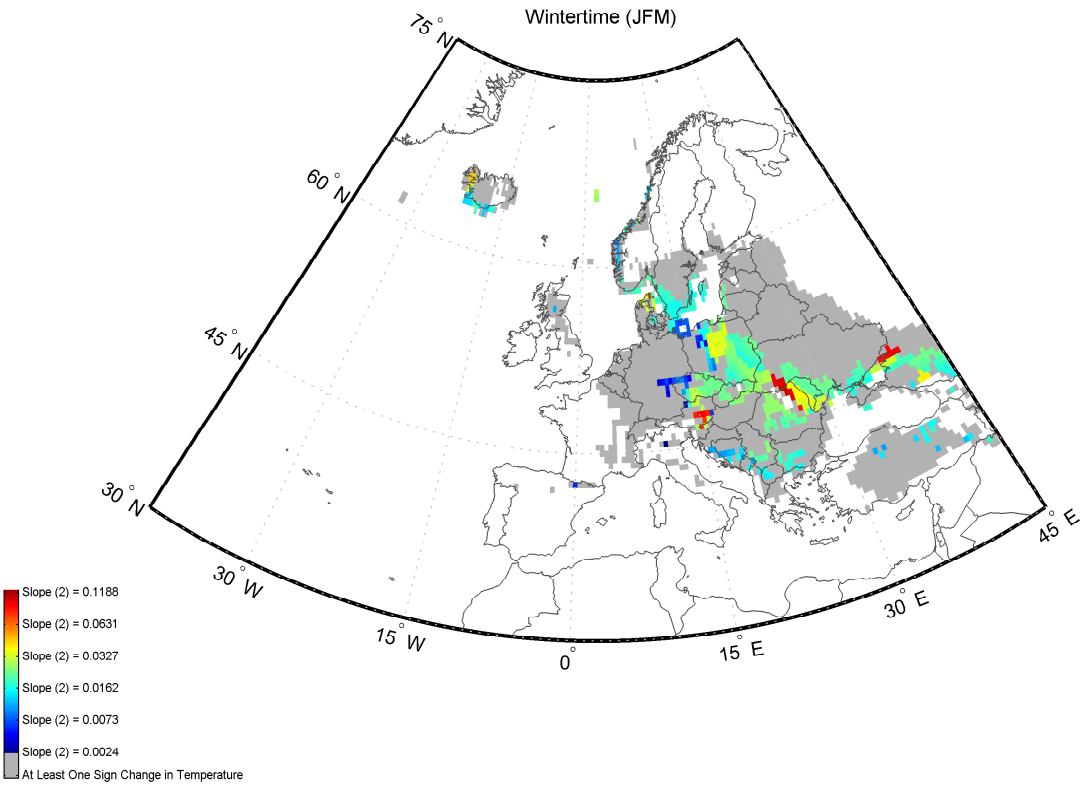


**Figure 5.164:** The same as Figure 5.162: zoomed in view of Europe

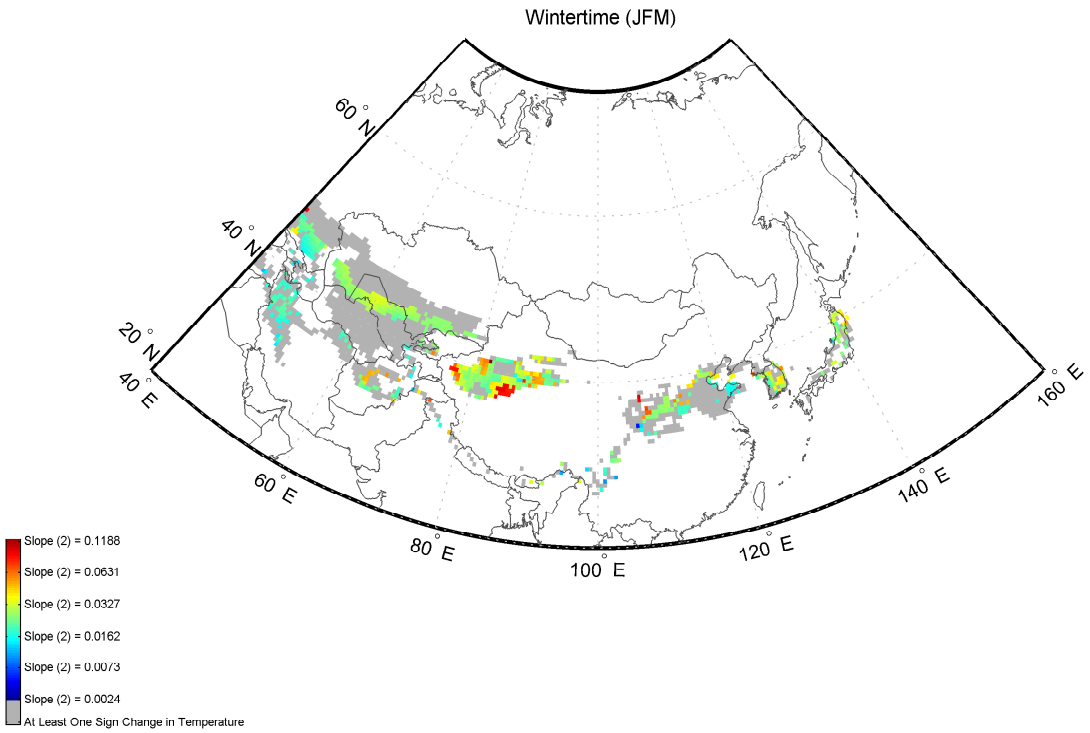


**Figure 5.165:** The same as Figure 5.162: zoomed in view of Asia

#### 5.6.4.2.4 H (1)

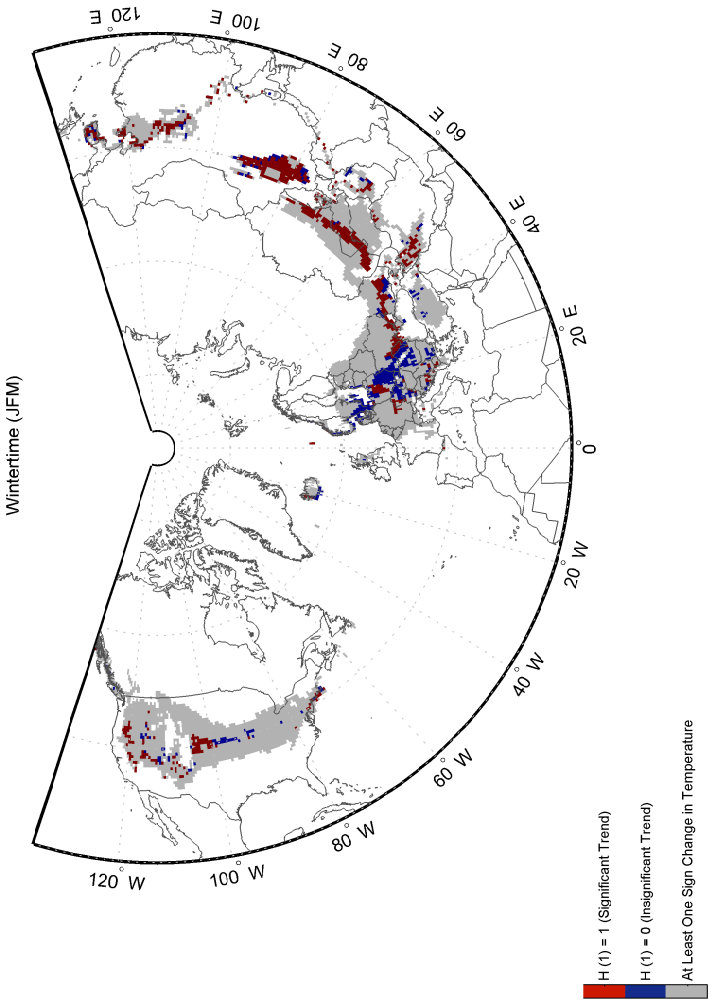


**Figure 5.166:** The map depicts the spatial distribution of H (1) in the Northern Hemisphere during **JFM**. The results are obtained using the **R method**, and the input parameters are as indicated in Section 5.6.3. The reader is referred to Section 5.6.1 for the definition of 'H (1)'.

#### 5.6.4.2.5 H (2)

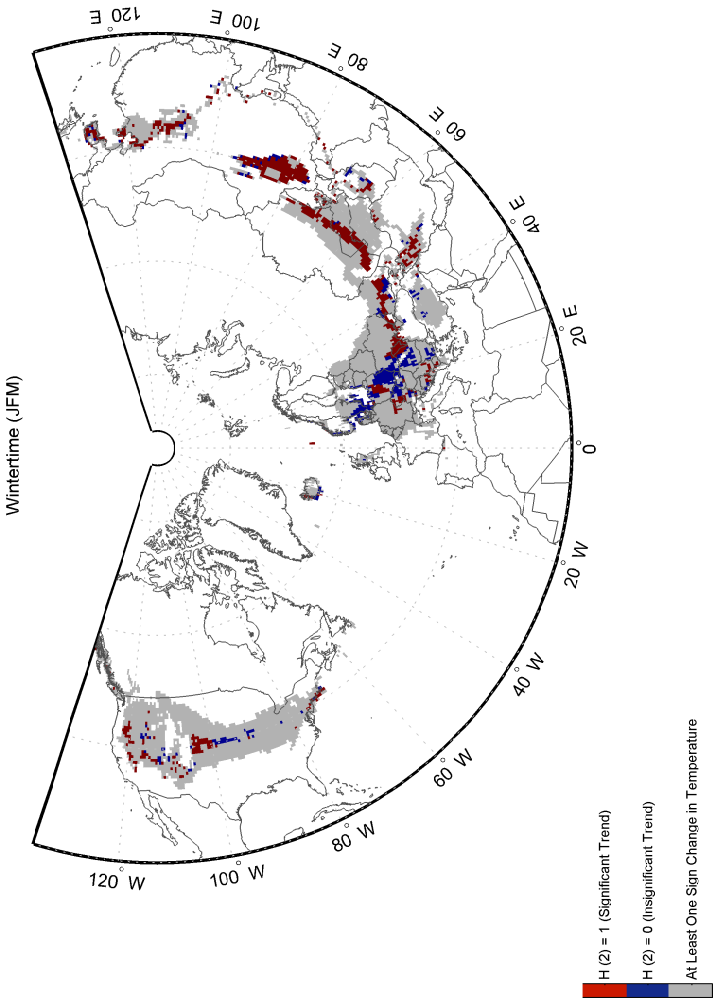


**Figure 5.167:** The map depicts the spatial distribution of H (2) in the Northern Hemisphere during **JFM**. The results are obtained using the **R method**, and the input parameters are as indicated in Section 5.6.3. The reader is referred to Section 5.6.1 for the definition of 'H (2)'.

#### 5.6.4.3 Maps of the R Method for MAM

##### 5.6.4.3.1 $y_0$

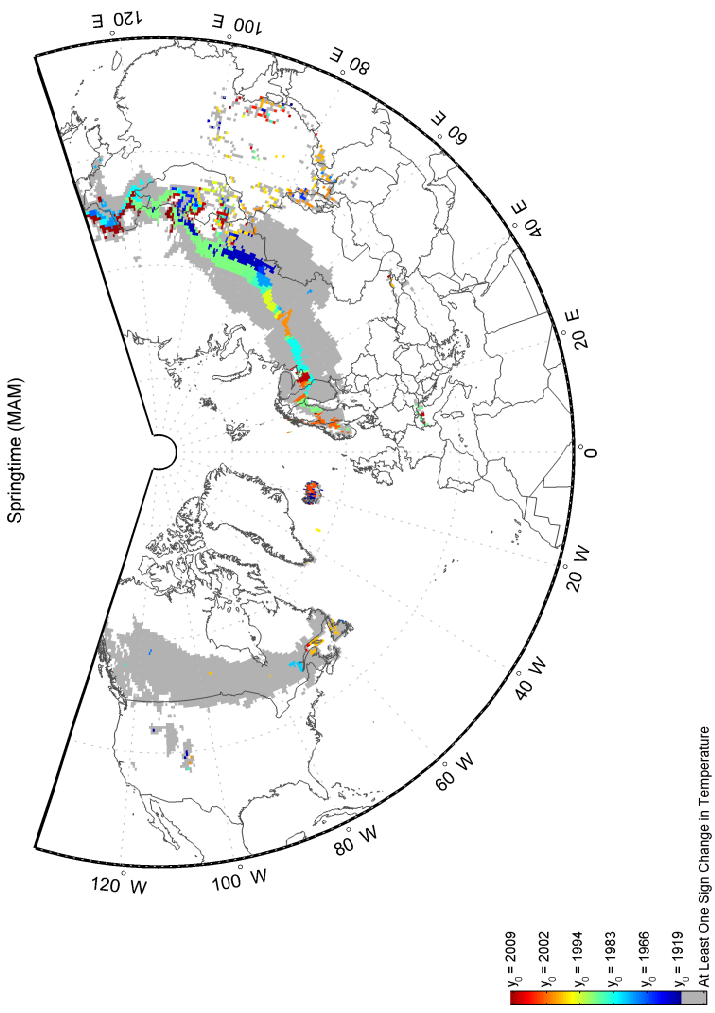


**Figure 5.168:** The map depicts the spatial distribution of $y_0$ in the Northern Hemisphere during **MAM**. The results are obtained using the **R method**, and the input parameters are as indicated in Section 5.6.3.

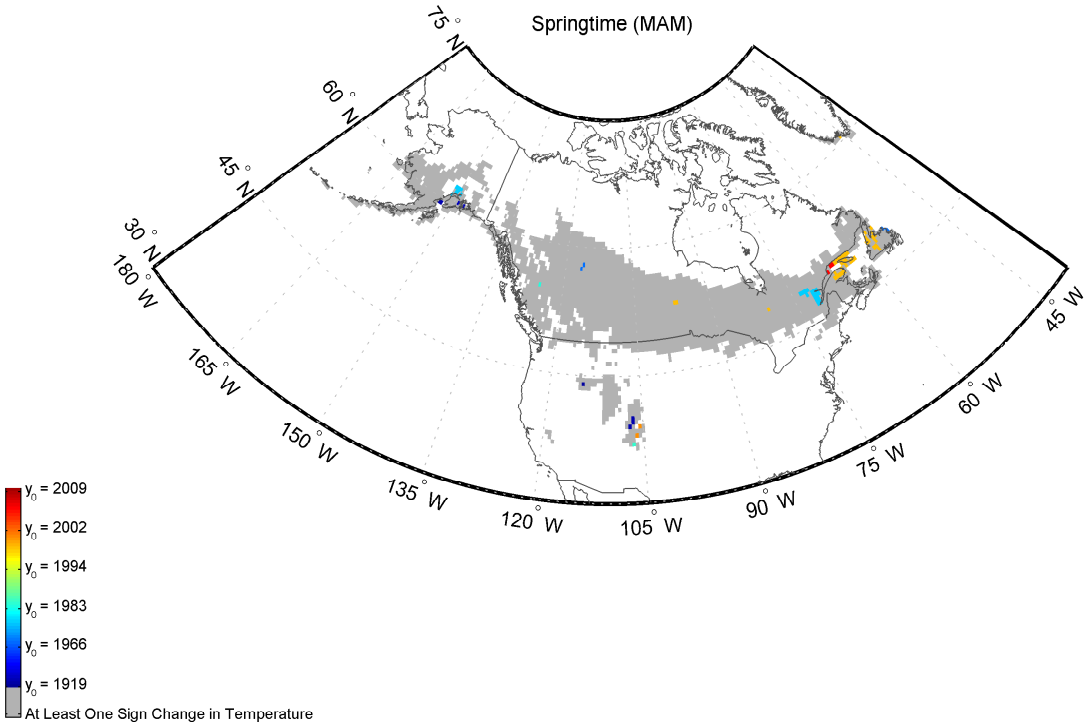


**Figure 5.169:** The same as Figure 5.168: zoomed in view of North America

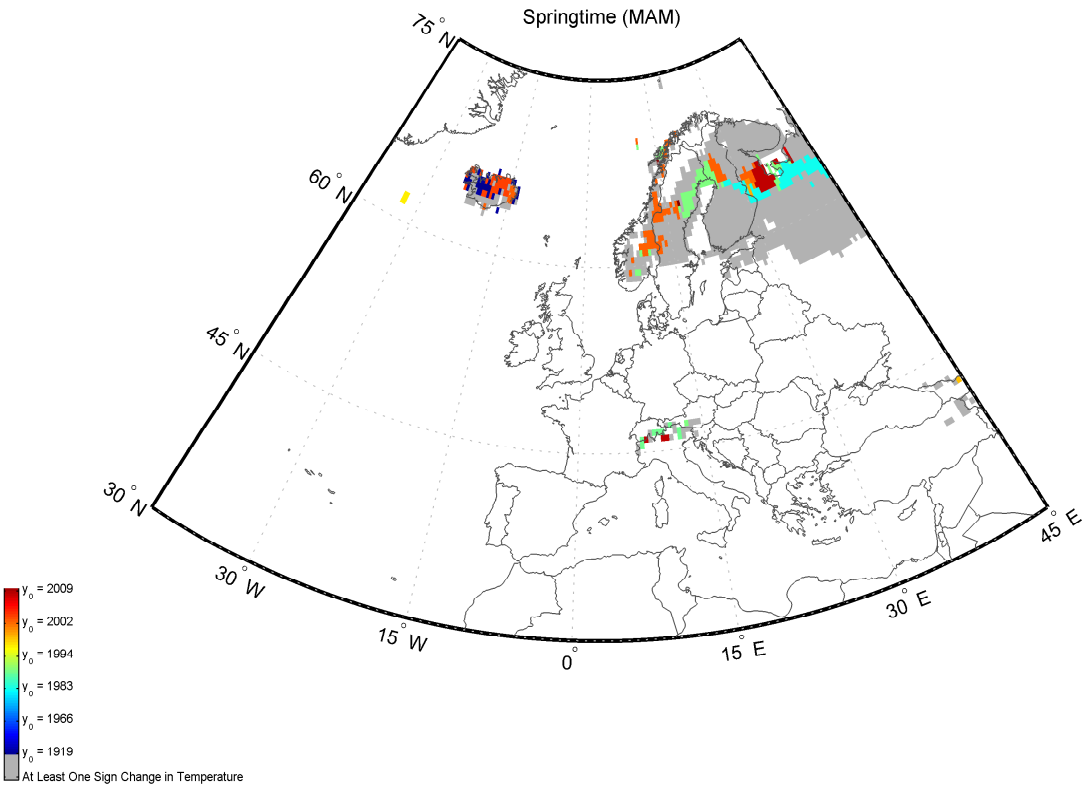


**Figure 5.170:** The same as Figure 5.168: zoomed in view of Europe

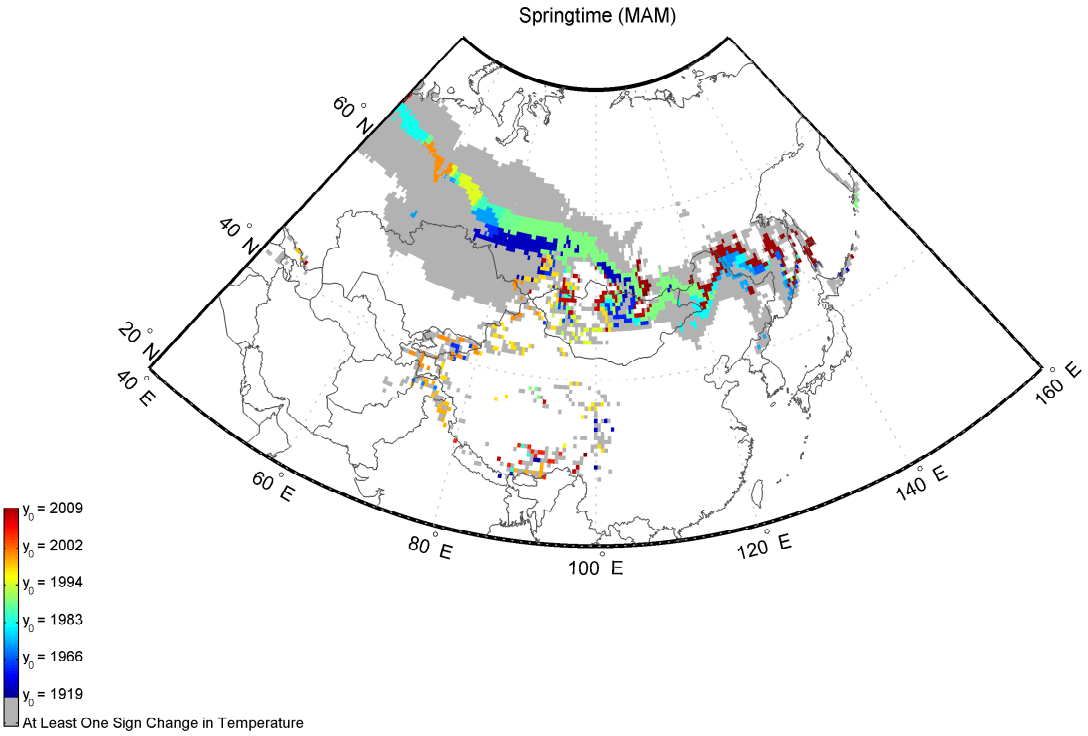


**Figure 5.171:** The same as Figure 5.168: zoomed in view of Asia

#### 5.6.4.3.2 Slope (1)

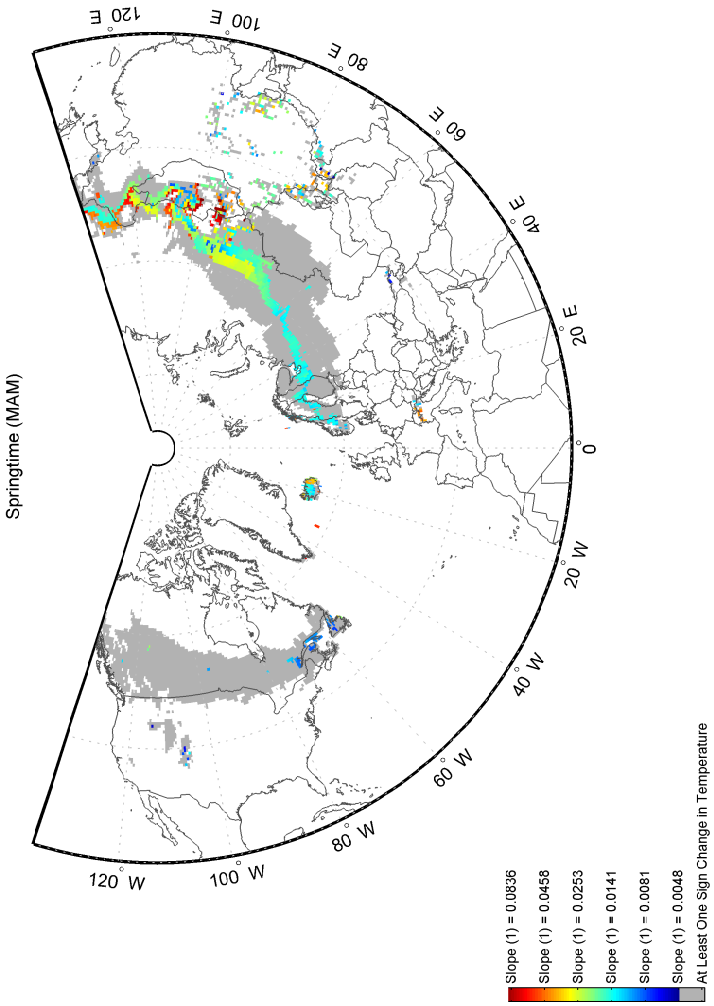


**Figure 5.172:** The map depicts the spatial distribution of Slope (1) in the Northern Hemisphere during **MAM**. The results are obtained using the **R method**, and the input parameters are as indicated in Section 5.6.3. The reader is referred to Section 5.6.1 for the definition of 'Slope (1)'.

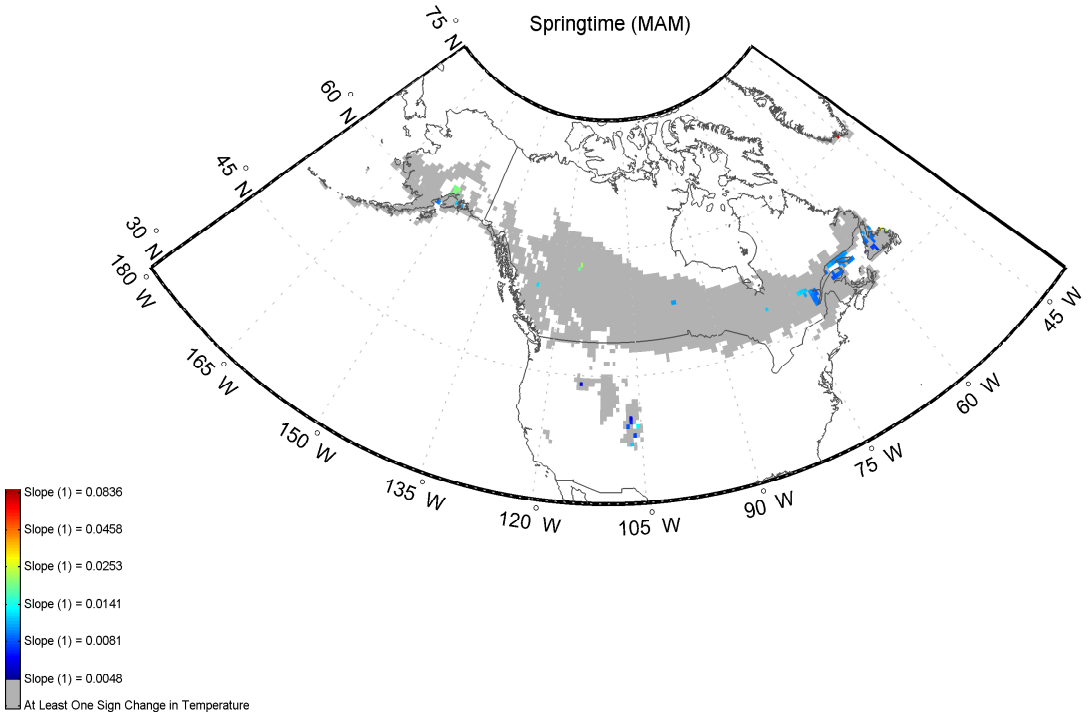


**Figure 5.173:** The same as Figure 5.172: zoomed in view of North America

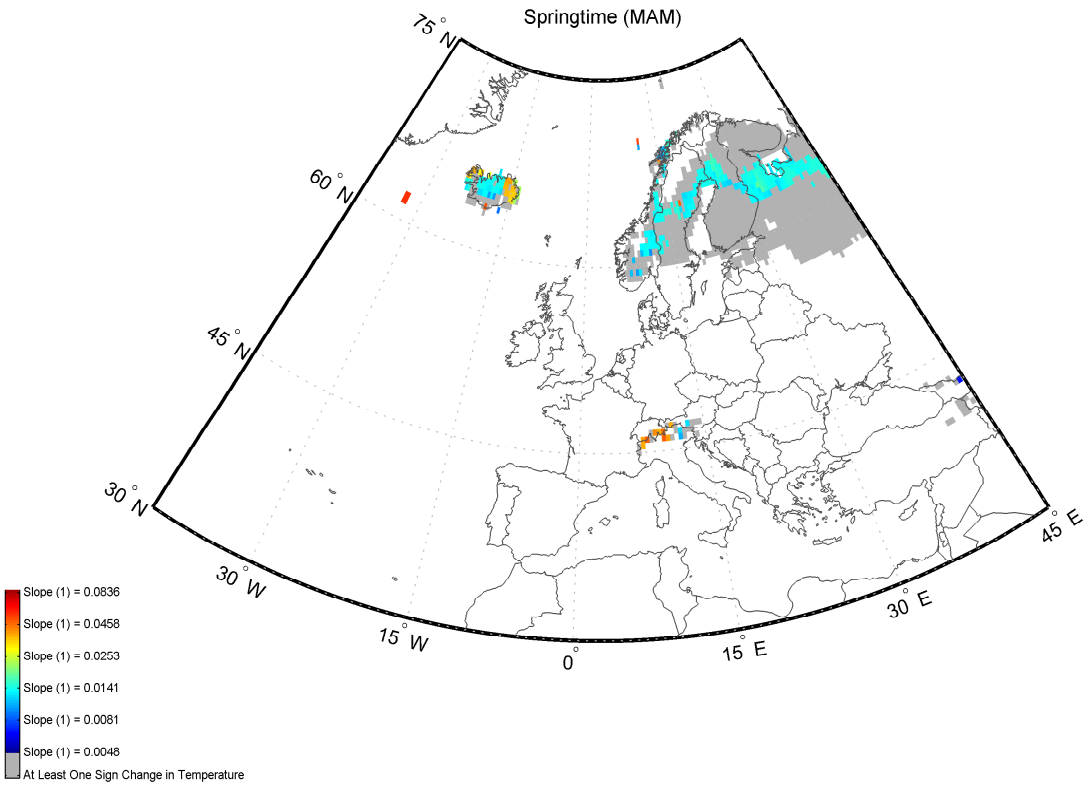


**Figure 5.174:** The same as Figure 5.172: zoomed in view of Europe

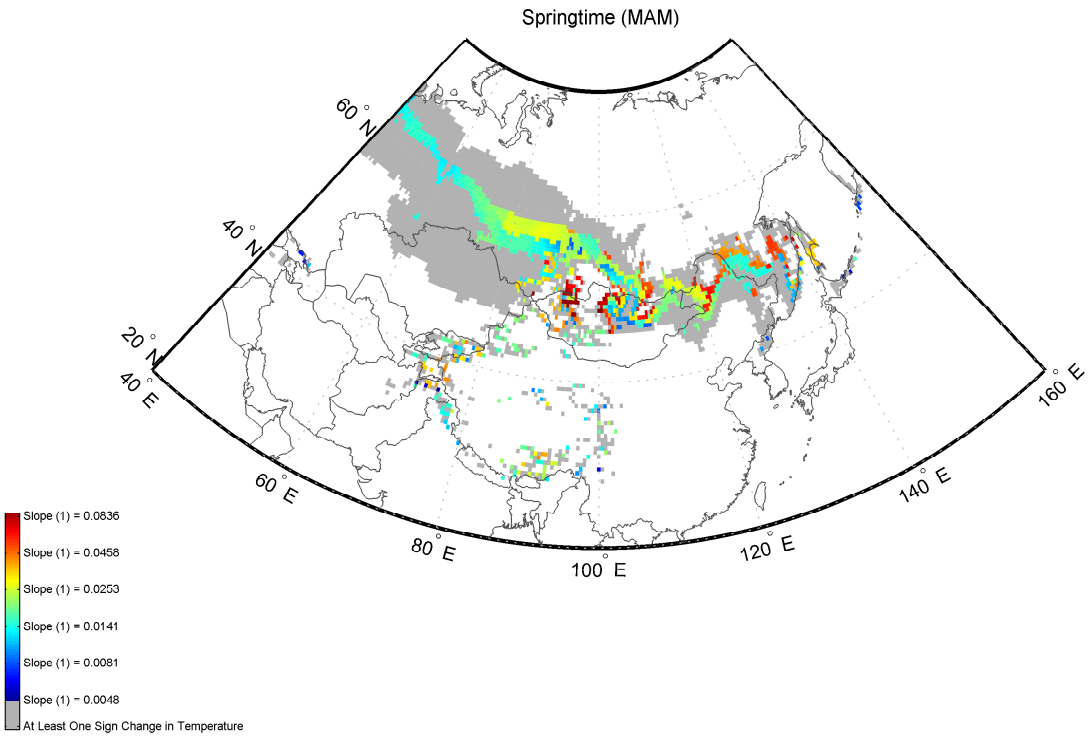


**Figure 5.175:** The same as Figure 5.172: zoomed in view of Asia

#### 5.6.4.3.3 Slope (2)

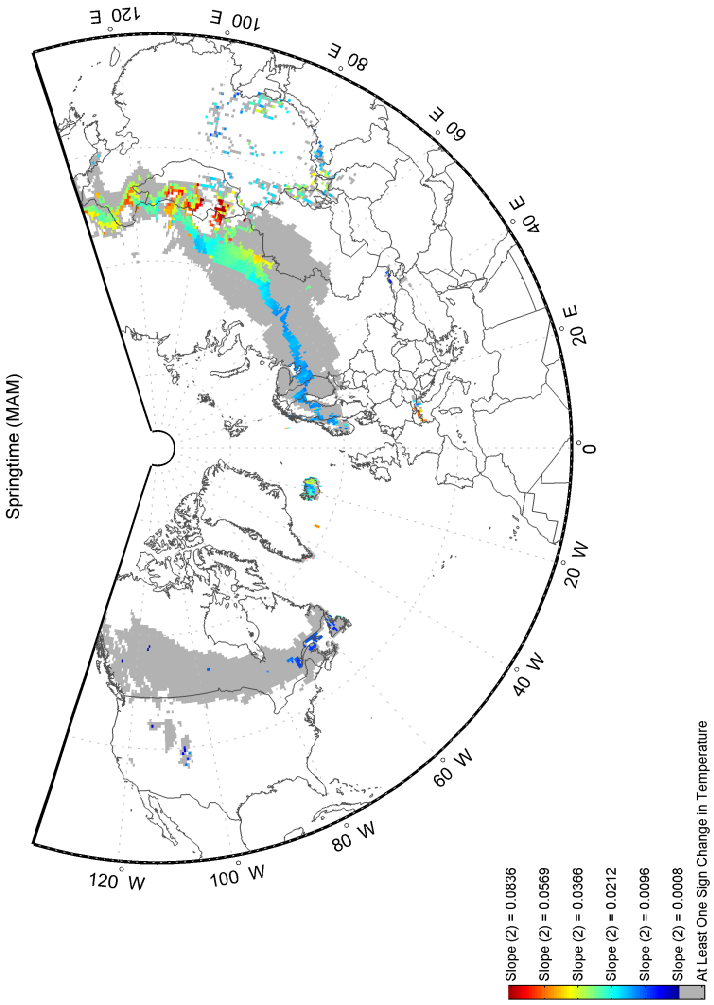


**Figure 5.176:** The map depicts the spatial distribution of Slope (2) in the Northern Hemisphere during **MAM**. The results are obtained using the **R method**, and the input parameters are as indicated in Section 5.6.3. The reader is referred to Section 5.6.1 for the definition of 'Slope (2)'.

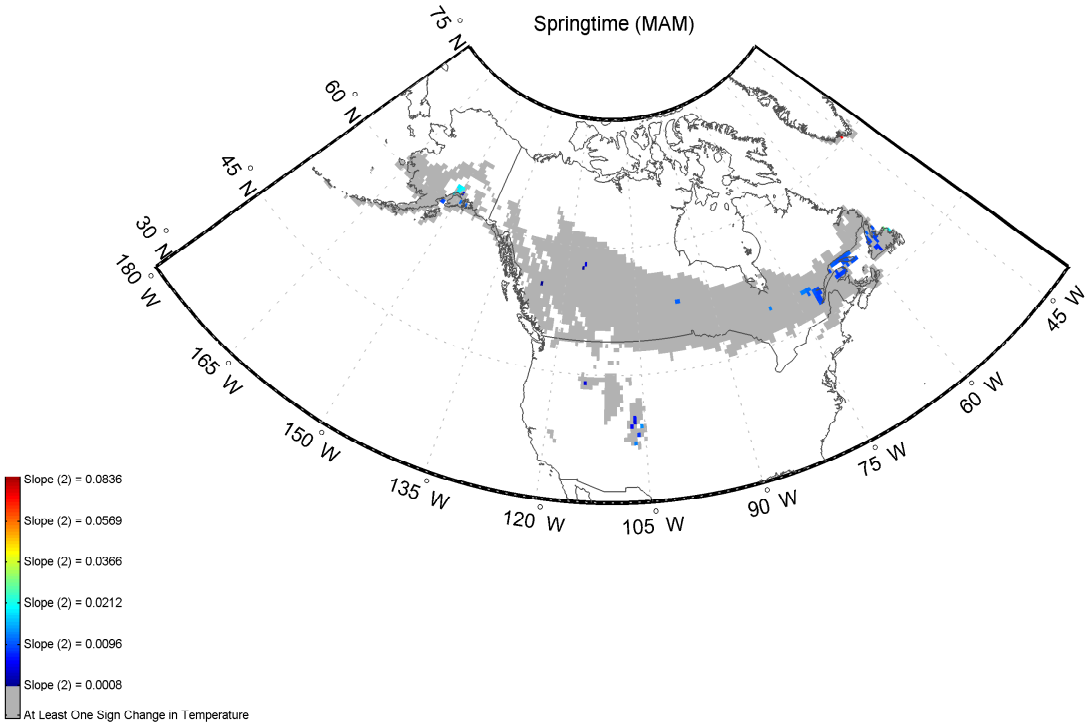


**Figure 5.177:** The same as Figure 5.176: zoomed in view of North America

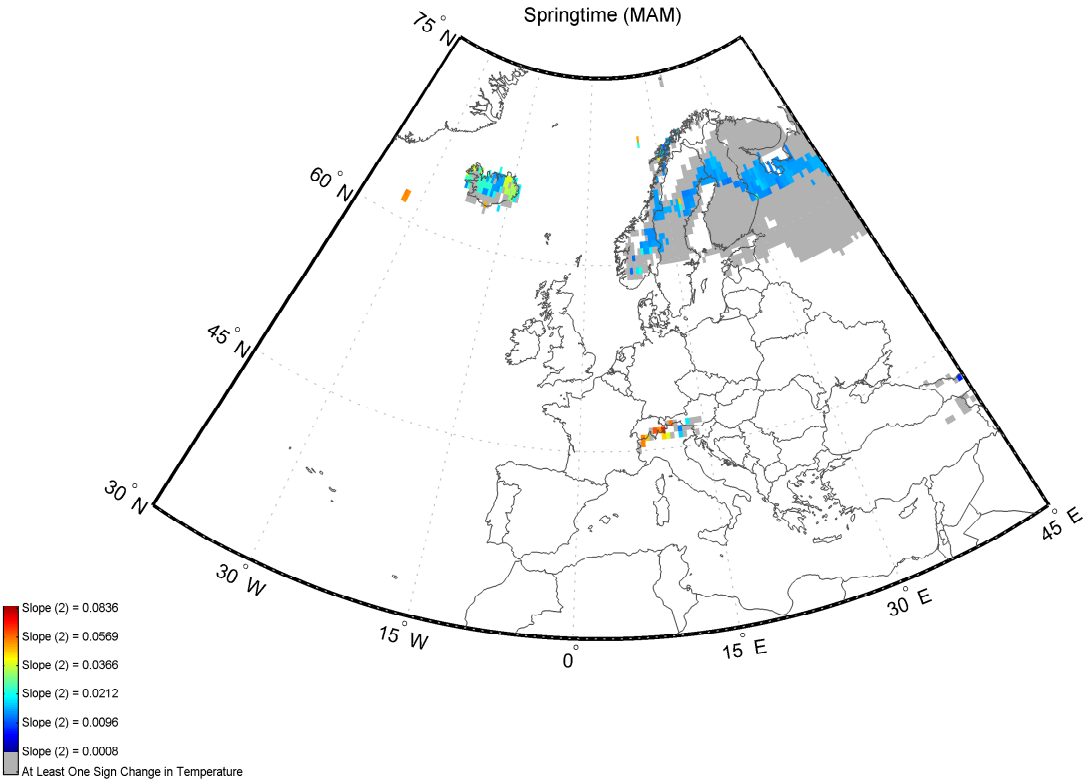


**Figure 5.178:** The same as Figure 5.176: zoomed in view of Europe

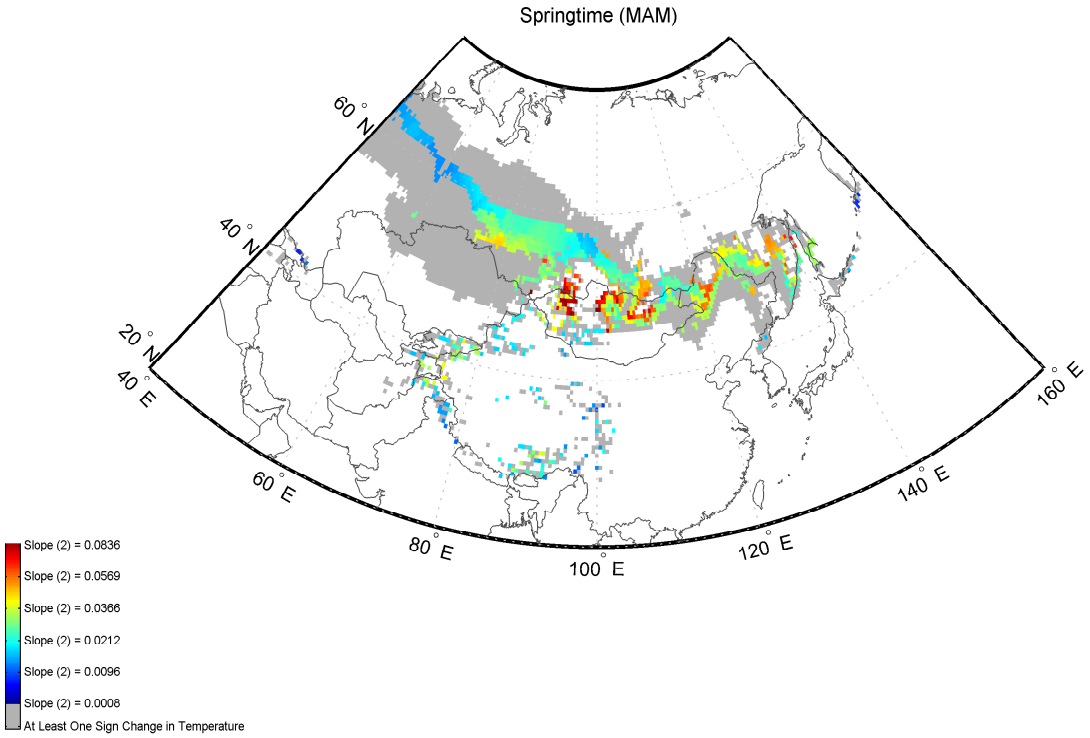


**Figure 5.179:** The same as Figure 5.176: zoomed in view of Asia

#### 5.6.4.3.4 H (1)

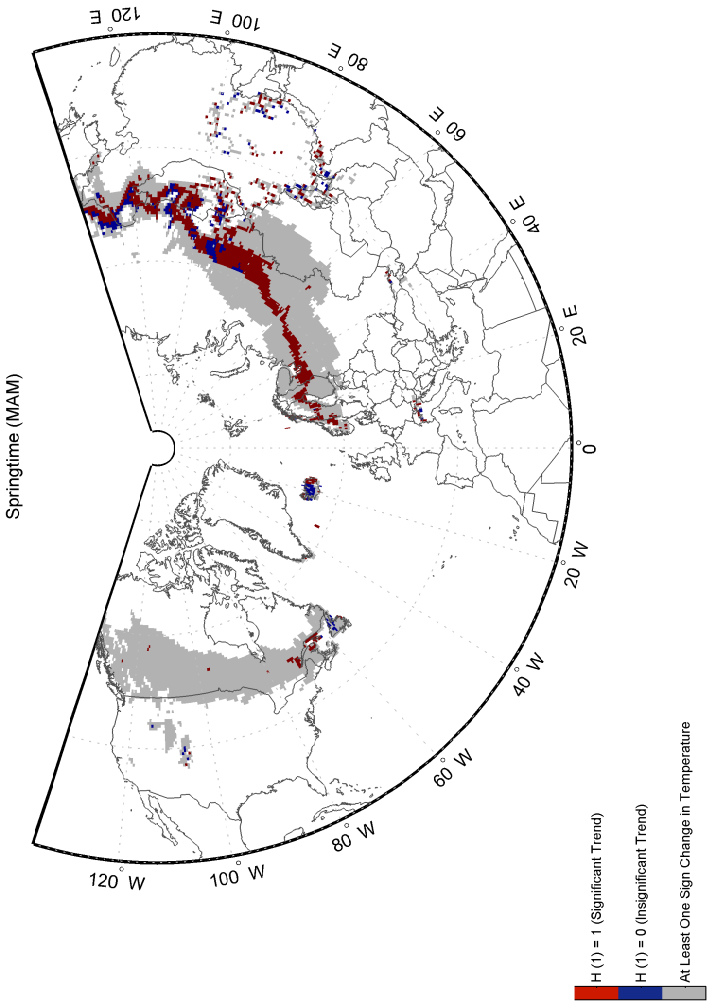


**Figure 5.180:** The map depicts the spatial distribution of H (1) in the Northern Hemisphere during **MAM**. The results are obtained using the **R method**, and the input parameters are as indicated in Section 5.6.3. The reader is referred to Section 5.6.1 for the definition of 'H (1)'.

#### 5.6.4.3.5 H (2)

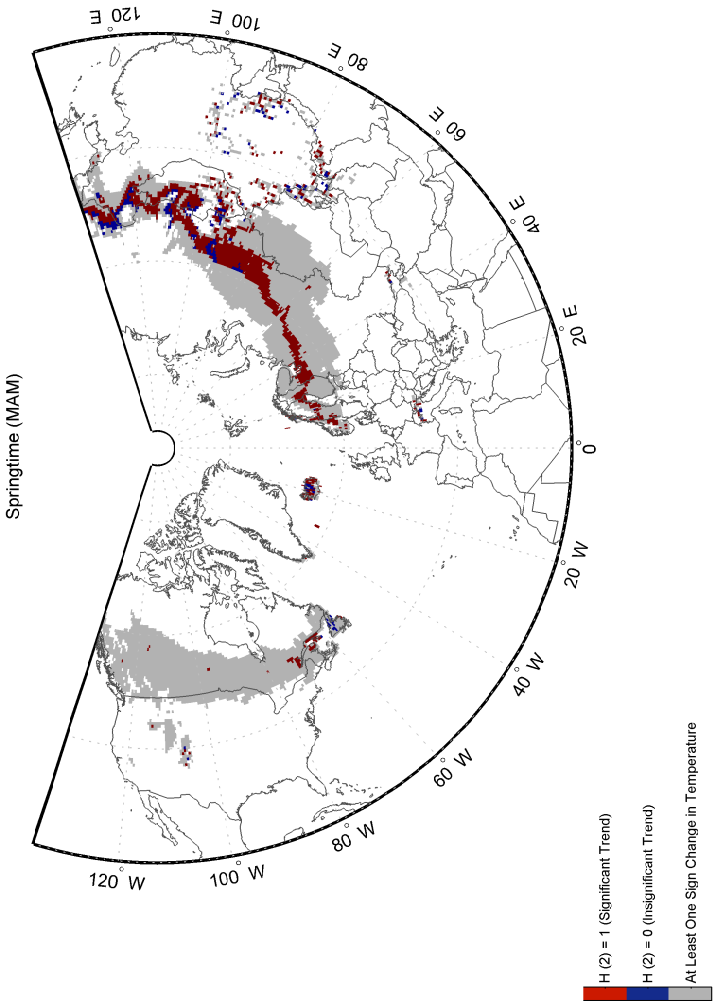


**Figure 5.181:** The map depicts the spatial distribution of H (2) in the Northern Hemisphere during **MAM**. The results are obtained using the **R method**, and the input parameters are as indicated in Section 5.6.3. The reader is referred to Section 5.6.1 for the definition of 'H (2)'.

## 5.7 Testing Global Significance

As indicated earlier in this document, a bootstrap algorithm is applied to investigate whether the percentage of the observed locally significant trends for each technique is high enough to consider them globally significant. The thorough description of the algorithm is given in Section 3.5.3. All the grid cells included in the final database are used for the analysis.

Tables 5.5 to 5.8 present the results. The tables contain the 5% critical values of the distributions of the percentage of tests which result in locally significant trends at the significance level of 0.05. Three types of distribution are obtained: i) 'all trends': distribution of the percentage of tests which are locally significant. The significant trends are either decreasing or increasing, ii) 'increasing trends': distribution of the percentage of tests which exhibit significant increasing trends, iii) 'decreasing trends': distribution of the percentage of tests which favour significant negative trends. Tables 5.5 to 5.8 also include the P-values. For more details on how to evaluate the test statistics and P-values, refer to Section 3.5.3. As is displayed below, except the decreasing trends, all of the trends are globally significant.

### 5.7.1 Model 2

**Table 5.5:** Results of the bootstrap analysis for **Model 2**

| Time | JFM | | | MAM | | |
|---|---|---|---|---|---|---|
| Data | $y_w$-$y_0$ | $S_{interest}$ | $Sw_{total}$ | $y_w$-$y_0$ | $S_{interest}$ | $Sw_{total}$ |
| One-sided 5% Critical Value (All Trends) | 0.10076 | 0.19185 | 0.16367 | 0.089844 | 0.15877 | 0.16247 |
| One-sided 5% Critical Value (Increasing Trends) | 0.067645 | 0.11751 | 0.1193 | 0.06218 | 0.11806 | 0.11288 |
| One-sided 5% Critical Value (Decreasing Trends) | 0.070317 | 0.14397 | 0.10132 | 0.059944 | 0.097335 | 0.10511 |
| One-sided P-value (All Trends) | 0 | 0 | 0 | 0 | 0 | 0 |
| One-sided P-value (Increasing Trends) | 0 | 0 | 0 | 0 | 0 | 0 |
| One-sided P-value (Decreasing Trends) | 1 | 1 | 1 | 0.9130 | 1 | 1 |

### 5.7.2 Model 3

**Table 5.6:** Results of the bootstrap analysis for **Model 3**

| Time | JFM | | | MAM | | |
|---|---|---|---|---|---|---|
| Data | $y_W$-$y_0$ | $S_{interest}$ | $S_{W_{total}}$ | $y_W$-$y_0$ | $S_{interest}$ | $S_{W_{total}}$ |
| One-sided 5% Critical Value (All Trends) | 0.12892 | 0.19171 | 0.15704 | 0.11223 | 0.17376 | 0.16883 |
| One-sided 5% Critical Value (Increasing Trends) | 0.077786 | 0.13052 | 0.10061 | 0.067861 | 0.11688 | 0.10748 |
| One-sided 5% Critical Value (Decreasing Trends) | 0.081006 | 0.11761 | 0.11761 | 0.068816 | 0.11285 | 0.11599 |
| One-sided P-value (All Trends) | 0 | 0 | 0 | 0.001 | 0 | 0 |
| One-sided P-value (Increasing Trends) | 0 | 0 | 0 | 0.004 | 0 | 0 |
| One-sided P-value (Decreasing Trends) | 0.8070 | 1 | 1 | 0.8130 | 1 | 1 |

### 5.7.3 MARS

**Table 5.7:** Results of the bootstrap analysis for **MARS**

| Time | JFM | | | MAM | | |
|---|---|---|---|---|---|---|
| Data | $y_W$-$y_0$ | $S_{interest}$ | $S_{W_{total}}$ | $y_W$-$y_0$ | $S_{interest}$ | $S_{W_{total}}$ |
| One-sided 5% Critical Value (All Trends) | 0.095004 | 0.17058 | 0.15719 | 0.090178 | 0.14583 | 0.1503 |
| One-sided 5% Critical Value (Increasing Trends) | 0.060266 | 0.099257 | 0.1004 | 0.054362 | 0.093588 | 0.11062 |
| One-sided 5% Critical Value (Decreasing Trends) | 0.065855 | 0.13253 | 0.10827 | 0.051452 | 0.093588 | 0.094122 |
| One-sided P-value (All Trends) | 0 | 0 | 0 | 0 | 0 | 0 |
| One-sided P-value (Increasing Trends) | 0 | 0 | 0 | 0 | 0 | 0 |
| One-sided P-value (Decreasing Trends) | 0.9550 | 1 | 1 | 0.8590 | 1 | 1 |

### 5.7.4 R Method

**Table 5.8:** Results of the bootstrap analysis for the **R method**

| **Time** | **JFM** | | **MAM** | |
|---|---|---|---|---|
| **Data** | $\mathbf{S_{interest}}$ | $\mathbf{S_{W_{total}}}$ | $\mathbf{S_{interest}}$ | $\mathbf{S_{W_{total}}}$ |
| **One-sided 5% Critical Value (All Trends)** | 0.18656 | 0.18958 | 0.17738 | 0.20472 |
| **One-sided 5% Critical Value (Increasing Trends)** | 0.12915 | 0.13595 | 0.11951 | 0.12487 |
| **One-sided 5% Critical Value (Decreasing Trends)** | 0.11405 | 0.11178 | 0.11844 | 0.14148 |
| **One-sided P-value (All Trends)** | 0 | 0 | 0 | 0 |
| **One-sided P-value (Increasing Trends)** | 0 | 0 | 0 | 0 |
| **One-sided P-value (Decreasing Trends)** | 1 | 1 | 1 | 1 |

## 5.8 Discussion

### 5.8.1 Mathematical Comparison of Various Techniques

As stated earlier in Chapter 2, all the techniques used in this document have some common characteristics that make them suitable for this research. Those features are once again listed below:

1. They could be easily automated and used in the analysis of large data sets.
2. They can analyse the original data directly, and the techniques do not necessitate the use of anomalies. The conversion of the original data requires the determination

of a base period. By using the original data, the ambiguity regarding the definition of a base period is avoided.

3. *A priori* assumptions regarding the timing of the shifts are not required.

Due to the relatively short length of the time series (109 years), it is difficult to attribute a definite function to them. This was the main reason that motivated the inclusion of the various methods to inspect the time series in this research. Before inspecting the differences and similarities between the results generated by different techniques, it is worthwhile to summarize the specific points that distinguish these methods and help understand their strengths and weaknesses based on the research goals. First, key characteristics of each technique are highlighted in Section 5.8.1.1 and summarized in Table 5.9. Then, some insight regarding the connection between these methods and their theoretical frameworks is provided (Section 5.8.1.2).

#### 5.8.1.1 Key Characteristics of Each Method

- **Model 2 and Model 3:** As indicated in Section 2.3.4, the time series of annual mean anomalies of the air temperature in the Northern Hemisphere seem to be non-stationary during the $20^{\text{th}}$ century. A number of studies have been devoted to investigating whether the underlying process is trend-stationary or has a unit root. Ivanov and Evtimov (2010) applied Kim and Perron's (2009) test to the time series of annual mean anomalies of the air temperature in the Northern Hemisphere. They concluded that the underlying process is trend-stationary. This implies that the long-term changes in climate follow a trend function, and short-term changes (climatic noises) are best described by a stationary process. As indicated earlier, an abrupt shift may occur in the slope and/or intercept of the trend function of a climate time series. Model 2 and Model 3 detect abrupt shifts in slope and simultaneous shifts in slope and intercept, respectively. The data generating process is given by Equation 3.14:

  $$y_t = x_t' \Psi + u_t$$

  The noise component ($u_t$) is assumed to be an AR(1) process; however, it could be generalized to a higher order ($p$) as well. Furthermore, as indicated earlier, one of the key features of this technique is that the noise component could be described by

either a stationary process or a unit root process. Based on Equations 3.19 and 3.20, Model 2 and Model 3 take the following final forms:

**Model 2:**

$$y_t = \mu_0 + \beta_0 t + \beta_1 DT_t + u_t$$

**Model 3:**

$$y_t = \mu_0 + \mu_1 DU_t + \beta_0 t + \beta_1 DT_t + u_t$$

Therefore, as could be inferred from Equations 3.14, 3.19, and 3.20, time series are modelled by a trend-stationary process with AR(1) (or higher order) noise component.

- **MARS:** If a simple form of splines like the piecewise linear splines is taken, and the right locations for knots are selected automatically, the resulting spline solution that is required to be continuous at each knot location is called MARS. To have a powerful knot selection algorithm that could be applied to cases with more than one independent variable or with interactions, Friedman (1991) used the concept of basis functions. The data generating process is illustrated by the following Equations (Equations 3.12 and 3.13):

$$\hat{f}(\mathbf{x}) = \sum_{m=1}^{M} a_m B_m(\mathbf{x})$$
$$B_m(\mathbf{x}) = I[\mathbf{x} \in R_m]$$

  As described in detail in Section 3.3.1, the two types of BF used in the MARS algorithm are as follows:

  - Direct BF: $max\ (0, x - c)$
  - Mirror image BF: $max\ (0, c - x)$

  MARS considers constructing such BF's with all permissible data points taken as $c$. Basically, $c$ stands for knot locations. An over-fit model is deliberately developed in the forward knot placement process and is pruned back in the knot cleaning step.

- **R method:** As indicated in Section 2.3.2, this technique belongs to the category of the methods that detect changes in the means of time series. This implies that

it is suitable for detecting sharp changes in mean rather than trend inhomogeneities in time series. The technique is capable of detecting the most recent changes (i.e., shifts close to both ends of time series).

As described in Section 3.2, the R method models a time series with the following equation, which implies that the time series contains both red noise and regime shifts:

$$(X_t - f_t) = \rho(X_{t-1} - f_{t-1}) + \varepsilon_t \quad \rightarrow \quad X_t = \rho X_{t-1} + f'_t + \varepsilon_t$$

where $f'_t = f_t - \rho f_{t-1}$. In this case, $f_t$ is a polynomial of degree zero and equal to the mean of the regime within which it falls. The red noise is removed using $X_t - \hat{\rho} X_{t-1}$, and the sequential algorithm applies to $Z'_t = f'_t + \varepsilon_t$.

#### 5.8.1.2 Examination of the Connection Between Various Methods

According to the above-mentioned points about MARS and Models 2 and 3, a close connection exists between MARS and Models 2 and 3. MARS approximates time series with polynomials of degree zero or one that are continuous at the boundaries. Models 2 and 3 assume that the long-term changes follow a linear trend, and the climatic noises could be modelled by an auto-regressive process. According to Figures 5.99 and 5.104, the maximum number of MARS segments among grid cells of the final database is 5 during both JFM and MAM. Models 2 and 3, on the other hand, approximate time series with two linear segments that are separated from each other by the break point. Model 2 is continuous at the break time, whereas Model 3 is discontinuous at the break point since it exhibits a shift in intercept in addition to slope.

A close examination of the histograms and result matrices of MARS reveals that the maximum number of positive 0°C crossing is 2 among the locations included in the final database, during both JFM and MAM (Figures 5.99 and 5.104). Locations with 2 positive 0°C crossings form a small subset of the final database during both JFM (185 out of 1498 locations) and MAM (216 out of 2520 locations). Therefore, most of the locations in the final database exhibit only one positive 0°C crossing. It is worthwhile to note that since MARS is continuous at the boundaries, all of the locations with two positive 0°C crossings are modelled with more than 2 segments and most commonly with 4 segments (JFM: 177 out of 185 locations, MAM: 210 out of 216 locations). Further investigations show that the behaviour of MARS in many locations with 2 segments resembles that of Model 2

(Figures C.14 and C.16). Furthermore, among locations with more than two segments, some of them are modelled as if the approximation technique is Model 3 of IO type. In all of these cases, there is a steep segment with a short duration which indeed plays the role of transitional period in the case of IO models. This segment leads to the simultaneous shift in slope and intercept as with Model 3 (Figures C.12 and C.24). As will be observed later in this section, due to all of these features, $y_0$'s reported by Models 2 and Model 3 are close to that of MARS. However, this conclusion cannot be extended to $y_w$. The reason is that in the case of Models 2 and 3, each time series is modelled with only two segments separated by the break time. Thus, $y_w$, which is the beginning of $S_{interest}$, is either the break time or 1901. However, in the case of MARS, the entire domain of the time series may be split into more than two segments. Hence, a different $y_w$ may be reported for the time series. Furthermore, the larger number of segments produced by MARS may affect the selection of $S_{interest}$, which leads to different values of $y_w$. An example of this case is Figure C.24; MARS models the time series with four segments, and the first and last segments cross 0°C. The first segment has a positive slope and is followed by another segment of positive slope. Since the first segment has a smaller slope, the last segment is selected as $S_{interest}$. Using Model 3, the first two segments of MARS are approximated by one line of positive slope. This line has a larger temperature accumulation and a larger rate of increase than the second segment. Therefore, it is selected as $S_{interest}$. Different $S_{interest}$'s imply different $y_w$'s.

At this point it should be noted that MARS is an adaptive regression technique that has been developed to model any type of data and not necessarily time series. It is accurate and applicable to cases with up to 20 independent variables. Furthermore, it generates precise results if there are interactions between a few independent variables. MARS is capable of handling missing values and categorical variables as well. All these characteristics make MARS a powerful method that could be used to model intricate situations. Since MARS does not belong to the category of techniques used in the analysis of time series, its algorithm does not include autoregressive terms. Hence, a more complicated path is followed to model the data. Due to the adaptive and complex nature of the algorithm, it requires the analyst to provide more input parameters compared to the other algorithms used in this study, and this is one of the drawbacks of MARS. As indicated earlier, MARS has no intuition of its own. These input arguments are open to wide experimentation. Therefore, it may be necessary to study the difference that it takes to run the model with different values of the input arguments and examine which of the possibilities yields the

best performance and the best bias-variance trade-off. Due to the large number of locations under study in this thesis, it is not feasible to investigate each case separately. To partially offset this problem, three groups of input parameters are used in the MARS analysis (refer to Section 5.5.1 for more details). In contrast to MARS, Models 2 and 3 as well as the R method, which are specifically developed for the analysis of time series, require few inputs. This makes these techniques more suitable for analysing large databases where it is not feasible to inspect all cases one by one and modify the inputs accordingly.

According to Section 5.8.1.1, the R method has some distinct features that make it different from MARS and Models 2 and 3. In the R method, the function of the underlying data generating process consists of polynomials of degree zero. This is different from MARS and Models 2 and 3, which embed linear functions of time. Another unique characteristic (unique advantage) of the R method is its ability to detect shift points close to the ends of time series since the analysis includes observations in sequence, and the number of observations included in each step is not fixed *a priori*. MARS and Models 2 and 3 lack this ability: Models 2 and 3 exclude some data points (based on the value of $\epsilon$ (Section 5.4.1)) from both ends of a time series. Due to the restriction on the number of data points required in each step for knot placement, the behaviour of MARS deteriorates close to the ends of time series, which could be partially controlled using the input argument 'End Span' (Section 5.5.1).

Since the R method detects the sharp changes in the mean of time series, the upward shifts that cross the 0°C line could be directly considered as $y_0$ candidates, and the model requires minimum rules on the determination of $y_0$. This implies that $y_0$ reported by the R method is the year of 0°C crossing when the mean of the time series moves above 0°C as opposed to MARS and Models 2 and 3 where the long-run path (trend function) of temperature crosses 0°C. Like MARS, the R method is capable of detecting multiple shifts. However, it differs from MARS and Models 2 and 3; as described in Section 3.2, the R method sequentially includes data points in the analysis and performs the Student's t-test for testing the significance of the difference between the mean levels under study in each step.

**Table 5.9:** Key features of the techniques applied in the analysis of time series

| | | |
|---|---|---|
| **Common** | 1. They could be easily automated and used in the analysis of large data sets.<br>2. They can analyse the original data directly, and the techniques do not necessitate the use of anomalies. The conversion of the original data requires the determination of a base period. By using the original data, the ambiguity regarding the definition of a base period is avoided.<br>3. *A priori* assumptions regarding the timing of the shifts are not required. | |
| **Specific** | Models 2 and 3 | Model 2 and Model 3 detect abrupt shifts in slope and simultaneous shifts in slope and intercept, respectively. The data generating process is given by Equation 3.14. The noise component ($u_t$) is assumed to be an AR(1) process; however, it could be generalized to a higher order ($p$) as well. Furthermore, one of the key features of the models is that the noise component could be described by either a stationary process or a unit root process (Kim and Perron, 2009; Perron and Yabu, 2009b). |
| | MARS | MARS is a subset of the methods used in adaptive computations. MARS is a hybrid of the classical spline approach and a more modern way of partitioning data into subregions; knots are predetermined in the classical spline approach. However, MARS identifies best knot placements automatically. To have a powerful knot selection algorithm that could be applied to cases with more than one independent variable or with interactions, the concept of basis functions is used (Friedman, 1991). |
| | R method | The technique belongs to the category of the methods that detect changes in the mean level of time series. This implies that it is suitable for detecting sharp changes in mean rather than trend inhomogeneities in time series. Due the sequential nature of its algorithm, the R method is capable of detecting the most recent changes (i.e., shifts close to both ends of time series) (Rodionov, 2004, 2006). |

### 5.8.2 Non-parametric Comparison of Results

The methodology of the non-parametric comparison techniques used in this study is provided in Section 3.6. Two methods will be used for comparing $y_w$ and $y_0$ results generated by MARS, Models 2 and 3, and the R method: Wilcoxon signed-rank test for paired observations and Wilcoxon rank-sum test. As could be inferred from the terminology, the former only compares the results of the common subset of locations selected by any two techniques. The latter, on the other hand, compares all the results obtained from one technique to the outputs of the other technique. Basically, the goal of using Wilcoxon rank-sum test is to investigate whether both techniques generally report similar results. Sometimes, one method selects a location for analysis, and the other method selects its neighbouring grid cell. Wilcoxon signed-rank test excludes these locations from the analysis. However, Wilcoxon rank-sum test has the advantage of including all these locations.

**Note:** All the sample sizes are larger than 20 in this study. Therefore, in the application of Wilcoxon signed-rank test, if there is no 0 present in the vector of differences, the distribution of the test statistic ($W_1$) is assumed to be normal. However, if 0's are present, the approach proposed by Pratt (1959) to handle 0's is followed. In this case, the distribution of $W_1$ is found based on 100,000 random permutations from the reference distribution of all $2^n$ permutations (refer to Section 3.6.1 for more details).

Prior to presenting the results of the tests, the techniques are compared graphically following the diagonal line approach (Figures 5.182 to 5.184). Each point on the figures represents a location that has been selected by the techniques shown on the x and y axes, and the values attributed to that location define its (x,y) coordinates on the page. The total number of paired locations used in each case is mentioned in Table 5.10. It should be noted that each of Figures 5.182 (JFM) and 5.183 (MAM) presents 6 double model comparisons of $y_0$ values. However, in the case of $y_w$, only 3 plots are presented for JFM or MAM (Figure 5.184). This is due to the fact that $y_w$ is not determined by the R method and only the $y_w$ values determined by MARS, Model 2, and Model 3 are compared.

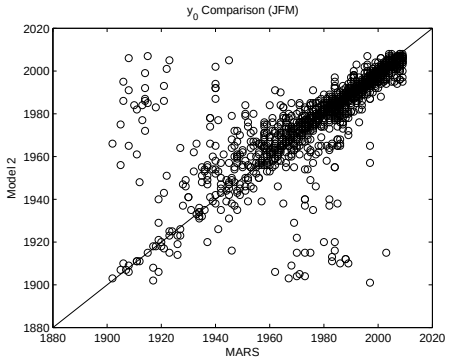


**(a)** MARS and Model 2

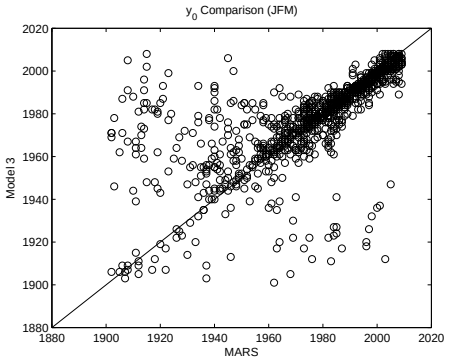


**(b)** MARS and Model 3

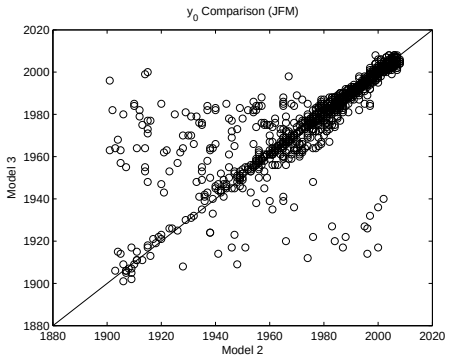


**(c)** Model 2 and Model 3

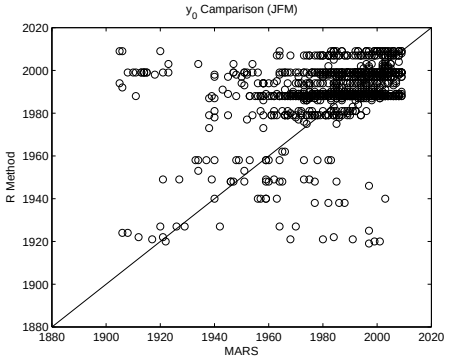


**(d)** MARS and R method

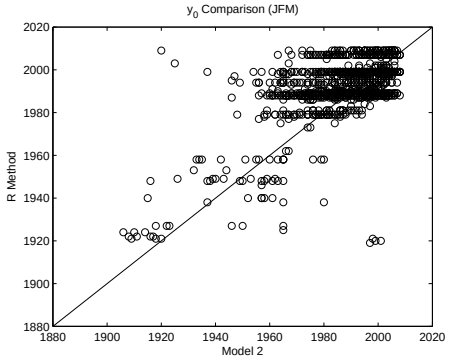


**(e)** Model 2 and R method

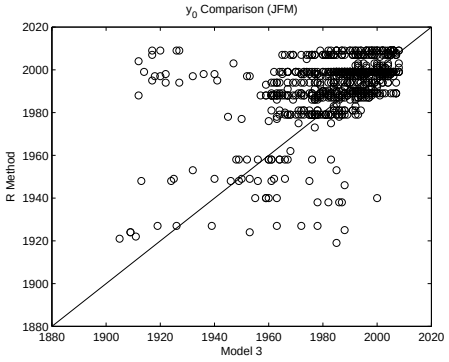


**(f)** Model 3 and R method

**Figure 5.182:** Graphical comparison of $\mathbf{y_0}$ results obtained for **JFM**

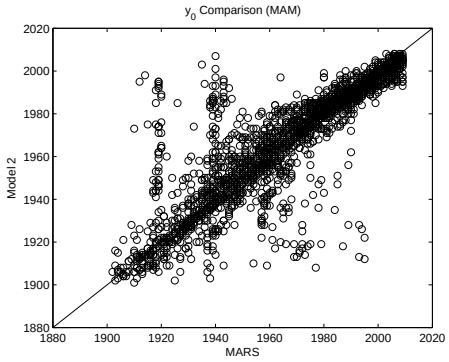


**(a)** MARS and Model 2

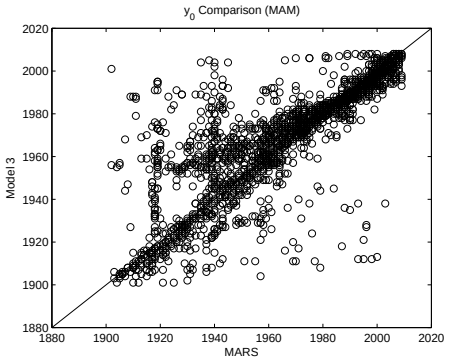


**(b)** MARS and Model 3

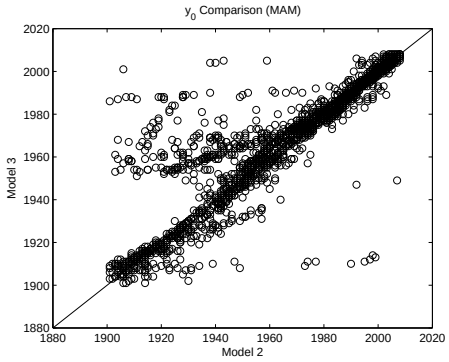


**(c)** Model 2 and Model 3

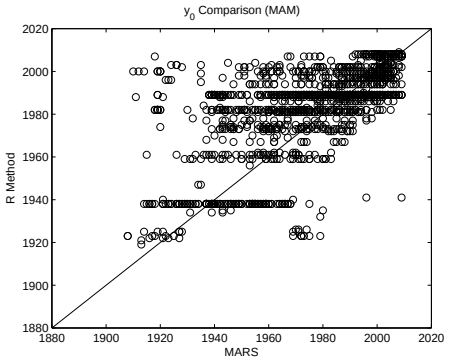


**(d)** MARS and R method

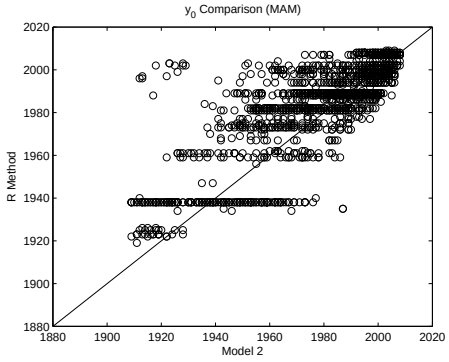


**(e)** Model 2 and R method

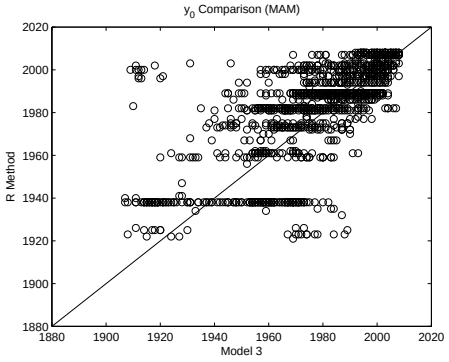


**(f)** Model 3 and R method

**Figure 5.183:** Graphical comparison of $\mathbf{y_0}$ results obtained for **MAM**

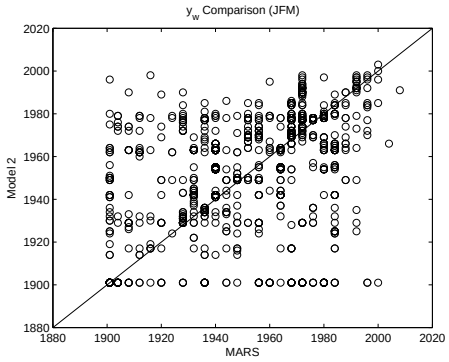


**(a)** MARS and Model 2 (JFM)

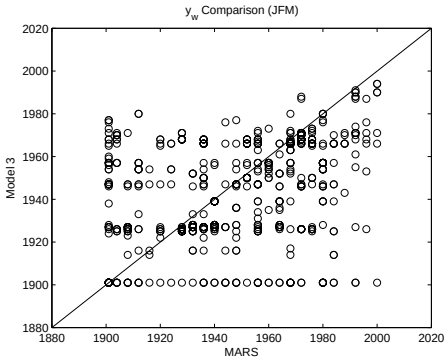


**(b)** MARS and Model 3 (JFM)

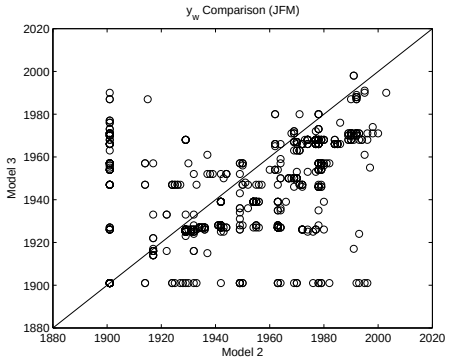


**(c)** Model 2 and Model 3 (JFM)

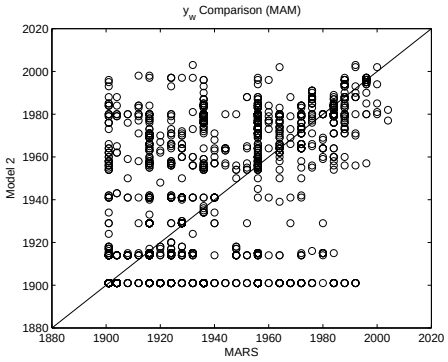


**(d)** MARS and Model 2 (MAM)

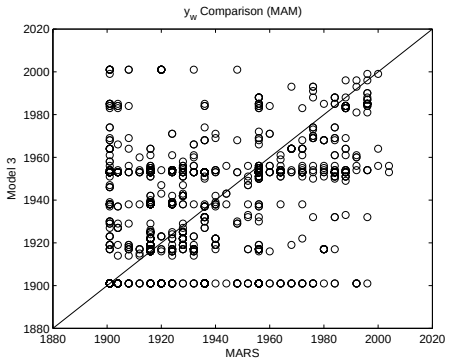


**(e)** MARS and Model 3 (MAM)

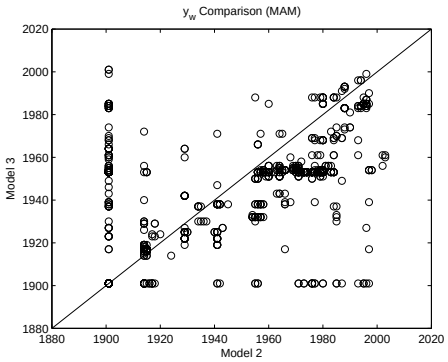


**(f)** Model 2 and Model 3 (MAM)

**Figure 5.184:** Graphical comparison of $\mathbf{y_w}$ results obtained for **JFM** (a, b, c) and **MAM** (d, e, f)

As depicted by the plots, during both JFM and MAM, Model 2 and Model 3 generate the most similar $y_0$ results. This implies that in the grid cells selected as the common subset of Model 2 and Model 3, the break times in slope (detected by Model 2) and in both intercept and slope (identified by Model 3) as well as the slopes of the OLS lines preceding or following the shift times are such that they lead to generally similar $y_0$ results.

As indicated earlier, the R method detects shifts in the mean level of time series as opposed to Model 2, Model 3, and MARS that identify trend inhomogeneities (refer to Section 5.8.1.2 for more details on the distinct features of the R method). Therefore, the $y_0$ outputs from the R method differ from those of Model 2, Model 3, and MARS. Plots d, e, and f in Figures 5.182 and 5.183 exhibit single-value trendings of the R method for $y_0$, i.e., the R method reports a single value as $y_0$ of a number of locations while $y_0$ determined by the other technique varies over a range. These results may be due to the high spatial coherence of the outcomes of the R method. As depicted by the $y_0$ maps of the R method (Figures 5.154 and 5.168), over some regions, $y_0$ values determined by the R method are the same or very close where other techniques report a range of values.

No close relationship between $y_w$'s of different techniques is detected. In the plots of Model 2 and Model 3 (Figure 5.184), data points are less scattered around the diagonal line compared to the other plots; however, the deviation from the diagonal line is significant. In the comparison of MARS and Model 2 or MARS and Model 3, as indicated earlier, the reason for having rather similar $y_0$'s and different $y_w$'s is that Models 2 and 3 approximate each time series with only two segments separated by the break time. Thus, $y_w$, which is the beginning of $S_{interest}$, is either the break time or 1901. However, in the case of MARS, the entire domain of the time series may be split into more than two segments. Hence, different $y_w$'s may be reported for the time series. In the comparison of Model 2 and Model 3, dissimilar $y_w$'s could be explained by different break times as is inferred from the comparison of break time histograms (JFM: Figures 5.1 and 5.47, MAM: Figures 5.5 and 5.52). In these cases, the slopes of the regression lines that approximate data are such that the 0°C crossing times of the selected paired observations are close; however, the breaks (the beginning of the lines) occur at different times. Furthermore, a close examination of Figure 5.184 reveals that there are locations where Model 2 identifies the first segment as $S_{interest}$ (i.e., $y_w = 1901$), whereas Model 3 determines the second segment as $S_{interest}$, and vice versa. Most of these locations are located in northeastern U.S. and western China during JFM (Figures 5.9 and 5.57) and southern Russia during MAM (Figures 5.28 and 5.76).

**Table 5.10:** The results of the comparison of different techniques using **Wilcoxon signed-rank test for paired observations** are presented below in the form of P-values. The null hypothesis of the test is $\mu_{\text{group 1}} = \mu_{\text{group 2}}$ (refer to Section 3.6.1 for more details on the hypothesis test).

| **Time** | **JFM** | | | **MAM** | | |
|---|---|---|---|---|---|---|
| **Data** | No. Paired Observations | $\mathbf{y_w}$ | $\mathbf{y_0}$ | No. Paired Observations | $\mathbf{y_w}$ | $\mathbf{y_0}$ |
| **MARS - Model 2** | 1292 | 0 | 0.0841 | 2199 | 0 | 0.0838 |
| **MARS - Model 3** | 1044 | 0 | 0.1220 | 1752 | 0 | 0.0698 |
| **MARS - R method** | 1026 | N/A | 0 | 1553 | N/A | 0 |
| **Model 2 - Model 3** | 1131 | 0 | 0.0853 | 1885 | 0 | 0.0506 |
| **Model 2 - R method** | 1162 | N/A | 0 | 1702 | N/A | 0 |
| **Model 3 - R method** | 839 | N/A | 0 | 1352 | N/A | 0 |

Wilcoxon signed-rank test for paired observations (Table 5.10) and Wilcoxon rank-sum test (Table 5.11) produce similar results to those obtained from the graphical comparison. Based on these tables, a few points should be highlighted: i) The null hypothesis of these tests is the equality of the population means of the two models being compared. Therefore, if large P-values are obtained, the tests fail to reject the null hypothesis. Hence, the results of the two groups are considered equal in the specified significance level, ii) Wilcoxon rank-sum test generates larger P-values in favour of the null hypothesis since it performs an overall comparison between all results, iii) Based on the P-values, it could be inferred that generally, different techniques produce closer $y_0$ results during JFM than MAM, iv) Except the P-value obtained using Wilcoxon signed-rank test during MAM, Model 3 and MARS have the most similar $y_0$ values (largest P-values) during both JFM and MAM.

### 5.8.3 Discussion on the Tabulated Results and Histograms

So far, the discussion was focussed on the comparison of different techniques in terms of methodology and overall agreement between $y_w$ and $y_0$ results. In this section, more in-depth discussion on the results is provided by inspecting all the tables, histograms, and maps presented earlier in this chapter.

**Table 5.11:** The results of the comparison of different techniques using **Wilcoxon rank-sum test** are presented below in the form of P-values. The null hypothesis of the test is $\mu_{\text{group 1}} = \mu_{\text{group 2}}$ (refer to Section 3.6.2 for more details on the hypothesis test).

| **Time** | **JFM** | | **MAM** | |
|---|---|---|---|---|
| **Data** | $\mathbf{y_w}$ | $\mathbf{y_0}$ | $\mathbf{y_w}$ | $\mathbf{y_0}$ |
| **MARS - Model 2** | 0 | 0.1781 | 0 | 0.0922 |
| **MARS - Model 3** | 0 | 0.3971 | 0 | 0.2696 |
| **MARS - R method** | N/A | 0 | N/A | 0 |
| **Model 2 - Model 3** | 0 | 0.2895 | 0 | 0.1080 |
| **Model 2 - R method** | N/A | 0 | N/A | 0 |
| **Model 3 - R method** | N/A | 0 | N/A | 0 |

The first point that needs to be discussed is whether the different methods used in this study analyse approximately the same locations. This is important to explore since only in that case is the comparison of histograms presented for each technique meaningful. According to Tables 5.1 to 5.4, the numbers of locations in the final database selected by the techniques are very close during JFM. The same applies to MAM. In both cases of JFM and MAM, although the numbers are very close, the R method and Model 2 select the minimum and maximum number of locations, respectively. Similarly, maps reveal that the grid cells selected for the final database exhibit small variance between different techniques. The most evident differences are as follows:

1. During JFM, using the R method, no location in northeastern U.S. fulfils the requirements of Rule 2 of *transition area* (Section 4.3).

2. During MAM, in contrast to Model 2 and MARS, no location is selected over southern Canada using Model 3. The R method detects only a few locations in North America based on Rule 2 of *transition area* for further investigations.

Since the number of locations and area of focus of different techniques are close, the discussion continues by examining the histograms that provide summary graphs showing

counts of locations for each variable. First, the conclusions drawn by inspecting JFM histograms are provided followed by the investigation of the MAM time series.

#### 5.8.3.1 JFM

1. **$y_w$**
   As discussed in Sections 5.8.1 and 5.8.2, the difference between $y_w$ results of the techniques is significant. As is depicted by JFM histograms (Figures 5.1, 5.47, and 5.95), $y_w$ values do not exhibit any specific behaviour; however, several points could be drawn from these figures:

   - The analysis of the $y_w$ histogram of Model 3 reveals that two periods during which warming in most of the locations started are the 1920s and 1960s. The number of locations that experience the onset of warming during these two decades is considerably larger than the numbers reported for the other decades. In the case of Model 2 and MARS, the numbers reported for different decades are not significantly different; however, the periods during which warming starts in most of the locations are identified as follows:
     Model 2: the 1940s and the period of 1960-1980
     MARS: the 1940s and the period of 1960-1990
     In both cases, 1970s contains the maximum number of locations.
   - The strong resemblance of the break time and $y_w$ histograms of both Model 2 and Model 3 and the small numbers of locations with $y_w = 1901$ indicate that the break time is the start year of warming for most of the locations.
   - Except the peak during the 1920s decade, the overall behaviours of the break time distributions (and consequently $y_w$ histograms) of Model 2 and Model 3 are close.
   - Using any modelling technique (MARS, Model 2 and Model 3), there are always some locations with the values of $y_w$ that fall within the first decade of the $20^{th}$ century. In the case of Models 2 and 3, the first columns of the $y_w$ histograms only contain locations with $y_w = 1901$ (Model 2: 157 locations and Model 3: 105 locations). There are 143 locations modelled by MARS whose $y_w$'s occur during the 1900s decade. However, only 88 locations belong to the category of $y_w = 1901$. This implies that some of the models generated by MARS have

first segments with the lengths less than 10 years followed by segments selected as $S_{interest}$. This is one of the undesirable properties of the MARS algorithm. This behaviour could be partially controlled with the input parameter Minimum Span (Section 5.5.1). To avoid introducing any bias into the modelling process and due to the large number of locations under study, this value is set to the automatic mode in this study. This lets the algorithm find the appropriate knot locations. Therefore, in some cases, MARS exhibits abrupt changes. It should be noted that another reason for this behaviour is the deterioration of the knot placement algorithm close to the ends of the time series. The discussion on $y_w = 1901$ has been provided in Section 5.3.1.

2. **$y_0$**

- According to Figures 5.1 (Model 2), 5.47 (Model 3), and 5.95 (MARS), the results of Model 2, Model 3, and MARS indicate that the number of locations experiencing the temperature sign change from negative to positive increases exponentially during the $20^{th}$ century. The results obtained from modelling the time series using the R method (Figure 5.144) reveal that the mean levels of most of the locations in the final database have risen above 0°C during the last two decades of the $20^{th}$ century and the first decade of the $21^{st}$ century (i.e., 1980-2009). A very small number of locations experience earlier 0°C crossings of their mean levels.
- According to the $y_0$ histogram of the R method (Figure 5.144), the mean level of no location changes sign from negative to positive during the first decade of the $20^{th}$ century. However, the $y_0$ histograms of MARS and Models 2 and 3 show that there are locations with $y_0$ occurring during the 1900s decade. These locations are categorized as follows: i) locations with $y_w = 1901$ and a steep first line that moves the time series above 0°C during the first decade of the $20^{th}$ century, ii) locations with $y_w$ values in the range of 1902-1910: These cases, which are only produced by MARS, have very short first segments (3-5 years) followed by second segments with large positive slopes. The second segments cross 0°C in a short time.

**Note:**

(a) The above-indicated model behaviours (i.e., $y_0$ occurs in the 1900s decade)

may be due to the very localised approximations. If more data points were available prior to 1901, more precise models would be obtained, and it might be concluded that the models are positive during the 1901-2009 period. It should be noted that the numbers of locations with $y_0$ occurring in the 1900s are 31, 28, and 24 for MARS, Model 2, and Model 3, respectively, which are negligible compared to the large final databases.

(b) As could be interpreted from the above note, the comparison of $y_w$ and $y_0$ histograms indicates that not all the locations with $1901 \leq y_w \leq 1910$ cross the 0°C line during the first decade of the $20^{th}$ century.

- Although there is some ambiguity regarding the determination of $y_0$ when a model crosses 0°C more than one time, the histograms (Model 3: Figure 5.51, MARS: Figure 5.99, R method: Figure 5.148) reveal that the majority of the locations in the final databases have only one positive 0°C crossing accepted as $y_0$.
- Histograms reveal that for most of the locations $S_{W_{total}}$ is the same as $S_{interest}$. This is indicative of one of the following three situations that are mentioned in descending order of number of locations under each group:
  (a) $S_{interest}$ is the last segment.
  (b) $S_{interest}$ is followed by a segment with a negative slope (MARS, Model 2, and Model 3) or smaller mean (R method) but still above the 0°C line. In such cases, the increase in temperature does not continue right after $S_{interest}$. However, the important points are the change in the sign of temperature as well as the fact that the segments following $S_{interest}$ remain above 0°C. In the case of MARS and the R method, warming may resume later or temperature fluctuates above the 0°C line.
  (c) $S_{interest}$ is followed by a segment with a negative slope (MARS) or smaller mean (the R method), and the model crosses 0°C in the negative direction; however, it turns positive in a short time.

3. **Duration, Accumulation, and Slope**
Figures 5.2 (Model 2), 5.48 (Model 3), 5.96 (MARS), and 5.145 (R method) are provided to visualize the distributions of duration and accumulation over different time periods. Since these two concepts could not be interpreted separately in the

frame of this discussion, the histograms of their quotient (slope) are presented in Figures 5.3 (Model 2), 5.49 (Model 3), 5.97 (MARS), and 5.146 (R method). Following conclusions could be drawn from these figures:

(a) MARS: Slope (1) and Slope (2) (Section 5.2) exhibit the exponential decay of number of locations as slope increases. Slope (1) and Slope (2) of the majority of the locations modelled by MARS are in the range of $0.03 - 0.06$ (°C/year) and $0 - 0.03$ (°C/year), respectively.

(b) Model 2: Slope (1) and Slope (2) (Section 5.2) exhibit positive skewness with the mode of approximately $0.03 - 0.05$ (°C/year) and $0.01 - 0.04$ (°C/year), respectively.

(c) Model 3: Slope (1) and Slope (2) (Section 5.2) exhibit positive skewness with the mode of approximately $0.02 - 0.05$ (°C/year).

(d) the R method: Similar to Models 2 and 3, positive skewness is observed in the histograms of Slope (1) and Slope (2) (Section 5.6.1). The modes are approximately $0.01 - 0.03$ (°C/year) in both cases.

**Note:** The means of Slope (1) and Slope (2) are larger using Model 3; a considerable number of locations show Slope (1) and Slope (2) in the range of $0.1 - 0.15$ (°C/year), whereas, in the case of Model 2, only a very small subset of the final database exhibit slopes larger than 0.1 (°C/year). Similar results apply to MARS; only a few locations exceed the value of 0.15 (°C/year). The slopes reported using the R method are generally smaller than the other techniques. According to Figure 5.146, the number of locations with Slope (1) and Slope (2) larger than 0.04 (°C/year) is negligible.

4. **Theil Slope**

Theil slope, a robust estimate of the rate of change, is also evaluated for all the three time periods of $y_w$-$y_0$, $S_{interest}$, and $S_{W_{total}}$ if the model is MARS, Model 2, or Model 3 (Figures 5.4, 5.50, and 5.98). In the case of the R method (Figure 5.147), Theil Slope (1) and Theil Slope (2) are estimated using the data points within the time periods determined as 'Duration' and 'Total Duration' (Section 5.6.1). The goal is to compare this non-parametric estimate to the parametric estimates obtained from different techniques. The following points should be highlighted as a result of this comparison:

(a) Using any technique except the R method, for which $y_w$ is not defined, Slope (1) is the slope of both time periods of $y_w$-$y_0$, $S_{interest}$. However, Theil slope estimates of these two time periods are different. Theil slope estimates of $y_w$-$y_0$ are negative for some locations. However, the results of the MK test reveal that none of the locations with negative Theil slope estimates exhibit significant decreasing trends. The same conclusion applies to the grid cells with negative Theil slope (1) or Theil Slope (2) in the case of the R method.

(b) The distributions of Theil slope during $S_{interest}$ and $S_{W_{total}}$ determined by Models 2 and 3 are very close to the distributions of Slope (1) and Slope (2). For MARS, slight differences are observed. The distributions of Theil slope exhibit positive skewness rather than exponential decay. However, the ranges of slopes are close. In the case of the R method, overall, Theil slope histograms resemble those of Slope (1) and Slope (2); however, there are a small number of locations with negative and insignificant Theil slopes.

5. **H**

To understand whether significant warming has occurred during the time period of $y_w$-$y_0$, $S_{interest}$, or $S_{W_{total}}$, the MK is performed using the original data within these sections. If the magnitude of the increase in temperature is not significant during $S_{interest}$ or $S_{W_{total}}$, it implies that the observed positive 0°C crossing ($y_0$) may only reflect the fluctuations of temperature. According to Figures 5.4 (Model 2), 5.50 (Model 3), 5.98 (MARS), and 5.147 (R method), generally, insignificant trends are reported for the period of $y_w$-$y_0$, whereas most of the trends over $S_{interest}$ and $S_{W_{total}}$ are significant.

#### 5.8.3.2 MAM

The points highlighted regarding the specific behaviours of the models, such as the discussion on the $y_0$ values in the range of 1900-1910, are explained in detail when investigating the JFM results. In this section, only the results drawn from the MAM histograms are presented. It is very important to note again that the MAM results apply to completely different grid cells from those of JFM. These are the regions whose temperature is negative during JFM from 1901 to 2009. However, the MAM temperature of these locations has changed sign from negative to positive during the period of 1901-2009. As depicted by the

MAM maps, these grid cells are located in higher latitudes.

1. **$y_w$**
   Similar to JFM, the $y_w$ histograms (Model 2: Figure 5.5, Model 3: Figure 5.51, MARS: Figure 5.100) do not show any specific behaviour; however, the following points should be highlighted:

   - For any technique except the R method, to which $y_w$ does not apply, one of the peaks of the $y_w$ histogram occurs during the first decade of the $20^{th}$ century. In the case of Models 2 and 3, $y_w$'s of all the locations comprising the first columns are equal to 1901. In addition to the 1900s decade, the following periods, which are mentioned in ascending order of number of locations, embed the maximum numbers of locations:
     MARS: 1920s and 1960s. Based on the $y_w$ histogram of MARS, it could be concluded that overall, in most of the locations, $y_w$ occurs in the first half of the $20^{th}$ century.
     Model 2: 1920s and 1970s
     Model 3: 1950s
   - The form of the break time histogram of Model 3 is close to its $y_w$ histogram. In the case of Model 2, in most of the locations, breaks occur in the latter half of the $20^{th}$ century. The same trend is not observed in the $y_w$ histogram. The large number of locations with $y_w = 1901$ in this case implies that the second segment of Model 2 in the majority of locations is above 0°C, and the first segment is $S_{interest}$.
   - In contrast to JFM, the behaviours of the break time histograms of Models 2 and 3 are not similar.
   - As indicated earlier, in the case of Models 2 and 3, the $y_w$ values of all the locations that fall under the category of 1900-1910 are equal to 1901. However, for MARS, 135 locations exhibit $1902 \leq y_w \leq 1910$. This implies that any location from this category has a very short (less than 10 years) first segment followed by $S_{interest}$ (For further details on such cases, refer to the $y_w$ section of JFM indicated above (Page 297))

2. **$y_0$**

- The $y_0$ histogram of MARS (Figure 5.100) illustrates that during MAM, the number of locations whose temperatures turn positive is increasing uniformly from the beginning of the $20^{th}$ century. In both cases of Models 2 and 3 (Model 2: Figure 5.5, Model 3: Figure 5.52), a considerable number of locations experience $y_0$ occurring in the first half of the $20^{th}$ century. The numbers of locations within each time category are approximately equal and half of the numbers observed within the second half of the $20^{th}$ century and the first decade of the $21^{st}$ century. The most noticeable difference between the $y_0$ histograms of the locations analysed during JFM and MAM, using MARS and Models 2 and 3 is that the MAM histograms do not exhibit the exponential growth observed in the JFM case. This observation as well as the $y_w$ histograms, which are denser in the beginning during MAM compared to JFM, may imply that although the JFM temperatures of these locations are still negative during the past century, warming during MAM has started from the beginning of the $20^{th}$ century (or perhaps earlier). The analysis of the JFM time series of these locations to understand the warming trend is beyond the scope of this research. It is possible that significant increases in temperature have occurred during JFM; however, since the temperatures were well below 0°C, no 0°C crossing is observed. The $y_0$ histogram of the R method is similar to the JFM histogram in that the mean levels of most of the locations in the final database have risen above 0°C during 1980-2009. A very small number of locations experience earlier 0°C crossings.
- As observed in the JFM histograms, except for the R method, all the techniques show locations whose $y_0$'s fall within the 1900s decade. All possible cases and notes on these locations are provided in the above-indicated $y_0$ section for JFM (Page 298). The numbers of locations with this characteristic are still small compared to the large final databases: 67, 118, and 138 for MARS, Model 2, and Model 3, respectively.
- As with JFM, the majority of locations modelled by MARS, Models 3, and the R method have only one positive 0°C crossing accepted as $y_0$ (Model 3: Figure 5.56, MARS: Figure 5.104, R method: 5.153). Hence, the uncertainty regarding the definition of $y_0$ for locations with more than one positive 0°C crossing influences small subsets of the final databases.
- In most of the locations, $S_{interest}$ is the same as $S_{W_{total}}$. All possible cases are listed in the $y_0$ section for JFM indicated in Page 299.

3. **Duration, Accumulation, and Slope**
   Figures 5.6 (Model 2), 5.53 (Model 3), 5.101 (MARS), and 5.150 (R method) depict the accumulation and duration histograms. These two concepts are analysed jointly as slope (Model 2: Figure 5.7, Model 3: Figure 5.54, MARS: Figure 5.102, R method 5.151). Slope (1) and Slope (2) exhibit positive skewness using any modelling technique. The results obtained from the slope histograms are as follows:

   (a) Since in the majority of locations, $S_{interest}$ and $S_{W_{total}}$ are the same, the distribution of Slope (2) strongly resembles that of Slope (1). The modes of the Slope (1) and Slope (2) histograms of MARS, Model 2, Model 3, and the R method are approximately 0.01-0.05, 0.01-0.04, 0.03-0.07, and 0.01-0.03 (°C/year), respectively.

   (b) The means of MARS, Model 2, Model 3, and the R method are approximately 0.1, 0.1, 0.15, and 0.04 (°C/year), respectively. Similar to the JFM analysis, modelling by the R method yields the smallest slopes.

4. **Theil Slope**
   Figures 5.8 (Model 2), 5.55 (Model 3), 5.103 (MARS), and 5.152 (R method) illustrate the histograms of Theil Slope. The following points should be highlighted from the histograms:

   - Some locations with negative slopes are observed in the histograms of Theil slope over $y_w$-$y_0$; however, based on the results of the MK test, none of these decreasing trends are significant. Similarly, the negative slopes in the histograms of Theil Slope (1) and Theil Slope (2) for the R method are insignificant.
   - In terms of the form of distribution, range, mode, and mean, the distributions of Theil Slope over $S_{interest}$ and $S_{W_{total}}$ resemble those obtained by different modelling techniques.

5. **H**
   According to Figures 5.8 (Model 2), 5.55 (Model 3), 5.103 (MARS), and 5.152 (R method), generally, insignificant trends are reported for the period of $y_w$-$y_0$, whereas most of the trends over $S_{interest}$ and $S_{W_{total}}$ are significant. For more details, refer to the discussion on H histograms indicated in Page 301.

### 5.8.4 Maps

A comprehensive discussion on the maps is provided below. The discussion first focuses on the JFM results and is followed by MAM results. Under each category, the *transition area* is divided into three parts, North America, Europe, and Asia. For each continent, the behaviour of all the techniques are compared.

#### 5.8.4.1 JFM

- **North America**
  Due to the high degree of spatial variability of the results, particularly those of MARS and Model 2, over North America, the *transition area* in North America is divided longitudinally into three regions: i) Western U.S.: 125°W − 105°W, ii) Central U.S.: 105°W−90°W, iii) Eastern U.S.: 90°W−70°W. The $y_w$, $y_0$, Slope (1), Slope (2), H of $S_{interest}$, and H of $S_{W_{total}}$ histograms of each of these regions are provided in Appendix B. In addition to the visual analysis of the maps, these histograms are investigated to make conclusions (MARS: Figures B.1 to B.3, Model 2: Figures B.8 to B.10, Model 3: Figures B.15 to B.17, R method: Figures B.22 to B.24). It should be noted that the discussion is limited to the locations with significant warming trends over $S_{interest}$ and $S_{W_{total}}$.

  1. **MARS**
     The analysis of the results of the MK test (Figures 5.122 and 5.123) reveals that the grid cells with insignificant warming during $S_{interest}$ and $S_{W_{total}}$ form approximately half of the total locations in North America. These grid cells are distributed (without a specific pattern) among the locations with significant increase in temperature. Furthermore, no specific trend or spatial integrity is observed.
     - In western U.S. (total of 97 locations with significant warming), the start of warming most commonly occurs during the 1900s, 1930s, and 1940s decades. $y_0$ of most of the locations is reported to be in the range of 1960-2000 (Figure B.1) .
     - Most of the grid cells in central U.S. (total of 37 locations with significant warming) exhibit insignificant warming. The start of warming among those

pixels with significant increasing trend takes place most commonly during the 1920s decade. The pixels cross 0°C ($y_0$) later in the 1960s decade and the time period of 1980-2009 (Figure B.2).

- In eastern U.S. (total of 48 locations with significant warming), $y_w$ of most of the locations happens some time in the first decade of the $20^{th}$ century or during the time period of 1950-1980. The 0°C crossing ($y_0$) occurs during 1960-2009 (Figure B.3).

Slope (1) and Slope (2) of the majority of grid cells fall within the range of $0.004 - 0.06$ (°C/year).

2. **Model 2**

   - In western U.S. (total of 135 locations with significant warming), the start of warming most commonly occurs during the 1940s decade. The majority of $y_0$'s fall within the range of 1960-2008 (Figure B.8).
   - As depicted by Figures 5.26 and 5.27, most of the locations in central U.S. exhibit insignificant warming trends. Only 39 locations show significant increase in warming that starts in the 1960s decade in most of the grid cells. $y_0$'s most commonly take place after 1960 with a peak in the 1980s decade (Figure B.9).
   - Only 13 locations, majority of which are located in northeastern U.S., exhibit significant warming trends that started in the 1970s decade. $y_0$ is distributed over the entire century with a small peak in the 1990s (Figure B.10).

   Slope (1) and Slope (2) of the majority of locations in western U.S. fall within the range of $0.015 - 0.05$ (°C/year). In central U.S., the histograms are dense in the range of $0.04 - 0.05$ (°C/year). In eastern U.S., no specific trend is observed.

3. **Model 3**
   In contrast to MARS and Model 2, Model 3 detects few locations with insignificant trends during $S_{interest}$ and $S_{W_{total}}$ (Figures 5.74 and 5.75). In other words, it builds the segments such that the increasing trends are significant.

   - In western U.S. (total of 96 locations with significant warming), warming begins in the 1940s in most of the locations. The peak of $y_0$ happens during

the 1960s. A considerable number of locations experience $y_0$ in the following decades (Figure B.15).

- In central U.S. (total of 101 locations with significant warming), $y_w$ in the majority of the locations occurs in the 1950s. $y_0$ is distributed evenly during the time period of 1960-2008 (Figure B.16). The inspection of Figure 5.62 reveals that there is a pattern in the spatial distribution of $y_0$: the higher the latitude is, the larger the value of $y_0$ is.
- In eastern U.S. (total of 86 locations with significant warming), $y_w$'s occur during the 1950s. Similar to central U.S., $y_0$ is distributed over the time period of 1960-2008 and shows the same pattern as that of central U.S. (Figure B.17).

Slope (1) and Slope (2) of the majority of locations are approximately in the range of $0.015-0.04$, $0.015-0.06$, and $0.03-0.05\,(^{\circ}\mathrm{C/year})$ in western, central, and eastern U.S., respectively.

4. **R method**

The R method selects the minimum number of locations compared to the other techniques. Particularly, over eastern regions, it analyses only few locations (13 locations). It is worthwhile to note again that the R method detects the shifts in the mean levels of the time series. Therefore, it produces unique results. The reader is referred to Section 5.8.1 for detailed information on the distinct characteristics of this technique. As indicated below, $y_0$'s reported by this method, which determines the time of sign change in mean levels, occur later compared to the other techniques. Another point that should be highlighted is the spatial integrity of the results.

- In western U.S. (total of 62 locations with significant warming), the means of time series change sign from negative to positive ($y_0$) during the 1990s decade (Figure B.22).
- In Central U.S. (total of 41 locations with significant warming), all $y_0$'s occur in the time period of 1980-2009 (Figure B.23).
- Similar to the results of Model 2, only 13 locations, most commonly located in northeastern U.S., exhibit significant warming. $y_0$'s are distributed over the 1920s, 1940s, 1980s, and 1990s decades with no specific pattern (Figure B.24).

**Table 5.12:** All the results indicated in Section 5.8.4.1 for North America are summarized in the table below. * Only locations that exhibit significant warming trends are considered to draw conclusions about the spatial distributions of $y_w$ and $y_0$. $\mathbf{N_t}$ is the total number of locations in the specified region that are in the final database. $\mathbf{N_s}$ is the number of locations in the subset of $N_t$ that experience significant increase in temperature.

| **Model** | **Regions** | | | | | | | | | | | |
|---|---|---|---|---|---|---|---|---|---|---|---|---|
| | **Western U.S.** | | | | **Central U.S.** | | | | **Eastern U.S.** | | | |
| | $\mathbf{N_t^*}$ | $\mathbf{N_s^*}$ | $\mathbf{y_w}$ | $\mathbf{y_0}$ | $\mathbf{N_t}$ | $\mathbf{N_s}$ | $\mathbf{y_w}$ | $\mathbf{y_0}$ | $\mathbf{N_t}$ | $\mathbf{N_s}$ | $\mathbf{y_w}$ | $\mathbf{y_0}$ |
| **MARS** | 154 | 97 | 1900s 1930s 1940s | 1960-2000 | 85 | 37 | 1920s | 1960s 1980-2009 | 80 | 48 | 1900s 1950-1980 | 1960-2009 |
| **Model 2** | 191 | 135 | 1940s | 1960-2008 | 106 | 39 | 1960s | 1980-2000 | 63 | 13 | 1970s | 1990s |
| **Model 3** | 127 | 96 | 1940s | 1960-2008 | 114 | 101 | 1950s | 1960-2008 | 100 | 86 | 1950s | 1960-2008 |
| **R method** | 86 | 62 | N/A | 1990s | 65 | 41 | N/A | 1980-2009 | 21 | 13 | N/A | No Pattern |

Except for eastern U.S. with a negligible number of locations, Slope (1) and Slope (2) fall within the range of $0.01 - 0.02$ (°C/year) over the entire region. Therefore, as illustrated earlier by the histograms of the R method (Section 5.6.4), smaller slopes are reported by this technique.

All the above-mentioned results are summarized in Table 5.12.

- **Europe**
  In Europe, the region under study is confined to the longitudes of 30°W and 45°E (Sections 5.4.3.2 (Model 2), 5.4.4.2 (Model 3), 5.5.3.2 (MARS), and 5.6.4.2 (R method)). The density of the selected locations by any of the modelling techniques is higher in eastern Europe. However, except northern Europe, the grid cells are distributed over entire Europe. The results below are obtained by inspecting the locations with significant increase in temperature.

  1. **MARS**
     There are 181 locations with insignificant warming during $S_{\text{interest}}$ (Figure 5.122). Excluding these locations, 338 locations remain to investigate. As observed in

Figures 5.107 and 5.111, in contrast to North America, $y_w$'s and $y_0$'s exhibit a pattern. The two variables increase with latitude. According to Figure B.4, $y_w$ occurs during the 1930s decade in the majority of locations. As is inferred from the comparison of Figures 5.107 and 5.122, in most of the locations with large values of $y_w$ ($y_w > 1980$), warming is not significant over $S_{interest}$. The time of 0°C crossing ($y_0$) is most commonly within the range of 1940-2009 (Figure B.4). As depicted by Figure 5.111, $y_0$ increases in the diagonal direction from southern Europe toward eastern Europe. In the similar fashion, Slope (1) and Slope (2) increase from approximately 0.004 to 0.1 (°C/year) (Figures 5.115 and 5.119).

2. **Model 2**
   The map of $y_w$ (Figure 5.11) shows high spatial integrity. Most of 126 locations with insignificant warming are concentrated in southern Europe, and the rest of the grid cells (504 grid cells) exhibit significant increase in temperature over $S_{interest}$. According to $y_w$ histogram of Europe (Figure B.11), if locations with insignificant warming in southern Europe and eastern Europe (Romania) are excluded, $y_w$ of the remaining locations takes place during the 1920s and 1940-1970; in higher latitudes, $y_w$ occurs later. The year of 0°C crossing ($y_0$) falls within the time period of 1960-2008 for most of the locations. Similar to MARS, $y_0$ values increase from west to east in the diagonal direction. In the north of Black Sea, in eastern Europe, $y_0$ increases with latitude. The values of Slope (1) and Slope (2) are in the range of $0.02 - 0.1$ (°C/year) and increase in the same way as $y_0$.

3. **Model 3**
   Similar to North America, the first noticeable point is the small number of grid cells with insignificant warming (33 out of 351 locations selected by Model 3). $y_w$ in higher latitudes occurs in the 1930s. The locations in lower latitudes experience $y_w$ earlier in the 1920s (Figure 5.59). $y_0$ values of most of the locations increase from west to east and from south to north in the range of 1940-2008 (Figure 5.63). Slope (1) and Slope (2) increase with latitude from approximately 0.02 to 0.04 (°C/year) (Figures 5.67 and 5.71).

4. **R method**
   Over Europe, the minimum number of locations in the final database is selected by Model 3. However, in terms of locations with significant warming, the R

method builds the smallest subset, which contains 185 grid cells (out of 541 locations selected for the final database using the R method). Most of these grid cells are concentrated in eastern Europe (in the north of Black Sea and in the south of Baltic Sea) (Figures 5.166 and 5.167). $y_0$'s of the majority of these locations occur in the 1980s (Figure 5.156), and Slope (1) and Slope (2) for these locations are in the range of 0.01 to 0.03 (°C/year) (Figures 5.160 and 5.164).

Table 5.13 summarizes the results obtained using different techniques over Europe. The comparison of Figures 5.74 and 5.122 reveals that in terms of locations selected for the final database, MARS and Model 3 strongly resemble each other over Europe. The advantage of Model 3 is that following Rules 1 and 2 of *transition area* (Section 4.3), Model 3 does not select most of the locations that are selected by MARS and then proved to experience insignificant increase in temperature. The overall spatial distribution of Model 2 is close to that of MARS if all the locations with significant and insignificant warming in the map of MARS are considered. However, Model 2 approximates time series such that, particularly over Poland, the results of the MK test favour significant increasing trends, whereas the same results are not obtained for MARS. If all the grid cells (with significant or insignificant increasing trends) selected by the models were considered, the spatial distribution of the R method would be close to those of the other methods. However, the R method builds the segments such that only in the north of Black Sea (in Ukraine) and in the south of Baltic Sea (in Poland) is significant warming over $S_{interest}$ observed.

- **Asia**
  The vast region of Asia is divided into three parts for the analysis: i) Southwestern and Central Asia (45°E to 75°E), ii) Central-Eastern Asia (75°E to 100°E), iii) Eastern Asia (100°E to 150°E). The *transition area* in southwestern and central Asia covers a small region that consists of some parts of Turkmenistan, Uzbekistan, Kazakhstan, and Iran. In central-eastern Asia, only a small region in western China meets the criteria set by Rules 1 and 2 of *transition area*. This region is located in the north of Tibet and south of Xinjiang and is surrounded by high mountains and shows interesting results. Most of the region lies in the Taklamakan Desert, and it will be referred to as 'western China' hereafter. In eastern Asia, the final database only includes some grid cells from east central China, South Korea, and Japan. Sim-

**Table 5.13:** All the results indicated in Section 5.8.4.1 for Europe are summarized in the table below. * Only locations that exhibit significant warming trends are considered to draw conclusions about the spatial distributions of $y_w$ and $y_0$. $\mathbf{N_t}$ is the total number of locations in the specified region that are in the final database. $\mathbf{N_s}$ is the number of locations in the subset of $N_t$ that experience significant increase in temperature.

| **Model** | **Europe** | | | |
|---|---|---|---|---|
| | $\mathbf{N_t^*}$ | $\mathbf{N_s^*}$ | $\mathbf{y_w}$ | $\mathbf{y_0}$ |
| **MARS** | 519 | 338 | most commonly in the 1930s: $y_w$ increases with latitude | most commonly within the range of 1940-2009: $y_0$ values increase in the diagonal direction from southern Europe toward eastern Europe |
| **Model 2** | 630 | 504 | 1920s and 1940-1970: $y_w$ increases with latitude | 1960-2008: $y_0$ values increase from west to east in the diagonal direction. In the north of Black Sea, in eastern Europe, $y_0$'s increase with latitude. |
| **Model 3** | 351 | 318 | 1920s in lower latitudes, 1930s in higher latitudes | increase from west to east and from south to north in the range of 1940-2008 |
| **R method** | 541 | 185 | N/A | 1980s (Grid cells with significant warming are concentrated in the north of Black Sea and south of Baltic Sea.) |

ilar to the other parts of the Northern Hemisphere, only locations with significant increasing trends are considered to make conclusions. Detailed histograms for each region of Asia are provided in Appendix B (MARS: Figures B.5 to B.7, Model 2: Figures B.12 to B.14, Model 3: Figures B.19 to B.21, R method: Figures B.26 to B.28).

1. **MARS**
   In Asia, the numbers of locations with insignificant trends over $S_{\text{interest}}$ and $S_{W_{\text{total}}}$ are small (Figures 5.122 and 5.123), and these grid cells are distributed over the entire *transition area* in Asia.
   - In most of the locations in southwestern and central Asia as well as eastern Asia, $y_w$ occurs during the 1970s and 1960s decades, respectively. Over western China, first, $y_w$ increases in the west to east direction (from 1930s

to 1970s), which is followed by a decrease (from 1960s to 1950s) (Figure 5.108).

- Over southwestern and central Asia, $y_0$ increases with latitude. However, no specific trend is observed in western China and eastern Asia, except generally smaller values of $y_0$ in the west of the region termed 'western China' compared to the rest of the grid cells in that region. $y_0$ is in the range of 1970-2009 in Asia (Figure 5.112).
- The largest values of Slope (1) and (2) are observed in central Asia. In the rest of the *transition area*, Slope (1) and Slope (2) are in the range of $0.004 - 0.1$ (°C/year) (Figures 5.116 and 5.120).

2. **Model 2**
   Most of the locations in southwestern Asia show insignificant warming over $S_{interest}$ and $S_{W_{total}}$. In central Asia, grid cells that are located in Uzbekistan do not show significant increasing trends either (Figures 5.26 and 5.27).
   - Excluding pixels indicated above, in terms of $y_w$ values, a high spatial integrity is observed in central Asia and western China. $y_w$ of the majority of locations occurs during the 1970s decade in central Asia and western China. Similar to the results obtained using MARS, in western China, a bell-shaped behaviour of $y_w$ is observed. This implies that $y_w$ values increase from 1930s (in the west) to 1970s (in the center) and decline to 1960s (in the east). In Eastern Asia, $y_w$ occurs during the 1960s and 1980s decades in China and during the time period of 1901-1940 in most of the locations in Japan and South Korea (Figure 5.12).
   - As with MARS, over central Asia, $y_0$ increases with latitude. In western China, earlier $y_0$'s are observed in the west of that region; however, overall, no specific trend is detected. The same conclusion applies to eastern Asia. $y_0$ of the majority of grid cells is in the range of 1970-2008 (Figure 5.16).
   - Slope (1) and Slope (2) of most of the locations over central Asia, western China, and eastern Asia are in the range of $0.02 - 0.15$, $0.03 - 0.1$, and $0.02 - 0.13$ (°C/year), respectively. It should be noted that the minimum values are concentrated over easternmost Asia (Figures 5.20 and 5.24).

3. **Model 3**
   Similar to other continents, most of the locations selected by Model 3 show

significant warming in $S_{interest}$ and $S_{W_{total}}$ (Figures 5.74 and 5.75).

- The spatial integrity of the $y_w$ values is more significant compared to Model 2. $y_w$ in most of the locations in southwestern and central Asia, western China, and eastern Asia occurs during the 1960s decade. It should be noted that although the dominant decade of $y_w$ is the 1960s in western China, similar to Model 2, distinct boundaries exist. $y_w$ most commonly occurs during the 1920s, 1960s, and 1940s decades in the west to east direction (Figure 5.60).
- The $y_0$ patterns observed in Figure 5.64 are clearer than Model 2. The values reported by Model 3 are in the range of 1960-2008. In central Asia, $y_0$ increases with latitude. In western China, similar to MARS and Model 2, the minimum values of $y_0$ are concentrated in the west of the region.
- Slope (1) and Slope (2) have larger values in southwestern and central Asia ($0.02 - 0.14$ (°C/year)). Slopes are larger in western and eastern China compared to the slopes in easternmost Asia. The values are within the range of $0.03 - 0.1$ (°C/year) in western China with the minimum values in the west of the region. Over eastern Asia, values generally fall within $0.06 - 0.08$ (°C/year) except the grid cells in easternmost Asia. These locations have smaller slopes (approximately $0.02 - 0.04$ (°C/year)) (Figures 5.68 and 5.72).

4. **R method**

According to Figures 5.166 and 5.167, few locations show insignificant warming over $S_{interest}$ and $S_{W_{total}}$.

- In southwestern and central Asia, the highest spatial integrity is observed in the $y_0$ results of the R method. The time of 0°C crossing ($y_0$) for almost all the locations is in the 1990s decade. It should be noted that the pattern observed using the other techniques (increase of $y_0$ with latitude) is replaced by very close values of $y_0$ in this part of Asia. In western China and eastern Asia, no pattern is observed, except that similar to the other techniques, minimum values in western China are concentrated in the west of the region. In western China and eastern Asia, $y_0$ generally occurs in the time periods of 1970-2000 and 1980-2000, respectively (Figure 5.157).
- As with the other parts of the Northern Hemisphere, the R method reports

the smallest slopes. Slope (1) and Slope (2) in southwestern and central Asia as well as eastern Asia are in the range of $0.01 - 0.03$ (°C/year). Over Asia, the minimum slopes are observed in western China ($0.005 - 0.01$ (°C/year)) (Figures 5.161 and 5.165).

Table 5.14 summarizes the results obtained using different techniques over Asia.

#### 5.8.4.2 MAM

Similar to JFM, only locations whose temperature exhibits significant warming over $S_{interest}$ and $S_{W_{total}}$ are analysed. The numbers of locations with significant trends for all the methods are indicated in Tables 5.15 (North America) and 5.16 (Eurasia). Furthermore, the spatial distributions of the grid cells with significant increase in temperature over $S_{interest}$ and $S_{W_{total}}$ are illustrated by Figures 5.45 and 5.46 (Model 2), 5.93 and 5.94 (Model 3), 5.141 and 5.142 (MARS), as well as 5.180 and 5.181 (R method).

- **North America**

  1. **MARS**

     - As depicted by Figures 5.125 and B.29, $y_w$ in many locations occurs in the first decade of the 20$^{th}$ century.
     - $y_0$ increases with latitude, and it is approximately evenly distributed in the range of 1920-2000 (Figures 5.129 and B.29).
     - Slope (1) and Slope (2) are in the range of $0.005 - 0.04$ (°C/year) (Figures 5.133, 5.137, and B.29).

  2. **Model 2**

     - According to Figures 5.29 and B.31, the start of warming in the majority of grid cells is during 1900-1920. In the west-central grid cells, $y_w$ occurs in the 1900s, and in the central-eastern locations, the values most commonly fall within the second decade of the 20$^{th}$ century.

**Table 5.14:** All the results indicated in Section 5.8.4.1 for Asia are summarized in the table below. * Only locations that exhibit significant warming trends are considered to draw conclusions about the spatial distributions of $y_w$ and $y_0$. $\mathbf{N_t}$ is the total number of locations in the specified region that are in the final database. $\mathbf{N_s}$ is the number of locations in the subset of $N_t$ that experience significant increase in temperature.

| **Model** | **Regions** | | | | | | | | | | | |
|---|---|---|---|---|---|---|---|---|---|---|---|---|
| | **Southwestern and Central Asia** | | | | **western China** | | | | **Eastern Asia** | | | |
| | $\mathbf{N_t^*}$ | $\mathbf{N_s^*}$ | $\mathbf{y_w}$ | $\mathbf{y_0}$ | $\mathbf{N_t}$ | $\mathbf{N_s}$ | $\mathbf{y_w}$ | $\mathbf{y_0}$ | $\mathbf{N_t}$ | $\mathbf{N_s}$ | $\mathbf{y_w}$ | $\mathbf{y_0}$ |
| **MARS** | 303 | 269 | 1970s | Increase with latitude: 1970-2009 | 210 | 190 | In the west to east direction: 1930s, 1970s, 1960s, 1950s | No pattern: 1970-2009 | 150 | 124 | 1960s | No pattern: 1970-2009 |
| **Model 2** | 308 | 185 | 1970s | Increases with latitude: 1970-2008 | 228 | 201 | In the west to east direction: 1930s, 1970s, 1960s | No pattern: 1970-2008 | 145 | 130 | China: 1960s, 1980s, Japan and South Korea: 1901-1940 | No pattern: 1970-2008 |
| **Model 3** | 426 | 403 | 1960s | Increase with latitude: 1960-2008 | 233 | 231 | In the west to east direction: 1920s, 1960s, 1940s | No pattern: 1970-2008 | 117 | 98 | 1960s | No pattern: 1970-2008 |
| **R method** | 283 | 253 | N/A | Almost all locations: 1990s | 206 | 171 | N/A | No pattern: 1970-2000 | 143 | 112 | N/A | No pattern: 1980-2000 |

- $y_0$ of the majority of the west-central grid cells falls within the range of 1900-1950, and the pattern observed in this region is not as strong as the pattern in the central-eastern part where $y_0$ values increase with latitude. $y_0$ in the central-eastern region generally takes place during 1910-2000 (Figures 5.33 and B.31). It is worth noting again that locations that experience both $y_0$ and $y_w$ in the first few decades of the $20^{th}$ century might be modelled by positive segments if more data points were available prior to 1901.
- Slope (1) and Slope (2) of most of the locations are within the range of $0.01 - 0.04\,(°C/year)$. Slopes are slightly larger in the west compared to the east (Figures 5.37, 5.41, and B.31).

3. **Model 3**
   - Similar to MARS and Model 2, $y_w$ values reported by Model 3 occur in the 1900s. Although there are a lot of grid cells in the center of the *transition area* that do not meet the criteria set by Rules 1 and 2 of *transition area*, the same pattern as Model 2 is observed; in the western grid cells, $y_w$ occurs during the 1900s, whereas, generally, it takes place later in the east (Figures 5.77 and B.33).
   - $y_0$ is generally in the range of 1900-1940 (Figures 5.81 and B.33).
   - Slope (1) and Slope (2) are reported to be in the range of $0.001-0.07(°C/year)$ (Figures 5.85, 5.89, and B.33).
4. **R method**
   - As depicted by Figures 5.169 and B.35, few locations experience $y_0$. $y_0$ of these grid cells could be categorized into two time periods of 1970s and 1990s. The selection of these grid cells may be due to the maritime climate variability in these areas (Bonsal and Prowse, 2003).
   - Slope (1) and Slope (2) of this small subset are in the range of $0.008 - 0.02\,(°C/year)$ (Figures 5.173, 5.177, and B.35).

   Table 5.15 summarizes the above-indicated results for North America during MAM.

- **Eurasia**

  Prior to investigating the maps of Eurasia, it should be noted that over Eurasia,

**Table 5.15:** All the results indicated in Section 5.8.4.2 for North America are summarized in the table below. * Only locations that exhibit significant warming trends are considered to draw conclusions about the spatial distributions of $y_w$ and $y_0$. $\mathbf{N_t}$ is the total number of locations in the specified region that are in the final database. $\mathbf{N_s}$ is the number of locations in the subset of $N_t$ that experience significant increase in temperature.

| **Model** | **North America** | | | |
|---|---|---|---|---|
| | $\mathbf{N_t^*}$ | $\mathbf{N_s^*}$ | $\mathbf{y_w}$ | $\mathbf{y_0}$ |
| **MARS** | 594 | 465 | 1900s | 1920-2000 |
| **Model 2** | 554 | 411 | West:1900s, East: 1910s | 1910-2000 |
| **Model 3** | 303 | 207 | 1900s | 1900-1940 |
| **R method** | 79 | 61 | N/A | 1970s, 1990s |

the grid cells selected based on Rules 1 and 2 of *transition area* are located in lower latitudes in the eastern areas compared to the western regions. Furthermore, in contrast to JFM with disconnected regions over Eurasia (particularly in Asia), the *transition area* looks like a continuous band extending from northern Europe to eastern Asia. This implies that more locations experience $y_0$ during MAM. It is also worthwhile to note again that only the locations with significant increasing trends over $S_{\text{interest}}$ and $S_{W_{\text{total}}}$ are discussed below.

1. **MARS**
   - Generally, $y_w$ occurs earlier in western regions, i.e., over northern Europe (Sweden and Finland) and European Russia. Over Asia, in southern Russia, northern Mongolia, and northeastern China, $y_w$ increases with latitude. Looking at the big picture, $y_w$ generally increases in the west to east direction. However, moving toward easternmost Asia from the common boundaries of Russia, Mongolia, and China, $y_w$ decreases. In the western regions, $y_w$ of most of the locations is in the range of 1900-1940 . $y_w$ most commonly occurs in the 1950s in the grid cells located in the center and east of the band that extends from northern Europe to easternmost Asia (Figures 5.124 and B.30).

- According to the $y_0$ map (Figure 5.128), a clear pattern exists; $y_0$ increases with latitude. The histogram of $y_0$ values over Eurasia (Figure B.30) reveals that $y_0$ increases approximately uniformly from the beginning of the $20^{th}$ century.
- Slope (1) and Slope (2) are in the range of $0.005 - 0.1$ (°C/year). According to Figures 5.132, 5.136, and B.30, slopes are generally smaller over northern Europe and European Russia compared to the rest of the locations along the band.

2. **Model 2**
   - Similar to MARS, the highest values of $y_w$ are concentrated in the center and east of the band extending from northern Europe to easternmost Asia. However, a more detailed investigation reveals that the trends and values are different from MARS. Furthermore, the spatial integrity of the results is readily noticeable. In Europe, the value of $y_w$ decreases from west to east, from 1980 to 1910. In Asia, $y_w$ of most of the locations occurs in the 1970s, and generally, in a given longitude, $y_w$ increases with latitude. In the center of the band, in southern Russia, there is a region with a considerable number of grid cells whose $y_w$ occurs in the 1900s. Similar to MARS, moving eastward from the common boundaries of Mongolia and China, $y_w$ decreases (Figures 5.28 and B.32).
   - The $y_0$ pattern (increase with latitude) is clearer compared to MARS (Figure 5.32). According to the histogram of $y_0$ for Eurasia (Figure B.32), although the number of locations with $y_0$ in the range of 1900-1970 is considerable, the histogram is denser during the time period of 1970-2008. As indicated above, there is a large region over southern Russia (close to the common boundaries of Kazakhstan and Russia) where $y_w$ most commonly occurs during the 1900s. As is depicted by the $y_0$ map, some of the grid cells located in this region experience $y_0$ in the first decade of the $20^{th}$ century. This implies that these grid cells might be included in the category of locations whose models are positive during the entire period of study if more data points were available prior to 1901. The fact that the southern neighbours of these pixels are modelled by positive segments supports this idea.

- In the majority of locations, Slope (1) and Slope (2) are in the range of $0.01-0.1$(°C/year). Slopes in the center to east of the band are significantly larger than those of western (over Europe) and easternmost locations. It should be noted that the region in southern Russia where $y_w$ occurs in the 1900s decade exhibits smaller slopes compared to the rest of the locations in the center to east of the band (Figures 5.36, 5.40, and B.32).

3. **Model 3**
   Similar to the cases indicated earlier, Model 3 builds segments such that the minimum ratio of insignificant to significant trends over $S_{interest}$ and $S_{W_{total}}$ is observed.
   - According to Figure 5.76, the continuity observed using MARS and Model 2 is broken; however, similar to Model 2, the results are spatially coherent. The 1950s is the dominant decade of $y_w$ (Figure B.34). Over European Russia and easternmost Asia, $y_w$ takes place earlier during 1920-1940. Along the band, most commonly over southern Russia, there are disconnected regions with a considerable number of locations whose $y_w$ occurs in the 1900s.
   - As with MARS and Model 2, $y_0$ generally increases with latitude (Figure 5.80). As depicted by the $y_0$ histogram over Eurasia (Figure B.34), $y_0$ of most of the locations occurs during the second half of the $20^{th}$ century and the first decade of the $21^{st}$ century. In the region in southern Russia whose grid cells experience $y_w$ during the 1900s decade, $y_0$ most commonly occurs during the 1900s decade as well.
   - Slope (1) and Slope (2) of most of the locations fall within the range of $0.02 - 0.1$ (°C/year). However, along the band that extends from northern Europe to easternmost Asia, the slopes of western and easternmost regions are smaller than the central slopes, which are in the range of $0.05 - 0.14$ (°C/year) (Figures 5.84, 5.88, and B.34).

4. **R method**
   - In contrast to the other techniques, $y_0$ exhibits no pattern (Figure 5.168). Instead, the continuous band extending from northern Europe to easternmost Asia consists of approximately distinct regions of specific values of $y_0$ (similar to the $y_w$ maps of the other techniques). Over northern Europe

and European Russia, $y_0$ occurs during the time period of 1980-2009. In Asia, the majority of locations fall within the category of 1990s. Similar to Model 2 and Model 3, in southern Russia (close to the common boundaries of Kazakhstan and Russia), there is a region that includes a considerable number of grid cells experiencing $y_0$ early in the first decade of the $20^{th}$ century. In easternmost Asia, rather smaller values of $y_0$ are observed than the majority of locations in the center and east of the band (1960-1980) (Figure B.36). The grid cells with large values of $y_0$ located in easternmost Asia are in the category of the locations with insignificant increasing trends over $S_{interest}$ and $S_{W_{total}}$.

- The R method produces the smallest slopes. Slope (1) and Slope (2) are most commonly in the range of $0.01 - 0.03$ (°C/year). Slopes are generally smaller in the west of the band compared to the center and east of it (Figures 5.172, 5.176, and B.36).

The summary of all the above-mentioned points with regard to Eurasia during MAM is indicated in Table 5.16.

### 5.8.5 Picking the Best Model

The graphical comparison of the techniques reveals that the $y_0$ results of Model 2, Model 3, and MARS are close (Section 5.8.2: Figures 5.182 and 5.183). Furthermore, the similarity of the $y_0$ results of MARS, Model 2, and Model 3 is supported by Wilcoxon signed-rank test for paired observations and Wilcoxon rank-sum test (refer to Tables 5.10 and 5.11). On the other hand, as discussed in the previous sections (Sections 5.8.3 and 5.8.4), the histograms and maps of JFM and MAM exhibit different results over some regions of the Northern Hemisphere. Particularly over North America and during MAM, very significant differences between the techniques are observed. Several points should be noted to understand and solve this contradiction:

- The graphical comparison of any two techniques only considers the common points selected by the two methods. Therefore, the fact that one of the techniques does not cover the grid cells of a specific region does not influence the comparison results. Furthermore, the approach applied to graphically compare the paired results of any

**Table 5.16:** All the results indicated in Section 5.8.4.2 for Eurasia are summarized in the table below. * Only locations that exhibit significant warming trends are considered to draw conclusions about the spatial distributions of $y_w$ and $y_0$. $\mathbf{N_t}$ is the total number of locations in the specified region that are in the final database. $\mathbf{N_s}$ is the number of locations in the subset of $N_t$ that experience significant increase in temperature.

| **Model** | **Eurasia** | | | |
|---|---|---|---|---|
| | $\mathbf{N_t^*}$ | $\mathbf{N_s^*}$ | $\mathbf{y_w}$ | $\mathbf{y_0}$ |
| **MARS** | 1918 | 1538 | western regions: 1900-1940, central-eastern locations: 1950s | uniform increase with latitude: 1900-2009 |
| **Model 2** | 2142 | 1712 | Europe: west to east from 1980 to 1910, Asia: most commonly 1970s (a large region in southern Russia: 1900s) | increase with latitude, 1970-2008 |
| **Model 3** | 1924 | 1826 | Europe: west to east from 1950 to 1920, Asia: most commonly 1950s (disconnected regions with a considerable number of grid cells: 1900s) | increase with latitude, 1950-2008 |
| **R method** | 1781 | 1418 | N/A | no pattern or trend; northern Europe and European Russia: 1980-2009, Asia: 1990s (a large region in southern Russia: 1900s), easternmost Asia: 1960-1980 |

two techniques is not a precise statistical method. It is often used to gain some rough idea of the difference between methods. As an example, from $y_w$ graphs (Figure 5.184), it is readily observed that $y_w$'s are different.

- To statistically compare $y_0$ results of the paired observations, Wilcoxon signed-rank test for paired observations is applied. According to Table 5.10, which represents the results of the test, although the $y_0$ results of MARS-Model 2, MARS-Model 3, and Model 2-Model 3 are similar at the 5% significance level, the results are different if the significance level is assumed to be larger (e.g., 10%). As indicated earlier, during MAM, P-values are smaller. This implies that the $y_0$ results differ more during MAM. Furthermore, as mentioned in Section 3.6.1.2, care must be taken in analysing the environmental data using Wilcoxon signed-rank test. As an example, when the

observations within each group are correlated, the test becomes very conservative in rejecting the null hypothesis : $\mu_1 = \mu_2$ (Modarres et al., 2005).

- In regard to Wilcoxon rank-sum test, according to Table 5.11, large P-values are indicative of similar results. However, even in that case, particularly during MAM, P-values are rather small. For example, the $y_0$ results of MARS-Model 2 and Model 2-Model 3 could be considered different at the significance level of 10%. Furthermore, the goal of Wilcoxon rank-sum test is to investigate whether both techniques generally yield similar results. For instance, during MAM, significant differences between Model 3 and Model 2 or MARS are observed over North America; however, over Eurasia, the $y_0$ patterns are similar. Therefore, in Wilcoxon rank-sum test, since numbers are taken into account without considering the locations they refer to, the test favours the null hypothesis of equal means in such cases.

In this research, the analysis is based on the relatively short time series. Thus, it is very difficult to attribute definite functions to them. This was the reason that motivated the inclusion of various methods to analyse time series in this study. The specific points that distinguish these methods and help understand their advantages and disadvantages based on the research goals are discussed in detail in Chapters 2 and 3. In Section 5.8.1, the key characteristics of each technique (Section 5.8.1.1) and the connection between these methods and their theoretical frame work (Section 5.8.1.2) are highlighted again.

As described in Sections 5.8.1.1 and 5.8.1.2, from the mathematical point of view, a close connection exists between MARS, Model 2, and Model 3; MARS approximates time series with polynomials of degree zero or one that are continuous at the boundaries. Model 2 and Model 3 assume that the long-term changes follow a linear trend, and the climatic noises are modelled by an auto-regressive process. The significant differences between the results of MARS, Model 2, and Model 3, which are depicted by the histograms and maps over some regions of the Northern Hemisphere (Sections 5.8.3 and 5.8.4), indicate the necessity of a more in-depth comparison between these techniques. Since the most considerable differences are observed in North America and during MAM, an extensive investigation is performed on the grid cells of that region to understand the underlying reasons for observed differences.

The analysis starts with the comparison of Model 2 and Model 3. Following the assessment of the results of Model 2 and Model 3, MARS will be compared to Model 2 and

Model 3 (refer to Section 5.8.5.2). In regard to the R method, since it is conceptually different from the other techniques, different results were expected. The final discussion (Section 5.8.5.3) highlights some points on why the R method is included in this research despite its distinct mathematical basis.

#### 5.8.5.1 Model 2 versus Model 3

As indicated in Section 2.3.4, since climate can undergo abrupt shifts besides gradual changes (Ivanov and Evtimov, 2010), statistical tests developed to detect breaks in the structure of time series can be applied to the problem of finding break points in the trend function of climate time series. Abrupt shifts may occur in the slope and/or intercept of the trend function of a climate time series. Model 2 and Model 3 detect abrupt shifts in slope and simultaneous shifts in slope and intercept, respectively. To understand which of the two approximations is more in accord with the behaviour of the original temperature data, three cases are considered:

- **Case 1**
  Time series that i) are modelled by Model 3, ii) fulfil the criteria of Rules 1 and 2 of *transition area* (Section 4.3), iii) have significant increasing trends over $S_{interest}$ and $S_{W_{total}}$ selected by Model 3, iv) are not selected by Model 2 since either Rules 1 and 2 of *transition area* or trend significance over $S_{interest}$ and $S_{W_{total}}$ is not satisfied. In North America, during MAM, 77 time series (out of 207 grid cells selected by Model 3: Table 5.15) have the above characteristics.

- **Case 2**
  Time series that i) are modelled by Model 2, ii) fulfil the criteria of Rules 1 and 2 of *transition area* (Section 4.3), iii) have significant increasing trends over $S_{interest}$ and $S_{W_{total}}$ selected by Model 2, iv) are not selected by Model 3 since either Rules 1 and 2 of *transition area* or trend significance over $S_{interest}$ and $S_{W_{total}}$ is not satisfied. In North America, during MAM, 281 time series (out of 411 grid cells selected by Model 2: Table 5.15) have the above characteristics.

- **Case 3**
  If both of Model 2 and Model 3 fulfil the requirements of Rules 1 and 2 of *transition area* and exhibit significant increasing trends during $S_{interest}$ and $S_{W_{total}}$, these grid

cells form this category. In North America, during MAM, the number of these time series is 130 (out of 207 (Model 3) and 411 (Model 2)).

The analysis starts with considering all 77 time series of Case 1. All of these time series are inspected manually and divided into the categories described below. The sample plots of each category are presented in Appendix C. Note that in addition to Models 2 and 3, time series are modelled by MARS and the R method to understand how the behaviours of time series are approximated by these models and whether MARS and the R method provide some evidence in favour of Model 2 or Model 3:

1. Since climate can undergo abrupt shifts besides gradual changes (Ivanov and Evtimov, 2010), Models 2 and 3 are used to detect breaks in the trend function of climate time series. Model 3 detects simultaneous shifts in slope and intercept; hence, it is discontinuous at the break time. Due to the discontinuity at the shift point, trivial positive 0°C crossings are sometimes produced by Model 3 where Model 2 segments are entirely above 0°C or below 0°C. Each of Figures C.2, C.4, C.7, C.8, and C.10 illustrates one example from different categories encountered by investigating all the time series that have the above-indicated characteristics. Note the periodic behaviour of the time series in Figure C.8, which is partially captured by MARS. It is possible that if more data points were available, the model approximation at Time = 2007 would be the same as Time = 1964.

2. Model 2 detects the shift in the slope of the trend function of a time series; hence, it is continuous at the break point. Due to the continuity in the break time, Model 2 exhibits a rather smooth behaviour. In some situations where it seems that the time series under study is best approximated by a positive or negative function, both of Model 2 and Model 3 cross 0°C in the positive direction. However, due to the continuity of Model 2 at the shift time and its somewhat smooth behaviour, the increasing trend during $S_{\text{interest}}$ is not significant. On the other hand, Model 3 approximates the time series such that both the intercept and slope change at the break time. Therefore, it often builds segments such that the original data within $S_{\text{interest}}$ exhibit a significant increasing trend. This point is best described by Figures C.1, C.6, and C.9. Each of these figures provide one example from various categories with the above-indicated features. In Figure C.1, as an example, no significant trend is detected over $S_{\text{interest}}$ of Model 2 (1983-2009), whereas the $S_{\text{interest}}$ built by Model 3 (1972-2009) is such that a significant increasing trend is observed.

3. In some cases, although Model 2 experiences a positive 0°C crossing during the first segment, it eventually goes back below 0°C; hence, that grid cell is not selected according to Rule 2 of *transition area*. Figures C.3 and C.5 provide examples of various cases that occur under this category. As depicted by Figure C.3, MARS and the R method approximate the time series in a similar fashion. Model 3 detects an early 0°C crossing similar to Model 2, which is followed by a break. Temperature tends to increase again, however, the final decline in temperature is not captured by Model 3. It should be noted that the fact that the R method detects similar changes as Model 2 close to the end of the time series under this category increases the reliability of Model 2. The reason is that as indicated earlier, one of the key advantages of the R method is its ability to detect abrupt changes in the mean level of a time series close to the end of the time series.

As described above, the analysis of the grid cells selected using Model 3 but not Model 2 produces results in favour of Model 2. The next step involves investigating 281 grid cells of Case 2. These time series are modelled by Model 2 such that they meet all the requirements of Rules 1 and 2 *transition area* and have significant increasing trends over $S_{interest}$; however, one of these characteristics is missing if they are approximated by Model 3. Various cases observed could be categorized as follows:

1. The $y_w$ and $y_0$ determination rules for Model 3 (5.4.2) are set such that it looks for $y_0$ within each of the two segments, and $y_w$ is determined as the beginning of the segment that includes $y_0$. These rules do not identify the break point that is preceded by a negative line and followed by a positive segment as the time of positive 0°C crossing (similar to the R method). The reason is that it would not be feasible to determine $y_w$ for these grid cells similar to the locations whose $y_0$ occurs within one of the two segments and $y_w$ is definable. Figures C.12 and C.15 provide examples of these cases.

2. A small subset of the grid cells of Case 2 includes locations whose Model 3 segments are positive or negative. Model 2 in these cases shows early $y_0$'s (within the first two decades of the $20^{th}$ century). As emphasized frequently, it could be assumed that the model of these locations is positive during the entire time period of this study. Figure C.16 illustrates one example from this category.

3. Some of the cases not selected using Model 3 experience one positive 0°C crossing. However, either the second segment of Model 3 crosses 0°C in the negative direction

(Figure C.13) or the increasing trend over $S_{interest}$ is not significant (Figure C.14). In the former case, as is confirmed by inspecting the models produced by the R method, the problem arises due to the discontinuity of Model 3 at the break point.

The analysis of the grid cells that are selected by only one of Model 2 and Model 3 reveals that Model 2 is more suitable than Model 3 in this research. However, one more step should be taken before reaching the final conclusion. That is to examine the performance of both models when both of them fulfil all the requirements of Rules 1 and 2 *transition area* and have significant increasing trends over $S_{interest}$. It is worthwhile to note again that Model 2 and Model 3 follow two different goals; the former only looks for the time of break in the slope of the trend function, and the latter is in search of the time when both the intercept and slope of the trend function change. Most of the cases with similar $y_0$ results generated by Models 2 and 3 have close break times. In some situations, although the break times are not close, the orientation of lines is such that similar $y_0$'s are obtained. During JFM, since the distributions of break time are close (Figures 5.1 and 5.47) less differences between the $y_0$ results of the two techniques are observed compared to MAM. Figures C.18 and C.22 provide two examples whose Model 2 and Model 3 approximations resemble each other. Figures C.17, C.19, and C.20 are the examples of cases where different segments are produced by Model 2 and Model 3; however, $y_0$'s are close. The grid cells where the performances of Model 2 and Model 3 differ could be divided into the groups indicated below. The segments might be such that these differences do not affect the $y_0$ results. However, the purpose of the following classification is to understand which model provides a better approximation of the original data.

1. As indicated, in some locations, the discontinuity and level change at the break time lead to a very localised model. Figures C.17, C.21, and C.23 are examples of such cases. Figure C.23 illustrates how localised approximations of Model 3 may lead to significantly different $y_0$ results.

2. Due to the change in level as well as slope at the break time of Model 3, in some cases, the second segment of Model 3 is not able to capture the decline in temperature that occurs close to the end of a time series. These cases are depicted by Figures C.19 and C.20. It is worthwhile to note again that the behaviour of Model 2 close to the ends of time series is verified by the R method since it is capable of discovering changes close to the ends of time series with a minimum delay.

Based on the above discussion, it is concluded that Model 2 provides better approximations of the time series in this research compared to Model 3.

#### 5.8.5.2 MARS versus Models 2 and 3

As indicated in Section 5.8.1.2, the behaviour of MARS in many locations with 2 segments resembles that of Model 2 (Figures C.14 and C.16). Furthermore, among locations with more than two segments, some of them are modelled as if the approximation technique is Model 3 of IO type. In all of these cases, there is a steep segment with a short duration that indeed plays the role of transitional period in the case of IO models. This segment leads to the simultaneous shift in slope and intercept as with Model 3 (Figures C.12 and C.24). In some situations, the larger number of segments built by MARS may affect the selection of $S_{interest}$. An example of this case is provided by Figure C.24; the time series is modelled by four segments, and the first and last segments cross 0°C in the positive direction. The first segment has a positive slope and is followed by another segment of positive slope. Since the first segment has a smaller slope, the last segment is selected as $S_{interest}$. Model 3 approximates the first two segments of MARS as one line of positive slope with a larger rate of temperature increase and a larger accumulation than the second segment. Therefore, $S_{interest}$ of Model 3 is the first segment.

As mentioned earlier in Section 5.8.1.2, MARS is an adaptive regression technique that has been developed to model any type of data and not necessarily time series. It is accurate and applicable to cases with up to 20 independent variables. Furthermore, it generates precise results if there are interactions between a few independent variables. MARS is also capable of handling missing values and categorical variables. All these characteristics make MARS a powerful method that could be used to model intricate situations. Since MARS does not belong to the category of techniques used in the analysis of time series, its algorithm does not include autoregressive terms. Hence, a more complicated path is followed to model data. Due to the adaptive and complex nature of the algorithm, it requires the analyst to provide more input parameters compared to the other algorithms used in this study, and this is one of the drawbacks of MARS. MARS has no intuition of its own, and these input arguments are open to experimentation. Therefore, it may be necessary to study the difference that it takes to run the model with different values of the input arguments and examine which of the possibilities yields the best performance and the best bias-variance trade-off. Due to the large number of locations under study in this

thesis, it is not feasible to investigate each case separately. To partially offset this problem, three groups of input parameters are considered in the MARS analysis (refer to Section 5.5.1 for more details). In contrast to MARS, Models 2, which is specifically developed for the analysis of time series, requires few inputs. This makes the technique more suitable for analysing large databases where it is not feasible to inspect all cases individually and modify the inputs accordingly.

#### 5.8.5.3 R method versus Other Techniques

The R method has some distinct features that make it different from the other methods. As emphasized frequently in this thesis, the R method belongs to the category of the methods that detect changes in the mean levels of time series. This implies that it is suitable for detecting sharp changes in mean rather than trend inhomogeneities in time series. Another unique characteristic of the R method is its ability to detect shift points close to the ends of time series since the analysis includes observations in sequence, and the number of observations included in each step is not fixed *a priori*. MARS and Models 2 and 3 lack this ability.

Since the R method detects the sharp changes in the mean of time series, the upward shifts that cross the 0°C line could be directly considered as $y_0$ candidates. Therefore, the model requires minimum rules on the determination of $y_0$. This implies that $y_0$ reported by the R method is the year of 0°C crossing when the mean of the time series moves above 0°C as opposed to MARS and Models 2 and 3 where the long-run path (trend function) of temperature crosses 0°C. $y_w$ is not defined for the R method due to its specific characteristics (for more details, refer to Sections 2.3.2.2, 3.2, and 5.8.1.1).

Although the R method is conceptually different from the other techniques, it is included in this thesis due to its unique characteristics. It is one of the advanced climate regime shift detection techniques and presents interesting results regarding the sign of the mean level of the temperature time series. The analysis of the time series with the R method provides the opportunity to compare the time of positive 0°C crossing of the mean level and the long-run path of temperature. As depicted by the maps and histograms, in some grid cells, the shift in the sign of mean occurs some time close to the positive 0°C crossing of the trend function. Furthermore, the comparison of the *transition areas* of different techniques reveals that most of the locations whose trend functions rise above 0°C

experience positive 0°C crossing in the mean level as well. Most commonly the positive 0°C crossing in mean occurs later. Another advantage of the assessment of the results of the R method is that its algorithm is robust near the ends of time series. Hence, in some situations, it was used to verify the behaviour of Model 2 in the initial or final years of the time series.

#### 5.8.5.4 Conclusion

This research is more concerned with the time of the positive 0°C crossing of the long-run path of temperature. Therefore, based on the discussion above, in terms of the simplicity of input arguments as well as $y_0$ and shift point determination, Model 2 provides the best approximation of the temperature time series in this research.

### 5.8.6 Cryospheric Evidence for Observed Trends

As indicated in Chapter 2, many analyses of change (temporal and spatial) still rely on relatively simple climate variables such as air temperature, which acts as an index for a complex set of heat fluxes. For example, in the study by Cayan et al. (2001), the first significant snowmelt run-off pulse of high-elevation streams in the interior western U.S. is considered as one of the indicators of the spring onset. The study indicates that anomalous temperature has a great impact on the first significant snowmelt. Therefore, it is of key importance to examine critical changes in air temperature. The focus of this thesis is on 0°C, the point of cryospheric phase change. Cryospheric variables such as freeze and breakup dates, timing of snowmelt, and the snow-free period are strongly influenced by the change in the sign of temperature (Bonsal and Prowse, 2003). Duguay et al. (2006) and Prowse et al. (2010) note that spring 0°C isotherm could be used as an indicator of the timing of spring breakup events. The goal of this section is to compare the observed spatial trends of $y_0$ with the trends reported by other studies for some of these cryospheric variables.

Prior to examining the connection between detected trends in some cryospheric variables and the $y_0$ results obtained in this research, the $y_w$ and $y_0$ results of Model 2, presented in Sections 5.8.3 and 5.8.4, are compiled below. Several points should be noted regarding the terminology of regions:

1. During JFM, due to the high degree of spatial variability of the results over North America, the *transition area* in North America is divided longitudinally into three regions: i) Western U.S.: 125°W − 105°W, ii) Central U.S.: 105°W − 90°W, iii) Eastern U.S.: 90°W − 70°W.

2. During JFM, in Europe, the region under study is confined to the longitudes of 30°W and 45°E. The density of the selected locations is higher in central Europe. However, except northern Europe, the grid cells are distributed over entire Europe.

3. During JFM, the region of Asia is divided into three parts for the analysis: i) Southwestern and Central Asia (45°E to 75°E), ii) Central-Eastern Asia (75°E to 100°E), iii) Eastern Asia (100°E to 150°E). The *transition area* in southwestern and central Asia covers a small region that consists of some parts of Uzbekistan, Kazakhstan, and Iran. From central-eastern Asia, only a small area from western China meets the criteria set by Rules 1 and 2 of *transition area*. This region is located in the north of Tibet and south of Xinjiang and is surrounded by high mountains. Most of the region lies in the Taklamakan Desert, and it is referred to as western China. In eastern Asia, the final database only includes some grid cells from east central China, South Korea, and Japan.

4. During MAM, the majority of grid cells in North America are located in Canada.

5. During MAM, in contrast to JFM with disconnected regions over Eurasia (particularly in Asia), the *transition area* looks like a continuous band extending from northern Europe to eastern Asia. The western grid cells along the band are located in higher latitudes compared to the eastern pixels.

**Results:**

- **JFM**
  - **North America**
    In western U.S., the start of warming most commonly occurs during the 1940s decades. The majority of $y_0$'s fall within the range of 1960-2008. Most of the locations in central U.S. exhibit insignificant warming trends. Only 39 locations (out of 106) show significant increase in warming which starts in the 1960s

decade in most of the grid cells. $y_0$ most commonly takes place after 1960 with a peak in the 1980s decade. Only a few locations (most commonly located in northeastern U.S.) exhibit significant warming trends started in the 1970s decade. $y_0$ is distributed over the entire century with a small peak in the 1990s.

- **Europe**
  The map of $y_w$ shows high spatial integrity. Most of the grid cells with insignificant warming are located in southern Europe. The remaining locations experience $y_w$ during the 1920s and 1940-1970. In higher latitudes, $y_w$ occurs later. $y_0$ occurs during 1960-2008 in most of the locations. $y_0$ values increase from west to east in the diagonal direction. In the north of Black Sea, in eastern Europe, $y_0$ increases with latitude.
- **Asia**
  Most of the locations in southwestern Asia show insignificant warming over $S_{interest}$. In central Asia, the grid cells that are located in Uzbekistan do not exhibit significant increasing trends either. Excluding these pixels, in terms of $y_w$ values, high spatial integrity is observed in central Asia and western China. $y_w$ of the majority of locations occurs during the 1970s decade in central Asia and western China. In western China, a bell-shaped behaviour of $y_w$ is observed. This implies that $y_w$ increases from 1930s (in the west) to 1970s (in the center) and declines to 1960s (in the east). In eastern Asia, $y_w$ occurs during the 1960s and 1980s decades in eastern China and during the time period of 1901-1940 in most of the locations in Japan and South Korea. Over central Asia, $y_0$ increases with latitude. In western China, smaller $y_0$'s are observed in the west of the region; however, overall, no specific pattern is detected. The same conclusion applies to eastern Asia. The values of $y_0$ of the majority of grid cells are in the range of 1970-2008.

- **MAM**
  - **North America**
    The start of warming in the majority of grid cells is during 1900-1920. In the west-central grid cells, $y_w$ occurs in the 1900s, and in the central-eastern locations, the values most commonly fall within the second decade of the $20^{th}$ century. $y_0$ of the majority of the west-central grid cells occurs during 1900-1950, and the pattern observed in this region is not as strong as the pattern in

the central-eastern part where $y_0$ values increase with latitude. $y_0$ in this region generally takes place during 1970-2000.

– **Eurasia**
The largest values of $y_w$ are concentrated in the center and east of the band extending from northern Europe to easternmost Asia. The spatial integrity of the results is readily noticeable. In Europe (northern Europe and European Russia), the value of $y_w$ decreases from west to east from 1980 to 1910. In Asia, $y_w$ of most of the locations occurs in the 1970s, and generally, in a given longitude, $y_w$ increases with latitude. In the center of the band, in southern Russia, there is a region with a considerable number of grid cells whose $y_w$ occurs in the 1900s. From the common boundaries of Mongolia and China in the eastward direction, $y_w$ decreases. $y_0$ shows a clear pattern; it increases with latitude in a given longitude. According to the histogram of $y_0$ for Eurasia, although the number of locations with $y_0$ in the range of 1900-1970 is considerable, the histogram is denser during the time period of 1970-2008.

**Notes:**

1. During JFM, the locations that experience $y_0$ are distributed haphazardly in North America, and weak spatial coherence is observed over this region. These patterns may be indicative of the fact that generally, this area is not influenced by climate change to a degree that the sign of temperature changes during JFM.

2. The temperature of the locations where both $y_0$ and $y_w$ occur in the first few decades of the $20^{th}$ century might be approximated by positive models if more data points were available. For example, during MAM, a subset of the grid cells located in North America over western areas of Canada have this characteristic. A similar situation is observed in southern Russia (close to the common boundaries of Kazakhstan and Russia).

After compiling all the results of Model 2, the rest of this section is focussed on comparing its results to the outcomes from related work. This section is more concerned with providing cryospheric evidence for the observed trends. However, it should also be noted that according to the $y_w$ histograms of Model 2 (Figure 5.1 for JFM and Figure 5.5 for MAM), the peaks of the histograms occur in the 1960-1980 period and the 1970s decade

during JFM and MAM, respectively. This conclusion is in agreement with the studies that referred to the widespread climate change in the 1970s and/or 1980s decades (e.g., Kerr, 1992; Hare and Mantua, 2000; Rodionov and Overland, 2005; IPCC, 2007; Lo and Hsu, 2010). It is worth noting again that the MAM histogram displays another peak in the 1900s decade which is due to the fact that the time series are truncated in 1901 and is not supported by any environmental evidence (refer to Section 5.3 for more details).

According to the Model 2 (Model 3) histograms of break time during both JFM and MAM, over the entire Northern Hemisphere (Figures 5.1, 5.5, 5.47, and 5.52), the main peaks of the histograms occur in the 1960s-1970s (1960s) and 1970s (1950s), respectively. These results are in accord with the results of Ivanov and Evtimov (2010). The study applies Model 3 of IO type to the time series of annual Northern Hemisphere surface temperature. The data span the time period of 1850-2007. Ivanov and Evtimov (2010) report that the trend line of the time series breaks in 1963, and after the transition period of 6 years, a new regime starts. The slope of the new regime is 3 times greater than the slope of the first regime.

In the study by Bonsal and Prowse (2003), spring 0°C isotherm is determined as the date of positive 0°C crossing of mean daily temperature. Due to temperature fluctuations, this situation may be repeated several times. Therefore, Bonsal and Prowse (2003) calculated the 31-day running averages of the time series under study. The 31-day running averages of the majority of stations cross 0°C one time. The study accepts the last positive 0°C crossing as spring 0°C isotherm if there is more than one positive 0°C crossing. For each station, the spring 0°C isotherm of each year is determined during the time period of 1961-1990. The mean of these dates is accepted as spring 0°C isotherm for the given station during 1961-1990.

The contour plot of spring 0°C isotherm dates over Canada is provided in Bonsal and Prowse (2003). According to this plot, spring 0°C crossings over the west-central and eastern grid cells of the MAM *transition area* of Model 2 occur on April 15 and April 1, respectively. According to the results of this thesis, the MAM temperature of the grid cells located in the region approximately between April 15 and April 1 isotherms has crossed the 0°C line. $y_0$ most commonly occurs within the period of 1970-2000. Therefore, there is an inconsistency in the time of positive 0°C crossing reported by the two studies during MAM; Bonsal and Prowse (2003) indicates that average spring positive 0°C crossings take place in April during the time period of 1961-1990, in the locations selected by Model

2. On the other hand, according to this thesis, the temperature of the majority of those locations has permanently crossed 0°C during the time period of 1970-2000.

This contradiction may be due to the fact that in the study by Bonsal and Prowse (2003), the spring 0°C isotherm of each station is determined by analysing the running average of the time series of each year in the period of 1960-1990. Then, the average of these values is evaluated for the given location. On the other hand, in this study, the average of three months of March, April, and May is used for modelling. Furthermore, $y_0$ is determined as the time when the trend function (the long-run path) of a time series or the mean level of a time series crosses 0°C. Beyond all of these considerations, the time period of the study is 1901-2009. The larger the data window is, the more precise the estimates are.

If all $y_0$'s were in the range of 1990-2009, it would be concluded that the grid cells located between April 15 and April 1 isotherms may have experienced $y_0$ in the following decades. It should be noted that the models in this study have the ability to change slope and/or level. Therefore, it is not required to reduce the analysis window to the latter half of the $20^{th}$ century to capture abrupt shifts. Even MARS and Model 3, which are capable of capturing abrupt shifts in level and slope, report rather early $y_0$'s for the region during MAM.

Burn (1994) selected a set of rivers from the west-central region of Canada to examine the trends of Julian day of the peak spring snowmelt run-off. These time series are collected from gauging stations in northwestern Ontario, Manitoba, Saskatchewan, and Alberta. The final year of the period of study is 1990, and the record length varies between stations with the median length of 37 years. The number of stations with significant decreasing trends (in 5% and 10% significance levels) is such that it could not have occurred by chance. Moreover, the study indicates that there is an inversely proportional relationship between the MAM temperature and Julian day of peak flood. According to the study, the spatial distribution of significant decreasing trends follows no specific pattern. However, these stations are located either within the MAM *transition area* produced by Model 2 (with significant trends over $S_{interest}$ and $S_{W_{total}}$) or in the neighbouring regions. The study does not provide any detail on the approximation of the Julian day of peak flood in the last year of each station. If this day falls within the time period of March-May, the following two conclusions could be drawn: i) Since the temperature of these locations has risen above 0°C during MAM (based on this thesis), the changes in the spring peak flood timing lag

behind observed increases in temperature, ii) Using Model 2, there are grid cells located in the central region of the MAM *transition area* with $y_0$ occurring in the time period of 1990-2008. Thus, the stations with the peak flood day during MAM may have experienced $y_0$ later during the period of 1990-2008.

Zhang et al. (2001) analysed the monthly mean streamflow data that span the time period of 1947-1996. The study reveals that significant increasing trends are only observed in March and April. This is indicative of an advancing spring freshet and ice breakup in these regions. The stations with positive and significant trends are most commonly located in British Columbia (southern British Columbia) and the Atlantic regions. According to the results of Model 2, in southern British Columbia, the model either has permanently risen above 0°C some time in the $20^{th}$ century or is positive during the entire time period of study. Similar to the spring peak flood timing, there is a lag between the identified temperature trends in this study and the hydrological events reported by Zhang et al. (2001). The reasons for this lag could be the usage of the average temperature of March to May and the models of the time series to determine $y_0$. Furthermore, if the temperature has recently crossed 0°C in a specific region, this lag could be explained by the fact that it takes some time before temperature changes are reflected in the cryospheric variables such that these events take place earlier than March. In the Atlantic regions, Model 2 identifies locations with $y_0$ in the range of 1995-2008. Thus, it could be concluded that the spring freshet timing in these regions has recently changed, and it occurs earlier.

The lag discussed above also exists between the results of Dibike et al. (2011a) and this study. Dibike et al. (2011a) analysed the influence of climate change on ice-cover characteristics (e.g., ice breakup) in North America using 'Multi-year simulation model for Lake thermo- and phytoplankton dynamics' (MyLake). Mean breakup dates are obtained by simulating the lake-ice phenology over the time period of 1979-2006. The depth of the lake is assumed to be 20 m. The breakup dates produced by MyLake for the MAM *transition area* of Model 2 are in the range of 130-140 Julian day (mid-May).

Zhang et al. (2000) investigated the ratio of snowfall to total precipitation during the time period of 1900-1998 in Canada. Negative trends are observed in the eastern and central regions of Canada. This complies with the observed trends on the $y_0$ map of Model 2 during MAM (Figure 5.33). It should be noted that these trends are significant only in the Atlantic regions. The study shows that if the time period of 1950-1998 is considered, only the western regions of Canada exhibit significant decreasing trends. As indicated in

Section 2.2.1.1.2, the change in the sign of temperature influences the precipitation type (e.g., Hamlet et al., 2005; Knowles et al., 2006). In this thesis, even Model 3 and MARS, which are capable of changing level as well as slope, do not identify locations with positive 0°C crossings ($y_0$) during the time period of 1950-1998 in the western regions reported to show significant decreasing trends by Zhang et al. (2000). However, the majority of the grid cells in the area are modelled by positive segments.

To study the impact of climate change on cold-region lakes, Dibike et al. (2011b) used MyLake to simulate the ice-cover characteristics in the Northern Hemisphere ($40° - 75°$N) during the time period of 1960–1999. The study detects significant negative trends (earlier) in mean breakup dates approximately in the eastern parts of the band extending from northern Europe to easternmost Asia in the MAM *transition area* of Model 2. Significant negative trends are observed in the western areas of Canada and Alaska as well. In this thesis, the modelled temperature is below 0°C during both JFM and MAM over a vast region of Alaska. However, a few locations in southern Alaska have crossed 0°C during MAM in the latter half of the $20^{\text{th}}$ century. With regard to significant negative trends in western Canada, as discussed above, according to Model 2, these regions are either modelled by positive segments or exhibit positive 0°C crossing.

Prowse et al. (2010) analysed the temporal and spatial changes of spring 0°C isotherm (Bonsal and Prowse, 2003) in the main-stem reaches of four large northward flowing Arctic rivers: Lena, Mackenzie, Ob and Yenisey. The study focuses on the regions within 2000 km from the headwaters. The source of one of these rivers, Yenisey (in Russia), is in the MAM *transition area* of Model 2. The *transition area* includes approximately 800 km from the main-stem reach of this river. The results of Model 2 agree with Prowse et al. (2010) in that spring 0°C isotherm increases (in Julian day) with latitude. This implies that higher latitudes experience later dates. Spring 0°C isotherm increases from approximately 100 to 120 Julian day (April) within 800 km from the main-stem headwater of the river. Since spring 0°C crossing occurs in April, the discussion indicated above (Page 333) with regard to the study by Bonsal and Prowse (2003) applies to this situation as well. The increase in $y_0$ with latitude increases the risk and severity of ice jam floods (Prowse et al., 2010).

As indicated in Section 2.2.1.3, due to recent changes in climate, the duration of cold season is subject to change. So are the mass balance season for glaciers as well as the net accumulation. Casassa et al. (2009) investigated run-off and discharge peaks in the mountain basin caused by melting of glaciers. The study indicates that in some regions like

southern and central British Columbia and low-middle elevations in the Alps, run-off has reduced. The reason is the decreasing snow cover and/or the great glacial mass loss that has occurred in the past. In other regions such as northwest of British Columbia, southwest of Yukon, high elevations in the Swiss and Austrian Alps, the Tianshan Mountains, and Tibet, records show increased run-off. The comparison between the maps of Casassa et al. (2009) and this thesis shows that all of these regions are identified as locations that experience $y_0$. In northwest of British Columbia and southwest of Yukon, both of the JFM and MAM maps of this thesis show positive 0°C crossings. The locations with reduced run-off in southern and central British Columbia are modelled by positive segments. As mentioned, in Europe, Casassa et al. (2009) only focuses on the regions in Switzerland and Austria. These regions show reduced run-off in low elevations and increased run-off in high elevations. During MAM, in Europe (Figure 5.34), these regions are the only locations that have recently crossed 0°C surrounded by the grid cells with positive temperature. A few grid cells experience $y_0$ during JFM in these regions. The glacierized basins in central Asia depicted by the maps of Casassa et al. (2009) are identified as the grid cells that show recent positive 0°C crossings during MAM (Figure 5.35). These grid cells are surrounded by the locations whose temperature is modelled by positive segments.

The comparison of the map of permafrost extent in Frey and McClelland (2009) with the MAM maps of Model 2 reveals that the east of the area selected in Asia based on Rule 1 of *transition area* (Section 4.3) is covered with isolated patches of permafrost. In Asia, in the west of the *transition area* selected based on Rule 1 of *transition area* ($60° - 90°$E and above 60°N), the region is covered with isolated patches of permafrost as well as sporadic and discontinuous permafrost. The comparison of the maps shows that most of the grid cells located in the regions indicated above are identified with positive 0°C crossings. In fact, in Asia, the shape of the *transition area* (selected based on Rules 1 and 2 of *transition area*) resembles the region covered by isolated patches shown on the maps of Lawrence et al. (2008) and Frey and McClelland (2009). This is indicative of permafrost degradation and deepening of the active later. Similar to Asia, in North America, the northern regions of the *transition area* selected based on Rule 1 of *transition area* are covered with isolated patches of permafrost as well as sporadic permafrost. However, none of these grid cells meet the criteria set by Rule 2 of *transition area* (i.e., experience $y_0$ during MAM).

The map of the active layer depth trends (1980-2002) is provided by Oelke et al. (2004) using a finite difference model for one-dimensional heat conduction with phase change. The comparison of this map with the JFM and MAM maps of Model 2 in Asia reveals that the

observed trends in Oelke et al. (2004) match the observations in this thesis. In the study by Oelke et al. (2004), the trends are only displayed over sporadic, discontinuous, and continuous permafrost. The map reveals that the depth of the active layer has decreased with the rate of approximately 2-8 (cm/year) in southeastern Russia, northeastern China, and Mongolia. All of these regions experience $y_0$ during MAM (Figure 5.35). As depicted by the JFM map of Asia (Figure 5.16), there is an isolated region in west-central China (located in the north of Tibet and south of Xinjiang) that includes a considerable number of grid cells whose temperature has risen above 0°C recently. The same area is shown on the map of Oelke et al. (2004) as the region where the depth of permafrost has been increasing since 1980 with the rate of approximately 2-8 (cm/year).

During JFM, in North America, the maximum number of locations whose temperature has risen above 0°C are found in western U.S. $y_0$ in western U.S. has most commonly occurred during the time period of 1960-2008 according to the results of Model 2. Numerous studies have been devoted to examine the hydrological impacts of climate change in this area. Some of these studies concerning our research are cited in Chapter 2, and the studies that provide direct spatial evidence for the observed trends in this thesis are presented below.

The hydrologic response of mountain snowpack and snowmelt to changing climate in this region is investigated by Stewart (2009). According to the map of changes in SWE during the time period of 1949-2004, most of the stations in western U.S. exhibit significant decreasing trends except the stations that are located in cold and high-elevation areas or regions with an overall increase in precipitation that offsets the decrease in SWE. According to the map of spring pulse onset in Stewart (2009), most of the stations in western U.S. experience earlier spring pulse onset (approximately 15-20 days).

The analysis of the elevation maps in Hamlet et al. (2005) reveals how the grid cell selection in western U.S. is influenced by elevation. According to the JFM map (Figure 5.14), the temperature of the coastal regions (inside and outside of the area selected based on Rule 1 of *transition area*) with approximately zero elevation is above 0°C during JFM. The spatial distribution of the locations with average SWE greater than 50 mm on April 1 (during 1916-2003) and decreasing SWE are depicted for March 1, April 1, and May 1 in Hamlet et al. (2005). The distribution approximately matches that of the grid cells that experience $y_0$. This implies that warmer temperatures in these regions have influenced snow cover and snowmelt. Studying streamflow data in western U.S. during 1950-1999,

Regonda and Rajagopalan (2005) reported a decrease in SWE and a general increase in winter precipitation most of which occurs in the form of rain. The observed changes are more significant in lower elevations and in the northwest Pacific (at elevations between 1000 and 2000 m (Leung and Ghan, 1999)). The reason is that winter temperatures are closer to 0°C in these regions, and small changes in climate have a significant effect on the hydrology of them.

The study by Knowles et al. (2006) reveals a decreasing trend in the ratio of the 'winter-total snowfall water equivalent' (SFE) to 'winter-total precipitation' (P) in western U.S., during the time period of 1949-2004. Similar to the previous studies, this research indicates that these changes most commonly happen in the regions with near freezing temperatures. If temperatures are low enough, increasing temperatures do not change the type of precipitation in the region. The study indicates that the widespread warming in March has caused the reduction of the ratio of SFE/P across the region. According to this study, March temperatures over western U.S. are high enough to cause region-wide decreases in SFE/P. However, in January, only coastal regions (very low elevations) exhibit a decline in SFE/P. Similar to the above-mentioned studies, the study by Knowles et al. (2006) provides cryospheric evidence for the results of this thesis during JFM; as depicted by the JFM maps of Model 2, the JFM temperature of the west coast is positive during the time period of 1901-2009, and as indicated above, across western U.S., $y_0$ in the majority of grid cells occurs during the period of 1960-2008.

During JFM, in Europe, the maximum number of grid cells are located in Poland. According to the JFM map of Model 2, $y_0$ shows a pattern; $y_0$ increases from west to east in Poland. The temperature of the western grid cells has risen above 0°C during the 1960s decade, whereas the temperature of the eastern regions has recently crossed 0°C. According to the maps of Falarz (2004), the variation coefficient of seasonal snow cover duration from 1948–49 to 1997–98, relative change (decrease) of snow cover duration from 1848–49 to 1997–98, and variation coefficient of maximum depth of snow cover in winter season from 1948–49 to 1997–98 decreases from west to east. This implies that larger variations are observed in the western regions. This could be explained by the fact that the change in the sign of temperature in the western grid cells has occurred earlier. It should be noted that Falarz (2004) defines snow cover duration as the number of days with snow cover $\leq 1$ cm in winter season.

The map of percentage changes in SCA between 1967–1987 and 1988–2004 in the North-

ern Hemisphere during MAM is depicted by IPCC (2007) (Figure 4.3). In the entire Northern Hemisphere, the area covered with the grid cells that experience reductions in average SCA resembles the combination of the JFM and MAM *transition area* (selected based on Rules 1 and 2 *transition area*) in this thesis. As described in Section 2.2.1.1.3, due to the snow-albedo feedback phenomenon, temperature variations have a great impact on the extent of the SCA in the Northern Hemisphere (IPCC, 2007). Therefore, the consistency between the map of changes in SCA and the maps of this thesis verifies the observed patterns in this research.

# Chapter 6

# Conclusions and Future Work

## 6.1 Conclusions

In the temperate regions of the Northern Hemisphere, the seasonal rise of temperature above 0°C marks the most pronounced changes in the environment like ice breakup events, breakage of ice dams, and spring floods; hence, it has significant impacts on hydrological and ecological processes as well as human activities. In this thesis, an extensive analysis is performed to locate the $0.5° \times 0.5°$ land grid cells in the extra-tropical Northern Hemisphere (20.25°N-89.75°N) with the mean temperature that was primarily negative during months of JFM or MAM and changed sign in the time period of 1901-2009. Furthermore, it is of interest to determine the year of positive 0°C crossing ($y_0$). Due to the high degree of variability of temperature data, to determine $y_0$, the time series are approximated by four different modelling techniques: i) trend shift detection techniques: Model 2 and Model 3 (Perron and Yabu, 2009b, Kim and Perron, 2009), ii) Multivariate Adaptive Regression Splines (MARS) (Friedman, 1991), iii) the R method (Rodionov, 2004, 2006). These models divide the entire domain of the time series into sub-regions. The sub-regions are modelled by the polynomials of degree zero or one. $y_0$ is then determined as the time when the models cross 0°C and remain above 0°C. The segment that includes $y_0$ is termed 'segment of interest' ($S_{\text{interest}}$). The 'start year of warming' ($y_w$) is determined as the beginning of $S_{\text{interest}}$, and it is the year that marks the onset of the warming that leads to the permanent positive 0°C crossing. The combination of $S_{\text{interest}}$ and the segment(s) of positive slope that immediately follows $S_{\text{interest}}$ is termed the 'section of total warming' ($S_{W_{\text{total}}}$). In some

situations, the models may pose some challenges since they exhibit more than one positive 0°C crossing. The rules set in Chapter 5 assisted with the determination of $y_0$ in such cases.

The thorough analysis of the results leads to the following conclusions:

- Except a small number of grid cells in western China and the southern portion of the Rocky Mountains in U.S., the MAM *transition area* is located in higher latitudes than that of JFM. It should be noted that the grid cells in western China, whose temperature was primarily negative during MAM and has recently risen above 0°C, form the outer boundary of a high-elevation region that embeds rather low-elevation areas like the Taklamakan Desert.

- According to the graphical comparison and the non-parametric comparison techniques (Wilcoxon signed-rank test for paired observations and Wilcoxon rank-sum test), significant differences exist between the $y_w$ results of MARS, Model 2, and Model 3. $y_w$ is determined as the beginning of $S_{interest}$; therefore, it is influenced by the behaviour of the models and how they determine the sub-regions (refer to Section 5.8.2 for more details). Due to the specific characteristics of the R method (Section 5.6.2), $y_w$ is not determined using this technique.

- The results of Wilcoxon signed-rank test for paired observations, which only compares the common subset of any two techniques, indicate that although the $y_0$ results of MARS-Model 2, MARS-Model 3, and Model 2-Model 3 are not different at the significance level of 5%, the results are different considering a larger significance level (e.g., 10%). During MAM, P-values are smaller, which is indicative of larger differences between the $y_0$ results during MAM.

- Wilcoxon rank-sum test reveals that considering the *transition area* as a whole, the $y_0$ results of MARS-Model 2, MARS-Model 3, and Model 2-Model are similar. However, it should be noted that Wilcoxon rank-sum test compares numbers without considering the locations they refer to. Therefore, it is not capable of detecting local differences (over individual continents).

- Both of the above-indicated non-parametric tests favour the alternative hypothesis of inequality of the means of the R method with the other techniques. The R method has some distinct features that make it different from the other techniques. The $y_0$

reported by the R method is the time when the mean of the time series rises above 0°C; whereas, in the case of MARS and Models 2 and 3, the long-run path (trend function) of temperature crosses 0°C.

- The mathematical comparison of the techniques highlights the following points:
  - The R method is suitable for detecting sharp changes in the mean level of the time series rather than trend inhomogeneities since the function of the underlying data generating process consists of polynomials of degree zero. Due to the sequential nature of the algorithm of the R method, it is capable of detecting the shift points close to the ends of the time series.
  - Model 2, Model 3, and MARS are similar in that they embed linear functions of time. MARS approximates the time series with the polynomials of degree zero or one, which are continuous at the boundaries. Model 2 and Model 3 assume that the long-term changes follow a linear trend, and climate noises are modelled by an auto-regressive process.

  The significant differences between the results of MARS, Model 2, and Model 3 depicted by the maps and histograms, particularly in North America and during MAM, necessitated a thorough assessment of the plots of the grid cells in North America to understand the model behaviour that causes the differences. Based on this extensive investigation, it is concluded that Model 2 is more in accord with the research objectives than Model 3. With regard to MARS, in many locations with two MARS segments, the MARS segments resemble those of Model 2. Furthermore, some of the models built by MARS with more than two segments resemble the approximations of Model 3 of IO type. In such cases, there is a MARS segment with a short duration and a relatively large slope that leads to the simultaneous shift in slope and intercept. This segment resembles the transitional period in the case of IO models. It should be noted that in some situations, the choice of $S_{\text{interest}}$ is influenced by the larger number of segments built by MARS compared to Models 2 and 3. From the mathematical points of view, MARS is a powerful method that could be used to model complex situations. It is an adaptive regression technique that has been developed to model any type of data, and it does not belong to the category of the techniques specifically developed to analyse time series. Thus, an intricate algorithm is followed to model data. This algorithm demands more input parameters compared

to the other algorithms used in this study. It may be required to experiment with different sets of input arguments to examine which of the possibilities leads to the best model and the best bias-variance trade-off. This is the undesired feature of MARS when it is applied to analyse a large data set such as was the case in this study.

In terms of the simplicity of input arguments as well as $y_0$ and shift point determination, Model 2 provides the best approximation of the temperature time series in this research. It is worth noting again that the $y_0$ determined by Model 2 is the time of positive 0°C crossing of the long-run path of temperature.

With regard to the R method, the mathematical comparison reveals that it is conceptually different from MARS, Model 2, and Model 3. However, due to the unique characteristics of the R method, highlighted earlier, it is selected as a suitable technique to examine changes in the mean level of the temperature time series. It is an advanced tool to compare the changes in the sign of the mean level of the time series to the shifts in the long-run path (trend function) of them. The assessment of the results of the R method reveals that in many locations, the time of the positive 0°C crossing of the mean level is close to that of the trend function. Furthermore, the *transition areas* of the R method during JFM and MAM resemble those of the other techniques. Since the R method is capable of detecting shifts close to the ends of time series, in some situations, it is used to verify the outcomes of Model 2 in the initial or final years of the time series.

- The results obtained by Model 2 are presented below. Only the grid cells with significant warming trends during $S_{\text{interest}}$ and $S_{W_{\text{total}}}$ are considered.

  1. **JFM**

     (a) North America
     The *transition area* in North America is located in the contiguous U.S. Most of the grid cells with significant warming during $S_{\text{interest}}$ and $S_{W_{\text{total}}}$ are located in western U.S. According to Model 2, $y_w$ and $y_0$ of most of these locations occur in the 1940s and during the time period of 1960-2008, respectively. In western U.S., the rate of warming during $S_{\text{interest}}$ and $S_{W_{\text{total}}}$ is $\sim 0.015 - 0.05\,(°\text{C/year})$. The haphazardly distributed grid cells in North

America and the weak spatial coherence of the results may be interpreted such that overall, this area is not influenced by climate change to a degree that the sign of temperature changes during JFM.

(b) Europe

In Europe, most of the grid cells are concentrated in central Europe. $y_w$ occurs during the time periods of 1920s and 1940-1970; generally, in higher latitudes, $y_w$ occurs later. As reported by Model 2, most of the locations experience $y_0$ during 1960-2008, and $y_0$ values increase from west to east in the diagonal direction. $y_0$ of the grid cells in the north of Black Sea, in eastern Europe, increases with latitude. The slopes of $S_{interest}$ and $S_{W_{total}}$ are in the range of $\sim 0.02 - 0.1$ (°C/year) and increase in the same way as $y_0$.

(c) Asia

In Asia, the *transition area* roughly consists of three regions: i) a small region in southwestern and central Asia, which covers some parts of Uzbekistan, Kazakhstan, and Iran, ii) a small area in western China, which is located in the north of Tibet and south of Xinjiang. Most of the region lies in the Taklamakan Desert, iii) few grid cells in east-central China, South Korea, and Japan. $y_w$ of the majority of locations occurs in the 1970s. $y_w$ occurs earlier (1901-1940) in easternmost locations. Model 2 reveals that the values of $y_0$ of the majority of grid cells are in the range of 1970-2008. In central Asia, $y_0$ increases with latitude; however, no specific pattern is observed in western China and eastern Asia. The rate of warming over $S_{interest}$ and $S_{W_{total}}$ is in the range of $\sim 0.02 - 0.15$ (°C/year). It should be noted that the minimum values are concentrated over easternmost Asia.

2. **MAM**

(a) North America

Most of the grid cells selected by Model 2 are located in Canada and extend from northeastern British Columbia to the Atlantic regions. $y_w$ occurs during the 1900s and 1910s in the west-central grid cells and central-eastern locations, respectively. The west-central locations experience $y_0$ during 1900-1950. It is worthwhile to note that when both of $y_w$ and $y_0$ occur in the first few decades of the $20^{th}$ century, the model could be considered positive for

almost the whole study period. If the time series spanned a wider time window, particularly prior to 1901, a more accurate model would be obtained for the initial years of the $20^{th}$ century, and the time series of these locations might be approximated by positive functions. $y_0$ of the central-eastern regions generally takes place during 1970-2000, and the values increase with latitude. The rate of warming during $S_{interest}$ and $S_{W_{total}}$ is in the range of $\sim 0.01 - 0.04$ (°C/year).

(b) Eurasia
In Eurasia, the *transition area* is like a continuous band extending from northern Europe to eastern Asia. The eastern regions are lower in latitude compared to the western grid cells. In Europe (northern Europe and European Russia), $y_w$ decreases from 1980 to 1910 in the eastward direction. In Asia, $y_w$ most commonly occurs in the 1970s. The maps of Model 2 depict that in a given longitude, $y_0$ exhibits an increasing pattern with latitude. Although a considerable number of locations experience $y_0$ prior to the 1970s, the histogram of Eurasia is denser during the time period of 1970-2008. The slopes of $S_{interest}$ and $S_{W_{total}}$ are in the range of $\sim 0.01 - 0.1$ (°C/year); the largest slopes are observed in the central-eastern regions of the band.

**Note:**

According to the $y_w$ histograms of Model 2 (Figure 5.1 for JFM and Figure 5.5 for MAM), considering the entire *transition area*, the peaks of the histograms occur in the 1960-1980 period and the 1970s decade during JFM and MAM, respectively. This conclusion is in agreement with the studies that referred to the widespread climate change in the 1970s and/or 1980s decades (e.g., Kerr, 1992; Hare and Mantua, 2000; Rodionov and Overland, 2005; IPCC, 2007; Lo and Hsu, 2010).

## 6.2 Future Work

This research may be extended in different directions:

- Since the distribution of thermal energy on the earth surface is influenced by large-scale air and ocean circulations, these patterns significantly influence the earth cli-

mate on the annual to decadal time scale. The next step of the analysis presented in this thesis could be examining the links between large-scale atmospheric and oceanic oscillation patterns and the observed spatial and temporal characteristics of $y_w$ and $y_0$. The time series of the indices may be analysed by the techniques introduced in this thesis for any abrupt shift in the trend function or mean level.

- The focus of this thesis was on the late-winter (JFM) and spring (MAM) time series. The analysis could be extended to other seasons to investigate if $y_0$ has taken place in the grid cells located in lower (higher) latitudes than the JFM (MAM) *transition area*.

- The topography map of the Northern Hemisphere could be analysed to understand the connections between the spatial characteristics depicted by the $y_w$ and $y_0$ maps and elevation. For example, in western U.S. or western China, the observed $y_0$ patterns may be explained based on the elevation characteristics of the regions. Some of these points are highlighted in this thesis; however, the thorough analysis of the topography maps may reveal interesting outcomes.

- As indicated in Chapter 4, the CRU data (University of East Anglia Climate Research Unit, 2011) exhibit long-term monthly or yearly changes in temperature at the earth's surface, not changes experienced only due to GHG emissions. Therefore, the data embed widespread and gradual changes. Due to this reason, it is of interest to explore if some of the observed patterns are the artefact of gradual changes like urbanization or industrial advancement, particularly in isolated regions.

- Since the air temperature influences the timing of many hydrological processes such as ice breakup, snowmelt, and spring streamflow, the time series of these variables could be analysed with the techniques applied in this research to determine the shift points. The spatial patterns of these shift dates could be compared to the $y_0$ maps to examine how closely they resemble each other.

- Many studies report the results of trend analyses on hydrological variables in Julian day. Therefore, it is not feasible to directly compare these results with the outcomes of the analysis performed using the mean temperature of three months. If the steps involved in this thesis are applied to individual months, this helps locate grid cells that experience $y_0$ in a specific month. The results obtained for individual months

could then be used to draw conclusions regarding the link between $y_0$ and the trends reported by the related work.

# References


Alexandersson, H. (1986). '**A homogeneity test applied to precipitation data**'. *International Journal of Climatology*, 6(6): 661–675

Allan, R. P. and Soden, B. J. (2008). '**Atmospheric warming and the amplification of precipitation extremes**'. *Science*, 321(5895): 1481–1484

Alley, R. B., Marotzke, J., Nordhaus, W. D., Overpeck, J. T., Peteet, D. M., Pielke Jr., R. A., Pierrehumbert, R. T., Rhines, P. B., Stocker, T. F., Talley, L. D., and Wallace, J. M. (2003). '**Abrupt Climate Change**'. *Science*, 299(5615): 2005–2010

Alpert, P., Ben-gai, T., Baharad, A., Benjamini, Y., Yekutieli, D., Colacino, M., Diodato, L., Ramis, C., Homar, V., Romero, R., Michaelides, S., and Manes, A. (2002). '**The paradoxical increase of Mediterranean extreme daily rainfall in spite of decrease in total values**'. *Geophysical Research Letters*, 29(10): 31.1–31.4

Andrews, D. W. K. and Ploberger, W. (1994). '**Optimal tests when a nuisance parameter is present only under the alternative**'. *Econometrica*, 62(6): 1383–1414

Anisimov, O. A. and Nelson, F. E. (1996). '**Permafrost distribution in the Northern Hemisphere under scenarios of climatic change**'. *Global and Planetary Change*, 14(1-2): 59–72

Anisimov, O. A. and Nelson, F. E. (1997). '**Permafrost zonation and climate change in the Northern Hemisphere: results from transient general circulation models**'. *Climatic Change*, 35(2): 241–258

Arora, V. K. and Boer, G. J (2001). '**Effects of simulated climate change on the hydrology of major river basins**'. *Journal of Geophysical Research*, 106(D4): 3335–3348

BADC (2011). NCAS British Atmospheric Data Centre, `http://badc.nerc.ac.uk/view/badc.nerc.ac.uk__ATOM__dataent_1256223773328276`

Barnett, T. P., Pierce, D. W., Hidalgo, H. G., Bonfils, C., Santer, B. D., Das, T., Bala, G., Wood, A. W., Nozawa, T., Mirin, A. A., Cayan, D. R., and Dettinger, M. D. (2008). '**Human-induced changes in the hydrology of the western United States**'. *Science*, 319(5866): 1080–1083

Barnston, A. G. and Livezey, R. E. (1987). '**Classification, seasonality and persistence of low-frequency atmospheric circulation patterns**'. *Monthly Weather Review*, 115(6): 1083–1126

Belkin, I. M. (2009). '**Rapid warming of large marine ecosystems**'. *Progress In Oceanography*, 81(1-4): 207–213

Beltaos, S. (2002). '**Effects of climate on mid-winter ice jams**'. *Hydrological Processes*, 16(4): 789–804

Beltaos, S. and Prowse, T. D. (2009). '**River-ice hydrology in a shrinking cryosphere**'. *Hydrological Processes*, 23(1): 122–144

Bonsal, B. R. and Prowse, T. D. (2003). '**Trends and variability in spring and autumn 0°C-isotherm dates over Canada**'. *Climatic Change*, 57(3): 341–358

Bradley, R. S. and Jones, P. D. (1985). **Detecting the Climatic Effects of Increasing Carbon Dioxide**, chapter **Data bases for isolating the effects of increasing carbon dioxide concentration**. US Department of Energy, Carbon Dioxide Research Division

Breiman, L. and Friedman, J. H. (1985). '**Estimating optimal transformations for multiple regression and correlation**'. *Journal of the American Statistical Association*, 80(391): 580–598

Breiman, L. and Meisel, W. S. (1976). '**General estimates of the intrinsic variability of data in nonlinear regression models**'. *Journal of the American Statistical Association*, 71(354): 301–307

Brown, R. J. E. (1964). '**Permafrost investigations on the MacKenzie highway in Alberta and MacKenzie district**'. Technical report, NRC Institute for Research in Construction; National Research Council Canada

Brown, R. D. and Mote, P. W. (2009). '**The response of Northern Hemisphere snow cover to a changing climate**'. *Journal of Climate*, 22(8): 2124–2145

Burn, D. H. (1994). '**Hydrologic effects of climatic change in west-central Canada**'. *Journal of Hydrology*, 160(1-4): 53–70

Burn, D. H. (2008). '**Climatic influences on streamflow timing in the headwaters of the Mackenzie River Basin**'. *Journal of Hydrology*, 352(1-2): 225–238

Burn, D. H., Cunderlik, J. M., and Pietroniro, A. (2004). '**Hydrological trends and variability in the Liard River basin**'. *Hydrological Sciences Journal*, 49(1): 53–67

Burn, D. H. and Hag Elnur, M. A. (2002). '**Detection of hydrologic trends and variability**'. *Journal of Hydrology*, 255(1-4): 107–122

Camill, P. (2005). '**Permafrost thaw accelerates in boreal peatlands during late-20th century climate warming**'. *Climatic Change*, 68(1-2): 135–152

Carlson, A. B. (1986). **Communication Systems: An Introduction to Signals and Noise in Electrical Communication**. McGraw-Hill

Casassa, G., Lopez, P., Pouyaud, B., and Escobar, F. (2009). '**Detection of changes in glacial run-off in alpine basins: examples from North America, the Alps, central Asia and the Andes**'. *Hydrological Processes*, 23(1): 31–41

Cayan, D. R., Kammerdiener, S. A., Dettinger, M. D., Caprio, J. M., and Peterson, D. H. (2001). '**Changes in the onset of spring in the western United States**'. *Bulletin of the American Meteorological Society*, 82(3): 399–415

Chelliah, M. and Arkin, P. (1992). '**Large-scale interannual variability of monthly outgoing longwave radiation anomalies over the global tropics**'. *Journal of Climate*, 5(4): 371–389

Comiso, J. C. (2003). '**Warming trends in the Arctic from clear sky satellite observations**'. *Journal of Climate*, 16(21): 3498–3510

Conrad, V. and Pollak, L. W. (1962). **Methods in Climatology**. Harvard University Press

Cunderlik, J. M and Burn, D. H. (2002). '**Local and regional trends in monthly maximum flows in southern British Columbia**'. *Canadian Water Resources Journal*, 27(2): 191–212

De Boor, C. (2001). **A practical guide to splines**. Springer

Dibike, Y., Prowse, T. D., Bonsal, B., de Rham, L., and Saloranta, T. (2011a). '**Simulation of North American lake-ice cover characteristics under contemporary and future climate conditions**'. *International Journal of Climatology*, Early View (Online Version of Record published before inclusion in an issue)

Dibike, Y., Prowse, T. D., Saloranta, T., and Ahmed, R. (2011b). '**Response of Northern Hemisphere lake-ice cover and lake-water thermal structure patterns to a changing climate**'. *Hydrological Processes*, 25(19): 2942–2953

Duguay, C. R., Flato, G. M., Jeffries, M. O., Menard, P., Morris, K., and Rouse, W. R. (2003). '**Ice-cover variability on shallow lakes at high latitudes: model simulations and observations**'. *Hydrological Processes*, 17(17): 3465–3483

Duguay, C. R., Prowse, T. D., Bonsal, B. R., Brown, R. D., Lacroix, M. P., and Menard, P. (2006). '**Recent trends in Canadian lake ice cover**'. *Hydrological Processes*, 20(4): 781–801

Dye, D. G. (2002). '**Variability and trends in the annual snow-cover cycle in Northern Hemisphere land areas, 1972–2000**'. *Hydrological Processes*, 16(15): 3065–3077

Dyurgerov, M. B. and Meier, M. F. (2005). '**Glaciers and the changing earth system: a 2004 snapshot**'. Occasional Paper 58, Institute of Arctic and Alpine Research, University of Colorado

Easterling, D. R. and Peterson, T. C. (1995). '**A new method for detecting undocumented discontinuities in climatological time series**'. *International Journal of Climatology*, 15(4): 369–377

Falarz, M. (2004). '**Variability and trends in the duration and depth of snow cover in Poland in the 20th century**'. *International Journal of Climatology*, 24(13): 1713–1727

Fleming, S. W. and Clarke, G. K. C. (2002). '**Autoregressive noise, deserialization, and trend detection and quantification in annual river discharge time series**'. *Canadian Water Resources Journal*, 27(3): 335–354

Forchhammer, M. and Boertmann, D. (1993). '**The muskoxen Ovibos moschatus in north and northeast Greenland: population trends and the influence of abiotic parameters on population dynamics**'. *Ecography*, 16(4): 299–308

Frey, K. E. and McClelland, J. W. (2009). '**Impacts of permafrost degradation on arctic river biogeochemistry**'. *Hydrological Processes*, 23(1): 169–182

Friedman, J. H. (1979). **Lecture Notes in Mathematics, Smoothing Techniques for Curve Estimation**, volume 757, chapter **A tree-structured approach to nonparametric multiple regression**. Springer

Friedman, J. H. (1991). '**Multivariate adaptive regression splines**'. *The Annals of Statistics*, 19(1): 1–67

Furgal, C. and Prowse, T. D. (2008). **From Impacts to Adaptation: Canada in a Changing Climate 2007**, chapter **Northern Canada**. Natural Resources Canada

Georgiadi, A. G., Milyukova, I. P., and Kashutina, E. A. (2010). **Environmental Change in Siberia: Earth Observation Field Studies and Modelling, Advances in Global Change Research**, volume 40, chapter **Response of river runoff in the cryolithic zone of eastern Siberia (Lena River Basin) to future climate warming**. Springer

Gerland, S., Liston, G. E., Winther, J. G., Orbaek, J. B., and Ivanov, B. V. (2000). '**Attenuation of solar radiation in Arctic snow: field observations and modelling**'. *Annals of Glaciology*, 31(1): 364–368

Gibbons, J. D. and Chakraborti, S. (2003). **Nonparametric Statistical Inference**. Marcel Dekker

Glantz, S. A. (2002). **Primer of Biostatistics**. McGraw-Hill

Goulding, H. L., Prowse, T. D., and Bonsal, B. R. (2009). '**Hydroclimatic controls on the occurrence of break-up and ice-jam flooding in the Mackenzie Delta, NWT, Canada**'. *Journal of Hydrology*, 379(3-4): 251–267

Greene, A. M. (2005). '**A time constant for hemispheric glacier mass balance**'. *Journal of Glaciology*, 51(174): 353–362

Groisman, P. Y., Karl, T. R., and Knight, R. W. (1994). '**Observed impact of snow cover on the heat balance and the rise of continental Spring temperatures**'. *Science*, 263(5144): 198–200

Gullet, D. W., Vincent, L., and Malone, L. (1991). '**Homogeneity testing of monthly temperature series: application of multiple-phase regression models with mathematical changepoints**'. Technical report, Atmospheric Environment Service

Hahn, C. J. and Warren, S. G. (1999). '**Extended edited synoptic cloud reports from ships and land stations over the globe, 1952-1996**'. Technical report, Environmental Sciences Division, Office of Biological and Environmental Research, United States Department of Energy

Hamilton, J. D. (1994). **Time Series Analysis**. Princeton University Press

Hamlet, A. F., Mote, P. W., Clark, M. P., and Lettenmaier, D. P. (2005). '**Effects of temperature and precipitation variability on snowpack trends in the western United States**'. *Journal of Climate*, 18(21): 4545–4561

Hanssen-Bauer, I. and Forland, E. J. (1994). '**Homogenizing long Norwegian precipitation series**'. *Journal of Climate*, 7(6): 1001–1013

Hare, S. R. and Mantua, N. J. (2000). '**Empirical evidence for North Pacific regime shifts in 1977 and 1989**'. *Progress In Oceanography*, 47(2-4): 103–145

Hastie, T. and Tibshirani, R. (1986). '**Generalized additive models**'. *Statistical Science*, 1(3): 297–318

Helsel, D. R. and Hirsch, R. M. (2002). **Hydrologic Analysis and Interpretation**, chapter **Statistical Methods in Water Resources**. United States Geological Survey (USGS)

Hinzman, L. D., Bettez, N. D., Bolton, W. R., Chapin, F. S., Dyurgerov, M. B., Fastie, C. L., Griffith, B., Hollister, R. D., Hope, A., Huntington, H. P., et al. (2005). '**Evidence and implications of recent climate change in northern Alaska and other Arctic regions**'. *Climatic Change*, 72(3): 251–298

Hirsch, R. M., Slack, J. R., and Smith, R. A. (1982). '**Techniques of trend analysis for monthly water quality data**'. *Water Resources Research*, 18(1): 107–121

Huber, P. J. (2005). '**Robust estimation of a location parameter**'. *The Annals of Mathematical Statistics*, 35(1): 73–101

Humlum, O., Instanes, A., and Sollid, J. L. (2003). '**Permafrost in Svalbard: a review of research history, climatic background and engineering challenges**'. *Polar Research*, 22(2): 191–215

Instanes, D. A. (2006). '**Impacts of a changing climate on infrastructure: buildings, support systems, and industrial facilities**'. *EIC Climate Change Technology, 2006 IEEE*: 1–4

IPCC (2007). '**Climate change 2007: The physical science basis**'. Technical report, Contribution of Working Group I to the fourth assessment report of the Intergovernmental Panel on Climate Change (IPCC)

IPCC (2008). '**Climate change and water**'. Technical report, IPCC (Intergovernmental Panel on Climate Change) Technical Paper VI

Ivanov, M. A. and Evtimov, S. N. (2010). '**1963: The break point of the Northern Hemisphere temperature trend during the twentieth century**'. *International Journal of Climatology*, 30(11): 1738–1746

Jacques, J. M. S. and Sauchyn, D. J. (2009). '**Increasing winter baseflow and mean annual streamflow from possible permafrost thawing in the Northwest Territories, Canada**'. *Geophysical Research Letters*, 36(L01401): 6 PP

Jekabsons, G. (2010). ARESLab: Adaptive Regression Splines toolbox for Matlab/Octave, `http://www.cs.rtu.lv/jekabsons/`

Jones, P. D. and Moberg, A. (2003). '**Hemispheric and large-scale surface air temperature variations: An extensive revision and an update to 2001**'. *Journal of Climate*, 16(2): 206–223

Jones, P. D., Raper, S. C. B., Bradley, R. S., Diaz, H. F., Kellyo, P. M., and Wigley, T. M. L. (1986). '**Northern Hemisphere surface air temperature variations 1851-1984**'. *Journal of Applied Meteorology*, 25(2): 161–179

Karl, T. R. and Trenberth, K. E. (2003). '**Modern global climate change**'. *Science*, 302(5651): 1719–1723

Karl, T. R. and Williams Jr., C. N. (1987). '**An approach to adjusting climatological time series for discontinuous inhomogeneities**'. *Journal of Climate and Applied Meteorology*, 26(12): 1744–1763

Karl, T. R., Williams Jr., C. N., Young, P. J., and Wendland, W. M. (1986). '**A model to estimate the time of observation bias associated with monthly mean maximum, minimum, and mean temperatures for the United States**'. *Journal of Climate and Applied Meteorology*, 25(2): 145–160

Kendall, M. G. (1975). **Rank correlation measures**. Charles Griffin

Kerr, R. A. (1992). '**Unmasking a shifty climate system**'. *Science*, 255(5051): 1508–1510

Kiehl, J. T. and Trenberth, K. E. (1997). '**Earth's annual global mean energy budget**'. *Bulletin of the American Meteorological Society*, 78(2): 197–208

Kim, D. and Perron, P. (2009). '**Unit root tests allowing for a break in the trend function at an unknown time under both the null and alternative hypotheses**'. *Journal of Econometrics*, 148(1): 1–13

Knowles, N., Dettinger, M. D., and Cayan, D. R. (2006). '**Trends in snowfall versus rainfall in the western United States**'. *Journal of Climate*, 19(18): 4545–4559

Kohler, M. A. (1949). '**On the use of double-mass analysis for testing the consistency of meteorological records and for making required adjustments**'. *Bulletin of the American Meteorological Society*, 30(5): 188–189

Kundzewicz, Z. W. and Robson, A. J. (2004). '**Change detection in hydrological records-a review of the methodology**'. *Hydrological Sciences Journal*, 49(1): 7–19

Kwong, Y. T. J. and Gan, T. Y. (1994). '**Northward migration of permafrost along the Mackenzie Highway and climatic warming**'. *Climatic Change*, 26(4): 399–419

Lambert, S. J. (1990). '**Discontinuities in the long-term Northern Hemisphere 500-millibar heights dataset**'. *Journal of Climate*, 3(12): 1479–1484

Lanzante, J. R. (1996). '**Resistant, robust and non-parametric techniques for the analysis of climate data: theory and examples, including applications to historical radiosonde station data**'. *International Journal of Climatology*, 16(11): 1197–1226

Lawrence, D. M., Slater, A. G., Romanovsky, V. E., and Nicolsky, D. J. (2008). '**Sensitivity of a model projection of near-surface permafrost degradation to soil column depth and representation of soil organic matter**'. *Journal of Geophysical Research*, 113(F02011): 14 PP

Leung, L. R. and Ghan, S. J. (1999). '**Pacific Northwest climate sensitivity simulated by a regional climate model driven by a GCM. Part II: 2×$CO_2$ simulations**'. *Journal of Climate*, 12(7): 2031–2053

Leung, L. R. and Wigmosta, M. S. (1999). '**Potential climate change impacts on mountain watersheds in the Pacific Northwest**'. *Journal of the American Water Resources Association*, 35(6): 1463–1471

Lo, T. T. and Hsu, H. H. (2010). '**Change in the dominant decadal patterns and the late 1980s abrupt warming in the extratropical Northern Hemisphere**'. *Atmospheric Science Letters*, 11(3): 210–215

Madden, R. A. and Williams, J. (1978). '**The correlation between temperature and precipitation in the United States and Europe**'. *Monthly Weather Review*, 106(1): 142–147

Magnuson, J. J., Robertson, D. M., Benson, B. J., Wynne, R. H., Livingstone, D. M., Arai, T., Assel, R. A., Barry, R. G., Card, V., Kuusisto, E., Granin, N. G., Prowse, T. D., M., Stewart K., and Vuglinski, V. S. (2000). '**Historical trends in lake and river ice cover in the Northern Hemisphere**'. *Science*, 289(5485): 1743–1746

Mann, H. B. (1945). '**Nonparametric tests against trend**'. *Econometrica*, 13(3): 245–261

Menne, M. J. and Williams Jr., C. N. (2009). '**Homogenization of temperature series via pairwise comparisons**'. *Journal of Climate*, 22(7): 1700–1717

Menne, M. J., Williams Jr., C. N., and Vose, R. S. (2009). '**The U.S. Historical Climatology Network monthly temperature data, version 2**'. *Bulletin of the American Meteorological Society*, 90(7): 993–1007

Miller, R. G. (1986). **Beyond ANOVA, Basics of Applied Statistics**. John Wiley & Sons

Min, S., Zhang, X., and Zwiers, F. W. (2010). '**Human-induced Arctic moistening**'. *Science*, 320(5875): 518–520

Min, S., Zhang, X., Zwiers, F. W., and Hegerl, G. C. (2011). '**Human contribution to more-intense precipitation extremes**'. *Nature*, 470(7334): 378–381

Mitchell, T. D. and Jones, P. D. (2005). '**An improved method of constructing a database of monthly climate observations and associated high-resolution grids**'. *International Journal of Climatology*, 25(6): 693–712

Modarres, R., Gastwirth, J. L., and Ewens, W. (2005). '**A cautionary note on the use of non-parametric tests in the analysis of environmental data**'. *Environmetrics*, 16(4): 319–326

Montgomery, D. C. and Runger, G. C. (2003). **Applied Statistics and Probability for Engineers**. John Wiley & Sons

Moore, R. D., Fleming, S. W., Menounos, B., Wheate, R., Fountain, A., Stahl, K., Holm, K., and Jakob, M. (2009). '**Glacier change in western North America: influences on hydrology, geomorphic hazards and water quality**'. *Hydrological Processes*, 23(1): 42–61

Morgan, J. N. and Sonquist, J. A. (1963). '**Problems in the analysis of survey data, and a proposal**'. *Journal of the American Statistical Association*, 58(302): 415–434

Mungall, C. and McLaren, D. J., eds. (1990). **Planet under stress: the challenge of global change**, chapter **Fresh Waters in Cycle**. Oxford University Press

Nelson, F. E., Anisimov, O. A., and Shiklomanov, N. I. (2001). '**Subsidence risk from thawing permafrost**'. *Nature*, 410: 889–890

New, M., Hulme, M., and Jones, P. (2000). '**Representing twentieth-century space-time climate variability. Part II: Development of 1901-96 monthly grids of terrestrial surface climate**'. *Journal of Climate*, 13(13): 2217–2238

NRC (2008). '**Potential impacts of climate change on U.S. transportation**'. Transportation research board special report 290, Committee on Climate Change and U.S. Transportation, National Research Council (U.S.)

Oelke, C., Zhang, T., and Serreze, M. C. (2004). '**Modeling evidence for recent warming of the Arctic soil thermal regime**'. *Geophysical Research Letters*, 31(L07208): 4 PP

Pederson, G. T., Gray, S. T., Woodhouse, C. A., Betancourt, J. L., Fagre, D. B, Littell, J. S., Watson, E., Luckman, B. H., and Graumlich, L. J. (2011). '**The unusual nature of recent snowpack declines in the North American cordillera**'. *Science*, 333(6040): 332–335

Perron, P. (1989). '**The great crash, the oil price shock, and the unit root hypothesis**'. *Econometrica*, 57(6): 1361–1401

Perron, P. and Yabu, T. (2009a). '**Estimating deterministic trends with an integrated or stationary noise component**'. *Journal of Econometrics*, 151(1): 56–69

Perron, P. and Yabu, T. (2009b). '**Testing for shifts in trend with an integrated or stationary noise component**'. *Journal of Business and Economic Statistics*, 27(3): 369–396

Peterson, T. C. and Easterling, D. R. (1994). '**Creation of homogeneous composite climatological reference series**'. *International Journal of Climatology*, 14(6): 671–679

Peterson, T. C., Vose, R., Schmoyer, R., and Razuvaev, V. (1998). '**Global historical climatology network (GHCN) quality control of monthly temperature data**'. *International Journal of Climatology*, 18(11): 1169–1179

Polyakov, I. V., Bekryaev, R. V., Alekseev, G. V., Bhatt, U. S., Colony, R. L., Johnson, M. A., Maskshtas, A. P., and Walsh, D. (2003). '**Variability and trends of air temperature and pressure in the maritime Arctic, 1875-2000**'. *Journal of Climate*, 16(12): 2067–2077

Portman, D. A. (1993). '**Identifying and correcting urban bias in regional time series: surface temperature in China's northern plains**'. *Journal of Climate*, 6(12): 2298–2308

Powell, A. M. and Xu, J. (2011). '**A new assessment of the mid-1970s abrupt atmospheric temperature change in the NCEP/NCAR reanalysis and associated solar forcing implications**'. *Theoretical and Applied Climatology*, 104(3-4): 443–458

Pratt, J. W. (1959). '**Remarks on zeros and ties in the Wilcoxon signed rank procedures**'. *Journal of the American Statistical Association*, 54(287): 655–667

Prowse, T. D. and Beltaos, S. (2002). '**Climatic control of river-ice hydrology: a review**'. *Hydrological Processes*, 16(4): 805–822

Prowse, T. D., Bonsal, B. R., Duguay, C. R., Hessen, D. O., and Vuglinsky, V. S. (2007). '**River and lake ice**'. Technical report, United Nations Environment Programme (UNEP)

Prowse, T. D. and Ommanney, C. S. L., eds. (1990). **Northern Hydrology: Canadian Perspectives**. National Hydrology Research Institute (Canada)

Prowse, T. D., Shrestha, R., Bonsal, B., and Dibike, Y. (2010). '**Changing spring air-temperature gradients along large northern rivers: Implications for severity of river-ice floods**'. *Geophysical Research Letters*, 37(L19706): 6 PP

Putkonen, J. and Roe, G. (2003). '**Rain-on-snow events impact soil temperatures and affect ungulate survival**'. *Geophysical Research Letters*, 30(4): 37.1–37.4

Radic, V. and Hock, R. (2010). '**Regional and global volumes of glaciers derived from statistical upscaling of glacier inventory data**'. *Journal of Geophysical Research*, 115(F01010): 10 PP

Regonda, S. K. and Rajagopalan, B. (2005). '**Seasonal cycle shifts in hydroclimatology over the western United States**'. *Journal of Climate*, 18(2): 372–384

de Rham, L. P., Prowse, T. D., and Bonsal, B. R. (2008). '**Temporal variations in river-ice break-up over the Mackenzie River Basin, Canada**'. *Journal of Hydrology*, 349(3-4): 441–454

Rhoades, D. A. and Salinger, M. J. (1993). '**Adjustment of temperature and rainfall records for site changes**'. *International Journal of Climatology*, 13(8): 899–913

Rodionov, S. N. (2004). '**A sequential algorithm for testing climate regime shifts**'. *Geophysical Research Letters*, 31(L09204): 4 PP

Rodionov, S. N. (2006). '**Use of prewhitening in climate regime shift detection**'. *Geophysical Research Letters*, 33(L12707): 4 PP

Rodionov, S. N. (2007). Regime Shift Detector, `http://www.beringclimate.noaa.gov/`

Rodionov, S. N. and Overland, J. E. (2005). '**Application of a sequential regime shift detection method to the Bering Sea ecosystem**'. *ICES Journal of Marine Science*, 62(3): 328–332

Rohli, R. V. and Vega, A. J. (2008). **Climatology**. Jones and Bartlett Publishers

Schweizer, J., Jamieson, J. B., and Schneebeli, M. (2003). '**Snow avalanche formation**'. *Reviews of Geophysics*, 41(4): 2.1–2.25

Smith, L. C., Pavelsky, T. M., MacDonald, G. M., Shiklomanov, A. I., and Lammers, R. B. (2007). '**Rising minimum daily flows in northern Eurasian rivers: A growing influence of groundwater in the high-latitude hydrologic cycle**'. *Journal of Geophysical Research*, 112(G04S47): 18 PP

Steinberg, D. and Colla, P. (1995). '**CART: tree-structured non-parametric data analysis**'. Salford Systems

Stendel, M. and Christensen, J. H. (2002). '**Impact of global warming on permafrost conditions in a coupled GCM**'. *Geophysical Research Letters*, 29(13): 10.1–10.4

Stewart, I. T. (2009). '**Changes in snowpack and snowmelt runoff for key mountain regions**'. *Hydrological Processes*, 23(1): 78–94

Stone, R. S., Dutton, E. G., Harris, J. M., and Longenecker, D. (2002). '**Earlier spring snowmelt in northern Alaska as an indicator of climate change**'. *Journal of Geophysical Research*, 107(D10): ACL 10–1

Storch, H. and Zwiers, F. W. (1999). **Statistical Analysis in Climate Research**. Cambridge University Press

SWIPA (2011). '**Snow, water, ice and permafrost in the Arctic (SWIPA): Executive Summary**'. Technical report, Coordinated by AMAP and produced in collaboration with IASC, WMO/Clic and IASSA

Syed, T. H., Famiglietti, J. S., Zlotnicki, V., and Rodell, M. (2007). '**Contemporary estimates of Pan-Arctic freshwater discharge from GRACE and reanalysis**'. *Geophysical Research Letters*, 34(L19404): 6 PP

Tiana, Y., Uenob, Y., Sudaa, M., and Akaminea, T. (2004). '**Decadal variability in the abundance of Pacific saury and its response to climatic/oceanic regime shifts in the northwestern subtropical Pacific during the last half century** '. *Journal of Marine Systems*, 52(1-4): 235–257

Trenberth, K. E. and Shea, D. J. (2005). '**Relationships between precipitation and surface temperature**'. *Geophysical Research Letters*, 32(L14703): 4 PP

University of East Anglia Climate Research Unit (2011). '**CRU Time Series (TS) high resolution gridded datasets**'. NCAS British Atmospheric Data Centre, `http://badc.nerc.ac.uk/view/badc.nerc.ac.uk__ATOM__dataent_1256223773328276`

Vogelsang, T. (1999). '**Testing for a shift in trend when serial correlation is of unknown form**'. Tinbergen Institute Discussion Papers, `https://www.msu.edu/~tjv/trendbrk.pdf`

Vogelsang, T. J. and Perron, P. (1998). '**Additional tests for a unit root allowing the possibility of breaks in the trend function**'. *International Economic Review*, 39(4): 1073–1100

Walvoord, M. A. and Striegl, R. G. (2007). '**Increased groundwater to stream discharge from permafrost thawing in the Yukon River basin: potential impacts on lateral export of carbon and nitrogen**'. *Geophysical Research Letters*, 34(L12402): 6 PP

Watanabe, M. and Nitta, T. (1999). '**Decadal changes in the atmospheric circulation and associated surface climate variations in the Northern Hemisphere winter**'. *Journal of Climate*, 12(2): 494–510

Woo, M. K., Kane, D. L., Carey, S. K., and Yang, D. (2008). '**Progress in permafrost hydrology in the new millennium**'. *Permafrost and Periglacial Processes*, 19(2): 237–254

Yue, S. and Pilon, P. (2003). '**Canadian streamflow trend detection: impacts of serial and cross-correlation**'. *Hydrological Sciences Journal*, 48(1): 51–63

Yue, S. and Pilon, P. (2004). '**A comparison of the power of the t-test, Mann-Kendall and bootstrap tests for trend detection**'. *Hydrological Sciences Journal*, 49(1): 21–37

Yue, S., Pilon, P., Phinney, B., and Cavadias, G. (2002). '**The influence of autocorrelation on the ability to detect trend in hydrological series**'. *Hydrological Processes*, 16(9): 1807–1829

Zhang, T., Frauenfeld, O. W., Serreze, M. C., Etringer, A., Oelke, C., McCreight, J., Barry, R. G., Gilichinsky, D., Yang, D., Ye, H., Ling, F., and Chudinova, S. (2005). '**Spatial and temporal variability in active layer thickness over the Russian Arctic drainage basin**'. *Journal of Geophysical Research*, 110(D16101): 14 PP

Zhang, X., Harvey, K. D., Hogg, W. D., and Yuzyk, T. R. (2001). '**Trends in Canadian streamflow**'. *Water Resources Research*, 37(4): 987–998

Zhang, X., Vincent, L. A., Hogg, W. D., and Niitsoo, A. (2000). '**Temperature and precipitation trends in Canada during the 20th century**'. *Atmosphere-Ocean*, 38(3): 395–429

Zivot, E. and Andrews, D. W. K. (1992). '**Further evidence on the great crash, the oil-price shock, and the unit-root hypothesis**'. *Journal of Business and Economic Statistics*, 10(3): 25–44

# Appendix A

# Sample Plots of Different Techniques

# A.1 Model 2

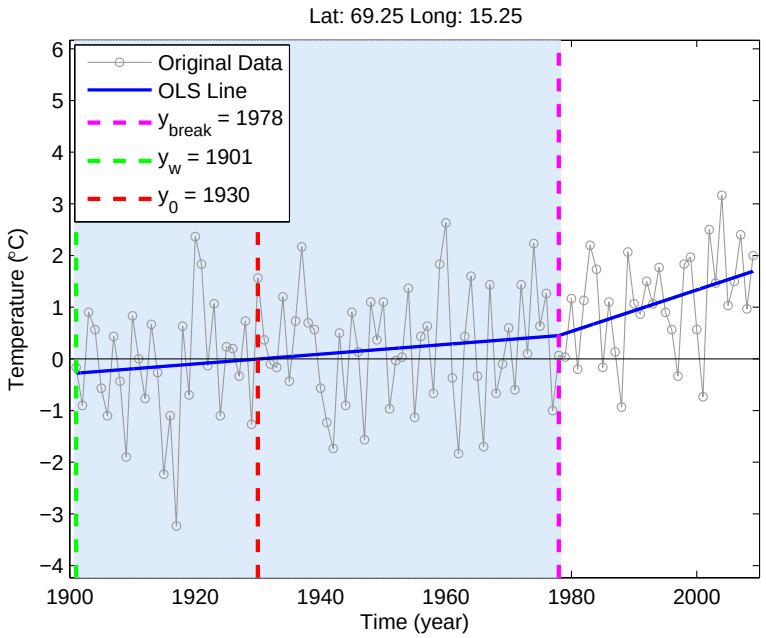


**Figure A.1:** The **MAM** time series above is approximated using **Model 2**. Following Rule 1a indicated in Section 5.4.2, $y_0$ and $y_w$ are evaluated. The segment shaded in blue is $S_{interest}$.

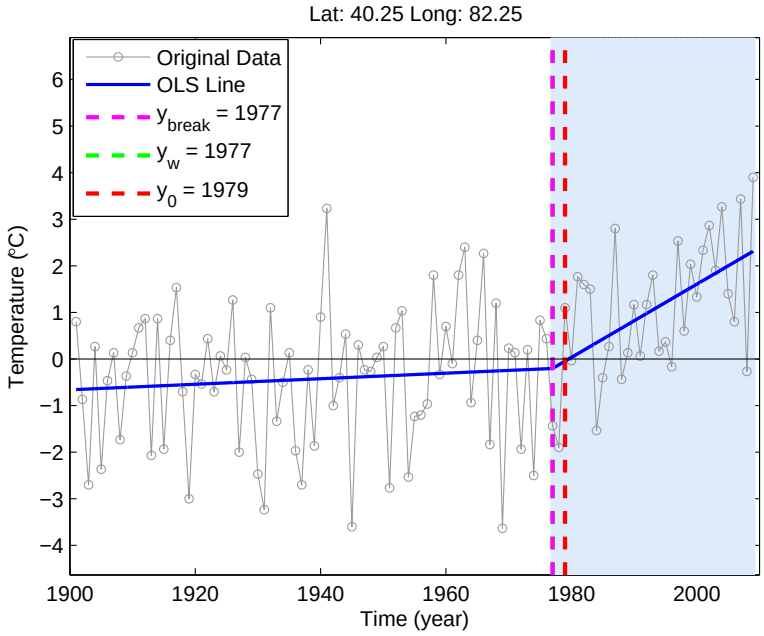


**Figure A.2:** The **JFM** time series above is approximated using **Model 2**. Following Rule 1b indicated in Section 5.4.2, $y_0$ and $y_w$ are evaluated. The segment shaded in blue is $S_{interest}$.

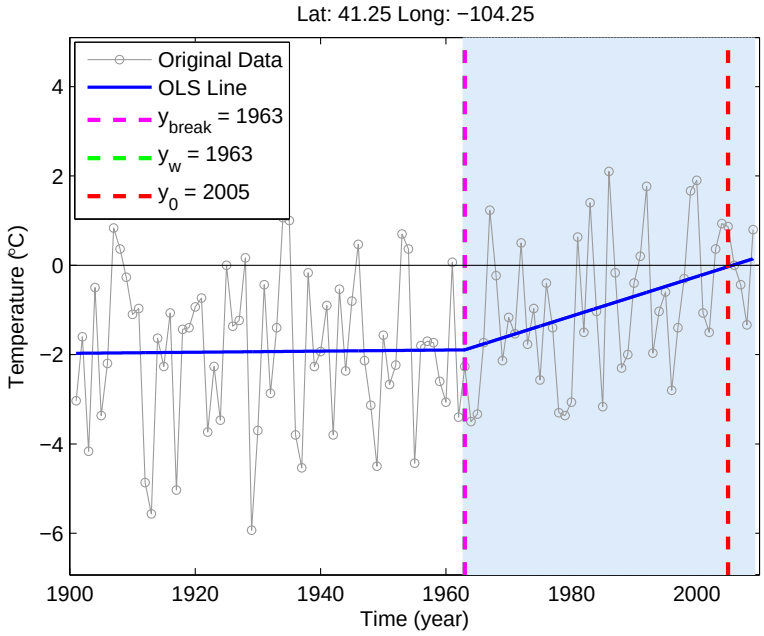


**Figure A.3:** The **JFM** time series above is approximated using **Model 2**. Following Rule 1b indicated in Section 5.4.2, $y_0$ and $y_w$ are evaluated. The segment shaded in blue is $S_{interest}$.

## A.2 Model 3

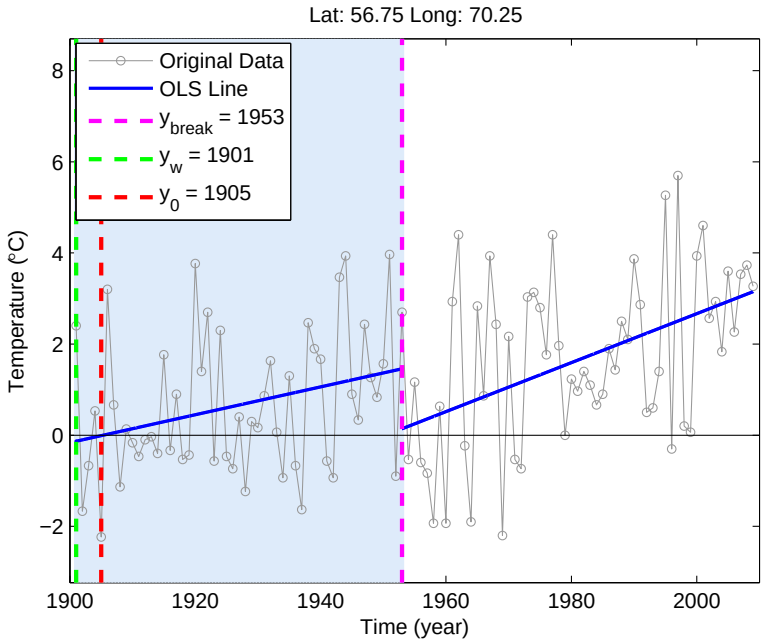


**Figure A.4:** The **MAM** time series above is approximated using **Model 3**. Following Rule 1a indicated in Section 5.4.2, $y_0$ and $y_w$ are evaluated. The segment shaded in blue is $S_{interest}$.

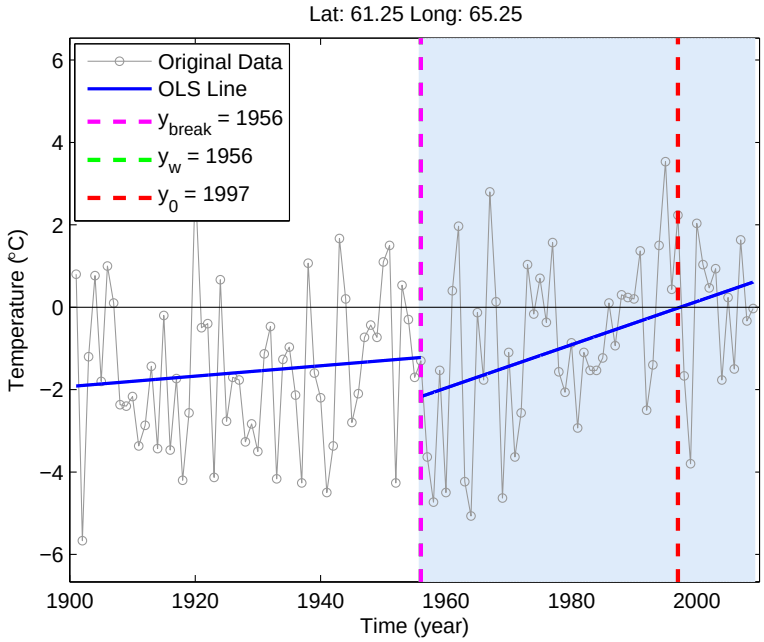


**Figure A.5:** The **MAM** time series above is approximated using **Model 3**. Following Rule 1b indicated in Section 5.4.2, $y_0$ and $y_w$ are evaluated. The segment shaded in blue is $S_{interest}$.

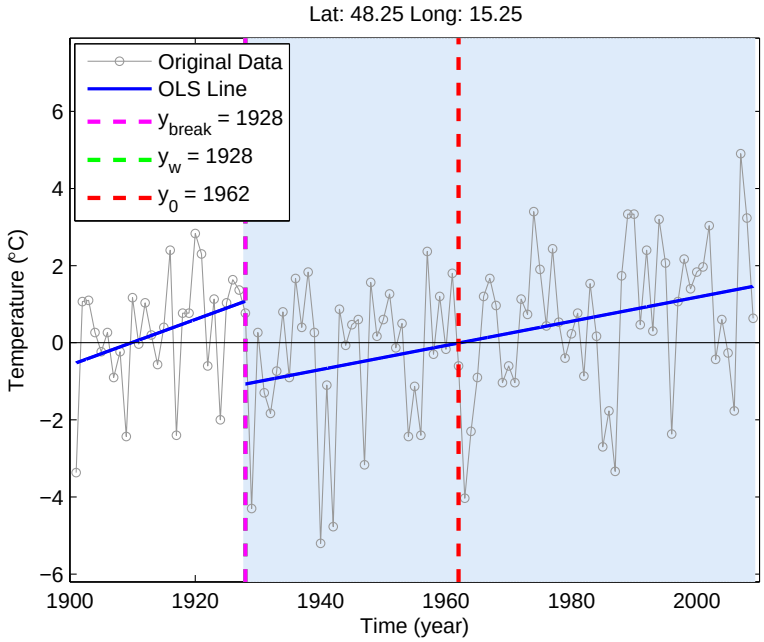


**Figure A.6:** The **JFM** time series above is approximated using **Model 3**. $y_0$ and $y_w$ are evaluated following Rule 2a indicated in Section 5.4.2: The first segment has a larger slope; however, the cumulative warming is larger over the second segment. Therefore, $S_{interest}$ is the second segment.

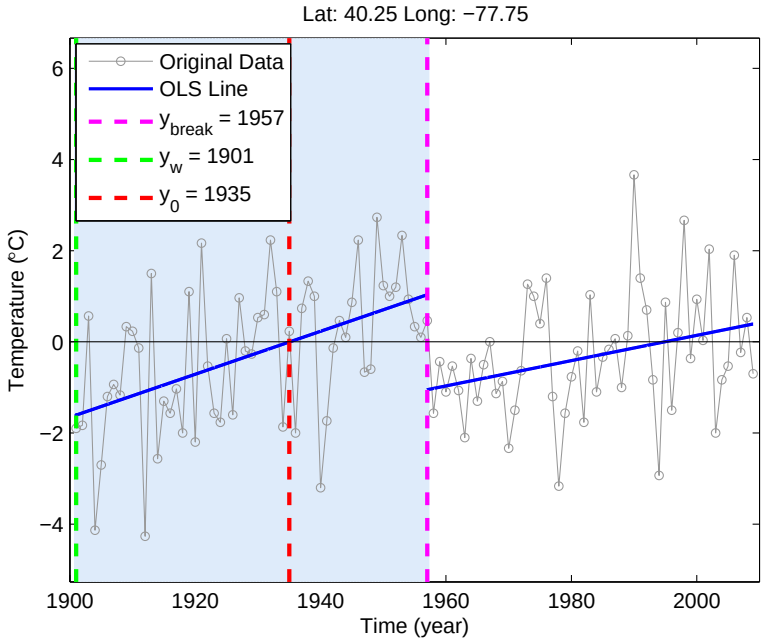


**Figure A.7:** The **JFM** time series above is approximated using **Model 3**. $y_0$ and $y_w$ are evaluated following Rule 2a indicated in Section 5.4.2: The first segment has the maximum slope and cumulative warming. Therefore, $S_{interest}$ is the first segment.

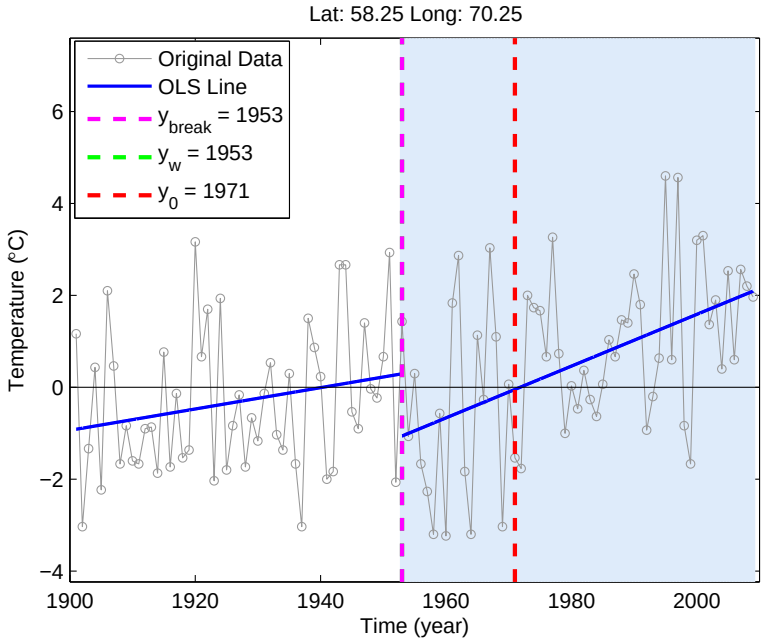


**Figure A.8:** The **JFM** time series above is approximated using **Model 3**. $y_0$ and $y_w$ are evaluated following Rule 2b indicated in Section 5.4.2: The second segment has the largest slope and cumulative warming. Therefore, $S_{interest}$ is the second segment.

## A.3 MARS

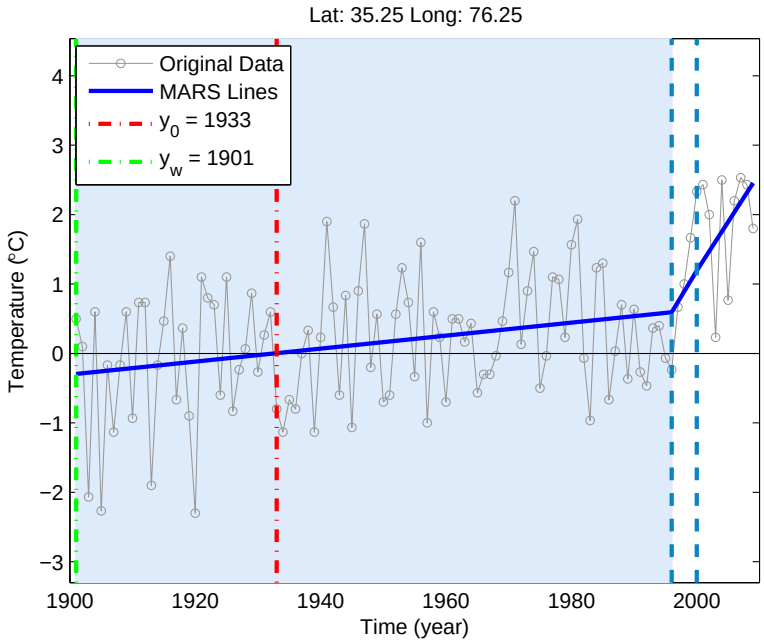


**Figure A.9:** The **MAM** time series above is approximated using **MARS**. The boundaries are the dashed blue lines, and the time series is modelled by three segments which are continuous at the boundaries. $y_0$ and $y_w$ are evaluated following Rule 1a indicated in Section 5.5.2: The only positive 0°C crossing takes place in the first segment, and it is selected as $S_{interest}$. Starting from 1901, temperature is constantly increasing.

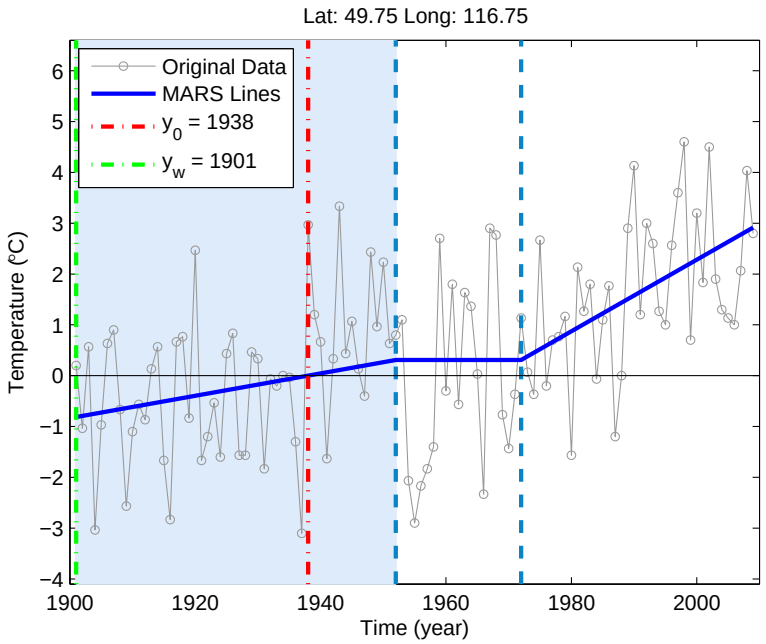


**Figure A.10:** The **MAM** time series above is approximated using **MARS**. The model consists of three segments separated by the dashed blue lines. $y_0$ and $y_w$ are evaluated following Rule 1a indicated in Section 5.5.2: The only positive 0°C crossing takes place in the first segment, and it is selected as $S_{interest}$. The increase in temperature initiates at 1901. Warming resumes in the third segment after a short period of constant average temperature.

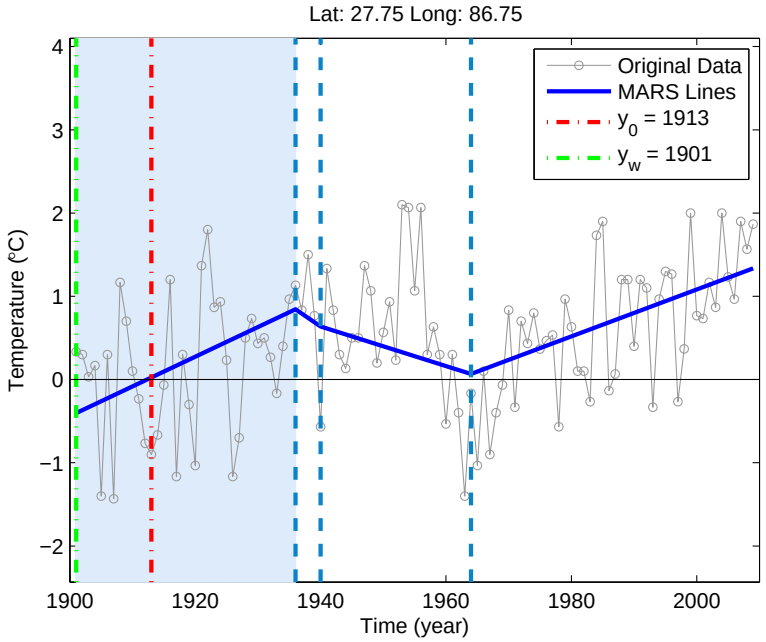


**Figure A.11:** The **MAM** time series above is approximated using **MARS**. It is modelled by four segments which are continuous at the boundaries. $y_0$ and $y_w$ are determined following Rule 1a indicated in Section 5.5.2: The only positive 0°C crossing takes place in the first segment, and it is selected as $S_{interest}$. Temperature moves above 0°C at 1913. Despite some fluctuations during the second and third segments, temperature stays above the 0°C line, and warming resumes at 1964.

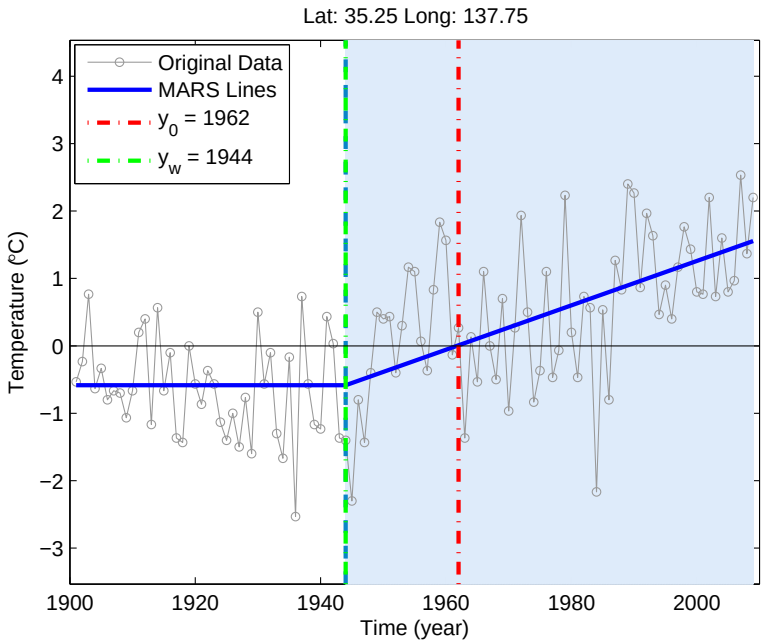


**Figure A.12:** The **JFM** time series above is approximated using **MARS**. $y_0$ and $y_w$ are determined following Rule 1b indicated in Section 5.5.2: The only positive 0°C crossing takes place in the second segment, and it is selected as $S_{interest}$.

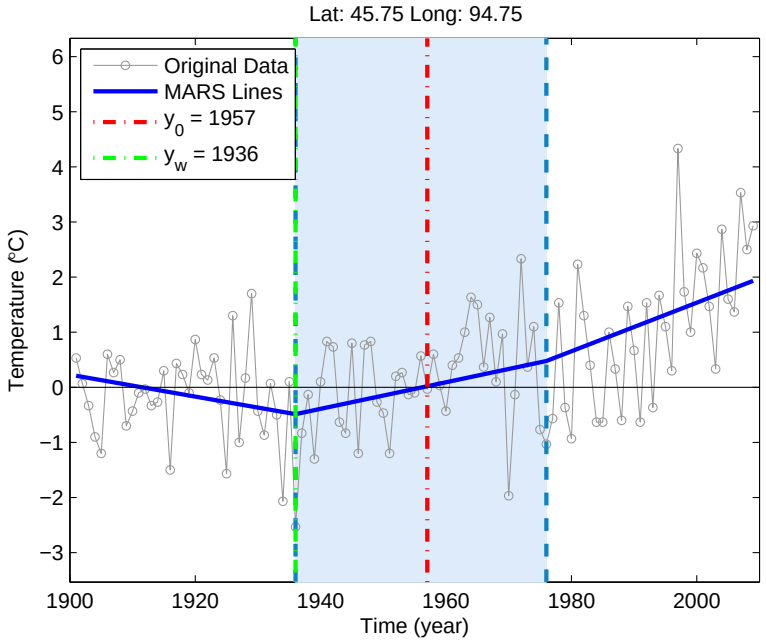


**Figure A.13:** The **MAM** time series above is approximated using **MARS**. $y_0$ and $y_w$ are determined following Rule 1b indicated in Section 5.5.2: The only positive 0°C crossing takes place in the second segment, and it is selected as $S_{interest}$.

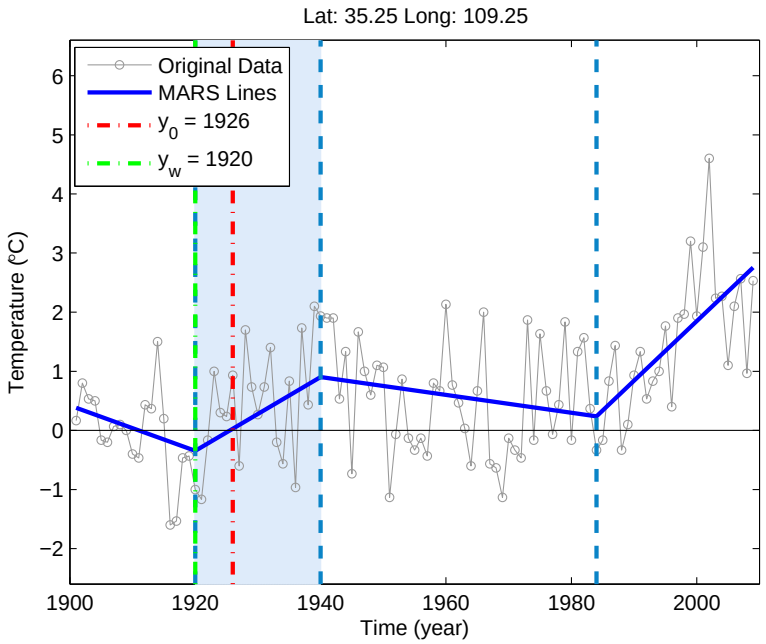


**Figure A.14:** The **JFM** time series above is approximated using **MARS**. The model consists of four segments which are continuous at the boundaries. $y_0$ and $y_w$ are determined following Rule 1b indicated in Section 5.5.2: The only positive 0°C crossing takes place in the second segment, and it is selected as $S_{interest}$. Warming starts at 1920, and the sign of temperature changes a few years later at 1926. Temperature remains positive despite the decreasing temperature during the third segment. The increase in temperature resumes at 1984.

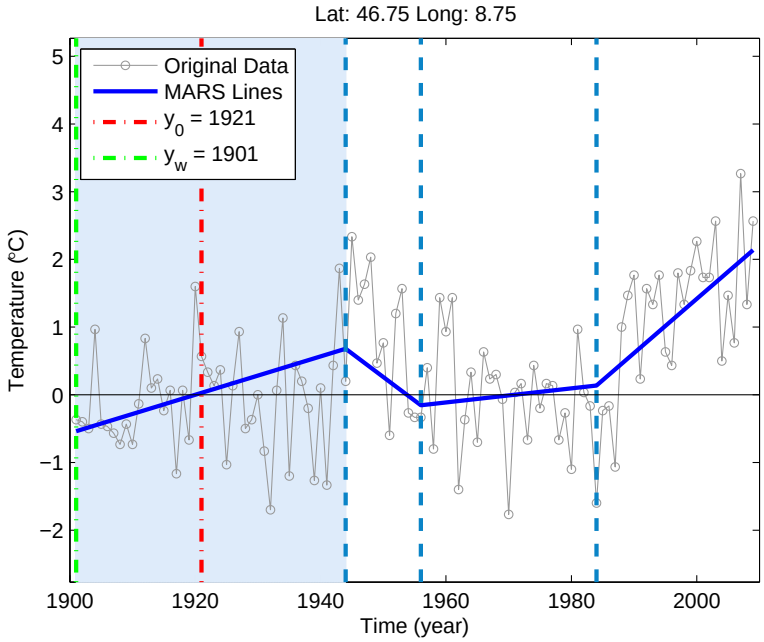


**Figure A.15:** The **MAM** time series above is approximated using **MARS**. The model consists of four segments which are continuous at the boundaries. $y_0$ and $y_w$ are determined following Rule 2a indicated in Section 5.5.2. There are two positive 0°C crossings, and the first segment has the maximum slope and cumulative warming; hence, it is selected as $S_{interest}$. Temperature crosses 0°C at 1921, and for a short period during the second and third segments, temperature turns negative. However, it goes back above 0°C and continues to increase.

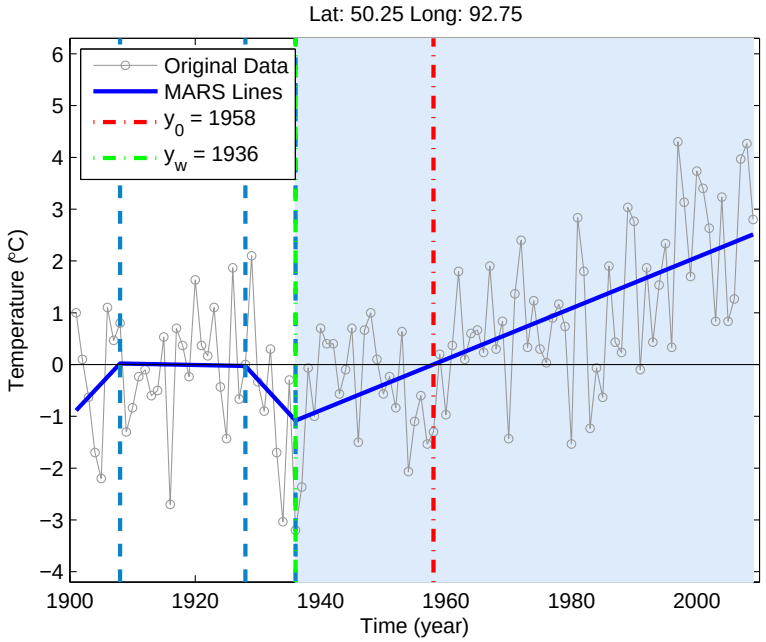


**Figure A.16:** The **MAM** time series above is approximated using **MARS**. The model consists of four segments which are continuous at the boundaries. $y_0$ and $y_w$ are determined following Rule 2a indicated in Section 5.5.2. There are two positive 0°C crossings, and the first segment has the maximum slope. However, it occurs over a short period, and the increase in temperature is insignificant until the beginning of the fourth segment. During this segment, significant warming takes place despite its smaller slope, and it is selected as $S_{interest}$

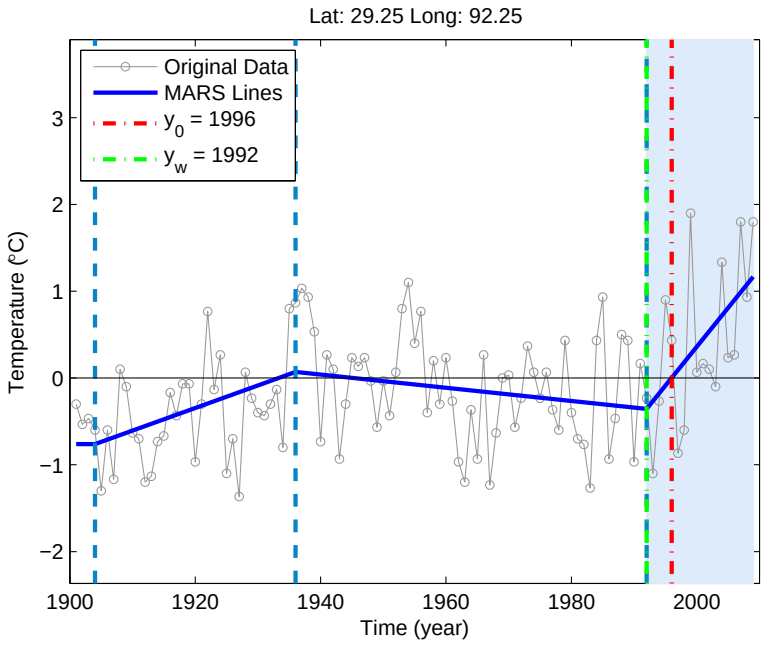


**Figure A.17:** The **MAM** time series above is approximated using **MARS**. The model consists of four segments which are continuous at the boundaries. $y_0$ and $y_w$ are determined following Rule 2b indicated in Section 5.5.2. There are two positive 0°C crossings which take place during the second and fourth segments. The last segment has the maximum slope and is selected as $S_{interest}$. Temperature fluctuates prior to 1992, and for a few years, it rises above 0°C. A sharp increase in temperature starts at 1992 and continues until the end of the time series.

## A.4 R Method

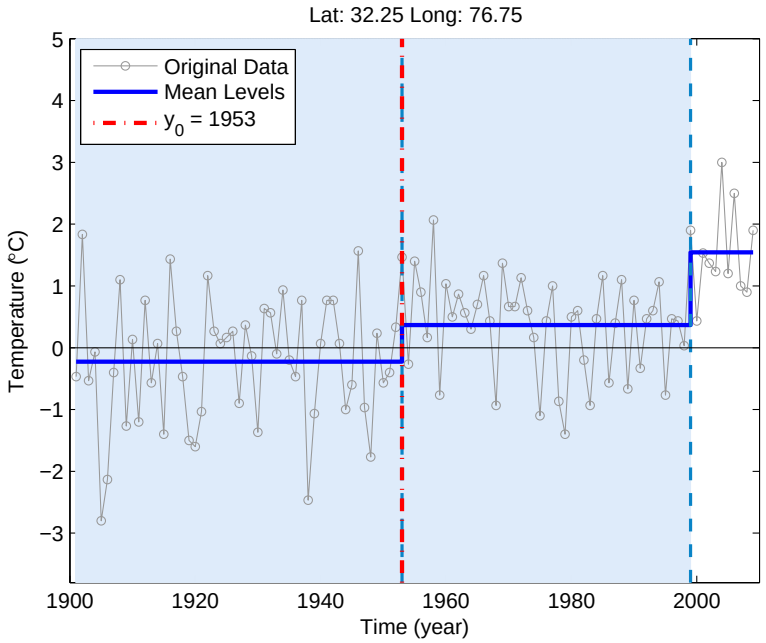


**Figure A.18:** The **JFM** time series above is approximated using the **R method**. The boundaries are the dashed blue lines, and the time series is modelled by three segments with disjoint boundaries. $y_0$ is determined based on Rule 1 (Section 5.6.2). The segment shaded in blue is $S_{interest}$.

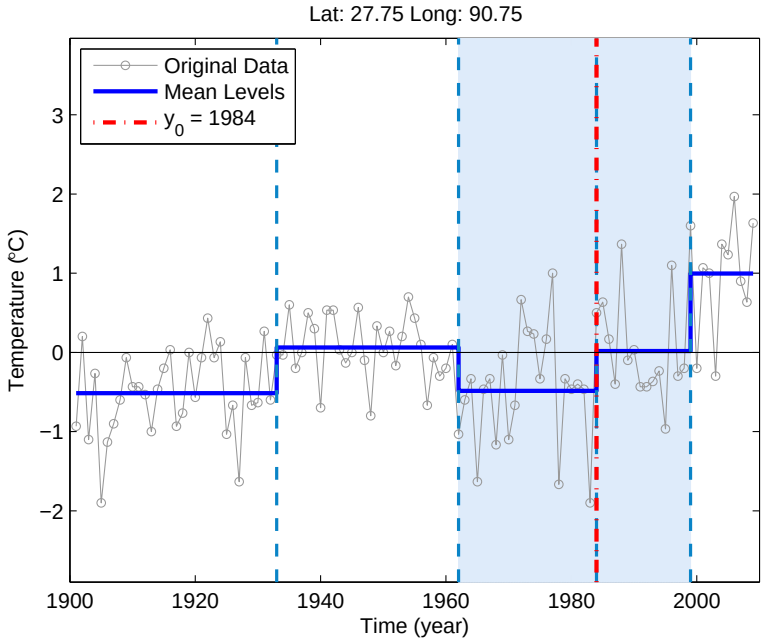


**Figure A.19:** The **JFM** time series above is approximated using the **R method**. The boundaries are the dashed blue lines, and the time series is modelled by five segments with disjoint boundaries. $y_0$ is determined based on Rule 2 (Section 5.6.2). The segment shaded in blue is $S_{\text{interest}}$.

# Appendix B

# Histograms of Different Techniques for Various Regions

# B.1 JFM

## B.1.1 MARS

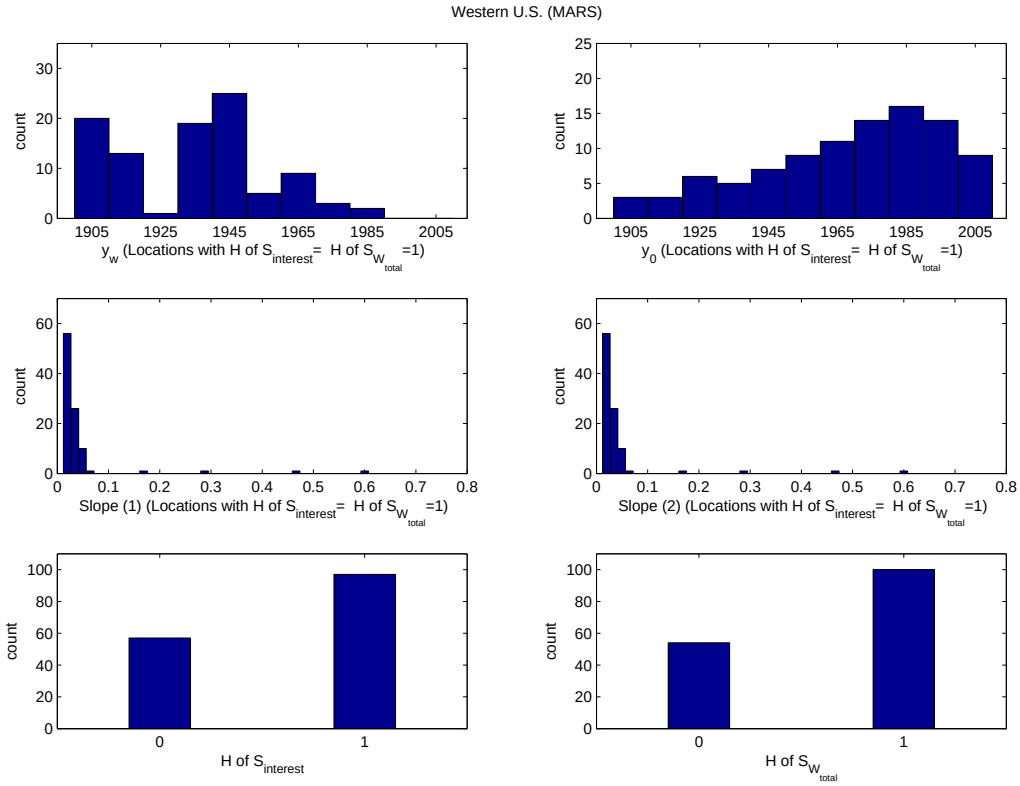


**Figure B.1:** Histograms of the analysed variables (Section 5.2) during **JFM** for western U.S. The results are obtained using **MARS**.

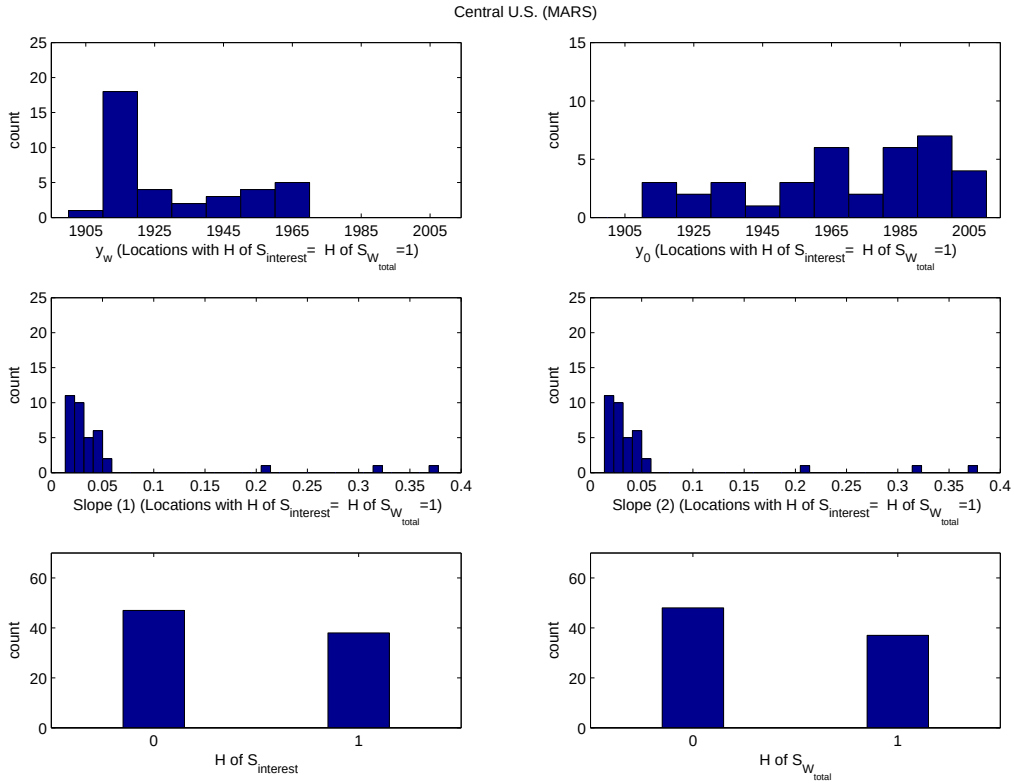


**Figure B.2:** Histograms of the analysed variables (Section 5.2) during **JFM** for central U.S. The results are obtained using **MARS**.

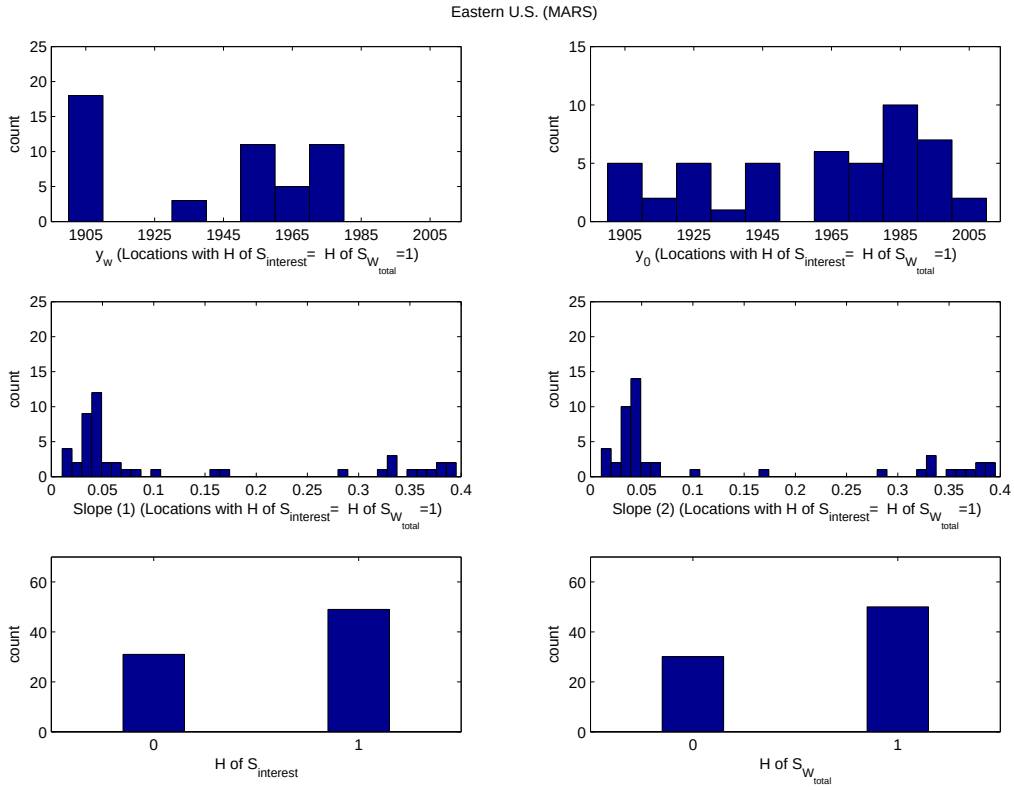


**Figure B.3:** Histograms of the analysed variables (Section 5.2) during **JFM** for eastern U.S. The results are obtained using **MARS**.

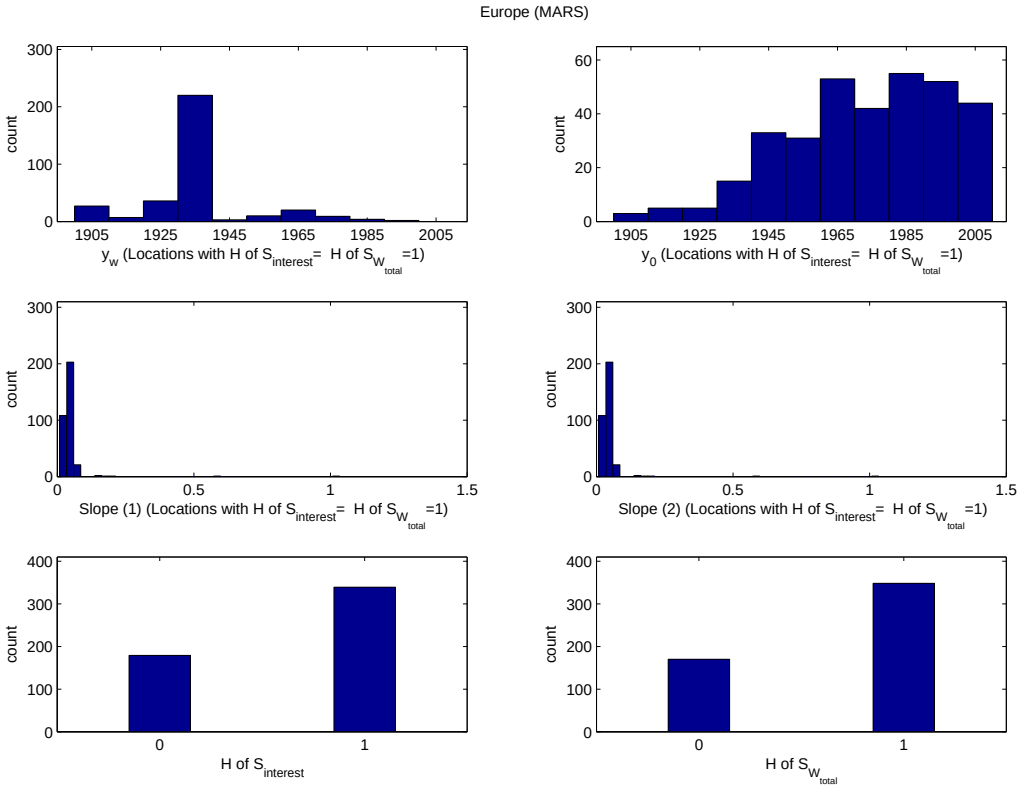


**Figure B.4:** Histograms of the analysed variables (Section 5.2) during **JFM** for Europe. The results are obtained using **MARS**.

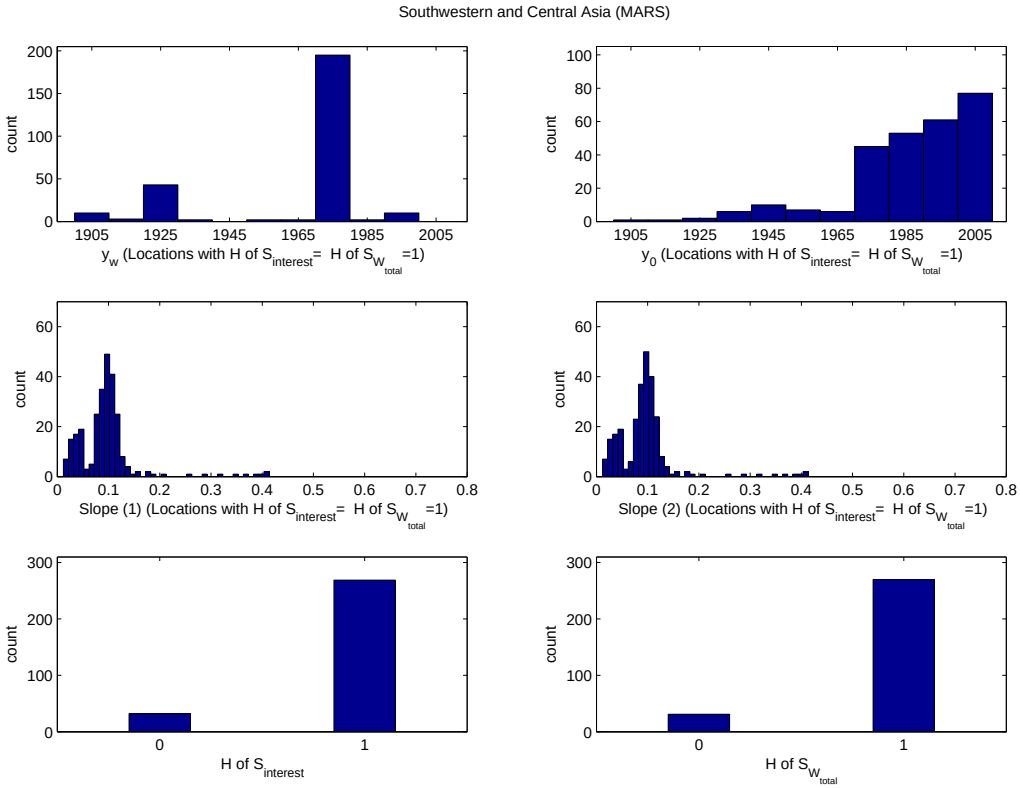


**Figure B.5:** Histograms of the analysed variables (Section 5.2) during **JFM** for southwestern and central Asia. The results are obtained using **MARS**.

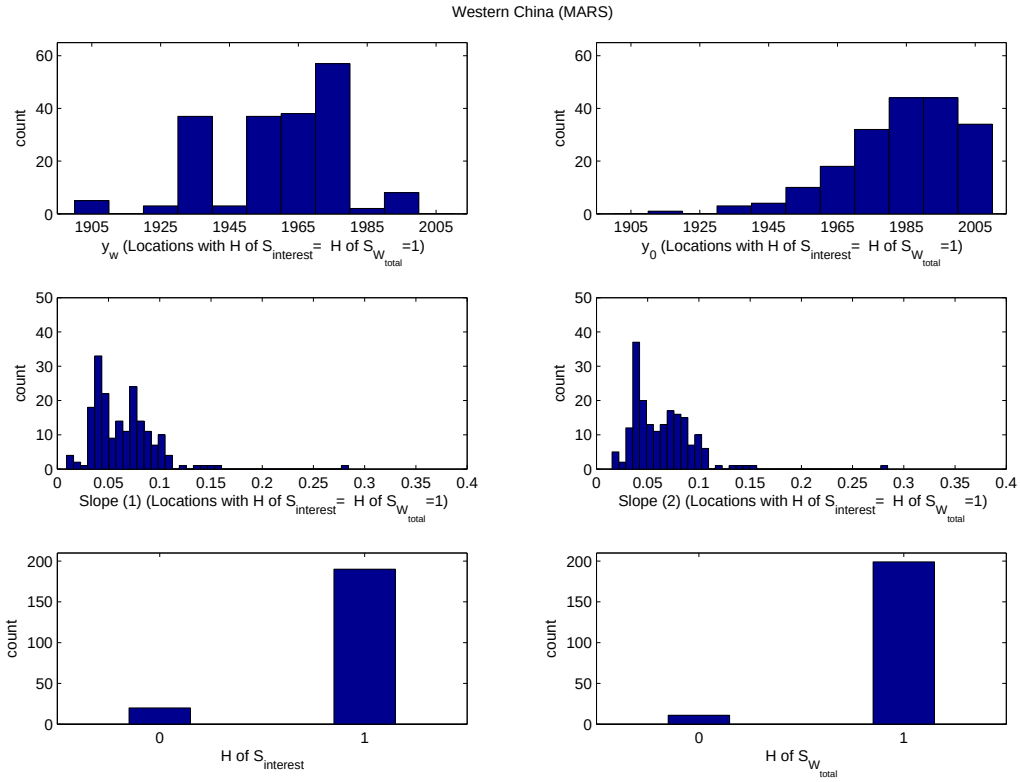


**Figure B.6:** Histograms of the analysed variables (Section 5.2) during **JFM** for western China. The results are obtained using **MARS**.

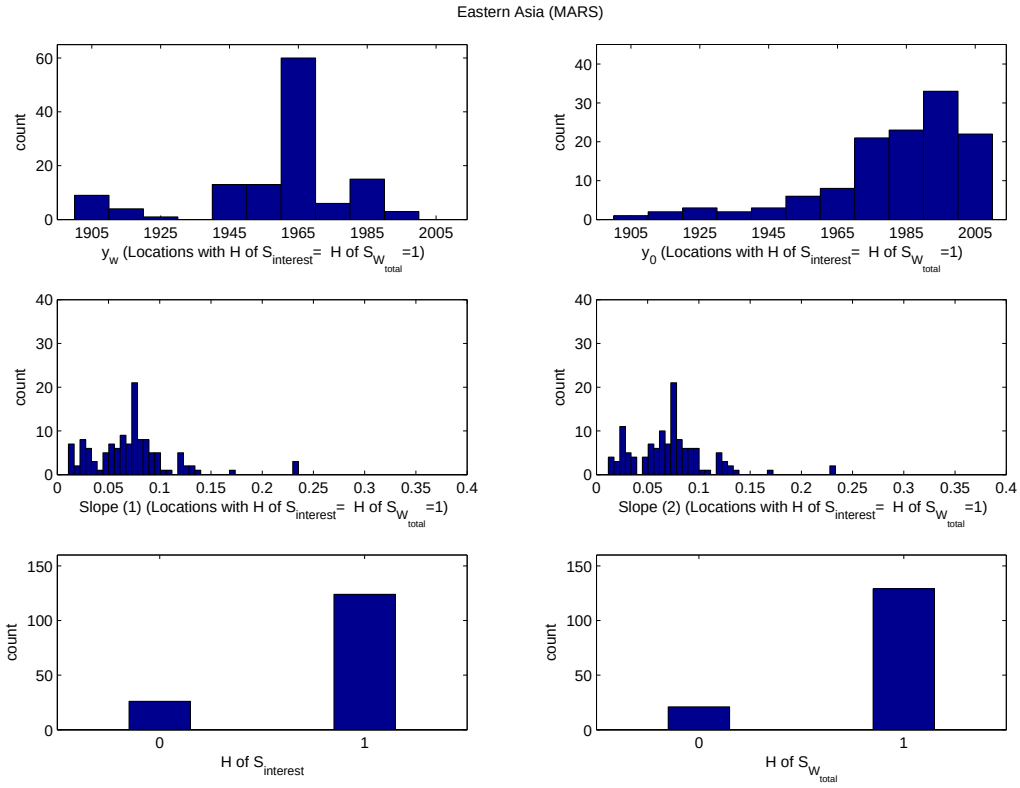


**Figure B.7:** Histograms of the analysed variables (Section 5.2) during **JFM** for eastern Asia. The results are obtained using **MARS**.

## B.1.2 Model 2

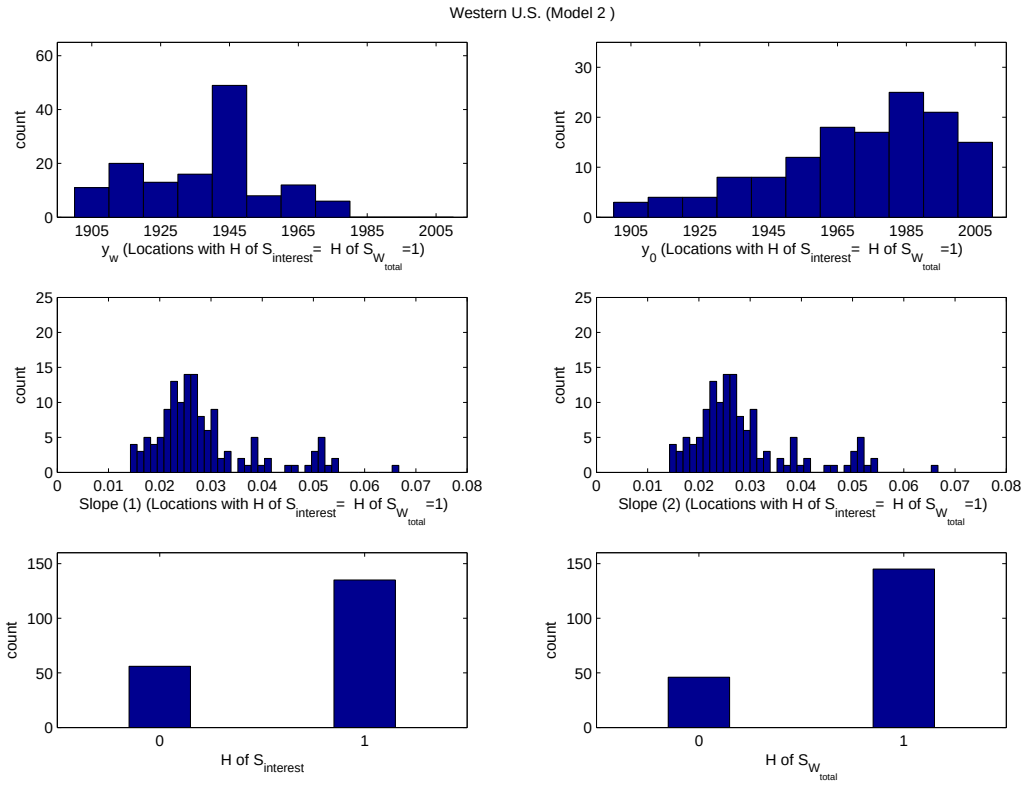


**Figure B.8:** Histograms of the analysed variables (Section 5.2) during **JFM** for western U.S. The results are obtained using **Model 2**.

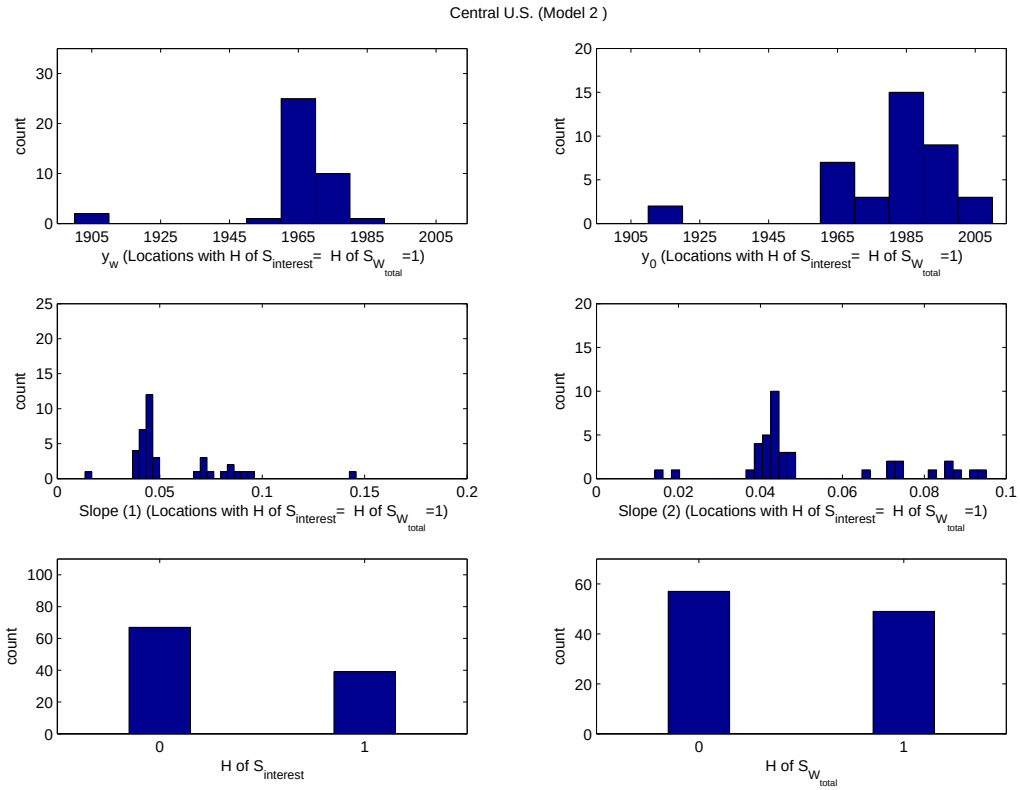


**Figure B.9:** Histograms of the analysed variables (Section 5.2) during **JFM** for central U.S. The results are obtained using **Model 2**.

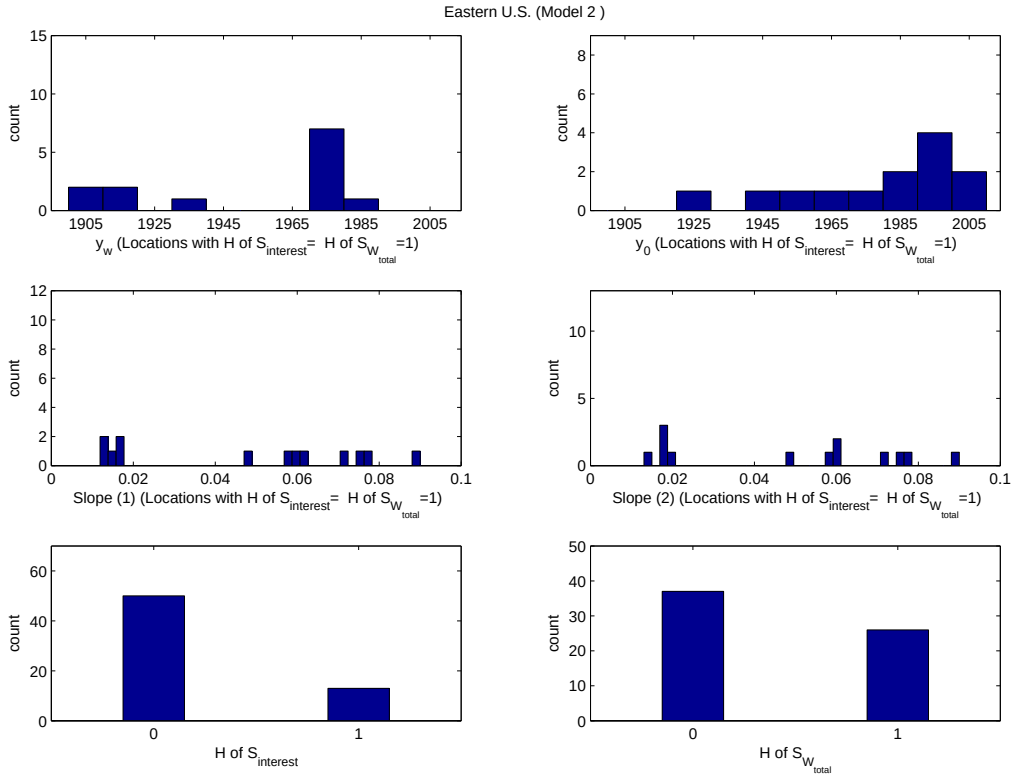


**Figure B.10:** Histograms of the analysed variables (Section 5.2) during **JFM** for eastern U.S. The results are obtained using **Model 2**.

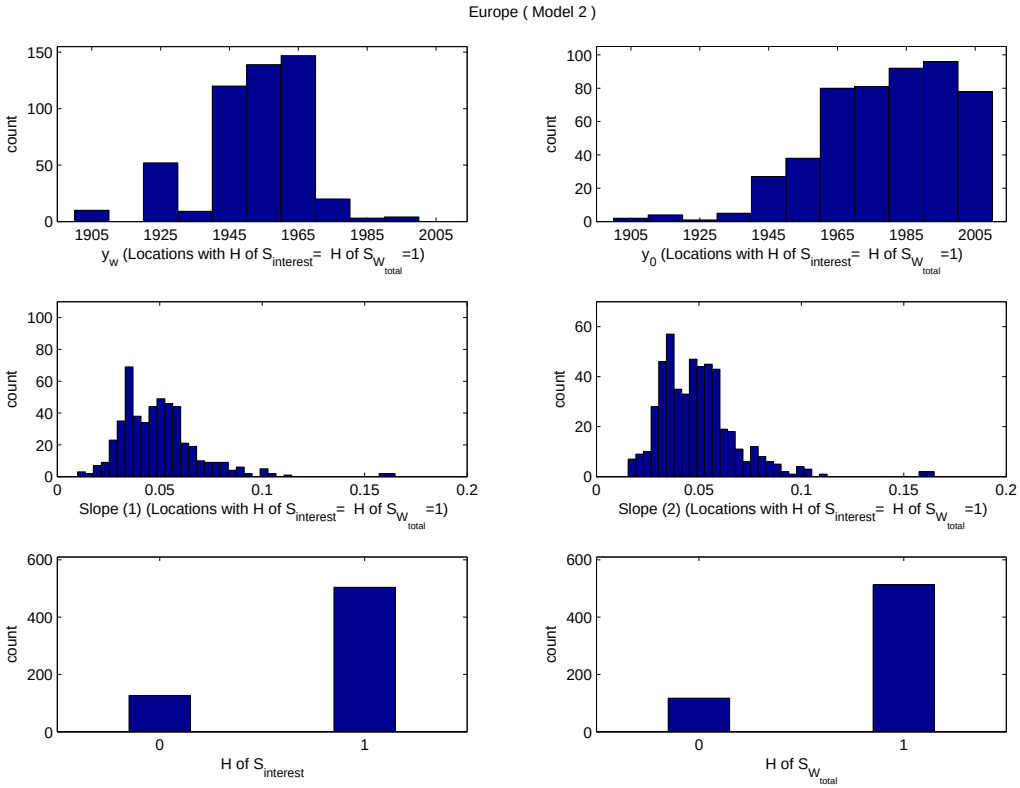


**Figure B.11:** Histograms of the analysed variables (Section 5.2) during **JFM** for Europe. The results are obtained using **Model 2**.

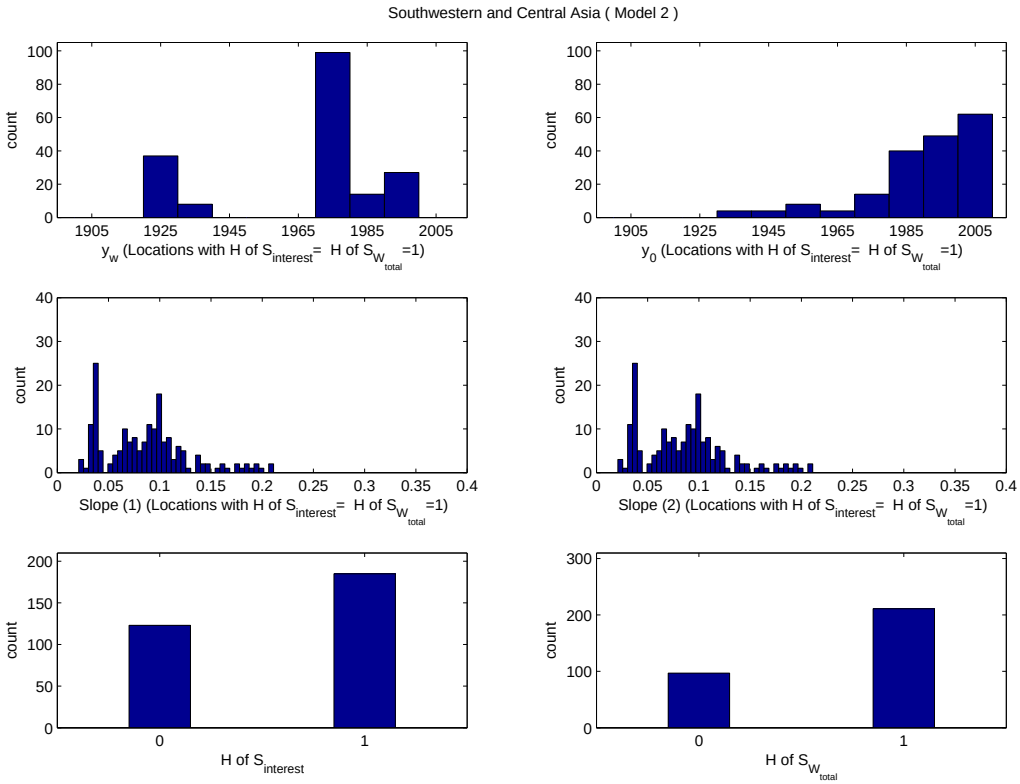


**Figure B.12:** Histograms of the analysed variables (Section 5.2) during **JFM** for southwestern and central Asia. The results are obtained using **Model 2**.

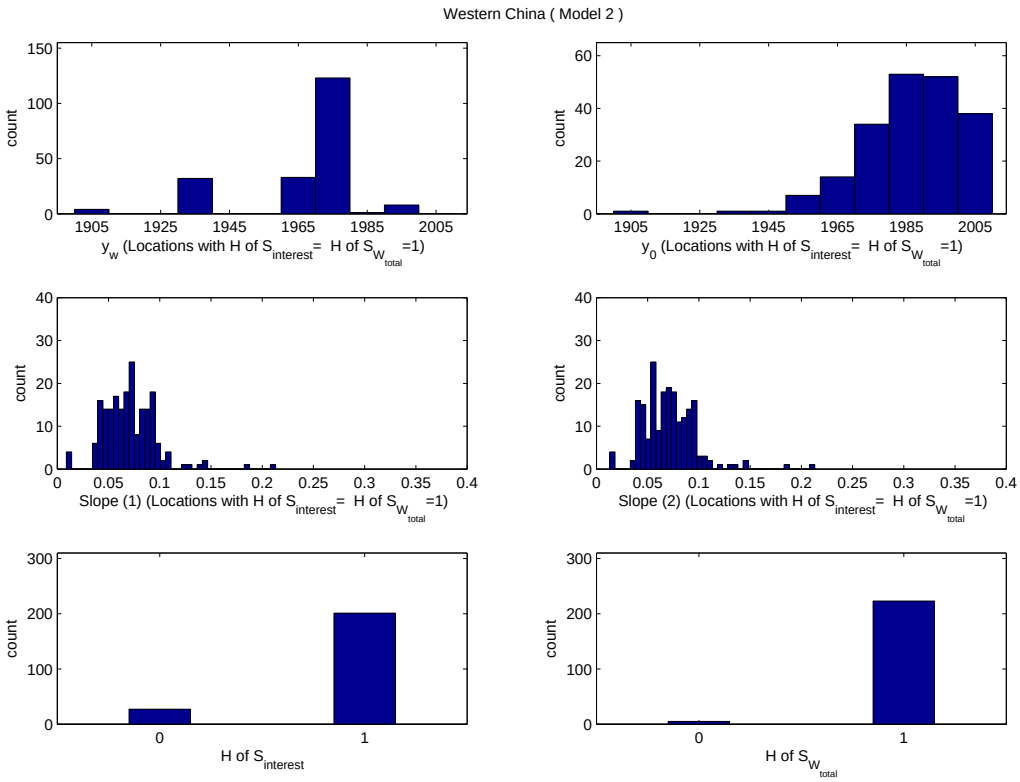


**Figure B.13:** Histograms of the analysed variables (Section 5.2) during **JFM** for western China. The results are obtained using **Model 2**.

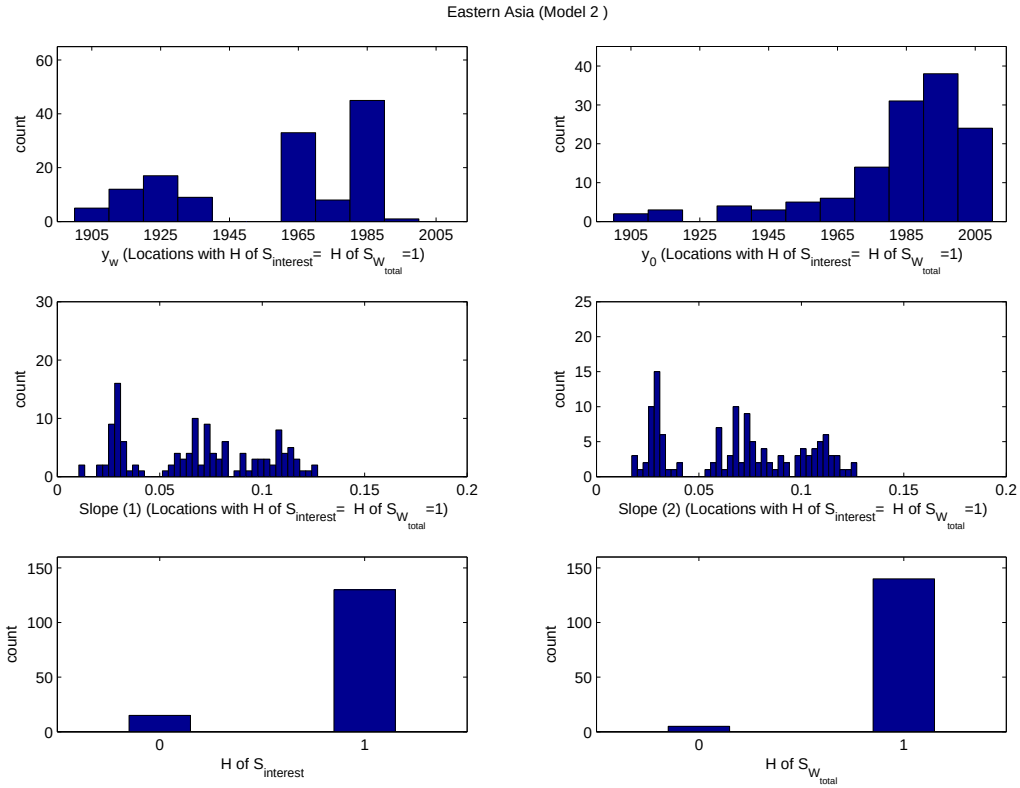


**Figure B.14:** Histograms of the analysed variables (Section 5.2) during **JFM** for eastern Asia. The results are obtained using **Model 2**.

### B.1.3 Model 3

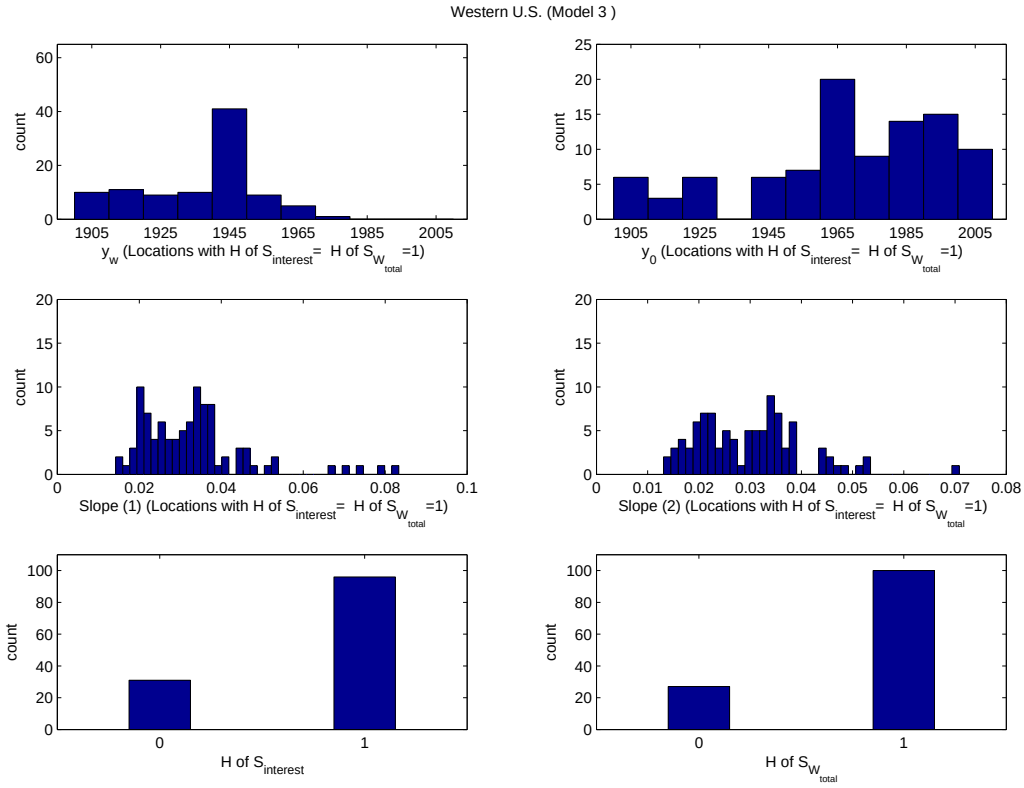


**Figure B.15:** Histograms of the analysed variables (Section 5.2) during **JFM** for western U.S. The results are obtained using **Model 3**.

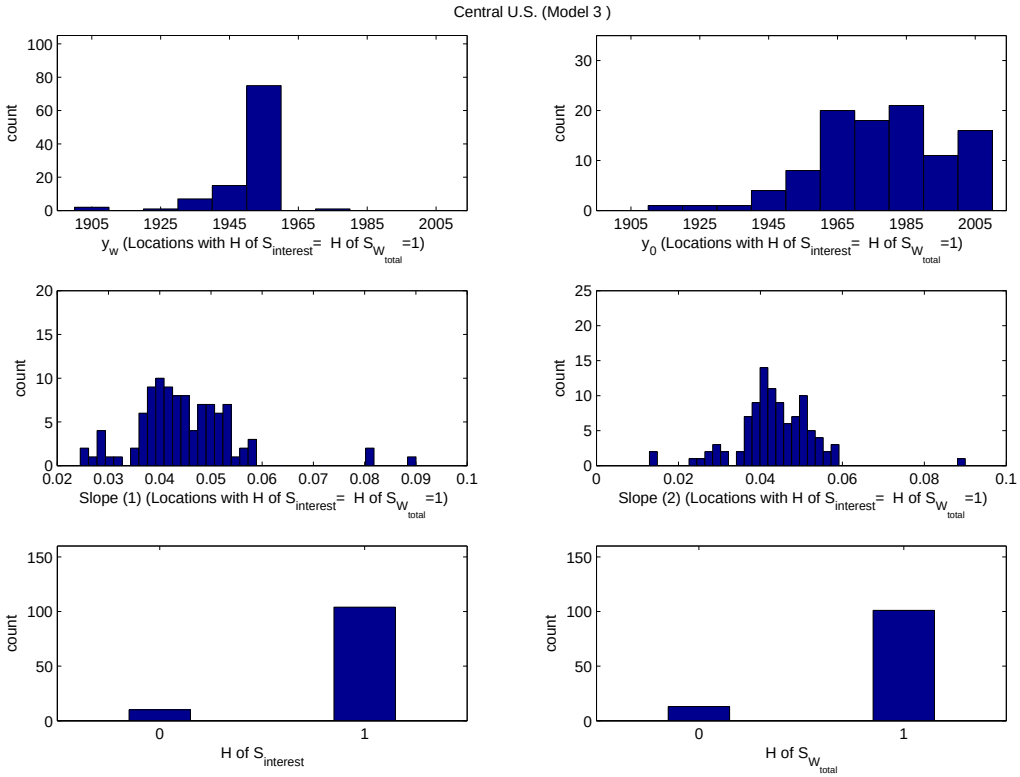


**Figure B.16:** Histograms of the analysed variables (Section 5.2) during **JFM** for central U.S. The results are obtained using **Model 3**.

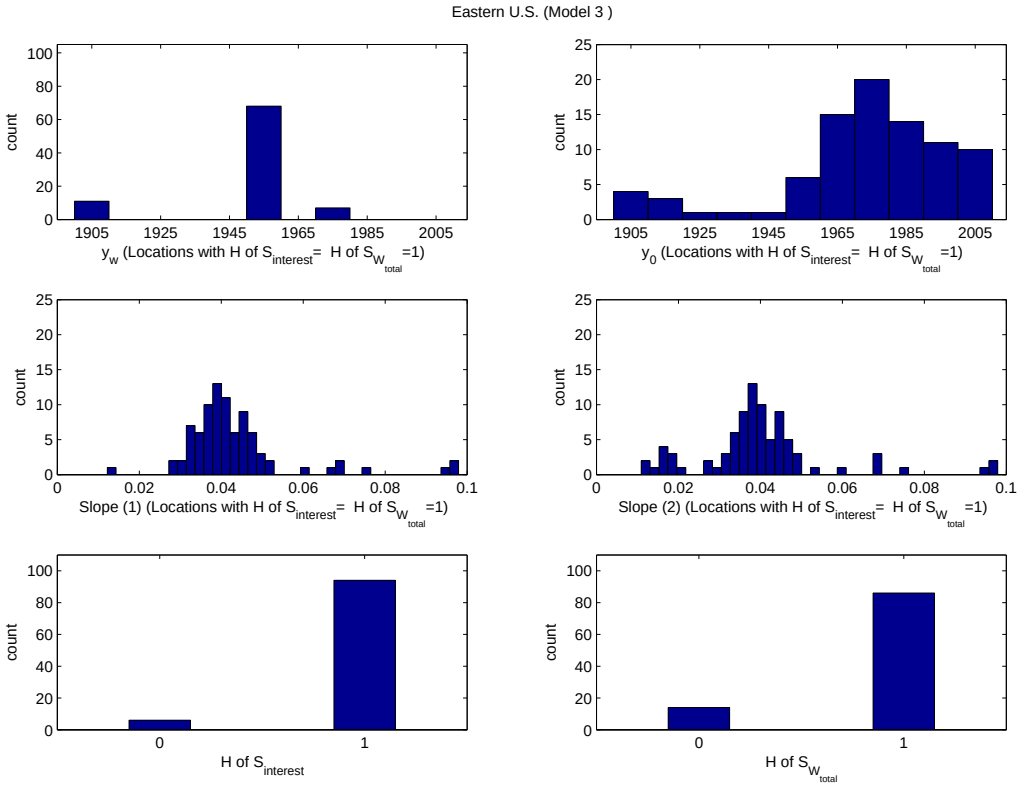


**Figure B.17:** Histograms of the analysed variables (Section 5.2) during **JFM** for eastern U.S. The results are obtained using **Model 3**.

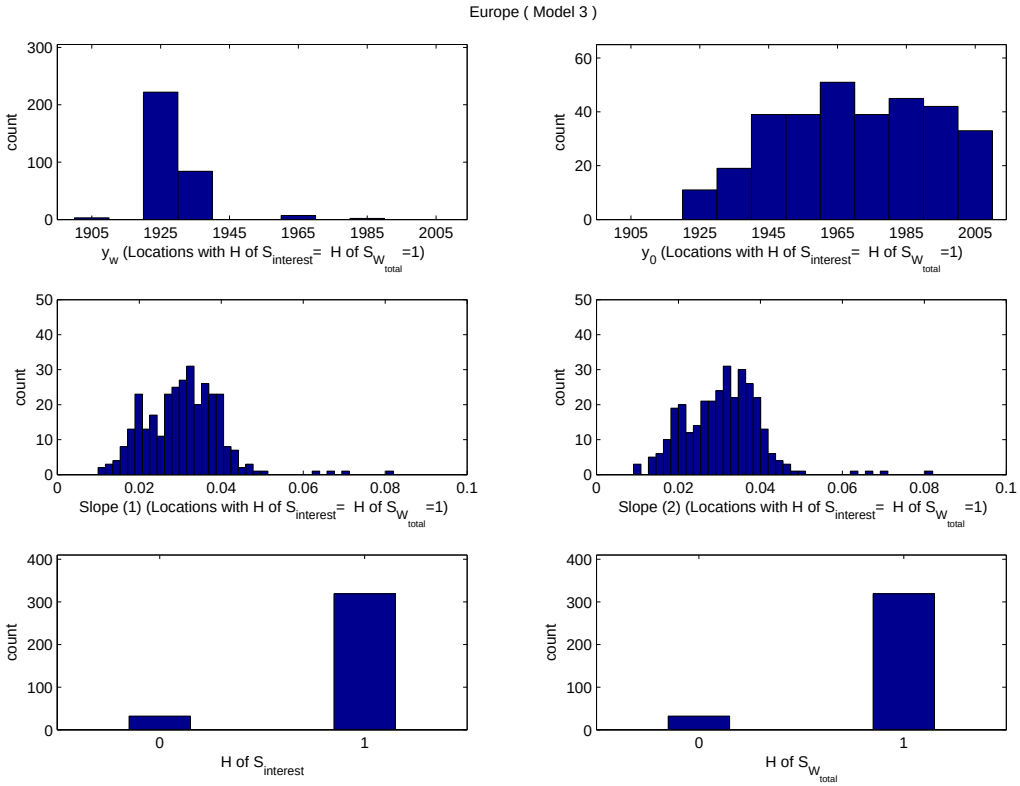


**Figure B.18:** Histograms of the analysed variables (Section 5.2) during **JFM** for Europe. The results are obtained using **Model 3**.

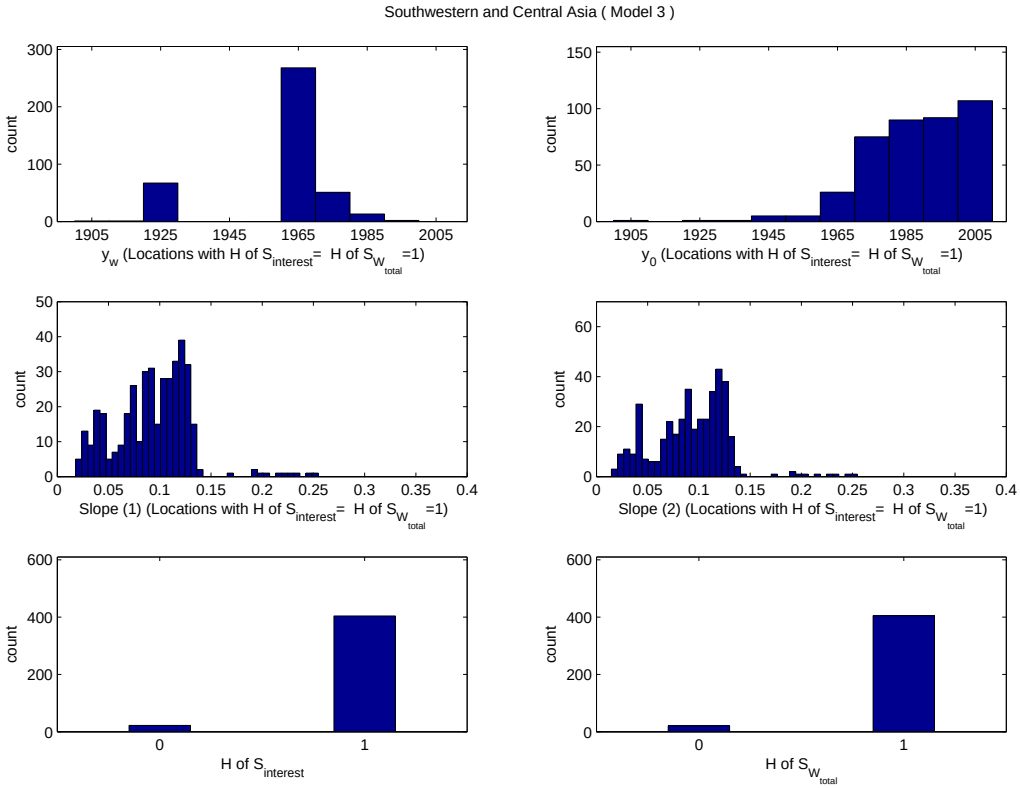


**Figure B.19:** Histograms of the analysed variables (Section 5.2) during **JFM** for southwestern and central Asia. The results are obtained using **Model 3**.

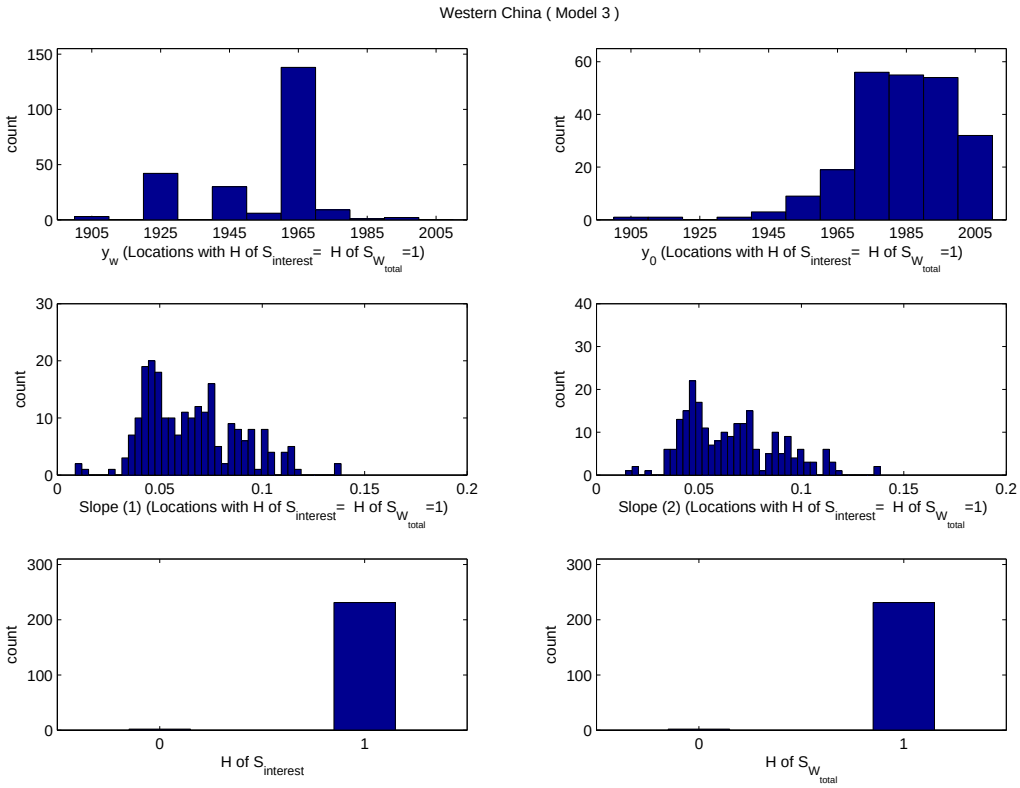


**Figure B.20:** Histograms of the analysed variables (Section 5.2) during **JFM** for western China. The results are obtained using **Model 3**.

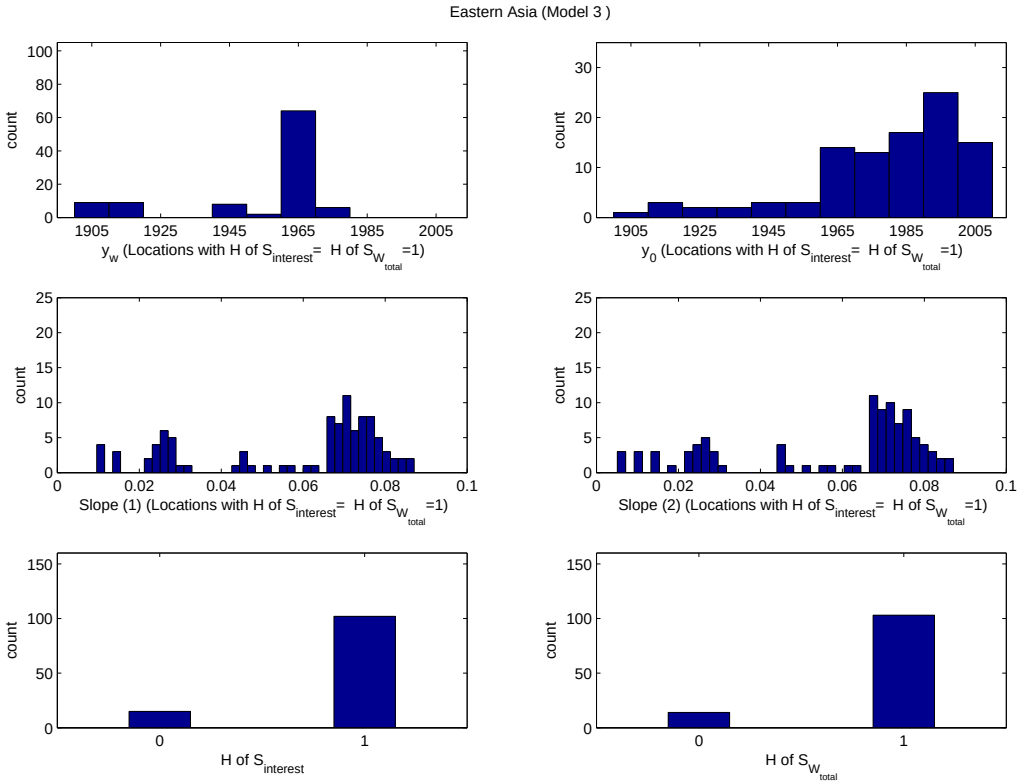


**Figure B.21:** Histograms of the analysed variables (Section 5.2) during **JFM** for eastern Asia. The results are obtained using **Model 3**.

### B.1.4 R Method

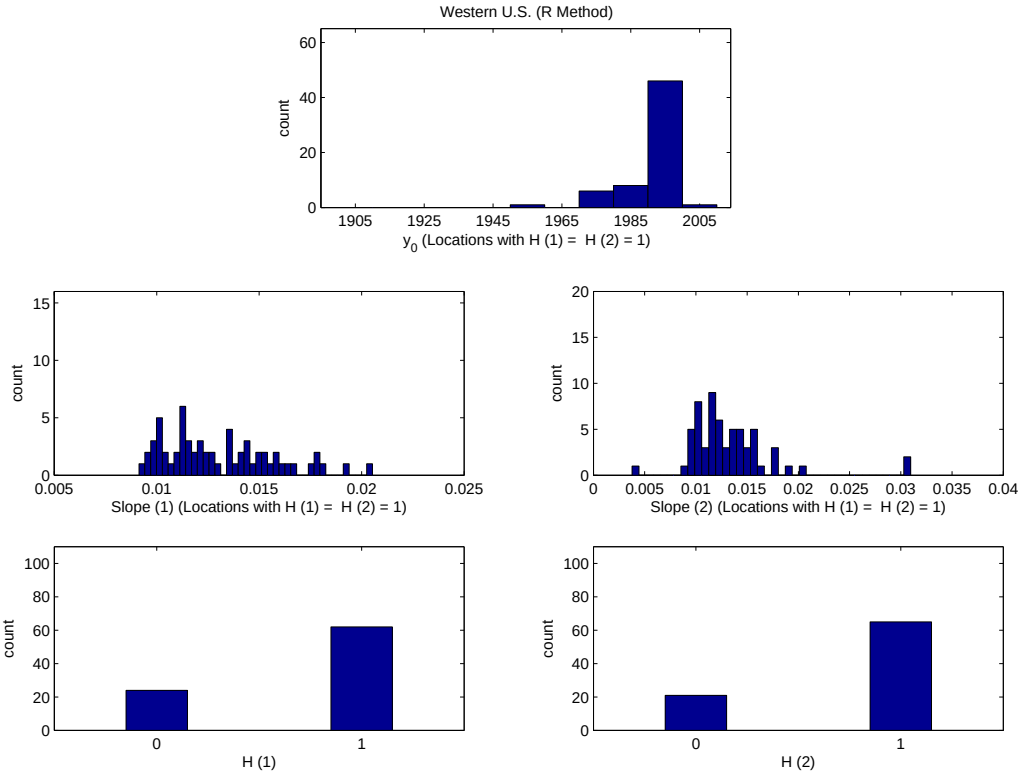


**Figure B.22:** Histograms of the analysed variables (Section 5.6.1) during **JFM** for western U.S. The results are obtained using the **R Method**.

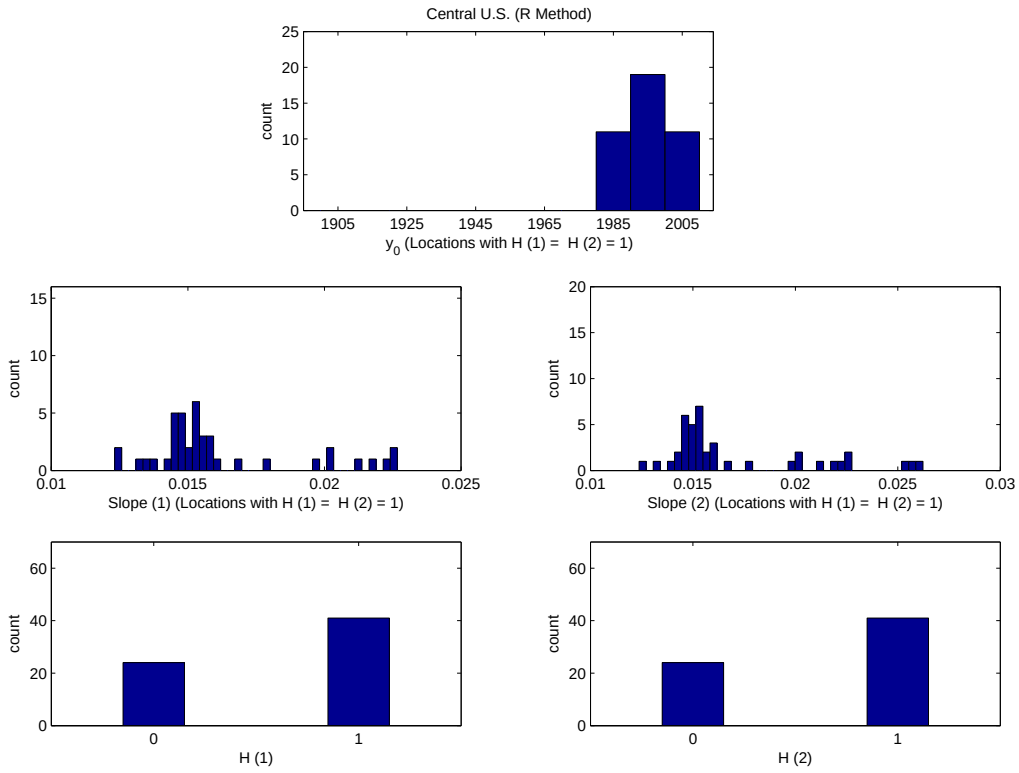


**Figure B.23:** Histograms of the analysed variables (Section 5.6.1) during **JFM** for central U.S. The results are obtained using the **R Method**.

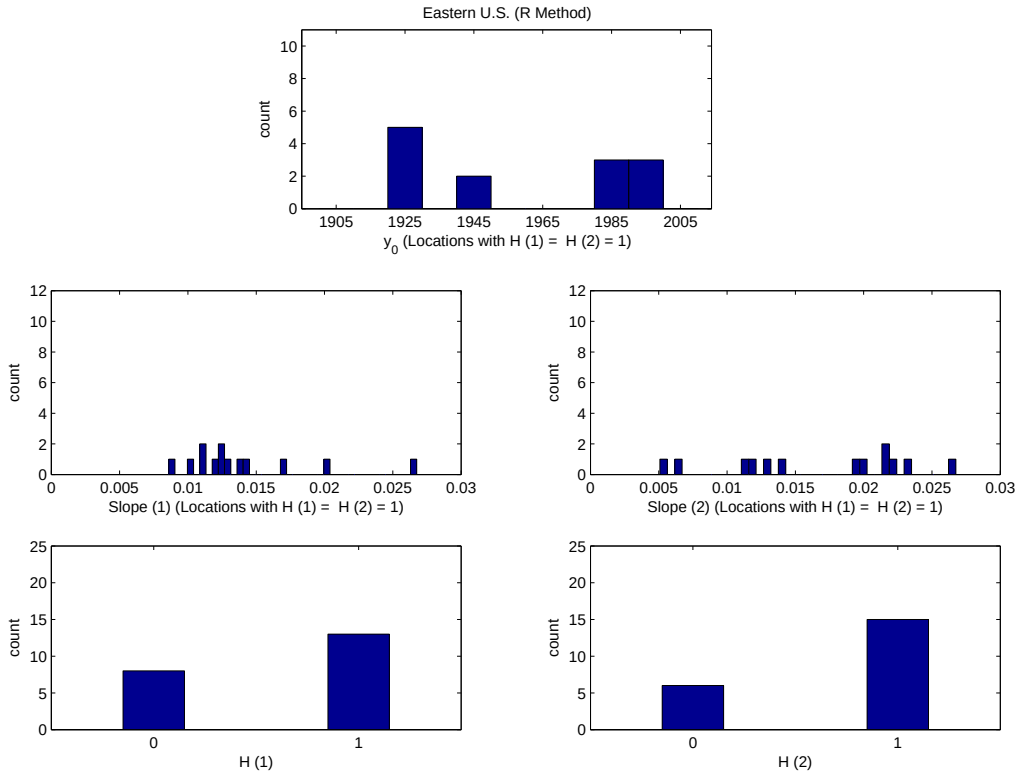


**Figure B.24:** Histograms of the analysed variables (Section 5.6.1) during **JFM** for eastern U.S. The results are obtained using the **R Method**.

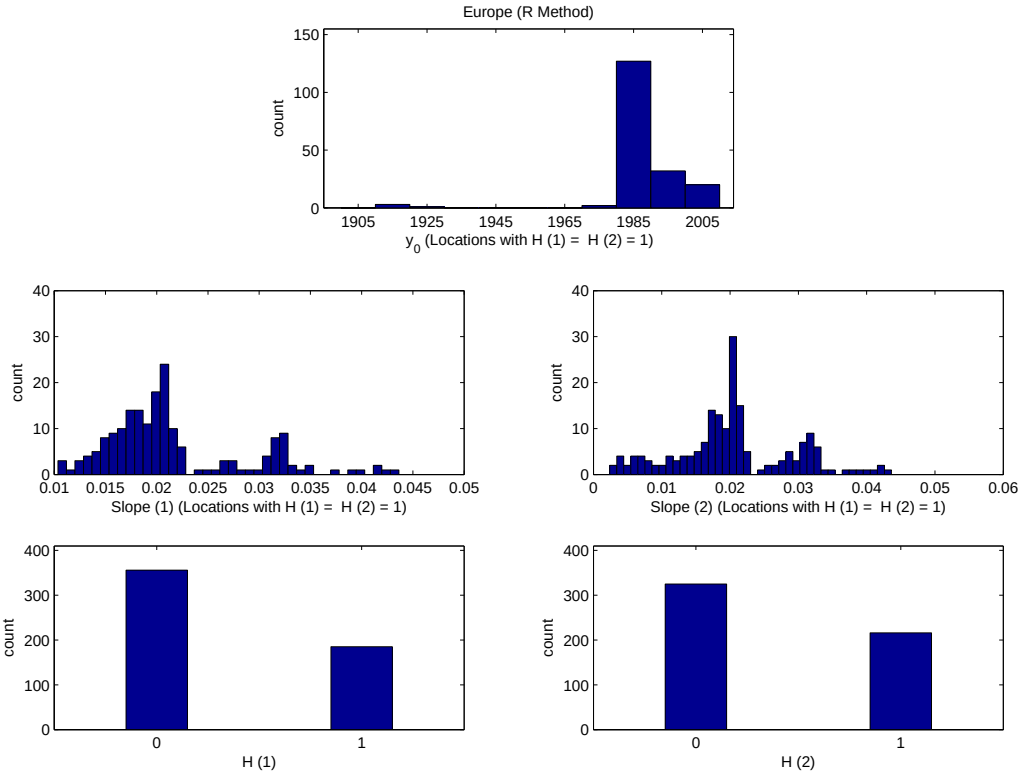


**Figure B.25:** Histograms of the analysed variables (Section 5.6.1) during **JFM** for Europe. The results are obtained using the **R Method**.

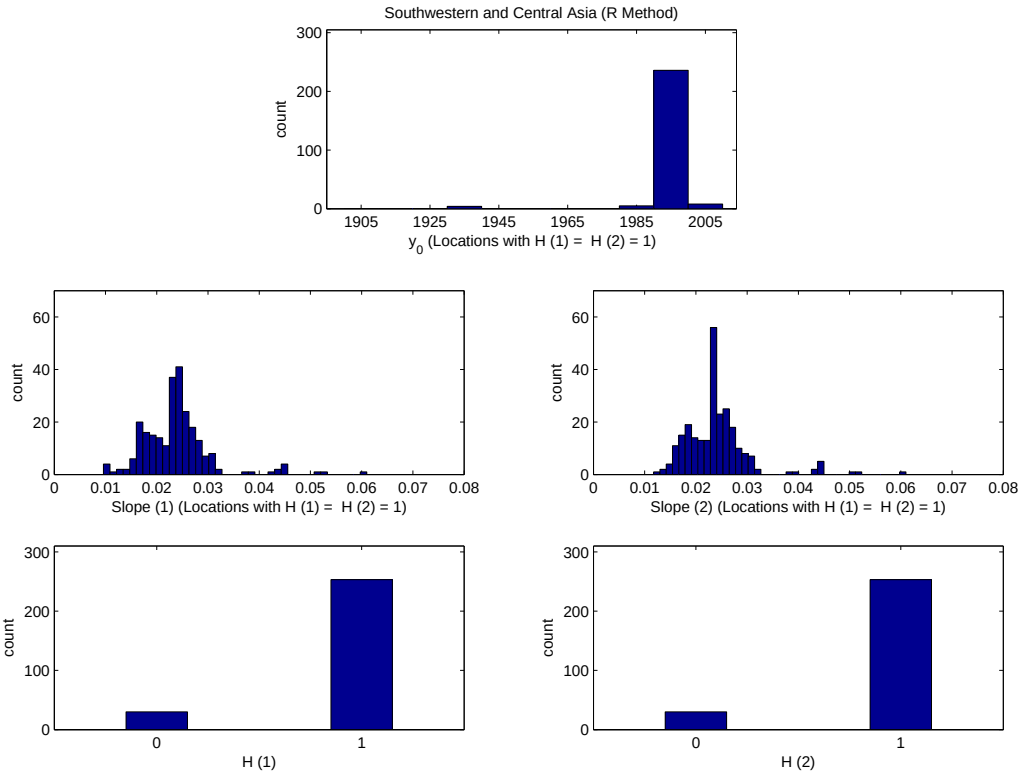


**Figure B.26:** Histograms of the analysed variables (Section 5.6.1) during **JFM** for southwestern and central Asia. The results are obtained using the **R Method**.

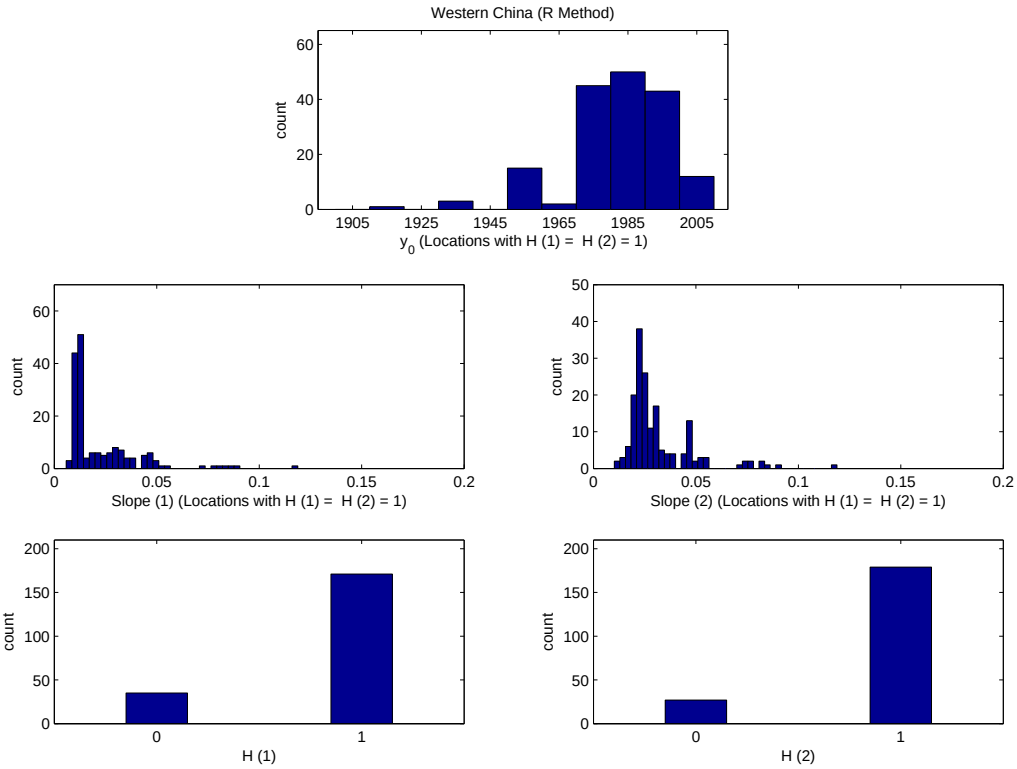


**Figure B.27:** Histograms of the analysed variables (Section 5.6.1) during **JFM** for western China. The results are obtained using the **R Method**.

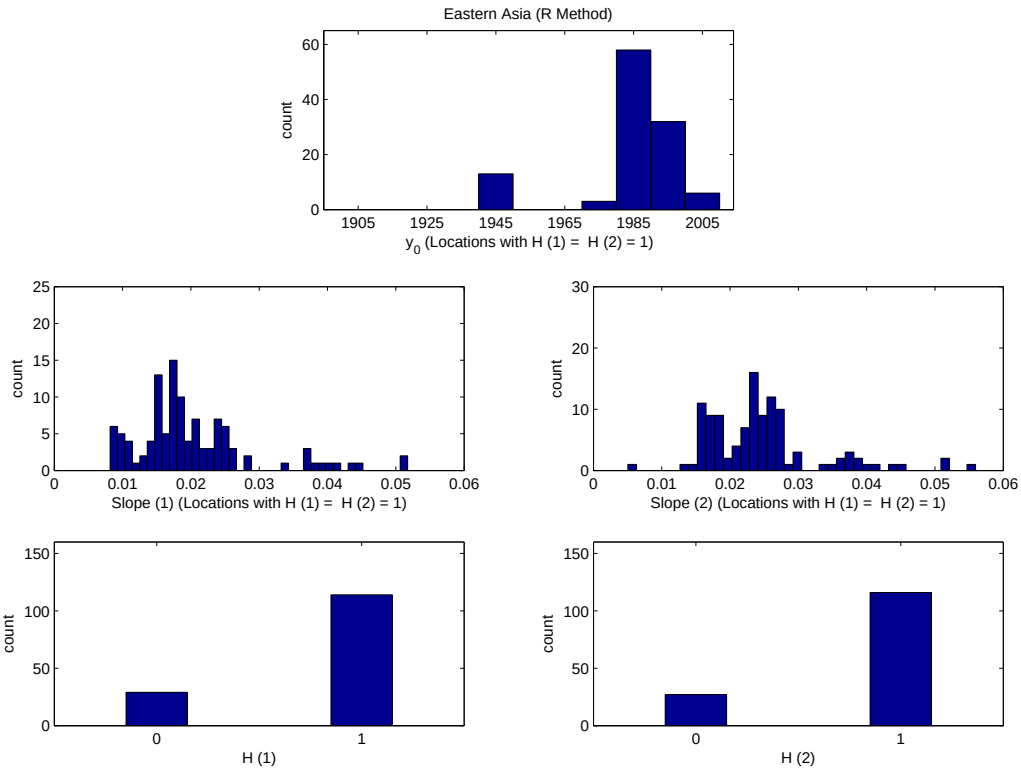


**Figure B.28:** Histograms of the analysed variables (Section 5.6.1) during **JFM** for eastern Asia. The results are obtained using the **R Method**.

# B.2 MAM

## B.2.1 MARS

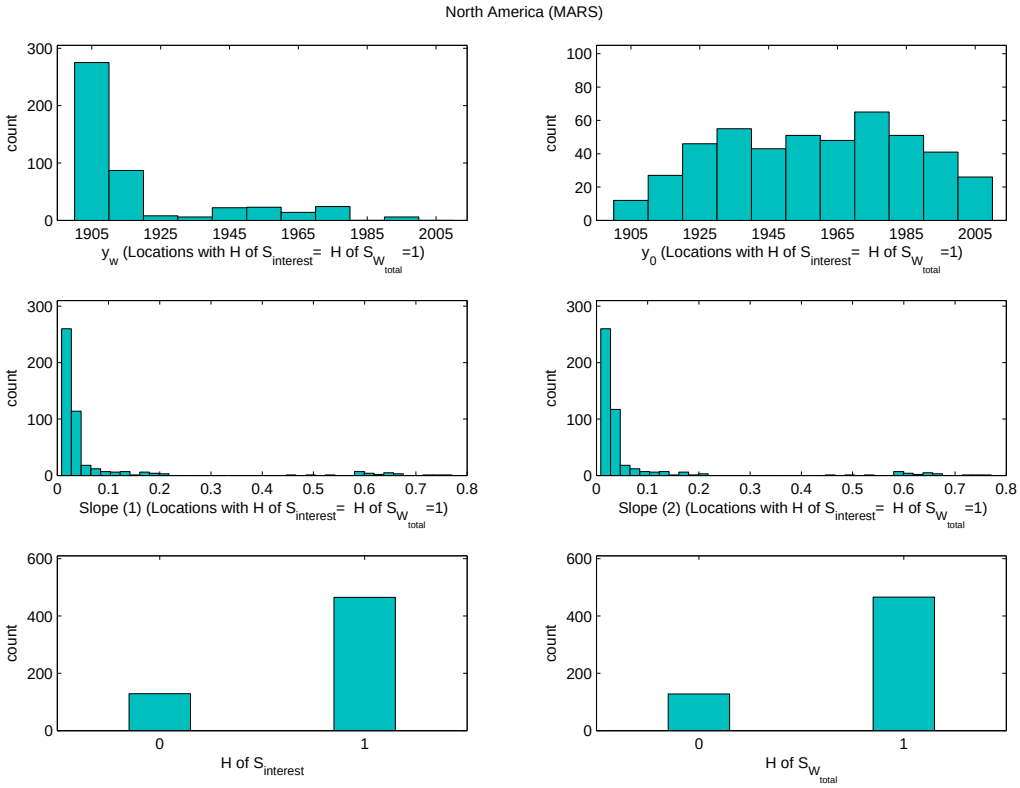


**Figure B.29:** Histograms of the analysed variables (Section 5.2) during **MAM** for North America. The results are obtained using **MARS**.

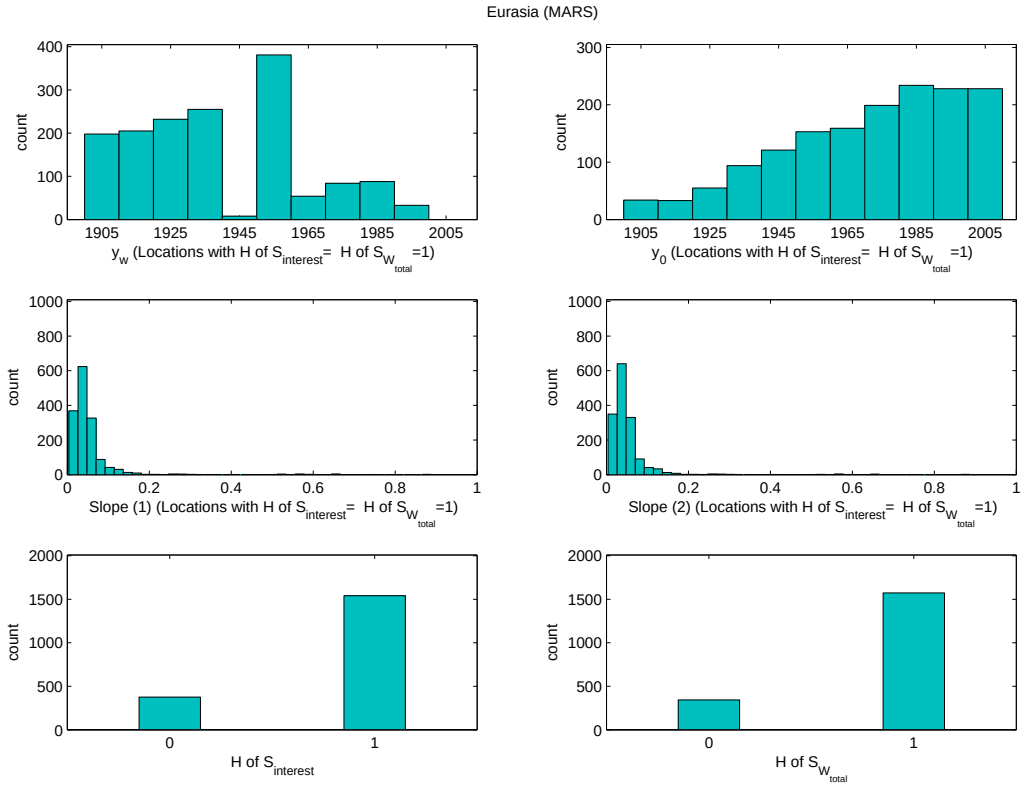


**Figure B.30:** Histograms of the analysed variables (Section 5.2) during **MAM** for Eurasia. The results are obtained using **MARS**.

### B.2.2 Model 2

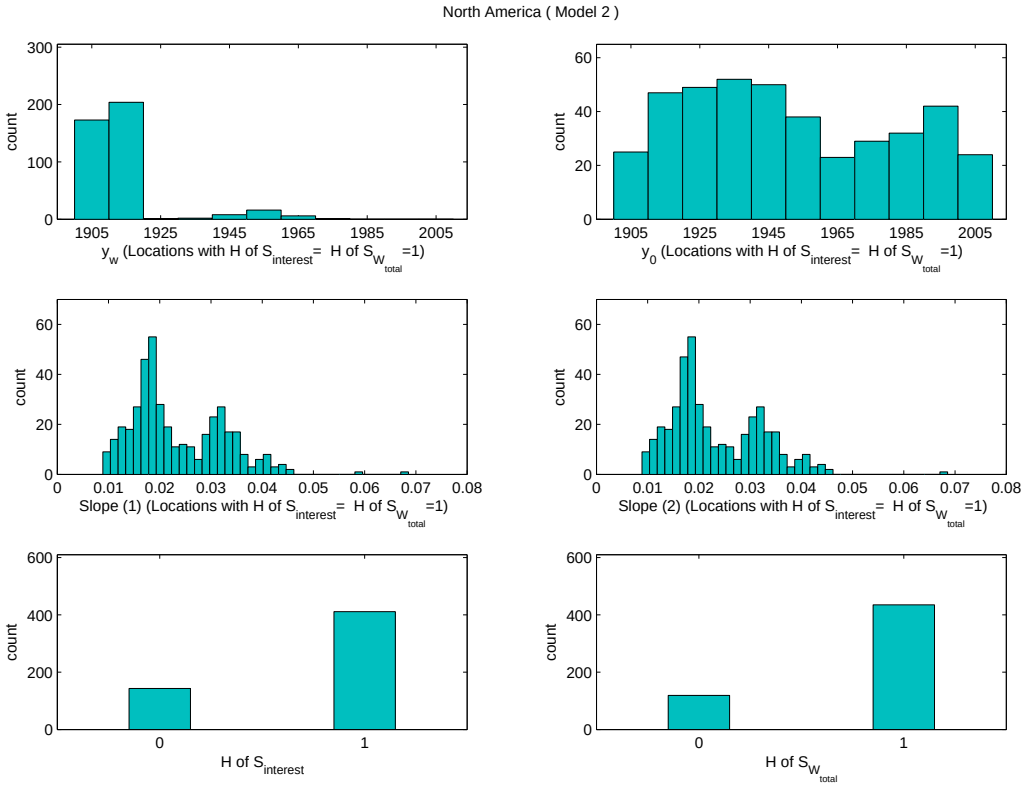


**Figure B.31:** Histograms of the analysed variables (Section 5.2) during **MAM** for North America. The results are obtained using **Model 2**.

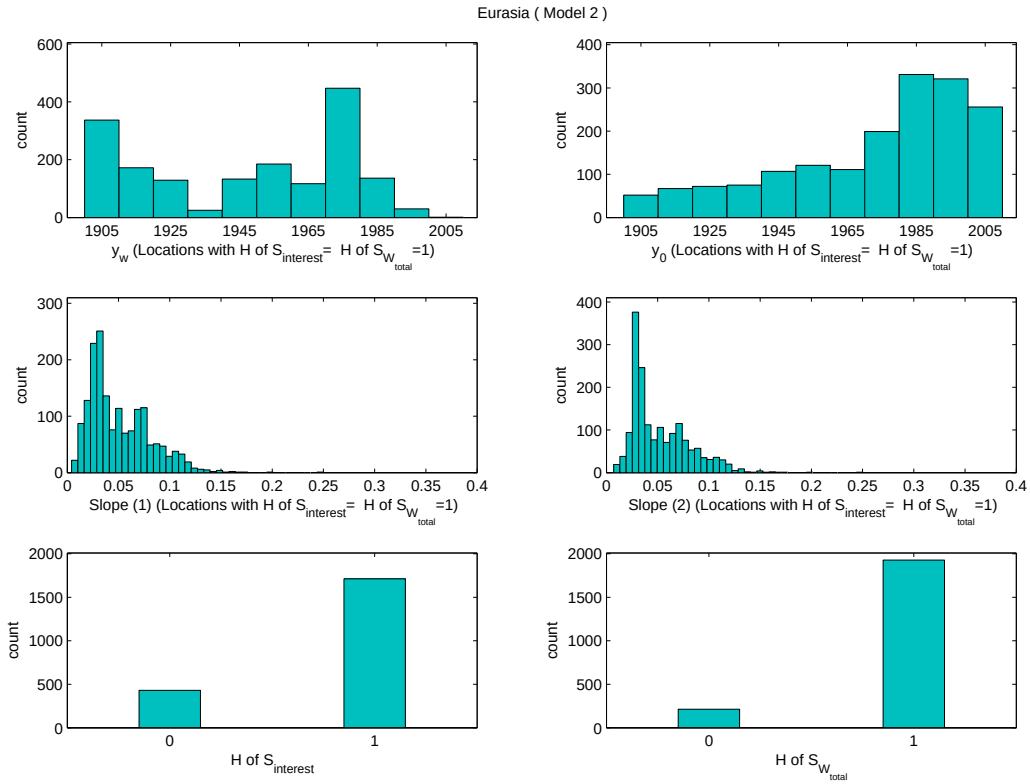


**Figure B.32:** Histograms of the analysed variables (Section 5.2) during **MAM** for Eurasia. The results are obtained using **Model 2**.

### B.2.3 Model 3

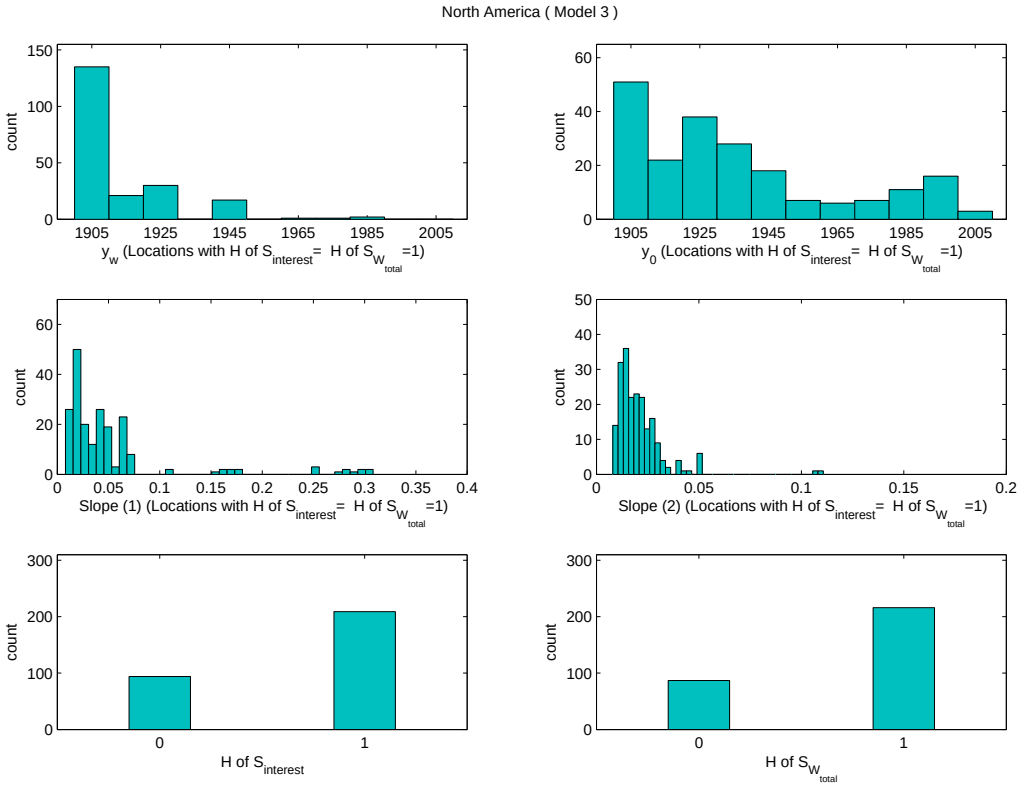


**Figure B.33:** Histograms of the analysed variables (Section 5.2) during **MAM** for North America. The results are obtained using **Model 3**.

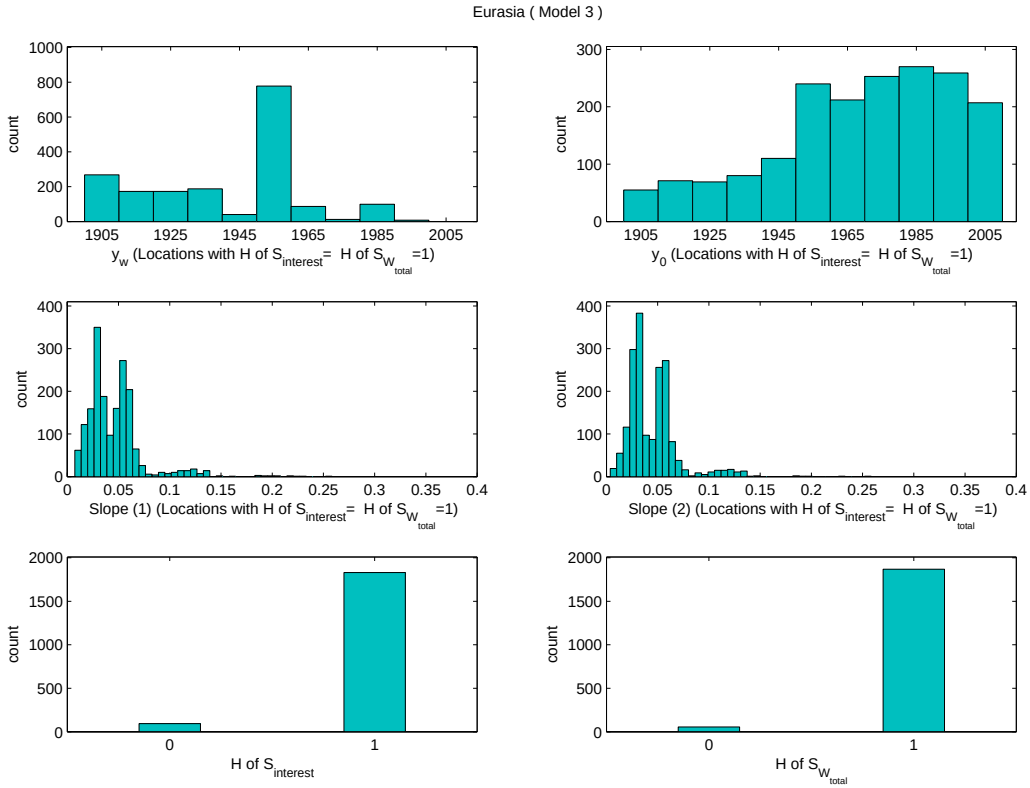


**Figure B.34:** Histograms of the analysed variables (Section 5.2) during **MAM** for Eurasia. The results are obtained using **Model 3**.

### B.2.4 R Method

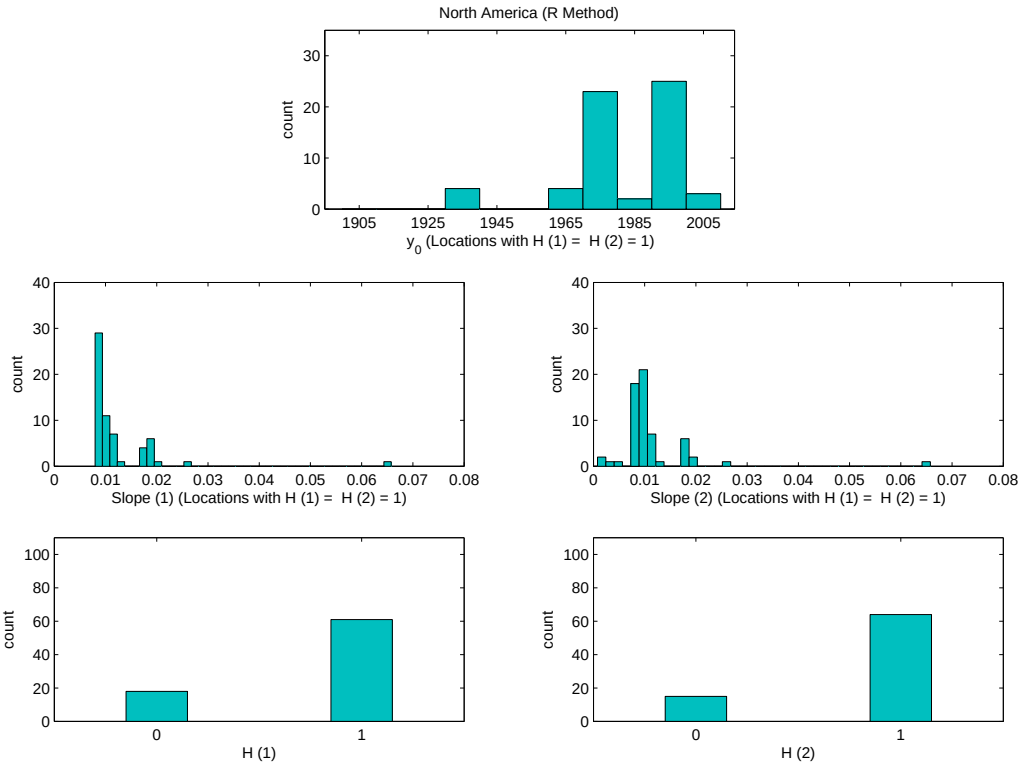


**Figure B.35:** Histograms of the analysed variables (Section 5.6.1) during **MAM** for North America. The results are obtained using the **R Method**.

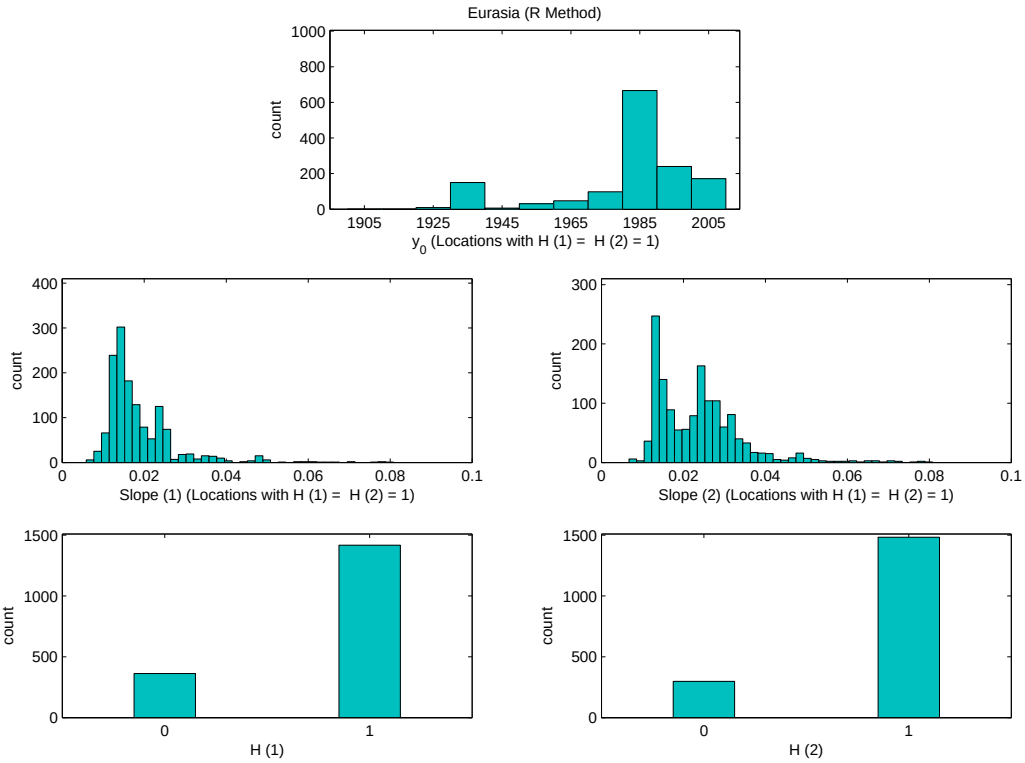


**Figure B.36:** Histograms of the analysed variables (Section 5.6.1) during **MAM** for Eurasia. The results are obtained using the **R Method**.

# Appendix C

# Sample Plots Used for Picking the Best Model

# C.1 Case 1

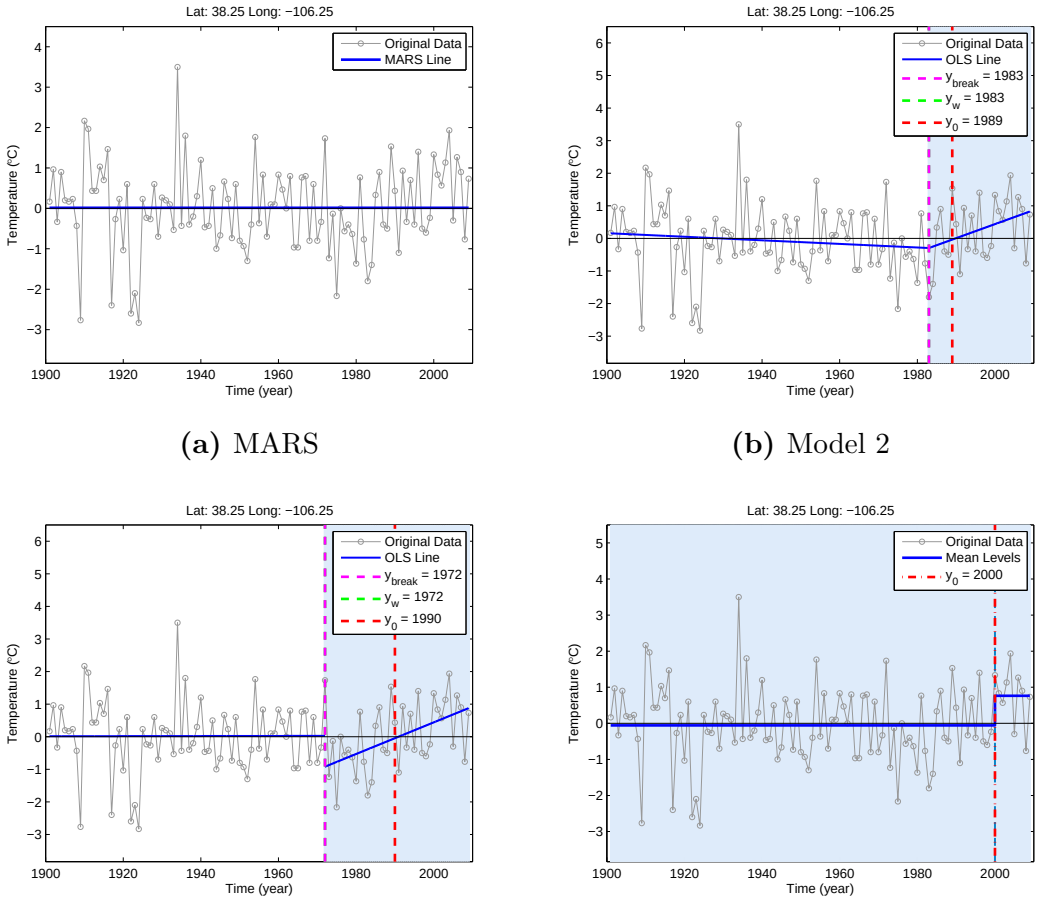


**(a)** MARS **(b)** Model 2

**(c)** Model 3 **(d)** R Method

**Figure C.1:** The **MAM** time series of the grid cell with latitude: 38.25°N and longitude: 106.25°W is modelled using (a) MARS, (b) Model 2, (c) Model 3, (d) the R Method. The figure is an example of Case 1 (Section 5.8.5).

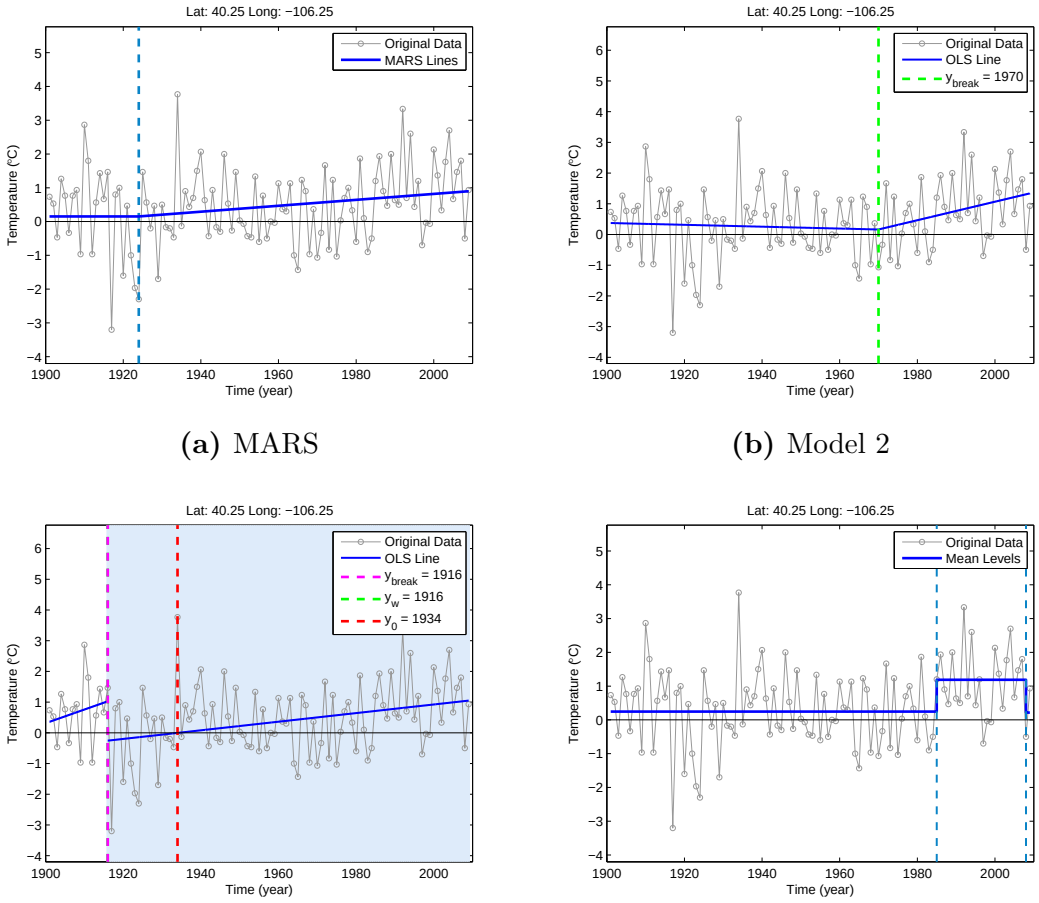


**(a)** MARS

**(b)** Model 2

**(c)** Model 3

**(d)** R Method

**Figure C.2:** The **MAM** time series of the grid cell with latitude: 40.25°N and longitude: 106.25°W is modelled using (a) MARS, (b) Model 2, (c) Model 3, (d) the R Method. The figure is an example of Case 1 (Section 5.8.5).

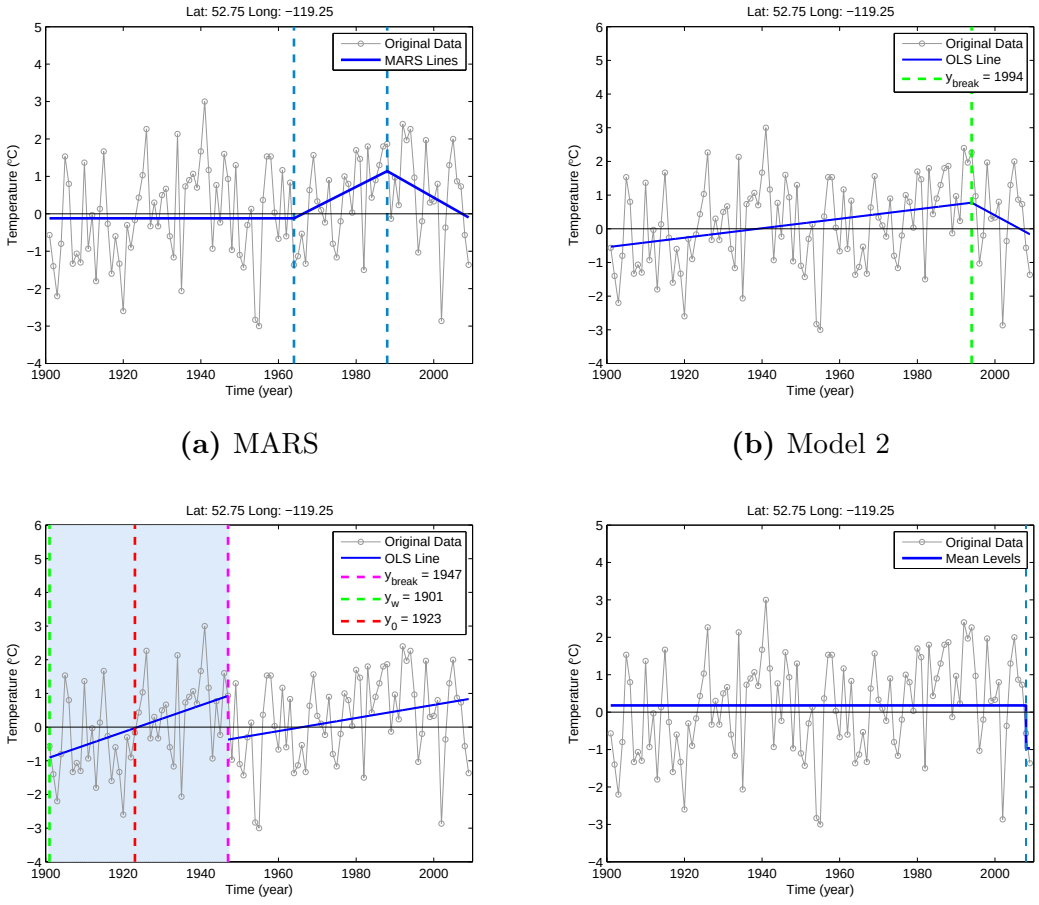


**(a)** MARS **(b)** Model 2

**(c)** Model 3 **(d)** R Method

**Figure C.3:** The **MAM** time series of the grid cell with latitude: 52.75°N and longitude: 119.25°W is modelled using (a) MARS, (b) Model 2, (c) Model 3, (d) the R Method. The figure is an example of Case 1 (Section 5.8.5).

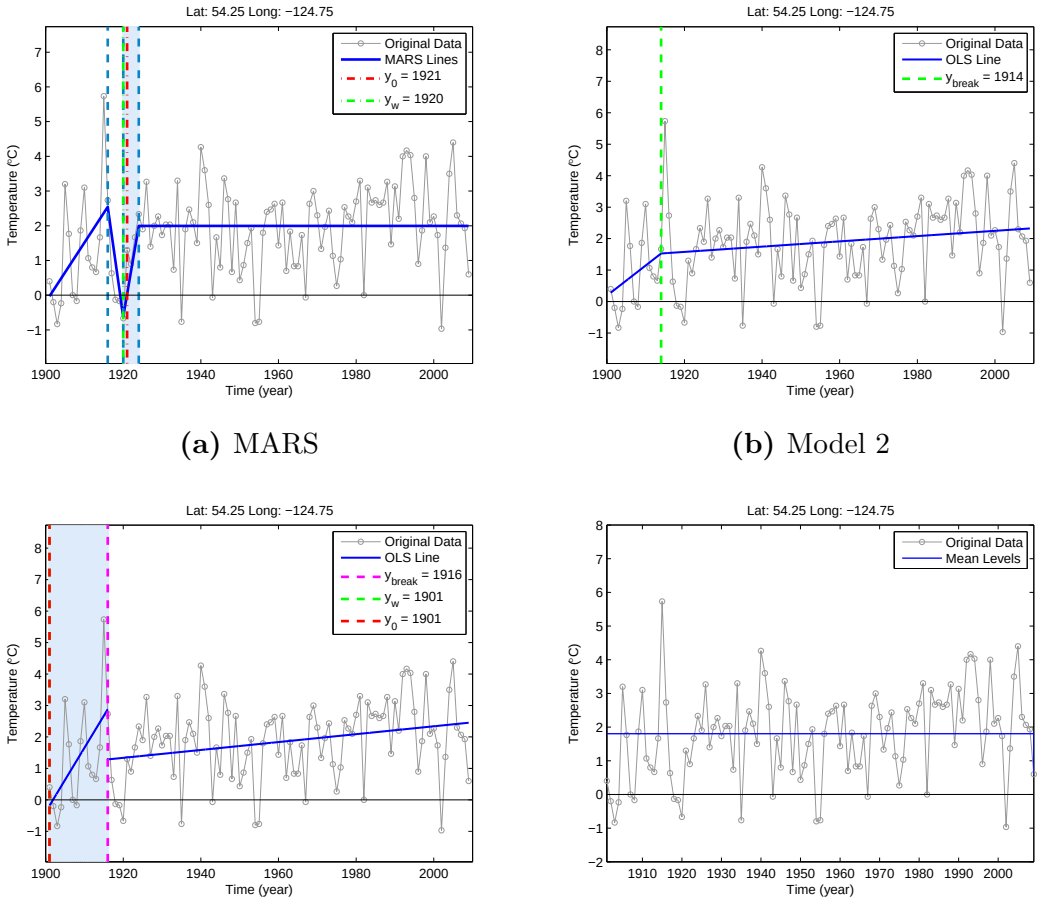


**(a)** MARS **(b)** Model 2

**(c)** Model 3 **(d)** R Method

**Figure C.4:** The **MAM** time series of the grid cell with latitude: 54.25°N and longitude: 124.75°W is modelled using (a) MARS, (b) Model 2, (c) Model 3, (d) the R Method. The figure is an example of Case 1 (Section 5.8.5).

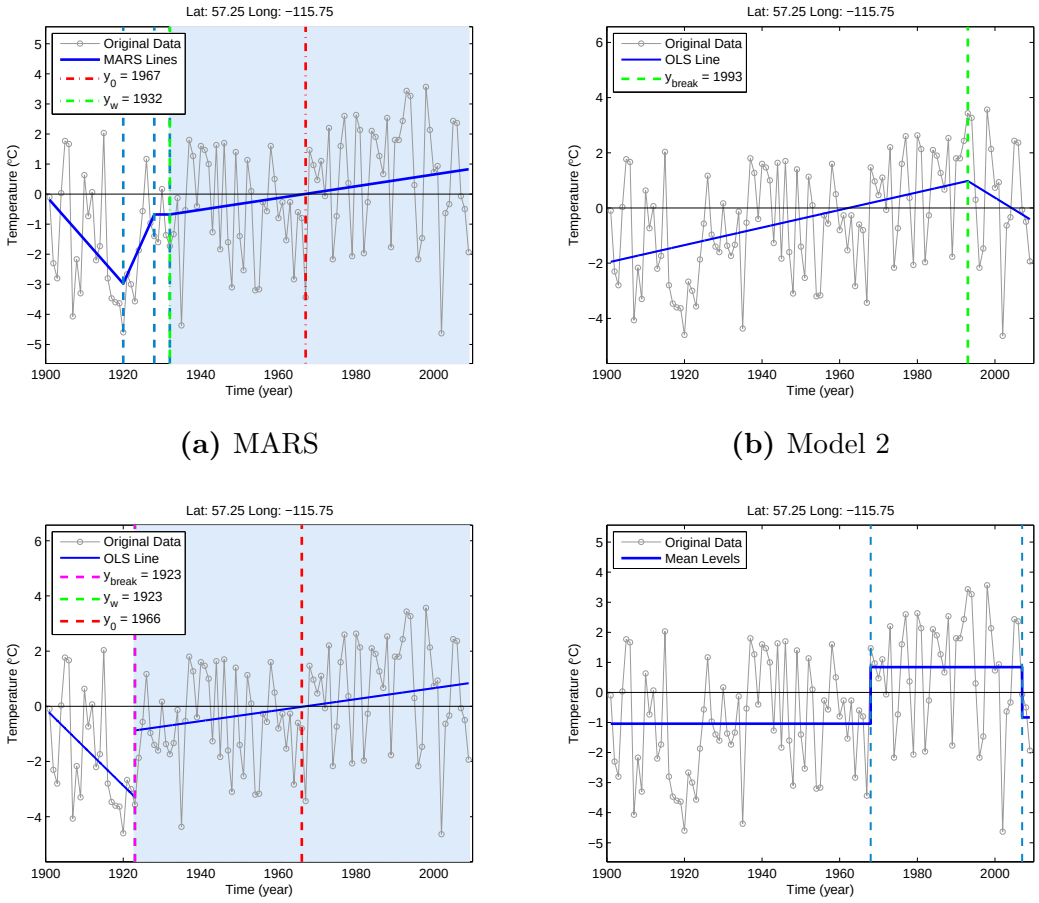


**(a)** MARS **(b)** Model 2

**(c)** Model 3 **(d)** R Method

**Figure C.5:** The **MAM** time series of the grid cell with latitude: 57.25°N and longitude: 115.75°W is modelled using (a) MARS, (b) Model 2, (c) Model 3, (d) the R Method. The figure is an example of Case 1 (Section 5.8.5).

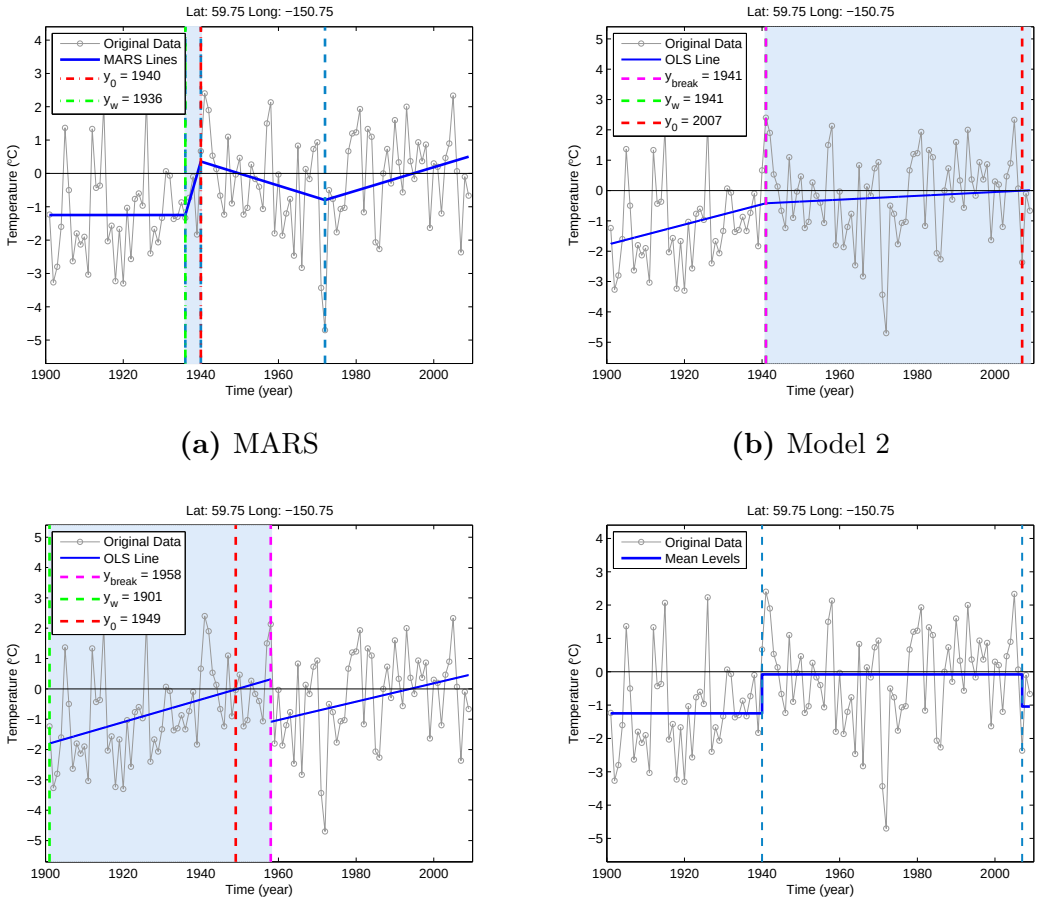


**(a)** MARS **(b)** Model 2

**(c)** Model 3 **(d)** R Method

**Figure C.6:** The **MAM** time series of the grid cell with latitude: 59.75°N and longitude: 150.75°W is modelled using (a) MARS, (b) Model 2, (c) Model 3, (d) the R Method. The figure is an example of Case 1 (Section 5.8.5).

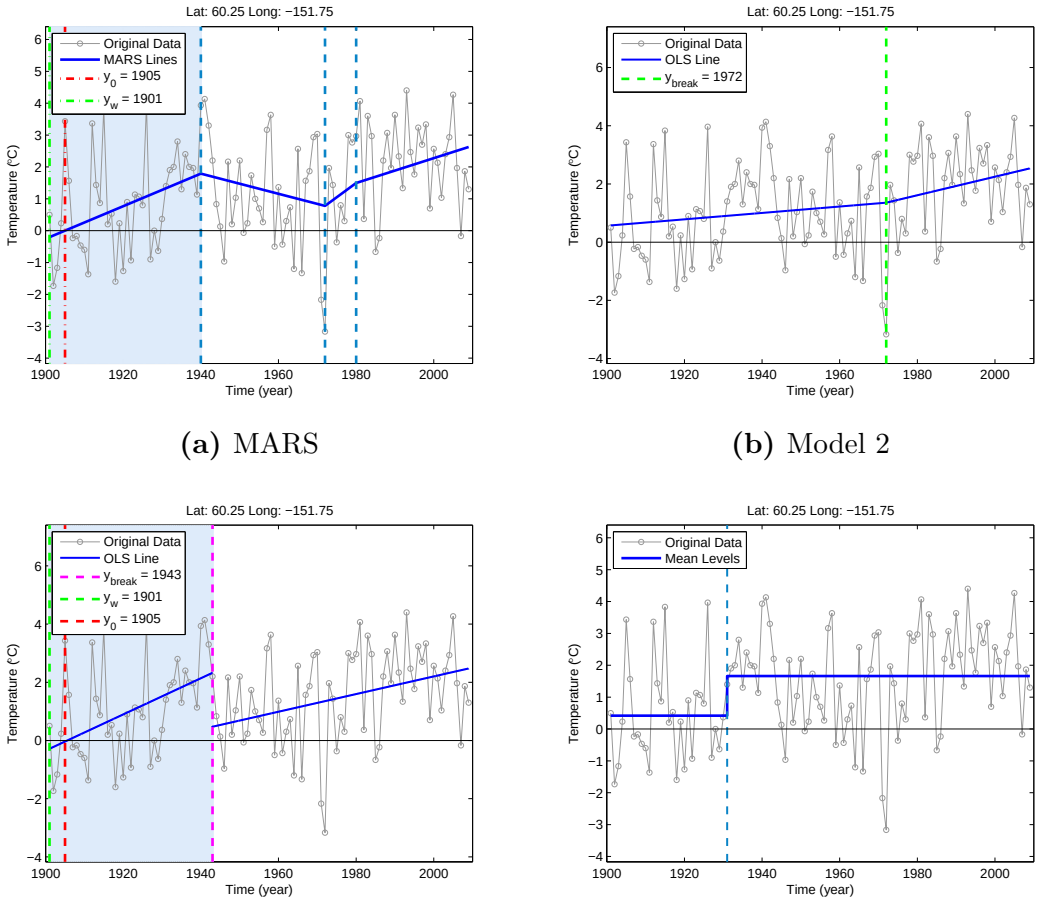


**(a)** MARS **(b)** Model 2

**(c)** Model 3 **(d)** R Method

**Figure C.7:** The **MAM** time series of the grid cell with latitude: 60.25°N and longitude: 151.75°W is modelled using (a) MARS, (b) Model 2, (c) Model 3, (d) the R Method. The figure is an example of Case 1 (Section 5.8.5).

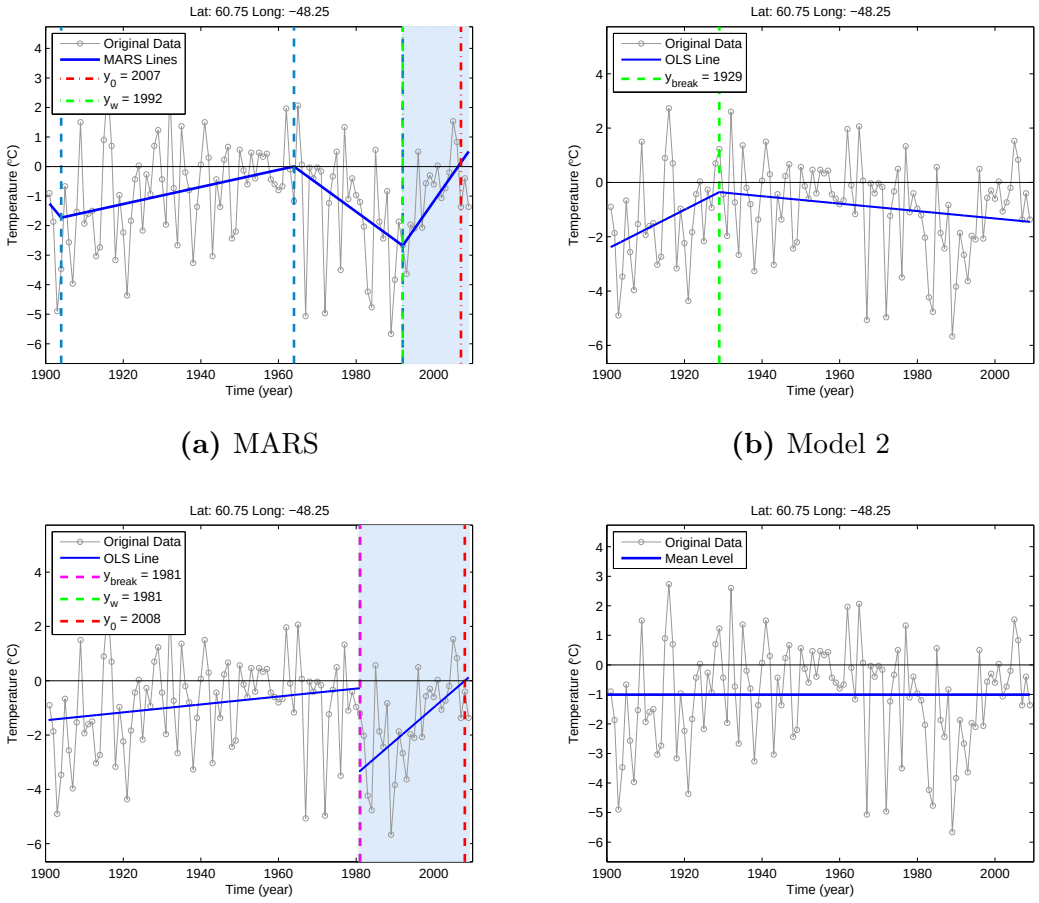


**(a)** MARS **(b)** Model 2

**(c)** Model 3 **(d)** R Method

**Figure C.8:** The **MAM** time series of the grid cell with latitude: 60.75°N and longitude: 48.25°W is modelled using (a) MARS, (b) Model 2, (c) Model 3, (d) the R Method. The figure is an example of Case 1 (Section 5.8.5).

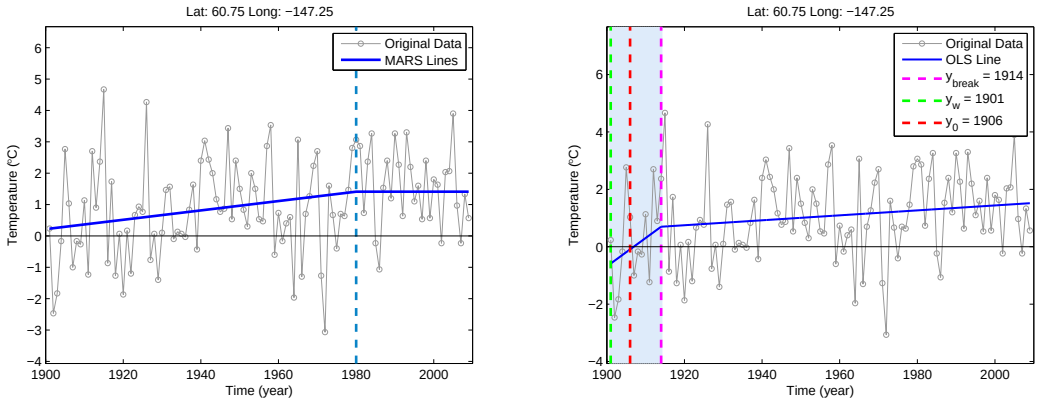


**(a)** MARS **(b)** Model 2

**(c)** Model 3 **(d)** R Method

**Figure C.9:** The **MAM** time series of the grid cell with latitude: 60.75°N and longitude: 147.25°W is modelled using (a) MARS, (b) Model 2, (c) Model 3, (d) the R Method. The figure is an example of Case 1 (Section 5.8.5).

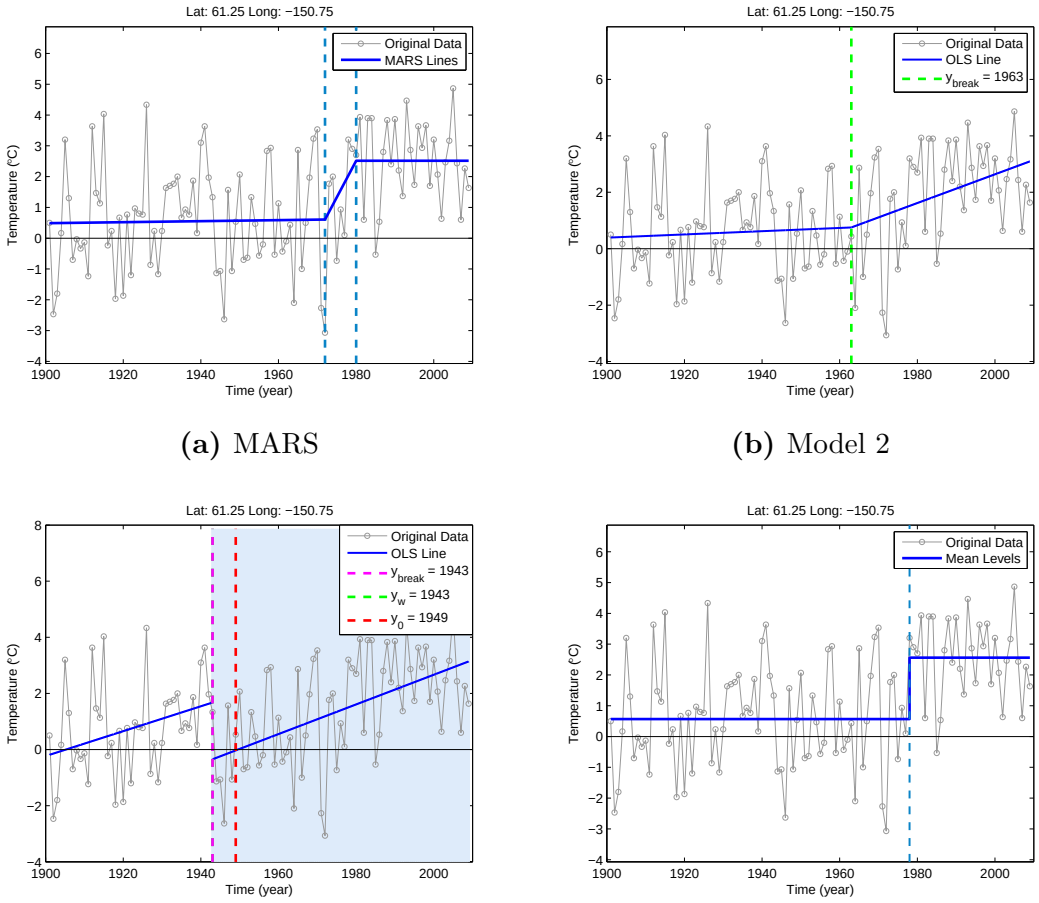


**(a)** MARS **(b)** Model 2

**(c)** Model 3 **(d)** R Method

**Figure C.10:** The **MAM** time series of the grid cell with latitude: 61.25°N and longitude: 150.75°W is modelled using (a) MARS, (b) Model 2, (c) Model 3, (d) the R Method. The figure is an example of Case 1 (Section 5.8.5).

## C.2 Case 2

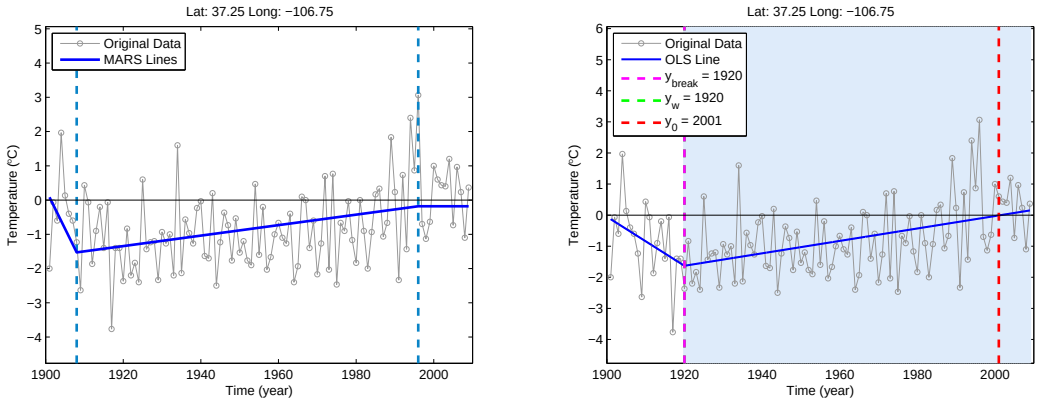


**(a)** MARS **(b)** Model 2

**(c)** Model 3 **(d)** R Method

**Figure C.11:** The **MAM** time series of the grid cell with latitude: 37.25°N and longitude: 106.75°W is modelled using (a) MARS, (b) Model 2, (c) Model 3, (d) the R Method. The figure is an example of Case 2 (Section 5.8.5).

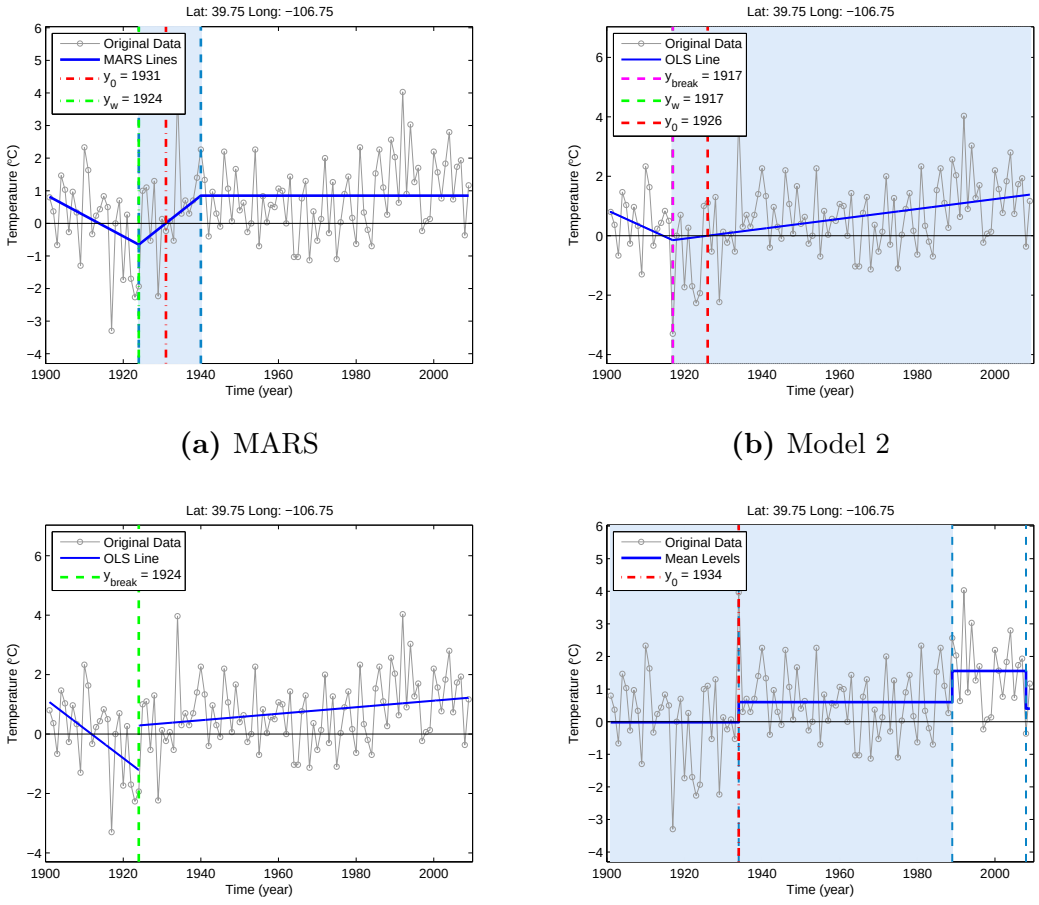


**(a)** MARS **(b)** Model 2

**(c)** Model 3 **(d)** R Method

**Figure C.12:** The **MAM** time series of the grid cell with latitude: 39.75°N and longitude: 106.75°W is modelled using (a) MARS, (b) Model 2, (c) Model 3, (d) the R Method. The figure is an example of Case 2 (Section 5.8.5).

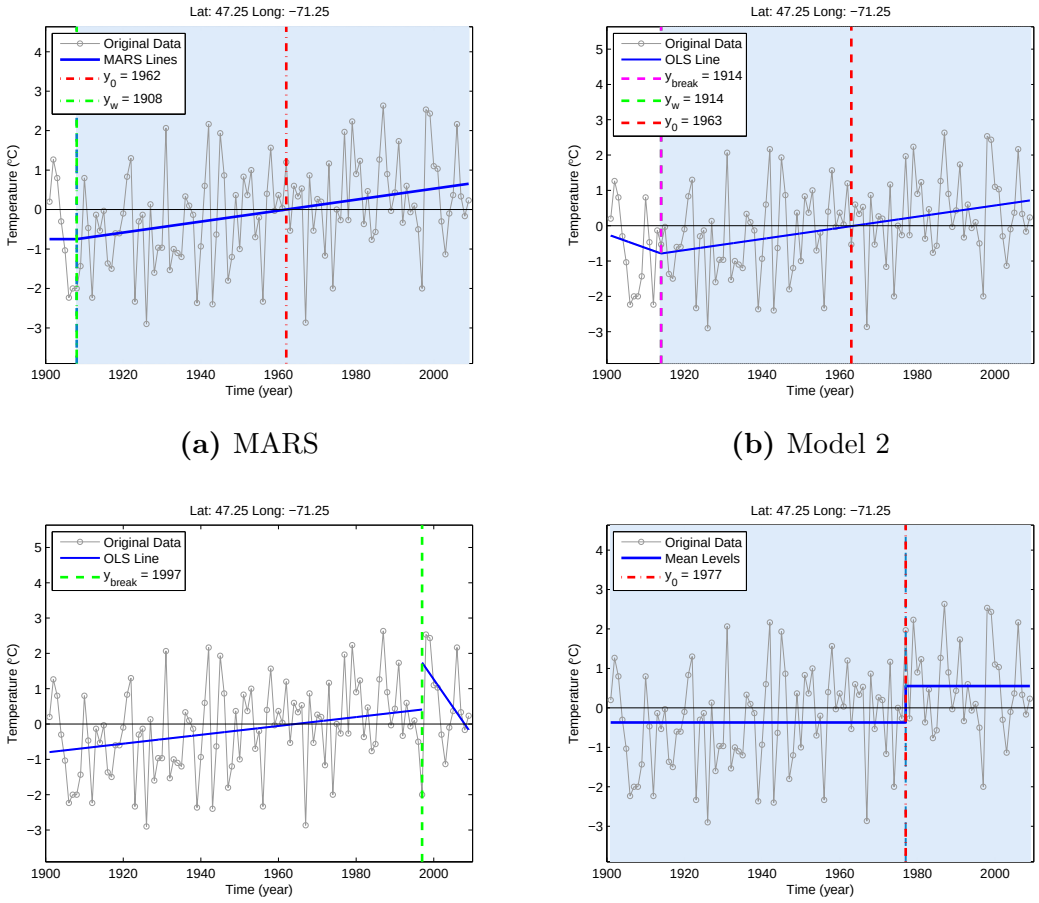


**(a)** MARS **(b)** Model 2

**(c)** Model 3 **(d)** R Method

**Figure C.13:** The **MAM** time series of the grid cell with latitude: 47.25°N and longitude: 71.25°W is modelled using (a) MARS, (b) Model 2, (c) Model 3, (d) the R Method. The figure is an example of Case 2 (Section 5.8.5).

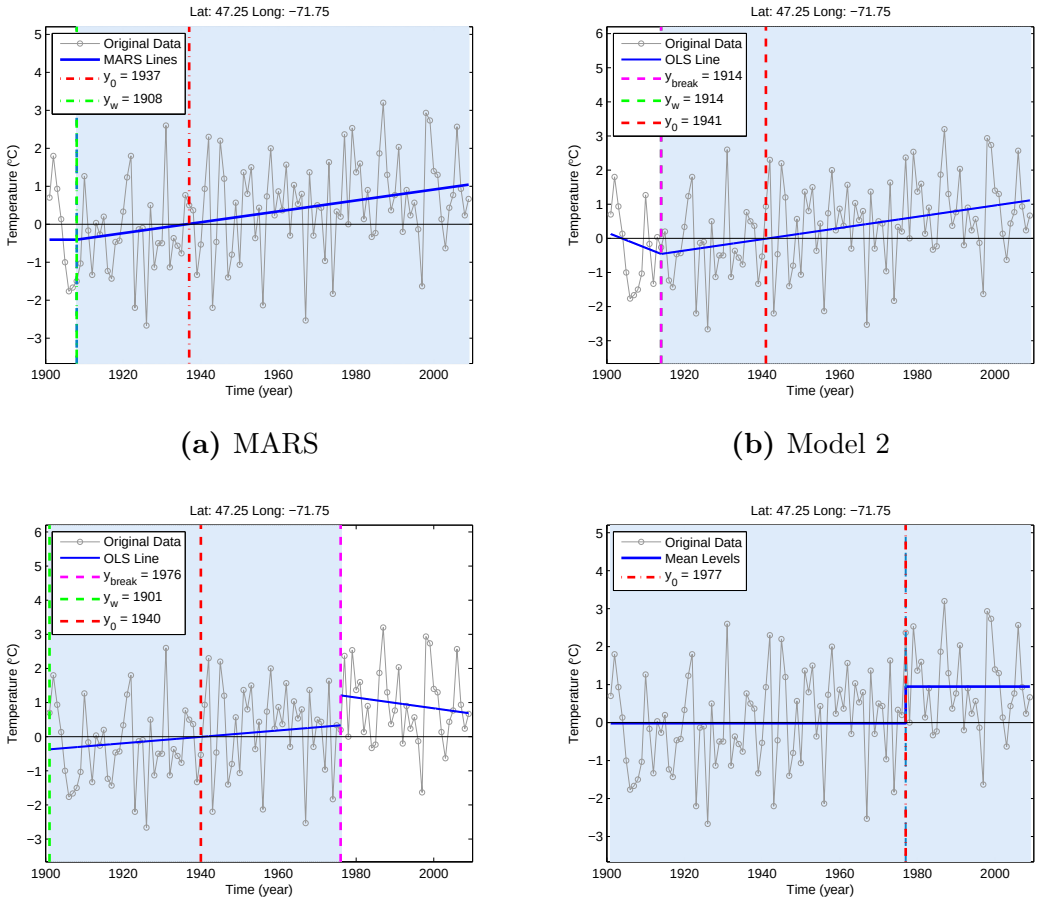


**(a)** MARS **(b)** Model 2

**(c)** Model 3 **(d)** R Method

**Figure C.14:** The **MAM** time series of the grid cell with latitude: 47.25°N and longitude: 71.75°W is modelled using (a) MARS, (b) Model 2, (c) Model 3, (d) the R Method. The figure is an example of Case 2 (Section 5.8.5).

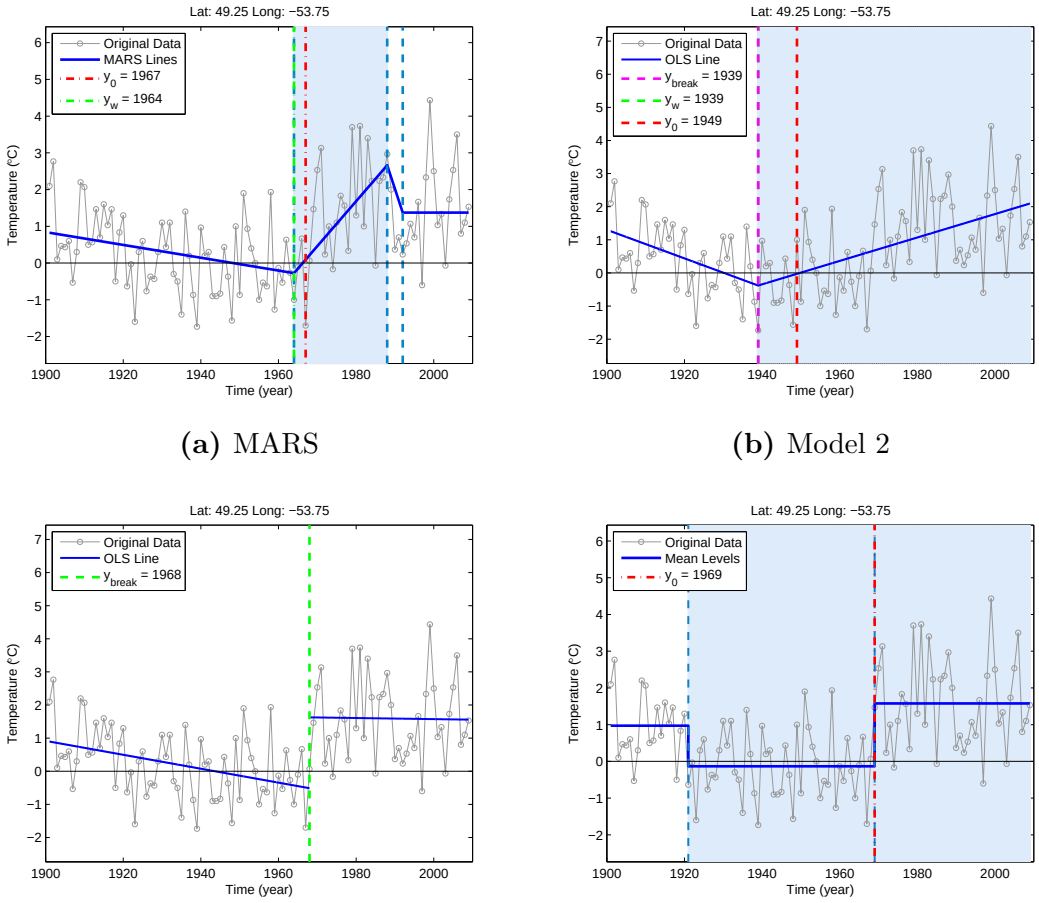


**(a)** MARS **(b)** Model 2

**(c)** Model 3 **(d)** R Method

**Figure C.15:** The **MAM** time series of the grid cell with latitude: 49.25°N and longitude: 53.75°W is modelled using (a) MARS, (b) Model 2, (c) Model 3, (d) the R Method. The figure is an example of Case 2 (Section 5.8.5).

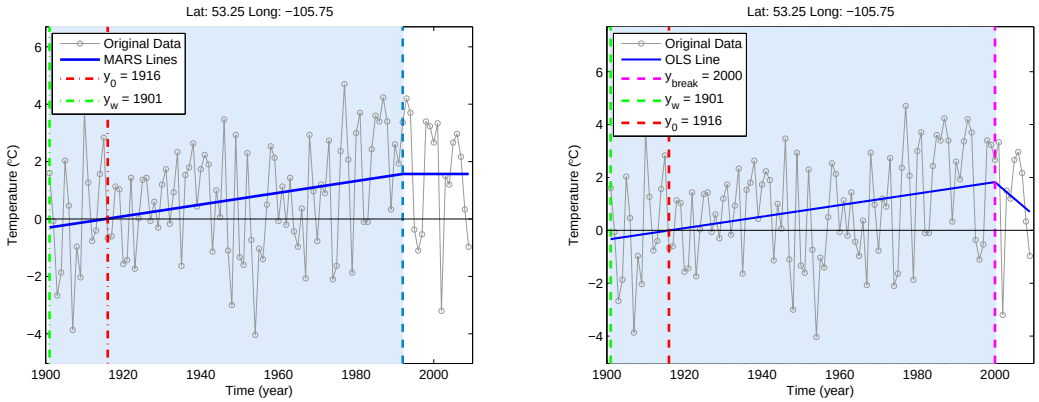


**(a)** MARS **(b)** Model 2

**(c)** Model 3 **(d)** R Method

**Figure C.16:** The **MAM** time series of the grid cell with latitude: 53.25°N and longitude: 105.75°W is modelled using (a) MARS, (b) Model 2, (c) Model 3, (d) the R Method. The figure is an example of Case 2 (Section 5.8.5).

## C.3 Case 3

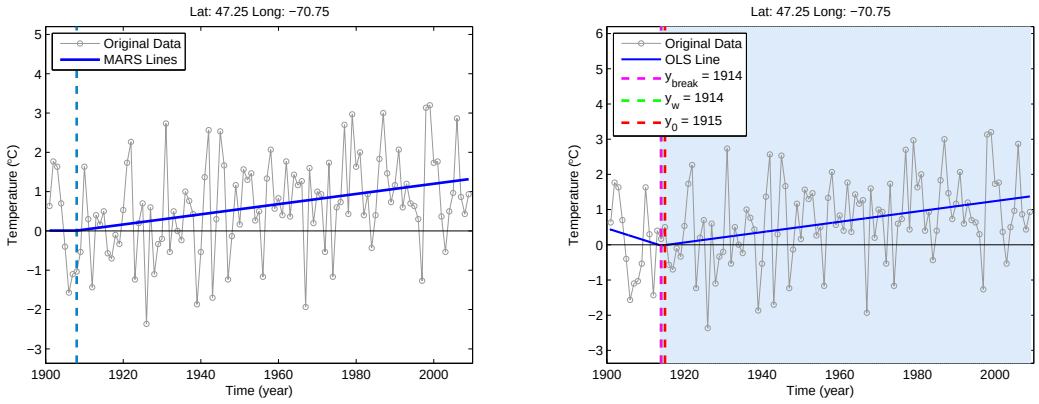


**(a)** MARS




**(b)** Model 2

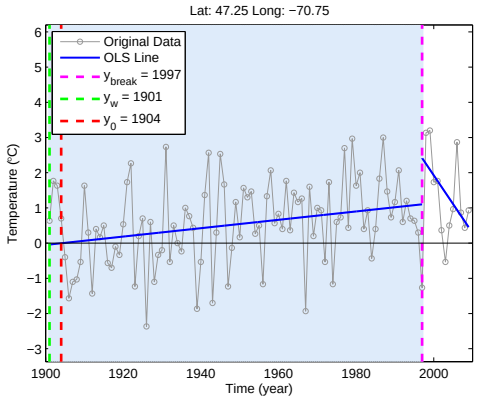


**(c)** Model 3

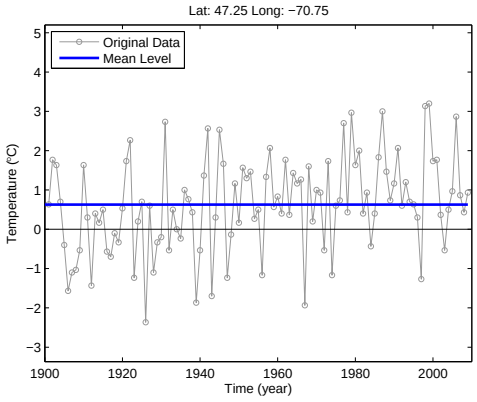


**(d)** R Method

**Figure C.17:** The **MAM** time series of the grid cell with latitude: 47.25°N and longitude: 70.75°W is modelled using (a) MARS, (b) Model 2, (c) Model 3, (d) the R Method. The figure is an example of Case 3 (Section 5.8.5).

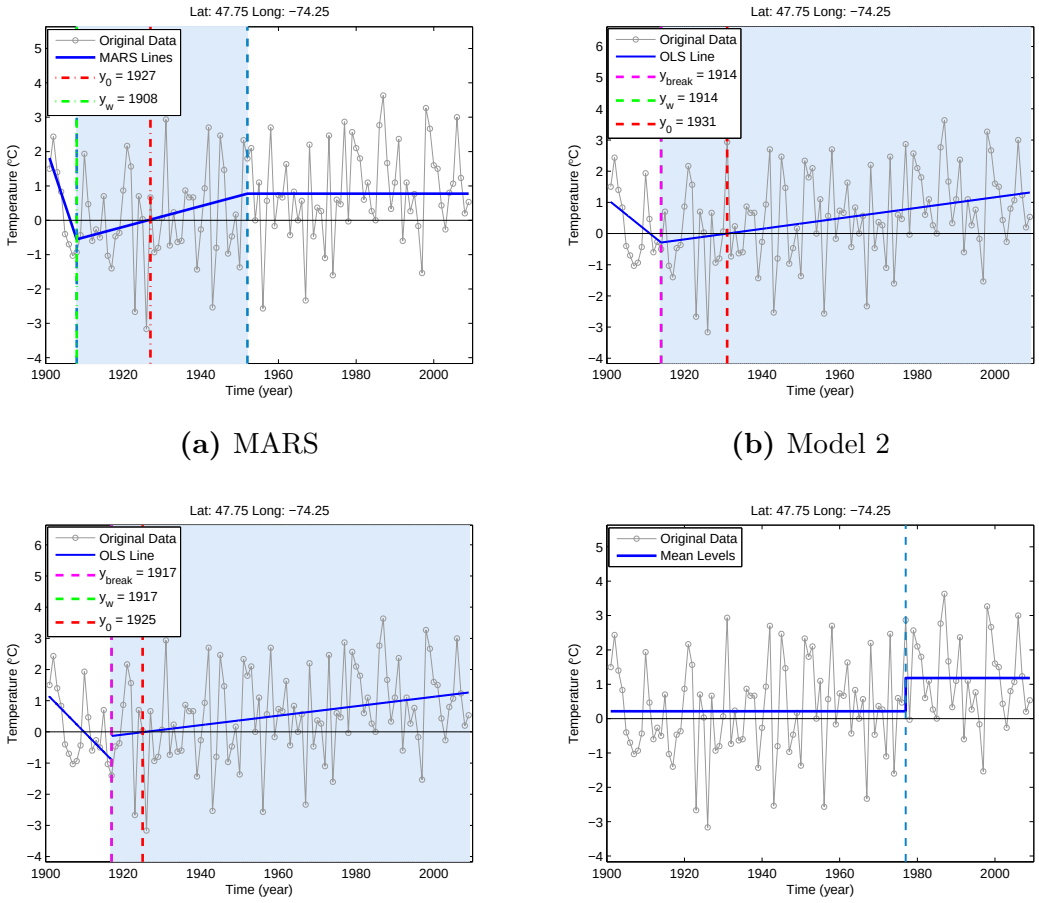


**(a)** MARS **(b)** Model 2

**(c)** Model 3 **(d)** R Method

**Figure C.18:** The **MAM** time series of the grid cell with latitude: 47.75°N and longitude: 74.25°W is modelled using (a) MARS, (b) Model 2, (c) Model 3, (d) the R Method. The figure is an example of Case 3 (Section 5.8.5).

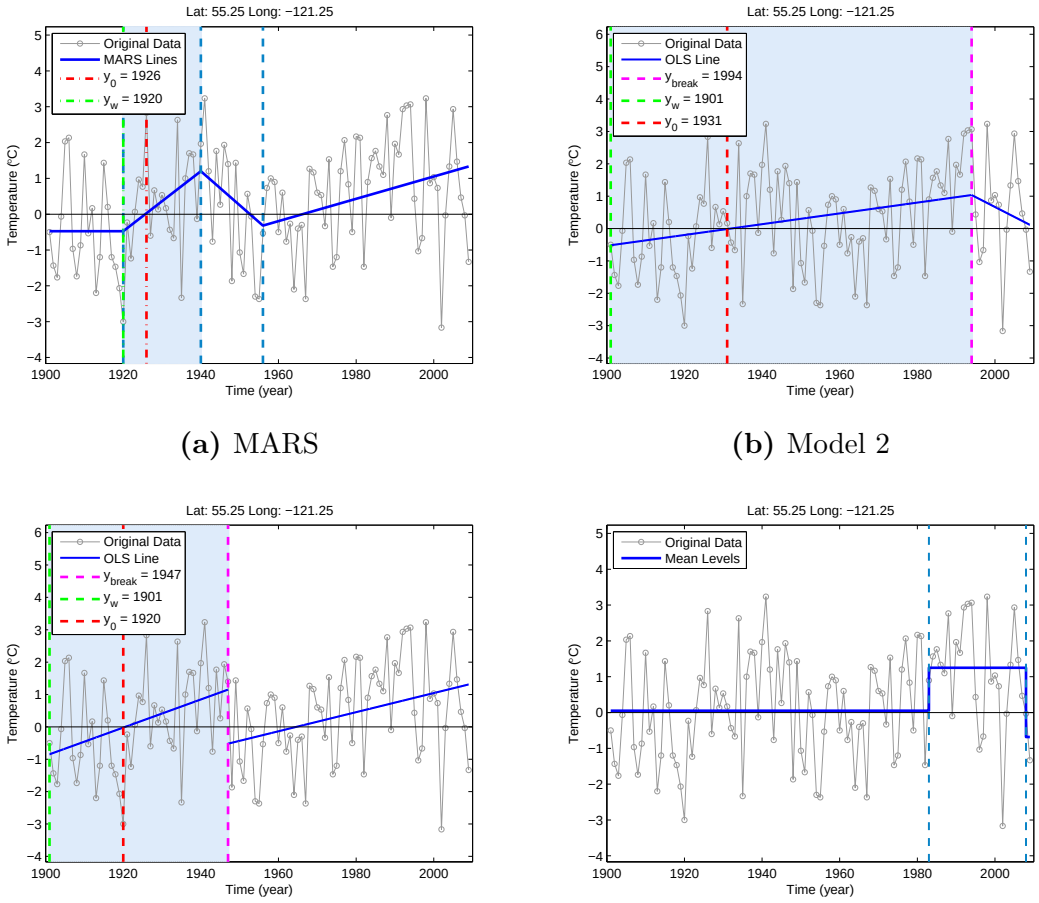


**(a)** MARS **(b)** Model 2

**(c)** Model 3 **(d)** R Method

**Figure C.19:** The **MAM** time series of the grid cell with latitude: 55.25°N and longitude: 121.25°W is modelled using (a) MARS, (b) Model 2, (c) Model 3, (d) the R Method. The figure is an example of Case 3 (Section 5.8.5).

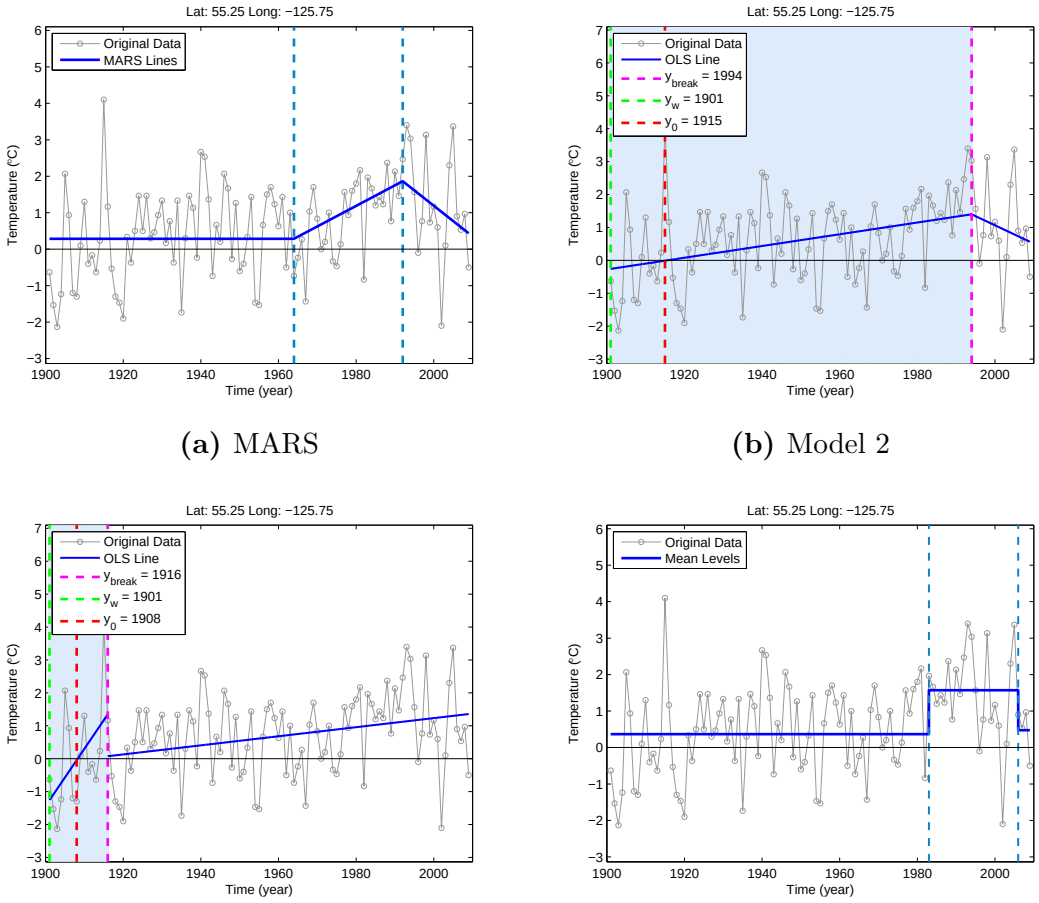


**(a)** MARS **(b)** Model 2

**(c)** Model 3 **(d)** R Method

**Figure C.20:** The **MAM** time series of the grid cell with latitude: 55.25°N and longitude: 125.75°W is modelled using (a) MARS, (b) Model 2, (c) Model 3, (d) the R Method. The figure is an example of Case 3 (Section 5.8.5).

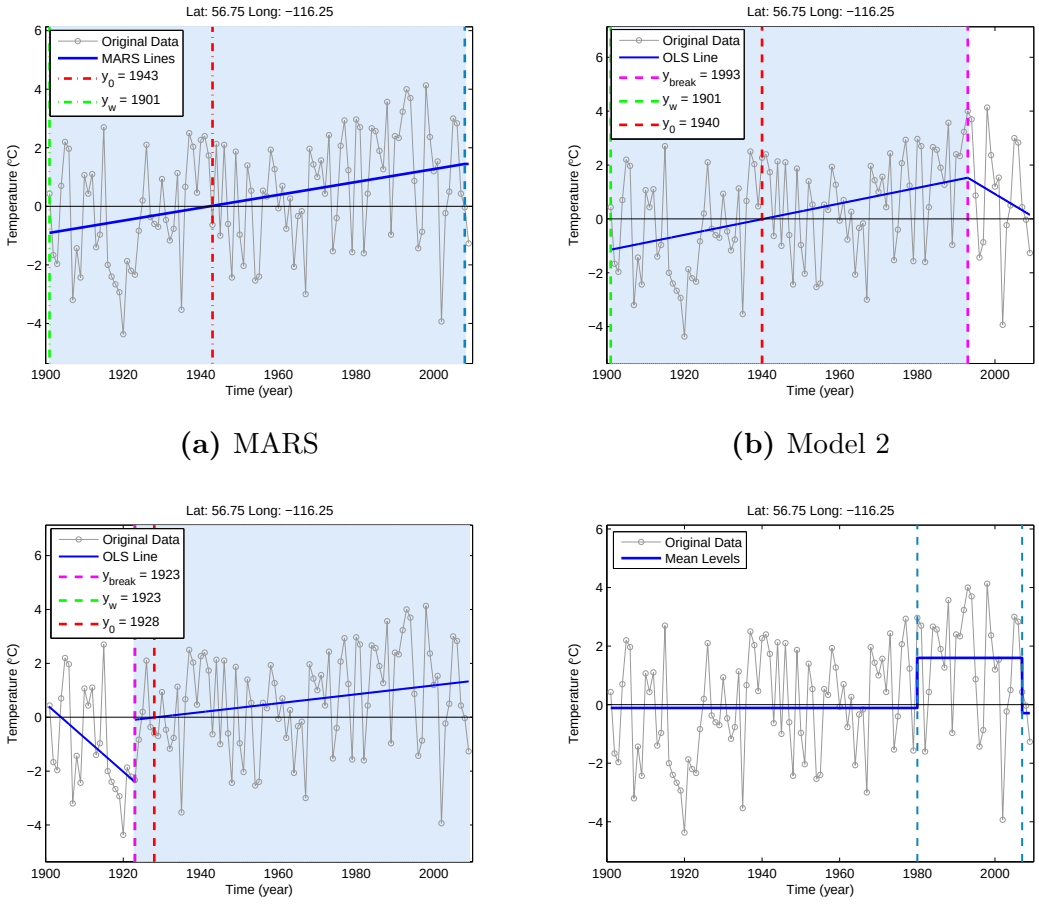


**(a)** MARS **(b)** Model 2

**(c)** Model 3 **(d)** R Method

**Figure C.21:** The **MAM** time series of the grid cell with latitude: 56.75°N and longitude: 116.25°W is modelled using (a) MARS, (b) Model 2, (c) Model 3, (d) the R Method. The figure is an example of Case 3 (Section 5.8.5).

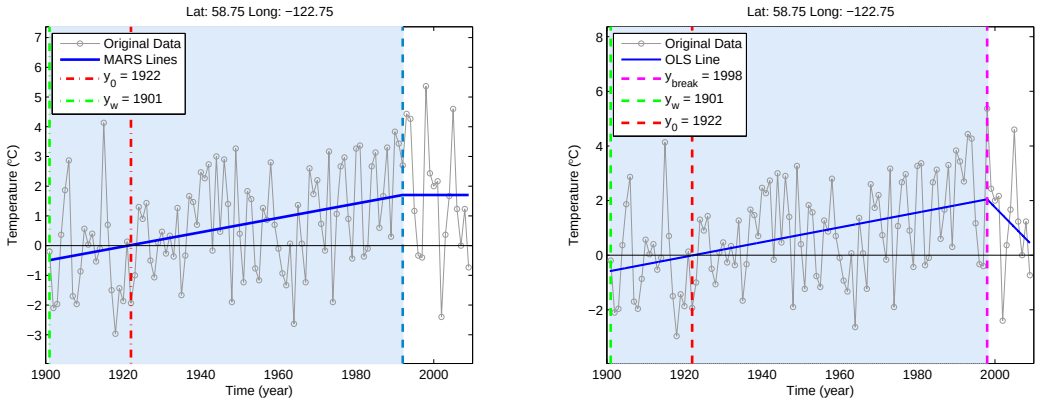


**(a)** MARS




**(b)** Model 2

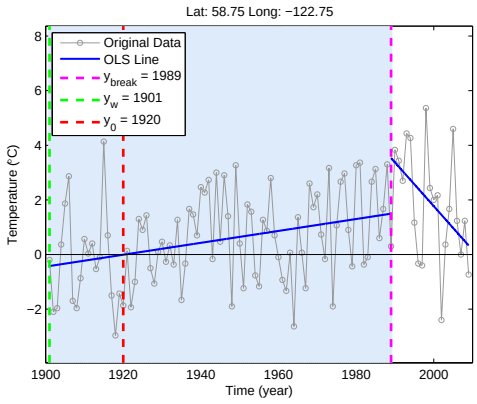


**(c)** Model 3

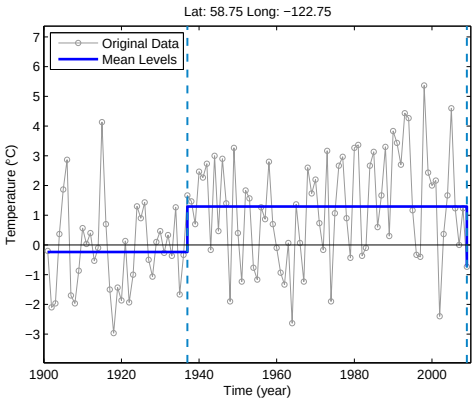


**(d)** R Method

**Figure C.22:** The **MAM** time series of the grid cell with latitude: 58.75°N and longitude: 122.75°W is modelled using (a) MARS, (b) Model 2, (c) Model 3, (d) the R Method. The figure is an example of Case 3 (Section 5.8.5).

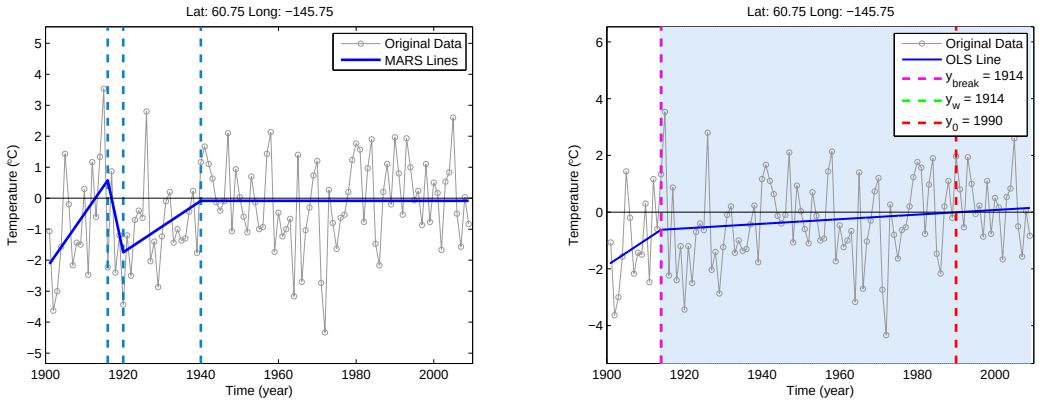


**(a)** MARS




**(b)** Model 2

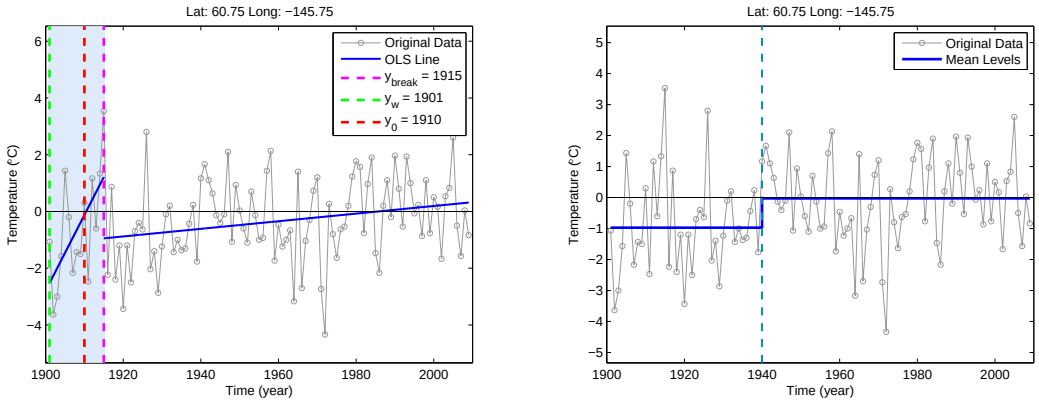


**(c)** Model 3




**(d)** R Method

**Figure C.23:** The **MAM** time series of the grid cell with latitude: 60.75°N and longitude: 145.75°W is modelled using (a) MARS, (b) Model 2, (c) Model 3, (d) the R Method. The figure is an example of Case 3 (Section 5.8.5).

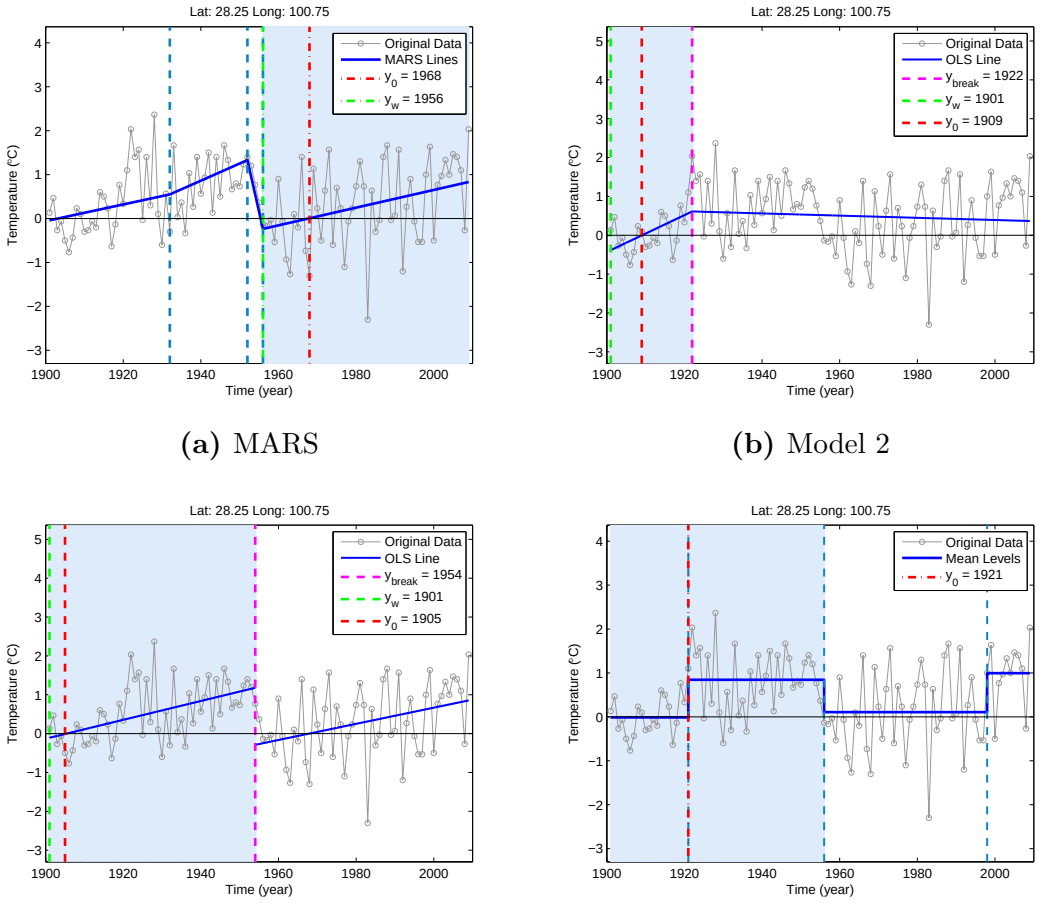


**(a)** MARS **(b)** Model 2

**(c)** Model 3 **(d)** R Method

**Figure C.24:** The **JFM** time series of the grid cell with latitude: 28.25°N and longitude: 100.75°E is modelled using (a) MARS, (b) Model 2, (c) Model 3, (d) the R Method. The figure is an example of Case 3 (Section 5.8.5).